Shale Gas and Tight Oil Reservoir Simulation

Wei Yu
Kamy Sepehrnoori

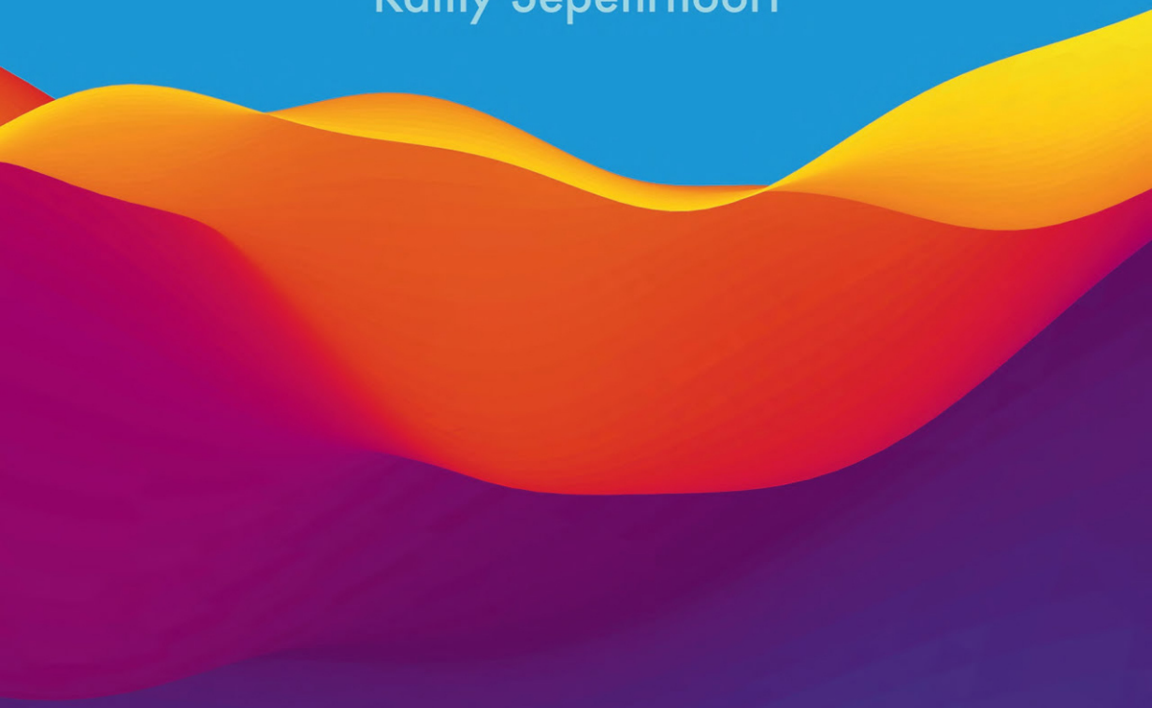

Shale Gas and Tight Oil Reservoir Simulation

Shale Gas and Tight Oil Reservoir Simulation

Wei Yu

Kamy Sepehrnoori

Gulf Professional Publishing
An imprint of Elsevier

Gulf Professional Publishing is an imprint of Elsevier
50 Hampshire Street, 5th Floor, Cambridge, MA 02139, United States
The Boulevard, Langford Lane, Kidlington, Oxford, OX5 1GB, United Kingdom

Notices
Knowledge and best practice in this field are constantly changing. As new research and experience broaden our understanding, changes in research methods, professional practices, or medical treatment may become necessary.

Practitioners and researchers must always rely on their own experience and knowledge in evaluating and using any information, methods, compounds, or experiments described herein. In using such information or methods they should be mindful of their own safety and the safety of others, including parties for whom they have a professional responsibility.

To the fullest extent of the law, neither the Publisher nor the authors, contributors, or editors, assume any liability for any injury and/or damage to persons or property as a matter of products liability, negligence or otherwise, or from any use or operation of any methods, products, instructions, or ideas contained in the material herein.

Library of Congress Cataloging-in-Publication Data
A catalog record for this book is available from the Library of Congress

British Library Cataloguing-in-Publication Data
A catalogue record for this book is available from the British Library

ISBN: 978-0-12-813868-7

Publishing Director: Joe Hayton
Senior Acquisition Editor: Katie Hammon
Editorial Project Manager: Naomi Robertson
Production Project Manager: Sruthi Satheesh
Cover Designer: Mark Rogers

Typeset by SPi Global, India

Dedication

To my parents Zhongzhao Yu and Ruie Sun, and my in-laws Guilao Wu and Chunyun Tang

Wei Yu

To my parents Mansour Sepehrnoori and Zamzam Soliman.

Kamy Sepehrnoori

Preface

This book is an essential reference for anyone interested in performing reservoir simulation of shale gas and tight oil reservoirs. The readers can be reservoir engineers, academics, and students who are involved in (1) modeling well performance of shale gas and tight oil reservoirs with simple and complex fracture geometries; (2) performing sensitivity studies, history matching, production forecasts, and economic optimization for shale gas and tight oil reservoirs; (3) investigating the impacts of complexities in fracture geometries and fluid transport mechanisms such as nanopore confinement, gas desorption, gas diffusion, gas slippage, and pressure-dependent matrix and fracture permeability on well performance; and (4) modeling CO_2 injection for enhanced oil recovery in tight oil reservoirs.

This book will provide important guidance on simulation of well performance in shale gas and tight oil reservoirs for learning (1) different methodologies to handle simple and complex fracture geometries, including an efficient semianalytical approach, local grid refinement (LGR) method, and an embedded discrete fracture model (EDFM) method; (2) an integrated reservoir simulation framework to perform sensitivity analysis and economic optimization; and (3) a methodology to perform phase equilibrium calculation considering the nanopore confinement effect.

For reservoir engineers in the petroleum industry, the most valuable aspect of the book is the probabilistic workflow for history matching and production forecasting. The practical application of the workflow is demonstrated step by step based on real field data. The workflow will not only generate reliable reserve estimation but also predict the effective range of reservoir and fracture properties through multiple history-matching solutions, which are important for helping field operators to characterize fracture treatment effectiveness and guiding the future field development optimization. This book also provides new insights into numerical modeling of CO_2 injection for enhanced oil recovery in tight oil reservoirs by considering CO_2 molecular diffusion mechanism. It provides a better understanding of the impacts of key reservoir properties and complex fractures on the CO_2 injection strategy. It also helps to determine and design the optimal injection-production scheme to maximize the oil recovery factor in multifractured horizontal wells.

For academics and students, this book can help them learn the theories and frontiers of advanced reservoir simulation for shale gas and tight oil reservoirs

with complex fracture geometries. Furthermore, it can provide some insights into the future research topics such as development of new generation reservoir simulator, new enhanced oil recovery methods in unconventional reservoirs, CO_2 sequestration in shale formation, and new applications of proposed methodologies in unconventional oil and gas reservoirs.

We welcome any feedback or comments with regard to the book, which will help us improve future editions of this book.

We would like to take this opportunity to thank the help and the support from Abdoljalil Varavei, Chowdhury Mamun, Jijun Miao, Kan Wu, Marut Wantawin, Pável Zuloaga Molero, Sutthaporn Tripoppoom, Weitong Sun, Yifei Xu, Youguang Chen, and Yuan Zhang. They provided help in different ways.

Chapter 1

Introduction of Shale Gas and Tight Oil Reservoirs

Chapter Outline

1.1 INTRODUCTION

Unconventional resources, such as shale gas and tight oil, are making a major contribution to the world energy. U.S. Energy Information Administration (EIA, 2013a) reported that the technically recoverable world shale oil resources are 345 billion barrels and world shale gas resources are 7299 trillion cubic feet (TCF). Fig. 1.1 shows the top reserve holders of shale gas resources throughout the world. As shown, the United States has 24.4 trillion cubic meters gas estimation, China has 36.1 trillion cubic meters gas estimation, and Argentina has 21.9 trillion cubic meters gas estimation. Fig. 1.2 shows U.S. shale gas and oil plays in the Lower 48 States. It is predicted that shale gas production will increase from 40% of total U.S. dry gas production in 2012 to 53% in 2040 (EIA, 2014). Fig. 1.3 shows the top 10 holders of tight oil resources throughout the world. Based on the early release overview of U.S. Energy Information Administration in 2013, onshore tight oil production will increase from 33% of total lower 48 onshore oil production to 51% in 2040 (EIA, 2013b).

Gas shales are typically characterized by ultralow permeability and low porosity and have a significant amount of total organic content (TOC). The permeability in shale gas reservoirs is around nano-Darcy.

In order to economically develop shale gas and tight oil reservoirs, two key technologies such as horizontal drilling and multistage fracturing are required, as shown in Fig. 1.4. The actual fracture stimulation process involves pumping large volume of fluids, which can create the complex fractures, and large amount of proppants, which can prevent the fractures closure. During hydraulic fracturing treatments, complex fracture networks are often generated and the interaction of hydraulic and natural fractures significantly impacts the complexity (Daniels et al., 2007; Maxwell et al., 2013). The complex fracture networks can create a huge contact area between the formation and horizontal wellbore (Cipolla and Wallace, 2014). The effectiveness of fracturing stimulation

Shale Gas and Tight Oil Reservoir Simulation. https://doi.org/10.1016/B978-0-12-813868-7.00001-8

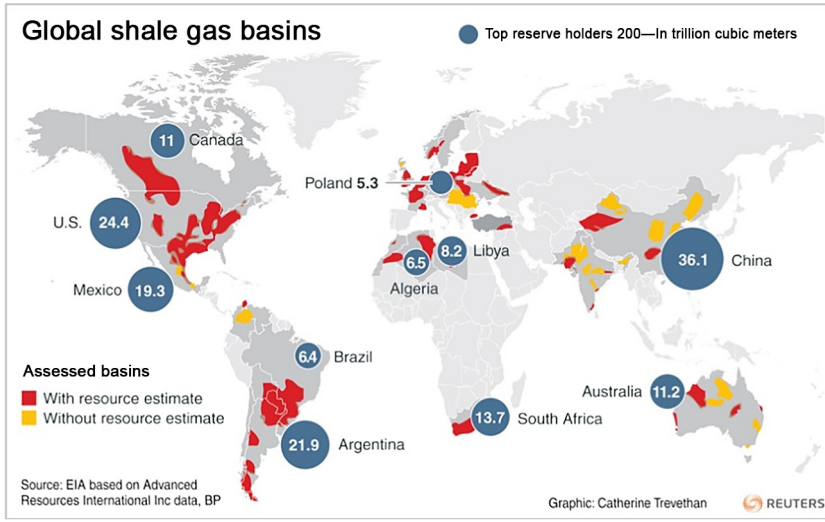

FIG. 1.1 Global shale gas basins distribution in the world (EIA, 2012).

treatment plays an important role in economic production of the unconventional reservoirs (Weng, 2014). Three to six perforation clusters per fracturing stage are typically used in most horizontal wells (Cipolla et al., 2010). EIA (2015) reported that four countries including the United States, Canada, China, and Argentina are currently producing commercial volumes of shale gas and tight oil and the United States is the dominant producer (Fig. 1.5).

Modeling complex hydraulic fracture propagation is important to understand fracture geometry. An acceptable fracture modeling should capture four critical physical processes, including (1) fracture deformation induced by internal pressure in the fracture; (2) fluid flow in the fracture; (3) fluid leak-off into the formation, and (4) fracture propagation (Veatch, 1986; Adachi et al., 2007). The most popular numerical method used for fracture modeling is boundary element method, which can efficiently simulate multiple fracture propagation (Wu et al., 2012; Wu and Olson, 2015a, 2016). In addition, a simplified three-dimensional displacement discontinuity method was proposed by Wu and Olson (2015b) to effectively simulate fracture opening and shearing. The complex fracture propagation model developed by Wu and Olson (2015a,b) couples rock deformation and fluid flow in the fractures and horizontal wellbore. The model fully captures the key physical mechanisms such as the stress shadow effects, flow rate distribution among multiple fractures, and interaction of hydraulic and natural fractures. It can simulate multiple fracture propagation in single well and multiple wells, as shown in Figs. 1.6 and 1.7, respectively. Hence, it is very important to develop reservoir models to perform production simulation considering the complex fracture geometries.

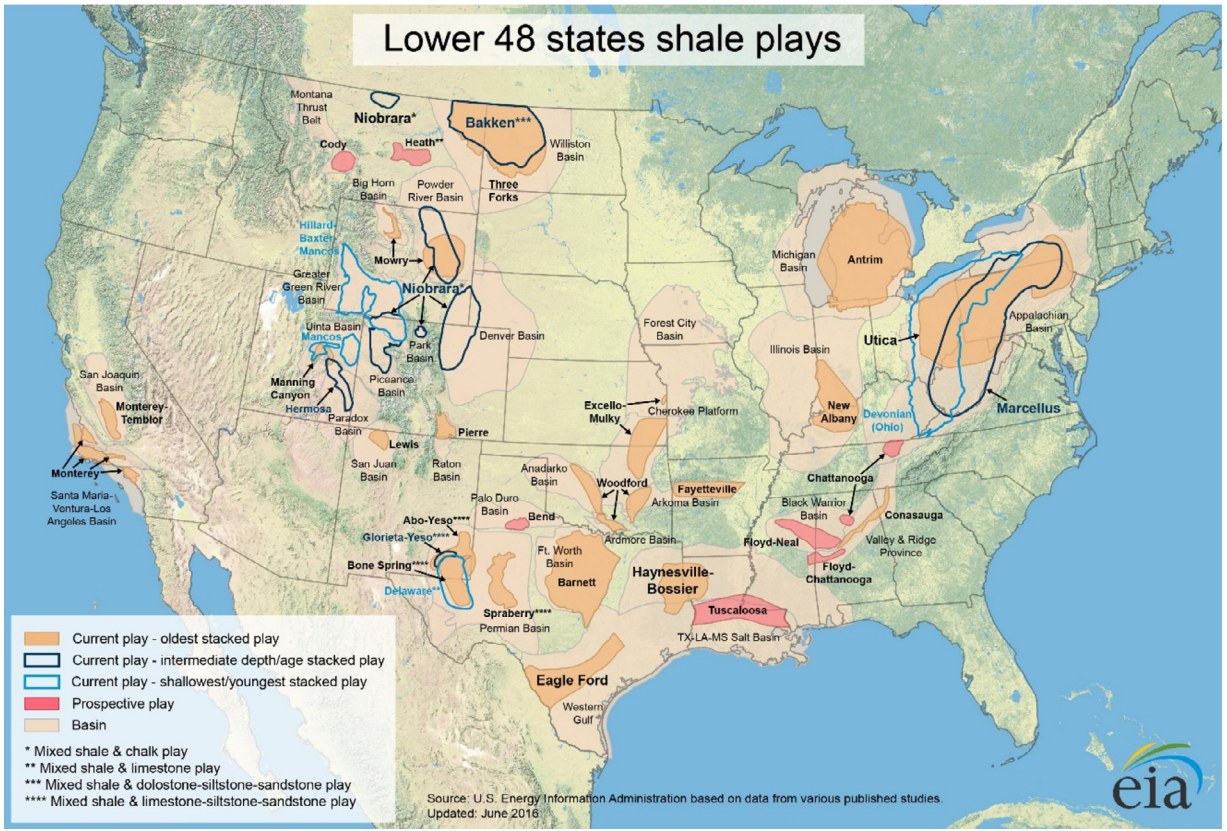

FIG. 1.2 U.S. shale gas and oil plays in the Lower 48 States. *(Source: U.S. Energy Information Administration based on data from various published studies, June 2016.)*

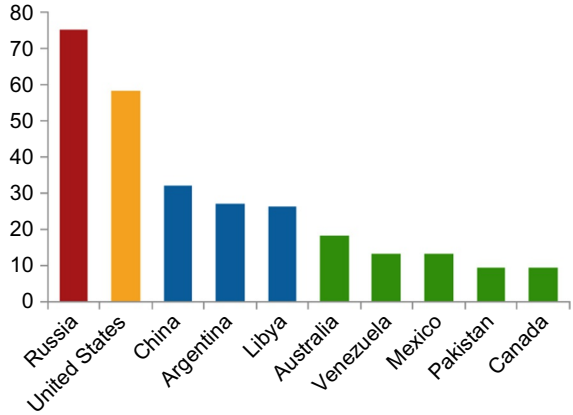

FIG. 1.3 Top 10 countries for technically recoverable tight oil resources (billion barrels) (EIA, 2013b).

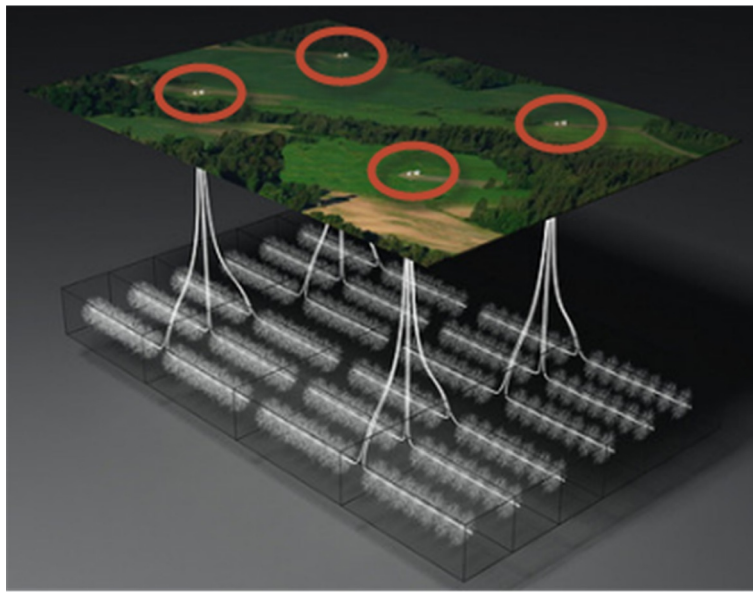

FIG. 1.4 Horizontal drilling and multistage hydraulic fracturing. *(Source: U.S. Energy Information Administration, September 2012.)*

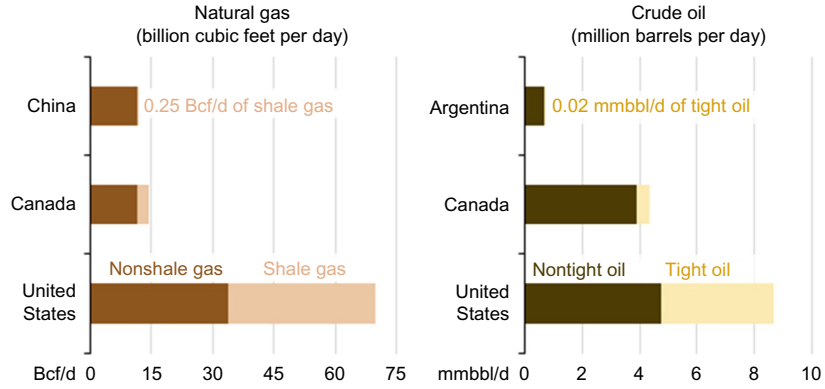

FIG. 1.5 Four countries producing commercial volumes of shale gas and tight oil (EIA, 2015). http://www.eia.gov/todayinenergy/detail.cfm?id=19991.

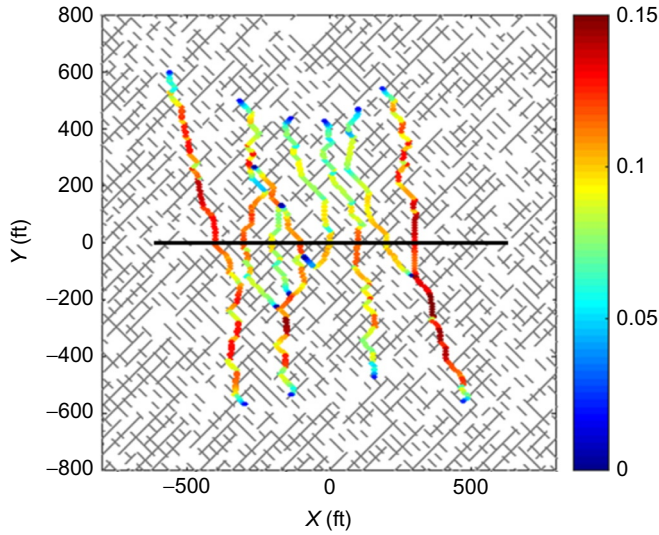

FIG. 1.6 Complex fracture propagation geometry in a single horizontal well generated using the fracture model developed by Wu and Olson (2015a,b).

The actual hydraulic fracturing process often generates complex nonplanar hydraulic fractures. The fracture width and fracture permeability change along fracture length. In general, some ideal fracture geometries such as biwing fractures and orthogonal fracture networks are used to represent the complex nonplanar fractures. Although there are numerical models to handle the

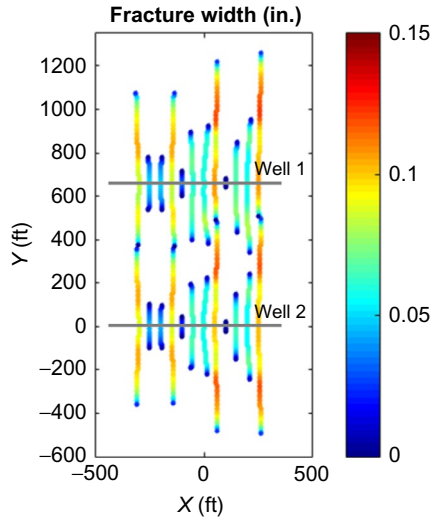

FIG. 1.7 Complex fracture propagation geometry in two horizontal wells generated using the fracture model developed by Wu and Olson (2015a,b).

complex fracture geometry, most of them are computationally more expensive. Also, there is the big challenge of gridding issue for modeling fractures. More importantly, the effects of varying fracture width and permeability along the fracture length are not considered by the existing models. Hence, an efficient model to simulate production from the complex nonplanar fractures is still lacking in the petroleum industry. In addition, there are very few work that have combined the realistic fracture geometry modeling as well as production simulation using such fracture geometries to analyze field well performance. Accordingly, it is significant to combine them together to evaluate well performance from shale gas and tight oil reservoirs.

Simulation of production from complex fracture geometries in shale reservoirs is challenging. We present an efficient semianalytical model by dividing fractures into segments to approximately represent the complex nonplanar fractures. It combines an analytical solution for the diffusivity equation about fluid flow in shale and a numerical solution for fluid flow in fractures. In addition, we present conventional numerical model to handle planar fractures and orthogonal fracture networks using local grid refinement (LGR). Moreover, we introduce an embedded discrete fracture model (EDFM) to efficiently deal with the complex fractures by dividing the fractures into segments using matrix cell boundaries and creating non-neighboring connections (NNCs). Fractures can have any strike and dip angels and variable width along fracture length. In addition, an EDFM preprocessor is introduced, which can be utilized by commercial reservoir simulators such as CMG and ECLIPSE and an in-house reservoir

simulator to model complex fracture geometries. The applications of these methods in simulation of well performance from shale gas and tight oil reservoirs are demonstrated.

Understanding the impact of complex fluid transport mechanisms on well performance of shale gas and tight oil reservoirs is important. The presence of large amount of nanopores in shale formation results in complex transport mechanisms, including nanopore confinement, non-Darcy flow, gas diffusion, gas slippage, and gas desorption. In addition, the pressure-dependent matrix and fracture permeabilities significantly affect well performance. We present the means to how to modify the traditional diffusivity equation by considering these complex fluid mechanisms. We present an in-depth analysis of these effects on well performance in combination of real field data. Especially, we present the analysis of some core measurements for methane adsorption at high pressure up to 7000 psi from Marcellus shale and the gas desorption behavior, which deviates from the Langmuir isotherm (Langmuir, 1918), but obeys the BET (Brunauer, Emmett, and Teller) isotherm (Brunauer et al., 1938). To the best of our knowledge, such behavior has not been reported in the literature for shale gas reservoirs in behaving like multilayer adsorption. The effect of different gas desorption models on calculation of original gas in place (OGIP) and gas recovery prediction is compared and discussed.

For shale gas reservoirs, the gas transport mechanisms are quite different from conventional gas reservoirs, which include not only gas advection, but also gas slippage, gas diffusion, and gas desorption. This is because the pore size distributions for shale gas reservoirs and conventional gas reservoirs are different. There are more nanopores in shale gas reservoirs compared with conventional gas reservoirs (Javadpour et al., 2007; Civan et al., 2010; Sakhaee-Pour and Bryant, 2012; Shi et al., 2013; Rezaveisi et al., 2014; Wu et al., 2014; Wu et al., 2015a,b). The diffusivity equation of conventional gas reservoir is not adequate to describe gas flow in shale. In addition, gas flow velocity in hydraulic fractures is so high that non-Darcy flow effect should be considered. Furthermore, multiple long hydraulic fractures with uniform proppant distribution and sufficient fracture conductivity play an important role in achieving effective well stimulation and economic production of shale gas reservoirs; however, it is very challenging to maintain such conductivity due to proppant settlement, proppant fines generation and migration in the fracture, proppant diagenesis, proppant embedment in softer rock, and proppant crushing in harder rock (Darin and Huitt, 1960; Pope et al., 2009; LaFollette and Carman, 2010; Fan et al., 2010). The effect of stress-dependent fracture conductivity should be taken into account. Consequently, a comprehensive model by considering the important mechanisms for gas flow in shale and the effects of nonplanar fractures, non-Darcy flow and stress-dependent fracture conductivity is highly required.

There is a high uncertainty in reservoir properties, which has a significant effect on shale gas and tight oil production. In reality, the order of magnitude

of permeability for shale gas reservoirs is nano-Darcy and for tight oil reservoirs is micro-Darcy. Typical shale gas reservoirs exhibit a net thickness of 50–600 ft, porosity of 2%–8%, TOC of 1%–14% and are found at depths ranging from 1000 to 13,000 ft (Cipolla et al., 2010). In addition, many fracture parameters are also uncertain and significantly affect well performance such as fracture spacing, fracture half-length, fracture height, and fracture conductivity. Moreover, the cost of hydraulic fracturing is expensive, although it can make shale gas and tight oil produced economically. The optimization of hydraulic fracture treatment design is important to obtain the most economical production scenario. Therefore, the development of a framework to perform sensitivity analysis and optimize shale gas and tight oil production in an efficient and effective way is clearly desirable.

With the development of unconventional resources, there is a considerable number of wells required for performing history matching and production forecasting using reservoir simulation approach. Generally, we use local grid refinement to model fractures and the size of matrix grids gradually becomes small when moving to the fracture grid. This results in a very complex gridding issue. In addition, when performing sensitivity studies and history matching, a large number of simulation cases are required and each case might have different fracture length and fracture number. It will be very time consuming to generate the input files for these simulation cases manually. Therefore, a user-friendly and efficient platform to generate multiple input files for reservoir simulators more easily and more efficiently is important. In addition, an efficient and practical approach to perform sensitivity studies, history matching, and production forecasts is clearly desirable. We present an assisted history matching workflow using proxy-modeling approach by integrating numerical reservoir simulators, design of experiment (DoE), response surface methodology (RSM), Markov chain Monte Carlo (MCMC), and Monte Carlo method. During the history matching process, an iterative procedure is introduced to gradually improve the accuracy of proxy models at the interested region with lower history matching errors. We demonstrate the application of the history-matching workflow step-by-step in field data analysis from Marcellus shale gas and Bakken tight oil reservoirs.

For tight oil reservoirs, the primary oil recovery factor is very low and substantial volumes of oil still remain in place. Hence, it is important to investigate the potential of CO_2 injection for enhanced oil recovery, which is a new subject and not well understood in tight oil reservoirs. We present how to accurately perform numerical modeling of CO_2 injection in tight oil reservoirs by considering the CO_2 molecular diffusion mechanism. We compare two scenarios of CO_2 injection: continuous injection of CO_2 and CO_2 Huff-n-Puff method. The impacts of various reservoir and fracture properties such as heterogeneity, complex fractures, and natural fractures on the comparison are discussed based on the typical reservoir and fluid properties from the Bakken formation.

REFERENCES

Adachi, J., Siebrits, E., Peirce, A., Descroches, J., 2007. Computer simulation of hydraulic fractures. Int. J. Rock Mech. Min. Sci. 44 (5), 739–757.

Brunauer, S., Emmett, P.H., Teller, E., 1938. Adsorption of gases in multimolecular layers. J. Am. Chem. Soc. 60, 309–319.

Cipolla, C.L., Wallace, J., 2014. Stimulated reservoir volume: a misapplied concept? Paper SPE 168596. SPE Hydraulic Fracturing Technology Conference, The Woodlands, Texas.

Cipolla, C.L., Mack, M., Maxwell, S., 2010. Reducing exploration and appraisal risk in low permeability reservoirs using microseismic fracture mapping—part 2. Paper SPE 138103. SPE Latin American and Caribbean Petroleum Engineering Conference, Lima, Peru.

Civan, F., Rai, C.S., Sondergeld, C.H., 2010. Shale-gas permeability and diffusivity inferred by improved formulation of relevant retention and transport mechanisms. Transp. Porous Media 86 (3), 925–944.

Daniels, J., Waters, G., LeCalvez, J., Lassek, J., Bentley, D., 2007. Contacting more of the Barnett shale through an integration of real-time microseismic monitoring, petrophysics, and hydraulic fracture design. Paper SPE 110562. SPE Annual Technical Conference and Exhibition, Anaheim, California.

Darin, S.R., Huitt, J.L., 1960. Effect of a partial monolayer of propping agent on fracture flow capacity. AIME Petroleum Trans. 219, 31–37.

Fan, L., Thompson, J.W., Robinson, J.R., 2010. Understanding gas production mechanism and effectiveness of well stimulation in the Haynesville shale through reservoir simulation. Paper SPE 136696. Canadian Unconventional Resources and International Petroleum Conference, Calgary, Canada.

Javadpour, F., Fisher, D., Unsworth, M., 2007. Nanoscale gas flow in shale gas sediments. J. Can. Pet. Technol. 46 (10), 55–61.

LaFollette, R.F., Carman, P.S., 2010. Proppant diagenesis: results so far. Paper SPE 131782. SPE Unconventional Gas Conference, Pittsburgh, Pennsylvania.

Langmuir, I., 1918. The adsorption of gases on plane surfaces of glass, mica and platinum. J. Am. Chem. Soc. 40, 1403–1461.

Maxwell, S.C., Weng, X., Kresse, O., Rutledge, J., 2013. Modeling microseismic hydraulic fracture deformation. Paper SPE 166312. SPE Annual Technical Conference and Exhibition, New Orleans, Louisiana.

Pope, C., Benton, T., Palisch, T., 2009. Haynesville shale-one operator's approach to well completions in this evolving play. Paper SPE 125079. SPE Annual Technical Conference and Exhibition, New Orleans, Louisiana.

Rezaveisi, M., Javadpour, F., Sepehrnoori, K., 2014. Modeling chromatographic separation of produced gas in shale wells. Int. J. Coal Geol. 121, 110–122.

Sakhaee-Pour, A., Bryant, S.L., 2012. Gas permeability of shale. SPE Reserv. Eval. Eng. 15 (4), 401–409.

Shi, J., Zhang, L., Li, Y., Yu, W., He, X., Liu, N., Wang, T., 2013. Diffusion and flow mechanisms of shale gas through matrix pores and gas production forecasting. Paper SPE 167226. SPE Unconventional Resources Conference, Calgary, Alberta, Canada.

U.S. Energy Information Administration, 2012. Global shale gas basins. http://blogthomsonreuters.com/index.php/global-shale-gas-basins-graphic-of-the-day.

U.S. Energy Information Administration, 2013a. Technically recoverable shale oil and shale gas resources: an assessment of 137 shale formations in 41 countries outside the United States. http://www.eia.gov/analysis/studies/worldshalegas/.

U.S. Energy Information Administration, 2013b. Early release overview. http://www.eia.gov/forecasts/aeo/er/pdf/0383er%282013%29.pdf.

U.S. Energy Information Administration, 2014. Annual energy outlook. http://www.eia.gov/forecasts/aeo/mt_naturalgas.cfm.

U.S. Energy Information Administration, 2015. Shale gas and tight oil are commercially produced in just four countries. http://www.eia.gov/todayinenergy/detail.cfm?id=19991.

Veatch, R.W., 1986. An overview of recent advances in hydraulic fracturing technology. Paper SPE 14085. International Meeting on Petroleum Engineering, Beijing, China.

Weng, X., 2014. Modeling of complex hydraulic fractures in naturally fractured formation. J. Unconventional Oil Gas Res. 9, 114–135.

Wu, K., Olson, J.E., 2015a. Simultaneous multi-frac treatments: fully coupled fluid flow and fracture mechanics for horizontal wells. SPE J. 20 (2), 337–346.

Wu, K., Olson, J.E., 2015b. A simplified three-dimensional displacement discontinuity method for multiple fracture simulations. Int. J. Fract. 193 (2), 191–204.

Wu, K., Olson, J.E., 2016. Numerical Investigation of complex fracture networks in naturally fractured reservoirs. SPE Prod. Oper. 31 (4), 300–309.

Wu, R., Kresse, O., Weng, X., Cohen, C., Gu, H., 2012. Modeling of interaction of hydraulic fractures in complex fracture networks. Paper SPE 152052. SPE Hydraulic Fracture Technology Conference, Texas, USA.

Wu, K., Li, X., Wang, C., Yu, W., Guo, C., Ji, D., Ren, G., Chen, Z., 2014. Apparent permeability for gas flow in shale reservoirs coupling effects of gas diffusion and desorption. Paper SPE 2014-1921039. SPE/AAPG/SEG Unconventional Resources Technology Conference, Denver, Colorado.

Wu, K., Li, X., Wang, C., Chen, Z., Yu, W., 2015a. A model for gas transport in microfractures of shale and tight gas reservoirs. AICHE J. 61 (6), 2079–2088.

Wu, K., Li, X., Wang, C., Yu, W., Chen, Z., 2015b. Model for surface diffusion of adsorbed gas in nanopores of shale gas reservoirs. Ind. Eng. Chem. Res. 54, 3225–3236.

Chapter 2

Numerical Model for Shale Gas and Tight Oil Simulation

Chapter Outline

2.1 INTRODUCTION

Shale gas and tight oil reservoirs have become increasingly important energy sources in the recent years. The combination of horizontal drilling and hydraulic fracturing technology has been widely used to create large and highly fractured network in shale reservoirs with ultralow permeability for economic production. Multiple transverse hydraulic fractures are generated when horizontal wellbores are drilled in the direction of the minimum horizontal stress. Maximizing the total stimulated reservoir volume (SRV) plays an important role in successful economic well production.

Shale Gas and Tight Oil Reservoir Simulation. https://doi.org/10.1016/B978-0-12-813868-7.00002-X

Shale gas reservoirs are organic-rich formations, varying from one shale formation to another, even within formation itself, and they serve as both reservoir and source rock together. Gas in the shale is mainly composed of free gas in natural fractures and matrix pore structure and adsorbed gas on the surface of shale matrix and in organic materials. The adsorption capacity of shales is related with the specific surface area, pressure, temperature, pore size, and sorption affinity (Leahy-Dios et al., 2011). Compared with conventional gas reservoirs, shale gas reservoirs may produce a considerable amount of gas from desorption (Mengal and Wattenbarger, 2011). Gas desorption may be a major gas production mechanism and can be an important factor for ultimate gas recovery. Neglecting the gas desorption effect might lead to underestimating gas potential, especially in shale formations with higher total organic content (TOC). The volume of TOC within shale gas reservoirs can occupy as high as 40% (*v*/*v*) of the reservoir rock in some of the organic rich shales, such as Woodford shale (Passey et al., 2010). Additionally, Thompson et al. (2011) demonstrated that gas desorption may have a significant impact on conventional Arps decline curve analysis (Arps, 1945) and that the hyperbolic decline exponent (*b*-value) would increase during the late time of gas production in the presence of gas desorption. The unprecedented growth of shale reservoirs has brought focus to the investigation of potential contributions of adsorbed gas to the estimated ultimate recovery (EUR) for short-term and long-term periods of production completely.

Some studies have suggested that gas desorption may contribute additional gas production for EUR in shale gas reservoirs. Cipolla et al. (2010a) reported that gas desorption may constitute 5%–15% of the total gas production in 30-year period for both Barnett shale and Marcellus shale, but the impact of gas desorption is primarily observable during the later time of well production, depending on reservoir permeability, flowing bottomhole pressure, and fracture spacing. Thompson et al. (2011) observed that gas desorption contributes to 17% increase in the EUR with respect to a 30-year forecasting result in a Marcellus shale well completed with 12 stages of hydraulic fracturing, located in North-East Pennsylvania. Mengal and Wattenbarger (2011) presented that gas desorption can result in approximately 30% increase in original gas in place (OGIP) estimates and 17% decrease in recovery factor (RF) estimates for Barnett shale and concluded that it is impossible to obtain accurate estimations and forecasting if the gas desorption is ignored. Das et al. (2012) performed experimental study of multicomponent adsorption/desorption effect on estimation and calculation of OGIP and EUR, and stated that the presence of CO_2 with CH_4 in the free gas makes the gas desorption behavior and measurement more complex. However, little attention has been given to the investigation and the comparison of the gas desorption effect for different shale gas reservoirs systematically. Hence, a detailed and systematic study of gas desorption contribution is still necessary.

In addition, the economic viability of shale gas developments hinges on sustaining sufficient fracture conductivity in propped hydraulic fractures after cleanup over the lifetime of a well. However, it has been very challenging to maintain such high fracture conductivity because of proppant fines generation and migration in the fracture (Pope et al., 2009), proppant diagenesis (LaFollette and Carman, 2010), also termed as proppant scaling, proppant embedment in softer rock and proppant crushing in harder rock (Fan et al., 2010). The hydraulic fracture permeability reduction as a function of pressure drawdown may be a significant component of overall gas recovery in many shale gas reservoirs. In addition, the effect of stress-dependent fracture conductivity on production profile and ultimate gas recovery is not understood completely. Also, it has been largely neglected by most fracture modeling work in the literature. Therefore, it is extremely important to study and evaluate its effect on well performance for different shale formations.

Uniform proppant distribution is a key aspect to achieve effective fracture stimulation and economic production of shale reservoirs. There have been many attempts in recent years to optimize proppant design for achieving uniform distribution in shale gas reservoirs (Woodworth and Miskimins, 2007; Warpinski et al., 2008; Warpinski, 2009; Cipolla et al., 2010b). Cipolla et al. (2008) studied the effect of proppant distribution on gas production when the fracture network is developed, and showed three limiting scenarios since it is very challenging to model proppant transport when fracture growth is complex: Case 1 is proppant evenly distributed throughout the complex fracture system; Case 2 is proppant concentrated in a dominant planar fracture, and Case 3 is proppant settling and forming "pillars" that are evenly distributed within the complex fracture system. Mahoney et al. (2013) developed a self-suspending proppant technology that makes complete proppant suspension until deposition in the fracture; this technique can eliminate the need for viscosity and suspension properties of a gel carrier; moreover, the hydraulic pumping pressure for proppant transport is reduced accordingly. Vincent (2012) suggested that it appears unreasonable to assume that the proppant within the narrower fractures could extend laterally for thousands of feet and vertically for hundreds of feet with a perfectly even distribution, possibly because of higher-stress lamina or other irregularities causing barriers that hinder flow within the fracture; hence, a better approach is required to predict proppant arrangement instead of a simplistic model. Daneshy (2013) has reported uneven proppant distribution between different perforation clusters in plug-and-perf fracturing operations and has pointed out that the proppant distribution is very different from fluid distribution and that most proppants enter the last perforation cluster. The proppant concentration of the last cluster is almost four times the proppant amount in the first cluster of four; this is because proppant grains with higher density and larger size and mass cannot easily change direction and enter the perforations, while fluids can easily do so. Crespo et al. (2013) conducted a large-scale experimental study mimicking the plug-and-perf operation and observed that uneven

proppant distribution within perforations existed in cases where proppant density was relatively high and at smaller flow rates with lower density proppant. However, the impact of uneven proppant distribution between different clusters on ultimate gas recovery has not been evaluated quantitatively. Additionally, most reservoir modeling works in the literature have usually assumed uniform proppant distribution among the fractures that are simultaneously taking fluid during pumping in a single stage. Cipolla et al. (2010c) have showed that about 40% of the perforation clusters were not producing gas. Hence, a detailed study for investigation of proppant distribution between different clusters on shale gas production is still significantly necessary.

2.2 NON-DARCY FLOW EFFECT

Gas flow rate along the fractures is high in shale gas reservoirs, especially at early stage of well production. The non-Darcy flow may occur, which is modeled using the Forchheimer (1901) modification to Darcy's law given here.

$$-\nabla P = \frac{\mu}{K} v + \beta \rho v^2, \tag{2.1}$$

where v is velocity, μ is viscosity, K is permeability, ρ is phase density, β is the non-Darcy Beta factor used in the Forchheimer correction and is determined using a correlation proposed by Evans and Civan (1994) as given here.

$$\beta = 1.485 \times 10^9 / K^{1.021}, \tag{2.2}$$

where the unit of K is md and unit of β is ft^{-1}. The β correlation was obtained using over 180 data points including those for propped fractures and was found to match the data very well with a correlation coefficient of 0.974 (Rubin, 2010). This equation has been implemented into the simulator and used for accounting for non-Darcy gas flow behavior.

In this study, we use reservoir simulator of CMG (CMG-IMEX, 2012; CMG-GEM, 2012) to model multiple hydraulic fractures and simulate fluid flow behavior in shale reservoirs. Hydraulic fracture is modeled explicitly using local grid refinement (LGR), which can capture the transient flow behavior from shale matrix to fracture (Rubin, 2010; Yu and Sepehrnoori, 2014a). The actual reservoir and fracture properties from the Marcellus Shale are used to investigate the non-Darcy flow effect. Table 2.1 summarized the basic parameters required for the simulation. A basic reservoir model including multistage fractures is shown in Fig. 2.1. In this model, the horizontal well length is 4500 ft with 18 fracturing stages, and four clusters are active in each stage. Hence, the total number of effective hydraulic fracture is 72. Stage spacing for each stage is set as 250 ft. Cluster spacing, defined as the distance between two neighboring clusters within each stage, is 50 ft. The distance between two outer clusters in two neighboring stages is assumed to be 100 ft. Bottomhole

TABLE 2.1 Basic Reservoir Simulation Parameter List for Marcellus Shale (Yu and Sepehrnoori, 2014b)

Parameter	Value	Unit
Initial reservoir pressure	5000	psi
Reservoir temperature	130	°F
Reservoir permeability	500	nD
Reservoir porosity	15%	–
Initial water saturation	20%	–
Total compressibility	3×10^{-6}	psi^{-1}
Horizontal well length	4500	ft
Number of stages	18	–
Cluster spacing	50	ft
Total number of fractures	72	–
Fracture half-length	355	ft
Fracture height	80	ft
Fracture conductivity	5	md-ft
Gas specific gravity	0.58	–

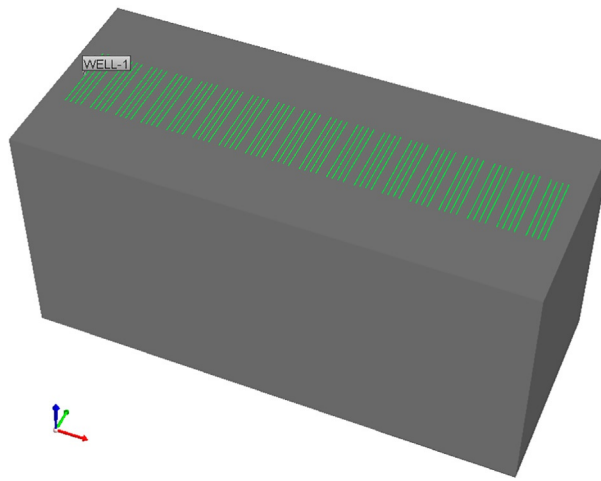

FIG. 2.1 A basic reservoir model including 18 fracturing stages and assuming four clusters per stage.

pressure (BHP) is used to constrain the reservoir simulations, and it is assumed to be constant with 1000 psi for the production period of 30 years.

The well performance with and without considering the non-Darcy effect under the condition of different fracture width is shown in Fig. 2.2. Fig. 2.2A illustrates that when the fracture width (w_f) is 0.0001 ft (0.03 mm), the non-Darcy effect is important at the early time of production (before 5 years), while it becomes negligible after 10 years of production. This is because the gas flow rate is high at the early time and fracture width is too small. However, Fig. 2.2B shows that the well performance is almost the same with and without considering the non-Darcy effect when the fracture width is 0.001 ft (0.3 mm) and 0.01 ft (3 mm). Gale et al. (2007) presented the natural fracture width in Barnett Shale is narrow and less than 0.05 mm. Wu and Olson (2013) simulated the width of hydraulic fractures and the average width is around 2.5 mm. Therefore, it can be implied that the non-Darcy effect is more important in narrower fractures while less important in wider fractures.

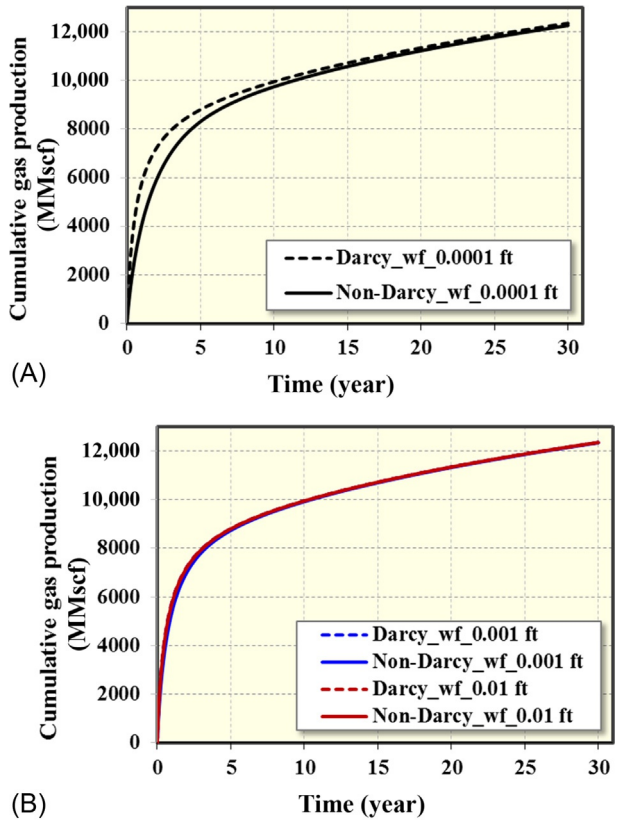

FIG. 2.2 Comparison of well performance with and without the non-Darcy effect (Yu and Sepehrnoori, 2014b). (A) Fracture width of 0.0001 ft. (B) Fracture width of 0.001 and 0.01 ft.

2.3 GAS DESORPTION EFFECT

2.3.1 Langmuir Isotherm

Gas shales are organic-rich formations. Gas storage in the shale is mainly divided into free gas in natural fractures and matrix pore structure and adsorbed gas in organic materials. Langmuir isotherm is widely used to describe the gas adsorption phenomenon. The amount of gas adsorbed on a solid surface is given by the Langmuir equation (Langmuir, 1918), characterizing physical desorption processes as a function of pressure at constant temperature:

$$G_s = \frac{V_L P}{P + P_L}, \tag{2.3}$$

where G_s is the gas content in scf/ton, V_L is the Langmuir volume in scf/ton, P_L is the Langmuir pressure in psi, and P is pressure in psi. The bulk density of shale (ρ_B) is needed to convert the typical gas content in scf/ft^3 to scf/ton. Langmuir pressure and Langmuir volume are two key parameters. Langmuir volume is referred to as the gas volume at the infinite pressure representing the maximum storage capacity for gas; Langmuir pressure is referred to as the pressure corresponding to one-half Langmuir volume. As the reservoir pressure is decreased, gas is desorbed from the surface of the matrix. Fig. 2.3 shows a graph of gas content with pressure for free gas and adsorbed gas used for a Barnett Shale example. Fig. 2.4 shows a graph of gas content with pressure for the adsorbed gas and total gas used for Barnett Shale (Montgomery et al., 2005). Both free gas and adsorbed gas add together to generate the total gas content. In Barnett Shale, the adsorbed gas is approximately 46% of the total gas. Contrary to conventional gas reservoirs, the amount of gas desorption in the matrix is commonly described by the Langmuir isotherm in a range of reservoir pressures. Fig. 2.5 illustrates an example of Langmuir isotherm of the Barnett Shale.

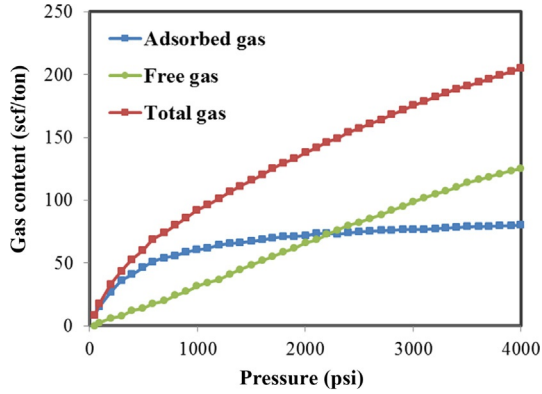

FIG. 2.3 An example of Barnett Shale gas content. *(Modified from Cipolla, C.L., Lolon, E.P., Erdle, J.C., Rubin, B., 2010. Reservoir modeling in shale-gas reservoirs. SPE Reserv. Eval. Eng. 13(4), 638–653.)*

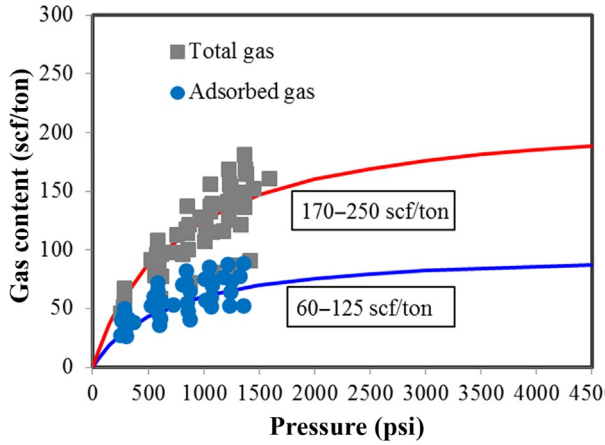

FIG. 2.4 Adsorption isotherms for Barnett Shale core samples. *(Modified from Montgomery, S.L., Jarvie, D.M., Bowker, K.A., Pollastro, R.M., 2005. Mississippian Barnett shale, Fort Worth basin, north-central Texas: gas-shale play with multi-trillion cubic foot potential. AAPG Bull. 89(2), 155–175.)*

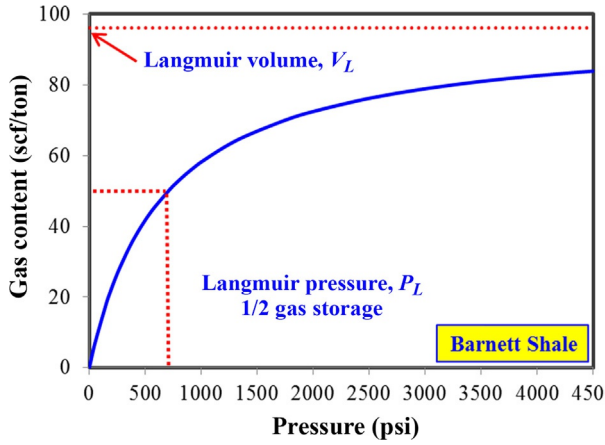

FIG. 2.5 An example of Langmuir isotherm curve for Barnett Shale with Langmuir volume of 96 scf/ton and Langmuir pressure of 650 psi (Yu and Sepehrnoori, 2013a).

It is clearly shown that higher Langmuir pressure releases more adsorbed gas and results in higher gas production. Generally, in early stage of production, when reservoir pressure is high, the gas desorption contribution to the gas production is insignificant; however, for long-term production, it is necessary to account for gas desorption, based on a laboratory measured isotherm due to the more substantial pressure depletion, resulting in more gas desorption.

2.3.2 Comparison of Black-Oil Model and Compositional Model

In reservoir simulator, both black-oil model and compositional model can be used to model the gas desorption effect. For the black-oil model, a technique developed by Seidle and Arri (1990) is used to model the effect of gas desorption from a shale gas reservoir. The Langmuir isotherm is replicated by a black-oil model's solution/gas ratio to represent the gas-desorption effect in shale. For the compositional model, the Langmuir isotherm is directly implemented in the reservoir simulator, which requires inputs of Langmuir volume, Langmuir pressure, and bulk density. We compared the black-oil model [using Computer Modelling Group's IMEX (CMG-IMEX, 2012)] with the compositional model [Computer Modelling Group's GEM (CMG-GEM, 2012)] with a porosity of 0.08, permeability of 0.0005 md, reservoir thickness of 200 ft, reservoir pressure of 3000 psi, BHP of 400 psi, fracture spacing of 250 ft, fracture half-length of 200 ft, and fracture conductivity of 10 md-ft. The reservoir model including 14 hydraulic fractures is shown in Fig. 2.6. The comparison results between the black-oil model and the compositional model for the case without gas desorption effect and the case with gas desorption effect are shown in Fig. 2.7. As shown, a good agreement is obtained for these two cases (the difference is within 1%–2%). This is because of the almost similar gas properties used in these two models. In addition, the difference between the case without gas desorption and the case with gas desorption is approximately 17% at the end of production, which is the gas desorption contribution to gas recovery for this Barnett Shale well.

2.3.3 Evaluation of Gas Desorption Effect for Five Shale Formations

In this simulation study, we set up a 3D reservoir model with dimensions of 5000 ft × 1600 ft × 200 ft for five shale formations including Barnett, Marcellus, Eagle Ford, Haynesville, and New Albany. Horizontal well length is 3500 ft. Fracture spacing is varied from 50 ft, 150 ft, to 250 ft corresponding to number of fracture of 70, 24, and 14, respectively. Fracture half-length is fixed at 350 ft

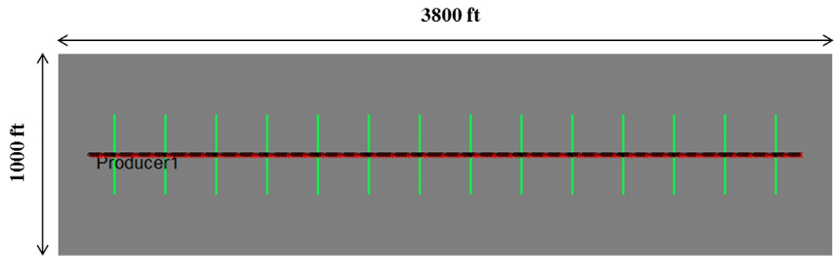

FIG. 2.6 A reservoir model including 14 hydraulic fractures for comparison of black-oil model and compositional model with and without considering gas desorption effect.

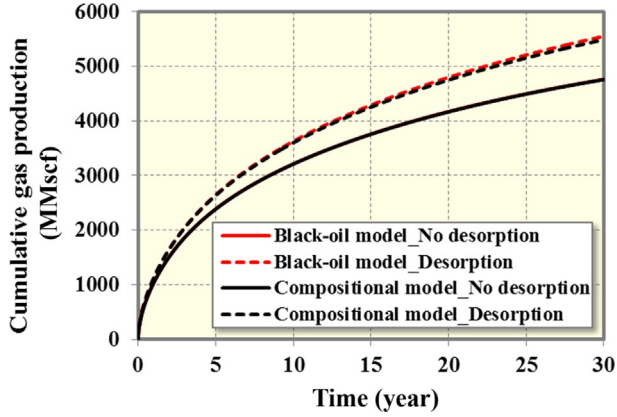

FIG. 2.7 Comparison of gas production between black-oil model and compositional model with and without considering gas desorption effect (Yu and Sepehrnoori, 2014c). ($V_L = 96$ scf/ton, $P_L = 650$ psi, $\rho_B = 2.58$ g/cm^3.)

and fracture conductivity is 10 md-ft for each case. The detailed reservoir data for the simulations are average values based on available data from these different shale formations in the literature and listed in Table 2.2. The reservoir is assumed to be homogeneous and the fractures are evenly spaced, with stress-independent porosity and permeability. Only gas is flowing in the reservoir, which is assumed to behave as non-Darcy flow. Langmuir pressure and Langmuir volume of these five shale formations published in the literature are listed in Table 2.3 and the corresponding Langmuir isotherm curves are shown in Fig. 2.8 (Zuber et al., 2002; Mengal and Wattenbarger, 2011; Nobakht et al., 2012; Boulis et al., 2012; Ikewun and Ahmadi, 2012). Increase in EUR is used to evaluate the contribution of gas desorption to ultimate gas recovery in this study, and it is defined as:

$$\text{Increase in EUR} = \frac{Q_{GasDesorption} - Q_i}{Q_{GasDesorption}}, \tag{2.4}$$

where $Q_{GasDesorption}$ is cumulative gas production considering gas desorption effect and Q_i is cumulative gas production without considering gas desorption effect.

Comparison of cumulative gas production with and without considering gas desorption for five different shale formations is shown in Fig. 2.9. It can be seen that the gas desorption contributes over 20% of increase in EUR at 30 years of gas production for New Albany Shale and Marcellus Shale; below 10% of increase in EUR for Haynesville Shale; between 10% and 20% increase in EUR for Barnett Shale and Eagle Ford Shale. This means that the effect of gas desorption for New Albany Shale is the highest because of the lower reservoir pressure and higher Langmuir pressure and for Haynesville Shale it is

TABLE 2.2 Basic Reservoir Simulation Parameter List for Five Shale Formations: Barnett, Marcellus, Eagle Ford, Haynesville, New Albany (Yu and Sepehrnoori, 2014a)

Parameter	Barnett	Marcellus	Eagle Ford	Haynesville	New Albany	Unit
Permeability	0.0001	0.0005	0.00005	0.0001	0.0001	md
Porosity	0.06	0.06	0.10	0.08	0.06	value
Initial pressure	3800	4000	8000	10,000	700	psi
BHP	1000	500	1500	1500	60	psi
Temperature	180	220	300	325	90	^{o}F
Gas saturation (%)	70	75	70	70	70	value
Compressibility	3×10^{-6}	3×10^{-6}	1×10^{-6}	1×10^{-6}	1×10^{-6}	psi^{-1}

TABLE 2.3 Langmuir Isotherm Data for Five Shale Formations: Barnett, Marcellus, Eagle Ford, Haynesville, New Albany (Yu and Sepehrnoori, 2014a)

Parameter	Barnett	Marcellus	Eagle Ford	Haynesville	New Albany	Unit
V_L	96	200	175	60	104.2	scf/ton
P_L	650	500	1500	1500	412.5	psi
ρ_B	2.58	2.46	2.6	2.6	2.4	g/cm^3

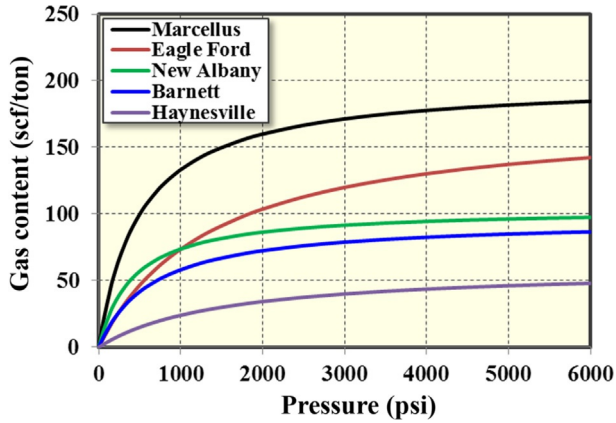

FIG. 2.8 Comparison of Langmuir isotherm curves of five shale formations (Yu and Sepehrnoori, 2014a).

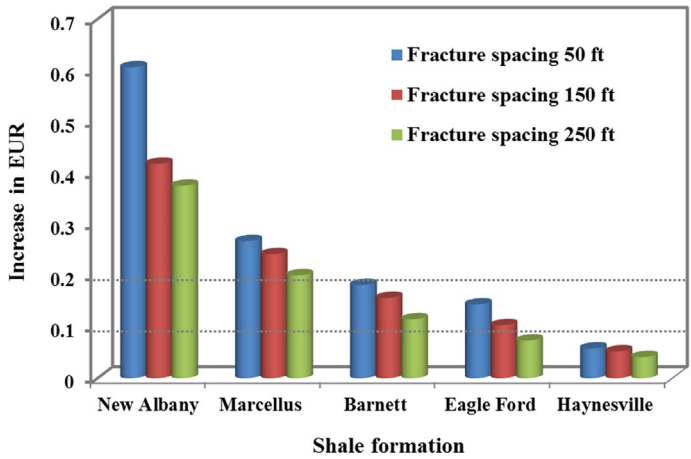

FIG. 2.9 Contribution of gas desorption to EUR at 30 years of five shale formations (Yu and Sepehrnoori, 2014a).

relatively negligible because of higher reservoir pressure and lower Langmuir pressure. Fan et al. (2010) also reported that in the Haynesville Shale, gas desorption contributes a very small amount of gas production because of the very high initial pore pressure and low initial TOC. In addition, the contribution of gas desorption to increase in EUR increases with the decreasing fracture spacing. The reason is that the decrease in fracture spacing results in more substantial pressure depletion, and, therefore, enhances the contribution of gas desorption.

2.4 GEOMECHANICS EFFECT

2.4.1 Pressure-Dependent Fracture Conductivity

In this study, the geomechanics effect is primarily focused on stress-dependent or pressure-dependent fracture conductivity, meaning that fracture conductivity is not a constant value, but decreases with the increasing closure stress due to proppant embedment. Alramahi and Sundberg (2012) presented the laboratory measurement data about the relationship between normalized fracture conductivity and closure stress due to proppant embedment for different shale samples from stiff shale to soft shale. Through fitting the laboratory measurement data, the expressions between normalized fracture conductivity and closure pressure are obtained (Yu and Sepehrnoori, 2014d):

$$\text{Stiff shale}: \ \log(FC_N) = -0.0001 \times \sigma - 0.1082, \ \ R^2 = 0.954, \tag{2.5}$$

$$\text{Medium shale}: \ \log(FC_N) = -0.0004 \times \sigma + 0.2191, \ \ R^2 = 0.998, \tag{2.6}$$

$$\text{Soft shale}: \ \log(FC_N) = -0.0006 \times \sigma + 0.4256, \ \ R^2 = 0.987, \tag{2.7}$$

where FC_N is normalized fracture conductivity by the initial fracture conductivity, and σ is closure pressure (psi). Using these equations in combination with the minimum horizontal stress, we can generate the pressure-dependent fracture conductivity curves for different shale formations.

2.4.2 Geomechanics Modeling

For modeling of geomechanics in hydraulic fractures, i.e., pressure-dependent fracture conductivity, a specific compaction table is used to account for the decreasing conductivities of propped fractures with the increase in closure stress or decrease in pressure, has been integrated in the reservoir simulator. The compaction table feature is assigned in the simulator to cells describing propped hydraulic fractures. The fracture conductivity is defined as the product of fracture width and fracture permeability as given here:

$$FC = w_f \times K_f, \tag{2.8}$$

where FC is fracture conductivity (md-ft), w_f is fracture width (ft), and K_f is fracture permeability (md).

Fig. 2.10 shows the relationships between the normalized fracture conductivity and reservoir pressure for different shale brittleness. As shown, the initial fracture conductivity corresponding to initial reservoir pressure of 5000 psi is 1 md-ft. The final fracture conductivity corresponding to the minimum flowing bottomhole pressure of 500 psi is 0.28, 0.03, and 0.0013 md-ft for stiff case, medium case, and soft case, respectively. Based on the same reservoir model for the Marcellus Shale, as shown in Fig. 2.1, we investigated the impacts of different pressure-dependent fracture conductivity curves on well performance,

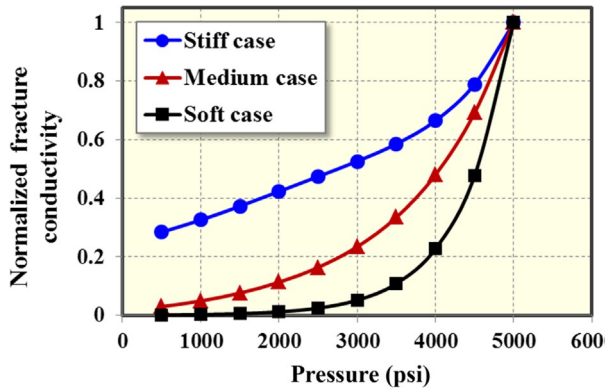

FIG. 2.10 Pressure-dependent fracture conductivity curves for different shale brittleness (Yu and Sepehrnoori, 2014b).

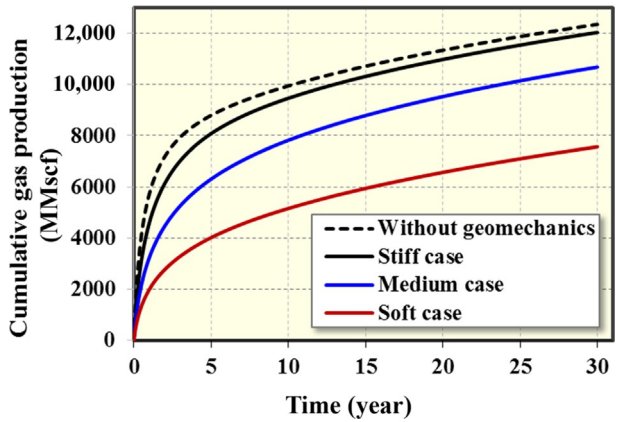

FIG. 2.11 Impact of geomechanics on well performance for difference shale brittleness (Yu and Sepehrnoori, 2014b).

as shown in Fig. 2.11. It illustrates that the geomechanics plays an important negative effect on well productivity. As shown, the cumulative gas production declines by 3%, 14%, and 39% corresponding to stiff case, medium case, and soft shale, respectively.

2.4.3 Sensitivity Study Based on a Field Well From Barnett Shale

In this case study, a field well from Barnett Shale was used to perform sensitivity study to investigate the geomechanics effect. Detailed reservoir information about the Barnett Shale well is listed in Table 2.4. Contribution from gas desorption to ultimate gas recovery is taken into account. Gas desorption is described by the Langmuir isotherm with Langmuir pressure of 650 psi,

TABLE 2.4 Reservoir and Fracture Properties for a Field Well From Barnett Shale (Yu and Sepehrnoori, 2013b)

Parameter	Value(s)	Unit
Initial reservoir pressure	3800	psi
Bottomhole pressure	1500	psi
Reservoir temperature	180	°F
Gas viscosity	0.02	cP
Reservoir depth	7000	ft
Pore pressure gradient	0.54	psi/ft
Closure pressure	5000	psi
Closure pressure gradient	0.71	psi/ft
Matrix permeability	0.00001	md
K_h/K_v	10	–
Matrix porosity	0.04	–
Initial gas saturation	0.67	–
Compressibility of shale	10^{-6}	psi^{-1}
Fracture conductivity	1	md-ft
Fracture half-length	245–595	ft
Fracture height	300	ft
Horizontal well length	2120	ft

Langmuir volume of 96 scf/ton, and bulk density of 2.58 g/cm^3. We set up a reservoir model with a volume of 3000 ft × 1500 ft × 300 ft. The fracture spacing is set at 100 ft, and the total number of hydraulic fractures is 20. In this well, the fracture half-length is varying: predictions of various values of fracture half-length were provided by the fracture maps obtained by using geophones installed in offset wells (Grieser et al., 2009). Reservoir modeling including hydraulic fractures for this well is shown in Fig. 2.12.

In the Barnett Shale, the closure stress is calculated from the horizontal stress of 5000 psi minus the pressure inside the fracture. Thus, the initial closure stress in this Barnett Shale example is 1200 psi corresponding to the initial reservoir pressure of 3800 psi, and the maximum closure stress is 3500 psi when the pressure inside the fracture reaches the flowing bottomhole pressure of 1500 psi. The pressure-dependent fracture conductivity data for these three different shale samples are normalized to the propped fracture conductivity measured

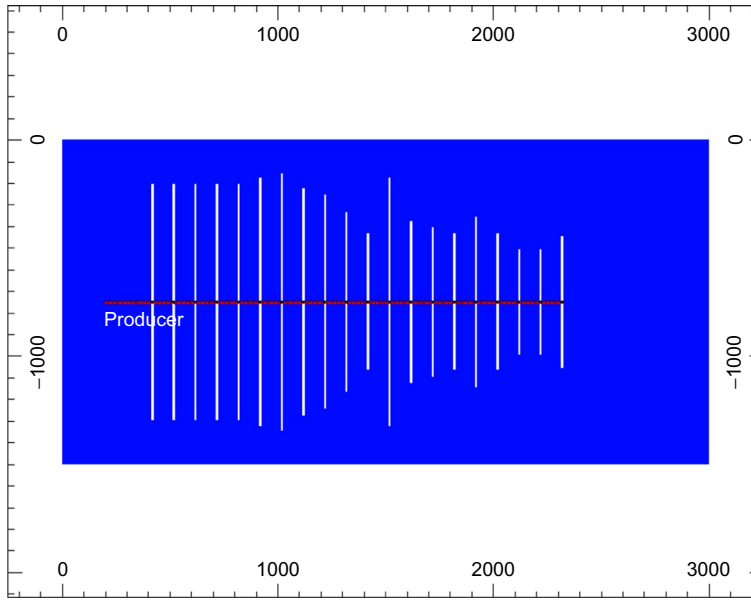

FIG. 2.12 A Barnett Shale well with varying hydraulic fracture half-length (Yu and Sepehrnoori, 2013b).

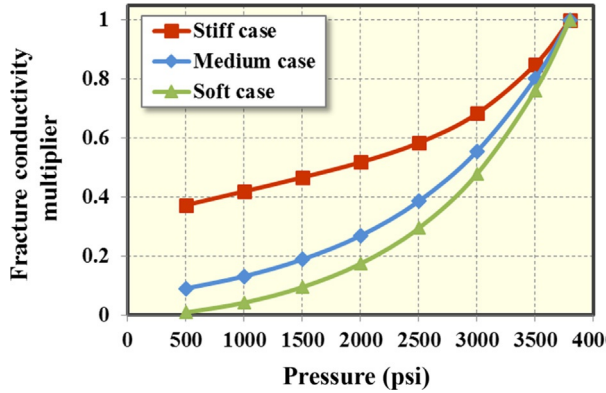

FIG. 2.13 Fracture conductivity multiplier versus pressure for different shale samples from stiff to soft (Yu and Sepehrnoori, 2013b).

at the initial closure stress of 1200 psi. The fracture conductivity multiplier versus pressure used in the reservoir modeling for different shale samples are generated from Eqs. (2.5)–(2.7), as illustrated in Fig. 2.13.

The history matching of field data with considering gas desorption and geomechanics effects together is shown in Fig. 2.14. It shows that there is a good

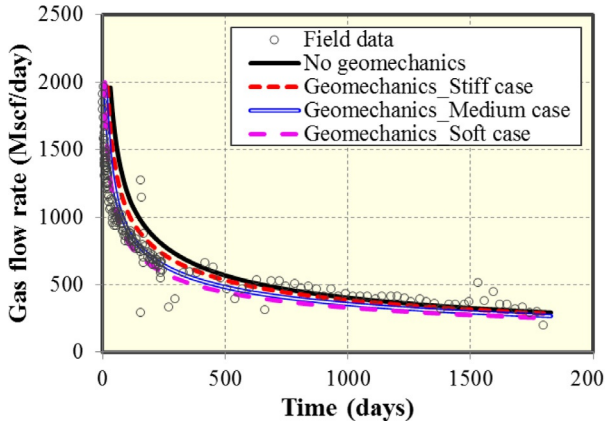

FIG. 2.14 History matching of a Barnett Shale well with gas desorption and pressure-dependent propped fracture conductivity effects (Yu and Sepehrnoori, 2013b).

early time match up to 300 days of production for three different geomechanics effects. After that, a more reasonable match between the numerical simulation results and the actual field gas flow data is obtained for the stiff case. For medium and soft cases, there is a small lower prediction of gas flow rate. This means that the effect of stress-dependent propped fracture conductivity plays an important role in history matching, especially in the early time of gas production, and a slight effect in well performance during the late time of gas production. Although a smaller reduction in fracture conductivity occurs in the early time with lower closure stress, it results in a larger decrease in gas production due to higher gas flow rate in the early time of production. During the late time of production, although there is a larger reduction in fracture conductivity with higher closure stress, the gas flow rate is lower, leading to a smaller decrease in gas production. Therefore, the effect of pressure-dependent fracture conductivity should be considered for history matching of shale gas production, especially in the early time of gas production with higher gas flow rate.

Fig. 2.15 shows the forecasting of gas production for a 30-year period with and without considering geomechanics. As shown, the cumulative gas production decreases when considering geomechanics compared with the base case without considering geomechanics. In addition, with the shale samples changing from stiff to soft, the reduction in cumulative gas production increases, illustrating that the geomechanics effect is crucial for accurate evaluation of ultimate gas recovery in shale gas reservoirs, especially for soft shales.

Fig. 2.16 shows the forecasting of gas flow rate for a 30-year period with and without considering the geomechanics effect. As shown, the gas flow rate decreases when considering the geomechanics compared with the base case without considering geomechanics. The decline of gas flow rate increases more with the shale samples changing from stiff to soft in the early time of production

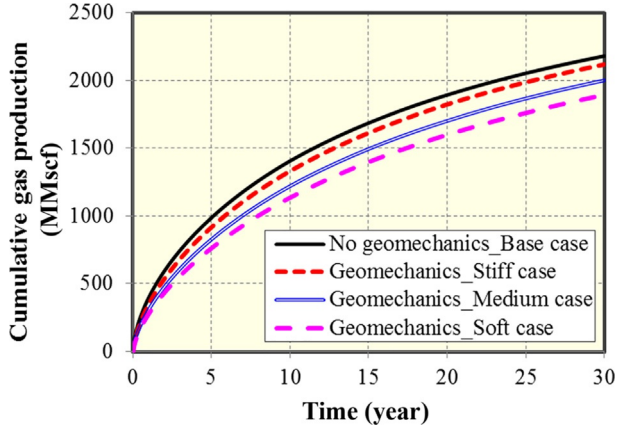

FIG. 2.15 Cumulative gas production at surface condition for 30 years with and without considering the geomechanics effect (Yu and Sepehrnoori, 2013b).

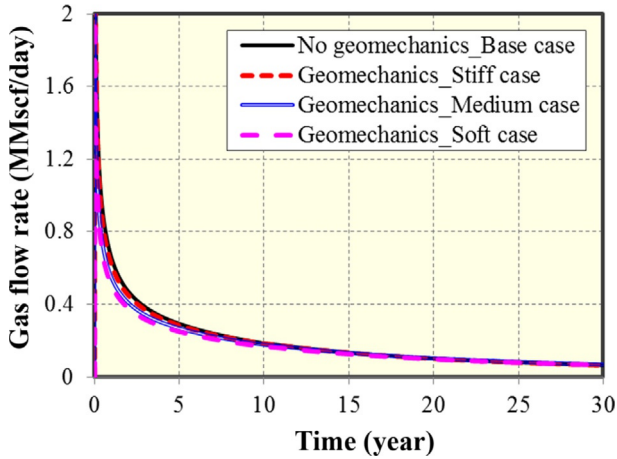

FIG. 2.16 Gas flow rate at surface condition for 30 years with and without considering the geomechanics effect (Yu and Sepehrnoori, 2013b).

and then less after approximately 3 years of production. Furthermore, the geomechanics effect is negligible for gas flow rate after around 10 years of production.

Decline rate of cumulative gas production is used to evaluate the effect of pressure-dependent fracture conductivity on gas recovery, and it is defined as:

$$\text{Decline rate} = \frac{Q_{Geomechanics} - Q_i}{Q_i}, \tag{2.9}$$

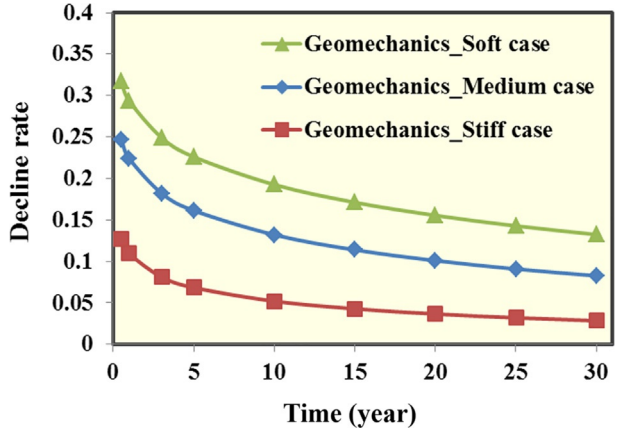

FIG. 2.17 Effect of geomechanics on decline rate of cumulative gas production for 30 years of production (Yu and Sepehrnoori, 2013b).

where $Q_{Geomechanics}$ is cumulative gas production with considering the geomechanics effect and Q_i is cumulative gas production without considering the geomechanics effect.

Fig. 2.17 shows the effect of geomechanics with three different shale samples on the decline rate of cumulative gas production in different years of production. It can be seen that the decline rate of cumulative gas production decreases significantly at the early time of production, especially before around 3 years of production for this case; after that, the decline rate trend decreases slowly. In addition, with the shale samples changing from stiff to soft, the contribution of the effect of geomechanics on the decline rate of cumulative gas production increases because of larger loss in fracture conductivity when the shale sample becomes more ductile. The comparison of the effect of geomechanics on reduction in gas recovery at 5, 10, 20, and 30 years of production for different cases is shown in Fig. 2.18. It shows that the final contribution of geomechanics on decline rate of gas recovery is around 15% for the soft case, 10% for the medium case, and 3% for the stiff case at 30 years of gas production. Thus, the impact of geomechanics cannot be ignored during the process of optimization of hydraulic fracturing design, performing history matching, and assessing production forecast of gas production, especially for the soft shales with lower Young's modulus.

2.4.3.1 *Effect of Matrix Permeability*

Effect of geomechanics on decline rate of cumulative gas production for 30 years with permeability of 0.00005 md and 0.0001 md is shown in Figs. 2.19 and 2.20, respectively. Compared with the base case with the permeability

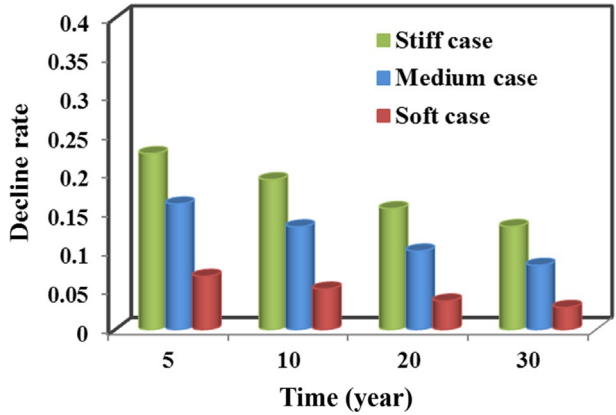

FIG. 2.18 Comparison of the effect of geomechanics on decline rate of cumulative gas production for different cases at different production time (Yu and Sepehrnoori, 2013b).

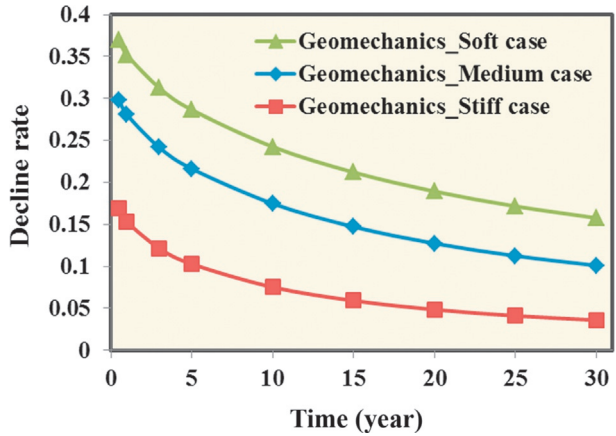

FIG. 2.19 Effect of geomechanics on decline rate of cumulative gas production for 30 years with permeability of 0.00005 md (Yu and Sepehrnoori, 2013b).

of 0.00001 md, the decline rate of cumulative gas production increases slowly with increasing permeability, and the decline rate trend is similar. The comparison of the effect of geomechanics on the decline rate of cumulative gas production at 30 years of production for different cases with different permeability is shown in Fig. 2.21. As shown, the permeability has a small effect on the contribution of geomechanics to the decline rate of gas recovery. For soft case, the range of decline rate with the increasing permeability is from 13.2% to 16.9%; for medium case, the range of decline rate is from 8.2% to 11.1%; for stiff case, the range of decline rate is from 2.8% to 4.1%.

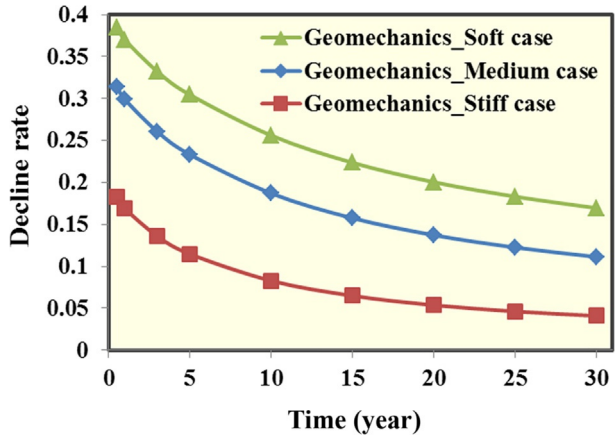

FIG. 2.20 Effect of geomechanics on decline rate of cumulative gas production for 30 years with permeability of 0.0001 md (Yu and Sepehrnoori, 2013b).

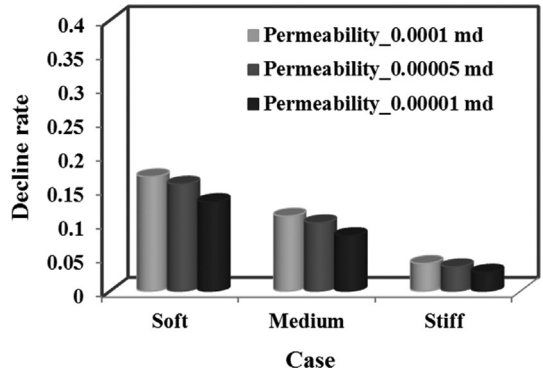

FIG. 2.21 The comparison of the effect of geomechanics on the decline rate of cumulative gas production at 30 years of production for different cases with different permeabilities (Yu and Sepehrnoori, 2013b).

2.4.3.2 Effect of Initial Fracture Conductivity

Effect of geomechanics on decline rate of cumulative gas production for 30 years with initial fracture conductivity of 0.1 and 10 md-ft is shown in Figs. 2.22 and 2.23, respectively. As shown, the decline rate of cumulative gas production is extremely sensitive to the initial fracture conductivity. When the initial fracture conductivity is smaller, the effect of geomechanics contributes more to the decline rate of gas production; while when the initial fracture conductivity is larger, the contribution of geomechanics on the decline rate is less, especially for the stiff case. The comparison of the effect of geomechanics on the decline rate of cumulative gas production at 30 years of production for

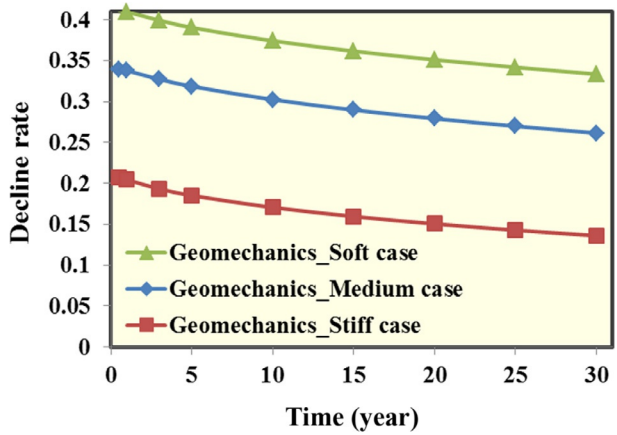

FIG. 2.22 Effect of geomechanics on decline rate of cumulative gas production for 30 years with initial fracture conductivity of 0.1 md-ft (Yu and Sepehrnoori, 2013b).

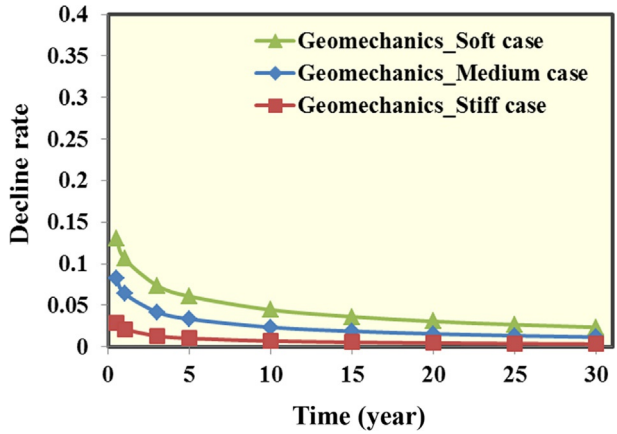

FIG. 2.23 Effect of geomechanics on decline rate of cumulative gas production for 30 years with initial fracture conductivity of 10 md-ft (Yu and Sepehrnoori, 2013b).

different cases with different initial fracture conductivity is shown in Fig. 2.24. It can be seen that the initial fracture conductivity has a significant effect on the contribution of geomechanics to the decline rate of gas recovery. For soft case, the range of decline rate with the decreasing initial fracture conductivity is from 2.3% to 33.3%; for medium case, the range of decline rate is from 1.2% to 26.1%; for stiff case, the range of decline rate is from 0.3% to 13.6%. Thus, there exists a critical initial fracture conductivity for different shale reservoirs to make the geomechanics effect become negligible over a lifetime of wells, which is important for optimization of hydraulic fracturing design. The critical

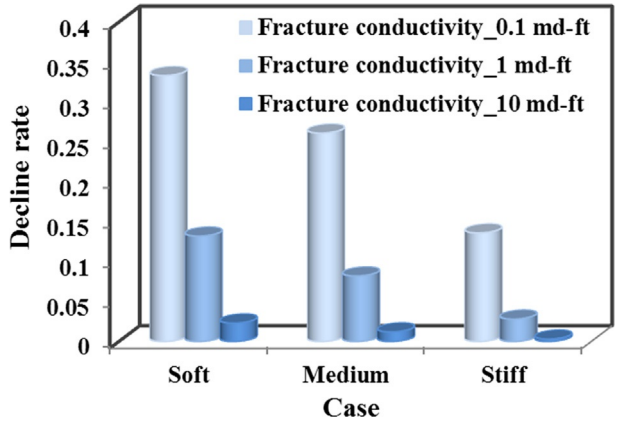

FIG. 2.24 The comparison of the effect of geomechanics on the decline rate of cumulative gas production at 30 years of production for different cases with different initial fracture conductivity (Yu and Sepehrnoori, 2013b).

fracture conductivity for the Barnett Shale with geomechanics of stiff case in this study is around 10 md-ft and the corresponding decline rate of cumulative gas production is below 5% over the lifetime of gas production.

2.4.3.3 *Effect of Bottomhole Pressure*

Effect of geomechanics on decline rate of cumulative gas production for 30 years with the bottomhole pressure of 500 and 1000 psi is shown in Figs. 2.25 and 2.26, respectively. Compared with the base case with the bottomhole pressure of 1500 psi, the decline rate of gas production decreases

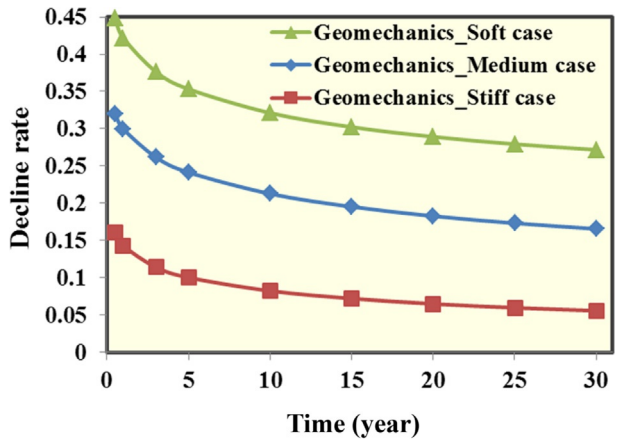

FIG. 2.25 Effect of geomechanics on decline rate of cumulative gas production for 30 years with bottomhole pressure of 500 psi (Yu and Sepehrnoori, 2013b).

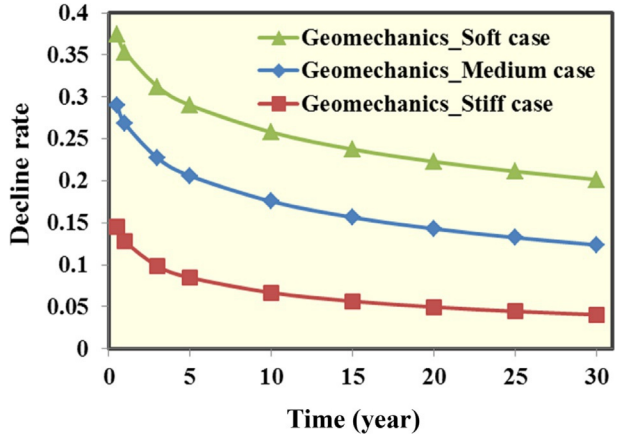

FIG. 2.26 Effect of geomechanics on decline rate of cumulative gas production for 30 years with bottomhole pressure of 1000 psi (Yu and Sepehrnoori, 2013b).

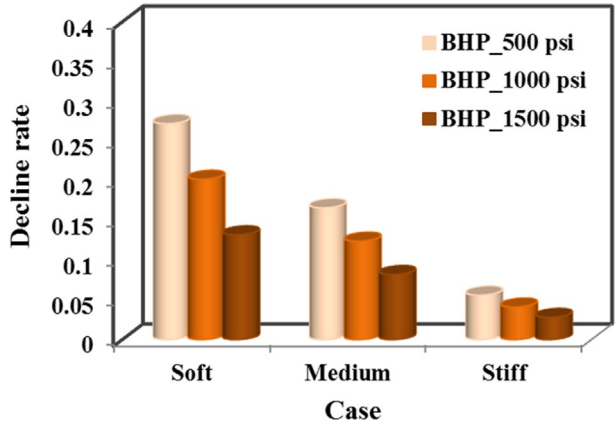

FIG. 2.27 The comparison of the effect of geomechanics on the decline rate of cumulative gas production at 30 years of production for different cases with different BHP (Yu and Sepehrnoori, 2013b).

slowly with the increasing bottomhole pressure, and the decline rate trend is similar. The comparison of the effect of geomechanics on the decline rate of cumulative gas production at 30 years of production for different cases with different bottomhole pressure is shown in Fig. 2.27. It shows that the effect of bottomhole pressure is more sensitive than the effect of permeability, while less than the effect of initial fracture conductivity. For soft case, the range of decline rate with the decreasing bottomhole pressure is from 13.2% to 27.2%; for medium case, the range of decline rate is from 8.2% to 16.6%; for stiff case, the range of decline rate is from 2.8% to 5.6%.

2.5 HISTORY MATCHING WITH GAS DESORPTION AND GEOMECHANICS EFFECTS

2.5.1 Barnett Shale

Average reservoir data for a Barnett Shale well were used for history matching (Al-Ahmadi et al., 2011). In this case, the well was stimulated by a multistage fracturing with a single, perforated interval for each stage. In this simulation study, we set up a reservoir with a volume of 3000 ft × 1500 ft × 300 ft. The fracture spacing and half-length is set at 100 and 150 ft, respectively, and the number of fractures is 28. Detailed reservoir information about this section of the Barnett Shale well is listed in Table 2.5.

TABLE 2.5 Reservoir and Fracture Properties Used for History Matching With a Field Well From Barnett Shale (Yu and Sepehrnoori, 2014a)

Parameter	Value(s)	Unit
Depth	5463	ft
Pore pressure gradient	0.54	psi/ft
Initial reservoir pressure	2950	psi
Closure pressure	3879	psi
Closure pressure gradient	0.71	psi/ft
BHP	500	psi
Production time	30	year
Reservoir temperature	150	°F
Gas viscosity	0.0201	cp
Initial gas saturation	0.70	–
Total compressibility	3×10^{-6}	psi^{-1}
Matrix permeability	0.00015	md
Matrix porosity	0.06	–
Fracture conductivity	1	md-ft
Fracture half-length	155	ft
Fracture spacing	100	ft
Fracture height	300	ft
Horizontal well length	2968	ft
Number of fractures	28	–

The history matching of field data considering gas desorption and geomechanics effects is presented in Fig. 2.28. The gas desorption parameters and the pressure-dependent fracture conductivity curve for the Barnett Shale well can be found in the work by Yu and Sepehrnoori (2014a). It shows a more reasonable match between the numerical simulation results and the actual field gas flow data. As shown, the gas desorption plays a positive effect on gas production, a smaller effect during early period of production while a higher contribution during late period of production because of substantial pressure depletion and larger gas drainage area, finally contributing to 15.8% of total gas production at around 4.5 years of gas production, and 20.7% of total gas production at 30 years of gas production. However, geomechanics plays a negative impact on gas production, a larger effect for early time of production while a smaller impact for late time of production, decreasing by 4.8% of total gas production at around 4.5 years of gas production, and 1.8% of total gas production at 30 years of gas production. Finally, the effect combining gas desorption and geomechanics together contributes to 11% increase in total gas production at around 4.5 years of gas production and 18.9% increase in total gas production at 30 years of gas production. In this Barnett Shale example, it can be noted that the gas desorption effect is dominant during the late period process of gas production, and geomechanics plays a negligible role in gas production. Thus, the impact of gas desorption should be considered while geomechanics might be ignored when performing history matching and assessing production forecast of gas production in formation with high Young's modulus, i.e., Barnett Shale.

2.5.2 Marcellus Shale

Average reservoir data for a Marcellus Shale well were used for history matching (Meyer et al., 2010). In this case, the well was stimulated by a multistage fracturing with a seven-stage treatment (five perforation clusters per stage) over a lateral of 2100 ft. The stage two has a minimal contribution of around 3% of the total production, while most stages produced gas mainly from a dominant cluster fracture (Meyer et al., 2010). Therefore, only six hydraulic fractures are used to perform history matching of production data. In this simulation study, we set up a reservoir with a volume of $3734\,\text{ft} \times 934\,\text{ft} \times 162\,\text{ft}$. The fracture spacing and half-length is set at 300 and 320 ft, respectively, and the number of fractures is 6. Detailed reservoir information about this section of the Marcellus Shale is listed in Table 2.6. The gas desorption parameters and the pressure-dependent fracture conductivity curve for the Marcellus Shale well can be found in the work by Yu and Sepehrnoori (2014a).

The history matching of field data is shown in Fig. 2.29. Similarly, the gas desorption plays a positive effect on gas production, contributing to 19.3% of total gas production at 30 years of gas production. The geomechanics plays a much more negative effect on gas production compared with the Barnett Shale example, especially a larger effect for early time of production rate, as shown in

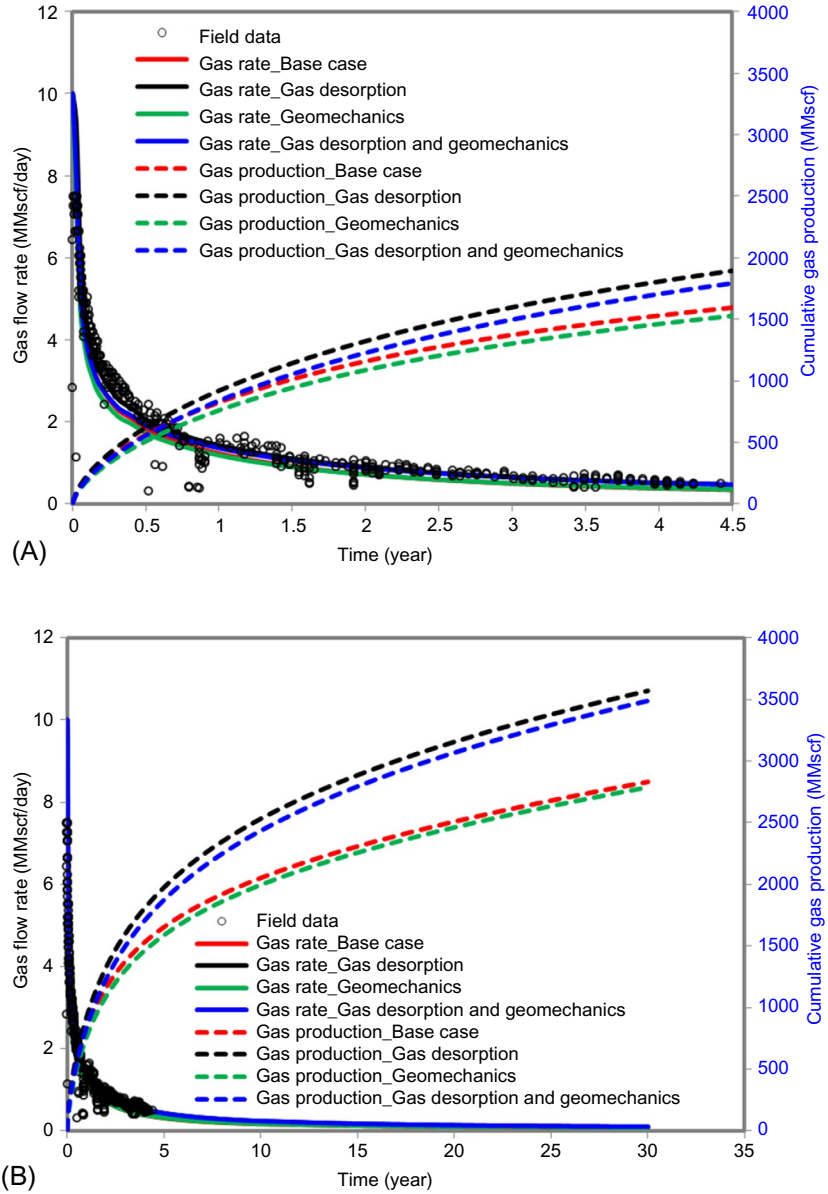

FIG. 2.28 History matching of Barnett Shale considering the gas desorption and geomechanics effects (Yu and Sepehrnoori, 2014a). (A) Gas production for a 4.5-year period. (B) Gas production for a 30-year period.

TABLE 2.6 Reservoir and Fracture Properties Used for History Matching With a Field Well From Marcellus Shale (Yu and Sepehrnoori, 2014a)

Parameter	Value(s)	Unit
Depth	8593	ft
Pore pressure gradient	0.55	psi/ft
Initial reservoir pressure	4726	psi
Closure pressure	6015	psi
Closure pressure gradient	0.70	psi/ft
BHP	535	psi
Production time	30	year
Reservoir temperature	175	°F
Gas viscosity	0.0201	cp
Initial gas saturation	0.70	–
Total compressibility	1×10^{-6}	psi^{-1}
Matrix permeability	0.0006	md
Matrix porosity	0.065	–
Fracture conductivity	3	md-ft
Fracture half-length	320	ft
Fracture spacing	300	ft
Fracture height	162	ft
Horizontal well length	2100	ft
Number of fractures	6	–

Fig. 2.29A; while a smaller impact for late time of production, decreasing by 23.3% of total gas production at 30 years of gas production, as shown in Fig. 2.29B. Finally, the impacts of combining gas desorption and geomechanics together make the gas production decrease by 4% in total gas production at 30 years of gas production. It should be pointed out that although a smaller reduction in fracture conductivity occurs in the early time with lower closure stress, it results in a larger decrease in gas production due to higher gas flow rate in the early time of production. During the late time of production, although there is a larger reduction in fracture conductivity with higher closure stress, the

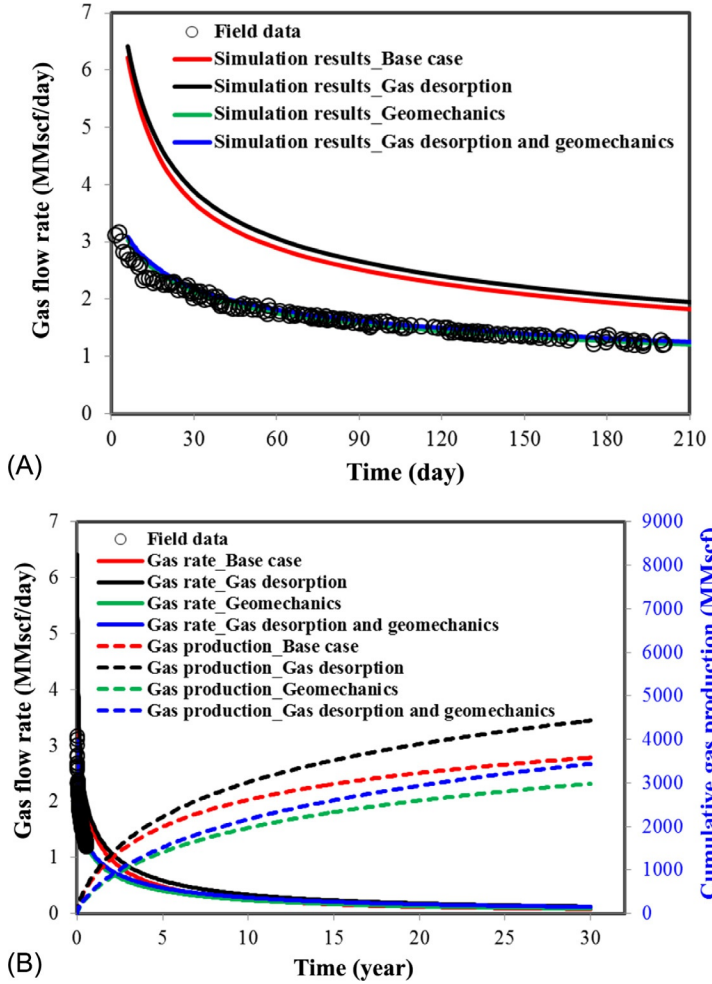

FIG. 2.29 History matching of Marcellus Shale considering the gas desorption and geomechanics effects (Yu and Sepehrnoori, 2014a). (A) Gas production for an around 200-day period. (B) Gas production for a 30-year period.

gas flow rate is lower, leading to a smaller decrease in gas production. In this Marcellus Shale example, the geomechanics effect is dominant during the early period of gas production compared with the gas desorption effect, while the gas desorption effect plays more important than that of geomechanics during the late period of gas production. Thus, the impacts of gas desorption and geomechanics should be considered together while performing history matching and assessing production forecast of gas production in formation with low Young's modulus, i.e., Marcellus Shale.

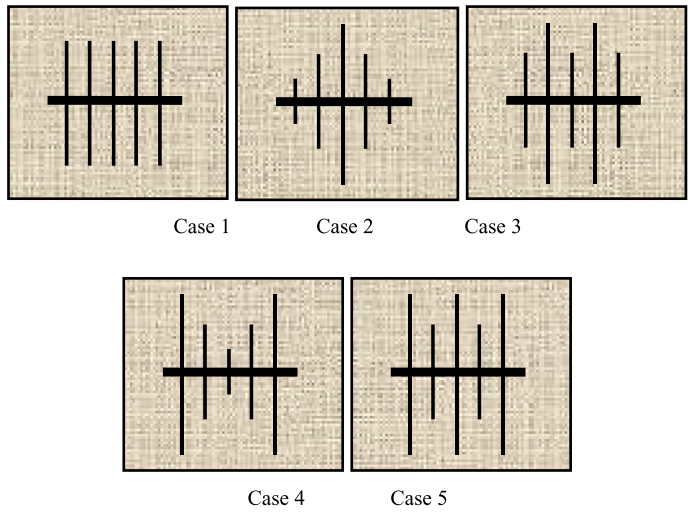

FIG. 2.30 Five different hydraulic fracture patterns within one perforation stage under the same total fracture length of 5000 ft (Yu et al., 2014a).

2.6 UNCERTAIN HYDRAULIC FRACTURES PATTERN[1]

2.6.1 Base Case

In this study, we presented five hydraulic fracture patterns with varying fracture half-length within one perforation stage, as illustrated in Fig. 2.30. Five clusters within one perforation stage are assumed. The total fracture length remains the same for each fracture pattern (5000 ft). The details for individual fracture half-length in each case are described here:

Case 1: Five fractures with an equal half-length of 500 ft.
Case 2: Middle fracture with a half-length of 740 ft, two longer fractures with a half-length of 500 ft, and two shorter fractures with a half-length of 380 ft.
Case 3: Two longer fractures with a half-length of 740 ft, and three shorter fractures with a half-length of 340 ft.
Case 4: Middle fracture with a half-length of 220 ft, two shorter fractures with a half-length of 400 ft, and two longer fractures with a half-length of 740 ft.
Case 5: Three longer fractures with a half-length of 740 ft, and two shorter fractures with a half-length of 140 ft.

We set up a basic reservoir model with a volume of 2000 ft × 2000 ft × 300 ft based on average reservoir data from Barnett Shale, as listed in Table 2.7.

1. Figures and text of Section 2.6 are reprinted from Yu et al. (2014a).

TABLE 2.7 Parameters Used in Simulations for Uncertain Fracture Patterns From Barnett Shale (Yu et al., 2014a)

Parameter	Value(s)	Unit
Initial reservoir pressure	3800	psi
BHP	1000	psi
Production time	30	year
Reservoir temperature	180	°F
Gas viscosity	0.02	cP
Matrix permeability	0.0001	md
Matrix porosity	0.06	–
Initial gas saturation	0.70	–
Compressibility of shale	10^{-6}	psi^{-1}
Cluster spacing	80	ft
Stage spacing	400	ft
Fracture conductivity	100	md-ft
Fracture height	300	ft

Cluster spacing for each case is set at 80 ft. Gas desorption effect and pressure-dependent fracture conductivity as illustrated in Fig. 2.31 are considered in all subsequent simulations. Gas desorption is described by the Langmuir isotherm with Langmuir pressure of 650 psi and Langmuir volume of 96 scf/ton.

Comparisons of gas flow rate and gas recovery at 30 years of production between these five cases are presented in Fig. 2.32, respectively. As shown, at early production time (less than 2 years), the well performance for each case remains the same, since the same total fracture length leads to the same contact area between fractures and reservoir before fracture interference occurs. However, after 2 years of production, the well performance for each case is very different. Among the five cases, Cases 1 and 5 show the lowest and the highest gas flow rate and gas recovery, respectively. The absolute and relative difference of gas recovery at 30 years of production between Cases 1 and 5 are around 591 MMscf and 35%, respectively. The gas recovery in Case 3 is larger than that of Cases 2 and 4 performs better than Case 3. This is simply because Cases 1 and 5 have the strongest and the weakest fracture interference, respectively. This may suggest that when performing history matching with short-term period of gas production, a good agreement can be obtained with each fracture pattern; while there will be a big uncertainty at late time of production because of the

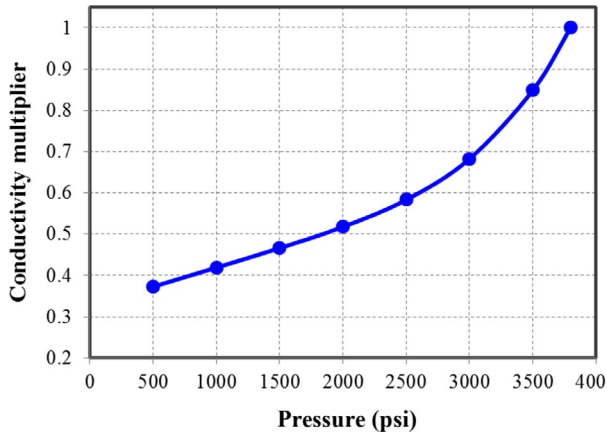

FIG. 2.31 Fracture conductivity multiplier versus pressure for Barnett Shale (Yu et al., 2014a).

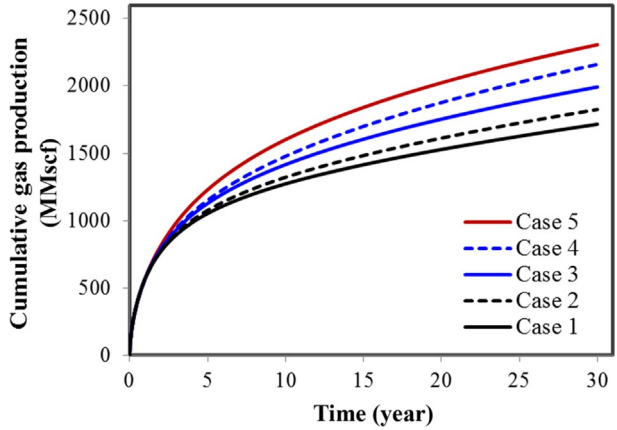

FIG. 2.32 Comparison of cumulative gas production with five cases (Yu et al., 2014a).

different degree of fracture interference. Therefore, it may imply that the hydraulic fracture pattern can be characterized based on history matching with long-term period of gas production. Fig. 2.33 shows pressure distribution of these five cases after 4 years of production. Clearly, Case 1 has the smallest drainage area between fractures and reservoir, leading to the lowest gas recovery, and Case 5 shows the largest drainage area, leading to the highest gas recovery. The drainage area in Cases 2–4 with the same total fracture length is between Cases 1 and 5. The drainage area in Case 4 is larger than that in Cases 2 and 3. It suggests that longer outer fractures lead to larger drainage area and higher gas recovery from low permeability shale gas reservoirs.

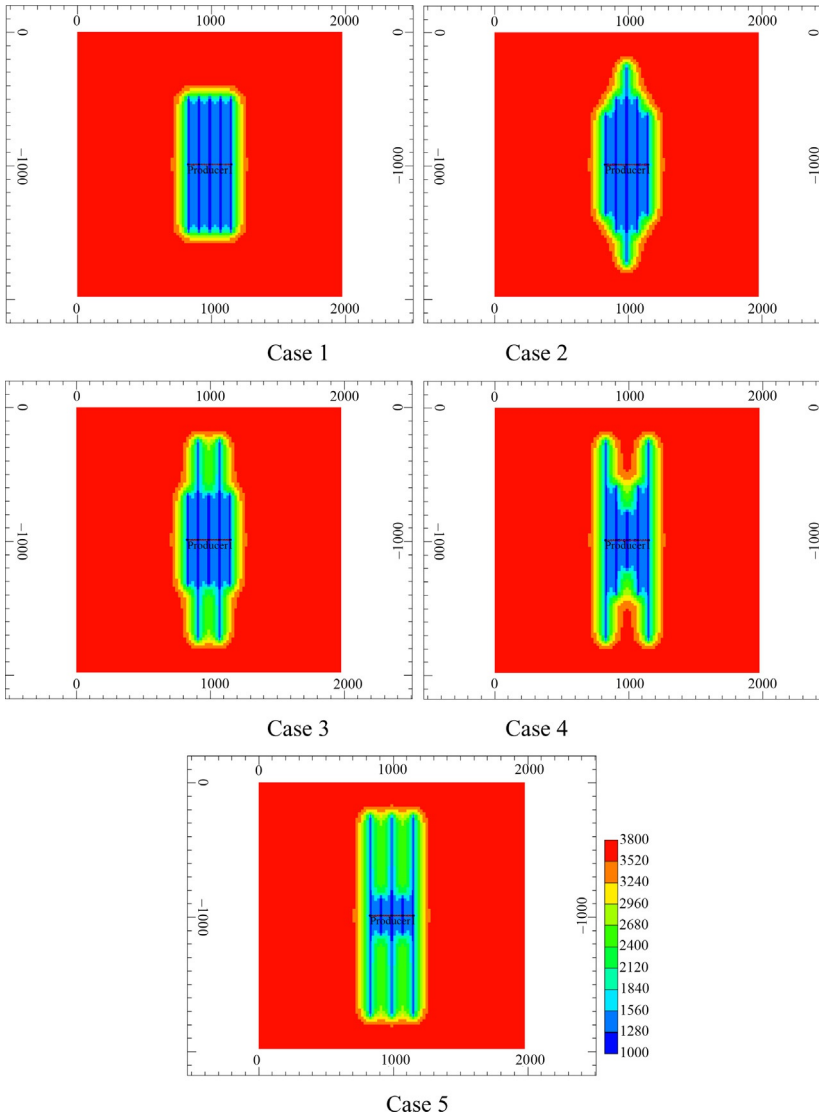

FIG. 2.33 Pressure distribution of five cases at 4 years of gas production (cluster spacing of 80 ft) (Yu et al., 2014a).

2.6.2 Sensitivity Study

2.6.2.1 Effect of Matrix Permeability

The shale matrix has ultralow permeability, typically in a range of tens to hundreds of nano-Darcy. The shale matrix permeability plays an important role in gas recovery in a hydraulic fractured horizontal well. The matrix permeability

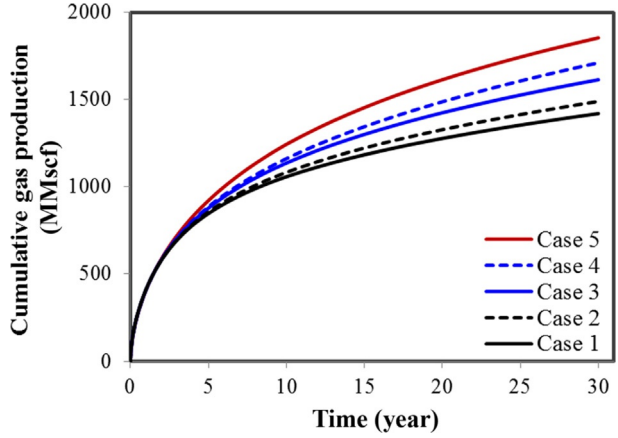

FIG. 2.34 Comparison of cumulative gas production with permeability of 50 nD (Yu et al., 2014a).

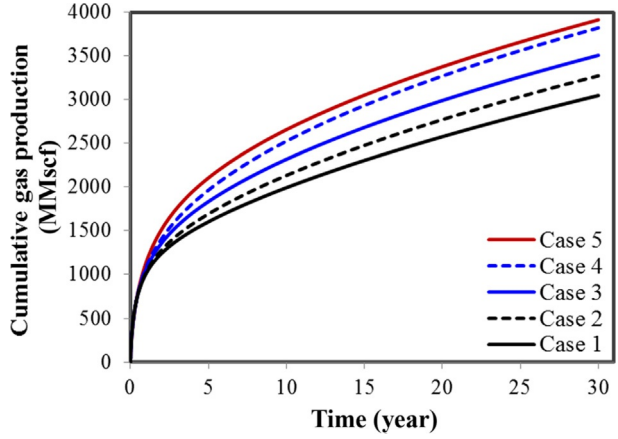

FIG. 2.35 Comparison of cumulative gas production with permeability of 500 nD (Yu et al., 2014a).

values of 50 and 500 nD are investigated with cluster spacing of 80 ft and fracture conductivity of 100 md-ft. Figs. 2.34 and 2.35 show the comparison of gas recovery for matrix permeability of 50 and 500 nD, respectively. As shown, the transition time of well performance change corresponding to permeability of 50 and 500 nD is around 3 years and 0.5 year, respectively, and the absolute difference of gas recovery at 30 years of production is about 434 MMscf and 866 MMscf, respectively. Hence, the gas recovery increases with the increasing shale matrix permeability. It means that proper characterization of hydraulic fracture pattern is very significant in shale reservoirs with higher matrix permeability.

2.6.2.2 *Effect of Cluster Spacing*

Cluster spacing in each stage of a hydraulic fracturing stimulation treatment is very important. The cluster spacing values of 60 and 100 ft are investigated with matrix permeability of 100 nD and fracture conductivity of 100 md-ft. The comparison of gas recovery for cluster spacing of 60 and 100 ft is shown in Figs. 2.36 and 2.37, respectively. It can be seen that the transition time of well performance change corresponding to cluster spacing of 60 and 100 ft is around 1 year and 2.5 years, respectively, and the absolute difference of gas recovery at

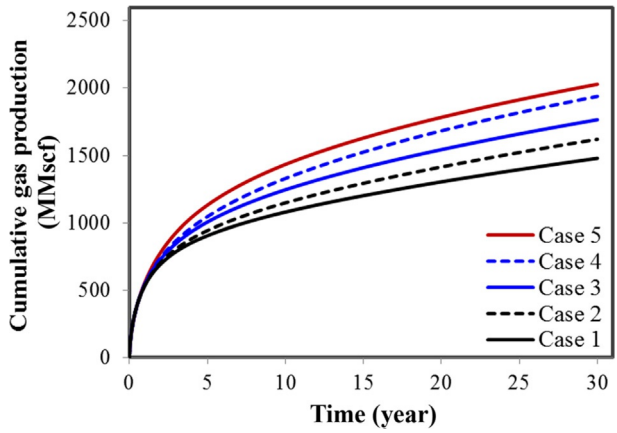

FIG. 2.36 Comparison of cumulative gas production with cluster spacing of 60 ft (Yu et al., 2014a).

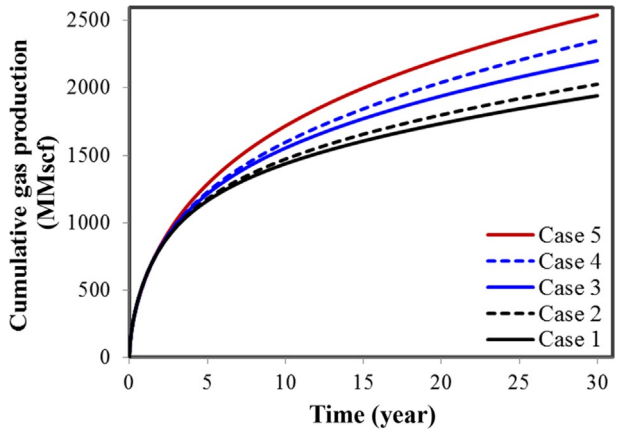

FIG. 2.37 Comparison of cumulative gas production with cluster spacing of 100 ft (Yu et al., 2014a).

30 years of production is about 550 MMscf and 600 MMscf, respectively. For all cases, the gas recovery increases slightly with the increasing cluster spacing.

2.6.2.3 *Effect of Fracture Conductivity*

Fracture conductivity is defined as fracture width multiplied by fracture permeability. The fracture conductivity values of 1 and 10 md-ft are investigated with cluster spacing of 80 ft and matrix permeability of 100 nD. Figs. 2.38 and 2.39 show the comparison of gas recovery for fracture conductivity of 1 and 10 md-ft, respectively. As shown, the transition time of well performance change corresponding to fracture conductivity of 1 and 10 md-ft is around 13 and 3 years,

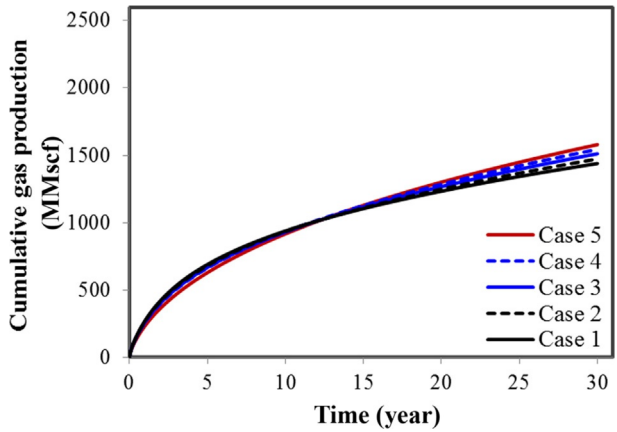

FIG. 2.38 Comparison of cumulative gas production with fracture conductivity of 1 md-ft (Yu et al., 2014a).

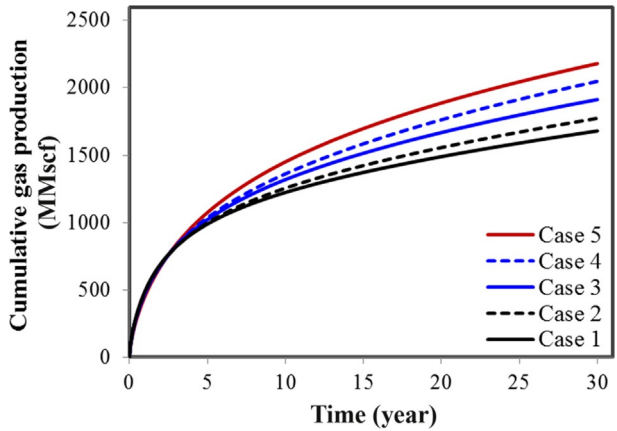

FIG. 2.39 Comparison of cumulative gas production with fracture conductivity of 10 md-ft (Yu et al., 2014a).

respectively, and the absolute difference of gas recovery at 30 years of production is about 140 MMscf and 500 MMscf, respectively. Hence, the gas recovery is very sensitive to the fracture conductivity, increasing significantly with the increasing fracture conductivity. It implies that quantification of fracture conductivity is very critical in characterization of hydraulic fracture pattern.

2.7 UNEVEN PROPPANT DISTRIBUTION

Uniform proppant distribution within multiple perforation clusters plays an important role in achieving high fracturing-treatment effectiveness in shale gas reservoirs. Although the technology of hydraulic fracturing has made significant progress over the last several years, proppant transport and distribution in multiple hydraulic fractures is still unclear. A numerical simulation study by Daneshy (2011) indicated that an uneven proppant distribution exists between four perforation clusters in one stage using plug-and-perf fracturing technique, as shown in Fig. 2.40. During his simulation study, many factors, such as fluid viscosity, injection rate, and proppant size and density, were considered. Among all scenarios, a highly uneven proppant distribution within different clusters was observed and most proppant entered the last perforation cluster; the proppant concentration of the last cluster was almost four times the proppant amount in the first cluster (Daneshy, 2011). The average ratio of proppant concentration within four clusters was approximately 1:1.5:2.5:4.

In this section, we evaluated three hypothetical scenarios of proppant distribution in four clusters within one fracturing stage, as shown in Fig. 2.41. Scenario

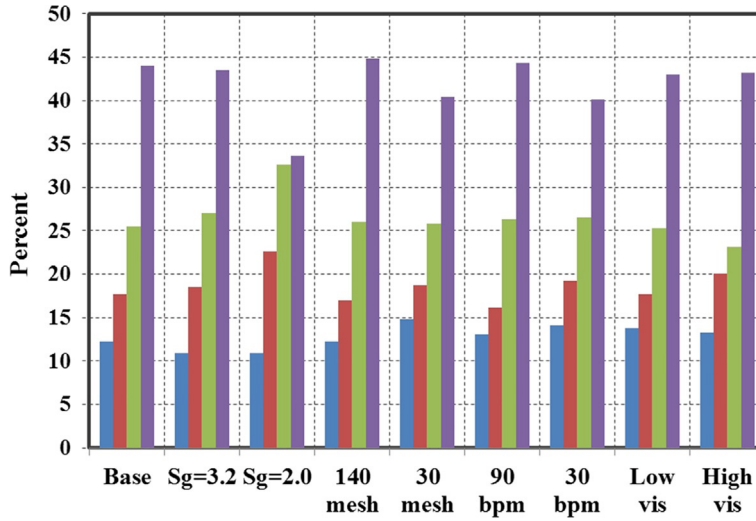

FIG. 2.40 Proppant distribution within four perforation clusters in one fracturing stage (Daneshy, 2011).

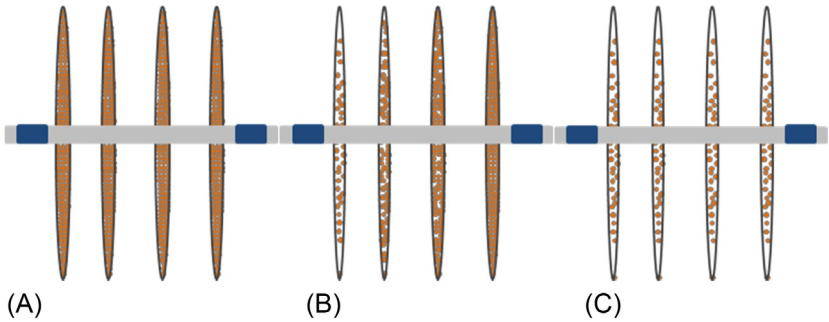

FIG. 2.41 Proppant distribution in four perforation clusters within one fracturing stage (Yu et al., 2015). (A) Scenario 1: uniform distribution with high proppant concentration. (B) Scenario 2: uneven distribution (proppant concentration ratio of 1:1.5:2.5:4). (C) Scenario 3: uniform distribution with low proppant concentration.

1 represents uniform distribution with high proppant concentration, which is the optimal design in the field operation; Scenario 2 represents uneven distribution with proppant concentration ratio of 1:1.5:2.5:4, which might be the real case in the field; Scenario 3 represents uniform distribution with low proppant concentration, which is poor design in field operations. In addition, proppant distribution in each cluster is assumed to be uniform laterally and vertically.

2.7.1 Base Case

We built a reservoir model with a volume of 5000 ft × 1600 ft × 300 ft with a well length of 3500 ft. In the base case, there are 11 fracturing stages and 4 clusters per stage. Therefore, the total number of hydraulic fractures is 44. The detailed reservoir properties for this model are the average values based on available data from published Marcellus Shale work and are listed in Table 2.8. The effects of gas desorption and geomechanics are considered for simulation. Langmuir pressure of 500 psi and Langmuir volume of 200 scf/ton are used in the gas desorption model. For the stress-dependent fracture conductivity effect, the relationship between fracture conductivity change with pressure is generated based on the Eq. (2.5).

In the base case, the cluster spacing is 80 ft, the initial reservoir pressure is 4000 psi, the minimum fracture conductivity is 1 md-ft, the fracture half-length is 300 ft, the fracture height is 200 ft, and the matrix permeability is 0.0001 md. The fracture conductivity in Scenario 1 is changed to 4 md-ft for all clusters. The fracture conductivity in Scenario 2 has a ratio of 1:1.5:2.5:4 md-ft for clusters one to four, respectively. In the base case, the fracture conductivity for Scenario 2 is 1, 1.5, 2.5, and 4 md-ft for clusters one to four within the single stage. The fracture conductivity of Scenario 3 is constant at 1 md-ft for all clusters. The comparison of cumulative gas production in a 30-year period between these three scenarios is shown in Fig. 2.42. Scenario 1

TABLE 2.8 Parameters Used in Simulation Study of Proppant Distribution Effect (Yu et al., 2015)

Parameter	Value(s)	Unit
Reservoir temperature	220	°F
Initial gas saturation	0.70	–
Gas gravity	0.58	–
Total compressibility	3×10^{-6}	psi^{-1}
Matrix porosity	0.06	–
Horizontal well length	3500	ft
BHP	500	psi

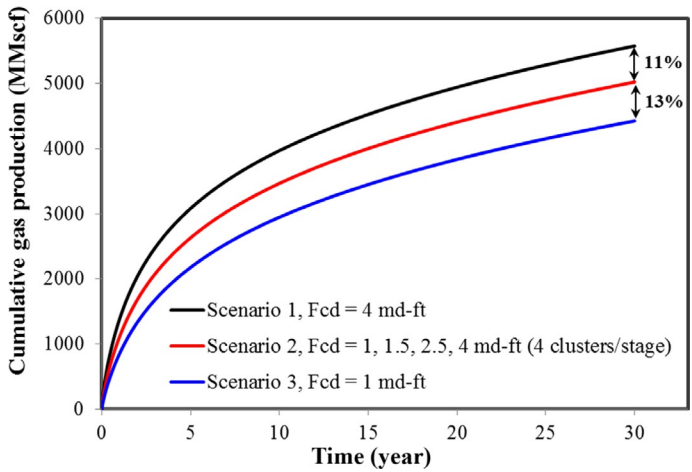

FIG. 2.42 Comparison of cumulative gas production in a 30-year period between three scenarios (Yu et al., 2015).

has the largest cumulative gas production and Scenario 2 has the smallest. The difference of cumulative gas production between Scenarios 1 and 2 is about 11%, between Scenarios 2 and 3 is about 13%, and between Scenarios 1 and 3 is about 24%. It suggests that the impact of proppant distribution on gas recovery is important and should be considered in the field development in order to optimize the shale gas production. Fig. 2.43 shows the pressure distribution after 1 year of production for Scenarios 1, 2, and 3. As shown, the drainage efficiency of Scenario 3 with low proppant concentration is the lowest, and the drainage efficiency of Scenario 2 is smaller than Scenario 1 with uniform proppant distribution and larger fracture conductivity.

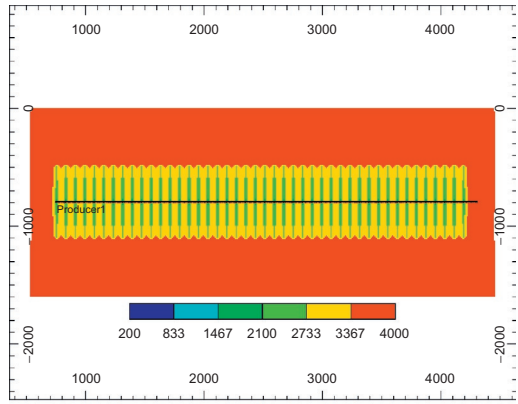

(A)

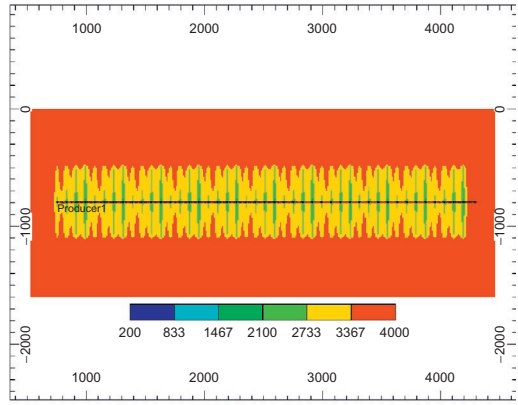

(B)

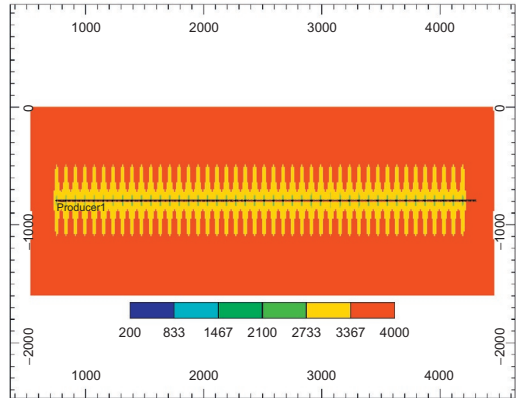

(C)

FIG. 2.43 Pressure (unit: psi) distribution after 1 year of gas production (Yu et al., 2015). (A) Pressure distribution of Scenario 1. (B) Pressure distribution of Scenario 2. (C) Pressure distribution of Scenario 3.

2.7.2 Sensitivity Study

In the subsequent simulation studies, we only chose Scenarios 1 and 2 to perform the sensitivity study for the purpose of determining the critical reservoir and fracture parameters controlling the difference in gas recovery between uneven proppant distribution in different perforation clusters and uniform proppant distribution with high fracture conductivity. Six uncertain parameters such as cluster spacing, initial reservoir pressure, fracture conductivity, fracture half-length, fracture height, and matrix permeability are investigated. The range of values used for those parameters is listed in Table 2.9. Cluster spacing of 50, 80, and 100 ft within a single fracturing stage is investigated, representing fracturing stage number (four clusters per stage) of 18, 11, and 9, respectively. The impacts of these six uncertainty parameters on the difference in gas production for 30 years between Scenarios 1 and 2 are summarized in a Tornado plot, as shown in Fig. 2.44. It illustrates that the most sensitive parameter is matrix permeability, followed by fracture height, fracture half-length, fracture conductivity, and initial reservoir pressure. The effect of cluster spacing is less sensitive based on the range investigated in this study. Also, the overall range of gas recovery difference between uneven proppant distribution and uniform proppant distribution is between 5.22% and 16.99% for the Marcellus Shale.

2.8 COMPARISON BIWING FRACTURE MODEL WITH FRACTURE NETWORK MODEL

Based on the basic reservoir model including multistage fractures, as shown in Fig. 2.1, we compared the impacts of biwing fracture and fracture network models on well performance for two scenarios assuming different number of active clusters within single perforation stage. Scenario 1 assumes that there are four active clusters within single perforation stage (Fig. 2.45). The cluster spacing is 50 ft. Scenario 2 assumes that there is only one active cluster within

TABLE 2.9 Six Uncertainty Parameters Used in Simulation Study of Proppant Distribution Effect (Yu et al., 2015)

Parameter	Minimum	Maximum	Unit
Cluster spacing	50	100	ft
Initial reservoir pressure	3000	5000	Psi
Fracture conductivity	0.1	10	md-ft
Fracture half-length	200	400	ft
Fracture height	100	300	ft
Matrix permeability	0.00001	0.001	md

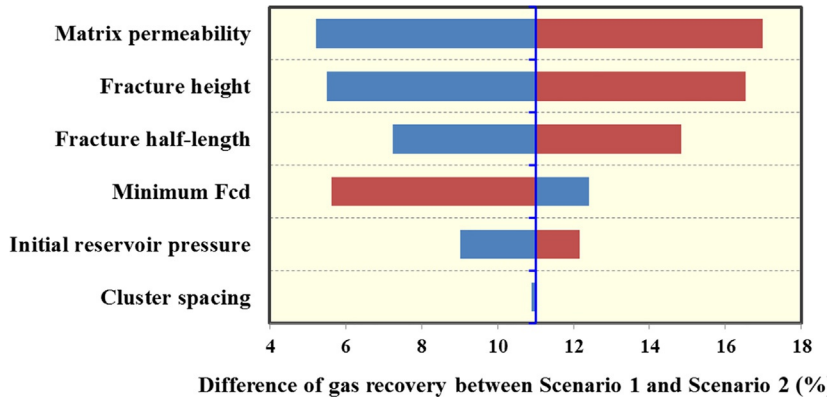

FIG. 2.44 Tornado chart of sensitivity study (Yu et al., 2015).

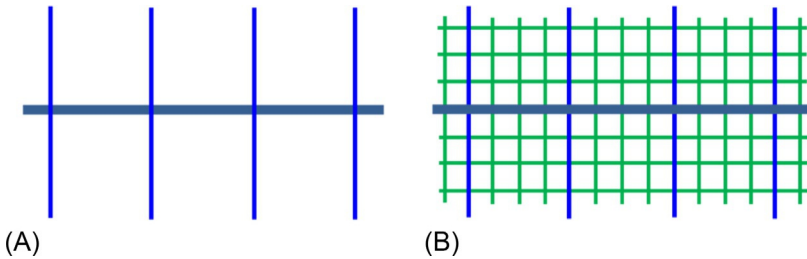

FIG. 2.45 Scenario 1: four active clusters within single perforation stage (Yu and Sepehrnoori, 2014b). (A) Biwing fracture model. (B) Fracture network model.

single perforation stage (Fig. 2.46). The orthogonal induced fractures are spaced 10 ft with secondary fracture conductivity ranging from 0.05 to 5 md-ft. The primary fracture conductivity in hydraulic fractures is 5 md-ft.

Fig. 2.47 compares the simulation results of cumulative gas production using biwing fracture and fracture network models for two scenarios, illustrating that there is a big difference between the two scenarios. For Scenario 1, there is a small difference (2%) between the biwing fracture and fracture network models, even when including high secondary fracture conductivity-induced fractures, as shown in Fig. 2.47A. This is because four effective hydraulic fractures for each stage can drain the reservoir effectively, and the fracture network contributes less to the total well performance. In addition, the computation time of the biwing fracture model is less than that of the fracture network model. Hence, the biwing fracture model is enough to perform history matching and evaluate well performance when there are multiple clusters within single perforation stage and cluster spacing is small (50 ft in this case study).

However, Fig. 2.47B shows that there is a big difference between the biwing fracture and fracture network models for Scenario 2. The difference is about

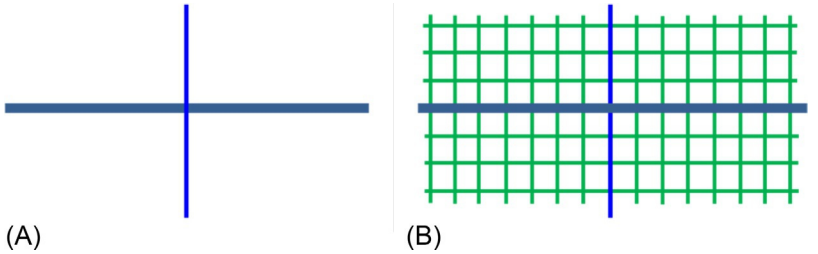

FIG. 2.46 Scenario 2: one effective cluster within single perforation stage (Yu and Sepehrnoori, 2014b). (A) Biwing fracture model. (B) Fracture network model.

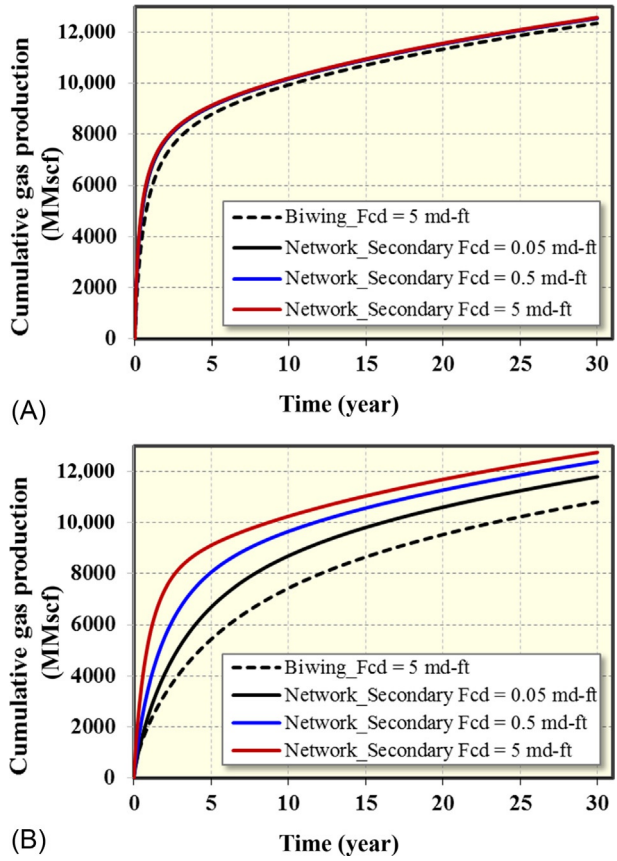

FIG. 2.47 Comparison of the biwing fracture and fracture network models (Yu and Sepehrnoori, 2014b). (A) Scenario 1: four clusters per stage. (B) Scenario 2: one cluster per stage.

10%, 15%, and 18%, corresponding to the secondary fracture conductivity of 0.05, 0.5, and 5 md-ft, respectively. Hence, the induced fracture network contributes significantly to the total well performance if there is only one primary hydraulic fracture within single perforation stage (stage spacing of 250 ft), since

single hydraulic fracture without fracture network cannot efficiently and completely deplete the reservoir.

2.9 MULTIPLE HORIZONTAL WELLS MODELING

Two scenarios describing multiple horizontal well placement were studied, as illustrated in Fig. 2.48. Scenario 1 is referred to as aligning fracturing, where hydraulic fracturing is between two wells in an aligned pattern; and Scenario 2 is referred to as alternating fracturing, where hydraulic fracturing is between two wells in a staggered pattern. We investigate the effect of fracture spacing

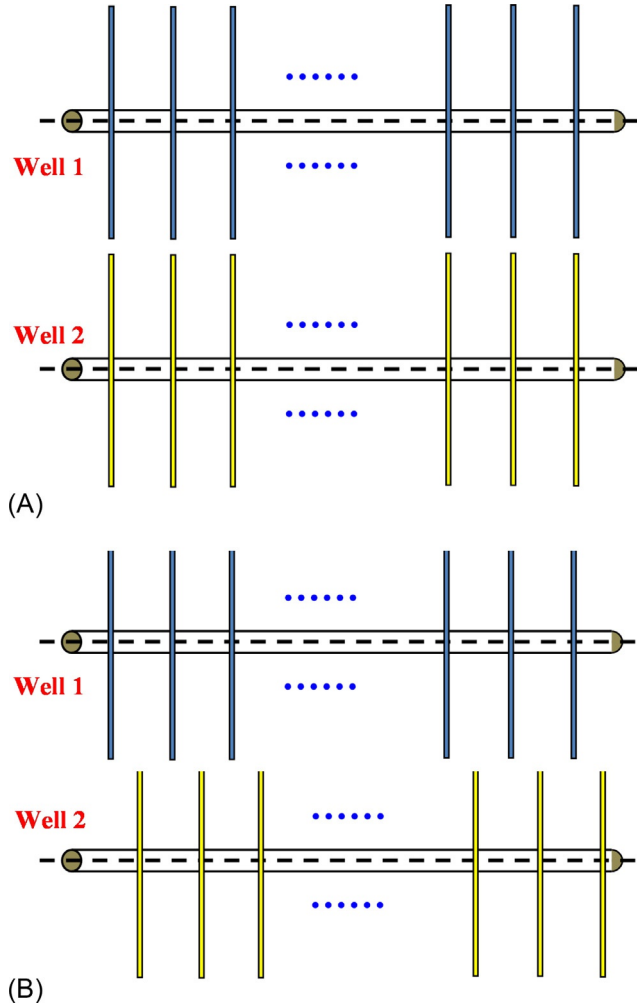

FIG. 2.48 Two scenarios of multiple horizontal well placement (Yu and Sepehrnoori, 2013a). (A) Scenario 1: aligning fracturing. (B) Scenario 2: alternating fracturing.

TABLE 2.10 Detailed Reservoir Information Used for Barnett Shale (Yu and Sepehrnoori, 2013a)

Parameter	Value(s)	Unit
Initial reservoir pressure	3800	psi
BHP	500	psi
Production time	30	year
Reservoir temperature	180	°F
Gas viscosity	0.0201	cp
Initial gas saturation	0.70	–
Total compressibility	3×10^{-6}	psi^{-1}
Matrix permeability	0.0001	md
Matrix porosity	0.06	–
Fracture conductivity	50	md-ft
Fracture half-length	300	ft
Fracture spacing	200, 400, 600	ft
Fracture height	200	ft
Well length per well	3600	ft
Number of fractures per well	9	–
Number of wells	2	–
Well distance	620	ft

toward comparison of gas production between these two scenarios. We set up a shale gas reservoir model with a volume of 5000 ft × 1600 ft × 200 ft. Detailed reservoir information used for Barnett Shale is listed in Table 2.10. Comparison of cumulative gas production is shown in Fig. 2.49. It shows that there is almost no difference of gas production for these two scenarios when fracture spacing is below 400 ft; however, Scenario 2 yields higher gas production than Scenario 1 when the fracture spacing is 400 ft or above. Fig. 2.50 presents the comparison of average reservoir pressure with fracture spacing of 600 ft. It can be seen that for Scenario 2, it has a larger average reservoir pressure drawdown, leading to higher cumulative gas production. Pressure distribution at 30 years of gas production for these two scenarios is shown in Fig. 2.51. It shows that more contact reservoir area is drained effectively by Scenario 2, compared to Scenario 1. In addition, Rafiee et al. (2012) reported that Scenario 2 design can increase the stress interference between fractures and create more effective stimulated reservoir volume to improve gas production. Therefore, Scenario 2 is suggested to optimize multiwell placement in shale gas reservoirs.

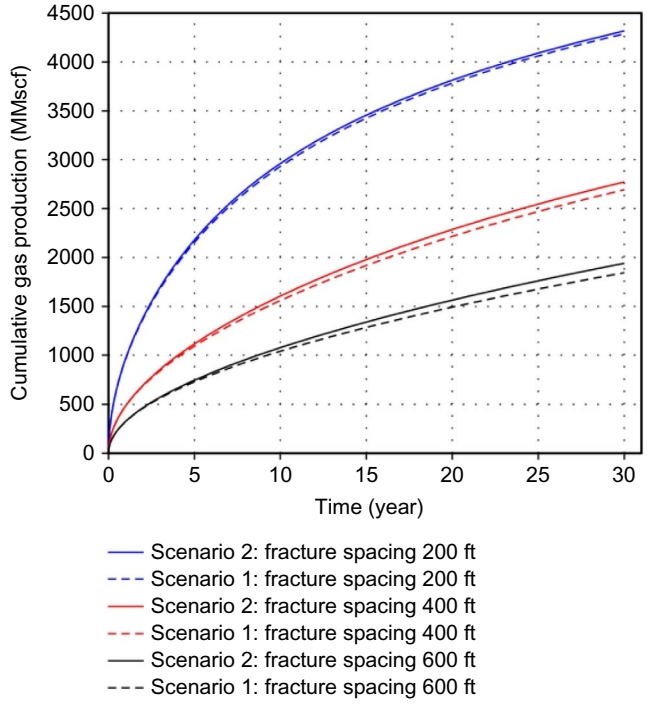

FIG. 2.49 Comparison of cumulative gas production (Yu and Sepehrnoori, 2013a).

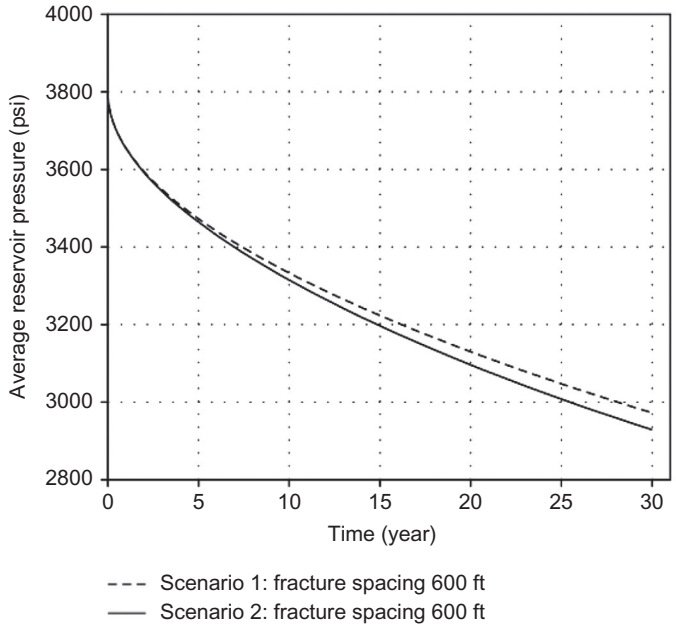

FIG. 2.50 Comparison of average reservoir pressure (Yu and Sepehrnoori, 2013a).

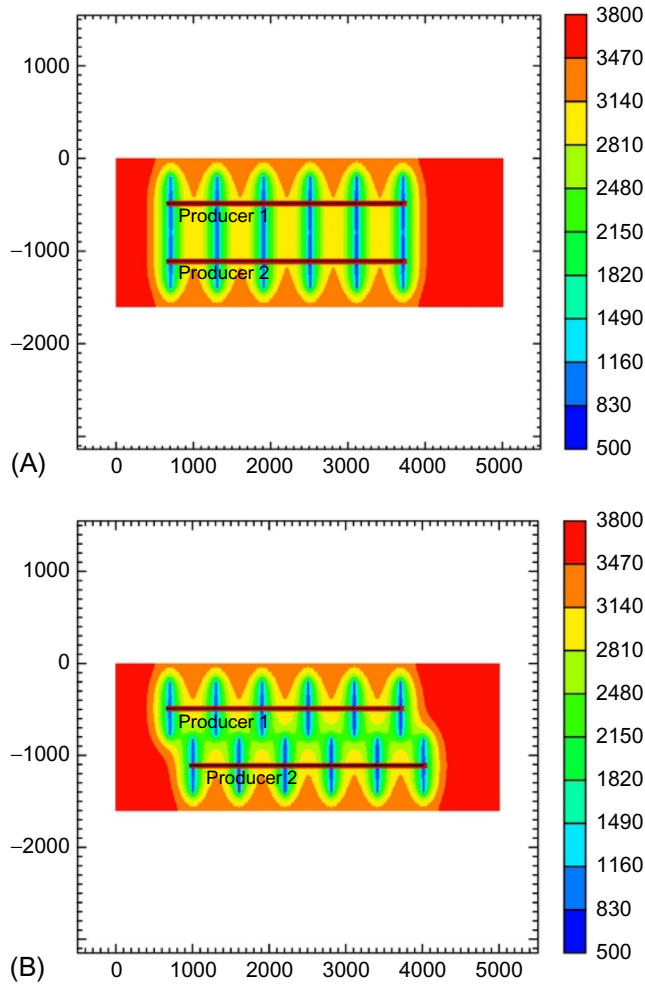

FIG. 2.51 Pressure distribution at 30 years of gas production (Yu and Sepehrnoori, 2013a). (A) Scenario 1: aligning fracturing. (B) Scenario 2: alternating fracturing.

2.10 RESERVOIR SIMULATION FOR TIGHT OIL RESERVOIRS

Reservoir simulation is an effective approach to simulate multiphase flow (gas-water-oil) in the tight oil reservoirs, especially in the early stage of field developments. In this study, reservoir simulator of CMG-IMEX (CMG-IMEX, 2012) is used to model multiple hydraulic fractures and fluid flow in the Bakken tight oil reservoirs. For reservoir modeling including multiple fractures, the LGR method is utilized to accurately model fluid flow from matrix to fractures. We set up a basic 3D reservoir model with dimensions of 10,560 ft × 1080 ft × 40 ft, which corresponds to length, width, and thickness, respectively. A biwing fracture model is used in the basic reservoir model.

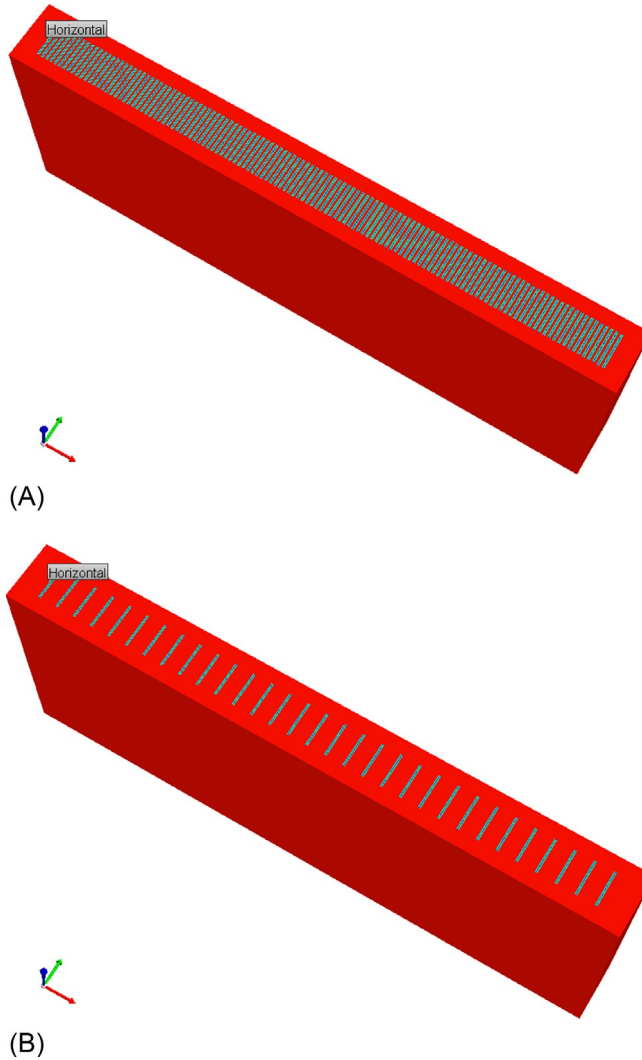

FIG. 2.52 A basic 3D reservoir model including 31 fracturing stages for Bakken tight oil reservoir. (A) Four effective fractures per stage. (B) One effective fracture per stage.

The horizontal well length is set at 10,000 ft with 31 perforation stages. Two scenarios are investigated based on the number of effective clusters in each stage, as shown in Fig. 2.52. Scenario 1 assumes that there are four clusters in each stage and the clusters are evenly spaced. Hence, there are totally 124 effective hydraulic fractures along the horizontal well. The stage spacing is 320 ft and the cluster spacing is 80 ft, which is defined as the distance between two neighboring fractures. Scenario 2 assumes that there is one active cluster per stage. Hence, there are totally 31 effective hydraulic fractures.

TABLE 2.11 Parameters Used for Simulations in the Middle Bakken (Yu and Sepehrnoori, 2014d)

Parameter	Value	Unit
Initial reservoir pressure	7500	psi
Reservoir temperature	240	°F
Reservoir permeability	5	μD
Reservoir porosity	7%	value
Initial water saturation	40%	value
Total compressibility	1×10^{-6}	psi^{-1}
Horizontal well length	10,000	ft
Fracture half-length	300	ft
Fracture conductivity	5	md-ft
Total number of fractures	124	value
Gas specific gravity	0.92	value
Bubble point	2500	psi

The typical fluid and rock properties from the Middle Bakken are used for the subsequent simulation study, as listed in Table 2.11. The reservoir is assumed to be homogeneous. Fracture height is equal to the reservoir thickness. A synthetic flowing bottomhole pressure curve is used to represent the real pressure drawdown, as illustrated in Fig. 2.53. The BHP decreases from 7000 to 1000 psi at the early time of production (around 1 year), after that, it stabilizes until the end of production (30 years). The relative permeability curves, such as water-oil relative permeability and liquid-gas relative permeability (Fig. 2.54), are obtained based on history matching with a field production data from the Middle Bakken (Yu et al., 2014b).

2.10.1 Effect of Fracture Conductivity

Effect of fracture conductivity on cumulative oil production for two scenarios is shown in Figs. 2.55 and 2.56, respectively. The range of fracture conductivity is from 0.1 to 100 md-ft. As shown, there is no big difference of cumulative oil production between 50 and 100 md-ft, illustrating that the fracture conductivity of 50 md-ft is close to infinite fracture conductivity in this case study.

2.10.2 Effect of Geomechanics

For the geomechanics effect, the pressure-dependent fracture conductivity curve used in this case study is shown in Fig. 2.57. As shown, the fracture conductivity corresponding to bottomhole pressure of 500 psi is about 20% of initial

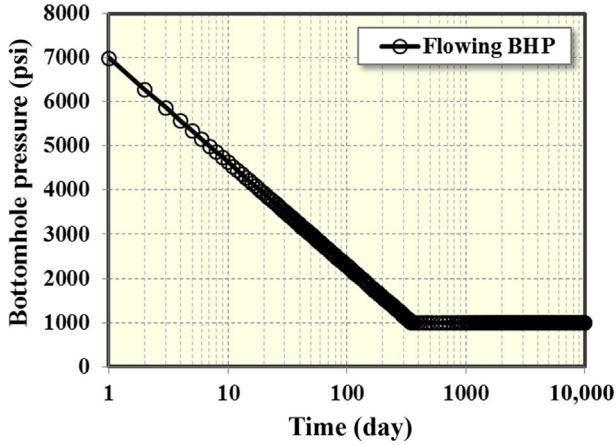

FIG. 2.53 Flowing bottomhole pressure used for simulation of the Middle Bakken tight oil reservoirs (Yu and Sepehrnoori, 2014d).

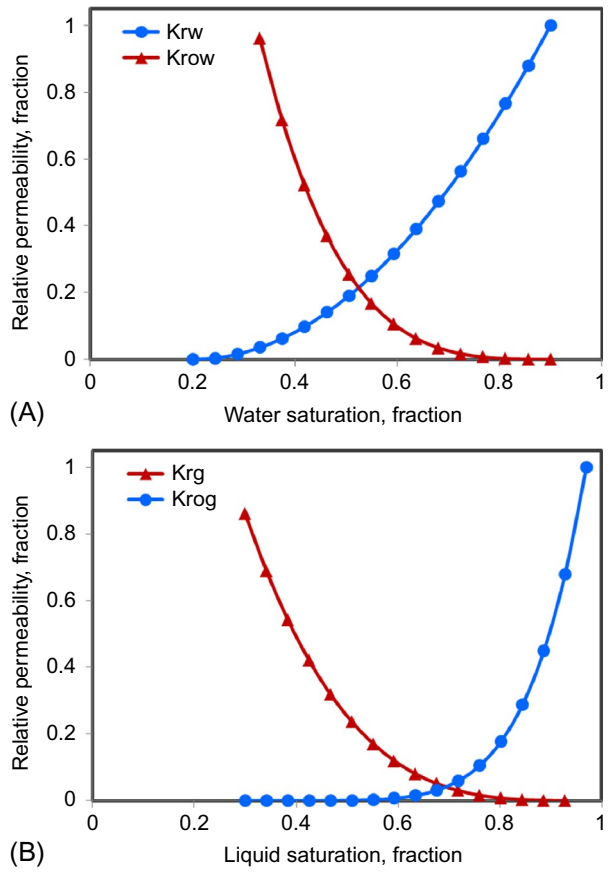

FIG. 2.54 Relative permeability curves for the Middle Bakken tight oil reservoirs (Yu et al., 2014b). (A) Water-oil relative permeability curve. (B) Liquid-gas relative permeability curve.

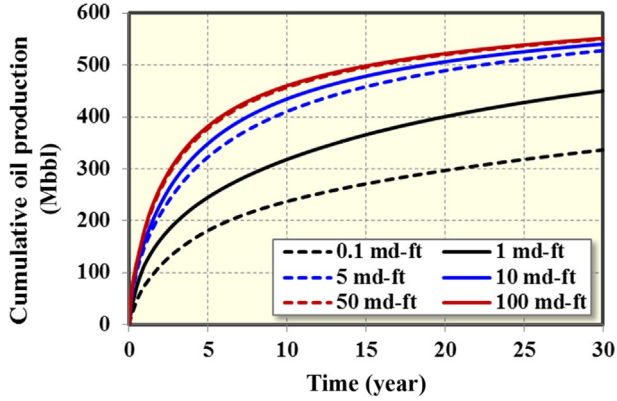

FIG. 2.55 Effect of fracture conductivity on well performance for Scenario 1 with four effective fractures per stage.

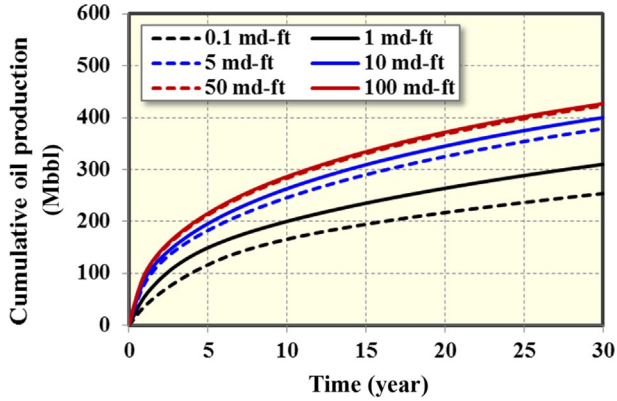

FIG. 2.56 Effect of fracture conductivity on well performance for Scenario 2 with one effective fracture per stage.

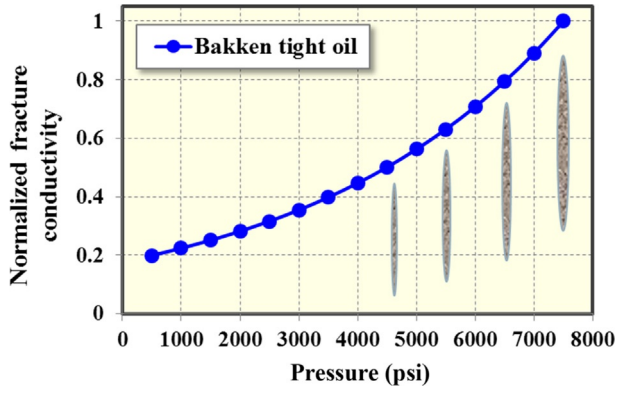

FIG. 2.57 The pressure-dependent fracture conductivity curve for the Middle Bakken (Yu and Sepehrnoori, 2014d).

fracture conductivity corresponding to the initial reservoir pressure of 7500 psi. The fracture conductivity of 5 md-ft is used for two scenarios. Fig. 2.58 shows the comparison of cumulative oil production with and without the geomechanics effect for two scenarios. It can be seen that cumulative oil production at 30 years of production decreases by around 11.4% and 14.4% for two scenarios, respectively. Hence, the geomechanics effect is important for history matching and completion optimization.

2.10.3 Effect of Fracture Network

Considering the possible brittle properties of the shale and consequently emphasizing the enhancement of the permeability of the formation around the hydraulic fractures, we compared the biwing fracture and fracture network models. Fig. 2.59 illustrates the fracture network model in conceptual consisting of primary and secondary fractures, representing primary hydraulic fractures and induced fractures. Fig. 2.60 shows the comparison of biwing fracture model

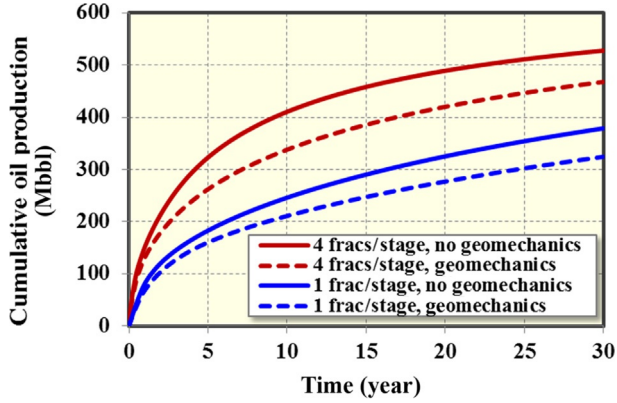

FIG. 2.58 The comparison of well performance with and without the geomechanics effect for two scenarios.

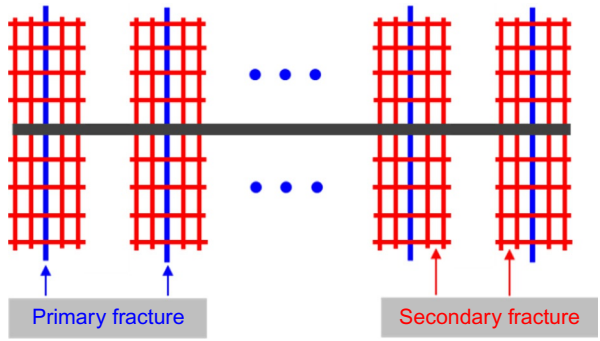

FIG. 2.59 A conceptual fracture network model comprising primary fractures and secondary fractures (Yu and Sepehrnoori, 2014d).

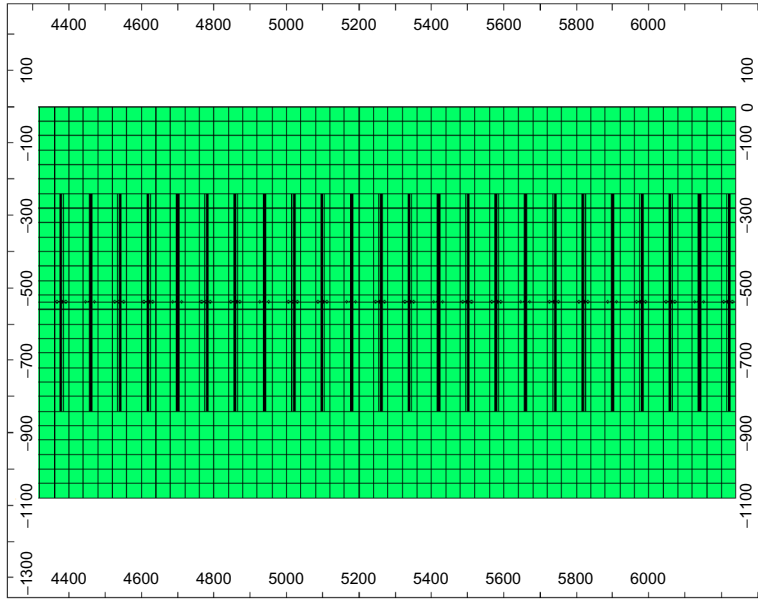

(A)

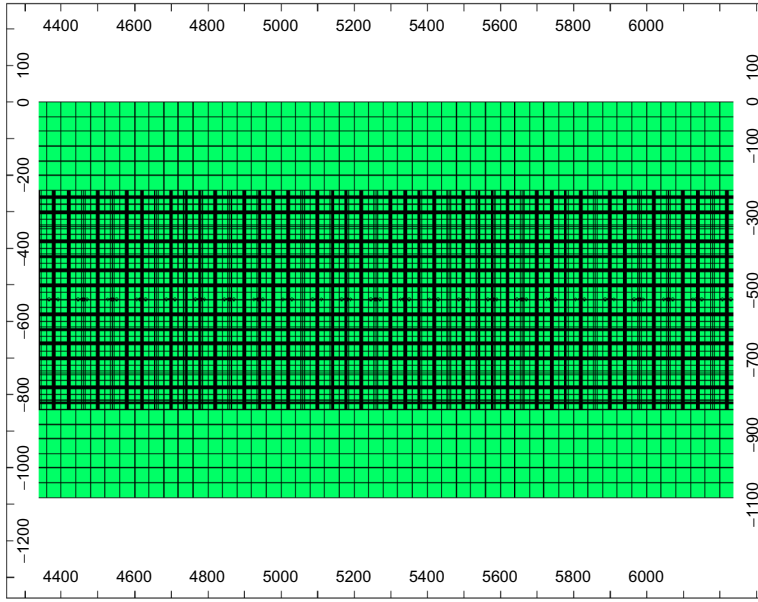

(B)

FIG. 2.60 Comparison of biwing fracture model and fracture network model in reservoir simulator. (A) Biwing fracture model. (B) Fracture network model.

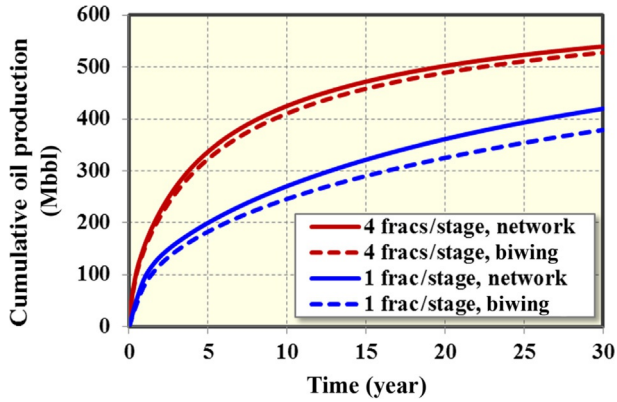

FIG. 2.61 Effect of fracture network on well performance for two scenarios.

and fracture network model in reservoir simulator. The grid size for fracture network is 40 ft × 40 ft in x and y directions. In this case study, the primary fracture conductivity of 5 md-ft and the secondary fracture conductivity of 0.5 md-ft is used.

The comparison result is shown in Fig. 2.61. It can be seen that the difference of cumulative oil production at 30 years of production is around 2.2% and 9.7% for two scenarios, respectively. For Scenario 1, there are four effective hydraulic fractures with a closer cluster spacing of 80 ft, resulting in no big difference of production between biwing fracture model and fracture network model and biwing fractures can effectively deplete the reservoir. However, for Scenario 2, the fracture spacing is larger (320 ft) and more induced fractures will significantly increase contact area between fracture and reservoir, resulting in a big difference of production between biwing fracture model and fracture network model. Therefore, the biwing fracture model can be effectively used to represent fracture network model to perform history matching and completion optimization for Scenario 1. The comparison of pressure distribution at 2 years of production between biwing fracture model and fracture network model is shown in Figs. 2.62 and 2.63 for two scenarios, respectively. As shown, there is a similar pressure distribution for Scenario 1 while a big difference of pressure distribution for Scenario 2.

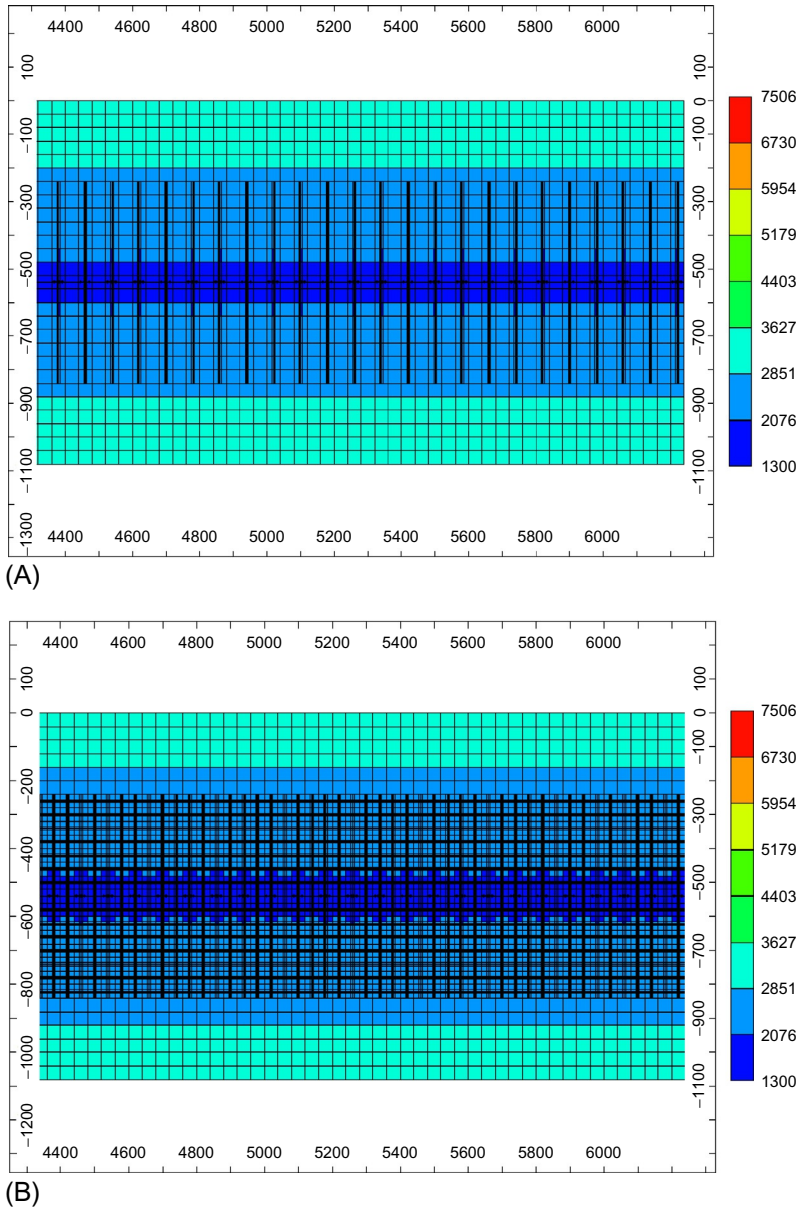

FIG. 2.62 Comparison of pressure distribution at 2 years of production for Scenario 1. (A) Biwing fracture model. (B) Fracture network model.

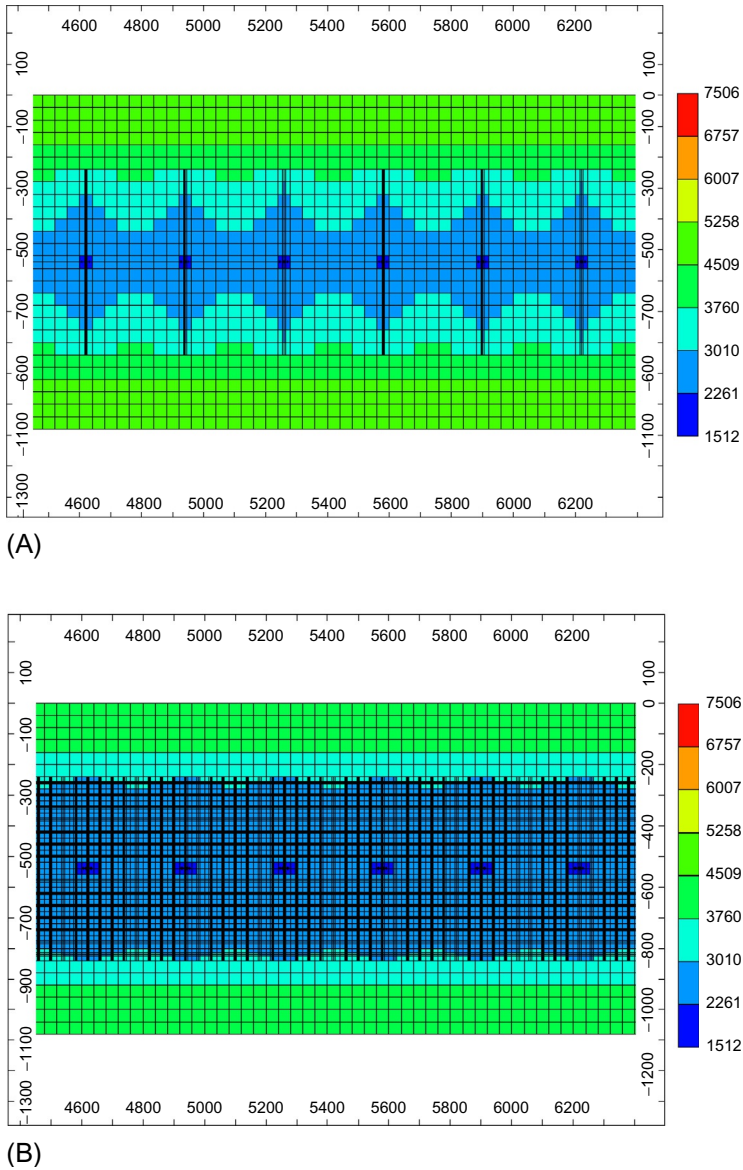

FIG. 2.63 Comparison of pressure distribution at 2 years of production for Scenario 2. (A) Biwing fracture model. (B) Fracture network model.

REFERENCES

Al-Ahmadi, H.A., Aramco, S., Wattenbarger, R.A., 2011. In: Triple-porosity models: one further step towards capturing fractured reservoirs heterogeneity.SPE/DGS Saudi Arabia Section Technical Symposium and Exhibition, Al-Khobar, Saudi Arabia. Paper SPE 149054.

Alramahi, B., Sundberg, M.I., 2012. In: Proppant embedment and conductivity of hydraulic fractures in shales. The 46th US Rock Mechanics/Geomechanics Symposium, Chicago, Illinois. Paper ARMA 12-291.

Arps, J.J., 1945. Analysis of decline curves. Trans. AIME 160 (1), 228–247.

Boulis, A., Jayakumar, R., lalehrokh, F., Lawal, H., 2012. In: Improved methodologies for more accurate shale gas assessments. Americas Unconventional Resources Conference, Pittsburgh, Pennsylvania. Paper SPE 154981.

Cipolla, C.L., Warpinske, N.R., Mayerhfer, M.J., Lolon, E.P., Vincent, M.C., 2008. In: The relationship between fracture complexity, reservoir properties, and fracture treatment design. SPE Annual Technical Conference and Exhibition, Denver, Colorado. Paper SPE 115769.

Cipolla, C.L., Lolon, E.P., Erdle, J.C., Rubin, B., 2010a. Reservoir modeling in shale-gas reservoirs. SPE Reserv. Eval. Eng. 13 (4), 638–653.

Cipolla, C.L., Lolon, E.P., Mayerhofer, M.J., Warpinski, N.R., 2010b. In: The effect of proppant distribution and un-propped fracture conductivity on well performance in unconventional gas reservoirs. SPE Hydraulic Fracturing Technology Conference, The Woodlands, Texas. Paper SPE 119368.

Cipolla, C., Mack, M., Maxwell, S., 2010c. In: Reducing exploration and appraisal risk in low permeability reservoirs using microseismic fracturing mapping – Part 2. SPE Latin American & Caribbean Petroleum Engineering Conference, Lima, Peru. Paper SPE 138103.

CMG-GEM, 2012. GEM User's Guide. Computer Modeling Group Ltd, Calgary.

CMG-IMEX, 2012. IMEX User's Guide. Computer Modeling Group Ltd, Calgary.

Crespo, F., Aven, N.K., Cortez, J., Soliman, M.Y., Bokane, A., Jain, S., Deshpande, Y., 2013. In: Proppant distribution in multistage hydraulic fractured wells: a large-scale inside-casing investigation. SPE Hydraulic Fracturing Technology Conference, The Woodlands, Texas. Paper SPE 163856.

Daneshy, A., 2011. Uneven distribution of proppants in perf clusters. World Oil. 232(4).

Daneshy, A., 2013. Horizontal well fracturing: a state-of-the-art report. World Oil. 234(7).

Das, M., Jonk, R., Schelble, R., 2012. In: Effect of multicomponent adsorption/desorption behavior on gas-in-place (GIP) calculations and estimation of free and adsorbed CH_4 and CO_2 in shale gas systems. SPE Annual Technical Conference and Exhibition, San Antonio, Texas. Paper SPE 159558.

Evans, R.D., Civan, F. 1994. Characterization of non-Darcy multiphase flow in petroleum bearing formations. Report, U.S. DOE Contract No. DE-AC22-90BC14659, School of Petroleum and Geological Engineering, University of Oklahoma.

Fan, L., Thompson, J.W., Robinson, J.R., 2010. In: Understanding gas production mechanism and effectiveness of well stimulation in the Haynesville shale through reservoir simulation. The Canadian Unconventional Resources and International Petroleum Conference, Calgary, Canada. CSUG/SPE 136696.

Forchheimer, P.H., 1901. Wasserbewegung durch boden [Movement of water through soil]. Zeitschr Ver deutsch Ing 49, 1736–1749.

Gale, J.F.W., Reed, R.M., Holder, J., 2007. Natural fractures in the Barnett shale and their importance for hydraulic fracture treatments. AAPG Bull. 91 (4), 603–622.

Grieser, B., Shelley, B., Soliman, M., 2009. In: Prediction production outcome from multi-stage, horizontal Barnett completions. SPE Production and Operations Symposium, Oklahoma City, Oklahoma. Paper SPE 120271.

Ikewun, P., Ahmadi, M., 2012. In: Production optimization and forecasting of shale gas wells using simulation models and decline curve analysis. SPE Western Regional Meeting, Bakersfield, California. Paper SPE 153914.

LaFollette, R.F., Carman, P.S., 2010. In: Proppant diagenesis: results so far. SPE Unconventional Gas Conference, Pittsburgh, Pennsylvania. Paper SPE 131782.

Langmuir, I., 1918. The adsorption of gases on plane surfaces of glass, mica and platinum. J. Am. Chem. Soc. 40, 1403–1461.

Leahy-Dios, A., Das, M., Agarwal, A., Kaminsky, R.D., 2011. In: Modeling of transport phenomena and multicomponent sorption for shale gas and coalbed methane in an unstructured grid simulator. SPE Annual Technical Conference and Exhibition, Denver, Colorado. Paper SPE 147352.

Mahoney, R.P., Soane, D., Kincaid, K.P., Herring, M., Snider, P.M., 2013. In: Self-suspending proppant. SPE Hydraulic Fracturing Conference, The Woodlands, Texas. Paper SPE 163818.

Mengal, S.A., Wattenbarger, R.A., 2011. In: Accounting for adsorbed gas in shale gas reservoirs. SPE Middle East Oil and Gas Show and Conference, Manama, Bahrain. Paper SPE 141085.

Meyer, B.R., Bazan, L.W., Jacot, R.H., Lattibeaudiere, M.G., 2010. In: Optimization of multiple transverse hydraulic fractures in horizontal wellbores. SPE Unconventional Gas Conference, Pittsburgh, Pennsylvania. Paper SPE 131732.

Montgomery, S.L., Jarvie, D.M., Bowker, K.A., Pollastro, R.M., 2005. Mississippian Barnett shale, Fort Worth basin, north-Central Texas: gas-shale play with multi-trillion cubic foot potential. AAPG Bull. 89 (2), 155–175.

Nobakht, M., Clarkson, C.R., Kaviani, D., 2012. New and improved methods for performing rate-transient analysis of shale gas reservoirs. SPE Reserv. Eval. Eng. 15 (3), 335–350.

Passey, Q.R., Bohacs, K.M., Esch, W.L., Klimentidis, R., Sinha, S., 2010. In: From oil-prone source rock to gas-producing shale reservoir-geologic and petrophysical characterization of unconventional shale-gas reservoirs. CPS/SPE International Oil & Gas Conference and Exhibition, Beijing, China. Paper SPE 131350.

Pope, C., Benton, T., Palisch, T., 2009. In: Haynesville shale-one operator's approach to well completions in this evolving play. SPE Annual Technical Conference and Exhibition, New Orleans, Louisiana. Paper SPE 125079.

Rafiee, M., Soliman, M.Y., Pirayesh, E., 2012. In: Hydraulic fracturing design and optimization: a modification to zipper frac. SPE Eastern Regional Meeting, Lexington, Kentucky. Paper SPE 159786.

Rubin, B., 2010. In: Accurate simulation of non-Darcy flow in stimulated fractured shale reservoirs. SPE Western Regional Meeting, Anaheim, California. Paper SPE 132093.

Seidle, J.P., Arri, L.E., 1990. In: Use of conventional reservoir models for coalbed methane simulation. CIM/SPE International Technical Meeting, Calgary, Canada. Paper SPE 21599.

Thompson, J.M., M'Angha, V.O., Anderson, D.M., 2011. In: Advancements in shale gas production forecasting—a Marcellus case study. SPE Americas Unconventional Gas Conference and Exhibition, The Woodlands, Texas. Paper SPE 144436.

Vincent, M.C., 2012. The next opportunity to improve hydraulic-fracture stimulation. J. Pet. Technol. 64 (3), 118–127.

Warpinski, N.R., 2009. In: Stress amplification and Arch dimensions in proppant beds deposited by waterfracs. SPE Hydraulic Fracturing Conference, The Woodlands, Texas. Paper SPE 119350.

Warpinski, N.R., Mayerhofer, M.J., Vincent, M.C., Cipolla, C.L., Lolon, E.P., 2008. In: Stimulating unconventional reservoirs: maximizing network growth while optimizing fracture conductivity. SPE Uncoventional Reservoirs Conference, Keystone, Colorado. Paper SPE 114173.

Woodworth, T.R., Miskimins, J.L., 2007. In: Extrapolation of laboratory proppant placement behavior to the field in slickwater fracturing applications. SPE Hydraulic Fracturing Technology Conference, College Station, Texas. Paper SPE 106089.

Wu, K., Olson, J.E., 2013. Investigation of the impact of fracture spacing and fluid properties for interfering simultaneously or sequentially generated hydraulic fractures. SPE Prod. Oper. 28 (4), 427–436.

Yu, W., Sepehrnoori, K., 2013a. Optimization of multiple hydraulically fractured horizontal wells in unconventional gas reservoirs. J. Pet. Eng. 1–18. Article ID 151898.

Yu, W., Sepehrnoori, K., 2013b. In: Numerical evaluation of the impact of geomechanics on well performance in shale gas reservoirs. 47th US Rock Mechanics/Geomechanics Symposium, San Francisco, California. Paper ARMA 13-555.

Yu, W., Sepehrnoori, K., 2014a. Simulation of gas desorption and geomechanics effects for unconventional gas reservoirs. Fuel 116, 455–464.

Yu, W., Sepehrnoori, K., 2014b. In: Sensitivity study and history matching and economic optimization for Marcellus shale. SPE/AAPG/SEG Unconventional Resources Technology Conference, Denver, Colorado. Paper SPE-2014-1923491.

Yu, W., Sepehrnoori, K., 2014c. An efficient reservoir simulation approach to design and optimize unconventional gas production. J. Can. Pet. Technol. 53, 109–121.

Yu, W., Sepehrnoori, K., 2014d. In: Optimization of well spacing for Bakken tight oil reservoirs. SPE/AAPG/SEG Unconventional Resources Technology Conference, Denver, Colorado. Paper SPE-2014-1922108.

Yu, W., Gao, B., Sepehrnoori, K., 2014a. Numerical study of the impact of complex fracture patterns on well performance in shale gas reservoirs. J. Pet. Sci. Res. 3 (2), 83–89.

Yu, W., Lashgari, H., Sepehrnoori, K., 2014b. In: Simulation study of CO_2 huff-n-puff process in Bakken tight oil reservoirs. SPE Western North American and Rocky Mountain Joint Regional Meeting, Denver, Colorado. Paper SPE 169575.

Yu, W., Zhang, T., Du, S., Sepehrnoori, K., 2015. Numerical study of the effect of uneven proppant distribution between multiple fractures on shale gas well performance. Fuel 142, 189–198.

Zuber, M.D., Williamson, J.R., hill, D.G., Sawyer, W.K., Frantz, J.H., 2002. In: A comprehensive reservoir evaluation of a shale reservoir – the New Albany shale. SPE Annual Technical Conference and Exhibition, San Antonio, Texas. Paper SPE 77469.

Chapter 3

Semianalytical Model for Shale Gas and Tight Oil Simulation

Chapter Outline

3.1 INTRODUCTION

In the last decade, the technical advancements in horizontal drilling and multistage fracturing had led to a boom in the development of unconventional resources such as shale gas and tight oil in the United States and abroad. The effectiveness of fracturing stimulation treatment plays an important role in economic production of these unconventional reservoirs (Weng, 2014). Microseismic monitoring of hydraulic fracture treatments plays a significant role in understanding the stimulation effectiveness and fracture geometry (Cipolla et al., 2012). Microseismic measurements indicate that the stimulation treatments often create complex fracture geometry, especially in the brittle shale reservoirs (Maxwell et al., 2002; Fisher et al., 2002; Warpinski et al., 2005; Cipolla

Shale Gas and Tight Oil Reservoir Simulation. https://doi.org/10.1016/B978-0-12-813868-7.00003-1

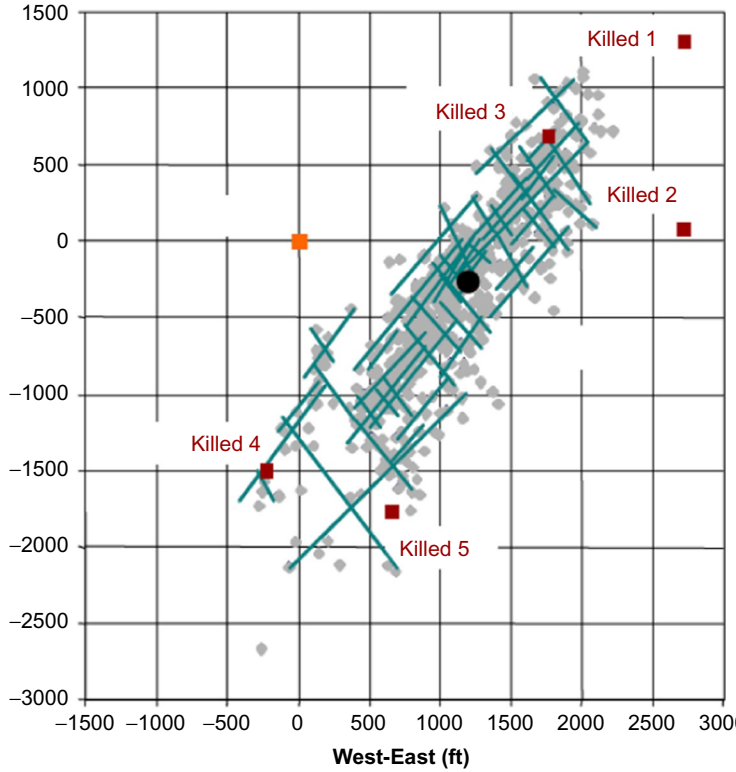

FIG. 3.1 Complex fracture geometry in a vertical well (Fisher et al., 2004).

and Wallace, 2014). Fig. 3.1 shows one an example indicating the complex fracture geometry created in a vertical well. The complex fracture geometry is strongly affected by in situ stresses and pre-existing natural fractures (Zhou et al., 2013; Weng, 2014). Although many attempts have been focused on developing hydraulic fracture propagation models to predict the complex nonplanar fracture geometry (Wu et al., 2012; Xu and Wong, 2013; Wu and Olson, 2013, 2014, 2015a; Wu, 2014), it is still challenging to measure the complex fracture geometry completely and exactly.

For the sake of simplicity, two idealized fracture geometries such as biwing fractures and orthogonal fracture networks are widely used to represent the complex geometry for simulation of well performance in unconventional reservoirs (Yu and Sepehrnoori, 2013a,b,c; Tavassoli et al., 2013a,b; Aybar et al., 2015), as shown in Fig. 3.2. In addition, such fracture geometries can be easily handled by analytical solutions, semianalytical solutions, and numerical solutions (Gringarten et al., 1972; Gringarten and Rameny, 1973; Cinco-Ley and Samaniego-V, 1981; Guppy et al., 1982; Blasingame and Poe, 1993; Chen and Raghavan, 1997; Khan et al., 2011; Yu et al., 2014a; Shakiba, 2014). In general, local grid refinement (LGR) is employed by using numerical solutions

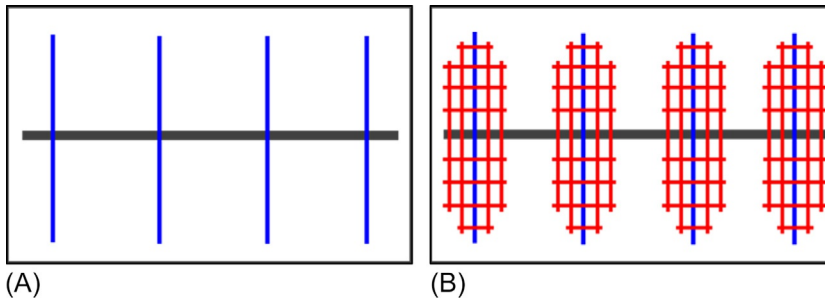

FIG. 3.2 Two ideal fracture geometries used for simulation of well production in shale reservoirs (Yu et al., 2014a). (A) Biwing fractures. (B) Orthogonal fracture networks.

to model hydraulic fracture explicitly with a small and constant fracture width but a larger permeability, which can effectively capture the transient flow behavior in fractured shale reservoirs (Rubin, 2010; Yu et al., 2014b,c,d; Yu and Sepehrnoori, 2014a,b,c; Yu et al., 2015a,b).

In recent years, significant efforts have been made to model well performance from the complex fracture geometry. Xu et al. (2010) developed a wire-mesh model to simulate the elliptical fracture network. However, the wire-mesh model is difficult to simulate nonorthogonal fracture network. Weng et al. (2011) developed an unconventional fracture model (UFM) to predict the complex fracture geometry, which can be integrated with a numerical reservoir simulator using the automatic generation of unstructured grids to properly simulate production from the complex fracture geometry (Cipolla et al., 2011; Mirzaei and Cipolla, 2012). However, this approach has some practical challenging such as the difficulties of model set-up and long turnaround time (Zhou et al., 2013). Olorode et al. (2013) proposed a 3D Voronoi mesh-generation application to generate the nonideal fracture geometry for simulator to investigate the effect of irregular fracture geometry on well performance of unconventional gas reservoirs. Moinfar et al. (2013) developed an embedded discrete fracture model (EDFM) based on the algorithm presented by Li and Lee (2008) to simulate fluid flow from unstructured fracture geometry. However, these numerical approaches are still challenging to use efficiently due to a very complicated gridding issue or an expensive computational cost or complexities in development of computational codes. In order to overcome these challenges, Zhou et al. (2013) proposed a semianalytical model to handle the complex fracture geometry efficiently. However, the semianalytical model did not consider the effects of gas slippage, gas diffusion, gas desorption, pressure-dependent fracture conductivity, and complex nonplanar fractures. In reality, the complex nonplanar fracture geometry with varying fracture width and fracture permeability is often generated, especially in the deviated wells (Olson, 1995; Olson and Wu, 2012), as shown in Figs. 3.3 and 3.4. However, most production simulation models only assume hydraulic fractures with

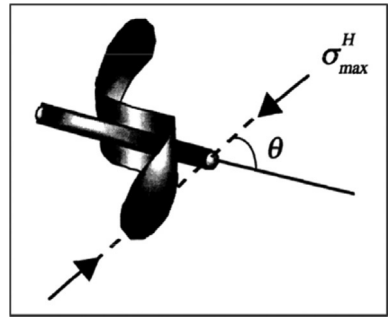

FIG. 3.3 A single curving nonplanar hydraulic fracture (Olson, 1995).

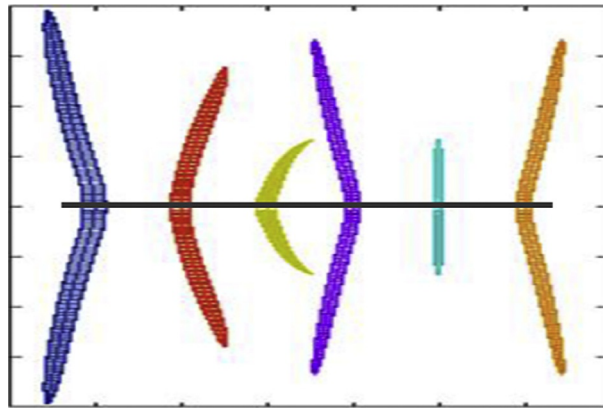

FIG. 3.4 Multiple curving nonplanar hydraulic fractures (Wu, 2014).

constant width. Furthermore, gas transport mechanisms such as gas slippage, gas diffusion, and gas desorption in shale reservoirs are still poorly understood. Hence, an efficient model to simulate production from the complex nonplanar fractures by considering the flow mechanisms stated here is still lacking in the petroleum industry. Henceforth, significant efforts are still required to develop an efficient model to fill this gap and evaluate the well performance of unconventional reservoirs with the complex nonplanar fractures.

In this chapter, we presented a semianalytical model to simulate production from multiple nonplanar fractures. Also, the effects of important gas transport mechanisms, non-Darcy flow, and pressure-dependent fracture conductivity are considered. More importantly, the diffusivity equation of conventional gas reservoirs was modified to model gas flow in shale reservoirs and fully implemented in the semianalytical model. We verified the semianalytical model against a numerical reservoir simulator of CMG-GEM (CMG-GEM, 2012) for rectangular fractures and planar fracture with varying width. We performed a series of

case studies for simulation of production from shale gas and tight oil reservoirs. This work provides an efficient production simulation model to simulate fluid flow from unconventional reservoirs with the complex nonplanar hydraulic fractures, which can provide critical insights into understanding the stimulation effectiveness for the field development of unconventional reservoirs.

3.2 MODEL ASSUMPTION AND FRACTURE DISCRETIZATION

The following assumptions are made for the semianalytical model development:

- the well is intercepted by fully penetrating fractures;
- the reservoir is bounded by an upper and a lower impermeable layer;
- the reservoir is isotropic and homogeneous with a constant height, porosity, and permeability;
- the initial reservoir pressure is uniform;
- for tight oil reservoirs, the reservoir contains a slightly compressible fluid with constant oil density, viscosity, and compressibility;
- fluid flow takes place only through fractures;
- there is no pressure loss along the wellbore;
- the pressure gradients are so small that the gravity effect is negligible.

Under these assumptions, the diffusivity equation can be used to describe the flow behavior (Matthews and Russell, 1967). The semianalytical model mainly consists of two parts describing fluid flow from reservoir to the wellbore. The first is fluid flow from shale to fractures. The second is fluid flow from fractures to wellbore, as shown in Fig. 3.5. More details about these two parts will be introduced and discussed in the following sections.

In order to capture the complex nonplanar fracture geometry, the hydraulic fracture in this model will be discretized into some fracture segments (N_f) and the associated nodes (N_v) connecting these segments. Fig. 3.6 presents two examples for the discretization of complex fractures. One example has a single well with three nonplanar hydraulic fractures, which are divided into 16 small fracture segments with 19 nodes. Another example has two horizontal wells with eight nonplanar hydraulic fractures, which are divided into 51 fracture segments (numbering in red color sequentially) and the corresponding 55 nodes (numbering in black color sequentially). Each fracture segment has specific properties such as fracture length, fracture orientation, and fracture aperture. The model thus approximately represents nonplanar fractures with nonuniform spatial distribution of fracture conductivity.

3.3 MODEL DEVELOPMENT FOR SHALE GAS SIMULATION

Gas transport through shale formation with a large amount of nanopores and extremely low permeability is quite different from conventional gas reservoirs,

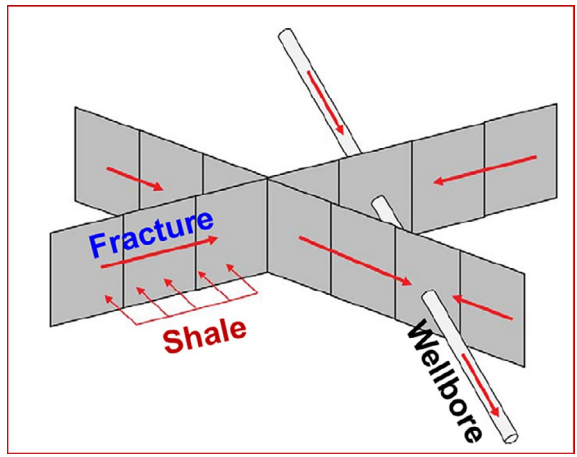

FIG. 3.5 Fluid flow from shale to fracture, then from fracture to wellbore, finally from wellbore to surface. *(Modified from Zhou, W., Banerjee, R., Poe, B., Spath, J., Thambynayagam, M., 2013. Semi-analytical production simulation of complex hydraulic-fracture networks. SPE J. 19 (1), 6–18.)*

where the laminar flow is dominant. It is generally agreed that the main flow mechanisms involved in shale gas reservoirs include not only gas advection, but also gas slippage, gas diffusion, and gas desorption. Hence, the diffusivity equation for conventional gas reservoirs should be modified by taking into account all these important flow mechanisms. In addition, gas velocity along the fracture is so high that non-Darcy flow effect should be considered. Also, the geomechanics effect, which is mainly focused on pressure-dependent fracture conductivity, should be taken into account in the model. More details about the modification of the diffusivity equation, non-Darcy flow effect, and geomechanics effect will be discussed in the following sections.

3.3.1 Continuity Equation for Conventional Gas Reservoirs

The well-known diffusivity equation is widely used in the petroleum industry to describe the conventional gas flow in porous media under the isotherm condition (Dake, 1978). It can be expressed below if neglecting the gas gravity effect and the source terms:

$$\frac{\partial\left(\rho_g\phi\right)}{\partial t}-\nabla\cdot\left(\frac{\rho_g k}{\mu_g}\nabla p\right)=0, \tag{3.1}$$

where ρ_g is gas density, ϕ is rock porosity, k is reservoir permeability, and μ_g is gas viscosity.

Al-Hussainy et al. (1966) introduced the concept of real gas pseudopressure to simplify the nonlinear diffusivity equation, which is defined by

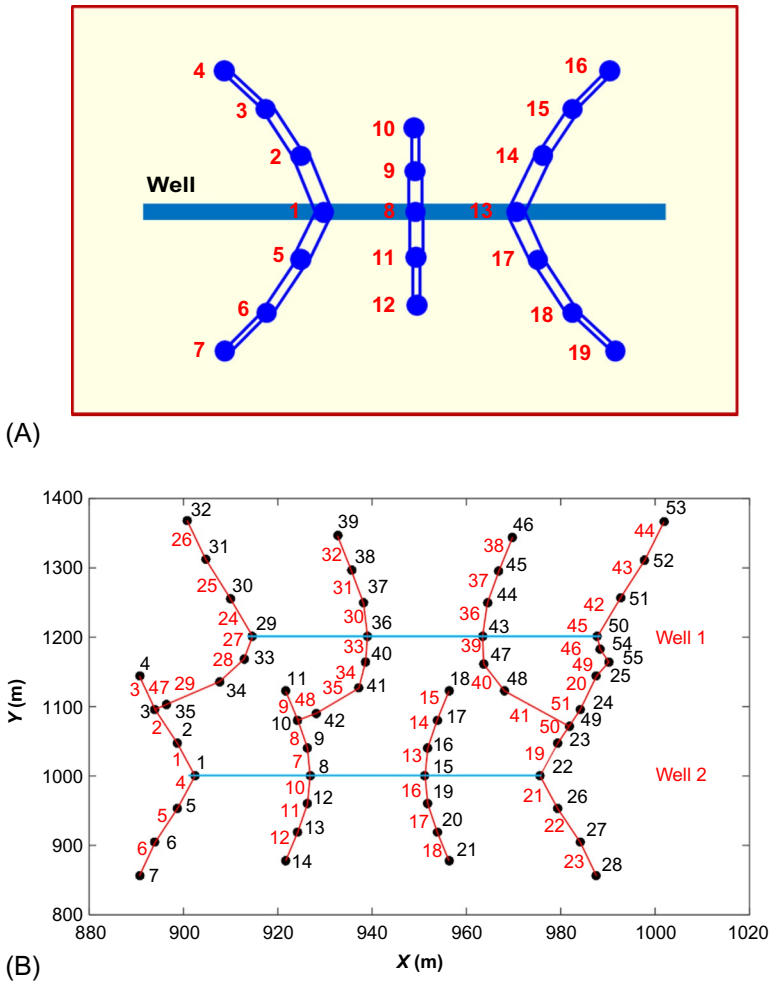

FIG. 3.6 Examples of fracture discretization. (A) Single well with 16 fracture segments and 19 nodes (Yu et al., 2017a). (B) Two wells with 51 fracture segments and 55 nodes (Yu et al., 2016b).

$$m(p) = 2\int_{p*}^{p} \frac{p}{\mu_g(p) Z_g(p)} dp, \tag{3.2}$$

where p^* is reference pressure. The final continuity equation is obtained as follows:

$$\frac{\partial^2 m(p)}{\partial x^2} + \frac{\partial^2 m(p)}{\partial y^2} + \frac{\partial^2 m(p)}{\partial z^2} = \frac{\phi c_g \mu_g}{k} \frac{\partial m(p)}{\partial t}. \tag{3.3}$$

This equation in combination with different initial and boundary conditions can be solved using exact numerical solution or approximate analytical solution. However, it is still inadequate to describe gas flow in shale reservoirs over the entire timescale of production due to many physical mechanisms such as gas diffusion, gas slippage, and gas desorption are ignored (Xu, 2014).

3.3.2 Continuity Equation for Shale Gas Reservoirs

In recent years, increased consideration has been given to modify the continuity for conventional gas transport to accurately model gas flow in shale reservoirs, which should fully couple the different gas transport mechanisms.

3.3.2.1 Gas Diffusion

Molecular diffusion occurs due to the molecules concentration difference, which is defined as "the process by which matter is transported from one part of a system to another as a result of random molecular motions" (Crank, 1975). Fig. 3.7 demonstrates the Darcian flow due to pressure gradient and Fickian flow due to concentration gradient. The green circles display the gas molecules. The big arrow represents the Darcian flow direction while the small arrows indicate the random flow. As shown in Fig. 3.7A, the difference of pressure is the driving force for the Darcian flow and there is a zero net effect for the Fickian flow due to the equal densities. However, as illustrated in Fig. 3.7B, the difference of density is the driving force for the Fickian flow.

The molecule diffusion process is governed by Fick's law (Ertekin et al., 1986; Bird et al., 2007):

$$J = -D\nabla C, \tag{3.4}$$

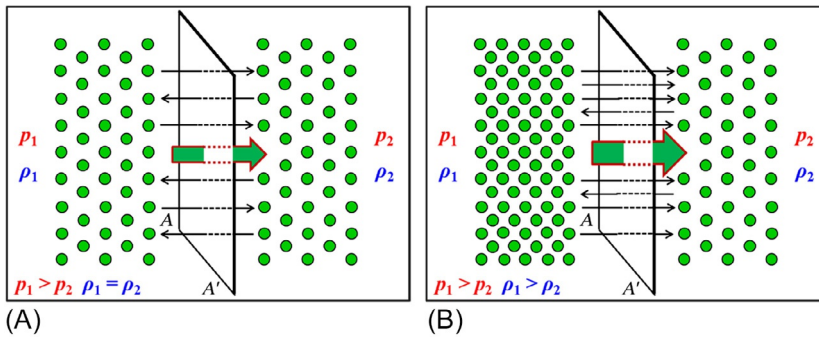

FIG. 3.7 Schematic representation of Darcian flow due to pressure gradient and Fickian flow due to concentration gradient. (A) Darcian flow. (B) Darcian flow and Fickian flow. *(Modified from Ertekin, T., King, G.R., Schwerer, F.C., 1986. Dynamic gas slippage: a unique dual-mechanism approach to the flow of gas in tight formations. SPE Form. Eval. 1 (1), 43–52.)*

where J is diffusion flux, C is molar concentration, and D is diffusivity coefficient, which is a property of the transported substance and the medium. In a saturated porous medium, Fick's law can be written as follows:

$$J = -D_{eff}\nabla C, \tag{3.5}$$

where D_{eff} is the effective diffusivity coefficient, which is related to the free-solution diffusion coefficient as (Xu, 2014):

$$D_{eff} = \frac{\delta}{\tau}\phi D_0, \tag{3.6}$$

where D_0 is bulk diffusivity in free solution, δ is a dimensionless constrictivity factor (≤ 1), which accounts for variation of the pore size along its length caused by small pores, and τ is a dimensionless tortuosity factor (≥ 1), accounting for the elongated diffusion path compared to the straight path (Carman, 1956). There are two classes to define the dimensionless tortuosity as follows (Dullien, 1979; McDuff and Ellis, 1979):

$$\tau = \frac{L_e}{L}, \tag{3.7}$$

or

$$\tau = \left(\frac{L_e}{L}\right)^2, \tag{3.8}$$

where L_e is the effective diffusion length and L is geometrical length of the medium. The tortuosity for the gas flow in porous medium can be estimated from porosity and gas saturation by (Dullien, 1979)

$$\tau = \frac{1}{\phi^{1/3}S_g^{7/3}}. \tag{3.9}$$

The dimensionless constrictivity factor, which depends on the ratio of molecule diameter to the pore diameter, is quantified by the empirical equation developed by Satterfield et al. (1973).

$$\delta = \left(1 - \frac{d_{\text{gas}}}{d_{\text{pore}}}\right)^2, \tag{3.10}$$

where d_{gas} is gas molecule diameter and d_{pore} is the pore diameter.

For a real gas, gas density is given by

$$\rho_g = \frac{pM}{ZRT}, \tag{3.11}$$

where p is pressure in kPa, M is the molecule weight of the gas ($M = \gamma_g M_{air}$, where γ_g is gas specific gravity and M_{air} is air molecular weight and equals 29 kg/kmol), R is the ideal gas constant with 8.3145 kPa m^3/(kmol·K), and T

is absolute temperature (K), Z is the gas compressibility factor. The gas molar concentration can be obtained as follows:

$$C = \frac{\rho_g}{M}. \tag{3.12}$$

The actual gas diffusion process is very complex, which might be the combination of three distinct mechanisms acting individually or simultaneously: bulk diffusion (molecule/molecule collisions dominate the gas transport), Knudsen diffusion (molecule-pore wall collisions dominate the gas transport), and surface diffusion (transport of adsorbed molecule layer) (Smith and Williams, 1984), as shown in Fig. 3.8.

The gas transport equation will be expressed here by considering the gas diffusion effect:

$$\frac{\partial\left(\rho_g\phi\right)}{\partial t} - \nabla\cdot\left(\frac{\rho_g k}{\mu_g}\nabla p + \frac{\delta}{\tau}\phi D_g \nabla\rho_g\right) = 0. \tag{3.13}$$

The relationship between gas density gradient and pressure gradient is given by

$$\nabla\rho_g = \rho_g c_g \nabla p, \tag{3.14}$$

where c_g is the isothermal gas compressibility factor, which can be determined as

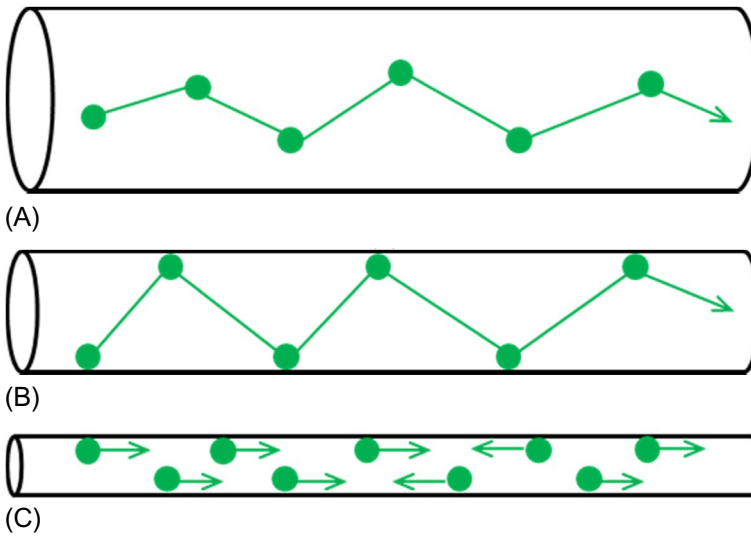

FIG. 3.8 Three distinct types of molecular diffusion. (A) Bulk diffusion. (B) Knudsen diffusion. (C) Surface diffusion.

$$c_g = \frac{1}{\rho_g}\left(\frac{\partial \rho_g}{\partial p}\right)_T. \tag{3.15}$$

Substituting Eq. (3.14) into Eq. (3.13), the gas transport equation can be modified as follows:

$$\frac{\partial\left(\rho_g \phi\right)}{\partial t} - \nabla \cdot \left(\frac{\rho_g k}{\mu_g}\nabla p + \frac{\delta}{\tau}\phi D_g \rho_g c_g \nabla p\right) = 0. \tag{3.16}$$

Eq. (3.16) can be simplified here through changing initial matrix permeability to apparent matrix permeability to account for the gas diffusion effect:

$$\frac{\partial\left(\rho_g \phi\right)}{\partial t} - \nabla \cdot \left(\frac{\rho_g k_a}{\mu_g}\nabla p\right) = 0, \tag{3.17}$$

$$k_a = k\left[1 + \frac{\mu_g}{k}\frac{\delta}{\tau}\phi D_g c_g\right], \tag{3.18}$$

where k_a is apparent matrix permeability.

3.3.2.2 Gas Slippage

Gas slippage is often described by the Klinkenberg effect, as shown in Fig. 3.9. The continuity equation will be expressed by the following expression by considering the Klinkenberg effect (Xu, 2014):

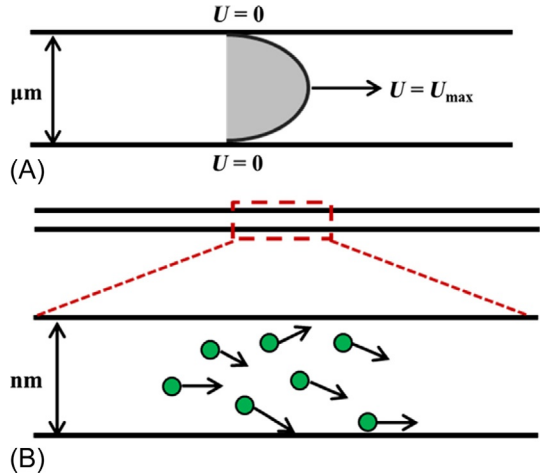

FIG. 3.9 Comparison of gas flow in micropores and nanapores. (A) Darcy flow in micropores. (B) Slip flow in nanopores. *(Modified from Javadpour, F., Fisher, D., Unsworth, M., 2007. Nanoscale gas flow in shale gas sediments. J. Can. Pet. Technol. 46 (10), 55–61.)*

$$u_g = -\frac{k(1+8\alpha K_n)}{\mu_g}\nabla p, \tag{3.19}$$

where α is a constant and close to 1, K_n is Knudsen number, which is defined by (Bird, 1994)

$$K_n = \frac{\lambda}{d}, \tag{3.20}$$

where d is the pore diameter, λ is the mean free path of gas molecules, which is defined by (Heidemann et al., 1984)

$$\lambda = \frac{k_B T}{\sqrt{2}\pi\sigma^2 p}, \tag{3.21}$$

where k_B is the Boltzmann constant (1.3805×10^{-23} J/K), T is temperature in K, p is pressure in Pa, and σ is diameter of gas molecules.

The gas transport equation will be altered by considering the gas diffusion and Klinkenberg effects together:

$$\frac{\partial\left(\rho_g\phi\right)}{\partial t} - \nabla\cdot\left[\frac{\rho_g k(1+8\alpha K_n)}{\mu_g}\nabla p + \frac{\delta}{\tau}\phi D_g \rho_g c_g \nabla p\right] = 0. \tag{3.22}$$

The apparent matrix permeability will become

$$k_a = k\left[1 + 8\alpha K_n + \frac{\mu_g}{k}\frac{\delta}{\tau}\phi D_g c_g\right]. \tag{3.23}$$

In addition, depending on the Knudsen number, Karniadakis and Beskok (2002) proposed four different flow regimes: (1) continuum flow regime ($K_n < 0.01$); (2) slip-flow regime ($0.01 < K_n < 0.1$); (3) transition regime ($0.1 < K_n < 10$); and (4) free molecular flow regime ($K_n > 10$). Florence et al. (2007) proposed an apparent permeability model to account for the gas slippage and gas diffusion effect in shale reservoirs with low and ultralow permeability:

$$k_a = k[1 + \alpha(K_n)K_n]\left(1 + \frac{4K_n}{1+K_n}\right), \tag{3.24}$$

where $\alpha(K_n)$ represents the rarefaction parameter, which is calculated by (Karniadakis and Beskok, 2002)

$$\alpha(K_n) = \frac{128}{15\pi^2}\tan^{-1}\left(4K_n^{0.4}\right). \tag{3.25}$$

3.3.2.3 Gas Desorption

The continuity equation to describe gas transport in shale reservoirs by considering the gas desorption effect is given as:

$$\frac{\partial\left[\rho_g\phi+(1-\phi)\rho_a\right]}{\partial t}-\nabla\cdot\left(\frac{\rho_g k_a}{\mu_g}\nabla p\right)=0, \tag{3.26}$$

where ρ_a is adsorbed gas mass per unit shale sample volume. Expansion of the left-side term of Eq. (3.26) results in the following expression:

$$\frac{\partial\left[\rho_g\phi+(1-\phi)\rho_a\right]}{\partial t}\approx\phi\frac{\partial\rho_g}{\partial p}\frac{\partial p}{\partial t}+(1-\phi)K_a\frac{\partial\rho_g}{\partial p}\frac{\partial p}{\partial t}, \tag{3.27}$$

where K_a is the differential equilibrium portioning coefficient of gas at a constant temperature, which is function of pressure and temperature and defined as (Cui et al., 2009; Patzek et al., 2013):

$$K_a=\left(\frac{\partial\rho_a}{\partial\rho_g}\right)_T. \tag{3.28}$$

Substituting Eqs. (3.27) and (3.28) into Eq. (3.26), the general nonlinear equation of transient gas flow in shale gas reservoirs is obtained:

$$\nabla\cdot\left(\frac{\rho_g k_a}{\mu_g}\nabla p\right)=[\phi+(1-\phi)K_a]c_g\rho_g\frac{\partial p}{\partial t}. \tag{3.29}$$

For the gas desorption effect, the mass balance of adsorbed gas in one unit bulk volume is described by

$$\rho_a V_b(1-\phi)=\rho_g(p_{ST},T_{ST})\rho_b V_b v, \tag{3.30}$$

where ρ_b is bulk density of shale, V_b is unit volume of bulk rock, v is the specific volume of gas adsorbed per unit mass of bulk rock (SCF/ton), which is measured at the reservoir pressure and temperature and then transferred to standard condition, $\rho_g(p_{ST},T_{ST})$ is the stock tank gas density. The adsorbed gas density per unit shale volume at the standard condition can be calculated as follows:

$$\rho_a=\frac{\rho_g(p_{ST},T_{ST})\rho_b v}{1-\phi}. \tag{3.31}$$

The differential equilibrium partitioning coefficient of gas can be expressed by

$$K_a=\left(\frac{\partial\rho_a}{\partial\rho_g}\right)_T=\frac{\rho_g(p_{ST},T_{ST})\rho_b}{1-\phi}\frac{\partial v}{\partial p}\frac{\partial p}{\partial\rho_g}=\frac{\rho_g(p_{ST},T_{ST})\rho_b}{(1-\phi)\rho_g c_g}\frac{\partial v}{\partial p}. \tag{3.32}$$

Adsorption at the gas/solid interface is referred to as the enrichment of one or more components in an interfacial layer (Sing et al., 1985). The organic matter in shale has a strong adsorption potential due to the large surface area and affinity to methane. In order to simulate gas production in shale gas reservoirs,

an accurate model of gas adsorption is very important. According to the International Union of Pure and Applied Chemistry (IUPAC) standard classification system (Sing et al., 1985), there are six different types of adsorption. The shape of the adsorption isotherm is closely related to the properties of adsorbate and solid adsorbent and the pore-space geometry (Silin and Kneafsey, 2012). The detailed description of the six isotherm classifications can be found in Sing et al. (1985).

The most commonly applied adsorption model for shale gas reservoirs is the classic Langmuir isotherm (Type I) (Langmuir, 1918), which is based on the assumption that there is a dynamic equilibrium at constant temperature and pressure between adsorbed and nonadsorbed gas. Also, it is assumed that there is only a single layer of molecules covering the solid surface, as shown in Fig. 3.10A. The Langmuir isotherm has two fitting parameters:

$$v = \frac{pv_L}{p + p_L}, \tag{3.33}$$

where v_L is the Langmuir volume, referred to as the maximum gas volume of adsorption at the infinite pressure, and p_L is the Langmuir pressure, which is the pressure corresponding to one-half Langmuir volume. Instantaneous equilibrium of the sorbing surface and the storage in the pore space is assumed to be established for the Langmuir isotherm (Freeman et al., 2012). Gao et al. (1994) demonstrated that the instantaneous equilibrium is a reasonable assumption because the ultralow permeability in shale leads to very low gas flow rate through the kerogen component of shale.

At high reservoir pressures, on can expect that natural gas sorbed on the organic carbon surfaces forms multimolecular layers. In other words, the Langmuir isotherm may not be a good approximation of the amount of gas sorbed on organic carbon-rich mudrocks. Instead, multilayer sorption of natural gas should be expected on organic carbon surfaces, and the gas adsorption isotherm of Type II should be a better choice. Type II isotherm often occurs in a

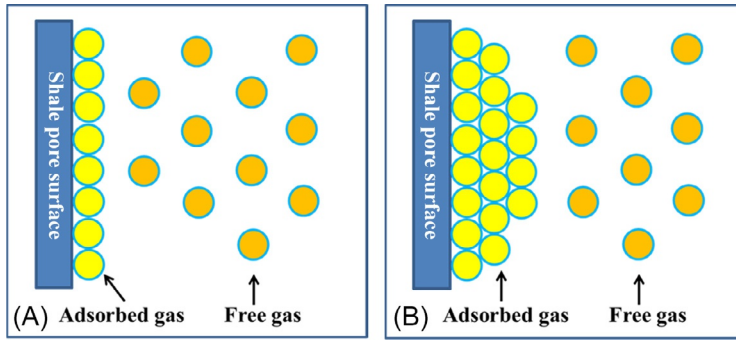

FIG. 3.10 Schematic plot of monolayer and multilayer gas adsorption (Yu et al., 2014e). (A) Monolayer Langmuir adsorption. (B) Multilayer BET adsorption.

nonporous or a macroporous material (Kuila and Prasad, 2013). In 1938, Stephen Brunauer, Paul Hugh Emmett, and Edward Teller (BET) published their theory in the *Journal of the American Chemical Society* (Brunauer et al., 1938). The BET isotherm model is a generalization of the Langmuir model to multiple adsorbed layers, as shown in Fig. 3.10B. The expression is shown as:

$$v = \frac{v_m C p}{(p_o - p)[1 + (C-1)p/p_o]}, \tag{3.34}$$

where p_o is the saturation pressure of the gas; v_m is the maximum adsorption gas volume when the entire adsorbent surface is being covered with a complete monomolecular layer; and C is a constant related to the net heat of adsorption, which is defined as:

$$C = \exp\left(\frac{E_1 - E_L}{RT}\right), \tag{3.35}$$

where E_1 is the heat of adsorption for the first layer, and E_L is that for the second and higher layers and is equal to the heat of liquefaction. The assumptions in the BET theory include homogeneous surface, no lateral interaction between molecules, and the uppermost layer is in equilibrium with gas phase. The standard BET isotherm assumes that the number of adsorption layers is infinite. But, in the case of n adsorption layers in some finite number, then a general form of BET isotherm is given:

$$v = \frac{v_m C \dfrac{p}{p_o}}{1 - \dfrac{p}{p_o}} \left[\frac{1 - (n+1)\left(\dfrac{p}{p_o}\right)^n + n\left(\dfrac{p}{p_o}\right)^{n+1}}{1 + (C-1)\dfrac{p}{p_o} - C\left(\dfrac{p}{p_o}\right)^{n+1}} \right]. \tag{3.36}$$

When $n = 1$, Eq. (3.36) reduces to the Langmuir isotherm, Eq. (3.33). When $n = \infty$, Eq. (3.36) will reduce to Eq. (3.34).

It should be noted that it is very challenging to apply the BET model to physically explain the supercritical methane adsorption since there is no concept of a liquid if the reservoir temperature is above the critical methane temperature. Consequently, the saturation pressure (p_o) also loses its physical meaning (Ozdemir, 2004). To avoid this issue, the saturation pressure (p_o) is treated as pseudosaturation pressure (p_s) for the high-pressure/temperature methane adsorption (Clarkson et al., 1997). Clarkson et al. (1997) summarized various methods to estimate the pseudosaturation pressure at any temperature above critical temperature. The method of extrapolation of the Antoine equation is used to calculate the pseudosaturation pressure for supercritical methane adsorption as follows (NIST, 2011; Hao et al., 2014):

$$\ln p_s = 7.7437 - \frac{1306.5485}{19.4362 + T}, \tag{3.37}$$

where T is temperature (K) and p_s is pseudosaturation pressure (MPa).

Consequently, for the Langmuir isotherm equation, the differential equilibrium partitioning coefficient of gas can be expressed as

$$K_a = \left(\frac{\partial \rho_a}{\partial \rho_g}\right)_T = \frac{\rho_g(p_{ST}, T_{ST})\rho_b}{(1-\phi)c_g\rho_g}\frac{v_L p_L}{(p_L+p)^2} = \frac{\rho_g(p_{ST}, T_{ST})\rho_b}{(1-\phi)c_g\rho_g}\frac{v^2 p_L}{v_L p^2}. \tag{3.38}$$

For the general form of BET isotherm, the differential equilibrium partitioning coefficient of gas can be expressed as

$$K_a = \left(\frac{\partial \rho_a}{\partial \rho_g}\right)_T = \frac{\rho_g(p_{ST}, T_{ST})\rho_b}{(1-\phi)c_g\rho_g} \times \left(A - B + \frac{v p_s}{p(p_s - p)}\right), \tag{3.39}$$

$$A = \frac{v_m C p}{p_s(p_s - p)} \times \frac{n(n+1)\left(\frac{p}{p_s}\right)^n - n(n+1)\left(\frac{p}{p_s}\right)^{n-1}}{1 + (C-1)\frac{p}{p_s} - C\left(\frac{p}{p_s}\right)^{n+1}}, \tag{3.40}$$

$$B = \frac{v}{p_s} \times \frac{C - 1 - C(n+1)\left(\frac{p}{p_s}\right)^n}{1 + (C-1)\frac{p}{p_s} - C\left(\frac{p}{p_s}\right)^{n+1}}. \tag{3.41}$$

In order to account for the adsorbed gas porosity, the adsorbed gas density is needed first. Note that the direct measurement of the adsorbed gas density is difficult and it is typically assumed that the adsorbed gas density is equal to the liquid-phase density; however, in many cases where the pore volume is dominated by micropores, the adsorbed gas density is larger than that of the liquid-phase density (Mosher et al., 2013). In addition, Mosher et al. (2013) pointed out that the molecular simulation can provide the unique opportunity to predict the adsorbed gas density. In this study, the adsorbed gas density of methane is calculated by the following equation, which was proposed by Riewchotisakul and Akkutlu (2015) based on the nonequilibrium molecular dynamic simulation to account for the change of adsorbed phase density with pressure in organic nanopores.

$$\rho_{ag} = 0.1057 \ln(p) - 0.4629, \tag{3.42}$$

where ρ_{ag} is adsorbed gas density within nanopores, g/cm^3; p is pressure, psi.

Ambrose et al. (2012) proposed a new method to calculate the free gas volume by considering the volume occupied by the adsorbed gas on the surface based on the Langmuir isotherm equation. The porosity occupied by adsorbed gas based on the Langmuir isotherm is

$$\phi_{ag} = 1.318 \times 10^{-6} M \frac{\rho_b}{\rho_{ag}} \times \left(\frac{v_L p}{p + p_L} \right). \tag{3.43}$$

The model can be modified for calculating original gas in place proposed by Ambrose et al. (2012) by considering the BET isotherm. The porosity occupied by adsorbed is modified as follows for the BET isotherm:

$$\phi_{ag} = 1.318 \times 10^{-6} M \frac{\rho_b}{\rho_{ag}} \times \frac{v_m C \frac{p}{p_o}}{1 - \frac{p}{p_o}} \left[\frac{1 - (n+1)\left(\frac{p}{p_o}\right)^n + n\left(\frac{p}{p_o}\right)^{n+1}}{1 + (C-1)\frac{p}{p_o} - C\left(\frac{p}{p_o}\right)^{n+1}} \right], \tag{3.44}$$

where M is molecular weight of adsorbed gas, lbm/lbmole. It should be noted that the adsorbed gas porosity should satisfy the criterion of $0 \le \phi_{ag} < \phi$. The diffusivity equation for gas transport in shale nanopores by considering the adsorbed gas porosity becomes

$$\nabla \cdot \left(\frac{\rho_g k_a}{\mu_g} \nabla p \right) = \left[\left(\phi - \phi_{ag} \right) + (1 - \phi) K_a \right] c_g \rho_g \frac{\partial p}{\partial t}. \tag{3.45}$$

In addition, the diffusivity equation by considering pore volume occupied by residual water saturation becomes

$$\nabla \cdot \left(\frac{\rho_g k_a}{\mu_g} \nabla p \right) = \left[\left(\phi - \phi_{ag} \right)(1 - S_{wr}) + (1 - \phi) K_a \right] c_g \rho_g \frac{\partial p}{\partial t}. \tag{3.46}$$

3.3.3 Gas Flow From Fractures to Wellbore

There are two scenarios for gas flow from fractures to wellbore based upon the fracture conductivity value, which is defined as the product of fracture width and fracture permeability. For the infinite fracture conductivity, it is often assumed that there is no pressure drop along the fracture (Gringarten et al., 1975). For the finite fracture conductivity, the pressure drop caused by gas flow along the jth fracture segment can be modeled as one dimension for the sake of simplicity, as shown in Fig. 3.11.

Zhou et al. (2013) provided the expressions for calculation of pressure drop along the jth fracture segment by considering both Darcy flow and non-Darcy flow behaviors. For the Darcy flow behavior, the pressure drop along the jth fracture segment is proportional to the fluid velocity and can be calculated as:

$$p_j - p_{j+1} = \int_{y_j}^{y_{j+1}} \left({}^{\mu}/_{\rho k_f w_f h_f} \right)_j \left[q_j + q_{fj}(y - y_j) \right] dy, \tag{3.47}$$

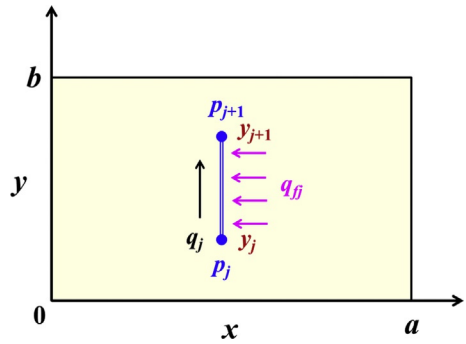

FIG. 3.11 Gas flow along the *j*th fracture segment for the finite fracture conductivity scenario (Yu et al., 2016a).

where k_f is fracture permeability, w_f is fracture width, h_f is fracture height, q_j is fluid flow rate at the node j of the jth fracture segment, q_{fj} is the flux of the jth fracture segment.

For the non-Darcy flow behavior, an additional pressure drop should be taken into account due to the inertial forces as given:

$$p_j - p_{j+1} = \int_{y_j}^{y_{j+1}} \left(\mu/\rho k_f w_f h_f\right)_j \left[q_j + q_{fj}\left(y - y_j\right)\right] dy + \rho\beta \int_{y_j}^{y_{j+1}} \left\{ \frac{\left[q_j + q_{fj}\left(y - y_j\right)\right]^2}{\left(\rho w_f h_f\right)_j^2} \right\} dy, \tag{3.48}$$

where β is the non-Darcy Forchheimer coefficient, which can be determined using the correlation proposed by Evans and Civan (1994) as given:

$$\beta = \frac{1.485 \times 10^9}{k_f{}^{1.021}}, \tag{3.49}$$

where the unit of fracture permeability k_f is md and the unit of β is ft^{-1}. This correlation was obtained based on over 180 data points including those for propped fractures and can match the data very well with the correlation coefficient of 0.974 (Rubin, 2010). This correlation is implemented into the semi-analytical model to account for the non-Darcy flow behavior occurrence in hydraulic fractures.

Mukherjee and Economides (1991) presented that there is a choke skin for radial convergent fracture flow due to inadequate contact between a vertical transverse fracture and a horizontal wellbore. The choking effect will result in an additional pressure drop when gas flow from fracture into wellbore, which is calculated by

$$\Delta p = \frac{Q\mu_g}{2\pi k h_f} s_c, \tag{3.50}$$

$$s_c = \frac{kh_f}{k_f w_f}\left[\ln\left(\frac{h_f}{2r_w}\right) - \frac{\pi}{2}\right], \tag{3.51}$$

where Δp is additional pressure drop, MPa; Q is gas volumetric flow rate, m^3/s; s_c is the choke skin; k_f is fracture permeability, m^2; w_f is fracture width, m; r_w is wellbore radius, m.

3.3.4 Fracture Width and Fracture Permeability Calculations

When the fracture initiation direction (perforation direction) is parallel to the maximum horizontal stress direction, planar fracture with varying fracture width will be generated, as shown in Fig. 3.12. Sneddon (1951) provided an analytical solution to calculate the corresponding fracture width distribution for such planar fracture geometry as follows:

$$w(x) = \frac{4(1-\nu^2)p_{net}}{E}\left(x_f^2 - x^2\right) = w_{\max}\left[1 - \left({}^{x}/_{x_f}\right)^2\right], \tag{3.52}$$

where w is fracture width, $w_{\max}$ is the maximum fracture width at the center of fracture, ν is Poisson ratio, E is Young's modulus, p_{net} is the net pressure (fluid pressure within the fracture minus normal stress acting on the fracture).

If the fracture initiation direction does not coincide with the maximum horizontal stress direction, a curving nonplanar fracture with fracture width restriction near the wellbore will be generated, as shown in Fig. 3.13. The fracture width as shown in the figure has been enlarged by a factor of 400. The

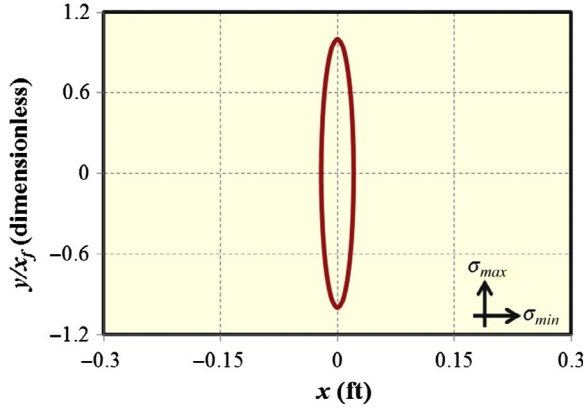

FIG. 3.12 Single planar fracture geometry with varying fracture width along fracture length (Yu et al., 2016a).

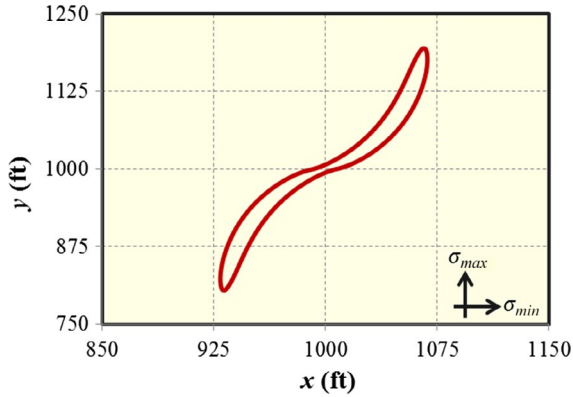

FIG. 3.13 Single curving nonplanar fracture with fracture width restriction near the wellbore (Yu et al., 2016a).

corresponding fracture width distribution is calculated using the fracture propagation model, which is provided by Wu (2014).

Fracture permeability corresponding to fracture width without considering the proppant effect can be calculated by the following expression (Witherspoon et al., 1980):

$$k_f = \frac{w_f^2}{12}, \tag{3.53}$$

where the unit of fracture permeability k_f is cm^2 and the unit of fracture width w_f is cm. In order to consider the effect of proppant inside the fracture, a coefficient multiplied by the Eq. (3.53) can be used.

3.3.5 Pressure-Dependent Fracture Conductivity

Pressure-dependent fracture conductivity means that fracture conductivity is not a constant value, but decreases with the increasing closure pressure due to proppant embedment (Terracina et al., 2010), as shown in Fig. 3.14. Alramahi and Sundberg (2012) presented the laboratory measurement data about the relationship between normalized fracture conductivity and closure pressure due to proppant embedment for different shale samples from stiff shale to soft shale, as shown in Fig. 3.15. Through fitting the laboratory measurement data, the expressions between normalized fracture conductivity and closure pressure are obtained (Yu and Sepehrnoori, 2014d):

$$\text{Stiff shale}: \log(FC_N) = -0.0001 \times \sigma - 0.1082, \quad R^2 = 0.954, \tag{3.54}$$

$$\text{Medium shale}: \log(FC_N) = -0.0004 \times \sigma + 0.2191, \quad R^2 = 0.998, \tag{3.55}$$

$$\text{Soft shale}: \log(FC_N) = -0.0006 \times \sigma + 0.4256, \quad R^2 = 0.987, \tag{3.56}$$

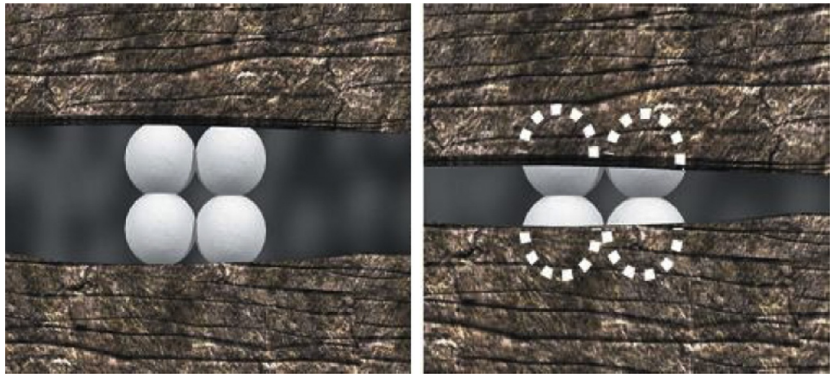

FIG. 3.14 Proppant embedment into the fracture faces resulting in a decrease of fracture width and fracture conductivity (Terracina et al., 2010).

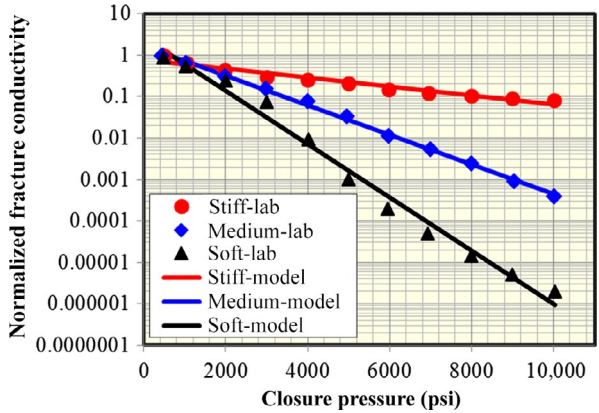

FIG. 3.15 The relationship between normalized fracture conductivity and closure pressure for different shale samples (Yu and Sepehrnoori, 2014d).

where FC_N is normalized fracture conductivity by the initial fracture conductivity, and σ is closure pressure (psi). As shown in Fig. 3.15, the magnitude of normalized fracture conductivity loss at the highest closure stress (10,000 psi) is about 1, 3.5, and 6 for the still shale, medium shale, and soft shale, respectively.

3.3.6 Real Gas Properties

The following equation of state is used to describe real gas properties such as density and Z factor:

$$pM = \rho_g ZRT, \tag{3.57}$$

where M is molecular weight, kg/mol; R is gas constant, J/mol K; T is temperature, K; Z is gas compressibility factor. The reduced pressure (p_r), reduced temperature (T_r), and reduced density (ρ_r) are needed to calculate the gas compressibility factor, which are defined by

$$p_r = \frac{p}{p_c}, \tag{3.58}$$

$$T_r = \frac{T}{T_c}, \tag{3.59}$$

$$\rho_r = \frac{\rho}{\rho_c}, \tag{3.60}$$

where p_c is critical pressure, MPa; T_c is critical temperature, K; ρ_c is critical density, kg/m^3, which can be calculated according to the critical Z factor of natural gas of 0.27:

$$\rho_c = \frac{p_c M}{0.27 R T_c}. \tag{3.61}$$

Substituting Eq. (3.61) into Eq. (3.57) gives

$$Z = \frac{0.27 p_r}{\rho_r T_r}. \tag{3.62}$$

In addition, the Z factor can be calculated by the following Benedict-Webb-Rubin equation based on reduced temperature and reduced density (Benedict et al., 1942):

$$\begin{aligned} Z = 1 &+ \left(A_1 + \frac{A_2}{T_r} + \frac{A_3}{T_r^3}\right) + \rho_r + \left(A_4 + \frac{A_5}{T_r}\right)\rho_r^2 \\ &+ \frac{A_5 A_6}{T_r}\rho_r^5 + \frac{A_7 \rho_r^2}{T_r^3}\left(1 + A_8 \rho_r^2\right) \exp\left(-A_8 \rho_r^2\right), \end{aligned} \tag{3.63}$$

where the coefficients were given by Dranchuk et al. (1973) through fitting the experimental data: $A_1 = 0.31506237$, $A_2 = -1.0467099$, $A_3 = -0.57832729$, $A_4 = 0.53530771$, $A_5 = -0.61232032$, $A_6 = -0.104888$, $A_7 = 0.68157001$, $A_8 = 0.6844549$. The Newton-Ralphson iteration procedure is used to solve Eqs. (3.62) and (3.63) to obtain the Z factor and reduced density based on the given reduced temperature and reduce pressure. Subsequently, the real gas compressibility can be calculated based on the correlation developed by Mahmoud (2014):

$$c_g = \frac{c_r}{p_c}, \tag{3.64}$$

$$c_r = \frac{1}{p_r} - \frac{1}{Z}\left[\left(1.404 e^{-2.5 T_r}\right) p_r - \left(5.524 e^{-2.5 T_r}\right)\right], \tag{3.65}$$

where c_r is reduced gas compressibility.

The gas viscosity is calculated by the formulation developed by Lee et al. (1966):

$$\mu_g = \frac{(9.4+0.02M)T^{1.5}}{209+19M+T}\exp\left(X\rho_g^Y\right), \tag{3.66}$$

$$X = 3.5+\frac{986}{T}+0.01M, \tag{3.67}$$

$$Y = 2.4-0.2X. \tag{3.68}$$

3.4 MODEL DEVELOPMENT FOR TIGHT OIL SIMULATION

In comparison with model development for shale gas simulation, the unique flow mechanisms such as gas slippage, gas diffusion, and gas desorption are not considered for model development in tight oil simulation. The unsteady-state oil flow from tight formation to fractures can be described by the traditional diffusivity equation without considering the source terms (Thambynayagam, 2011):

$$\eta_x\frac{\partial^2 p}{\partial x^2}+\eta_y\frac{\partial^2 p}{\partial y^2}+\eta_z\frac{\partial^2 p}{\partial z^2}=\frac{\partial p}{\partial t}, \tag{3.69}$$

where η is hydraulic diffusivity coefficient, which is defined as:

$$\eta_j = \frac{k}{\phi c_t \mu}, \tag{3.70}$$

where k is permeability, ϕ is porosity, c_t is total compressibility of the system, and μ is oil viscosity. For oil flow in fracture, the pressure drop along the fracture satisfies the Darcy flow behavior.

3.5 SEMIANALYTICAL MODEL UNKNOWNS AND GOVERNING EQUATIONS

There are three primary groups of unknown variables in the semianalytical model. The first one is gas flow rate at the nodes of fracture segments, which is defined as q_i. The second is gas flux at fracture segments, which is defined as q_{fj}. The third is pressure at the nodes, which is defined as p_i. All unknowns are listed in the following:

(1) N_v gas flow rates at all nodes, q_i, $i=1, \ldots, N_v$.
(2) N_f gas flux at fracture segments, q_{fj}, $j=1, \ldots, N_f$.
(3) N_v pressure at all nodes, p_i, $i=1, \ldots, N_v$.

Hence, the total number of unknown variables includes $2N_v+N_f$, which can be written by the following convenient vector form:

$$X^T = \left[q_1, q_2, \ldots, q_{Nv}, \quad q_{f1}, q_{f2}, \ldots, q_{fNf}, \quad p_1, p_2, \ldots, p_{Nv}\right], \tag{3.71}$$

Correspondingly, we have the same number of governing equations, which are described by the following three groups:

(1) N_v mass balance equations at all nodes:

$$(q_i)_{\text{inflow}} = (q_i)_{\text{outflow}}, \quad i = 1, \ \ldots, \ N_v. \tag{3.72}$$

(2) N_f Darcy or non-Darcy flow equations at all fracture segments, which are described by Eq. (3.47) or (3.48). The non-Darcy flow equation can be simplified as:

$$p_j - p_{j+1} = \int_{y_j}^{y_{j+1}} D_j q_j(y) + ND_j q_j(y)^2 dy, \quad j = 1, \ \ldots, \ N_f, \tag{3.73}$$

where

$$q_j(y) = q_j + q_{fj}\left(y - y_j\right), \tag{3.74}$$

$$D_j = \left({}^{\mu}/_{\rho k_f w_f h_f}\right)_j, \tag{3.75}$$

$$ND_j = {}^{\rho\beta}/_{\left(\rho w_f h_f\right)_j{}^2}. \tag{3.76}$$

In addition, there are $N_v - N_f$ wellbore nodes with constant flowing bottomhole pressure (BHP) constraint or constant flowing rate constraint. For constant BHP constraint:

$$p_k = BHP, \quad k = 1, \ \ldots, \ N_v - N_f. \tag{3.77}$$

For constant flow rate constraint (q_w):

$$\sum_{k=1}^{N_v - N_f} q_k = q_w, \ p_k = p_{k+1}, \quad k = 1, \ \ldots, \ N_v - N_f. \tag{3.78}$$

(3) N_f pressure solutions at the center of all fracture segments, which combines gas transport in shale and gas flow in fracture. The pressure solution (p_{jc}) at center of each fracture segment for gas transport in shale is equal to that for gas flow in fracture.

$$\left(p_{jc}\right)_{\text{fracture}} = \left(p_{jc}\right)_{\text{shale}}, \quad j = 1, \ \ldots, \ N_f. \tag{3.79}$$

For gas flow in the fracture, the pressure solution at center can be obtained by modifying the Eq. (3.73) as follows:

$$\left(p_{jc}\right)_{\text{fracture}} = p_j - \int_{y_j}^{y_{jc}} D_j q_j(y) + ND_j q_j(y)^2 dy. \tag{3.80}$$

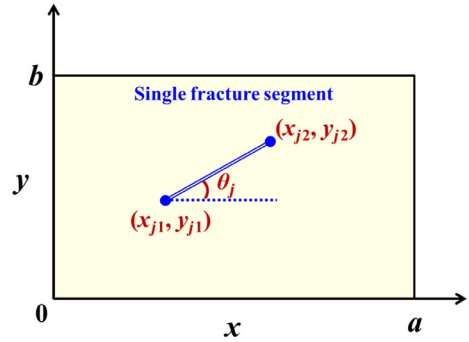

FIG. 3.16 Single fracture segment with an inclination angle of θ_j (Yu et al., 2017a).

For gas transport from shale matrix to single fracture segment as shown in Fig. 3.16, a 2D analytical solution for single fracture segment is obtained based on Green's functions and source solutions, which can be used to calculate pressure at any location with respect to time in an infinite reservoir (Gringarten et al., 1972; Gringarten and Rameny, 1973; Guppy et al., 1982):

$$p(x,y,t)=p_i-\frac{\mu_g}{4\pi h_f\rho_g k}\int_{t_1}^{t_2}\int_{-dy/2}^{dy/2}\frac{q_f(\tau)}{t-\tau}\times e^{-\frac{\left(x+x'\cos\theta-x_m\right)^2+\left(y+x'\sin\theta-y_m\right)^2}{4\eta(t-\tau)}}dx'd\tau, \tag{3.81}$$

where p_i is initial reservoir pressure, h_f is fracture height, dy is length of fracture segment, θ is an inclination angle of fracture segment along the x coordinate, x_m is the center coordinate of fracture segment in x direction, y_m is the center coordinate of fracture segment in y direction, q_f is the flux of fracture segment, η is the hydraulic diffusivity coefficient. Using the method of images, a 2D analytical solution for single fracture segment in a bounded reservoir ($0<x<x_e$, $0<y<y_e$) can be obtained as

$$\begin{aligned}p(x,y,t)=p_i-\frac{\mu_g}{4\pi h_f\rho_g k}&\int_{t_1}^{t_2}\int_{-dy/2}^{dy/2}\frac{q_f(\tau)}{t-\tau}\\&\times\sum_{n=-\infty}^{+\infty}\left[e^{-\frac{(x+x'\cos\theta-x_m-2nx_e)^2}{4\eta(t-\tau)}}+e^{-\frac{(x-x'\cos\theta+x_m-2nx_e)^2}{4\eta(t-\tau)}}\right]\\&\times\sum_{n=-\infty}^{+\infty}\left[e^{-\frac{(y+x'\sin\theta-y_m-2ny_e)^2}{4\eta(t-\tau)}}+e^{-\frac{(y-x'\sin\theta+y_m-2ny_e)^2}{4\eta(t-\tau)}}\right]dx'd\tau,\end{aligned} \tag{3.82}$$

According to the principle of superposition, the following equation is used to calculate the pressure solution at center of each fracture segment by considering interference from all other fracture segments (Fig. 3.17):

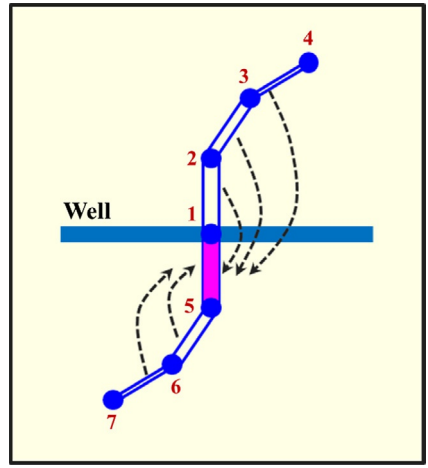

FIG. 3.17 An example illustrating production interference from other fracture segments on the target fracture segment.

$$
\begin{aligned}
\left(p_{jc}\right)_{\text{shale}} = p_i - \frac{\mu_g}{4\pi h_f \rho_g k} \sum_{i=1}^{N_f} \int_{t_1}^{t_2} \int_{-dy_i/2}^{dy_i/2} \frac{q_{fi}(\tau)}{t-\tau} \\
\times \sum_{n=-\infty}^{+\infty} \left[e^{-\frac{(x+x'\cos\theta_i - x_{mi} - 2nx_e)^2}{4\eta(t-\tau)}} + e^{-\frac{(x-x'\cos\theta_i + x_{mi} - 2nx_e)^2}{4\eta(t-\tau)}} \right] \\
\times \sum_{n=-\infty}^{+\infty} \left[e^{-\frac{(y+x'\sin\theta_i - y_{mi} - 2ny_e)^2}{4\eta(t-\tau)}} + e^{-\frac{(y-x'\sin\theta_i + y_{mi} - 2ny_e)^2}{4\eta(t-\tau)}} \right] dx' d\tau,
\end{aligned}
\tag{3.83}
$$

where θ_i is an inclination angle of the ith fracture segment along the x coordinate, x_{mi} is the center coordinate of the ith fracture segment in x direction, y_{mi} is the center coordinate of the ith fracture segment in y direction, q_{fi} is the flux of the ith fracture segment.

3.6 SEMIANALYTICAL MODEL SOLUTION

Fig. 3.18 presents the detailed flowchart for the semianalytical model to simulate well performance of shale gas or tight oil reservoirs with complex fracture geometry. It should be mentioned that varying time steps can be used to significantly improve the computational efficiency of the semianalytical model.

3.7 SEMIANALYTICAL MODEL VERIFICATION

We verify the semianalytical model against a numerical reservoir simulator (CMG-GEM, 2012) and an analytical solution (Ecrin-Topaze, 2013) for shale

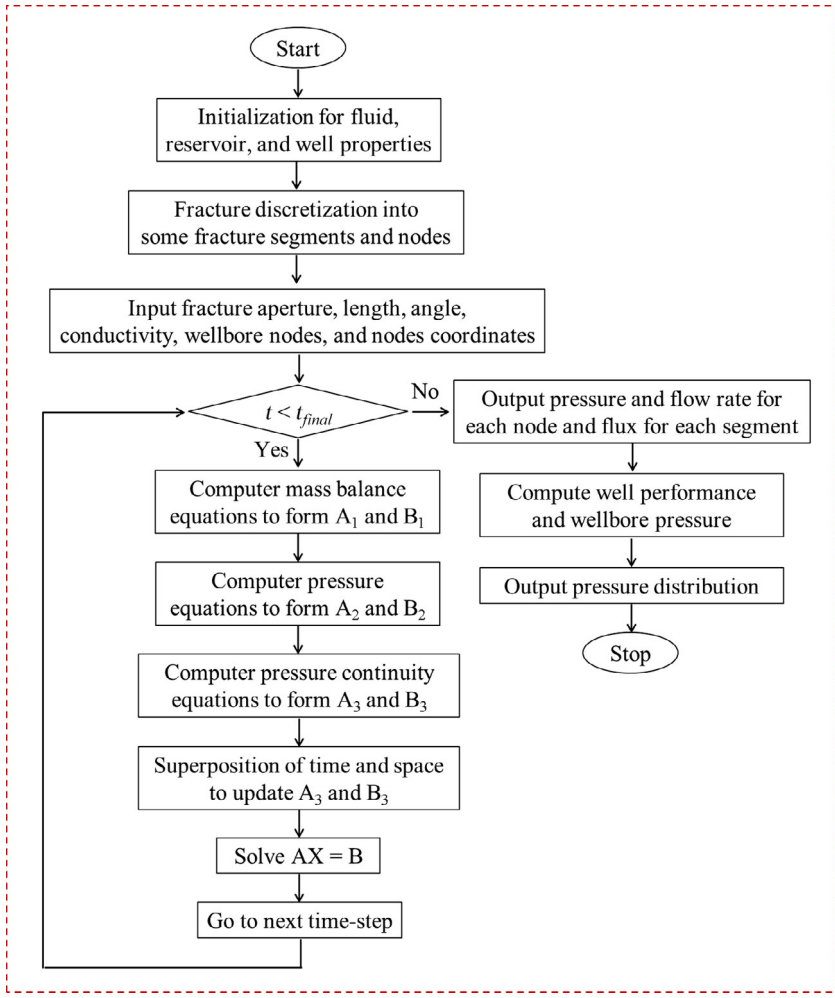

FIG. 3.18 Detailed flowchart of the semianalytical model for simulation of shale gas or tight oil production with complex fracture geometry (Yu et al., 2016b).

gas and tight oil simulations. The LGR approach is used to explicitly model hydraulic fractures for the numerical model.

3.7.1 Shale Gas Reservoirs

A case study with single planar fracture was performed with the purpose of verifying the semianalytical model. The basic reservoir and fracture properties used for the simulations are summarized in Table 3.1. The gas type is methane. The reservoir is assumed to be homogeneous with only gas flow

TABLE 3.1 Basic Reservoir and Fracture Properties Used for the Simulations (Yu et al., 2017a)

Parameter	Value
Initial reservoir pressure (psi)	4300
Reservoir temperature (°F)	130
Reservoir permeability (nD)	800
Reservoir porosity	12%
Initial gas saturation	90%
Gas gravity	0.58
Total compressibility (psi^{-1})	10^{-6}
Fracture half-length (ft)	350
Fracture conductivity (md-ft)	100
Fracture height (ft)	100
Fracture width (ft)	0.01

under the condition of residual water saturation. The value for BHP was held at 2000 psi for all simulations. Fracture height is assumed to be equal to the formation thickness. Note that fracture conductivity is 100 md-ft. The single fracture is divided into 20 segments with 35 ft for each segment, as shown in Fig. 3.19. The gas properties for the input of the semianalytical model are provided in Table 3.2, which is also used in the following shale-gas simulation studies.

3.7.1.1 Gas Desorption Effect

The Langmuir desorption model with Langmuir pressure of 535 psi, Langmuir volume of 196.4 scf/ton, and bulk density of 2.52 g/cm^3 is used for verification. The comparison of gas flow rate between this model, analytical model, and numerical model by considering the gas desorption effect is shown in Fig. 3.20, illustrating that a good match between them is obtained. Fig. 3.21 shows the effect of gas desorption on cumulative gas production. As shown, the gas desorption effect contributes to around 5% increase of gas recovery at the end of production (1000 days).

3.7.1.2 Geomechanics Effect

In this case study, the stiff shale case was selected to investigate the impact of geomechanics on well performance. Using Eq. (3.54) and assuming the

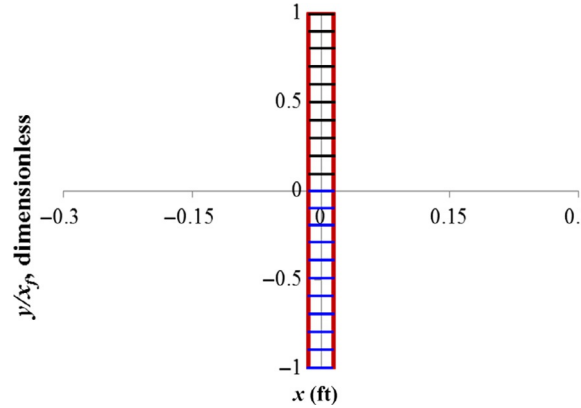

FIG. 3.19 Single planar fracture geometry with constant fracture width and 20 fracture segments (Yu et al., 2017a).

TABLE 3.2 Gas Properties for the Input of the Semianalytical Model (Yu et al., 2017a)

Pressure (psi)	*Z*-Factor	Viscosity (cp)	Density (g/cm^3)
400	0.960	0.013	0.018
800	0.924	0.013	0.037
1200	0.893	0.014	0.057
1600	0.871	0.015	0.078
2000	0.858	0.016	0.099
2400	0.854	0.017	0.120
2800	0.859	0.018	0.139
3200	0.872	0.020	0.156
3600	0.890	0.021	0.172
4000	0.913	0.022	0.187
4400	0.939	0.023	0.199
4800	0.969	0.024	0.211
5000	0.984	0.025	0.216

minimum horizontal stress of 5473 psi, the pressure-dependent fracture conductivity curve was generated, as shown in Fig. 3.22. It illustrates that the final fracture conductivity will reduce to 46% of initial fracture conductivity corresponding to the BHP of 2000 psi. The comparison of gas flow rate between

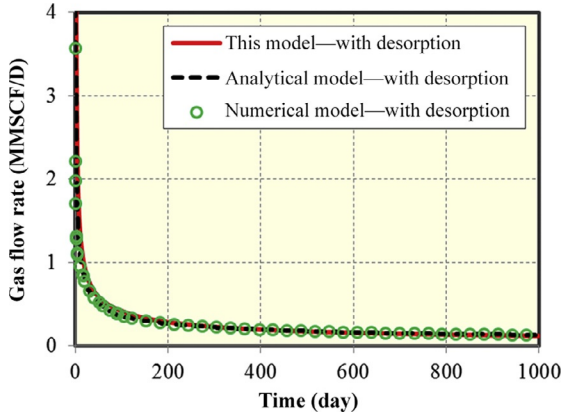

FIG. 3.20 Comparison of gas flow rate by considering the gas desorption effect between this model, analytical, and numerical models (Yu et al., 2017a).

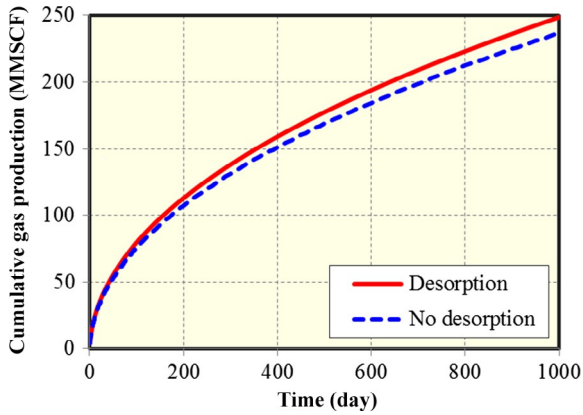

FIG. 3.21 Effect of gas desorption on cumulative gas production (Yu et al., 2017a).

this model and numerical model by considering the geomechanics effect is shown in Fig. 3.23, illustrating that a good match is obtained.

Figs. 3.24 and 3.25 show the effect of geomechanics on cumulative gas production with initial fracture conductivity of 100 and 5 md-ft, respectively. As shown, the geomechanics effect reduces the gas recovery at end of production (1000 days) by 0.5% for the initial fracture conductivity of 100 md-ft, while 13% for the initial fracture conductivity of 5 md-ft. It suggests that the geomechanics effect is important when the fracture conductivity is low.

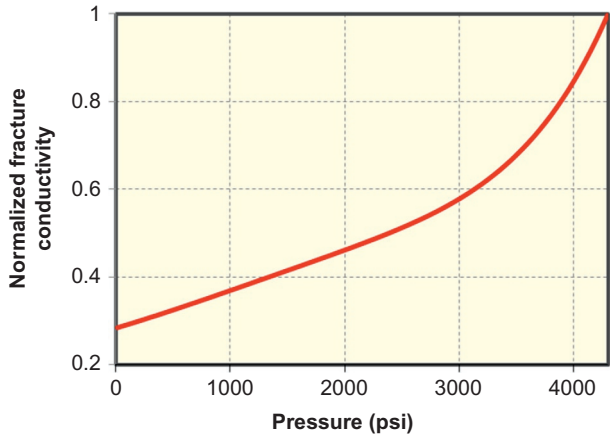

FIG. 3.22 Pressure-dependent fracture conductivity curve used for this case study (Yu et al., 2017a).

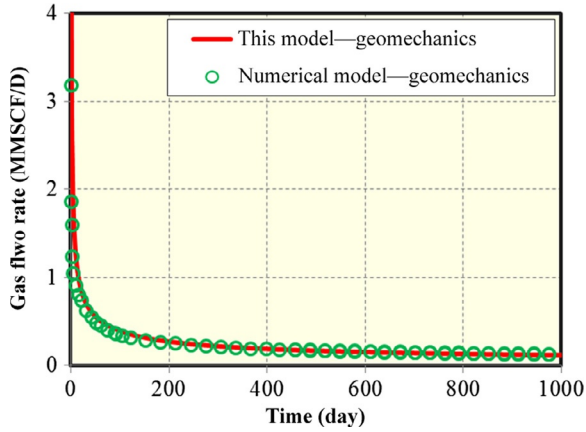

FIG. 3.23 Comparison of gas flow rate by considering the geomechanics effect between this model and numerical model (Yu et al., 2017a).

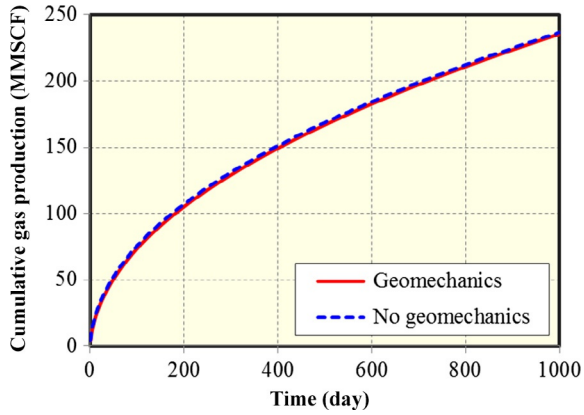

FIG. 3.24 Effect of geomechanics on cumulative gas production with initial fracture conductivity of 100 md-ft (Yu et al., 2017a).

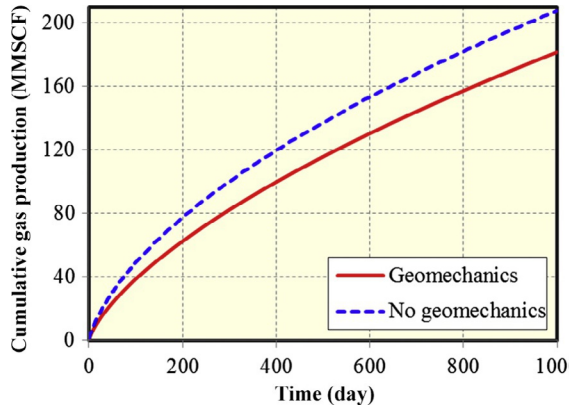

FIG. 3.25 Effect of geomechanics on cumulative gas production with initial fracture conductivity of 5 md-ft (Yu et al., 2017a).

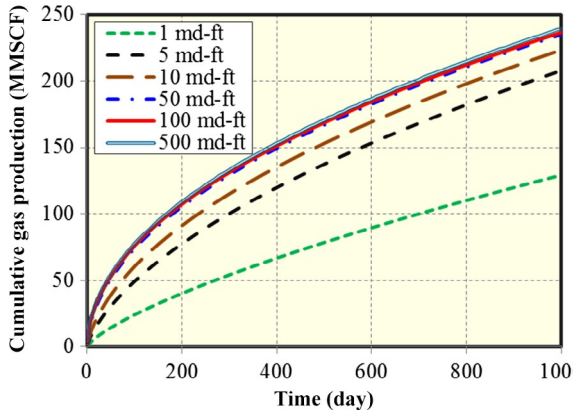

FIG. 3.26 Effect of fracture conductivity on cumulative gas production (Yu, 2015).

3.7.1.3 Fracture Conductivity Effect

The effect of fracture conductivity on cumulative gas production was studied and shown in Fig. 3.26, illustrating that the trend of increase in gas recovery with time decreases with the increasing fracture conductivity. In addition, the gas recovery of the fracture conductivity of 100 md-ft approaches that of 500 md-ft. Hence, it can be suggested that the 100 md-ft is very close to the infinite fracture conductivity in this case study.

3.7.1.4 Fracture Segment Number Effect

If the fracture is divided into more segments, the simulation results will be more accurate. However, the computation will be more time consuming. Hence, there

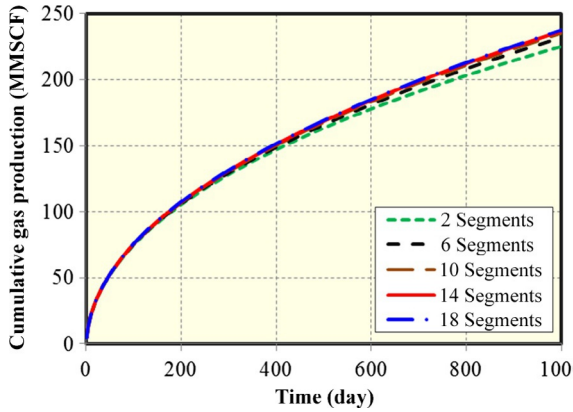

FIG. 3.27 Effect of number of fracture segment on cumulative gas production (Yu, 2015).

is a tradeoff between them. In this case study, the effect of number of fracture segments on cumulative gas production was studied and shown in Fig. 3.27, illustrating that 14 fracture segments with 50 ft for each one is very close to the real solution. It suggests that the length for each fracture segment, which is <50 ft, is good enough to obtain accurate results.

3.7.2 Tight Oil Reservoirs

In order to verify the semianalytical model against a numerical reservoir simulator, two cases for single planar fracture geometry with constant fracture width are considered next. Case 1: constant flow rate constraint without the geomechanics effect. Case 2: constant BHP constraint with the geomechanics effect. Table 3.3 summarizes the reservoir and fracture properties used for the following simulation studies. Fourteen equal fracture segments are used for each case. Based on the fracture half-length of 210 ft, each fracture segment length is 30 ft. Fracture width is 0.01 ft and facture conductivity is 420 md-ft. The dimensionless fracture conductivity is defined:

$$F_{cd} = \frac{k_f w_f}{k_m x_f}. \tag{3.84}$$

Hence, the dimensionless fracture conductivity is 20 corresponding to 420 md-ft.

3.7.2.1 Case 1: Constant Flow Rate Constraint

In Case 1, the constant flow rate constraint (25 STB/D) is used without considering the geomechanics effect. Fig. 3.28 presents the comparison of BHP between the semianalytical model and numerical model. The simulation results from the

TABLE 3.3 Reservoir and Fracture Properties Used for Simulation (Yu et al., 2016a)

Parameter	Value	Unit
Initial reservoir pressure	4200	psi
Reservoir permeability	0.1	mD
Reservoir porosity	10%	value
Reservoir thickness	50	ft
Total compressibility	3×10^{-6}	psi^{-1}
Fracture conductivity	420	md-ft
Fracture width	0.01	ft
Fracture half-length	210	ft
Oil viscosity	0.6	cp
Formation volume factor	1.273	bbl/STB
Production time	1000	day

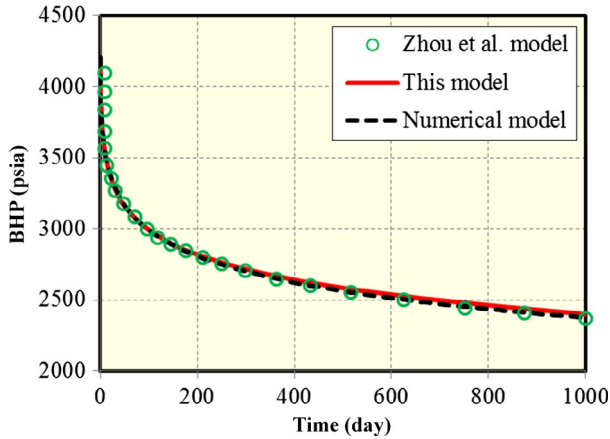

FIG. 3.28 Comparison of BHP for Case 1 with constant flow rate constraint and without the geomechanics effect (Yu et al., 2016a).

work by Zhou et al. (2013) with the same reservoir and fracture properties are also included. It can be seen that a good match between them is obtained.

After verification for Case 1, we investigated the impact of number of fracture segment on the BHP, as shown in Fig. 3.29. The fracture segment is assumed to be the same for each simulation study. As shown, the BHP of eight

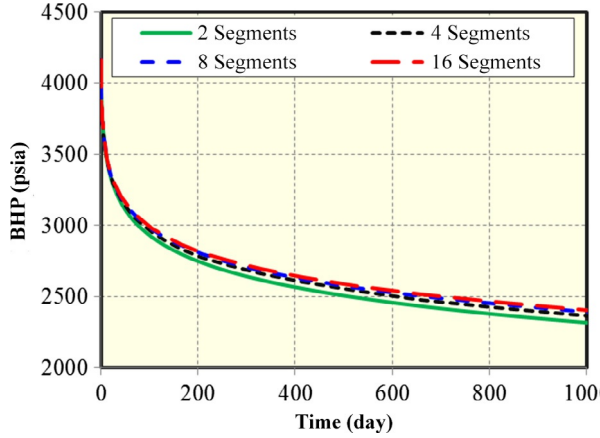

FIG. 3.29 Effect of number of fracture segment on the BHP of Case 1 (Yu et al., 2016a).

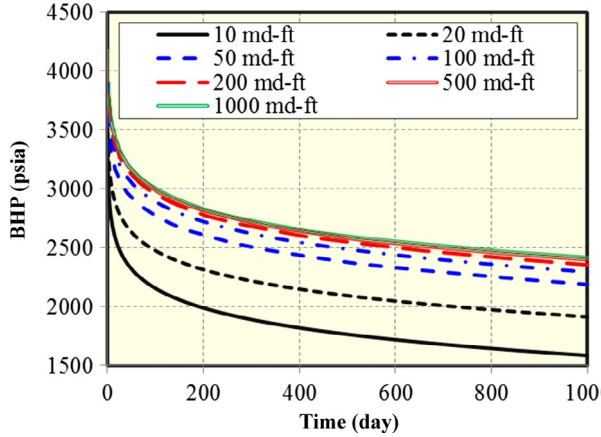

FIG. 3.30 Effect of fracture conductivity on the BHP of Case 1 (Yu et al., 2016a).

fracture segments approaches that of 16 fracture segments. The length of each fracture segment corresponding to eight segments is 52.5 ft. Hence, in the following simulation studies, it is suggested that the length of fracture segment is set up at most 52.5 ft in order to maintain the accuracy of simulation results.

In addition, the effect of fracture conductivity on the BHP is also studied and shown in Fig. 3.30, illustrating that the BHP drops more quickly with the smaller fracture conductivity. In addition, the BHP of the fracture conductivity of 200 md-ft approaches that of 1000 md-ft. Hence, it can be suggested that the 200 md-ft is very close to the infinite fracture conductivity in this case study and the corresponding dimensionless fracture conductivity is calculated as 9.5.

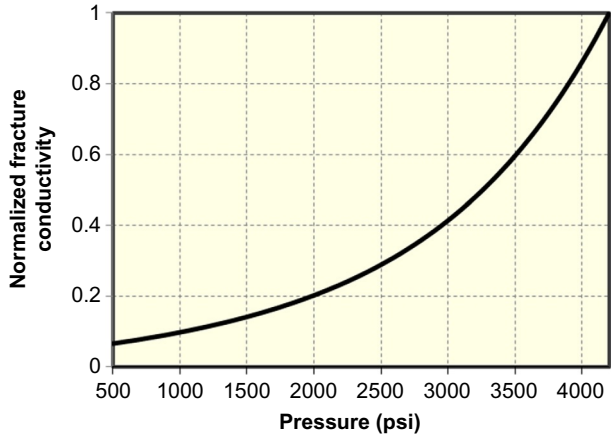

FIG. 3.31 Relationship between the normalized fracture conductivity and pressure at fracture segments (Yu et al., 2016a).

3.7.2.2 Case 2: Constant BHP Constraint

In Case 2, the geomechanics effect is considered and the curve as shown in Fig. 3.31 is used for simulation. The constant BHP of 2000 psi is used for simulation constraint. The initial fracture conductivity at each fracture segment is 420 md-ft, which will decrease as a function of pressure and production by considering the geomechanics effect. In the simulation, when the pressure drops as the production time increases, the value of fracture conductivity at each fracture segment will be updated based on the following formulation, which is a modified form of Eq. (3.55) by substituting the minimum horizontal stress of 5345 psi:

$$FC = FC_i \times 10^{-0.0004\times(5345-P)+0.2191}, \tag{3.85}$$

where FC is fracture conductivity with unit of md-ft, FC_i is initial fracture conductivity, P is average pressure at the fracture segment with unit of psi.

Fig. 3.32 presents the comparison of oil flow rate by considering the geomechanics effect. It can be seen that a good agreement between this model and the numerical model is obtained. Hence, it can be concluded that the semianalytical model can effectively simulate the effect of geomechanics on well performance of tight oil reservoirs. Additionally, Fig. 3.33 compares cumulative oil production with and without considering the geomechanics effect. As shown, the geomechanics effect makes the cumulative oil production at 1000 days decrease by around 6% for this case study.

3.8 SHALE GAS SIMULATION

3.8.1 Synthetic Case Study

A complex hydraulic fracture propagation model, developed by Wu and Olson (2015a), is used to generate the nonplanar fracture geometry. The complex

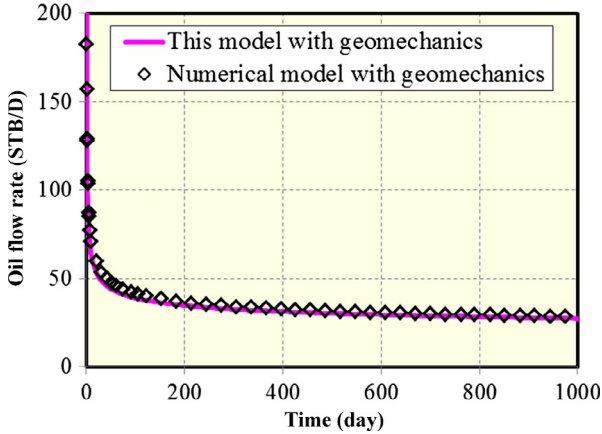

FIG. 3.32 Comparison of oil flow rate between this model and the numerical model for Case 2 with constant BHP constraint and with the geomechanics effect (Yu et al., 2016a).

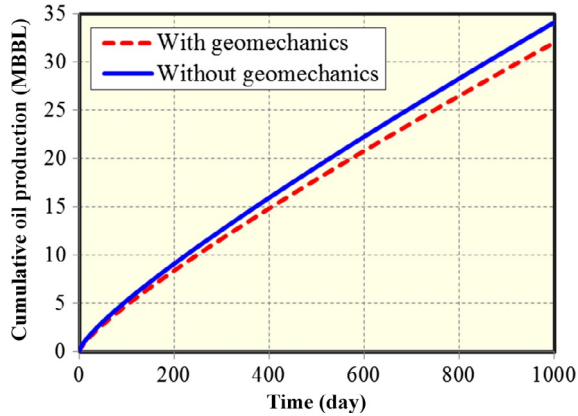

FIG. 3.33 Comparison of cumulative oil production with and without considering the geomechanics effect (Yu et al., 2016a).

fracture propagation model development is beyond the scope of this study. The model couples rock deformation and fluid flow in the fractures and horizontal wellbore. The core solid mechanics solution is three dimensional, such that fracture opening, shearing, and stress shadow effects are accurately determined for single and multifracture cases (Wu and Olson, 2015b). Fluid flow in the fracture and the associated pressure drop are based on lubrication theory, assuming the fracture is analogous to a slot between parallel plates and the fluid is non-Newtonian. A constant total fluid injection rate is given. Partitioning of flow rate into each fracture is dynamically calculated in such way that the wellbore pressure is constrained to gradually decrease along the lateral due to wellbore

friction. The interaction of hydraulic and natural fractures is described through analyzing induced stresses at the fracture tips. Stochastic realization methods were used to describe natural fracture patterns (Wu and Olson, 2016). Length of natural fractures follows a power-law distribution. The model has been validated against known analytical solutions for single hydraulic fracture growth (Olson and Wu, 2012). To demonstrate the validity of capturing the physical process of fracture interaction, the model has also been compared to a numerical model (Wu et al., 2012) in case of multiple fracture propagation. The primary assumptions for the current fracture model include: transverse fractures are initiated perpendicular to the horizontal wellbore with a nominal initial length; fracture height is constant; proppant transport is not considered.

We used three different fracture geometries to examine the difference between planar fractures and nonplanar fractures and the effect of natural fractures, as shown in Fig. 3.34. The fracture width as shown in the figure has been enlarged by a factor of 2000. The pre-existing natural fractures are assumed to be closed. The key inputs used for the fracture model include fluid injection rate of 20 bbl/min, injection time of 600 s, Poisson ratio of 0.23, Young's modulus of 3×10^6 psi, the maximum horizontal stress of 8100 psi, the minimum horizontal stress of 8000 psi, and the leak-off coefficient of 5×10^{-5} ft/min$^{0.5}$. The reservoir thickness is 100 ft and the fracture spacing is 50 ft. As shown, two outer

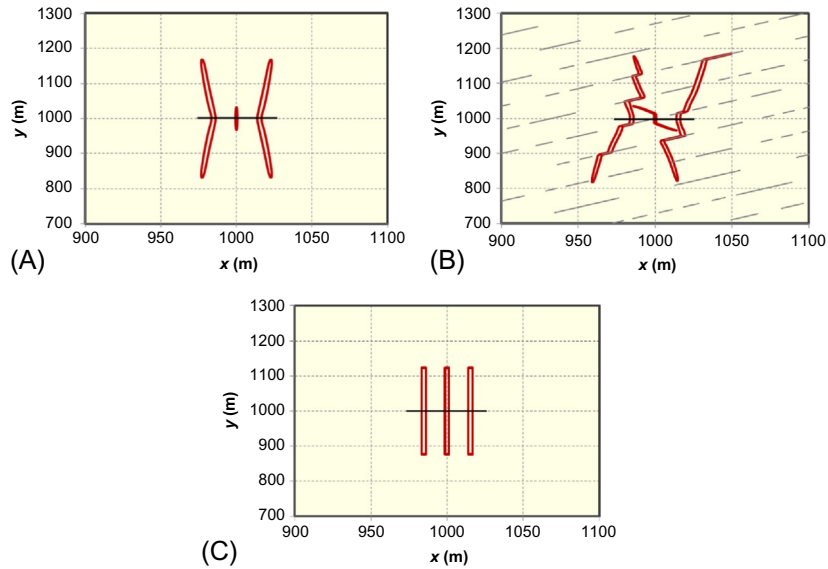

FIG. 3.34 Three different fracture geometries investigated in this study (Yu et al., 2017a). (A) Case 1: Nonplanar fracture geometry without the natural fracture effect. (B) Case 2: Nonplanar fracture geometry with the natural fracture effect. (C) Case 3: Converted planar fracture geometry with equal fracture half-length and fracture width.

fractures are curving and longer than the inner fracture because of the stress shadow effects and uneven flow rate distribution between three fractures. In addition, the natural fractures significantly affect the fracture propagation pattern, resulting in a complex and asymmetric nonplanar fracture geometry. For Case 1, fracture half-length is 555 ft for the outer fractures and 105 ft for the inner fracture. For Case 2, the upper and lower fracture half-length is 606 and 619 ft for the left outer fracture, 130 and 126 ft for the inner fracture, and 640 and 606 ft for the right outer fracture, respectively. For Case 3, we assumed the same total fracture length and fracture area in the *x*-*y* plane as in Case 1, so the fracture half-length is calculated as 404 ft and average fracture width is 0.0044 ft. Since the current fracture model did not consider the proppant transport, a coefficient is needed to multiply by fracture width obtained from the fracture model to calculate the fracture permeability and the corresponding fracture conductivity. In the following production simulations, a coefficient of 8.1×10^{-4} is used. The calculated fracture conductivity is around 550 md-ft for Case 3 with constant fracture width representing the high fracture conductivity scenario.

In order to simulate the production using the semianalytical model, each fracture for three cases is discretized into 20 small fracture segments. The key reservoir and gas properties are the same as Tables 3.1 and 3.2. The value for BHP was held at 2000 psi for all simulations. The non-Darcy flow and gas desorption effects are considered. Gas desorption used in the simulation is based on the core measurements from Marcellus shale (Yu et al., 2014e). The BET isotherm is used to model the gas desorption measurements with p_o of 9833.4 psi, v_m of 134.07 scf/ton, and C of 39.14. Fig. 3.35 presents the comparison of cumulative gas production between three cases. As shown, there is a very small difference between them at early period while a big difference occurs at long term. The nonplanar fracture geometry with the natural fracture effect has the largest gas recovery at end of production, illustrating that the natural fracture plays an important role in contributing to gas recovery. The relative difference between nonplanar fractures with and without considering the natural fracture effect is about 10%. Furthermore, the difference between the converted planar fractures and the nonplanar fractures without the natural fracture effect is big at end of production and the relative difference between them at 1000 days of production is around 41%. Also, we compared the transient flow behavior between them using a square root of time plot, as shown in Fig. 3.36. It can be seen that the linear flow time of the planar fracture geometry is much shorter than the two nonplanar fracture geometries, resulting in a more serious production interference for the planar fractures. Fig. 3.37 shows the pressure distribution at both short-term (100 days) and long-term (1000 days) periods for each case. It can be seen clearly that the drainage area of the nonplanar fractures is larger than the planar fractures and there is more serious production interference for the planar fractures compared to the nonplanar fractures.

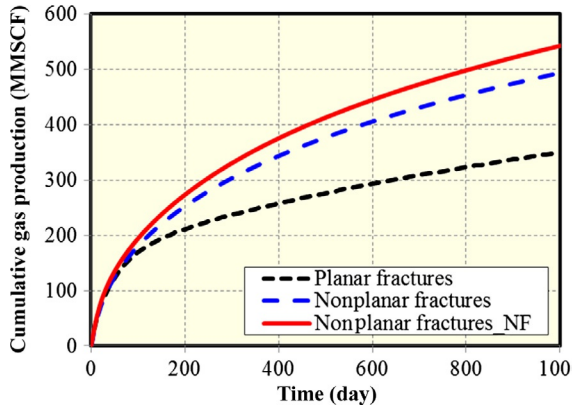

FIG. 3.35 Comparison of cumulative gas production for three cases (Yu et al., 2017a).

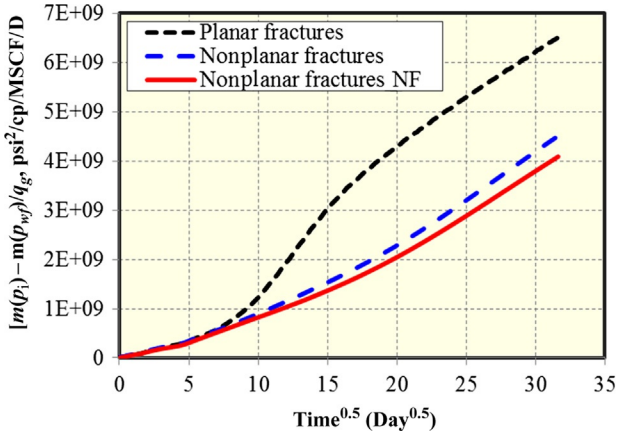

FIG. 3.36 Comparison of rate transient analysis for three cases (Yu et al., 2017a).

3.8.2 Field Case Study

One horizontal well from the Marcellus shale reservoir was selected to perform history matching and production forecasting using the semianalytical model. This well was completed using a lateral length of 1904 ft, seven fracturing stages, three perforation clusters per stage, and the cluster spacing is 68 ft. Almost 150 days of production data were available to perform history matching and to evaluate the well performance. Table 3.4 summarizes the detailed reservoir and fracture properties of the well required for simulation. Slick water was used for hydraulic fracturing. The injection rate is 60 bbl/min. Poisson ratio is 0.23. Young's modulus is 3×10^6 psi. The maximum horizontal stress is 7500 psi and the minimum horizontal stress is 7000 psi.

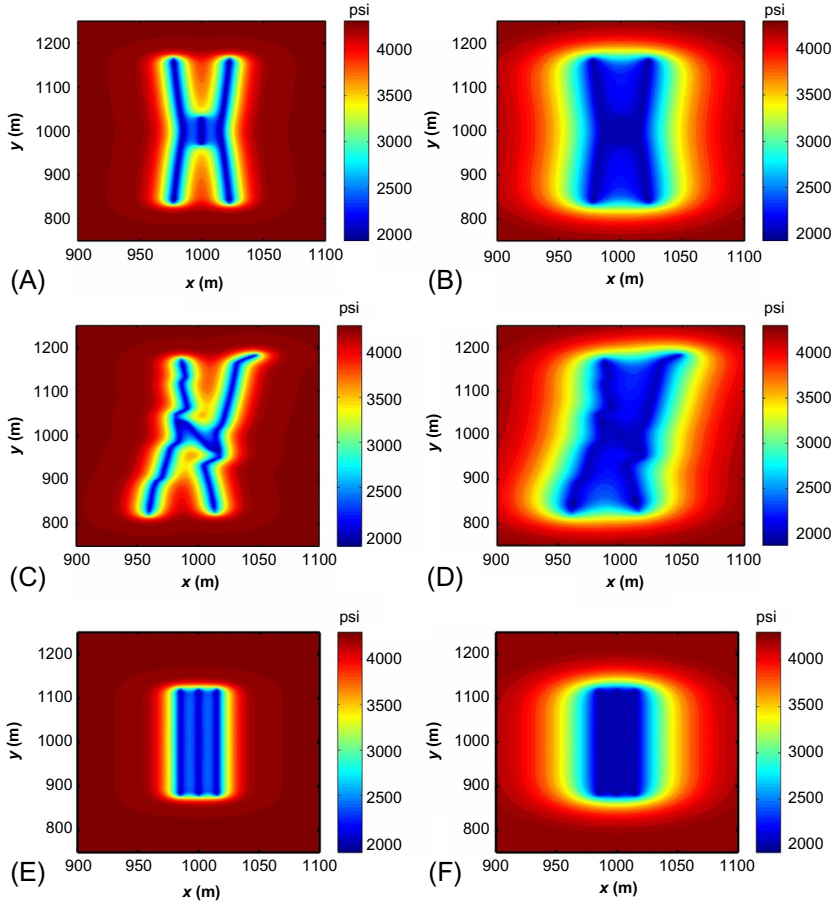

FIG. 3.37 Comparison of pressure distribution for three cases at short-term and long-term periods (Yu et al., 2017a). (A) Case 1 at 100 days of production. (B) Case 1 at 1000 days of production. (C) Case 2 at 100 days of production. (D) Case 2 at 1000 days of production. (E) Case 3 at 100 days of production. (F) Case 3 at 1000 days of production.

Based on these parameters, the nonplanar fracture geometry generated using the fracture propagation model is used for performing history matching and production forecasting. Flowing BHP in Fig. 3.38 is used to constrain the simulation and gas flow rate is the history-matching variable. The injection time for each stage, the coefficient multiplied by Eq. (3.53) used to calculate the fracture permeability, the leak-off coefficient, and matrix permeability were mainly used to run the fracture model and the semianalytical model to obtain a good match. Note that the injection time per each stage is not consistent with the field pumping time due to the limitation of current fracture model without considering proppant transport. The effects of flowback water and wettability of the

TABLE 3.4 Reservoir and Fracture Parameters for One Well in Marcellus Shale (Yu et al., 2017a)

Parameter	Value
Initial reservoir pressure (psi)	4300
Reservoir temperature (°F)	130
Reservoir porosity	12%
Reservoir thickness (ft)	100
Initial water saturation	10%
Horizontal well length (ft)	1904
Number of stages	7
Cluster spacing (ft)	68
Total number of fractures	21
Gas-specific gravity	0.58

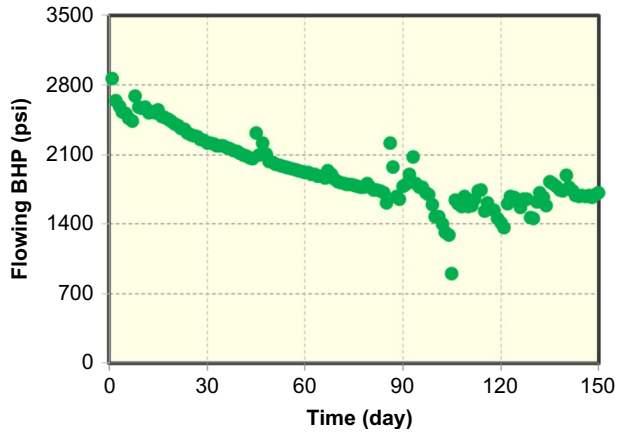

FIG. 3.38 Flowing BHP of the well in Marcellus shale (Yu et al., 2017a).

formation are not considered in the simulation. The non-Darcy flow effect is considered and gas desorption data are used. The history matching results for gas flow rate are shown in Fig. 3.39, illustrating that a reasonable match between simulation results and field data is obtained. Through history matching, the nonplanar fracture geometry per stage with fracture half-length of 365 ft for outer fractures and 170 ft for inner fracture is quantified, as shown in

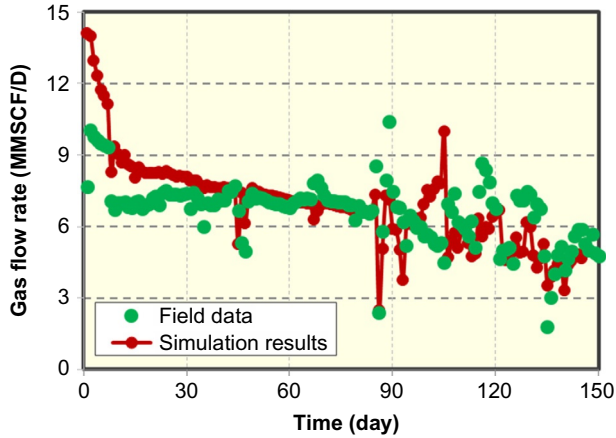

FIG. 3.39 History matching results for gas flow rate (Yu et al., 2017a).

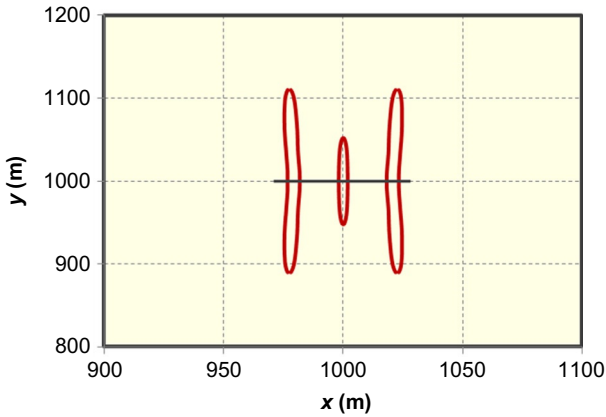

FIG. 3.40 The nonplanar fracture geometry within single stage used for a good history match (Yu et al., 2017a).

Fig. 3.40. The fracture width as shown in the figure has been enlarged by a factor of 2000. It is important to note that history matching is nonunique. Here we only present one possible nonplanar fracture geometry. The injection time is determined as 10 min for each stage. The leak-off coefficient used by the fracture model was 1.4×10^{-3} ft/min$^{0.5}$. The matrix permeability was determined as 800 nD. The coefficient multiplied by Eq. (3.53) used to correct the fracture permeability was determined as 1.16×10^{-6} in this case study (the unit of fracture permeability is cm^2). The corresponding fracture conductivity profile of two outer fractures and one inner fracture within single stage is displayed in Fig. 3.41. The pressure distribution at end of field production is shown in Fig. 3.42, clearly showing the effective drainage area of this well.

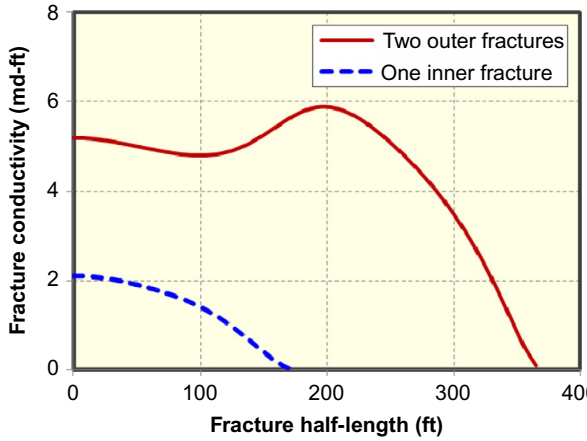

FIG. 3.41 Fracture conductivity profile of two outer fractures and one inner fracture within single stage (Yu et al., 2017a).

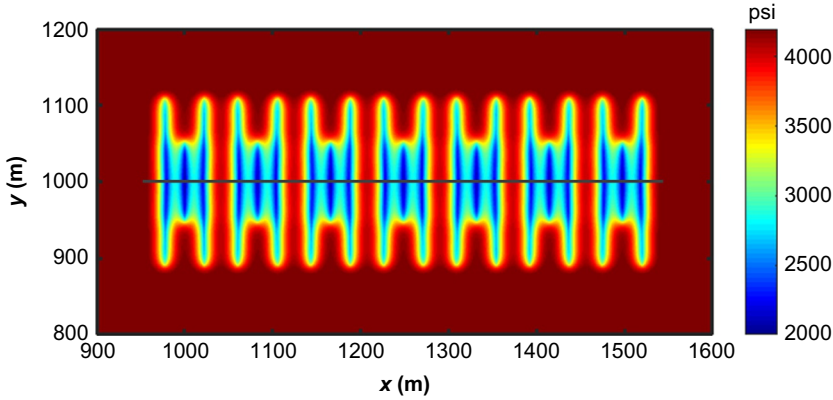

FIG. 3.42 Pressure distribution at end of field production (Yu et al., 2017a).

After history matching, we performed a production forecasting for 30 years. After history matching period, BHP of 1000 psi remained constant until 30 years of production. Fig. 3.43 shows the gas recovery at 30 years of production by considering the nonplanar fractures, the planar fractures, and the important flow mechanisms. The average pore diameter of 50 nm and the average diffusion coefficient of 1×10^{-6} m^2/s are assumed in this case study. The nonplanar fractures and the planar fractures have the same total fracture length and fracture area. Accordingly, the converted planar fractures have an equal fracture half-length of 300 ft and fracture width of 0.008 ft. The fracture conductivity is around 4 md-ft. It can be seen that the difference of cumulative gas production between the nonplanar fractures and the converted planar fractures is 12% at

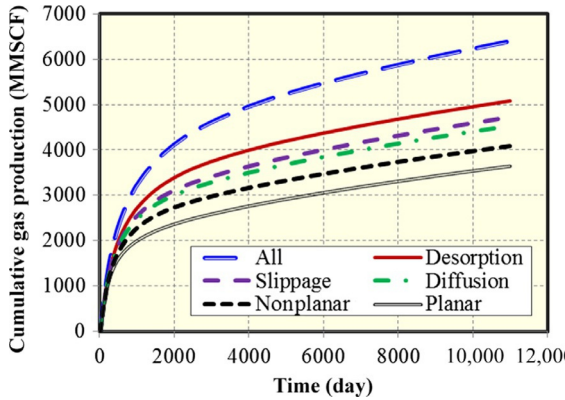

FIG. 3.43 Production forecasting at 30-year period by considering the nonplanar fractures and the converted planar fractures and the important gas flow mechanisms (Yu et al., 2017a).

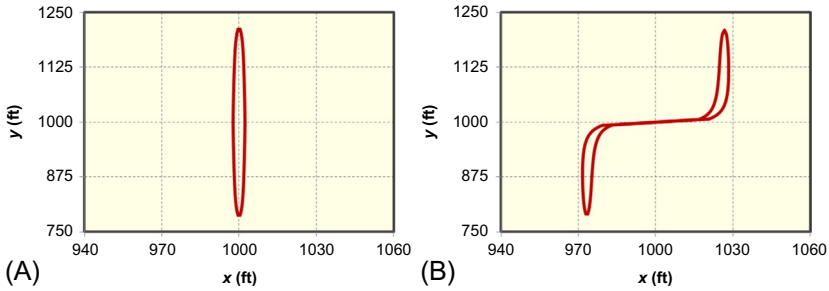

FIG. 3.44 Two fractures with different fracture geometries (Yu et al., 2016a). (A) Planar fracture with varying width. (B) Curving nonplanar fracture.

30 years of production. In addition, the contribution of gas diffusion, gas slippage, and gas desorption to gas recovery at 30 years of production compared to that without considering them is 11%, 16%, and 25%, respectively. Totally, the contribution of these three important mechanisms is about 56%. Hence, the key finding of this case study was that modeling of gas production from the nonplanar fractures as well as modeling the important gas flow mechanisms in shale gas reservoirs is significant.

3.9 TIGHT OIL SIMULATION

3.9.1 Two Fractures With Different Fracture Geometries

We applied the semianalytical model to perform simulation studies for two different fracture geometries, which were generated from the fracture propagation model by Wu (2014), as shown in Fig. 3.44. The fracture width as shown in the figure has been enlarged by a factor of 100. One is planar fracture geometry with

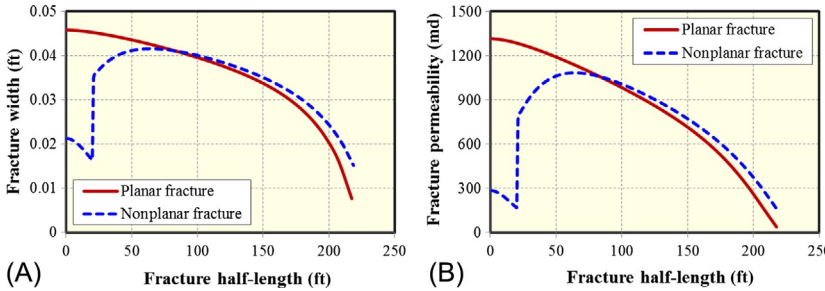

FIG. 3.45 Comparison of fracture width and fracture permeability of two fracture geometries along fracture half-length (Yu et al., 2016a). (A) Fracture width distribution. (B) Fracture permeability distribution.

varying fracture width, another is curving nonplanar fracture geometry and there is a severe fracture width restriction around the wellbore. The only difference between these two fracture geometries is the angle between fracture initiation direction and the maximum horizontal stress: 0 degrees for the planar fracture geometry and 70 degrees for the nonplanar fracture geometry. The other parameters are the same: Poisson ratio is 0.25, Young's modulus is 4×10^6 psi, the maximum horizontal stress is 5450 psi, the minimum horizontal stress is 4450 psi, injection fluid rate is 20 bbl/min, and injection time is 8 min.

The fracture width and fracture permeability distribution of these two fracture geometries along fracture half-length are shown in Fig. 3.45. It should be noted that fracture half-length in this study represents the distance measured from the first node at the fracture center to the node at the fracture tip. The other reservoir and fluid properties are the same as Table 3.3.

Comparison of BHP variation with time of these two fracture geometries is shown in Fig. 3.46. As shown, the curving nonplanar fracture has the larger pressure drop than the planar fracture. This is because there is a severe fracture width restriction around the wellbore for the curving nonplanar fracture, resulting in the larger pressure drop. Fig. 3.47 presents the comparison of pressure distribution at time of 1 h, illustrating that there is a larger pressure drop near the wellbore for the nonplanar fracture than the planar fracture. It can be concluded that the curving nonplanar fracture geometry plays a significant negative effect on well performance, which should be avoided in the field operation.

The transient flow regime analysis for these two fracture geometries with finite fracture conductivity is also investigated. Cinco-Ley and Samaniego-V (1981) proposed four flow periods for production of a vertically fractured well, which can be characterized based on different slops in the log-log graph of the dimensionless pressure drop (p_{wD}) and pressure drop derivative (p_{wD}') versus the dimensionless time (t_{Dx_f}). The dimensionless variables can be represented by

$$P_{wD} = \frac{kh\left(P_i - P_{wf}\right)}{141.2qB\mu}, \tag{3.86}$$

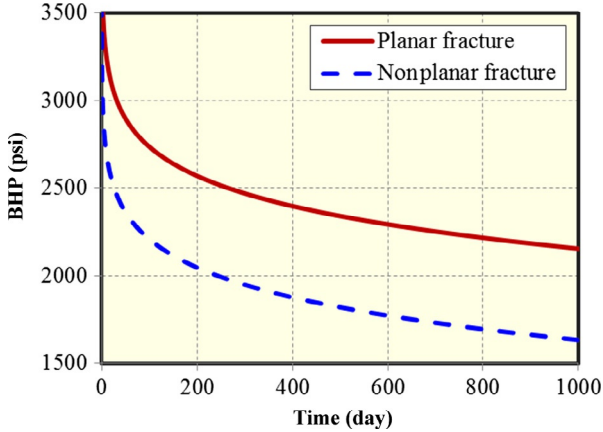

FIG. 3.46 Comparison of BHP variation with time of the two fracture geometries (Yu et al., 2016a).

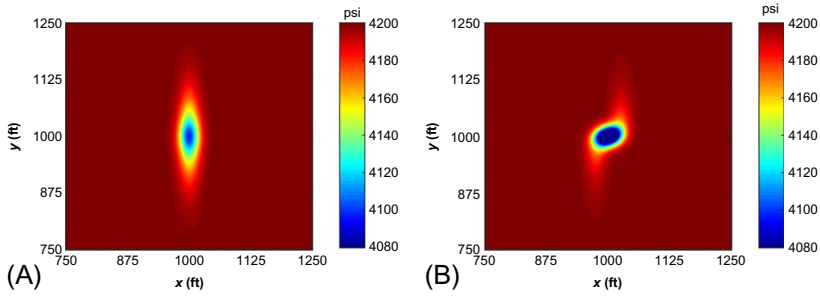

FIG. 3.47 Pressure distribution of the two fracture geometries at time of 1 h (Yu et al., 2016a). (A) Planar fracture with varying width. (B) Curving nonplanar fracture.

$$t_{Dx_f} = \frac{0.0002637kt}{\phi\mu c_t x_f^2}, \tag{3.87}$$

$$P'_{wD} = \frac{dP_{wD}}{d\ \ln t_{Dx_f}}, \tag{3.88}$$

where the units used are k in md, h in ft, P in psi, q in STB/D, B in bbl/STB, μ in cp, t in day, c_t in psi^{-1}, x_f in ft.

Fig. 3.48 presents the four time periods: (a) fracture linear flow with a 1/2 slope straight line for pressure and pressure derivative curves; (b) bilinear flow with a 1/4 slope straight line for pressure and pressure derivative curves; (c) formation linear flow with a 1/2 slope straight line for pressure and pressure derivative curves; (d) pseudoradial flow, which stabilizes at 0.5 line in the pressure derivative log-log plot (Bourdet et al., 1983). Cinco-Ley and Samaniego-V (1981) reported that the formation linear flow only occurs in the fracture with

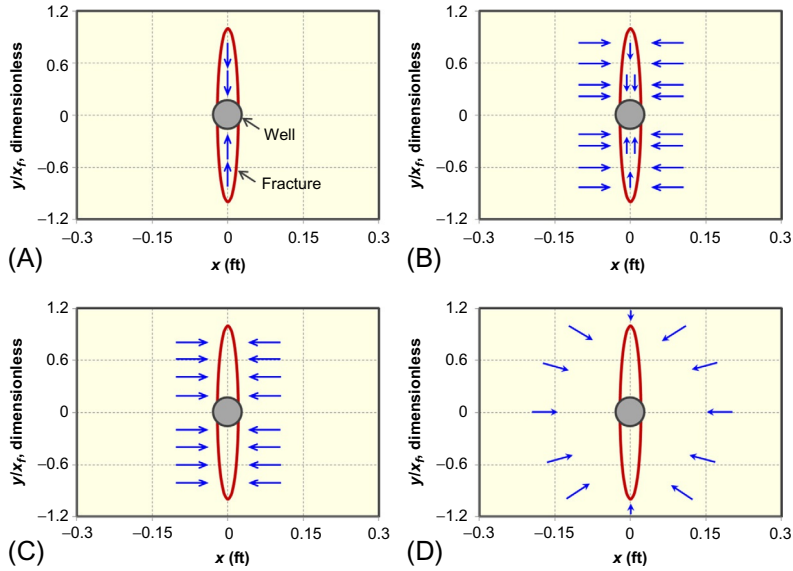

FIG. 3.48 Four flow periods for a vertically fractured well (Yu et al., 2016a). (A) Fracture linear flow. (B) Bilinear flow. (C) Formation linear flow. (D) Pseudoradial flow.

the large dimensionless conductivity such as 300. Comparison of transient flow behavior of these two fracture geometries is shown in Fig. 3.49. As shown, the bilinear flow and the pseudoradial flow exhibit for the planar fracture. However, the nonplanar fracture only shows the pseudoradial flow and the slope at early times is $<1/4$, which might be applied in the field analysis to identify whether or not there is a severe fracture width restriction around the wellbore. Fig. 3.50 compares cumulate oil production for these two fracture geometries under the constant BHP of 2000 psi. As shown, the planar fracture has the larger oil production than the nonplanar fracture. The oil production at 1000 days for the nonplanar fracture decreases by 24%, compared to the planar fracture. Hence, the curving nonplanar fracture geometry jeopardizes the well productivity compared to the planar fracture geometry, which should be examined carefully in production forecasting of tight oil reservoirs.

3.9.2 Well Interference Through Complex Fracture Hits

We performed a case study to investigate the pressure response of the shut-in well when well interference occurs due to the fracture hits (Yu et al., 2017b). Fig. 3.51 presents the configuration of fracture width distribution in two horizontal wells with multiple complex fracture hits with and without natural fractures, which were generated based on the complex fracture propagation model (Wu and Olson, 2015a, 2016). As shown, the fracture geometry is more complex at the presence of the natural fractures. The injection rate is 60 bpm for each well. Poisson ratio is 0.2. Young's modulus is 4×10^6 psi. The maximum

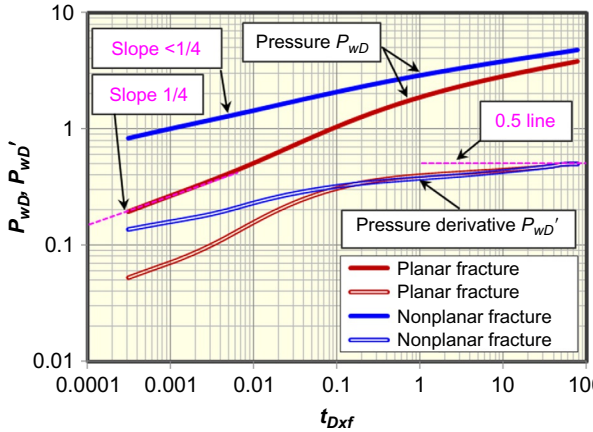

FIG. 3.49 Comparison of flow regime characterization of the two fracture geometries (Yu et al., 2016a).

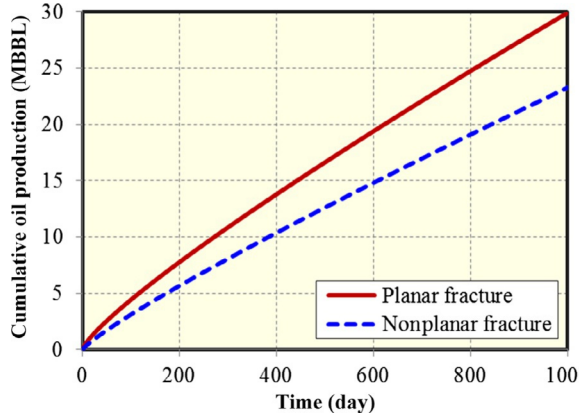

FIG. 3.50 Comparison of well performance of the two fracture geometries (Yu et al., 2016a).

horizontal stress is 4550 psi and the minimum horizontal stress is 4450 psi. The leak-off coefficient is 5×10^{-4} ft/min$^{0.5}$. Two sets of natural fractures have orientation of 45 and 135 degrees from x-axis, respectively. The other reservoir properties remain the same as in Table 3.4. Well 1 is shut in and Well 2 is producing. Fig. 3.52 compares the BHP of Well 1 for two cases, indicating that the pressure drop without natural fractures is larger than that with natural fractures. Fracture width gradually decreases from wellbore to fracture tips without perturbation of natural fractures. However, when a hydraulic fracture encounters a natural fracture and propagates along it, the fracture width on the natural fracture segment will be restricted. As shown in Fig. 3.51B, the colors that indicated fracture width distribution from wellbore to tips do not gradually change from red to blue. This width restriction acts as a choke to alleviate well interference.

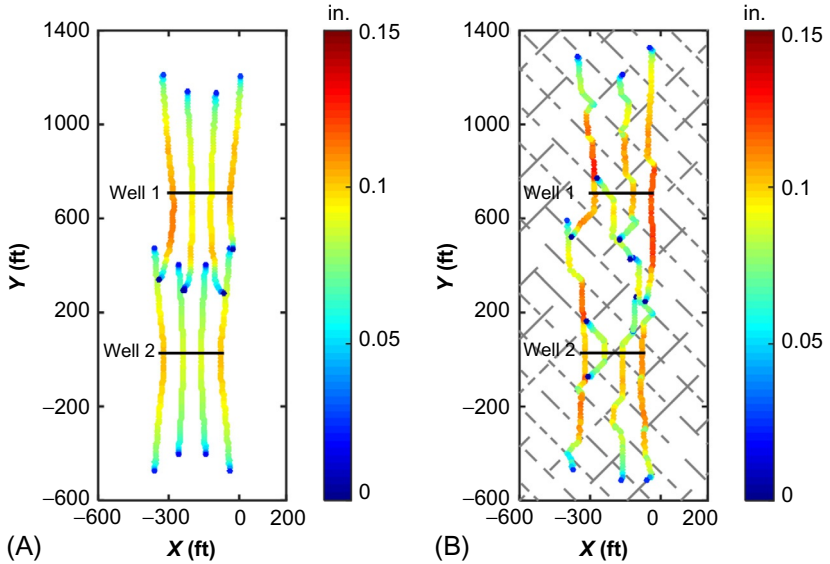

FIG. 3.51 Fracture width distribution in two horizontal wells with well interference through multiple complex fracture hits (Yu et al., 2016b). (A) Without natural fracture effect. (B) With natural fracture effect.

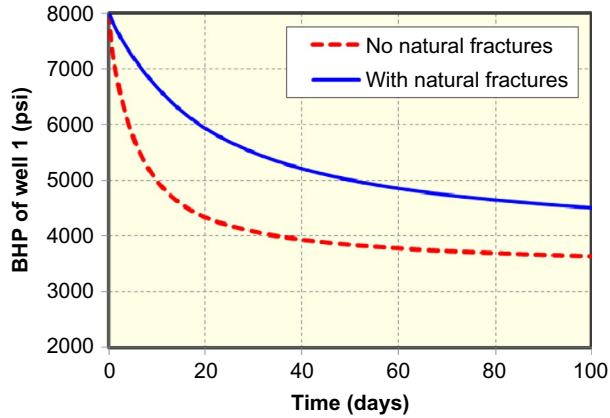

FIG. 3.52 Comparison of BHP of Well 1 between two cases with and without natural fractures (Yu et al., 2016b).

Hence, the complex nonplanar fractures in Fig. 3.51A make fluid transport from Well 1 to Well 2 much easier than that in Fig. 3.51B. Fig. 3.53 demonstrates the comparison of pressure distribution after 30 days of production, clearly indicating that the difference of intensity of well interference between two cases.

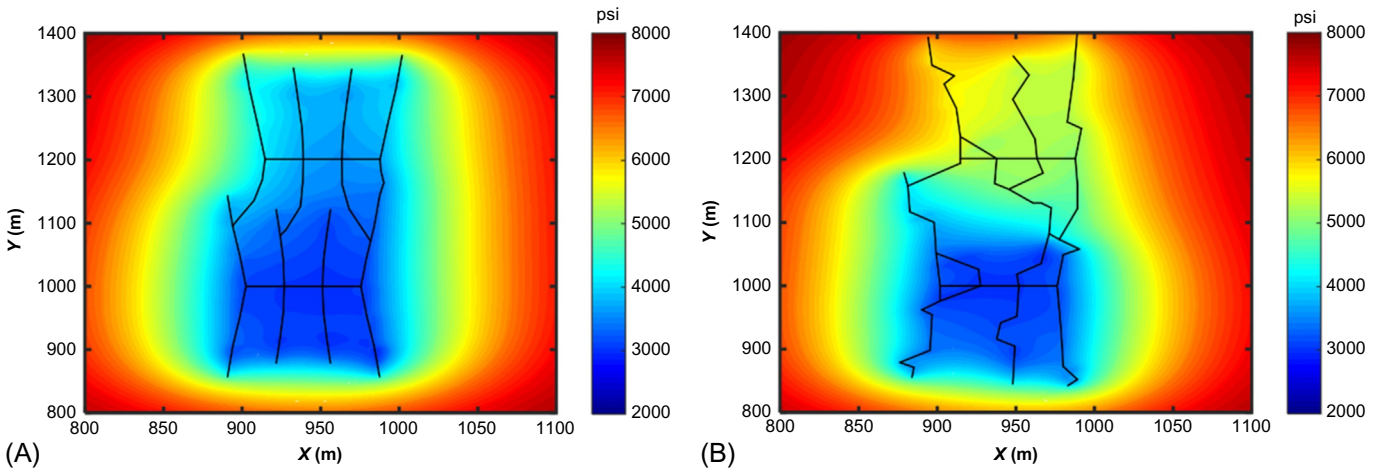

FIG. 3.53 Comparison of pressure distribution after 30 days for well interference with and without natural fractures (Yu et al., 2016b). (A) Without natural fracture effect. (B) With natural fracture effect.

REFERENCES

Al-Hussainy, R., Ramey Jr., H.J., Crawford, P.B., 1966. The flow of gases through porous media. J. Pet. Technol. 18 (5), 624–636.

Alramahi, B., Sundberg, M.I., 2012. In: Proppant embedment and conductivity of hydraulic fractures in shales. Paper ARMA 12-291, The 46th US Rock Mechanics/Geomechanics Symposium, Chicago, Illinois.

Ambrose, R.J., Hartman, R.C., Diaz-Campos, M., Akkutlu, I.Y., Sondergeld, C.H., 2012. Shale gas-in-place calculations part 1: new pore-scale considerations. SPE J. 17 (1), 219–229.

Aybar, U., Yu, W., Wshkalak, M.O., Sepehrnoori, K., 2015. Evaluation of production losses from unconventional shale reservoirs. J. Nat. Gas Sci. Eng. 23, 509–516.

Benedict, M., Webb, G.B., Rubin, L.C., 1942. An empirical equation for thermodynamic properties of light hydrocarbons and their mixtures II. Mixtures of methane, ethane, propane, and n-butane. J. Chem. Phys. 10 (12), 747–758.

Bird, G.A., 1994. Molecular Gas Dynamics and the Direct Simulation of Gas Flows. Oxford University Press, Oxford, UK.

Bird, R.B., Stewart, W.E., Lightfoot, E.N., 2007. Transport Phenomena. John Wiley & Sons, Inc, New York.

Blasingame, T.A., Poe Jr., B.D., 1993. In: Semianalytic solutions for a well with a single finite-conductivity vertical fracture. SPE Annual Technical Conference and Exhibition, Houston, Texas. Paper SPE 26424.

Bourdet, D.P., Whittle, T.M., Douglas, A.A., Pirard, Y.M., 1983. A new set of type curves simplifies well test analysis. World Oil 95–106. May.

Brunauer, S., Emmett, P.H., Teller, E., 1938. Adsorption of gases in multimolecular layers. J. Am. Chem. Soc. 60, 309–319.

Carman, P.C., 1956. Flow of Gases Through Porous Media. Academic Press Inc, New York.

Chen, C.C., Raghavan, R., 1997. A multiply-fractured horizontal well in a rectangular drainage region. SPE J. 2 (4), 455–465.

Cinco-Ley, H., Samaniego-V, F., 1981. Transient-pressure analysis for fractured wells. SPE J. 33 (9), 1749–1766.

Cipolla, C.L., Wallace, J., 2014. In: Stimulated reservoir volume: a misapplied concept?. SPE Hydraulic Fracturing Technology Conference, The Woodlands, Texas. Paper SPE 168596.

Cipolla, C.L., Fitzpatrick, T., Williams, M.J., Ganguly, U.K., 2011. In: Seismic-to-simulation for unconventional reservoir development. SPE Reservoir Characterisation and Simulation Conference and Exhibition, Abu Dhabi, UAE. Paper SPE 146876.

Cipolla, C.L., Maxwell, S., Mack, M., 2012. In: Engineering guide to the application of microseismic interpretations. SPE Hydraulic Fracturing Technology Conference, The Woodlands, Texas. Paper SPE 152165.

Clarkson, C.R., Bustin, R.M., Levy, J.H., 1997. Application of the monolayer/multilayer and adsorption potential theories to coal methane adsorption isotherms at elevated temperature and pressure. Carbon 35 (12), 1689–1705.

CMG-GEM, 2012. GEM User's Guide. Computer Modeling Group Ltd, Calgary.

Crank, J., 1975. The Mathematics of Diffusion. Clarendon Press, Oxford.

Cui, X., Bustin, A.M.M., Bustin, R.M., 2009. Measurements of gas permeability and diffusivity of tight reservoir rocks: different approaches and their applications. Geofluids 9 (3), 208–223.

Dake, L.P., 1978. Fundamentals of Reservoir Engineering. Elsevier Science Publishing Company, Amsterdam.

Dranchuk, P.M., Purvis, R.A., Robinson, D.B., 1973. In: Computer calculation of natural gas compressibility factors using the Standing and Katz correlation. Proceedings of Annual Technical Meeting, Edmonton.

Dullien, F.A.L., 1979. Porous Media, Fluid Transport and Pore Structure. Academic Press, New York.

Ecrin-Topaze, 2013. Version 4.30.08. KAPPA, Paris, France.

Ertekin, T., King, G.R., Schwerer, F.C., 1986. Dynamic gas slippage: a unique dual-mechanism approach to the flow of gas in tight formations. SPE Form. Eval. 1 (1), 43–52.

Evans, R.D., Civan, F. 1994. Characterization of non-Darcy multiphase flow in petroleum bearing formations. Report, U.S. DOE Contract No. DE-AC22-90BC14659, School of Petroleum and Geological Engineering, University of Oklahoma.

Fisher, M.K., Davidson, B.M., Goodwin, A.K., Fielder, E.O., Buckler, W.S., Steinberger, N.P., 2002. In: Integrating fracture mapping technologies to optimize stimulations in the Barnett shale. SPE Annual Technical Conference and Exhibition, San Antonio, Texas. Paper SPE 77411.

Fisher, M.K., Heinze, J.R., Harris, C.D., Davidson, B.M., Wright, C.A., Dunn, K.P., 2004. In: Optimizing horizontal completion techniques in the Barnett shale using microseismic fracture mapping. SPE Annual Technical Conference and Exhibition, Houston, Texas. Paper SPE 90051.

Florence, F.A., Rushing, J., Newsham, K.E., Blasingame, T.A., 2007. In: Improved permeability prediction relations for low permeability sands. SPE Rocky Mountain Oil & Gas Technology Symposium, Denver, Colorado.

Freeman, C.M., Moridis, G.J., Michael, G.E., Blasingame, T.A., 2012. In: Measurement, modeling, and diagnostics of flowing gas composition changes in shale gas wells. SPE Latin American and Caribbean Petroleum Engineering Conference, Mexico City, Mexico. Paper SPE 153391.

Gao, C., Lee, J.W., Spivey, J.P., Semmelbeck, M.E., 1994. In: Modeling multilayer gas reservoirs including sorption effects. SPE Eastern Regional Conference and Exhibition, Charleston, West Virginia. Paper SPE 29173.

Gringarten, A.C., Ramey Jr., H.J., Raghavan, R. 1975. Applied pressure analysis for fractured wells. J. Pet. Technol., 27 (7): 887–892.

Gringarten, A.C., Rameny Jr., H.J., 1973. The use of source and Green's functions in solving unsteady-flow problems in reservoirs. SPE J. 13 (5), 285–296.

Gringarten, A.C., Ramey Jr., H.J., Raghavan, R., 1972. Unsteady-state pressure distribution created by a well with a single infinite-conductivity vertical fracture. SPE J. 14 (4), 347–360.

Guppy, K.H., Cinco-Ley, H., Ramey Jr., H.J., Samaniego-V, F., 1982. Non-Darcy flow in wells with finite conductivity vertical fractures. SPE J. 22 (5), 681–698.

Hao, S., Chu, W., Jiang, Q., Yu, X., 2014. Methane adsorption characteristics on coal surface above critical temperature through Dubinin-Astakhov model and Langmuir model. Colloids Surf. A Physicochem. Eng. Asp. 444, 104–113.

Heidemann, R.A., Jeje, A.A., Mohtadi, F., 1984. An Introduction to the Properties of Fluids and Solids. University of Calgary Press, Calgary, Canada.

Karniadakis, G.E., Beskok, A., 2002. Micro-Flows, Fundamentals and Simulation. Spriger-Verlag, New York.

Khan, W.A., Rehman, S.A., Akram, A.H., Ahmad, A., 2011. In: Factors affecting production behavior in tight gas reservoirs. SPE/DGS Saudi Arabia Section Technical Symposium and Exhibition, Al-Khobar, Saudi Arabia, 15–18 May. Paper SPE 149045.

Kuila, U., Prasad, M., 2013. Specific surface area and pore-size distribution in clays and shales. Geophys. Prospect. 61, 341–362.

Langmuir, I., 1918. The adsorption of gases on plane surfaces of glass, mica and platinum. J. Am. Chem. Soc. 40, 1403–1461.

Lee, A., Gonzalez, M., Eakin, B., 1966. The viscosity of natural gases. J. Pet. Technol. 18 (8), 997–1000.

Li, L., Lee, S.H., 2008. Efficient field-scale simulation of black oil in a naturally fractured reservoir through discrete fracture networks and homogenized media. SPE Reserv. Eval. Eng. 11 (4), 750–758.

Mahmoud, M., 2014. Development of a new correlation of gas compressibility factor (Z-factor) for high pressure gas reservoirs. J. Energy Resour. Technol. 136, 1–11.

Matthews, C.S., Russell, D.G., 1967. Pressure Buildup and Flow Tests in Wells. AIME Monograph, vol. 1. SPE-AIME, New York.

Maxwell, S.C., Urbancic, T.I., Steinsberger, N.P., Zinno, R., 2002. In: Microseismic imaging of hydraulic fracture complexity in the Barnett shale. SPE Annual Technical Conference and Exhibition, San Antonio, Texas. Paper SPE 77440.

McDuff, R.E., Ellis, R.A., 1979. Determining diffusion coefficients in marine sediments: a laboratory study of the validity of resistivity techniques. Am. J. Sci. 279, 666–675.

Mirzaei, M., Cipolla, C.L., 2012. In: A workflow for modeling and simulation of hydraulic fractures in unconventional gas reservoirs. SPE Middle East Unconventional Gas Conference and Exhibition, Abu Dhabi, UAE. Paper SPE 153022.

Moinfar, A., Varavei, A., Sepehrnoori, K., Johns, R.T., 2013. In: Development of a coupled dual continuum and discrete fracture model for the simulation of unconventional reservoirs. SPE Reservoir Simulation Symposium, The Woodlands, Texas. Paper SPE 163647.

Mosher, K., He, J., Liu, Y., Rupp, E., Wilcox, J., 2013. Molecular simulation of methane adsorption in micro- and mesoporous carbons with applications to coal and gas shale systems. Int. J. Coal Geol. 109–110, 36–44.

Mukherjee, H., Economides, M.J., 1991. A parametric comparison of horizontal and vertical well performance. SPE Form. Eval. 6 (2), 209–216.

NIST, 2011. Thermophysical properties of fluid systems. http://webbook.nist.gov/chemistry/fluid/.

Olorode, O.M., Freeman, C.M., Moridis, G.J., Blasingame, T.A., 2013. High-resolution numerical modeling of complex and irregular fracture patterns in shale-gas reservoirs and tight gas reservoirs. SPE Reserv. Eval. Eng. 16 (4), 1–13.

Olson, J.E., 1995. In: Fracturing from highly deviated and horizontal wells: numerical analysis of non-planar fracture propagation. Low Permeability Reservoirs Symposium, Denver, Colorado. Paper SPE 29573.

Olson, J.E., Wu, K., 2012. In: Sequential vs. simultaneous multizone fracturing in horizontal wells: insights from a non-planar, multifrac numerical model. SPE Hydraulic Fracturing Technology Conference, The Woodlands, Texas. Paper SPE 152602.

Ozdemir, E., 2004. Chemistry of the Adsorption of Carbon Dioxide by Argonne Permium Coals and a Model to Simulate CO_2 Sequestration in Coal Seams. PhD Dissertation, University of Pittsburgh.

Patzek, T.W., Male, F., Marder, M., 2013. Gas production in the Barnett shale obeys a simple scaling theory. PNAS 110 (49), 19731–19736.

Riewchotisakul, S., Akkutlu, I.Y., 2015. In: Adsorption enhanced transport of hydrocarbons in organic nanopores. SPE Annual Technical Conference and Exhibition, Houston, Texas. Paper SPE 175107.

Rubin, B., 2010. In: Accurate simulation of non-Darcy flow in stimulated fractured shale reservoirs. SPE Western Regional Meeting, Anaheim, California. Paper SPE 132093.

Satterfield, C.N., Colton, C.K., Pitcher, W.H., 1973. Restricted diffusion in liquids within fine pores. AICHE J. 19 (3), 628–635.

Shakiba, M., 2014. Modeling and Simulation of Fluid Flow in Naturally and Hydraulically Fractured Reservoirs Using Embedded Discrete Fracture Model (EDFM). Master ThesisThe University of Texas at Austin.

Silin, D., Kneafsey, T., 2012. Shale gas: nanometer-scale observations and well modeling. J. Can. Pet. Technol. 51 (6), 464–475.

Sing, K.S.W., Everett, D.H., Haul, R.A.W., Moscou, L., Pierotti, R.A., Rouquerol, J., Siemieniewska, T., 1985. Reporting physisorption data for gas/solid systems with special reference to the determination of surface area and porosity (recommendations 1984). Pure Appl. Chem. 57 (4), 603–619.

Smith, D.M., Williams, F.L., 1984. Diffusional effects in the recovery of methane from coalbeds. SPE J. 24 (5), 529–535.

Sneddon, I.N., 1951. Fourier Transforms. McGraw-Hill, New York.

Tavassoli, S., Yu, W., Javadpour, F., Sepehrnoori, K., 2013a. Well screen and optimum refracturing time: a Barnett shale well. J. Pet. Eng. Article ID 817293.

Tavassoli, S., Yu, W., Javadpour, F., Sepehrnoori, K., 2013b. In: Selection of candidate horizontal wells and determination of the optimal time of refracturing in Barnett shale (Johnson county). SPE Unconventional Resources Conference, Calgary, Alberta, Canada. Paper SPE 167137.

Terracina, J.M., Turner, J.M., Collins, D.H., Spillars, S.E., 2010. In: Proppant selection and its effect on the results of fracturing treatments performed in shale formations. SPE Annual Technical Conference and Exhibition, Florence, Italy. Paper SPE 135502.

Thambynayagam, R.M.K., 2011. The Diffusion Handbook: Applied Solutions for Engineers. McGraw-Hill Professional, New York.

Warpinski, N.R., Kramm, R.C., Heinze, J.R., Waltman, C.K., 2005. In: Comparison of single and dual-array microseismic mapping techniques in the Barnett shale. SPE Annual Technical Conference and Exhibition, Dallas, Texas. Paper SPE 95568.

Weng, X., 2014. Modeling of complex hydraulic fractures in naturally fractured formation. J. Unconv. Oil Gas Resour. 9, 114–135.

Weng, X., Kresse, O., Cohen, C., Wu, R., Gu, H., 2011. Modeling of hydraulic-fracture-network propagation in a naturally fractured formation. SPE Prod. Oper. 26 (4), 368–380.

Witherspoon, P., Wang, J., Iwai, K., Gale, J., 1980. Validity of cubic law for fluid flow in a deformable rock fracture. Water Resour. Res. 16 (6), 1016–1024.

Wu, K., 2014. Numerical Modeling of Complex Hydraulic Fracture Development in Unconventional Reservoirs. PhD Dissertation, The University of Texas at Austin, Austin, TX.

Wu, K., Olson, J.E., 2013. Investigation of the impact of fracture spacing and fluid properties for interfering simultaneously or sequentially generated hydraulic fractures. SPE Prod. Oper. 28 (4), 427–436.

Wu, K., Olson, J.E., 2014. In: Mechanics analysis of interaction between hydraulic and natural fractures in shale reservoirs. SPE/AAPG/SEG Unconventional Resources Technology Conference, Denver, Colorado. Paper SPE-2014-1922946.

Wu, K., Olson, J.E., 2015a. Simultaneous multi-frac treatments: fully coupled fluid flow and fracture mechanics for horizontal wells. SPE J. 20 (2), 337–346.

Wu, K., Olson, J.E., 2015b. A simplified three-dimensional displacement discontinuity method for multiple fracture simulations. Int. J. Fract. 193 (2), 191–204.

Wu, K., Olson, J.E., 2016. Numerical investigation of complex fracture networks in naturally fractured reservoirs. SPE Prod. Oper. 31 (4), 300–309.

Wu, R., Kresse, O., Weng, X., Cohen, C., Gu, H., 2012. In: Modeling of interaction of hydraulic fractures in complex fracture networks. SPE Hydraulic Fracturing Technology Conference, The Woodlands, Texas. Paper SPE 152052.

Xu, W., 2014. In: Modeling gas transport in shale reservoir – conservation laws revisited. Unconventional Resources Technology Conference, Denver, Colorado. Paper URTeC 1924016.

Xu, G., Wong, S.W., 2013. In: Interaction of multiple non-planar hydraulic fractures in horizontal wells. International Petroleum Technology Conference, Beijing, China. Paper IPTC 17043.

Xu, W., Thiercelin, M., Ganguly, U., Weng, X., Gu, H., Onda, H., Sun, J., Calvez, J.L., 2010. In: Wiremesh: a novel shale fracturing simulator. International Oil and Gas Conference and Exhibition, Beijing, China. Paper SPE 132218.

Yu, W., 2015. Developments in Modeling and Optimization of Production in Unconventional Oil and Gas Reservoirs. PhD DissertationThe University of Texas at Austin, Austin, TX.

Yu, W., Sepehrnoori, K., 2013a. In: Optimization of multiple hydraulically fractured horizontal wells in unconventional gas reservoirs. SPE Production and Operation Symposium, Oklahoma, Oklahoma. Paper SPE 164509.

Yu, W., Sepehrnoori, K., 2013b. In: Numerical evaluation of the impact of geomechanics on well performance in shale gas reservoirs. 47th US Rock Mechanics/Geomechanics Symposium, San Francisco, California. Paper ARMA 13-555.

Yu, W., Sepehrnoori, K., 2013c. In: Simulation of proppant distribution effect on well performance in shale gas reservoirs. SPE Unconventional Resources Conference, Calgary, Alberta, Canada. Paper SPE 167225.

Yu, W., Sepehrnoori, K., 2014a. In: Sensitivity study and history matching and economic optimization for Marcellus shale. SPE/AAPG/SEG Unconventional Resources Technology Conference, Denver, Colorado. Paper SPE-2014-1923491.

Yu, W., Sepehrnoori, K., 2014b. An efficient reservoir simulation approach to design and optimize unconventional gas production. J. Can. Pet. Technol. 53, 109–121.

Yu, W., Sepehrnoori, K., 2014c. Simulation of gas desorption and geomechanics effects for unconventional gas reservoirs. Fuel 116, 455–464.

Yu, W., Sepehrnoori, K., 2014d. In: Optimization of well spacing for Bakken tight oil reservoirs. SPE/AAPG/SEG Unconventional Resources Technology Conference, Denver, Colorado. Paper SPE-2014-1922108.

Yu, W., Huang, S., Wu, K., Sepehrnoori, K., Zhou, W., 2014a. In: Development of a semi-analytical model for simulation of gas production in shale gas reservoirs. SPE/AAPG/SEG Unconventional Resources Technology Conference, Denver, Colorado. Paper SPE-2014-1922945.

Yu, W., Al-Shalabi, E.W., Sepehrnoori, K., 2014b. In: A sensitivity study of potential CO_2 injection for enhanced gas recovery in Barnett shale reservoirs. SPE Unconventional Resources Conference, The Woodlands, Texas. Paper SPE 169012.

Yu, W., Gao, B., Sepehrnoori, K., 2014c. Numerical study of the impact of complex fracture patterns on well performance in shale gas reservoirs. J. Pet. Sci. Res. 3, 83–89.

Yu, W., Luo, Z.Y., Javadpour, F., Varavei, A., Sepehrnoori, K., 2014d. Sensitivity analysis of hydraulic fracture geometry in shale gas reservoirs. J. Pet. Sci. Eng. 113, 1–7.

Yu, W., Sepehrnoori, K., Patzek, T.W., 2014e. In: Evaluation of gas adsorption in Marcellus shale. SPE Annual Technical Conference an Exhibition, Amsterdam, The Netherlands. Paper SPE 170801.

Yu, W., Zhang, T., Du, S., Sepehrnoori, K., 2015a. Numerical study of the effect of uneven proppant distribution between multiple fractures on shale gas well performance. Fuel 142, 189–198.

Yu, W., Varavei, A., Sepehrnoori, K., 2015b. Optimization of shale gas production using design of experiment and response surface methodology. Energy Sources A Recovery Util. Environ. Effects 37 (8), 906–918.

Yu, W., Wu, K., Sepehrnoori, K., 2016a. A semianalytical model for production simulation from nonplanar hydraulic-fracture geometry in tight oil reservoirs. SPE J. 21 (3), 1028–1040.

Yu, W., Wu, K., Zuo, L., Tan, X., Weijermars, R., 2016b. In: Physical models for inter-well interference in shale reservoirs: relative impacts of fracture hits and matrix permeability. Unconventional Resources Technology Conference, San Antonio, Texas.

Yu, W., Wu, K., Sepehrnoori, K., Xu, W., 2017a. A comprehensive model for simulation of gas transport in shale formation with complex hydraulic-fracture geometry. SPE Reserv. Eval. Eng. 20 (3), 547–561.

Yu, W., Xu, Y., Weijermars, R., Wu, K., Sepehrnoori, K., 2017b. In: Impact of well interference on shale oil production performance: a numerical model for analyzing pressure response of fracture hits with complex geometries. SPE Hydraulic Fracturing Technology Conference and Exhibition, The Woodlands, Texas.

Zhou, W., Banerjee, R., Poe, B., Spath, J., Thambynayagam, M., 2013. Semianalytical production simulation of complex hydraulic-fracture networks. SPE J. 19 (1), 6–18.

Chapter 4

Modeling Gas Adsorption in Marcellus Shale Using Langmuir and BET Isotherms

Chapter Outline

4.1 INTRODUCTION

In recent years, the boom of shale gas production was fueled by the improvements in horizontal drilling and multistage hydraulic fracturing technologies. As a result, shale gas has become an increasingly important source of natural gas supply in North America and around the world. In nature, gas shales are characterized by extremely small grain size, extremely low permeability on the order of nano-Darcy (10^{-6} md), small porosity, and high total organic carbon (TOC). For instance, the TOC in Marcellus Shale ranges 2–20 wt% and clay content is 10–45 wt% (Boyce et al., 2010). Shale can serve as both source and reservoir rock. The amount of gas in place in shale is strongly affected by TOC, clays, and adsorption ability of methane on the internal surface of solid (Martin et al., 2010). In general, complex fracture networks that are generated connect the shale formation and the horizontal well. Shale matrix has strong gas storage capacity but cannot transport the gas across long distance because it is very tight; a fracture network can transport the gas efficiently due to large hydraulic conductivity but has limited storage capacity (Lane et al., 1989; Carlson and Mercer, 1991). Since a part of gas in shale reservoirs is adsorbed, investigation of gas adsorption can provide critical insights into evaluation of well performance, shale characterization, and optimization of fracture design in shale gas reservoirs.

Generally, natural gas in shale reservoirs is stored as free gas in both organic matter (kerogen) and larger mineral pores and natural fractures, as well as

Shale Gas and Tight Oil Reservoir Simulation. https://doi.org/10.1016/B978-0-12-813868-7.00004-3

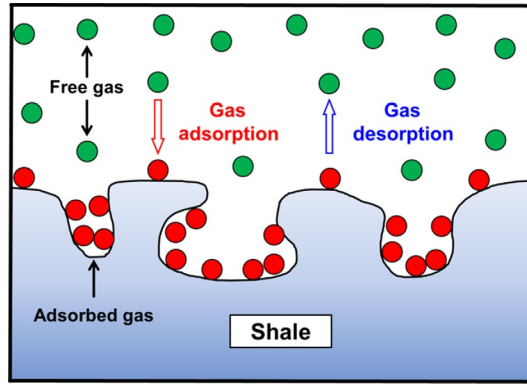

FIG. 4.1 Free gas and adsorbed gas in shale gas reservoirs (Yu, 2015).

adsorbed gas within organic matter (Leahy-Dios et al., 2011), as shown in Fig. 4.1. The adsorbed gas has higher density than the surrounding free gas. Clarkson and Haghshenas (2013) presented five mechanisms for methane existence in shale gas reservoirs: (1) adsorption on internal surface area; (2) conventional (compressed gas) storage in natural and hydraulic (induced) fractures; (3) conventional storage in matrix porosity (organic and inorganic); (4) solution in formation water; (5) absorption (solution) in organic matter. The organic matter is nanoporous material primarily consisting of micropores (pore length less than 2 nm) and mesopores (pore length between 2 and 50 nm) (Kang et al., 2011). The pore-size heterogeneity such as varying pore size, shape, and surface roughness greatly influences the gas transport and adsorption properties in shale gas reservoirs (Firouzi et al., 2014a,b). The organic matter occupies only a part of the bulk rock as connected clusters embedded in the rock or dispersion among mineral grains (Silin and Kneafsey, 2012). In the Appalachian Basin, the well performance from darker zones within Devonian Shale with higher organic content is better than that from organic-poor gray zones (Schmoker, 1980). Lu et al. (1995) showed that the relationship between gas adsorption capacity and TOC is approximately linear when the TOC is high; while for a very low TOC, illite plays an important role in gas storage in Devonian shales. The adsorption process in shale gas reservoirs is mainly physical adsorption, which means that the adsorption is fully reversible, allowing gas molecules to completely adsorb and desorb, and the interaction force between the solid surface and the adsorbed gas molecules is controlled by the weak van der Waals force. The specific surface area, defined as surface area per gram of solid, plays an important role in controlling the adsorption capacity. The rougher solid surface and the smaller pore sizes can contribute a larger specific surface area (Solar et al., 2010). The specific surface area can be calculated using the BET method (Brunauer et al., 1938). A rough solid surface with many nanometer-scale cavities can adsorb gas more strongly than an ideally polished surface (Rouquerol et al., 1999; Solar et al., 2010).

A recent study conducted by the U.S. Energy Information Administration (EIA, 2014) concludes that the Marcellus Shale is one of six key tight oil and shale gas regions, which account for 95% of domestic oil production growth and all domestic natural gas production growth during 2011–2013. The Marcellus Shale is located in the Appalachian basin across six states, including Pennsylvania, New York, West Virginia, Ohio, Virginia, and Maryland. The Marcellus Shale covers a total area of more than 100,000 mile^2, and the depth is in the range of 4000–8500 ft with an average thickness of 50–200 ft. (Department of Energy, 2013). The average estimated ultimate recovery (EUR) is about 2.325 BCF (billion cubic feet) per well and the average porosity is 8% and TOC is 12 wt% (EIA, 2011). The Marcellus Shale has 1500 TCF (trillion cubic feet) of original gas in place (OGIP) with 141 TCF of technically recoverable gas (Department of Energy, 2013). Reservoir temperature in the Marcellus Shale is observed to be around 140°F and bottomhole pressure is up to be 6000 psi (Williams et al., 2011). The kerogen type of Marcellus Shale is primarily Type II with a mixture of Type III (Weary et al., 2000).

Most publications to date have used the Langmuir isotherm to describe gas desorption in shale gas reservoirs. In this study, we observed that the gas desorption in some areas of the Marcellus Shale follows the BET isotherm based on laboratory measurements. The Langmuir and BET isotherms were compared with experimental data. In addition, through history matching with one production well in the Marcellus Shale, we evaluated the effect of gas adsorption on well performance at short and long production times.

4.2 ADSORPTION MODEL FOR SHALE GAS RESERVOIRS

Adsorption at the gas/solid interface is referred to as the enrichment of one or more components in an interfacial layer (Sing et al., 1985). The organic matter in shale has a strong adsorption potential due to large surface area and affinity to methane. In order to simulate gas production in shale gas reservoirs, an accurate model of gas adsorption is very important. According to the International Union of Pure and Applied Chemistry (IUPAC) standard classification system (Sing et al., 1985), there are six different types of adsorption, as shown in Fig. 4.2. The shape of the adsorption isotherm is closely related to the properties of adsorbate and solid adsorbent and the pore-space geometry (Silin and Kneafsey, 2012). The detailed description of the six isotherm classifications can be found in Sing et al. (1985).

The most commonly applied adsorption model for shale gas reservoirs is the classic Langmuir isotherm (Type I) (Langmuir, 1918), which is based on the assumption that there is a dynamic equilibrium at constant temperature and pressure between adsorbed and nonadsorbed gas. Also, it is assumed that there is only a single layer of molecules covering the solid surface. The Langmuir isotherm has two fitting parameters:

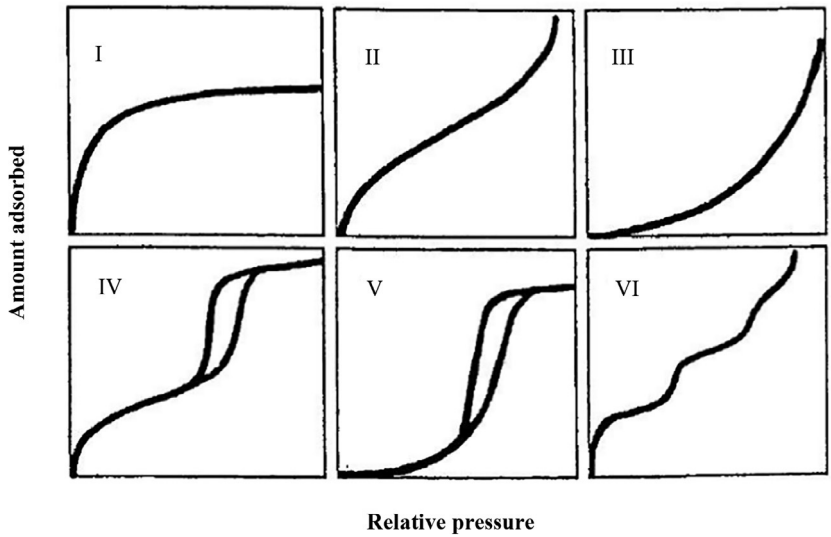

FIG. 4.2 Six types of physical sorption isotherms according to the IUPAC classification (Sing et al., 1985).

$$v(p) = \frac{v_L p}{p + p_L}, \tag{4.1}$$

where $v(p)$ is the gas volume of adsorption at pressure p, v_L is Langmuir volume, and p_L is Langmuir pressure. Instantaneous equilibrium of the sorbing surface and the storage in the pore space is assumed to be established for the Langmuir isotherm (Freeman et al., 2012).

At high reservoir pressures, on can expect that natural gas sorbed on the organic carbon surfaces forms multimolecular layers. In other words, the Langmuir isotherm may not be a good approximation of the amount of gas sorbed on organic carbon-rich mudrocks. Instead, multilayer sorption of natural gas should be expected on organic carbon surfaces, and the gas adsorption isotherm of Type II should be a better choice. Type II isotherm often occurs in a nonporous or a macroporous material (Kuila and Prasad, 2013). In 1938, Stephen Brunauer, Paul Hugh Emmett, and Edward Teller (BET) published their theory in the *Journal of the American Chemical Society* (Brunauer et al., 1938). The BET isotherm model is a generalization of the Langmuir model to multiple adsorbed layers. The expression is shown as follows:

$$v(p) = \frac{v_m C p}{(p_o - p)[1 + (C-1)p/p_o]}, \tag{4.2}$$

where p_o is the saturation pressure of the gas; v_m is the maximum adsorption gas volume when the entire adsorbent surface is being covered with a complete monomolecular layer; and C is a constant related to the net heat of adsorption, which is defined as:

$$C = \exp\left(\frac{E_1 - E_L}{RT}\right), \tag{4.3}$$

where E_1 is the heat of adsorption for the first layer, and E_L is that for the second and higher layers and is equal to the heat of liquefaction. The assumptions in the BET theory include homogeneous surface, no lateral interaction between molecules, and the uppermost layer is in equilibrium with gas phase.

The standard BET isotherm assumes that the number of adsorption layers is infinite. But, in the case of n adsorption layers in some finite number, then a general form of BET isotherm is given as:

$$v(p) = \frac{v_m C \frac{p}{p_o}}{1 - \frac{p}{p_o}} \left[\frac{1 - (n+1)\left(\frac{p}{p_o}\right)^n + n\left(\frac{p}{p_o}\right)^{n+1}}{1 + (C-1)\frac{p}{p_o} - C\left(\frac{p}{p_o}\right)^{n+1}} \right]. \tag{4.4}$$

When $n = 1$, Eq. (4.4) will reduce to the Langmuir isotherm, Eq. (4.1). When $n = \infty$, Eq. (4.4) will reduce to Eq. (4.2).

Here $v(p)$ is the specific volume of gas adsorbed at the reservoir pressure and temperature per unit mass of bulk rock, reference to a standard pressure and temperature (stock tank condition (ST) in the oil industry). The customary cubic fields are the standard cubic feet of sorbed gas per ton of bulk rock (scf/ton), or the standard cubic centimeters of gas per gram of rock. The conversion factor is

$$1\left(\frac{\text{scf}}{\text{ton of bulk rock}}\right) = \frac{1}{32}\left(\frac{\text{standard cm}^3}{\text{g of bulk rock}}\right). \tag{4.5}$$

It should be noted that it is very challenging to apply the BET model to physically explain the supercritical methane adsorption since there is no concept of a liquid if the reservoir temperature is above the critical methane temperature. Consequently, the saturation pressure (p_o) also loses its physical meaning (Ozdemir, 2004). To avoid this issue, the saturation pressure (p_o) is treated as pseudosaturation pressure (p_s) for the high-pressure/temperature methane adsorption (Clarkson et al., 1997). In this study, the method of extrapolation of the Antoine equation is used to calculate the pseudosaturation pressure for supercritical methane adsorption as follows (NIST, 2011; Hao et al., 2014):

$$\ln p_s = 7.7437 - \frac{1306.5485}{19.4362 + T}, \tag{4.6}$$

where T is temperature (K) and p_s is pseudosaturation pressure (MPa).

In this study, we mainly focus on fitting the experimental measurements of supercritical methane adsorption by fixing the pseudosaturation pressure and tuning three fitting parameters of v_m, C, and n. For practical application, the BET isotherm model can easily be utilized in a reservoir simulator to model the contribution of gas desorption on well performance in some shale gas reservoirs. Although there are some physical adsorption models such as the simplified local

density model, the 2D equation of state model (Chareonsuppanimit et al., 2012; Clarkson and Haghshenas, 2013), and molecular simulation (Firouzi and Wilcox, 2012; Firouzi et al., 2014b), we did not utilize the mentioned models in this study.

Fig. 4.3 compares shapes of the Langmuir and BET isotherms: gas desorption along the BET isotherm contributes more significantly at early time of production than that with the Langmuir isotherm curve. This is because the slope of the BET isotherm curve at high pressure is larger than that of the Langmuir isotherm curve, resulting in more adsorbed gas releasing at early production times. In addition, under the same pressure drop from the initial reservoir pressure to the bottomhole pressure (BHP), the amount of released adsorbed gas with the BET isotherm curve is larger than that with the Langmuir isotherm curve.

4.3 GAS FLOW MODEL IN SHALE

An equation to describe mass balance of gas flow in shale gas reservoirs by considering the gas desorption effect is given (Patzek et al., 2013; Yu et al., 2014a):

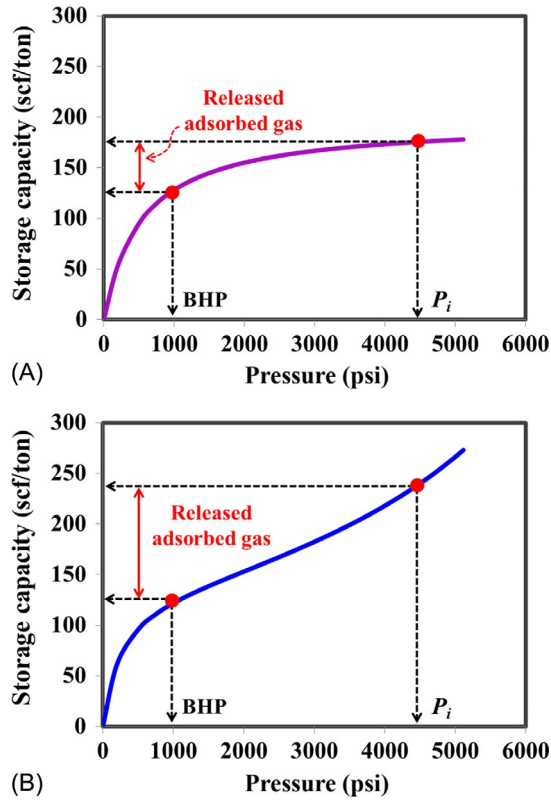

FIG. 4.3 Comparison of the Langmuir and BET isotherms (Yu, 2015). (A) Langmuir isotherm curve. (B) BET isotherm curve.

$$\frac{\partial\left[\rho_g S_g\phi+(1-\phi)\rho_a\right]}{\partial t}=-\left[\frac{\partial\left(\rho_g u_g\right)}{\partial x}+\frac{\partial\left(\rho_g u_g\right)}{\partial y}+\frac{\partial\left(\rho_g u_g\right)}{\partial z}\right], \tag{4.7}$$

where u_g is Darcy velocity of gas, S_g is initial gas saturation, ρ_g is the free gas density, and ρ_a is the adsorbed gas mass per unit shale volume (kilograms of adsorbed gas per cubic meter of solid).

The final governing nonlinear equation of transient gas flow in shale gas reservoirs, considering the gas desorption effect, is shown as follows and more details about the derivation can be found in our previous work (Yu et al., 2014a):

$$\left[\frac{\partial}{\partial x}\left(\frac{\rho_g k}{\mu_g}\frac{\partial p}{\partial x}\right)+\frac{\partial}{\partial y}\left(\frac{\rho_g k}{\mu_g}\frac{\partial p}{\partial y}\right)+\frac{\partial}{\partial z}\left(\frac{\rho_g k}{\mu_g}\frac{\partial p}{\partial z}\right)\right]=\left[\phi S_g+(1-\phi)K_a\right]c_g\rho_g\frac{\partial p}{\partial t}, \tag{4.8}$$

where k is reservoir permeability, c_g is the isothermal gas compressibility factor, K_a is the differential equilibrium partitioning coefficient of gas at a given temperature (Patzek et al., 2013), defined as follows:

$$K_a=\left(\frac{\partial\rho_a}{\partial\rho_g}\right)_T. \tag{4.9}$$

The mass balance of adsorbed gas in one unit bulk volume is described as

$$\rho_a V_b(1-\phi)=\rho_g(p_{ST},T_{ST})\rho_b V_b v, \tag{4.10}$$

where ρ_b is bulk density of shale; V_b is unit volume of bulk rock; v is the specific volume of gas adsorbed per unit mass of bulk rock (scf/ton), which is measured at the reservoir pressure and temperature and then transferred to standard condition; and $\rho_g(p_{st}, T_{st})$ is the stock tank gas density.

The adsorbed gas mass per unit shale volume at the standard condition can be calculated as follows:

$$\rho_a=\frac{\rho_g(p_{ST},T_{ST})\rho_b v}{1-\phi}. \tag{4.11}$$

The differential equilibrium partitioning coefficient of gas can be expressed by

$$K_a=\left(\frac{\partial\rho_a}{\partial\rho_g}\right)_T=\frac{\rho_g(p_{ST},T_{ST})\rho_b}{1-\phi}\frac{\partial v}{\partial p}\frac{\partial p}{\partial\rho_g}. \tag{4.12}$$

The isothermal gas compressibility factor can be determined as

$$c_g=\frac{1}{\rho_g}\left(\frac{\partial\rho_g}{\partial p}\right)_T. \tag{4.13}$$

The equation of state for real gas is given by

$$\rho_g = \frac{pM}{Z(p)RT}, \tag{4.14}$$

where p is pressure in kPa, M is the molecular weight of the gas ($M = \gamma_g M_{air}$, where $M_{air} = 29$ kg/kmol is the molecular weight of air), R is the ideal gas constant with 8.3145 kPa m^3/(kmol K), T is absolute temperature (K), and $Z(p)$ is the gas compressibility factor.

Mahmoud (2014) developed a new correlation for calculating the real gas compressibility as follows:

$$c_g = \frac{c_{pr}}{p_c}, \tag{4.15}$$

$$c_{pr} = \frac{1}{p_{pr}} - \frac{1}{Z(p)}\left[\left(1.404e^{-2.5T_{pr}}\right)p_{pr} - \left(5.524e^{-2.5T_{pr}}\right)\right], \tag{4.16}$$

$$p_{pr} = \frac{p}{p_c}, \tag{4.17}$$

$$T_{pr} = \frac{T}{T_c}, \tag{4.18}$$

where p_c is the gas critical pressure, c_{pr} is the reduced gas compressibility, p_{pr} is the reduced pressure, and T_{pr} is the reduced temperature.

Substituting Eq. (4.13) into Eq. (4.12) yields

$$K_a = \left(\frac{\partial \rho_a}{\partial \rho_g}\right)_T = \frac{\rho_g(p_{ST}, T_{ST})\rho_b}{(1-\phi)\rho_g c_g}\frac{\partial v}{\partial p}. \tag{4.19}$$

Consequently, for the Langmuir isotherm equation, the differential equilibrium partitioning coefficient of gas can be expressed as follows:

$$K_a = \left(\frac{\partial \rho_a}{\partial \rho_g}\right)_T = \frac{\rho_g(p_{ST}, T_{ST})\rho_b}{(1-\phi)c_g\rho_g}\frac{v_L p_L}{(p_L+p)^2} = \frac{\rho_g(p_{ST}, T_{ST})\rho_b}{(1-\phi)c_g\rho_g}\frac{v^2 p_L}{v_L p^2}. \tag{4.20}$$

For the general form of BET isotherm, the differential equilibrium partitioning coefficient of gas can be expressed as

$$K_a = \left(\frac{\partial \rho_a}{\partial \rho_g}\right)_T = \frac{\rho_g(p_{ST}, T_{ST})\rho_b}{(1-\phi)c_g\rho_g} \times \left(A - B + \frac{vp_s}{p(p_s-p)}\right), \tag{4.21}$$

$$A = \frac{v_m C p}{p_s(p_s-p)} \times \frac{n(n+1)\left(\frac{p}{p_s}\right)^n - n(n+1)\left(\frac{p}{p_s}\right)^{n-1}}{1 + (C-1)\frac{p}{p_s} - C\left(\frac{p}{p_s}\right)^{n+1}}, \tag{4.22}$$

$$B = \frac{v}{p_s} \times \frac{C - 1 - C(n+1)\left(\frac{p}{p_s}\right)^n}{1 + (C-1)\frac{p}{p_s} - C\left(\frac{p}{p_s}\right)^{n+1}}. \tag{4.23}$$

4.4 METHANE ADSORPTION MEASUREMENTS IN MARCELLUS SHALE

In this study, measurements for methane adsorption were conducted by Weatherford laboratories isotherm equipment featuring two independent covered oil baths, metal-to-metal seals on pressure cells in place of O-ring seals, pressure capabilities to 10,000 psi, and temperatures up to 350°F. The volumetric method is utilized with a reference cell connecting to a sample cell. Independent pressure transducers and a thermocouple or RTD (resistance temperature detectors) are utilized to monitor the pressure and temperature change within each cell. Pressure and temperature data are monitored by a computer data acquisition system that can collect data at 0.5-s intervals. Two cells are immersed in an oil bath maintained at constant temperature in order to minimize errors due to transient temperature fluctuations. Free gas is contained within the void volume of the cells while the sorbed gas is contained in the micropores of the shale material within the sample cell. There are two primary steps in measuring isotherm data including a calibration step and an isotherm measurement step. During calibration, the empty reference and sample cell volumes and the void volume within the sample cell after it is filled with a sorbing material are determined with helium as it does not adsorb into the sample. The isotherm measurement step involves repeated pressure steps with methane to determine the stabilized equilibrium pressure and temperature conditions for each step. A full computerized interpretation is implemented to account for slight temperature and pressure variations and improve the accuracy of the measured stabilized pressure and temperature conditions at the end of each isotherm step, which greatly increases the repeatability and consistency of the isotherm measurements. In addition, the shale samples were immediately preserved at the well site so that in situ fluids are not altered via desiccation or imbibition.

The Gibbs isotherm data determined from the experiments were corrected to the total isotherm based on the following equation (Sircar, 1999; Ambrose et al., 2012):

$$Gs = \frac{Gs'}{1 - \rho_f / \rho_s}, \tag{4.24}$$

where Gs' is Gibb's isotherm storage capacity, scf/ton; Gs is total isotherm storage capacity, scf/ton; ρ_f is free gas density, lbm/ft^3; ρ_s is sorbed gas density, lbm/ft^3. The free gas density is dependent upon the Z factors, which are calculated using the NIST REFPROP program (NIST, 2013).

For Marcellus Shale isotherm measurements of this study, a mass of about 250 g of shale samples were used and all experiments were conducted at 130°F. Total organic content is measured by a LECO carbon analyzer. We have analyzed gas adsorption laboratory measurements on four samples from the lower Marcellus Shale, as shown in Fig. 4.4. It can be seen that the adsorption measurements do not obey the Langmuir isotherm but obey the BET isotherm. We employed both the Langmuir and BET isotherms to fit the experimental measurements, as shown in Fig. 4.5. The fitting parameters of Langmuir and BET isotherms are listed in Tables 4.1 and 4.2, respectively. The coefficient of determination, also known as R^2, is used to evaluate goodness of fit. The measurements are better approximated by the BET isotherm than by the Langmuir isotherm. There are very few published high-pressure methane adsorption data for shale. Chareonsuppanimit et al. (2012) provided a summary of literature sources for high-pressure gas adsorption data on shales (Nuttall et al., 2005; Beaton et al., 2010; Weniger et al., 2010), where the highest pressure used to measure gas adsorption was around 4000 psi. However, the highest pressure used for measuring methane adsorption in this study was more than 7000 psi. Vermylen (2011) measured N_2, CH_4, and CO_2 adsorptions for four Barnett Shale samples with the maximum pressure of 1500 psi and found that CH_4 and N_2 obey the Langmuir isotherm while CO_2 obeys the BET isotherm. This study, to the best of our knowledge, for the first time shows that CH_4 adsorption at high pressure in some areas of Marcellus Shale behaves like multilayer adsorption and the BET isotherm fits the data well.

The relationship between the TOC and gas storage capacity at the reference pressure of 5000 psi is shown in Fig. 4.6, illustrating a good linear relationship.

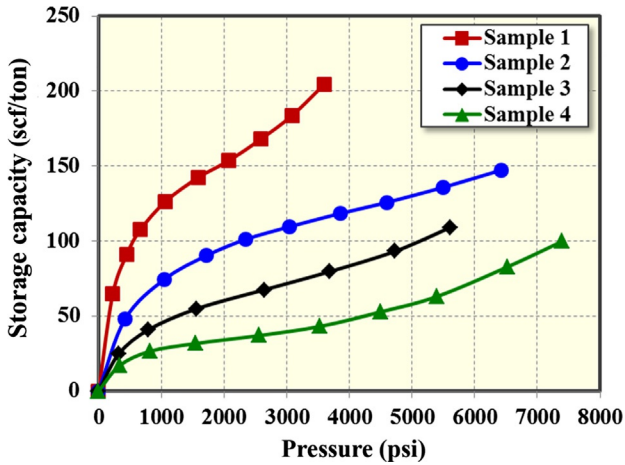

FIG. 4.4 Experimental measurements of gas adsorption from the lower Marcellus Shale (Yu et al., 2016).

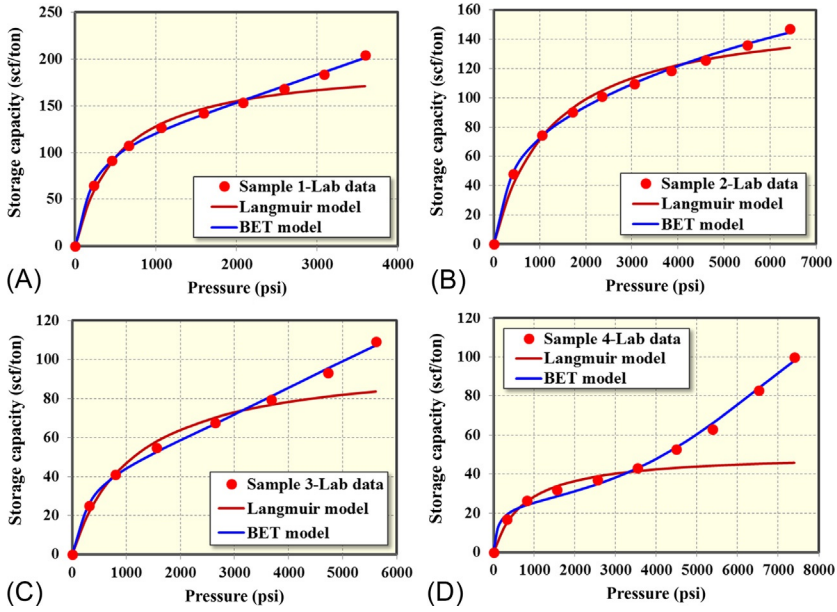

FIG. 4.5 Comparison of fitting results using the Langmuir and BET isotherms (Yu et al., 2016). (A) Sample 1. (B) Sample 2. (C) Sample 3. (D) Sample 4.

TABLE 4.1 Langmuir Isotherm Parameters Used for Fitting the Measurements (Yu et al., 2016)

Langmuir Parameters	Sample 1	Sample 2	Sample 3	Sample 4
p_L (psi)	535	1240	1144	776.4
v_L (scf/ton)	196.4	160.3	100.6	50.7
R^2	0.908	0.961	0.840	0.195

TABLE 4.2 BET Isotherm Parameters Used for Fitting the Measurements (Yu et al., 2016)

BET Parameters	Sample 1	Sample 2	Sample 3	Sample 4
v_m (scf/ton)	124.53	83.47	49.01	24.11
C	36.63	21.84	24.56	73.82
n	4.03	2.76	4.46	7.64
R^2	0.998	0.999	0.998	0.995

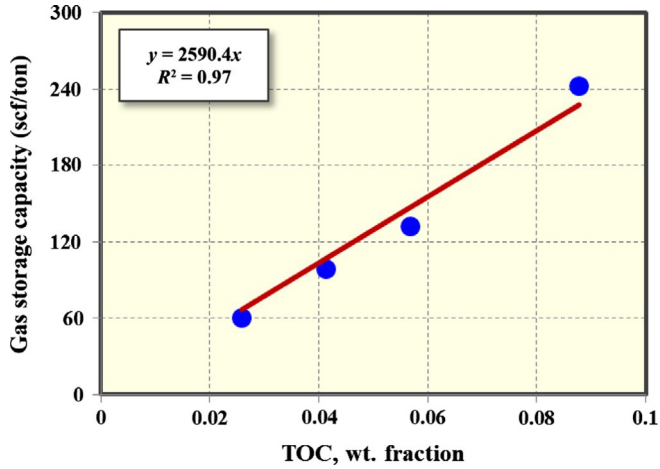

FIG. 4.6 Relationship between gas storage capacity and the TOC (Yu et al., 2016).

4.5 COMPARISON OF FREE GAS AND ADSORBED GAS

It can be seen from Eq. (4.8) that $(1-\phi)K_a$ and ϕS_g represent the contributions of adsorbed gas and free gas in shale. The actual reservoir properties of Marcellus Shale are used. Porosity of 0.142 and initial gas saturation of 90% are employed for calculation. We calculated $(1-\phi)K_a$ of four samples using Eq. (4.20) for the Langmuir isotherm and Eqs. (4.21)–(4.23) for BET isotherm, respectively, as shown in Fig. 4.7. For the Langmuir isotherm, Fig. 4.7A shows that gas desorption is comparable to free gas at low reservoir pressure, while gas desorption is less important at high reservoir pressure. However, for the BET isotherm, Fig. 4.7B illustrates that gas desorption is significant at both high and low reservoir pressure.

4.6 CALCULATION OF ORIGINAL GAS IN PLACE

The traditional method for calculating the original gas in place for free gas is expressed as (Ambrose et al., 2012):

$$v_f = 32.0368 \times \frac{\phi S_{gi}}{\rho_b B_g}, \tag{4.25}$$

where v_f is the free gas volume in scf/ton, ϕ is reservoir porosity, S_{gi} is the initial gas saturation, ρ_b is the bulk rock density, g/cm^3, and B_g is the gas formation volume factor in reservoir volume/surface volume.

Ambrose et al. (2012) proposed a new method to calculate the free gas volume by considering the volume occupied by the adsorbed gas on the surface based on the Langmuir isotherm equation. The porosity occupied by adsorbed gas based on the Langmuir isotherm is

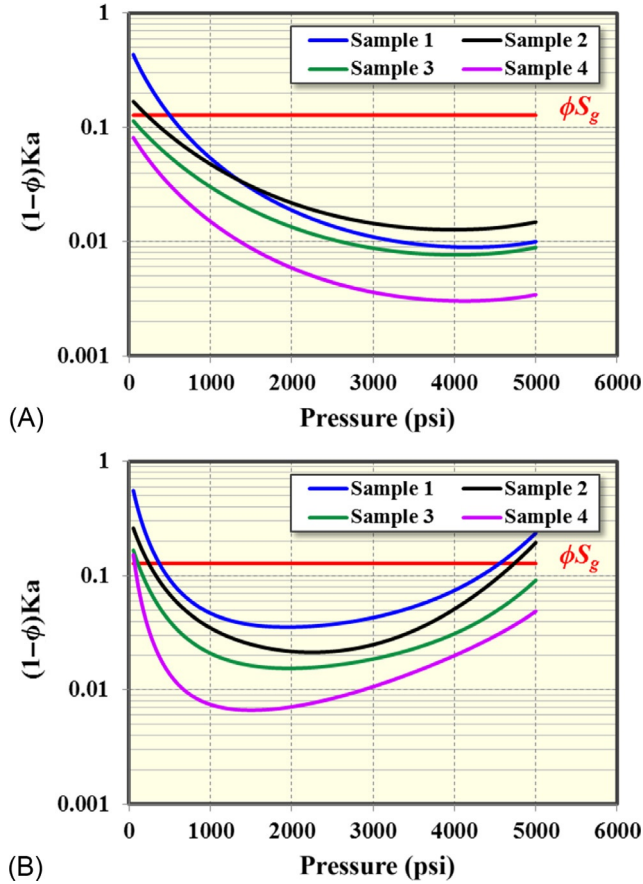

FIG. 4.7 Comparison of free gas and adsorbed gas with different isotherms (Yu et al., 2016). (A) Langmuir isotherm used for calculation. (B) BET isotherm used for calculation.

$$\phi_{a\_Langmuir} = 1.318 \times 10^{-6} M \frac{\rho_b}{\rho_s} \times \left(\frac{v_L p}{p + p_L} \right). \tag{4.26}$$

The final governing expression is shown here:

$$v_{f\_Langmuir} = \frac{32.0368}{B_g} \left[\frac{\phi(1 - S_w)}{\rho_b} - \frac{1.318 \times 10^{-6} M}{\rho_s} \times \left(\frac{v_L p}{p + p_L} \right) \right], \tag{4.27}$$

where S_w is the initial water saturation; and M molecular weight of natural gas, lbm/lbmole; ρ_s is the adsorbed gas density, g/cm^3. Note that the direct measurement of the adsorbed gas density is difficult and it is typically assumed that the adsorbed gas density is equal to the liquid-phase density; however, in many cases where the pore volume is dominated by micropores the adsorbed gas density is larger than that of the liquid-phase density (Mosher et al., 2013).

In addition, Mosher et al. (2013) pointed out that the molecular simulation can provide the unique opportunity to predict the adsorbed gas density. In this study, the adsorbed gas density of methane is calculated by the following equation, which was proposed by Riewchotisakul and Akkutlu (2015) based on the none-quilibrium molecular dynamic simulation to account for the change of adsorbed phase density with pressure in organic nanopores.

$$\rho_s = 0.1057 \ln(p) - 0.4629, \tag{4.28}$$

where the unit of adsorbed gas density (ρ_s) is g/cm^3 and pressure (p) is psi.

The total original gas in place can be obtained by summation of free gas volume and adsorbed gas volume:

$$v_{t\_Langmuir} = v_{f\_Langmuir} + v_{a\_Langmuir}, \tag{4.29}$$

where $v_{f\_Langmuir}$ is the free gas volume based on the Langmuir isotherm, scf/ton; $v_{a\_Langmuir}$ is the adsorbed gas volume based on the Langmuir isotherm, scf/ton; and $v_{t\_Langmuir}$ is the total gas volume based on the Langmuir isotherm, scf/ton.

In this work, we modified the model for calculating original gas in place proposed by Ambrose et al. (2012) by considering the BET isotherm. The porosity occupied by adsorbed is modified as follows for the BET isotherm:

$$\phi_{a\_BET} = 1.318 \times 10^{-6} M \frac{\rho_b}{\rho_s} \times \frac{v_m C \dfrac{p}{p_o}}{1 - \dfrac{p}{p_o}} \left[\frac{1 - (n+1)\left(\dfrac{p}{p_o}\right)^n + n\left(\dfrac{p}{p_o}\right)^{n+1}}{1 + (C-1)\dfrac{p}{p_o} - C\left(\dfrac{p}{p_o}\right)^{n+1}} \right]. \tag{4.30}$$

The governing equation is obtained as:

$$v_{f\_BET} = \frac{32.0368}{B_g} \left\{ \frac{\phi(1 - S_w)}{\rho_b} - \frac{1.318 \times 10^{-6} M}{\rho_s} \times \frac{v_m C \dfrac{p}{p_o}}{1 - \dfrac{p}{p_o}} \left[\frac{1 - (n+1)\left(\dfrac{p}{p_o}\right)^n + n\left(\dfrac{p}{p_o}\right)^{n+1}}{1 + (C-1)\dfrac{p}{p_o} - C\left(\dfrac{p}{p_o}\right)^{n+1}} \right] \right\}. \tag{4.31}$$

The total original gas in place can be obtained by summation of free gas volume and adsorbed gas volume:

$$v_{t\_BET} = v_{f\_BET} + v_{a\_BET}, \tag{4.32}$$

where v_{f_BET} is the free gas volume based on the BET isotherm in scf/ton, v_{a_BET} is the adsorbed gas volume based on the BET isotherm in scf/ton, and v_{t_BET} is the total gas volume based on the BET isotherm in scf/ton.

The actual reservoir properties of Marcellus Shale are used for the calculation of original gas in place, as shown in Table 4.3. Using Eqs. (4.26)–(4.32), the

porosities of gas adsorption, free gas in place, adsorbed gas in place, and the total original gas in place are calculated, as summarized in Tables 4.4 and 4.5. As shown, the average total original gas in place is 521 scf/ton, calculated using the BET isotherm, which is larger than the 510 scf/ton calculated using the

TABLE 4.3 Parameters Used for Calculation in the Marcellus Shale (Yu et al., 2016)

Parameter	Value	Unit
Initial reservoir pressure	5000	psi
Reservoir temperature	130	°F
Reservoir porosity	14%	–
Initial water saturation	10%	–
B_g	0.0033	–
M	20	lb/lb-mol
ρ_b	2.63	g/cm^3

TABLE 4.4 Original Gas in Place Calculation Based on the BET Isotherm (Yu et al., 2016)

Sample	ϕ_{a_BET}	v_{a_BET} (scf/ton)	v_{f_BET} (scf/ton)	v_{t_BET} (scf/ton)
1	0.038	242.36	323.30	565.66
2	0.021	132.30	387.69	519.99
3	0.016	99.14	407.10	506.24
4	0.010	60.42	429.75	490.17

TABLE 4.5 Original Gas in Place Calculation Based on the Langmuir Isotherm (Yu et al., 2016)

Sample	$\phi_{a\_Langmuir}$	$v_{a\_Langmuir}$ (scf/ton)	$v_{f\_Langmuir}$ (scf/ton)	$v_{t\_Langmuir}$ (scf/ton)
1	0.028	177.44	361.28	538.72
2	0.020	128.42	389.97	518.38
3	0.013	81.87	417.20	499.07
4	0.007	43.85	439.44	483.30

Langmuir isotherm. Hence, characterizing the gas adsorption isotherm is important for quantifying the total original gas in place and evaluating the economic potential of gas shales.

4.7 NUMERICAL SIMULATION METHODS

In this work, a compositional simulator is used to model multiple hydraulic fractures and gas flow in Marcellus Shale reservoirs (CMG-GEM, 2012). In our simulation model, the local grid refinement (LGR) with logarithmic cell spacing is used to accurately model gas flow from shale matrix to hydraulic fractures. Non-Darcy flow is considered for which the non-Darcy Beta factor, used in the Forchheimer number, is determined using a correlation proposed by Evans and Civan (1994). This approach has been extensively used to model transient gas flow in hydraulically fractured shale gas reservoirs (Rubin, 2010; Yu and Sepehrnoori, 2014a,b; Yu et al., 2014b). In the simulation model, the Langmuir isotherm is used to model gas desorption. Also, the adsorption data can be entered as a table form. Increase in gas recovery is used to assess the contribution of gas desorption in this work, and it is defined by

$$\text{Increase in gas recovery} = \frac{Q_{GasDesorption} - Q_i}{Q_{GasDesorption}}, \tag{4.33}$$

where $Q_{GasDesorption}$ is cumulative gas production with gas desorption effect, whereas Q_i is cumulative gas production without gas desorption effect.

A Marcellus Shale area of about 207 acres was simulated by setting up a basic 3D reservoir model with dimensions of 6000 ft × 1500 ft × 130 ft, which corresponds to length, width, and thickness, respectively, as shown in Fig. 4.8. The reservoir has two shale layers. Porosity of bottom and upper layers is around 14.2% and 7.1%, respectively. The horizontal well are stimulated in the bottom layer with 16 fracturing stages and four perforation clusters per stage with cluster spacing of 50 ft. The total well length is 3921 ft. There are almost 190 days of production data available for performing history matching and evaluating the effect of gas desorption on well performance.

Table 4.6 summarizes the detailed reservoir and fracture properties of this well. The reservoir is assumed to be homogeneous and the fractures are evenly spaced, with stress-independent porosity and permeability. The flowing bottomhole pressure in Fig. 4.9 is used to constrain the simulation and cumulative gas production is the history-matching variable. Table 4.7 lists reservoir permeability and fracture properties with a good history match without considering the gas desorption effect, as shown in Fig. 4.10.

In the subsequent simulation studies, we have performed history matching by considering gas desorption from the four shale samples and production forecasting for a 30-year period by gradually dropping the bottomhole pressure at 190 days to 200 psi within 1 month and then maintaining 200 psi until 30 years. The comparisons of gas desorption effect between the Langmuir and the BET

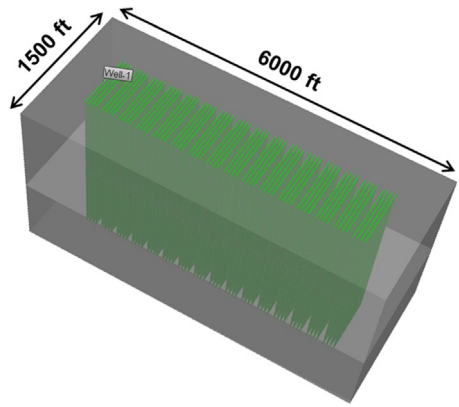

FIG. 4.8 A basic 3D reservoir model for the Marcellus Shale (Yu et al., 2016).

TABLE 4.6 Reservoir and Fracture Parameters for the Marcellus Shale Well (Yu et al., 2016)

Parameter	Value	Unit
Initial reservoir pressure	5100	psi
Reservoir temperature	130	°F
Reservoir permeability	800	nD
Reservoir porosity (upper layer)	7.1%	–
Reservoir porosity (bottom layer)	14.2%	–
Initial water saturation	10%	–
Total compressibility	3×10^{-6}	psi^{-1}
Horizontal well length	3921	ft
Number of stages	16	–
Cluster spacing	50	ft
Fracture half-length	400	ft
Fracture conductivity	3.5	md-ft
Fracture height	95	ft
Total number of fractures	64	–
Gas specific gravity	0.58	–

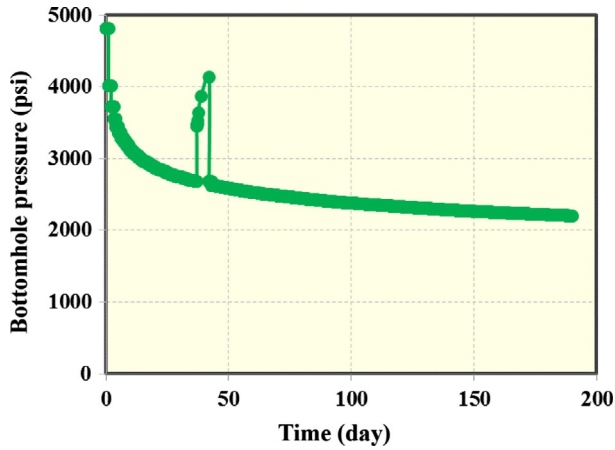

FIG. 4.9 Flowing bottomhole pressure of the Marcellus Shale well (Yu et al., 2016).

TABLE 4.7 Reservoir and Fracture Parameters Used for a Good History Match (Yu et al., 2016)

Parameter	Value	Unit
Reservoir permeability	800	nD
Fracture half-length	400	ft
Fracture conductivity	3.5	md-ft
Fracture height	95	ft

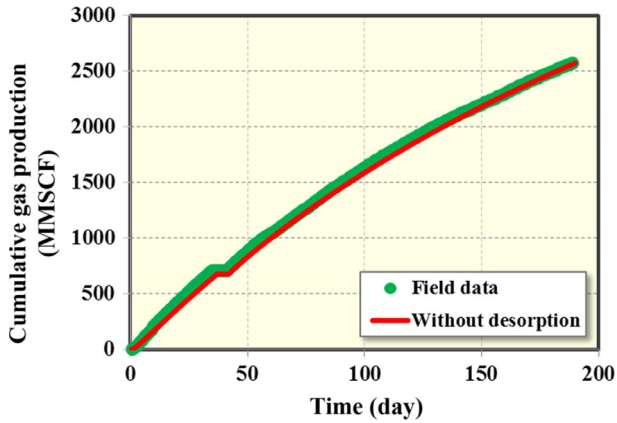

FIG. 4.10 Comparison between simulation data and the field data of the Marcellus Shale well (Yu et al., 2016).

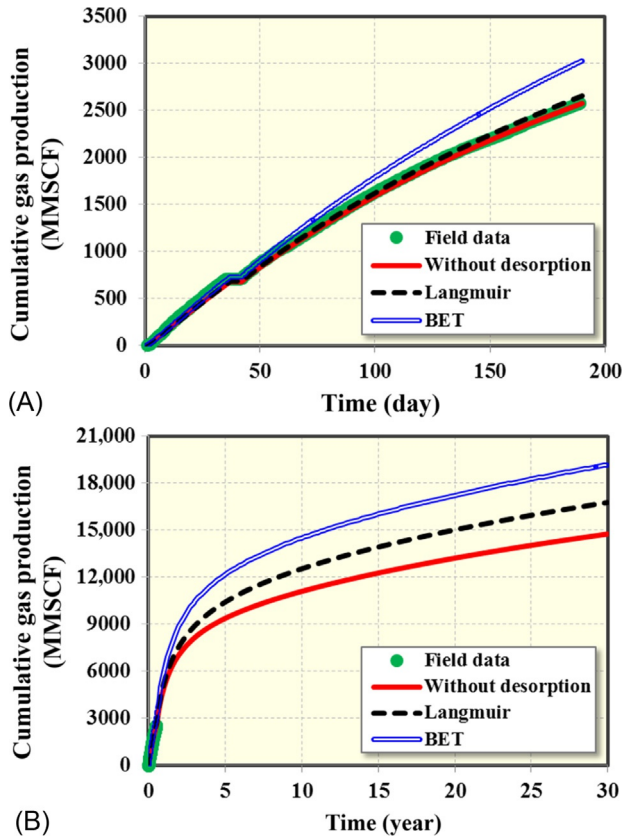

FIG. 4.11 Comparison of well performance with the Langmuir and BET isotherms for Sample 1 (Yu et al., 2016). (A) History matching. (B) Production forecasting.

isotherms for the four shale samples are shown in Figs. 4.11–4.14. It can be seen that gas desorption with the BET isotherm contributes more significantly to gas recovery than that with the Langmuir isotherm at the early time of production (190 days). The increase in gas recovery after 190 days of production with the BET isotherm is 17.6%, 7.4%, 9%, and 6.3%, while the increase in gas recovery with the Langmuir isotherm is 3%, 4.7%, 2.9%, and 1.1% for the samples 1–4, respectively. At 30 years of production, the increase in gas recovery with the BET isotherm is 30%, 15.2%, 13.5%, and 8.1%, while the increase in gas recovery with the Langmuir isotherm is 13.7%, 15.1%, 9.5%, and 4.3% for the samples 1–4, respectively.

Once again, we performed history matching by considering the BET isotherm for the four samples, as shown in Fig. 4.15. Two main parameters, fracture half-length and fracture height, were tuned to obtain a good match. The other parameters were kept the same as the history match case without considering

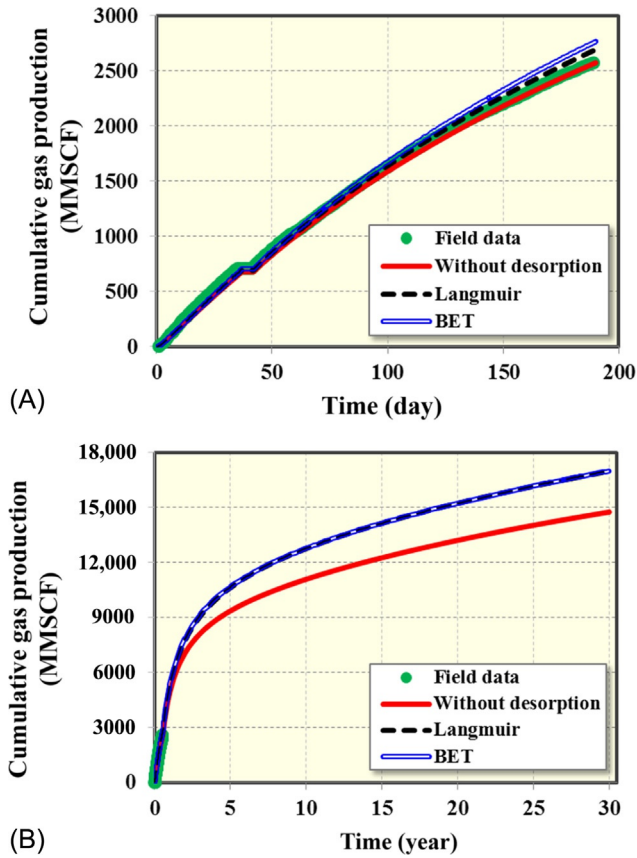

FIG. 4.12 Comparison of well performance with the Langmuir and BET isotherms for Sample 2 (Yu et al., 2016). (A) History matching. (B) Production forecasting.

desorption. As shown, a good match was obtained for each sample using fracture half-length and fracture height as shown in Table 4.8. In comparison to the case without desorption, the fracture half-length was reduced for each sample, although the fracture height was reduced from 95 to 85 ft for Sample 1. Hence, it can be suggested that the gas desorption effect using the BET isotherm plays an important role in performing history matching at early time of production.

4.8 SUMMARY

We have analyzed the laboratory measurements of gas adsorption from four shale samples in the Marcellus Shale using the Langmuir and the BET isotherms. The effect of gas adsorption on calculation of original gas in place

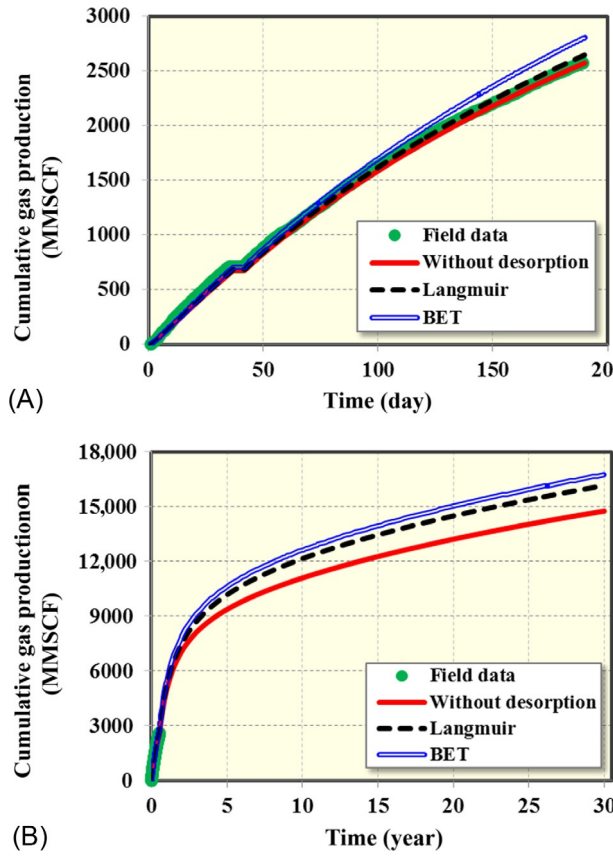

FIG. 4.13 Comparison of well performance with the Langmuir and BET isotherms for Sample 3 (Yu et al., 2016). (A) History matching. (B) Production forecasting.

and well performance has been investigated. The following conclusions can be drawn from this work:

(1) The measured gas adsorption in four samples from the lower Marcellus Shale is better described by the BET isotherm, rather than by the Langmuir isotherm.

(2) A good linear relationship between gas storage capacity and TOC is obtained.

(3) Gas desorption obeying the BET isotherm is comparable to the free gas at low and high reservoir pressure.

(4) The average total original gas in place is 521 scf/ton when calculated using the BET isotherm, and 510 scf/ton calculated using the Langmuir isotherm.

(5) For the horizontal well investigated in this study, the range of increase in gas recovery at 190 days of production with the BET isotherm is

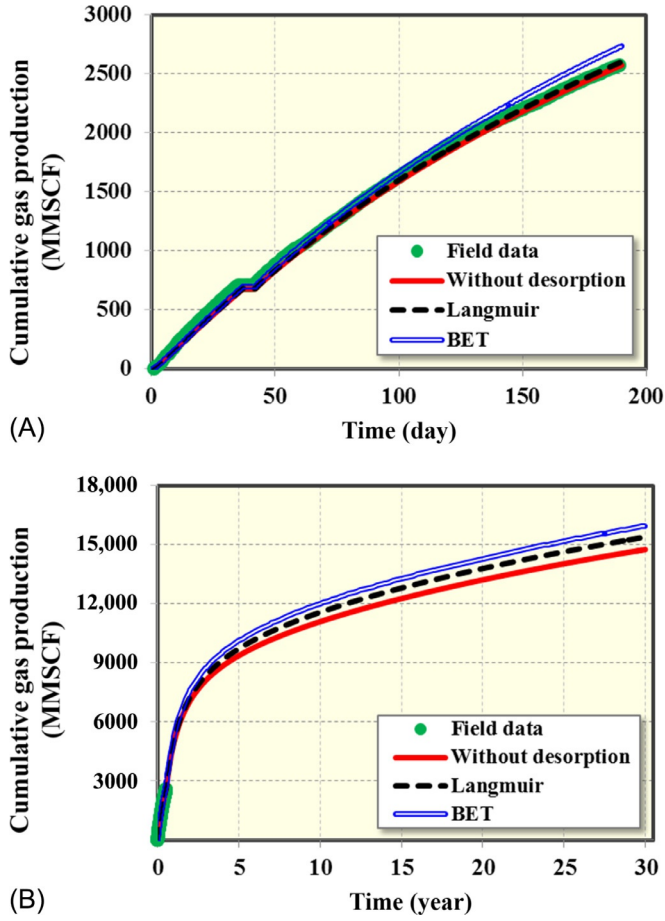

FIG. 4.14 Comparison of well performance with the Langmuir and BET isotherms for Sample 4 (Yu et al., 2016). (A) History matching. (B) Production forecasting.

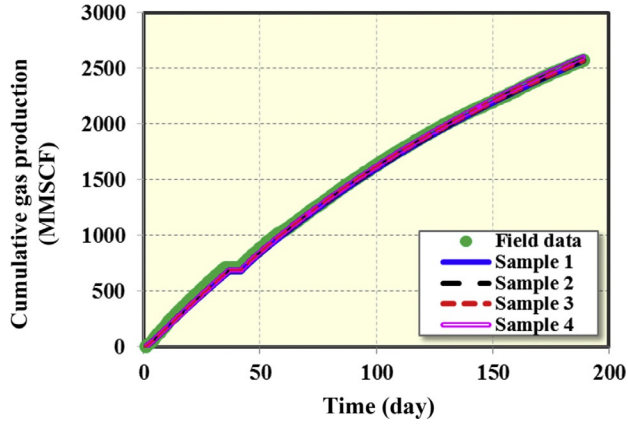

FIG. 4.15 History matching by considering the BET isotherm of four samples (Yu et al., 2016).

TABLE 4.8 Fracture Half-Length and Fracture Height Used for a Good History Match (Yu et al., 2016)

Parameter	Without Desorption	Desorption (Sample 1)	Desorption (Sample 2)	Desorption (Sample 3)	Desorption (Sample 4)
Fracture half-length (ft)	400	300	330	320	350
Fracture height (ft)	95	85	95	95	95

6.3%–17.6%, while the range with the Langmuir isotherm is 1.1%–4.7%. After 30 years of production, the range of increase in gas recovery with the BET isotherm is 8.1%–30%, while the range with the Langmuir isotherm is 4.3%–15.1%.

REFERENCES

Ambrose, R.J., Hartman, R.C., Diaz-Campos, M., Akkutlu, I.Y., Sondergeld, C.H., 2012. Shale gas-in-place calculations part 1: new pore-scale considerations. SPE J. 17 (1), 219–229.

Beaton, A.P., Pawlowicz, J.G., Anderson, S.D.A., Berhane, H., Rokosh, C.D., 2010. Rock Eval™, total organic carbon and adsorption isotherms of the Duvernay and Muskwa formations in Alberta: shale gas data release. ERCB/AGS Open File Report. Energy Resources Conservation Board, Edmonton, Alberta.

Boyce, M.L., Yanni, A.E., Carr, T.R., 2010. Depositional control of organic content in the middle Devonian Marcellus interval of west Virginia and western Pennsylvania. AAPG Hedberg Research Conference, Austin, Texas.

Brunauer, S., Emmett, P.H., Teller, E., 1938. Adsorption of gases in multimolecular layers. J. Am. Chem. Soc. 60, 309–319.

Carlson, E.S., Mercer, J.C., 1991. Devonian shale gas production: mechanisms and simple models. J. Pet. Technol. 43 (4), 476–482.

Chareonsuppanimit, P., Mohammad, S.A., Robinson Jr., R.L., Gasem, K.A.M., 2012. High-pressure adsorption of gases on shales: measurements and modeling. Int. J. Coal Geol. 95, 34–46.

Clarkson, C.R., Haghshenas, B., 2013. In: Modeling of supercritical fluid adsorption on organic-rich shales and coal.SPE Unconventional Resources Conference, The Woodlands, Texas. Paper SPE 164532.

Clarkson, C.R., Bustin, R.M., Levy, J.H., 1997. Application of the monolayer/multilayer and adsorption potential theories to coal methane adsorption isotherms at elevated temperature and pressure. Carbon 35 (12), 1689–1705.

CMG-GEM, 2012. GEM User's Guide. Computer Modeling Group Ltd, Calgary.

Department of Energy (DOE), 2013. Modern shale gas development in the United States: an update. http://www.netl.doe.gov/File%20Library/Research/Oil-Gas/shale-gas-primer-update-2013.pdf.

Evans, R.D., Civan, F. 1994. Characterization of non-darcy multiphase flow in petroleum bearing formations. Report, U.S. DOE Contract No. DE-AC22-90BC14659, School of Petroleum and Geological Engineering, University of Oklahoma.

Firouzi, M., Wilcox, J., 2012. Molecular modeling of carbon dioxide transport and storage in porous carbon-based materials. Microporous Mesoporous Mater. 158, 195–203.

Firouzi, M., Alnoaimi, K., Kovscek, A., Wilcox, J., 2014a. Klinkenberg effect on predicting and measuring helium permeability in gas shales. Int. J. Coal Geol. 123, 62–68.

Firouzi, M., Rupp, E.C., Liu, C.W., Wilcox, J., 2014b. Molecular simulation and experimental characterization of the nanoporous structures of coal and gas shale. Int. J. Coal Geol. 121, 123–128.

Freeman, C.M., Moridis, G.J., Michael, G.E., Blasingame, T.A., 2012. In: Measurement, modeling, and diagnostics of flowing gas composition changes in shale gas wells.SPE Latin American and Caribbean Petroleum Engineering Conference, Mexico City, Mexico. Paper SPE 153391.

Hao, S., Chu, W., Jiang, Q., Yu, X., 2014. Methane adsorption characteristics on coal surface above critical temperature through Dubinin-Astakhov model and Langmuir model. Colloids Surf. A Physicochem. Eng. Asp. 444, 104–113.

Kang, S.M., Fathi, E., Ambrose, R.J., Akkutlu, I.Y., Sigal, R.F., 2011. Carbon dioxide storage capacity of organic-rich shales. SPE J. 16 (4), 842–855.

Kuila, U., Prasad, M., 2013. Specific surface area and pore-size distribution in clays and shales. Geophys. Prospect. 61, 341–362.

Lane, H.S., Watson, A.T., Lancaster, D.E., 1989. Identifying and estimating desorption from Devonian shale gas production data. In: Paper SPE 19794.SPE Annual Technical Conference and Exhibition, San Antonio, Texas.

Langmuir, I., 1918. The adsorption of gases on plane surfaces of glass, mica and platinum. J. Am. Chem. Soc. 40, 1403–1461.

Leahy-Dios, A., Das, M., Agarwal, A., Kaminsky, R., 2011. In: Modeling of transport phenomena and multicomponent sorption for shale gas and coalbed methane in an unstructured grid simulator. SPE Annual Technical Conference and Exhibition, Denver, Colorado. Paper SPE 147352.

Lu, X., Li, F., Watson, A.T., 1995. Adsorption measurements in Devonian shales. Fuel 74 (4), 599–603.

Mahmoud, M., 2014. Development of a new correlation of gas compressibility factor (z-factor) for high pressure gas reservoirs. J. Energy Resour. Technol. 136, 1–11.

Martin, J.P., Hill, D.G., Lombardi, T.E., Nyahay, R., 2010. A primer on New York's gas shales. http://offices.colgate.edu/bselleck/AppBasin/GasshaleMartin.pdf.

Mosher, K., He, J., Liu, Y., Rupp, E., Wilcox, J., 2013. Molecular simulation of methane adsorption in micro- and mesoporous carbons with applications to coal and gas shale systems. Int. J. Coal Geol. 109–110, 36–44.

NIST, 2011. Thermophysical properties of fluid systems. http://webbook.nist.gov/chemistry/fluid/.

NIST, 2013. NIST Reference Fluid Thermodynamic and Transport Properties (REFPROP): Version 9.1.

Nuttall, B.C., Drahovzal, J.A., Eble, C.F., Bustin, R.M. 2005. Analysis of the Devonian black shale in Kentucky for potential carbon dioxide sequestration and enhanced natural gas production. Kentucky Geological Survey, University of Kentucky, Lexington, Kentucky.

Ozdemir, E., 2004. Chemistry of the Adsorption of Carbon Dioxide by Argonne Permium Coals and a Model to Simulate CO_2 Sequestration in Coal Seams. PhD Dissertation, University of Pittsburgh.

Patzek, T.W., Male, F., Marder, M., 2013. Gas production in the Barnett shale obeys a simple scaling theory. PNAS 110 (49), 19731–19736.

Riewchotisakul, S., Akkutlu, I.Y., 2015. Adsorption enhanced transport of hydrocarbons in organic nanopores.SPE Annual Technical Conference and Exhibition, Houston, Texas. Paper SPE 175107.

Rouquerol, J., Rouquerol, F., Sing, K.S.W., 1999. Adsorption by Powers and Porous Solids: Principles, Methodology and Applications. Academic Press, London.

Rubin, B., 2010. In: Accurate simulation of non-Darcy flow in stimulated fractured shale reservoirs. SPE Western Regional Meeting, Anaheim, California. Paper SPE 132093.

Schmoker, J.W., 1980. Organic content of Devonian shale in western Appalachian basin. AAPG Bull. 64 (12), 2156–2165.

Silin, D., Kneafsey, T., 2012. Shale gas: nanometer-scale observations and well modeling. J. Can. Pet. Technol. 51 (6), 464–475.

Sing, K.S.W., Everett, D.H., Haul, R.A.W., Moscou, L., Pierotti, R.A., Rouquerol, J., Siemieniewska, T., 1985. Reporting physisorption data for gas/solid systems with special reference to the determination of surface area and porosity (recommendations 1984). Pure Appl. Chem. 57 (4), 603–619.

Sircar, S., 1999. Gibbsian surface excess for gas adsorption-revisited. Ind. Eng. Chem. Res. 38, 3670–3682.

Solar, C., Blanco, A.G., Vallone, A., Sapag, K., 2010. Adsorption of methane in porous materials as the basis for the storage of natural gas. In: Potocnik, P. (Ed.), Natural Gas. Sciyo, Rijeka, Crootia. http://www.intechopen.com/books/natural-gas.

U.S. Energy Information Administration, 2011. Review of emerging resources: U.S. shale gas and shale oil plays. http://www.eia.gov/analysis/studies/usshalegas/pdf/usshaleplays.pdf.

U.S. Energy Information Administration, 2014. Drilling productivity report. http://www.eia.gov/petroleum/drilling/#tabs-summary-1.

Vermylen, J.P., 2011. Geomechanical Studies of the Barnett Shale, Texas, USA. PhD Dissertation, Stanford University.

Weary, D.J., Ryder, R.T., Nyahay, R., 2000. Thermal maturity patterns (CAI and %Ro) in the Ordovician and Devonian rocks of the Appalachian basin in New York State. U.S. Geological Survey Open File Report 00-496. http://pubs.usgs.gov/of/2000/of00-496/NY_TEXT.PDF.

Weniger, P., Kalkreuth, W., Busch, A., Krooss, B.M., 2010. High-pressure methane and carbon dioxide sorption on coal and shale samples from the Paraná Basin, Brazil. Int. J. Coal Geol. 84, 190–205.

Williams, H., Khatri, D., Keese, R., Roy-Delage, L., Roye, J., Leach, D., Rottler, P., Procherie, O., Rodriguez, J., 2011. In: Flexible, expanding cement system (FECS) successfully provides zonal isolation across Marcellus shale gas trends.Canadian Unconventional Resources Conference, Calgary, Alberta, Canada. Paper SPE 149440.

Yu, W., 2015. Developments in Modeling and Optimization of Production in Unconventional Oil and Gas Reservoirs. PhD Dissertation, The University of Texas at Austin, Austin, TX.

Yu, W., Sepehrnoori, K., 2014a. Simulation of gas desorption and geomechanics effects for unconventional gas reservoirs. Fuel 116, 455–464.

Yu, W., Sepehrnoori, K., 2014b. An efficient reservoir simulation approach to design and optimize unconventional gas production. J. Can. Pet. Technol. 53 (2), 109–121.

Yu, W., Huang, S., Wu, K., Sepehrnoori, K., Zhou, W., 2014a. In: Development of a semi-analytical model for simulation of gas production in shale gas reservoirs.Unconventional Resources Technology Conference, Denver, Colorado. Paper URTeC 1922945.

Yu, W., Luo, Z., Javadpour, F., Varavei, A., Sepehrnoori, K., 2014b. Sensitivity analysis of hydraulic fracture geometry in shale gas reservoirs. J. Pet. Sci. Eng. 113, 1–7.

Yu, W., Sepehrnoori, K., Patzek, T.W., 2016. Modeling gas adsorption in Marcellus shale with Langmuir and BET isotherms. SPE J. 21 (2), 589–600.

Chapter 5

Embedded Discrete Fracture Model (EDFM) for Complex Fracture Geometry

Chapter Outline

5.1 INTRODUCTION

Gas shales are characterized by extremely low permeability (nanodarcies), low porosity (2%–8%), and high total organic carbon (1%–14%), which can be both source rock and reservoir rock (Cipolla et al., 2010). In recent years, the economic viability of shale gas production has been enabled with the advances

Shale Gas and Tight Oil Reservoir Simulation. https://doi.org/10.1016/B978-0-12-813868-7.00005-5

in hydraulic fracturing technologies and horizontal drilling. It has been estimated by U.S. Energy Information Administration (EIA) that shale gas production accounts for over 50% of total U.S. natural gas production in 2015 (EIA, 2016). Hence, shale gas has contributed significantly to the total natural gas supply in the United States.

Gas transport in shale formation involves complex gas transport mechanisms due to the presence of a large amount of nanopores and organic matter, which include gas desorption, adsorbed gas porosity, gas slippage, Knudsen diffusion, etc. (Javadpour et al., 2007; Wang and Reed, 2009; Civan, 2010; Civan et al., 2011; Sakhaee-Pour and Bryant, 2012; Akkutlu and Fathi, 2012; Yu et al., 2016a). Yu et al. (2016a) reported that the adsorbed gas porosity can be up to as high as 3.8% based on the experimental measurements of gas adsorption isotherm in some area of Marcellus shale. However, this important effect has not yet been well documented and clearly understood in the literature. Furthermore, complex fracture networks are commonly observed based on microseismic measurements (Warpinski et al., 2005; Cipolla and Wallace, 2014) and fracture propagation models (Wu et al., 2012; Xu and Wong, 2013; Wu and Olson, 2013, 2015), especially in the presence of pre-existing natural fractures. In addition, fracture width and conductivity vary along fracture length, which has been observed and predicted by both experimental studies and fracture models (Wu and Olson, 2013, 2015; Weijers and de Pater, 1992; Abass et al., 1996). Moreover, the fracture conductivity is pressure dependent, which decreases with the reservoir depletion due to proppant embedment (LaFollette and Carman, 2010; Fan et al., 2010; Alramahi and Sundberg, 2012). Hence, the complex gas transport mechanisms and complex fracture geometries pose a great challenge to accurately and efficiently evaluate and simulate well performance in shale gas reservoirs.

In recent years, considerable efforts have been made to model well performance from shale reservoirs with complex fracture geometry analytically and semianalytically (Chen and Raghavan, 1997; Zhou et al., 2013; Yu et al., 2016b, 2017a; Yang et al., 2016; Chen et al., 2017; Wang et al., 2018). However, these analytical and semianalytical approaches are difficult to fully capture the complex physics that existed in shale gas reservoirs such as heterogeneity, multiphase flow (gas/water), pressure-dependent rock properties and fracture conductivity, disconnected natural fractures, fractures with any orientation in 3D dimension, etc. In accordance, Cipolla et al. (2010) stated that numerical reservoir simulation is the most rigorous method to model shale-gas reservoirs, which can incorporate the complex nature of fracture geometry and long-time transient gas flow behavior due to very low permeability of shale matrix. Regarding numerical methods with structured grid (single-porosity model), local grid refinement (LGR) is often used to model hydraulic fractures, where a small cell is placed for fracture and some cells with logarithmically increasing size are close to fracture (Rubin, 2010; Yu and Sepehrnoori, 2014a). However, this method is mainly limited to two simple fracture patterns such as biwing

fractures and orthogonal fracture networks. Such fracture geometries are inadequate to represent the complex nature of fracture geometry in reality. Similarly, the traditional dual-continuum (dual-porosity or dual-permeability) numerical models (Warren and Root, 1963) have the limitations for explicitly modeling complex fractures and cannot adequately account for anisotropy, heterogeneity, and fracture connectivity (Dershowitz et al., 1998; Xu et al., 2017a).

With the recent advances in discrete fracture models using unstructured gridding with local refinement near the fractures, the true complex fracture geometry can be better modeled (Sandve et al., 2012; Mirzaei and Cipolla, 2012; Hui et al., 2013). However, the unstructured grids are still challenging to use efficiently in the field scale due to very complicated gridding issues and an expensive computational cost. Recently, a multisegment well approach (Edwards et al., 2013; Du et al., 2016) has been developed to dynamically model hydraulic fractures. However, this approach is difficult to handle a large number of isolated natural fractures, which has no connection to primary hydraulic fractures and wellbore. In order to overcome these issues, a state-of-the-art embedded discrete fracture model (EDFM) was developed to use for in-house simulator developments (Moinfar et al., 2014; Cavalcante Filho et al., 2015; Shakiba and Sepehrnoori, 2015; Yu et al., 2017b). Recently, it has been widely extended to use in commercial reservoir simulators in a nonintrusive manner (Xu, 2015; Zuloaga-Molero et al., 2016; Xu et al., 2017a, 2017b; Zhang et al., 2017a, 2017b). In EDFM, the complex fractures are embedded in conventional structured matrix grids explicitly without the need of LGR in the vicinity of fractures. This approach is simpler and faster to capture the complex fracture geometries. Accordingly, the EDFM approach is fully implemented in the model development of this study. More details will be discussed later in the text. Although there are many existing numerical models for shale gas simulation (Cipolla et al., 2010; Wu et al., 2014; Sun et al., 2015; Li et al., 2015; Fung and Du, 2016; An et al., 2017), many of these complex phenomena have not been completely captured, and hence it is necessary to develop a powerful model to fill this gap in the petroleum industry.

Multiwell pads with high well density have been widely applied in the economic development of tight-oil reservoirs. Tighter well spacing often results in the phenomenon of well-to-well interference due to fracture hits (Lawal et al., 2013; King and Valencia, 2016). Such fracture hits may involve connecting both hydraulic fractures and natural fractures. Prior work has shown that the intensity of well interference increases with a decrease of well spacing (Ajani and Kelkar, 2012; Kurtoglu and Salman, 2015). Similarly, infill drilling often increases the risk of fracture hits between the infill well and its neighboring wells. The fracture hits may negatively affect well performance and play an important role in optimizing well spacing to maximize overall recovery (Yaich et al., 2014; Malpani et al., 2015). Hence, minimizing the possibility of fracture hits and well interference is significant.

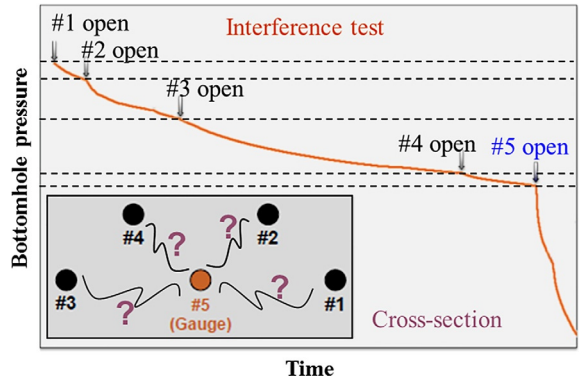

FIG. 5.1 Example of pressure test for identifying well interference in a multiwell pad. *(Modified from Scott, K.D., Chu, W.C., Flumerfelt, R.W., 2015. Application of real-time bottom-hole pressure to improve field development strategies in the Midland basin Wolfcamp shale. In: Paper URTeC 2154675, Unconventional Resources Technology Conference, San Antonio, Texas.)*

Field operators often utilize pressure tests to identify the intensity of well-to-well connections (Portis et al., 2013; Sardinha et al., 2014; Sani et al., 2015; Scott et al., 2015). During the pressure test process, all wells are first shut in for a certain period, then some wells are brought back on production sequentially. In the meantime, bottomhole pressure (BHP) or wellhead pressure of the shut-in well is measured and recorded (Lindner and Bello, 2015). Fig. 5.1 presents an example of a field pressure test with observed BHP changes of shut-in Well 5 when opening Wells 1–4 sequentially in Wolfcamp shale, which clearly revealed the different degrees of well interference between Well 5 and surrounding wells (Scott et al., 2015). The physical mechanisms for inducing well interference are very complex due to the combinatory effects of matrix permeability, connecting hydraulic fractures, and natural fractures (Yu et al., 2016c). However, to the best of our knowledge, the impacts of complex fracture hits such as nonplanar fractures and natural fractures on pressure response of well interference have not been thoroughly studied.

Although there are many pressure test data reported in the literature to demonstrate the existence of well interference (Portis et al., 2013; Sardinha et al., 2014; Sani et al., 2015; Scott et al., 2015), few studies quantitatively simulate pressure response of well interference accounting for complex hydraulic and natural fracture geometries. Complex fracture geometries are often generated during the actual fracturing process. The realization that such complex fracture patterns exist mandates modeling efforts should attempt to quantify their possible impact on well performance. Marongiu-Porcu et al. (2016) developed an integrated workflow through combining fracture model, reservoir simulation, and geomechanics model to reduce fracture hits and minimize interwell fracturing interference. However, the impacts of hydraulic fracture hits and natural fractures on pressure response of the shut-in well were not captured and investigated. Awada et al. (2016) built an analytical model to simulate the pressure

response of a shut-in vertically fractured well connected to another vertically fractured well through a single straight fracture hit. The impacts of matrix permeability and hydraulic fracture conductivity on pressure response were studied. However, the analytical solution is difficult to apply to multiple horizontal wells with complex fracture hits in the presence of natural fractures. Yu et al. (2016c) developed a semianalytical model to simulate the pressure response of multiple horizontal wells with complex nonplanar fracture hits. The effects of connecting fracture conductivity, number of connecting fractures, and complex nonplanar fracture hits on pressure response were investigated. The semianalytical solution cannot account for the effects of disconnected natural fractures and multiphase flow on pressure response. Hence, a new numerical model is still needed in the petroleum industry to simulate the impacts of complex hydraulic and natural fracture geometry on pressure response of well interference in tight-oil reservoirs.

5.2 NUMERICAL MODEL FOR SHALE GAS TWO-PHASE FLOW

Two-phase flows (gas/water) are considered for deriving the mass conservation equations for simulation of shale gas production. Each phase is present at equilibrium considering the viscous, gravity, and capillary forces. Gas and water can also be treated as two components. It is assumed that gas and water phases are independent without component interactions. The general mass conservation equation for component i ($i=g$ for gas and $i=w$ for water) can be written as

$$\frac{\partial W_i}{\partial t}+\vec{\nabla}\cdot\vec{F}_i-R_i=0, \tag{5.1}$$

where W_i, $\vec{F}_i$, R_i, and t are the accumulation, flux, source, and time terms, respectively (Lake, 1989). It should be mentioned that the unit of the equation is lb-moles per unit bulk volume per unit time.

The accumulation term for gas component considering gas saturation, gas adsorption, and pore volume occupied by adsorbed gas near the pore surface is expressed as:

$$W_g=\phi S_g\left(1-c_{ag}\right)\xi_g+(1-\phi)\rho_s v_{ag}\xi_{ag}, \tag{5.2}$$

where ϕ is porosity, S_g is gas saturation, c_{ag} is the volume fraction of adsorbed gas per unit pore volume, ξ_g is the molar density of gas phase, ρ_s is the rock density in ton per unit volume of solid, v_{ag} is the specific volume of gas adsorbed per unit mass of bulk rock (standard cubic feet per ton, scf/ton), ξ_{ag} is the molar density of adsorbed gas in lb-mole/ft^3.

The accumulation term for water component without considering water adsorption is below:

$$W_w=\phi S_w\xi_w, \tag{5.3}$$

where ξ_w is the molar density of water phase in lb-mole/ft^3 and S_w is water saturation.

The flux of gas and water components can be written as

$$\vec{F}_g = \xi_g \vec{u}_g, \tag{5.4}$$

$$\vec{F}_w = \xi_w \vec{u}_w, \tag{5.5}$$

where $\vec{u}_g$ and $\vec{u}_w$ represent the superficial velocity of gas phase and water phase, respectively.

Based on multiphase version of Darcy's law for fluid flow in porous media, the superficial velocity of phase j ($j = g$ for gas phase and $j = w$ for water phase) becomes

$$\vec{u}_j = -\frac{\vec{\vec{k}}\, k_{rj}}{\mu_j}\left(\nabla p_j - \gamma_j \nabla D\right), \tag{5.6}$$

where k_{rj} is relative permeability, μ_j is viscosity, γ_j is the specific weight of phase j, and D is depth.

The source term is written as

$$R_i = \frac{q_i}{V_b}, \tag{5.7}$$

where q_i is the molar flow rate of component i, which is positive for injection and negative for production, V_b is the bulk volume of a gridblock.

The final mass conservation equations for gas and water components are described below:

$$\frac{\partial}{\partial t}\left[\phi S_g\left(1 - c_{ag}\right)\xi_g + (1-\phi)\rho_s v_{ag}\xi_{ag}\right] + \vec{\nabla} \cdot \left(\xi_g \vec{u}_g\right) - \frac{q_g}{V_b} = 0, \tag{5.8}$$

$$\frac{\partial}{\partial t}\left(\phi S_w \xi_w\right) + \vec{\nabla} \cdot \left(\xi_w \vec{u}_w\right) - \frac{q_w}{V_b} = 0. \tag{5.9}$$

5.2.1 Gas Desorption Effect

In our previous studies (Yu et al., 2016a), it was found that four experimental measurements of methane adsorption from the Marcellus Shale core samples deviate from the Langmuir isotherm, but obey the BET isotherm (Brunauer et al., 1938). The standard BET isotherm assumes that the number of adsorption layers is infinite. Here, a general form of BET isotherm considering n adsorption layers is used as follows:

$$v_{ag} = \frac{v_m C p/p_o}{1 - p/p_o}\left[\frac{1 - (n+1)(p/p_o)^n + n(p/p_o)^{n+1}}{1 + (C-1)p/p_o - C(p/p_o)^{n+1}}\right], \tag{5.10}$$

where v_{ag} is the gas volume of adsorption, p_o is the saturation pressure of the gas, v_m is the maximum adsorption gas volume when the adsorbent surface

is being covered with a complete monomolecular layer, C is a constant. It is important to note that the saturation pressure loses its physical meaning when the reservoir temperature is above the critical methane temperature (Ozdemir, 2004). Instead, the saturation pressure can be treated as pseudosaturation pressure (p_s) for the high-pressure/temperature methane adsorption (Clarkson et al., 1997), which can be calculated using the following extrapolation of the Antoine equation (NIST, 2011; Hao et al., 2014):

$$\ln p_s = 7.7437 - \frac{1306.5485}{19.4362 + T}, \tag{5.11}$$

where T is temperature in K and p_s is pseudosaturation pressure in MPa. After calculation of p_s, three parameters such as v_m, n, and C are generally used to fit the experimental data of methane adsorption. When $n = 1$, the general BET isotherm will be simplified as the classic Langmuir isotherm (Langmuir, 1918):

$$v_{ag} = \frac{v_L p}{p + p_L}, \tag{5.12}$$

where v_L is Langmuir volume (scf/ton), which is the maximum adsorbed gas volume at the infinite pressure, p_L is Langmuir pressure, which is the pressure at which one-half of the gas is desorbed.

5.2.2 Adsorbed Gas Porosity

In this study, the adsorbed gas density of methane is calculated by the expression proposed by Riewchotisakul and Akkutlu (2015), which is obtained based on the nonequilibrium molecular dynamic simulation to account for the change of adsorbed phase density with pressure in organic nanopores:

$$\rho_{ag} = 0.1057 \ln(p) - 0.4629, \tag{5.13}$$

where ρ_{ag} is the adsorbed gas density in g/cm^3 and p is pressure in psi. Note that the molar density of adsorbed gas can be calculated by

$$\xi_{ag} = \frac{\rho_{ag}}{M_{ag}}, \tag{5.14}$$

where M_{ag} is molecular weight of adsorbed gas. Hence, the pore volume occupied by adsorbed gas can be calculated by

$$c_{ag} = \frac{(1-\phi)\rho_s v_{ag} \rho_{g,ST}}{\rho_{ag}\phi}, \tag{5.15}$$

where $\rho_{g,ST}$ is gas density at standard condition. Hence, the adsorbed gas porosity (ϕ_{ag}) is obtained as

$$\phi_{ag} = \frac{(1-\phi)\rho_s v_{ag} \rho_{g,ST}}{\rho_{ag}}. \tag{5.16}$$

It should be pointed out that the adsorbed gas porosity should satisfy the criterion of $0 \leq \phi_{ag} < \phi$.

Since the formation is assumed to be slightly compressible, the porosity is a function of pressure and calculated by

$$\phi = \phi_o \left[1 + c_f (p - p_o)\right], \tag{5.17}$$

where ϕ_o is the porosity at the reference pressure p_o, c_f is the formation compressibility. Accordingly, the porosity change for free gas not only considers the assumption of slightly compressible formation but also the pore volume occupied by adsorbed gas.

5.2.3 Gas Slippage and Diffusion Effect

In shale formations, a large amount of nanopores result in the presence of multiple gas flow regimes. Gas slippage and diffusion effect becomes important in shale nanopores, especially at low pressure with reservoir depletion. Four flow regimes were proposed by Karniadakis and Beskok (2002) depending on the Knudsen number (K_n): (1) continuum-flow regime ($K_n < 0.01$); (2) slip-flow regime ($0.01 < K_n < 0.1$); (3) transition regime ($0.1 < K_n < 10$); and (4) free molecular-flow regime ($K_n > 10$). The Knudsen number is defined by

$$K_n = \frac{\lambda}{d}, \tag{5.18}$$

where d is the pore diameter and λ is the mean free path of gas molecules, which is computed by (Heidemann et al., 1984)

$$\lambda = \frac{k_B T}{\sqrt{2}\pi\sigma^2 p}, \tag{5.19}$$

where k_B is the Boltzmann constant (1.3805×10^{-23} J/K), T is temperature in K, p is pressure in Pa, and σ is diameter of gas molecules.

For shale gas reservoirs with low and ultra-low permeability, the following apparent permeability model proposed by Florence et al. (2007) is used to account for the gas slippage and diffusion effect:

$$k_a = k_i \left[1 + \alpha(K_n) K_n\right] \left(1 + \frac{4K_n}{1 + K_n}\right), \tag{5.20}$$

where k_a is apparent matrix permeability, k_i is the initial matrix permeability, $\alpha(K_n)$ represents the rarefaction parameter, which can be calculated by (Karniadakis and Beskok, 2002)

$$\alpha(K_n) = \frac{128}{15\pi^2} \tan^{-1}\left(4K_n^{0.4}\right). \tag{5.21}$$

Similarly, the other existing apparent permeability models considering complex nanopore phenomena such as surface diffusion of adsorbed gas in

the literature can be easily added in the current numerical model (Javadpour et al., 2007; Civan, 2010; Civan et al., 2011; Sakhaee-Pour and Bryant, 2012; Wu et al., 2015). However, the comparison of different apparent permeability models is beyond the scope of this chapter.

5.2.4 Non-Darcy Flow Effect

It is assumed that the non-Darcy flow effect only occurs for gas flow inside fractures. The non-Darcy flow is widely modeled using the Forchheimer modification to Darcy's law and is written as

$$-\nabla\Phi_g = \frac{\mu_g}{k \cdot k_{rg}}\vec{u}_g + \beta_g \rho_g |\vec{u}_g| \vec{u}_g, \tag{5.22}$$

where Φ_g is the potential of gas phase, ρ_g is gas density, β_g is the non-Darcy Forchheimer coefficient, which can be determined using the correlation proposed by Evans and Civan (1994) as given here:

$$\beta_g = \frac{1.485 \times 10^9}{k^{1.021}}, \tag{5.23}$$

where the unit of permeability is md and the unit of β_g is ft^{-1}. This correlation was obtained based on more than 180 data points including those for propped fractures and a good match is obtained with a correlation coefficient of 0.974 (Rubin, 2010). This correlation will be implemented into the numerical model in this study.

5.2.5 Pressure-Dependent Matrix Permeability

We use the empirical equation developed by Jones (1988) according to experimental data to handle the correlation between the change of matrix permeability and net effective stress as follows:

$$\frac{k}{k_i} = \exp\{a_k[\exp(-\sigma_e/\sigma^*) - 1]\}/(1 + C'\sigma_e), \tag{5.24}$$

where a_k is a constant, σ^* is a decay constant, which is arbitrarily given as 3000 psi, C' is a constant, which is arbitrarily set to 3×10^{-6} psi^{-1} (Jones, 1988), σ_e is the net effective stress, which is defined by

$$\sigma_e = \sigma - \alpha p_r, \tag{5.25}$$

where σ is the confining stress, p_r is pore pressure, α is Biot's constant, which can be calculated for an ideal uniaxial strain scenario (Chu et al., 2012):

$$\alpha = 1 - \frac{c_m}{c_b}, \tag{5.26}$$

where c_m is rock matrix compressibility and c_b is rock bulk compressibility.

5.2.6 Pressure-Dependent Fracture Permeability

It has been recognized that fracture conductivity, which refers to fracture permeability multiplied by fracture width, is challenging to maintain a constant high value in reality, whereas it often declines with the increasing closure pressure due to proppant embedment, proppant crushing, etc. This phenomenon is more serious when the shale rock is soft. Through fitting the laboratory measurement data in the proppant embedment test for different shale core samples ranging from still to soft (Alramahi and Sundberg, 2012), the following relationships between normalized fracture conductivity and closure pressure were obtained (Yu and Sepehrnoori, 2014b):

$$\text{Stiff shale}: \ \log(FC_N) = -0.0001 \times \sigma_c - 0.1082, \ \ R^2 = 0.954 \tag{5.27}$$

$$\text{Medium shale}: \ \log(FC_N) = -0.0004 \times \sigma_c + 0.2191, \ \ R^2 = 0.998 \tag{5.28}$$

$$\text{Soft shale}: \ \log(FC_N) = -0.0006 \times \sigma_c + 0.4256, \ \ R^2 = 0.987 \tag{5.29}$$

where FC_N is normalized fracture conductivity divided by the initial fracture conductivity, and σ_c is closure pressure in psi. These equations will be implemented in the numerical model in this study.

Finally, the finite difference method is utilized to solve the coupled and highly nonlinear partial differential equations. Under the assumption of isothermal shale-gas reservoir, the unknowns should be specified initially to include reservoir pressure and the number of moles for each component. In addition, no flow boundary condition is considered. An implicit pressure, explicit composition technique is used to solve for the unknowns such as pressure and component moles. More details can be found in the work by Chang (1990). The physical properties of real gas such as density, viscosity, and compressibility are calculated using Peng-Robinson equation of state (Lohrenz et al., 1964; Peng and Robinson, 1976).

5.3 NUMERICAL MODEL FOR TIGHT-OIL THREE-PHASE FLOW

The material balance equations are discretized with a finite-difference scheme using a block-centered grid. An IMPEC (implicit pressure and explicit composition) solution scheme is applied where the pressure equation is solved implicitly and the component molar balance equation is solved explicitly. Three-phase flow (water, oil, and gas) is considered for deriving the mass conservation equations for shale/tight-oil simulation in this study. The general mass conservation equation for each component can be written as

$$\frac{\partial W_i}{\partial t} + \vec{\nabla} \cdot \vec{F}_i - R_i = 0, \tag{5.30}$$

where t is time, W_i, $\vec{F}_i$, R_i are the accumulation, flux, and source terms, respectively (Lake, 1989). For component i, the terms in Eq. (5.30) can be expressed as

$$W_i = \phi \sum_{j=1}^{N_p} S_j \xi_j x_{ij}, \tag{5.31}$$

$$\vec{F}_i = \sum_{j=1}^{N_p} \xi_j \vec{u}_j x_{ij}, \tag{5.32}$$

$$\vec{u}_j = -\frac{\vec{\vec{k}} k_{rj}}{\mu_j} \left(\nabla p_j - \gamma_j \nabla D \right), \tag{5.33}$$

$$R_i = \frac{q_i}{V_b}, \tag{5.34}$$

where ϕ is porosity; V_b is bulk volume; N_p refers to number of phases, which is three in our study; subscript j refers to fluid phases; S is fluid phase saturation; ξ is molar density; x is mole fraction of component in phase; $\vec{u}$ is phase velocity; $\vec{\vec{k}}$ is permeability tensor; k_r is relative permeability; μ is phase viscosity; D is depth; γ is specific gravity; p is pressure; q is molar injection or production rate.

Therefore, the overall mass conservation equation for the component i is

$$\frac{\partial}{\partial t} \left[\phi \sum_{j=1}^{N_p} S_j \xi_j x_{ij} \right] - \vec{\nabla} \cdot \left[\sum_{j=1}^{N_p} \xi_j x_{ij} \frac{\vec{\vec{k}} k_{rj}}{\mu_j} \left(\nabla p_j - \gamma_j \nabla D \right) \right] - \frac{q_i}{V_b} = 0. \tag{5.35}$$

The equation considers fluid convection and Darcy's law. Physical dispersion and adsorption in solid phase are not considered in this study.

To solve the pressure in gridblocks, the basic assumption is that the total pore volume is the same as the total fluid volume. If we assume a slightly compressible formulation and use the chain rule, the pressure equation can be obtained as

$$\left(V_P^0 c_f - \frac{\partial V_t}{\partial p} \right) \frac{\partial p}{\partial t} - V_b \sum_{i=1}^{N_c+1} \vec{V}_{ti} \vec{\nabla} \cdot \sum_{j=1}^{N_p} \xi_j x_{ij} \frac{\vec{\vec{k}} k_{rj}}{\mu_j} \nabla p = V_b \sum_{i=1}^{N_c+1} \vec{V}_{ti} \vec{\nabla} \cdot$$

$$\sum_{j=1}^{N_p} \xi_j x_{ij} \frac{\vec{\vec{k}} k_{rj}}{\mu_j} \left(\nabla p_{cj} - \gamma_j \nabla D \right) + \sum_{i=1}^{N_c+1} \vec{V}_{ti} q_i, \tag{5.36}$$

where N_c refers to number of hydrocarbon components; V_P^0 is pore volume at reference pressure; p is pressure of reference phase (oleic phase); $\vec{V}_t$ is partial molar volume; p_{cj} is capillary pressure between phase j and reference phase.

Every time step, Eq. (5.36) is solved implicitly to obtain the pressure at each gridblock. After that, Eq. (5.35) is solved explicitly to get the component moles. Saturation of each phase can be calculated by means of flash calculations (Mehra et al., 1983; Perschke et al., 1989). The fluid properties are calculated with Peng-Robinson equation of state (Lohrenz et al., 1964; Peng and Robinson, 1976). This procedure is repeated until the maximum simulation time is reached.

5.4 EMBEDDED DISCRETE FRACTURE MODEL

We use the state-of-the-art EDFM approach to handle complex fracture geometries. The EDFM has been approved to be a powerful method to model complex fracture geometries in unconventional oil and gas reservoir simulation. The EDFM method borrows concepts from both dual-continuum model and discrete fracture models. In this method, a fracture with any shape is discretized into small segments based on the matrix block boundaries. Correspondingly, in the computational domain, some additional virtual cells are created to represent these segments. To accurately simulate fluid flow associated with these fracture segments, the non-neighboring connections (NNCs) are defined for these virtual blocks and transmissibility factors are calculated.

In the EDFM approach, all connections can be classified into four basic types, including flow between matrix blocks and fractures, flow between fracture segments inside an individual fracture, flow between intersecting fracture segments, and flow between fracture segment and the wellbore it intersects, as shown in Fig. 5.2.

The first three types of connections are simulated using transmissibility factors between blocks, and the volume flow rate (q) of phase l between blocks in an NNC pair can be expressed as

$$q = \lambda_l T_{NNC} \Delta p, \tag{5.37}$$

where λ_l is the relative mobility of phase l, T_{NNC} is the transmissibility factor, and Δp is the potential difference between corresponding blocks.

Generally, T_{NNC} can be expressed as

$$T_{NNC} = \frac{k_{NNC} A_{NNC}}{d_{NNC}}, \tag{5.38}$$

where k_{NNC}, A_{NNC}, and d_{NNC} represent the permeability, common area, and distance for the connection, respectively.

For flow between fracture and matrix, k_{NNC} is the matrix permeability, A_{NNC} is the area of the fracture segment, and d_{NNC} is the average normal distance from matrix block to fracture segment. For flow between fracture segments (within individual fracture or between intersecting fractures), k_{NNC} is the fracture permeability, A_{NNC} is the common area between fracture segments, and d_{NNC} is the distance between fracture segments. Using the transmissibility factor calculated

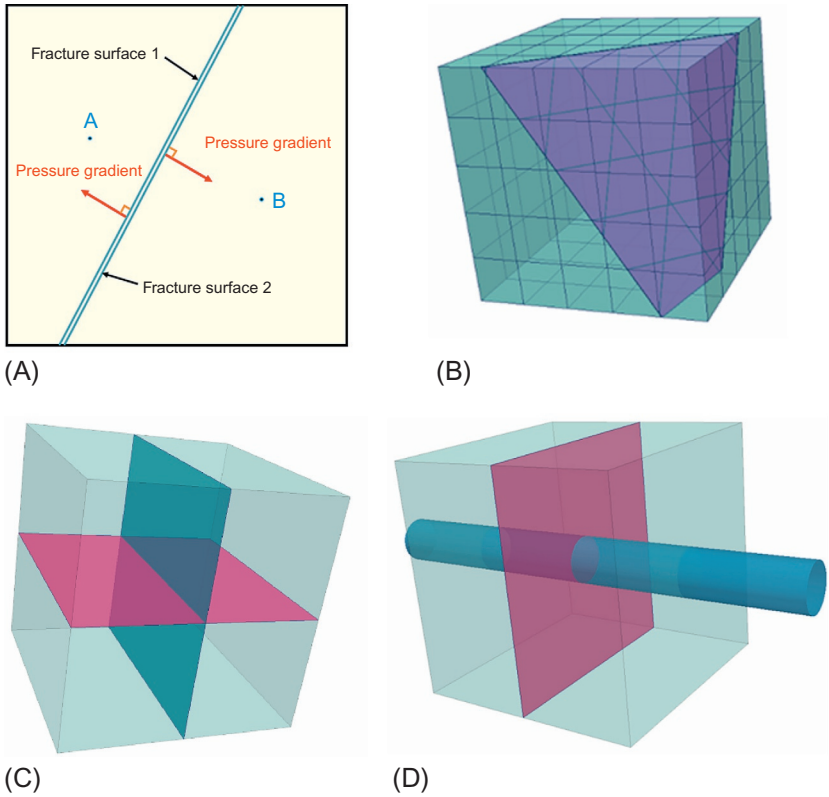

FIG. 5.2 Four types of non-neighboring connections (NNCs) (Xu, 2015; Xu et al., 2017a). (A) Flow between matrix blocks and fractures; (B) Flow between fracture segments inside an individual fracture; (C) Flow between intersecting fracture segments; (D) Flow between fracture segment and the wellbore it intersects.

from Eq. (5.38), the convective terms in Eqs. (5.8), (5.9), (5.35), and (5.36) are modified to incorporate the NNCs.

Similarly, fracture-wellbore intersections are modeled by treating fracture segments as wellblocks and assigning well indices. The calculation of well indices is similar to Peaceman's model.

$$WI_f = \frac{2\pi k_f w_f}{\ln(r_e/r_w)}, \tag{5.39}$$

$$r_e = 0.14\sqrt{L^2 + W^2}, \tag{5.40}$$

where w_f is the fracture aperture, k_f is the fracture permeability, L is the length of the fracture segment, and W is the height of the fracture segment. More details of the transmissibility factor and well index calculation can be found in Moinfar et al. (2014) and Xu et al. (2017a).

Our numerical model through fully implementation of EDFM can easily, quickly, and accurately handle complex hydraulic and natural fractures in unconventional reservoirs. The new model overcomes the key limitations of available numerical reservoir simulators with structured gridding and local grid refinement to handle complex fracture geometries. In addition, the new model does not have the complex gridding issue and low computational efficiency, which are often existing in numerical reservoir simulators with unstructured gridding technique.

5.5 MODEL VERIFICATION

5.5.1 Shale Gas Simulation

We set up a basic 3D reservoir model with dimensions of 2020 ft × 1500 ft × 130 ft, which corresponds to reservoir length, width, and thickness, respectively, as shown in Fig. 5.3. The dimension of grid size is 20 ft × 20 ft × 130 ft. A synthetic shale-gas case with 11 planar hydraulic fractures was simulated with the purpose of verifying the new developed model against a commercial reservoir simulator (CMG-GEM, 2012). The commercial simulator utilizes the LGR approach to handle hydraulic fracture. Each block containing hydraulic fracture is refined by 5 × 1 × 1. Our model uses the EDFM approach to deal with hydraulic fracture without the need of grid refinement near the fracture. The other reservoir and fracture properties used for the simulations are summarized in Table 5.1. The gas type is methane. The reservoir is assumed to be homogeneous with two-phase flow of gas and water. The initial water saturation is assumed to be 50% for the purpose of verification. It should be mentioned that the effects of capillary pressure and nanopore confinement are not included in the current study (Wu et al., 2017). Fig. 5.4 presents different relative permeability curves for the matrix and fracture system, respectively. The constant flowing bottomhole pressure (BHP) of 500 psi is assumed

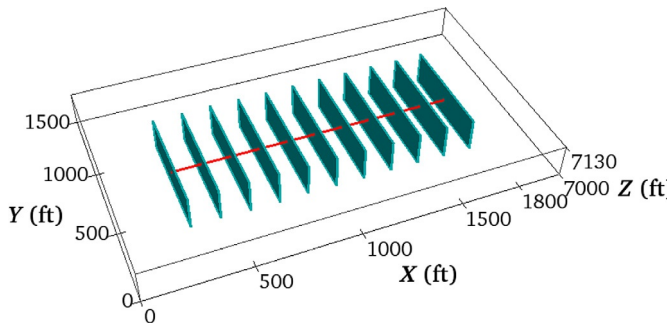

FIG. 5.3 A basic 3D reservoir model for a horizontal well with 11 planar hydraulic fractures (Yu et al., 2018a).

TABLE 5.1 Basic Parameters Used for the Simulations (Yu et al., 2018a)

Parameter	Value	Unit
Initial reservoir pressure	4000	psi
Reservoir temperature	130	°F
Reservoir thickness	130	ft
Reservoir permeability	800	nD
Reservoir porosity	12%	–
Initial gas saturation	50%	–
Gas gravity	0.58	–
Total compressibility	3×10^{-6}	psi^{-1}
Fracture half-length	350	ft
Fracture conductivity	100	md-ft
Fracture height	130	ft
Fracture width	0.01	ft
Fracture spacing	140	ft
Langmuir pressure	1300	psi
Langmuir volume	140	scf/ton
Rock density	2.5	g/cm^3

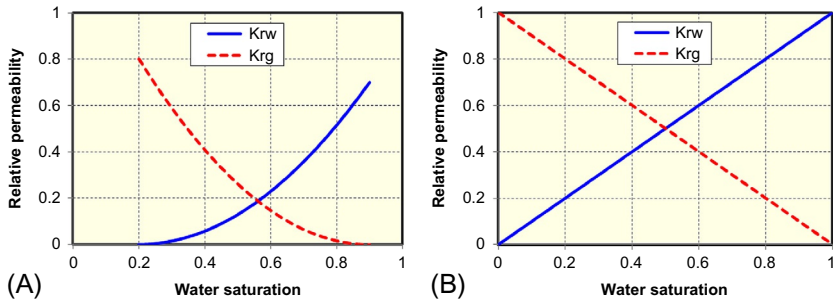

FIG. 5.4 Different relative permeability curves used for two-phase shale-gas simulation (Yu et al., 2018a). (A) Matrix system; (B) Fracture system.

for the simulation constraint over time. Fracture height is assumed to fully penetrate reservoir thickness. Gas desorption is considered using Langmuir isotherm, which is available in the commercial reservoir simulator. The non-Darcy flow effect is also considered.

Fig. 5.5 compares the simulation results of both flow rates and cumulative production for gas and water at a 30-year period between our model and the commercial reservoir simulator. As can be seen, a good match is obtained between them. It implies that our numerical model in conjunction with the EDFM approach can simulate shale-gas production with planar fractures by considering gas desorption and non-Darcy flow effects. Fig. 5.6 shows the pressure distribution after 30 years of production. It can be observed that the effective drainage area can be clearly demonstrated.

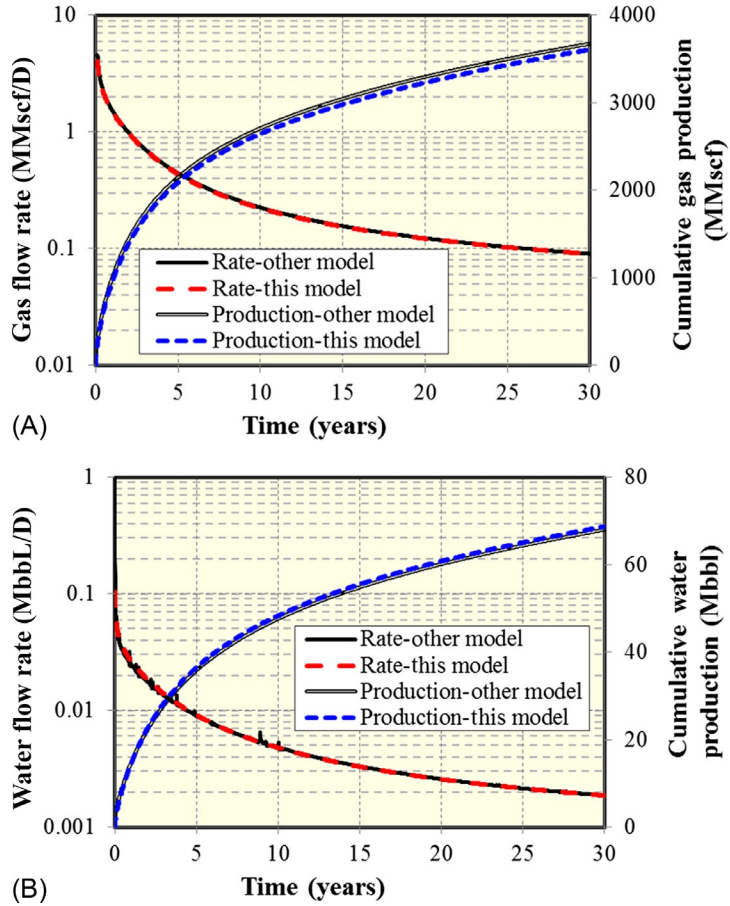

FIG. 5.5 Comparison of simulation results of flow rates and cumulative production at a 30-year period between this model and commercial reservoir simulator (Yu et al., 2018a). (A) Gas-flow rate and cumulative gas production; (B) Water-flow rate and cumulative water production.

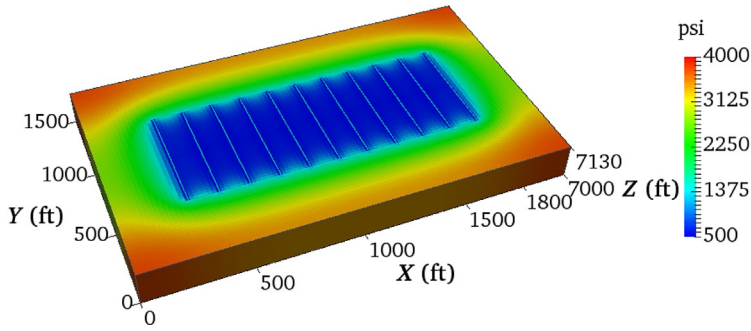

FIG. 5.6 Pressure distribution using this model after 30 years of production (Yu et al., 2018a).

5.5.2 Tight-Oil Simulation

A synthetic tight-oil case was built based on publicly available Eagle Ford data in order to verify the new developed numerical model (Orangi et al., 2011; Simpson et al., 2016). Fluid types in the Eagle Ford range from black oils with low gas oil ratio (GOR) to volatile oils with high GOR (Orangi et al., 2011). In our study, black oil with low GOR is considered. Fluid characterization data for Eagle Ford shale are scarce in literature. In our study, we assume crude oil of the Eagle Ford formation consists of five pseudocomponents, i.e., CO_2, N_2-C_1, C_2-C_5, C_6-C_{10}, and C_{11+}. The corresponding molar fractions are 0.01821, 0.44626, 0.17882, 0.14843, and 0.20828, respectively. According to the critical properties of these pseudocomponents and the other inputs in Tables 5.2 and 5.3, the key oil properties were determined using the Peng-Robinson equation of state and flash calculations under the reservoir temperature of 270°F: oil gravity is 41 °API, GOR is 1000 scf/stb, formation volume factor is 1.65 rb/stb, and bubble point is 3446 psi, which are the same as the data reported by Orangi et al. (2011).

We set up a basic reservoir model with length, width, and thickness of 6550 ft × 2150 ft × 100 ft, which corresponds to reservoir dimensions shown in Fig. 5.7. Two horizontal wells with multiple planar hydraulic fractures are modeled first. The separation of the two wells is 700 ft and each well contains 30 transverse hydraulic fractures with fracture half-length of 225 ft. The EDFM method is applied to model hydraulic fractures, which do not require any local grid refinement (LGR). LGR was still needed to account for the hydraulic fractures in the numerical reservoir simulator, in order to fully capture the transient flow behavior of fluid transfer from the matrix to fractures (Yu et al., 2016a). The basic reservoir and fracture properties used in the simulations are listed in Table 5.4.

A constant flowing initial BHP of 2000 psi is assumed for each well at the start of the simulations. Hydraulic fractures are assumed to fully

TABLE 5.2 Compositional Data for the Peng-Robinson Equation of State in the Eagle Ford Formation (Yu et al., 2017b)

Component	Molar Fraction	Critical Pressure (atm)	Critical Temperature (K)	Critical Volume (L/mol)	Molar Weight (g/gmol)	Acentric Factor	Parachor Coefficient
CO_2	0.01821	72.80	304.20	0.0940	44.01	0.2250	78.00
N_2-C_1	0.44626	45.24	189.67	0.0989	16.21	0.0084	76.50
C_2-C_5	0.17882	32.17	341.74	0.2293	52.02	0.1723	171.07
C_6-C_{10}	0.14843	24.51	488.58	0.3943	103.01	0.2839	297.42
C_{11+}	0.20828	15.12	865.00	0.8870	304.39	0.6716	661.45

TABLE 5.3 Binary Interaction Parameters for Oil Components in the Eagle Ford Formation (Yu et al., 2017b)

Component	CO_2	N_2-C_1	C_2-C_5	C_6-C_{10}	C_{11+}
CO_2	0	0.1036	0.1213	0.1440	0.1500
N_2-C_1	0.1036	0	0	0	0
C_2-C_5	0.1213	0	0	0	0
C_6-C_{10}	0.1440	0	0	0	0
C_{11+}	0.1500	0	0	0	0

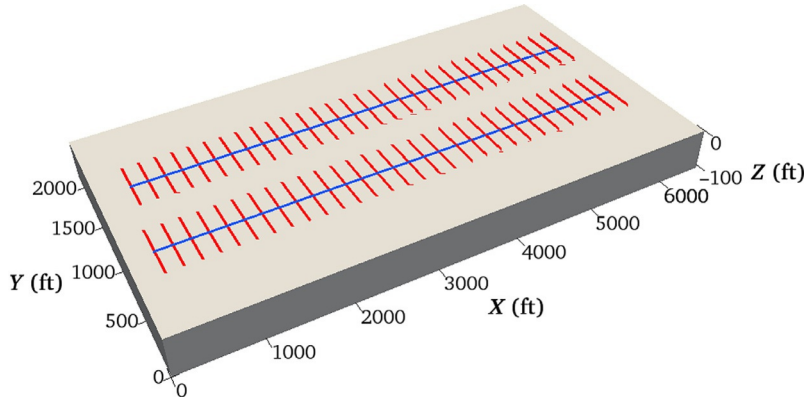

FIG. 5.7 A basic reservoir model including 2 horizontal wells *(blue lines)* each with 30 planar hydraulic fractures *(red lines)* (Yu et al., 2017b).

penetrate the reservoir thickness. The assumed relative permeability curves, such as water-oil relative permeability and liquid-gas relative permeability, are given in Fig. 5.8. The comparison of gas- and oil-flow rates between this model and numerical reservoir simulator (CMG-GEM, 2012) is shown in Fig. 5.9, illustrating that a good agreement was obtained. The pseudocomponents for tight oil adopted in our model ensure fluid properties (density, viscosity, and composition) correspond to values under reservoir condition at all times. The formation volume factor follows from the ratio of fluid volume at surface and under reservoir conditions, as is GOR, both of which are obtained from the pseudocomponents flash calculations in the results of Fig. 5.9.

TABLE 5.4 Basic Reservoir and Fracture Properties Used for the Simulations (Yu et al., 2017b)

Parameter	Value	Unit
Initial reservoir pressure	8000	psi
Reservoir temperature	270	°F
Reservoir permeability	470	nD
Reservoir porosity	12%	–
Initial water saturation	17%	–
Total compressibility	3×10^{-6}	psi^{-1}
Fracture half-length	225	ft
Fracture conductivity	100	md-ft
Fracture height	100	ft
Fracture width	0.01	ft
Fracture spacing	200	ft
Well spacing	700	ft

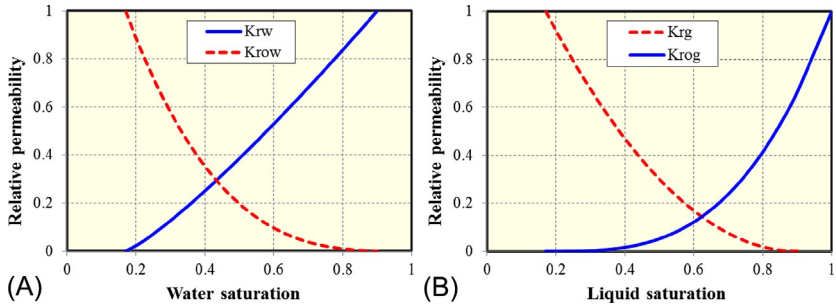

FIG. 5.8 Relative permeability curves used in this study (Yu et al., 2017b). (A) Water-oil relative permeability curve; (B) Liquid-gas relative permeability curve.

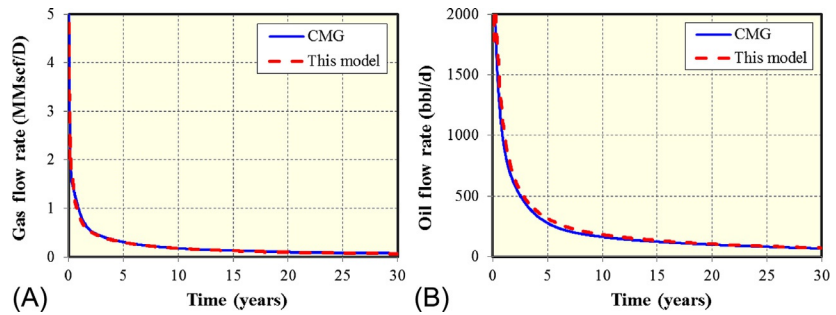

FIG. 5.9 Comparison of well performance between this model and numerical reservoir simulator (Yu et al., 2017b). (A) Gas-flow rate; (B) Oil-flow rate.

5.6 CASE STUDIES FOR WELL PERFORMANCE IN SHALE GAS RESERVOIRS

5.6.1 Complex Gas Transport Mechanisms

In the following sections, we examined the impacts of complex gas transport mechanisms on well performance such as gas desorption, gas slippage, and gas diffusion in more detail. It is important to point out that the initial water saturation is changed to 20%, which is the residual water saturation. Hence, there is only gas flow for the following case studies. The other input parameters remain the same as those in Table 5.1.

In our previous study associated with gas desorption (Yu et al., 2016a), it has been found that the BET isotherm performs a better match than Langmuir isotherm with the measured methane adsorption under high reservoir pressure. The fitting parameters of BET isotherm such as $v_m = 49.01$ scf/ton, $C = 24.56$, and $n = 4.46$ are used in this study. Fig. 5.10 shows the effects of gas adsorption using BET isotherm with and without considering adsorbed gas porosity on well performance. It can be illustrated that the relative contribution of gas desorption on well performance after 30 years without considering the adsorbed gas porosity is around 11% compared to the case without considering gas desorption. However, it will decrease to around 5% when considering the adsorbed gas porosity. Hence, the adsorbed gas porosity effect significantly affects well performance, which has been usually neglected in the literature.

Fig. 5.11 presents the effect of gas slippage and diffusion on well performance by considering various nanopore sizes between 5 and 50 nm. It can be observed that the smaller the nanopore size, the higher ultimate gas recovery. This is because the smaller pore size leads to larger Knudsen number, and then the ratio of apparent permeability to initial matrix permeability increases accordingly, especially at lower reservoir pressure, resulting in higher gas recovery.

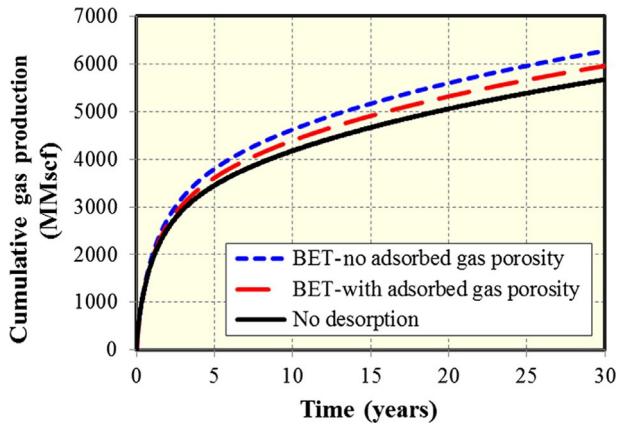

FIG. 5.10 Effects of gas adsorption and adsorbed gas porosity well performance (Yu et al., 2018a).

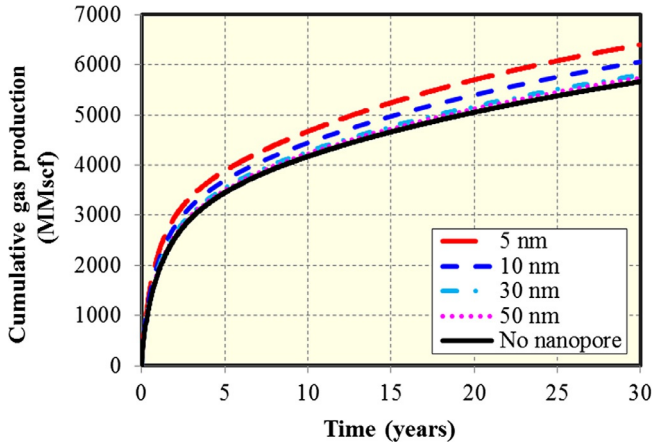

FIG. 5.11 Effect of gas slippage and diffusion on well performance with various nanopore sizes between 5 and 50 nm (Yu et al., 2018a).

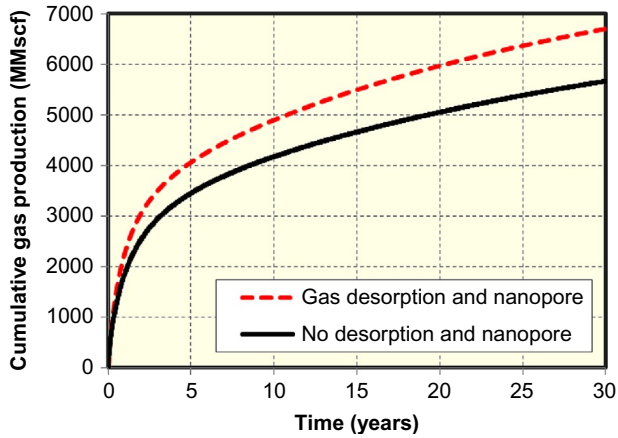

FIG. 5.12 Effects of the combination effects of gas desorption, adsorbed gas porosity, gas slippage, and diffusion on well performance (Yu et al., 2018a).

The positive contribution of gas slippage and diffusion effect to ultimate gas recovery after 30 years is about 13% and 7% with respect to the nanopore size 5 and 10 nm, respectively, when compared to the case without considering the effect. However, the nanopore size of 50 nm has negligible impact on well performance in this study.

Fig. 5.12 shows the combining effects of gas desorption, adsorbed gas porosity, gas slippage and diffusion discussed in the preceding on well performance. The nanopore size of 5 nm is assumed. It clearly shows that a significant increase of ultimate gas recovery of 18% after 30 years of production is

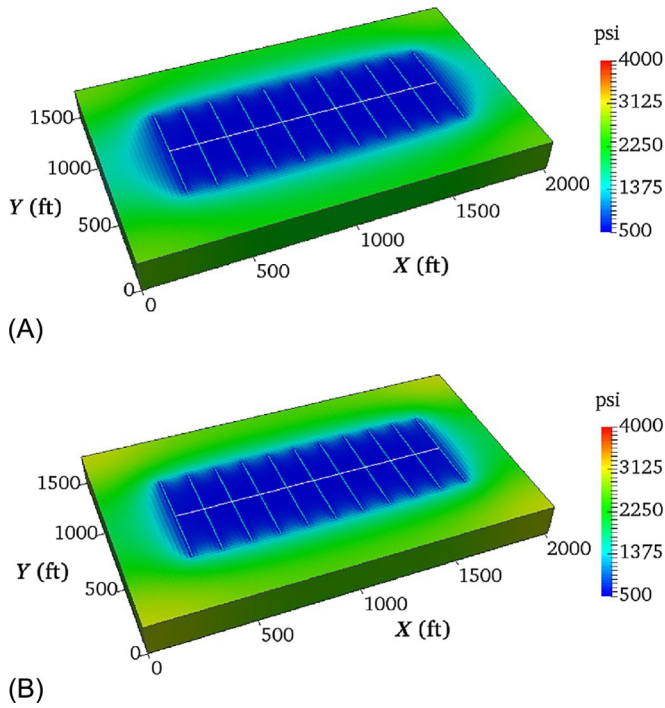

FIG. 5.13 Comparison of pressure distribution after 30 years with and without considering the combining effects of gas desorption, adsorbed gas porosity, and gas slippage, and diffusion (Yu et al., 2018a). (A) With the combing effects; (B) Without the combing effects.

determined when compared to the case without considering the combining effects. Fig. 5.13 shows the comparison of pressure distribution after 30 years with and without considering the combining effects. As shown, a faster reservoir depletion occurs when considering the combing effects. Accordingly, it can be concluded that it is extremely important to consider all of these important complex gas transport mechanisms in nanopores and organic matter in order to accurately simulate shale gas production.

5.6.2 Complex Natural Fracture Geometry

Next, the effect of complex natural fractures in combination with 11 planar hydraulic fractures described in the preceding on well performance is investigated. We designed three cases with different number and set of natural fractures, as shown in Fig. 5.14. Case 1 is with 100 one-set natural fractures. Case 2 is with 200 one-set natural fractures. Case 3 is with 200 two-set natural fractures. The natural fractures are randomly distributed in the reservoir of interest. For cases 1 and 2, the natural fractures are oriented at 5–10 degree

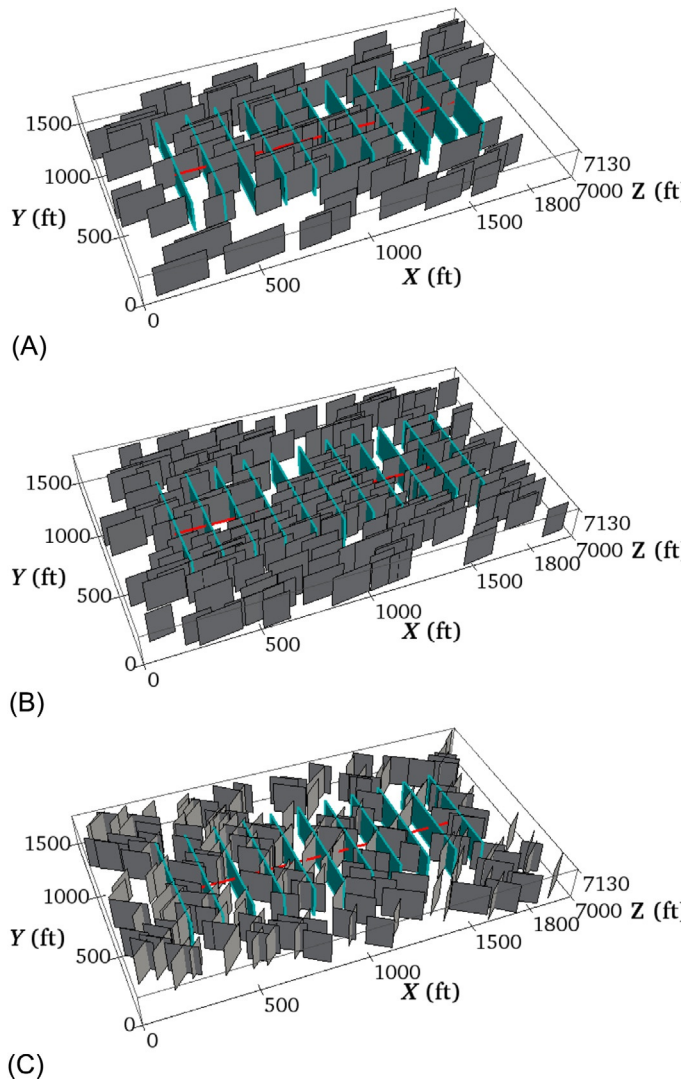

FIG. 5.14 Three cases with different natural fracture settings (*gray color* represents natural fractures) (Yu et al., 2018a). (A) Case 1 with 100 one-set natural fractures; (B) Case 2 with 200 one-set natural fractures; (C) Case 3 with 200 two-set natural fractures.

along the horizontal wellbore, which are almost perpendicular to hydraulic fractures. The natural fractures length ranges from 100 to 300 ft, which satisfies a normal distribution. For Case 3, one set of natural fractures is oriented at 45–55 degree and another set is 135–145 degree. Similarly, the length of natural fractures ranges from 100 to 300 ft. The conductivity of natural fractures for each case is assumed to be 10 md-ft and the conductivity of hydraulic fractures is

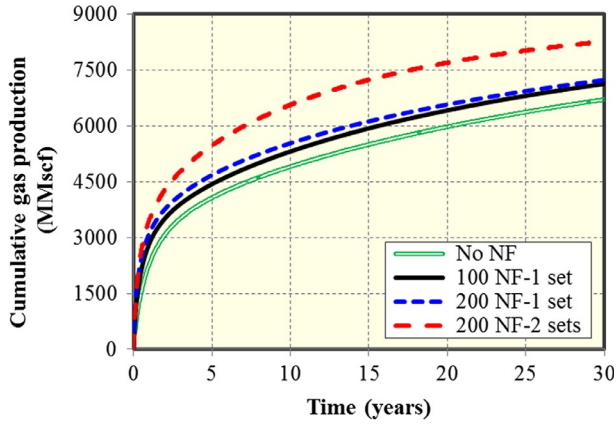

FIG. 5.15 Effects of different number and sets of natural fractures on well performance (NF represents natural fracture) (Yu et al., 2018a).

100 md-ft. The effects of non-Darcy flow, gas desorption, adsorbed gas porosity, and nanopore size of 5 nm are considered.

Fig. 5.15 compares the effects of different number and sets of natural fractures on well performance. As shown, the natural fractures have a critical effect on well performance. The increase of ultimate gas recovery after 30 years compared to base case without natural fractures is 6.3%, 7.8%, and 23.2% for Cases 1, 2, and 3, respectively. Fig. 5.16 shows the comparison of pressure distribution after 1000 days and 30 years of production for each case. It can be clearly demonstrated that there is a larger effective drainage area for cases 1–3 than that for base case without natural fractures (Fig. 5.16A and B). In addition, there is a little difference between Cases 1 and 2. This is because the number of natural fractures connected with hydraulic fractures increases slightly with an increase of fracture number from 100 to 200, resulting in a little bit increase of drainage area (Fig. 5.16E and F vs. Fig. 5.16C and D). However, there are more number of natural fractures connected to hydraulic fractures directly or indirectly for Case 3, leading to a much more complex connected fracture network and a bigger expansion of drainage area than cases 1 and 2 (Fig. 5.16G and H). Hence, it can be predicted that it is important to create a better connected complex fracture network during the actual fracturing process, which is vital to maximizing the stimulation effectiveness and production optimization. The influences of detailed natural fracture conductivity, density, orientation, distribution on well performance will be examined in more detail in future study.

5.6.3 Complex Hydraulic Fracture Geometry

In this study, a complex hydraulic fracture propagation model, developed by Wu and Olson (2016), is used to predict complex nonplanar fracture geometry

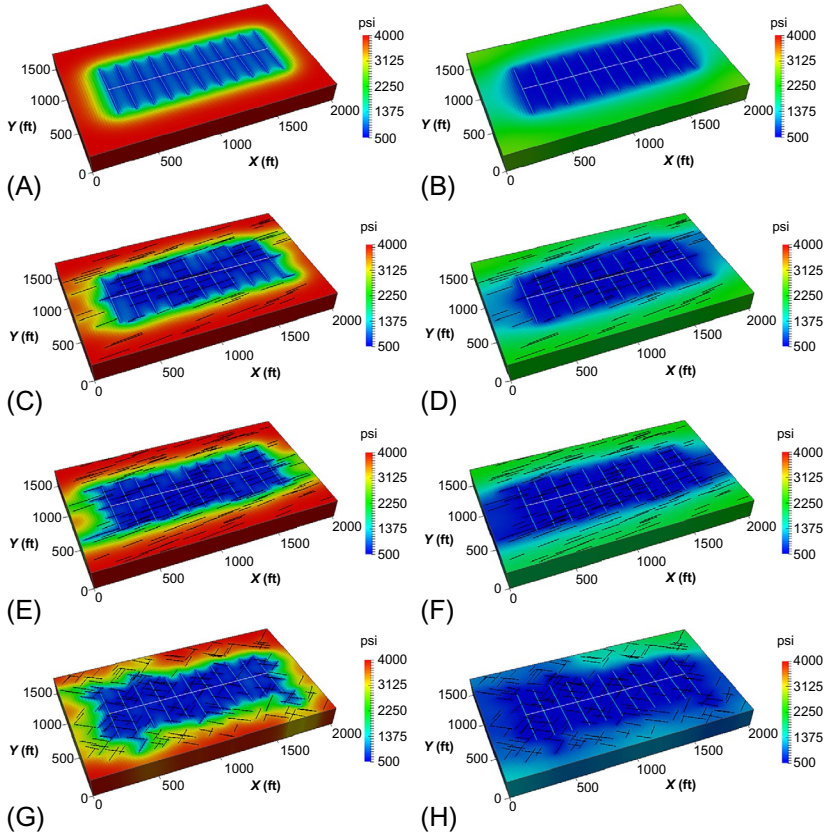

FIG. 5.16 Comparison of pressure distribution for different cases after 1000 days and 30 years (Yu et al., 2018a). (A) Base case without NF after 1000 days; (B) Base case without NF after 30 years; (C) Case 1 after 1000 days; (D) Case 1 after 30 years; (E) Case 2 after 1000 days; (F) Case 2 after 30 years; (G) Case 3 after 1000 days; (H) Case 3 after 30 years.

through modeling the interaction between hydraulic fractures and natural fractures. The model couples rock deformation and fluid flow in the fractures and horizontal wellbore. The core solid mechanics solution is three dimensional, such that fracture opening, shearing, and stress shadow effects are accurately determined for single and multifracture cases (Wu and Olson, 2015). Fluid flow in the fracture and the associated pressure drop are based on lubrication theory, assuming the fracture is analogous to a slot between parallel plates and the fluid is non-Newtonian. A constant total fluid injection rate is given. Partitioning of flow rate into each fracture is dynamically calculated in such way that the wellbore pressure is constrained to gradually decrease along the lateral due to wellbore friction. The interaction of hydraulic and natural fractures is described through analyzing induced stresses at the fracture tips. Stochastic

realization methods were used to describe natural fracture patterns (Wu and Olson, 2016). Length of natural fractures follows a power-law distribution. The model has been validated against known analytical solutions for single hydraulic fracture growth (Olson and Wu, 2012). To demonstrate the validity of capturing the physical process of fracture interaction, the model has also been compared to a numerical model (Wu et al., 2012) in case of multiple fracture propagation. The primary assumptions for the current fracture model include: transverse fractures are initiated perpendicular to the horizontal wellbore with a nominal initial length; fracture height is constant; proppant transport and poroelastic effects are not considered. In this study, the parameters used for the fracture model include fluid injection rate of 20 barrels per minute (bbl/min) and injection time of 10 min for each fracture, Young's modulus of 3×10^6 psi, Poisson ratio of 0.23, the difference of minimum and maximum horizontal stress of 500 psi, and fluid leak-off coefficient of 5×10^{-3} ft/min$^{0.5}$. Fig. 5.17 shows the distribution of fracture width of the generated complex nonplanar fracture geometry for a synthetic shale-gas case. For this case study, there are 11 nonplanar fractures evenly spaced 140 ft and 100 natural fractures. As shown, the distribution of fracture width is highly nonuniform.

Next, the complex fracture geometry was transformed to reservoir model, as shown in Fig. 5.18. The nonuniform fracture width results in varying fracture conductivity across the fractures ranging from 0.1 to 48 md-ft. The natural fracture conductivity is 10 md-ft. The other input parameters are kept the same as those in Table 5.1. The combing effects of non-Darcy flow, gas desorption, adsorbed gas porosity, and nanopore size of 5 nm are considered. In addition, the effects of pressure-dependent matrix permeability and fracture conductivity are included. We use Eq. (5.24) with a_k of 2.7442 and Eq. (5.28) to generate the pressure-dependent matrix permeability and fracture conductivity, respectively,

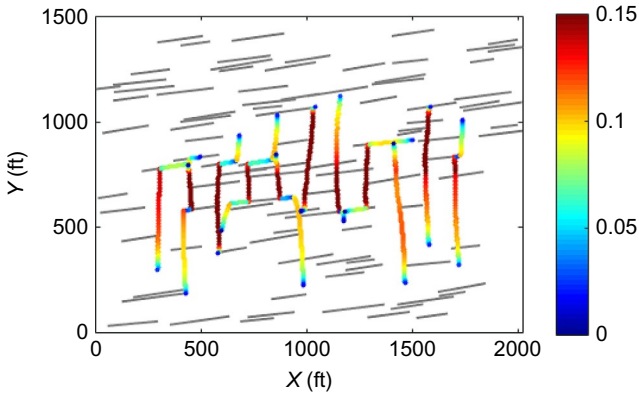

FIG. 5.17 Distribution of fracture width of generated complex nonplanar fracture geometry predicted by the fracture model for a synthetic shale-gas case (*gray lines* represent natural fractures) (Yu et al., 2018a).

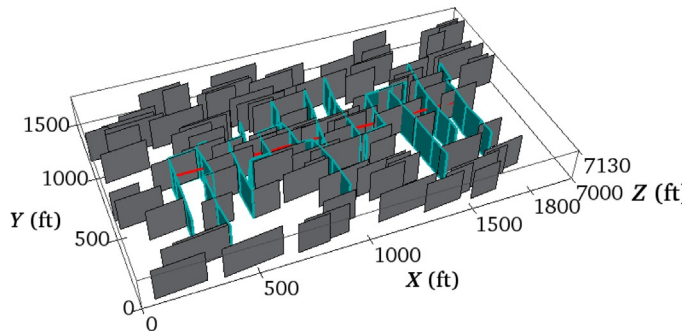

FIG. 5.18 Complex nonplanar fracture geometry with 100 natural fractures in a synthetic shale-gas case (Yu et al., 2018a).

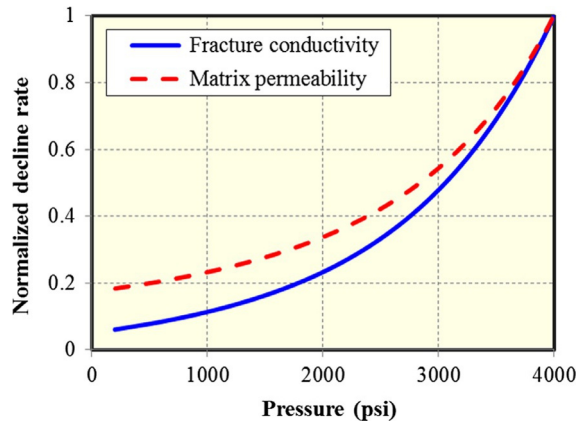

FIG. 5.19 Pressure-dependent curves of matrix permeability and fracture conductivity used in this study (Yu et al., 2018a).

as shown in Fig. 5.19. The normalized decline rate means that the matrix permeability and fracture conductivity at different pressure divided initial matrix permeability and fracture conductivity. As shown, the matrix permeability and fracture conductivity at BHP of 500 psi are about 20% and 8% of initial values for this case study. Fig. 5.20 presents the effects of pressure-dependent matrix permeability and fracture conductivity on well performance individually or simultaneously. It can be clearly observed that pressure-dependent effect significantly declines the gas recovery. The ultimate gas recovery after 30 years is decreased by 16%, 20%, and 31% for pressure-dependent matrix permeability, fracture conductivity, and both, respectively, when compared to the case without considering these effects. Fig. 5.21 presents the comparison of pressure distribution of different scenarios after 1000 days and 30 years. As shown,

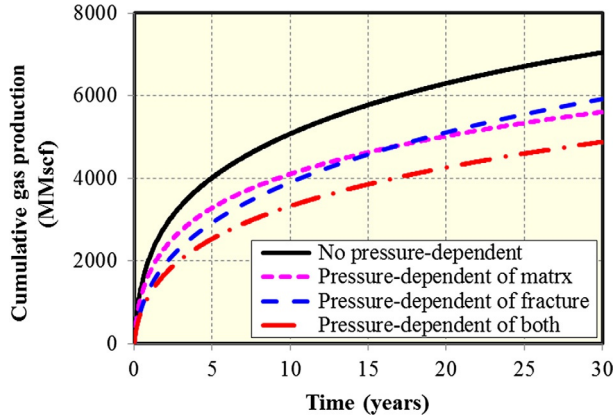

FIG. 5.20 Effects of pressure-dependent matrix permeability and fracture conductivity on well performance (Yu et al., 2018a).

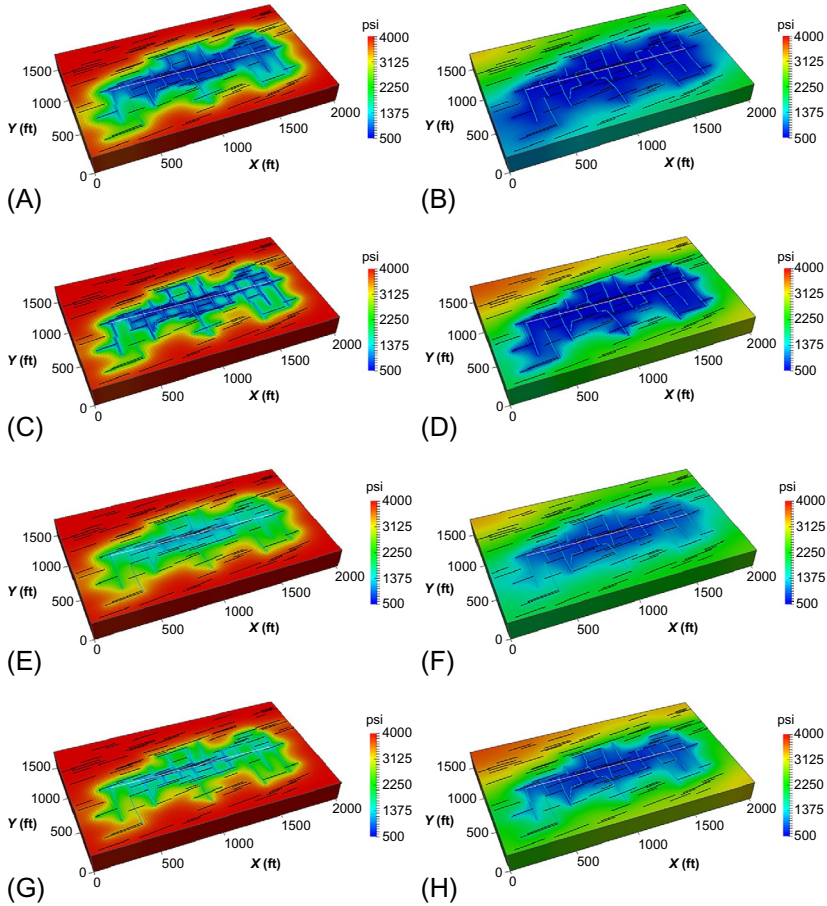

FIG. 5.21 Comparison of pressure distribution for different scenarios after 1000 days and 30 years (Yu et al., 2018a). (A) Without pressure-dependent effect after 1000 days; (B) Without pressure-dependent effect after 30 years; (C) Pressure-dependent matrix permeability after 1000 days; (D) Pressure-dependent matrix permeability after 30 years; (E) Pressure-dependent fracture conductivity after 1000 days; (F) Pressure-dependent fracture conductivity after 30 years; (G) Pressure dependent of both after 1000 days; (H) Pressure dependent of both after 30 years.

the drainage area is mainly concentrated nearby the fractures when only considering pressure-dependent matrix permeability (Fig. 5.21C and D vs. Fig. 5.21A and B). However, when only taking into account pressure-dependent fracture conductivity, the effective drainage area becomes further smaller after 1000 days (Fig. 5.21C vs. Fig. 5.21E), whereas the reservoir depletion becomes more wider after 30 years due to the dominate role of matrix permeability at later times (Fig. 5.21D vs. Fig. 5.21F). When the effects of pressure-dependent of both matrix permeability and fracture conductivity are included, the drainage area and reservoir depletion are much smaller than the case without these effects (Fig. 5.21G and H vs. Fig. 5.21A and B). Hence, it is highly recommended that pressure-dependent rock and fracture properties should be carefully characterized based on laboratory measurements in order to achieve an optimal treatment design in shale gas reservoirs.

We investigate the impact of reservoir heterogeneity on well performance. A range of matrix permeability between 0.0001 md (100 nD) and 0.001 md (1000 nD) is considered. Fig. 5.22 represents the distribution of matrix permeability in the reservoir. Correspondingly, the average equivalent matrix permeability is calculated as about 0.0005 md (500 nD). The comparison of well performance between the homogeneous and heterogeneous scenarios is shown in Fig. 5.23. It can be clearly seen that the relative difference of ultimate gas recovery after 30 years between the heterogeneous case and the homogeneous case with the minimum permeability of 0.0001 md is as high as 35%. It is about 27% between the heterogeneous case and the homogeneous case with the maximum permeability of 0.001 md. However, the difference between the heterogeneous case and the homogeneous case with average equivalent permeability of 0.0005 md is small, which is about 5% after 30 years. Hence, it is important to properly characterize the distribution of matrix permeability in order to perform a better production prediction in shale gas reservoirs.

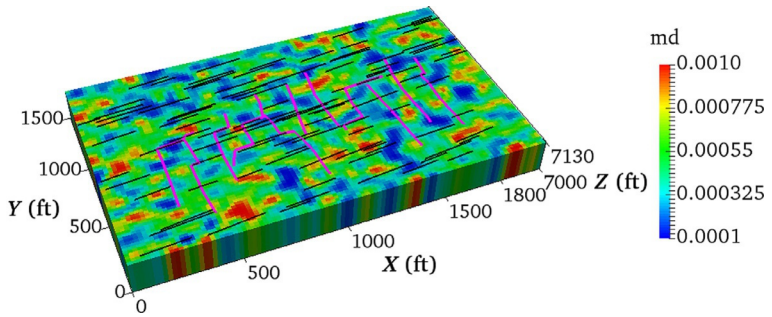

FIG. 5.22 Distribution of matrix permeability in the reservoir with complex nonplanar fracture geometry and natural fractures (Yu et al., 2018a).

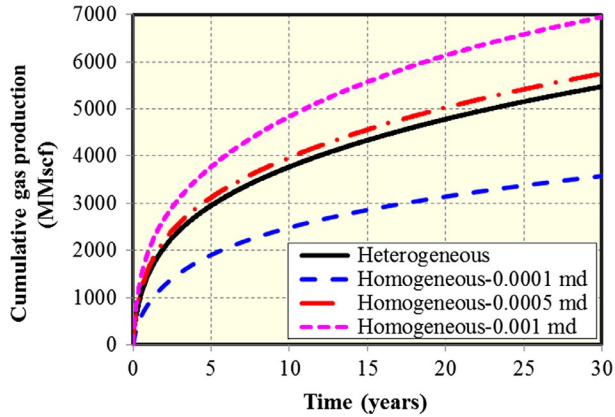

FIG. 5.23 Comparison of well performance between homogeneous and heterogeneous scenarios (Yu et al., 2018a).

5.7 CASE STUDIES FOR WELL INTERFERENCE IN TIGHT-OIL RESERVOIRS

In order to examine the impacts of different physical mechanisms such as matrix permeability, hydraulic fracture hits, and natural fractures on pressure response of well interference, we designed four synthetic cases, each comprising two parallel horizontal wells, but with different degrees of fracture density (and connectivity), as illustrated in Fig. 5.24. Case 1 represents well interference through matrix permeability with neither having any natural fractures nor any connecting hydraulic fractures. Case 2 represents well interference through both the matrix permeability and via natural fractures partly connected to the regular set of hydraulic fractures. The natural fractures occur in two dominant orientations and the total number of natural fractures is 1000 in the reservoir volume studied (black lines). More specifically, a statistical method was used to generate the natural fracture sets. The angle with respect to the x axis for one set ranges from 5 to 25 degree and the other set ranges from 95 to 115 degree. The length of the natural fractures varies between 100 and 300 ft. The conductivity of the natural fractures is fixed at 1 md-ft. The natural fracture height in our model is assumed equal to the reservoir thickness. Case 3 represents well interference through both matrix permeability and via hydraulic fracture hits, but without any natural fractures. The two wells are interconnected via five hydraulic fracture hits each with fracture conductivity of 100 md-ft. Case 4 represents well interference through the combination of matrix permeability, natural fractures, and connecting hydraulic fractures. The other reservoir and fracture properties remain the same as those in Tables 5.2–5.4. The simulation time is 1000 days. It is assumed that the upper horizontal well is producing under the constant BHP of 2000 psi while the lower horizontal well remains

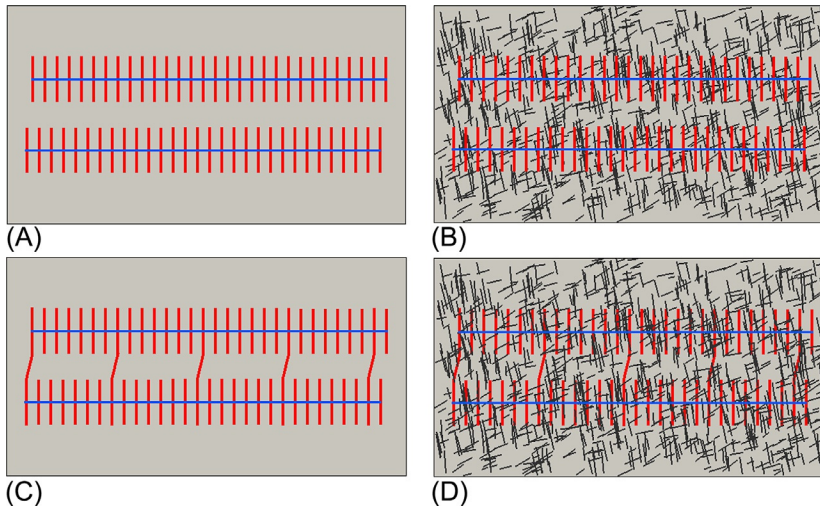

FIG. 5.24 Map view of four cases demonstrating the different mechanisms inducing well interference such as matrix permeability, hydraulic fracture hits, natural fractures, and the combination of them (Yu et al., 2017b). (A) Case 1; (B) Case 2; (C) Case 3; (D) Case 4.

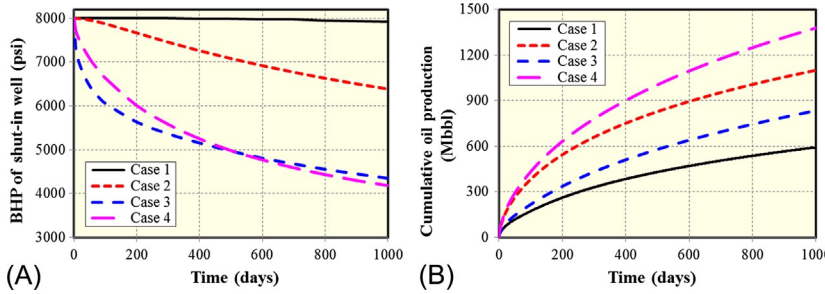

FIG. 5.25 Comparison for four cases of (A) pressure response of the shut-in lower well after opening upper well and (B) cumulative oil production of the producing well (Yu et al., 2017b).

shut-in at all times. It is necessary to point out that this assumption may not be realistic in the field operations. However, the key purpose here is to examine the impacts of various physical mechanisms on pressure response of well interference. More practical scenarios in the field operations such as the shut-in well are considered undrilled for some period of time and then drilled and will be investigated systematically in the future study.

The pressure response of the shut-in well and cumulative oil production of the producing well for each of the four cases is presented in Fig. 5.25. For Case 1, the effect of matrix permeability on BHP decline of the shut-in well within 1000 days is negligible due to the low matrix permeability of 470 nD and assuming an otherwise constant porosity for all cases. For Case 2, the BHP decline is

small at early times and subsequently decreases almost linearly at later times. For Case 3, the BHP declines relatively fast at early times but then the decline rate slows at later times. Comparing Cases 2 and 3 indicates that the connectivity via hydraulic fracture hits in our model is more important for well interference than the effect of natural fractures. For Case 4, the BHP declines at early times slower than for Case 3 but then faster at later times. For Case 4, oil production from natural fractures likely helps sustain productivity of the open well. Fig. 5.25B confirms that the presence of natural fractures (Cases 2 and 4) significantly boosts the performance of the producing well.

Fig. 5.26 shows the pressure distribution in the reservoir for each case after 1000 days of production. For Case 1 (Fig. 5.26A), well interference is absent and reservoir depletion around the shut-in well cannot occur. When well interference occurs due to the existence of natural fractures as in Case 2 (Fig. 5.26B), the drainage area of the producing well becomes somewhat enhanced as compared to Case 1. Fluid flows from the shut-in well to the producing well via some connected natural fractures. Since the conductivity of the connecting natural fractures is very small (1 md-ft), any reservoir depletion around the shut-in well remains negligible. When well interference increases due to connection of the two wells by hydraulic fracture hits as in Case 3 (Fig. 5.26C), fluid flows faster from the shut-in well to the producing well, aided by larger conductivity of the connecting hydraulic fractures, resulting in some discernable drainage around the shut-in well. When well interference occurs due to a combination of effects as in Case 4 (Fig. 5.26D), the drainage area encompasses both the producing well and the shut-in well, and consequent reservoir depletion area is largest.

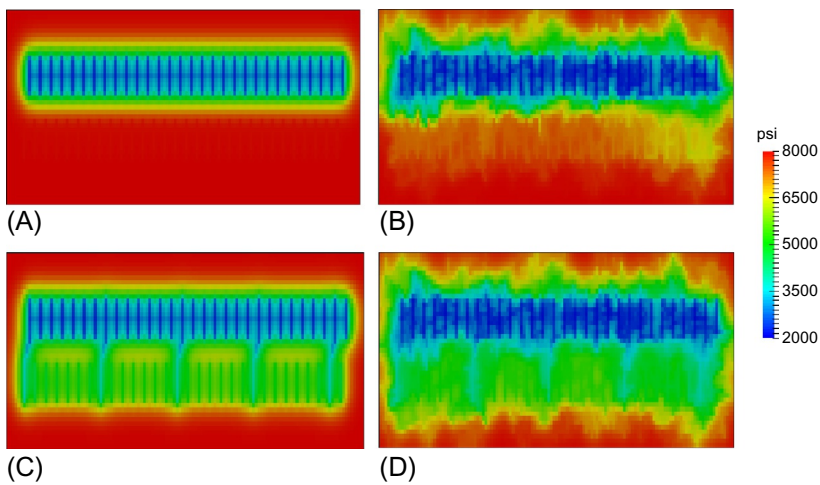

FIG. 5.26 Comparison of pressure distribution between four cases after 1000 days of production (Yu et al., 2017b). (A) Case 1; (B) Case 2; (C) Case 3; (D) Case 4.

5.8 SENSITIVITY ANALYSIS

5.8.1 Effect of Connecting Fracture Conductivity

On the basis of Case 3 with five fracture hits, we investigated the impact on pressure response of four discrete cases with different conductivity for the set of fracture hits, namely, 0.1, 1, 10, and 100 md-ft, as shown in Fig. 5.27. The BHP of the shut-in well decreases most rapidly when the conductivity of the connecting fractures is higher. In addition, the profile of BHP decline changes from convex to concave with an increase in fracture conductivity. The BHP result for the low fracture conductivity (0.1 md-ft) suggests that the pressure response of well interference is difficult to identify at early times of production even though there are multiple hydraulic fracture hits. Fig. 5.27B graphs the cumulative oil production for the upper, open well for each set of fracture hit conductivities. As to be expected, cumulative production increases with increasing conductivity of the connecting fractures. The reservoir pressure distribution after 1000 days of production is shown in Fig. 5.28 for each fracture hit conductivity. Fluids flow faster from the shut-in well to the producing well when the conductivity of the connecting fractures is higher, as can be physically expected.

5.8.2 Effect of Number of Connecting Hydraulic Fractures

We separately investigated the impact on pressure response for a discrete number of fracture hits, referring to the number of hydraulic fractures connecting the well pair, comparing the effect of 3, 5, 8, and 15 hits, as shown in Fig. 5.29. The conductivity of all fracture hits was kept constant at 100 md-ft. The resulting BHP of the shut-in well and the cumulative oil production of the open well for each case is shown in Fig. 5.30. The BHP of the shut-in well decreases faster when the fracture hits increase, confirming that the number of connecting fractures plays an important role in pressure response of well interference. Similarly, cumulative oil production of the open well increases when the number of connecting hydraulic fractures increases. The pressure

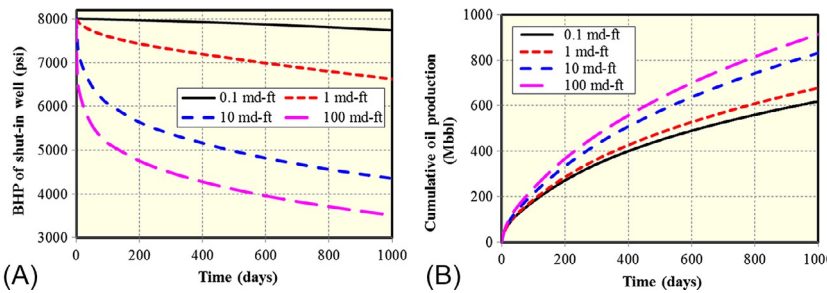

FIG. 5.27 Effect of connecting fracture conductivity on pressure response of the shut-in well and cumulative oil production of the producing well (Yu et al., 2017b). (A) BHP of the shut-in well; (B) Cumulative oil production.

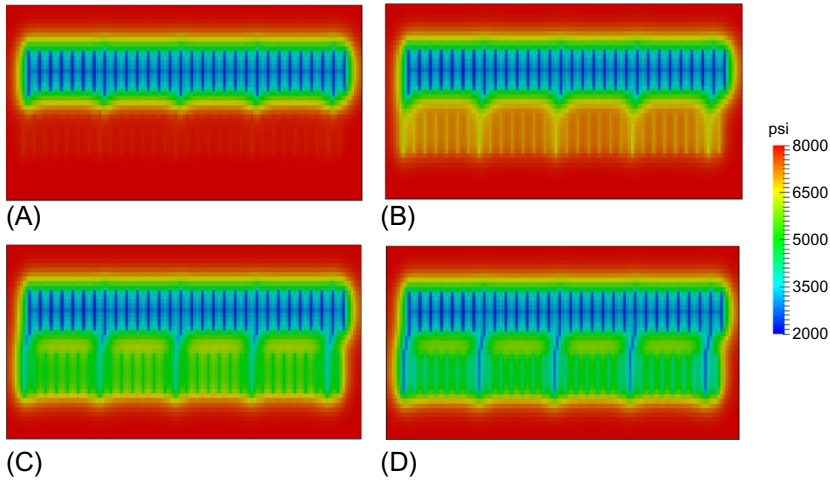

FIG. 5.28 Comparison of pressure distribution under different connecting fracture conductivities after 1000 days of production (Yu et al., 2017b). (A) 0.1 md-ft; (B) 1 md-ft; (C) 10 md-ft; (D) 100 md-ft.

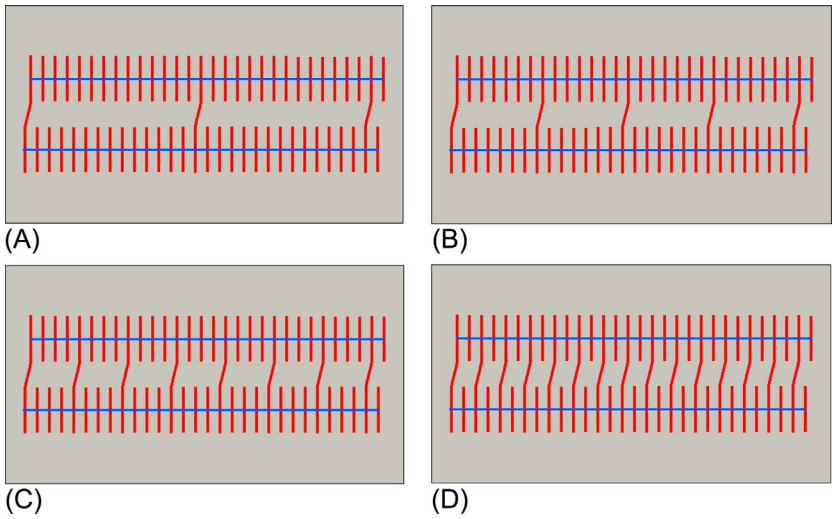

FIG. 5.29 Map view of different number of connecting hydraulic fractures inducing well interference (Yu et al., 2017b). (A) 3 connecting hydraulic fractures; (B) 5 connecting hydraulic fractures; (C) 8 connecting hydraulic fractures; (D) 15 connecting hydraulic fractures.

distribution pattern in the reservoir after 1000 days of production for each case is shown in Fig. 5.31. These pressure images clearly demonstrate that fluid migrates faster away from the shut-in well to the producing well when the number of connecting hydraulic fractures increases. Depletion of the reservoir

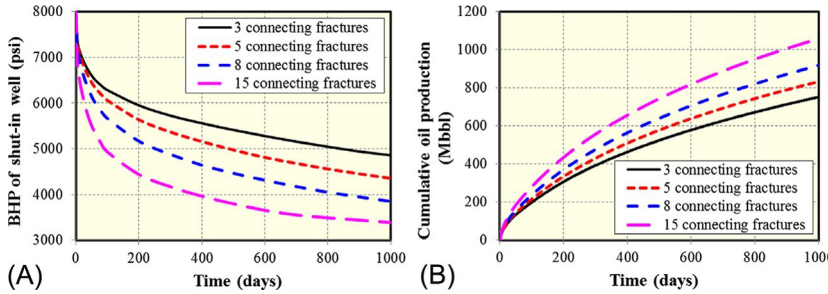

FIG. 5.30 Effect of number of connecting hydraulic fractures on pressure response of the shut-in well and cumulative oil production of the producing well (Yu et al., 2017b). (A) BHP of the shut-in well; (B) Cumulative oil production.

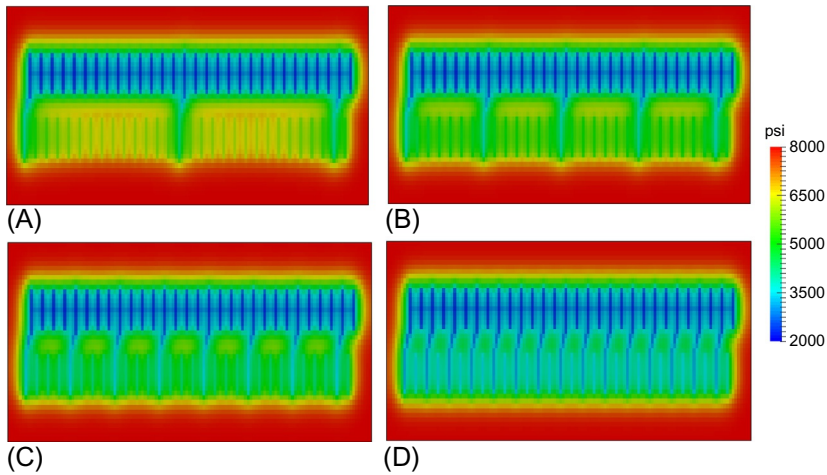

FIG. 5.31 Comparison of pressure distribution under different number of connecting hydraulic fractures after 1000 days of production (Yu et al., 2017b). (A) 3 connecting fractures; (B) 5 connecting fractures; (C) 8 connecting fractures; (D) 15 connecting fractures.

section drained by the well pair benefits from fracture hits, when one well is kept shut-in. However, simultaneous production by keeping both wells under production will certainly be faster, but requires a double set of pumps and separators, offsetting some of the net present value gains due to faster production.

5.8.3 Effect of Number of Natural Fractures

We investigated the impact on pressure response and well productivity for four discrete cases with different natural fracture density, namely, 100, 500, 1000, and 1500 fractures per study area volume, as shown in Fig. 5.32. The natural fracture parameters such as natural fracture length, angle, and height remain the same as in Case 4. The resulting impacts on BHP of the shut-in well and the cumulative oil production of the producing well are shown in Fig. 5.33A

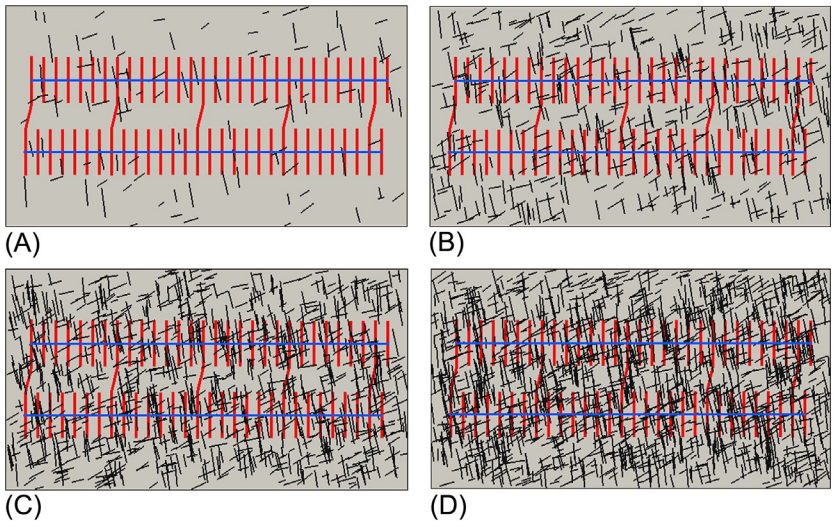

FIG. 5.32 Map view of different number of natural fractures inducing well interference (Yu et al., 2017b). (A) 100 natural fractures; (B) 500 natural fractures; (C) 1000 natural fractures; (D) 1500 natural fractures.

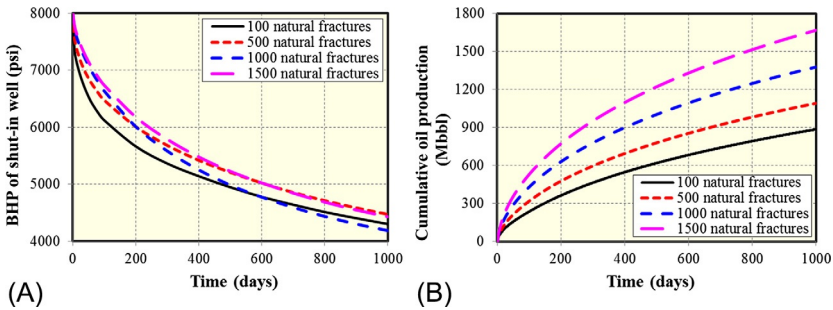

FIG. 5.33 Effect of number of natural fractures on pressure response of the shut-in well and cumulative oil production of the producing well (Yu et al., 2017b). (A) BHP of the shut-in well; (B) Cumulative oil production.

and B, respectively. The BHP of the shut-in well consistently decreases faster at early flow times when natural fracture density increases. However, the pressure decline rate is inconsistent at later times, which we attribute to detailed interference effects connected to natural fracture location and variations in degree of connectivity between natural fractures and hydraulic fractures. More efforts will be made in future studies to explain in detail why the change in pressure response varies over time when natural fractures and hydraulic fractures interfere. The cumulative oil production of the open well consistently increases when the natural fracture density increases (Fig. 5.33B). The reason is that overall drainage by fractures (both hydraulic and natural) is more effective for higher density of natural fractures.

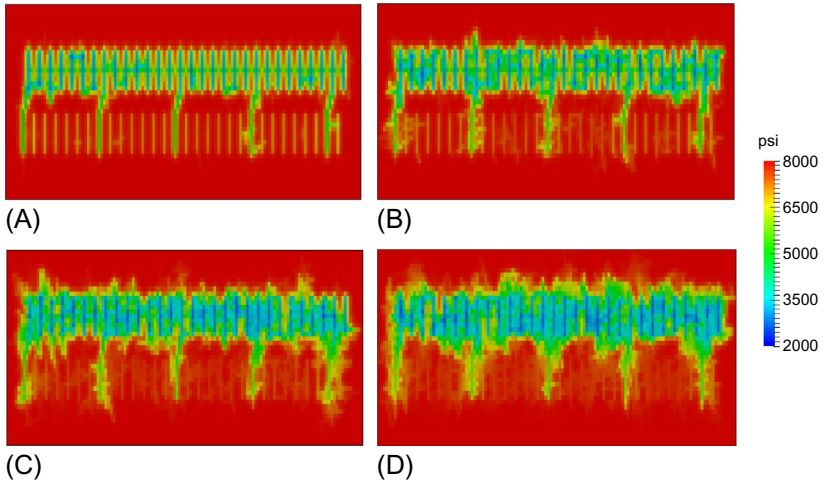

FIG. 5.34 Comparison of pressure distribution under different number of natural fractures after 100 days of production (Yu et al., 2017b). (A) 100 natural fractures; (B) 500 natural fractures; (C) 1000 natural fractures; (D) 1500 natural fractures.

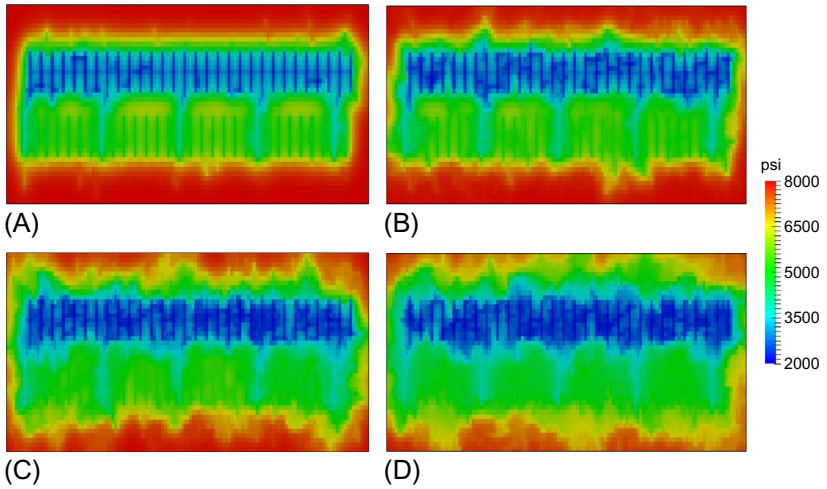

FIG. 5.35 Comparison of pressure distribution under different number of natural fractures after 1000 days of production (Yu et al., 2017b). (A) 100 natural fractures; (B) 500 natural fractures; (C) 1000 natural fractures; (D) 1500 natural fractures.

A comparison of pressure distributions after 100 days of production is shown in Fig. 5.34A–D for various densities of natural fractures. These results reveal that the drainage area of the producing well increases when the number of natural fractures increases. The more advanced pressure drawdown pattern after 1000 days of production is shown in Fig. 5.35. Even for such longer

production times, the drainage area of the producing well is consistently larger when natural fractures are more abundant.

5.9 WELL SHUT-IN TEST SIMULATION

In order to examine the different well interference intensity between the target well and its surrounding wells, we expanded the width of the basic reservoir model to 2850 ft, in order to accommodate three horizontal wells, as shown in Fig. 5.36. The distance between two neighboring wells is still 700 ft and each well has 30 nonplanar hydraulic fractures. Additionally, the model includes 2000 natural fractures and their parameter settings such as fracture length, angle, and height are similar as before. The simulation time is 100 days.

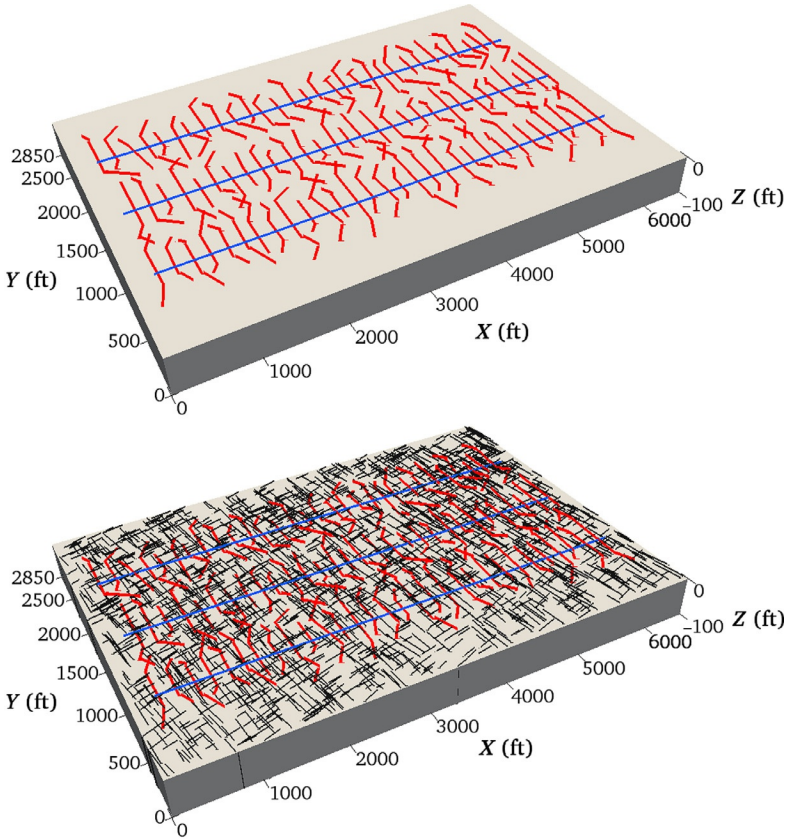

FIG. 5.36 The extended basic reservoir model including three horizontal wells, multiple nonplanar hydraulic fractures and natural fractures (Yu et al., 2017b). (A) Three horizontal wells with only 90 nonplanar hydraulic fractures; (B) Three horizontal wells with 90 nonplanar hydraulic fractures and 2000 natural fractures.

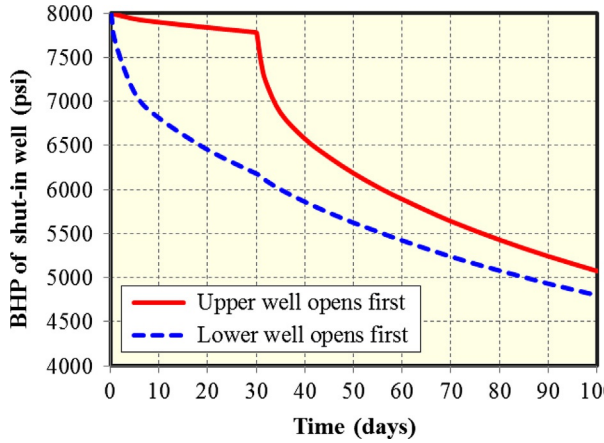

FIG. 5.37 Comparison of BHP decline behavior of the shut-in well for two different scenarios (Yu et al., 2017b).

The middle well is always shut-in. We designed two scenarios for the other two wells to identify well interference effects on well productivity. Scenario 1: the upper well first opens to produce for 1 month, then the lower well opens to produce. Scenario 2: the lower well first opens to produce for 1 month, then the upper well is also opened to produce.

Fig. 5.37 compares the BHP decline behavior for each of the two scenarios. For Scenario 1, the BHP of the shut-in well decreases slowly when the upper well opens first. However, the BHP rapidly declines when the lower well is also opened to produce after 30 days. The lower well has a much stronger well interference with the middle well than the upper well. For Scenario 2, the BHP of the shut-in well decreases quickly when the lower well opens first and there is a slower, but continuous decline after 30 days when the upper is additionally opened to produce. The upper well has a smaller well interference with the middle well as compared to the lower well. Hence, scenario 1 performs better than scenario 2 to identify the well interference intensity between the middle well with its neighboring wells. Fig. 5.38 compares the pressure distribution pattern of the two scenarios after 30 days prior to opening of the other well. The well interference between the middle well and lower well is larger than the well interference between the middle and the upper well.

5.10 WELL SPACING EFFECTS

5.10.1 All Wells Open

Next, we simulated the reservoir depletion effectiveness by varying well spacing in the study area from one well (Case 1) to 2 wells (Case 2) to 3 parallel horizontal wells (Case 3) (Fig. 5.39). The location and density of natural

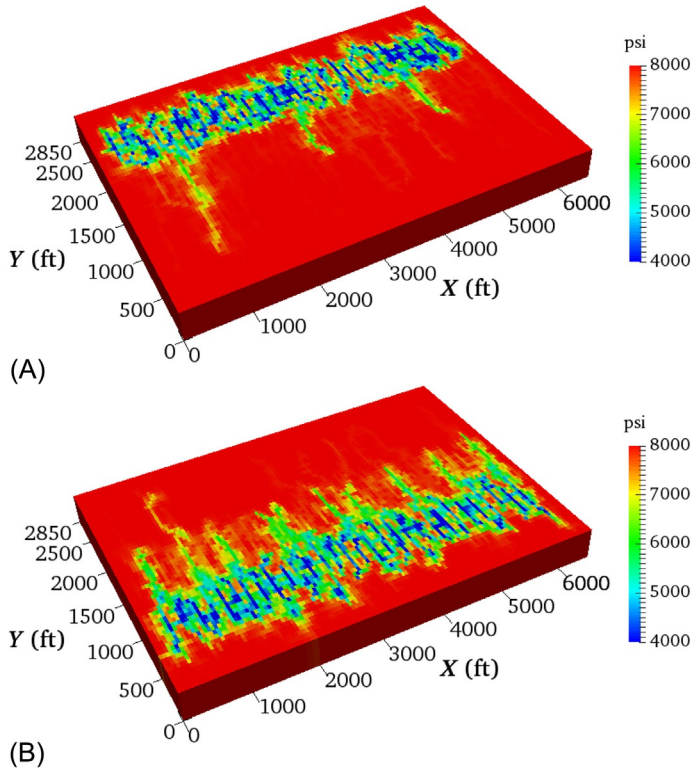

FIG. 5.38 Comparison of pressure distribution between two different scenarios after 100 days of production (Yu et al., 2017b). (A) Scenario 1; (B) Scenario 2.

fractures remains the same for each case. Fig. 5.40 presents a comparison of the cumulative oil and gas production for each of the three cases over a 30-year production period. Total production of the region after 30 years with one well is only 51% and with two wells 96% as compared to production from three wells. A full economic analysis to determine the optimal number of wells was needed. Fig. 5.41 shows the reservoir pressure distribution for each case after 1000 days of production, clearly illustrating that three wells drainage the reservoir much faster than both single well and two wells at early times.

5.10.2 Production With Some Wells Shut-in

For the case with three producing wells shown in Fig. 5.39C, we also plotted cumulative production if some wells are kept shut-in. Cumulative oil and gas production after 30 years are compared in Fig. 5.42. Production of the region with only the upper well open is only 66% as compared to production with all three wells open. Production with only the middle well or the lower well

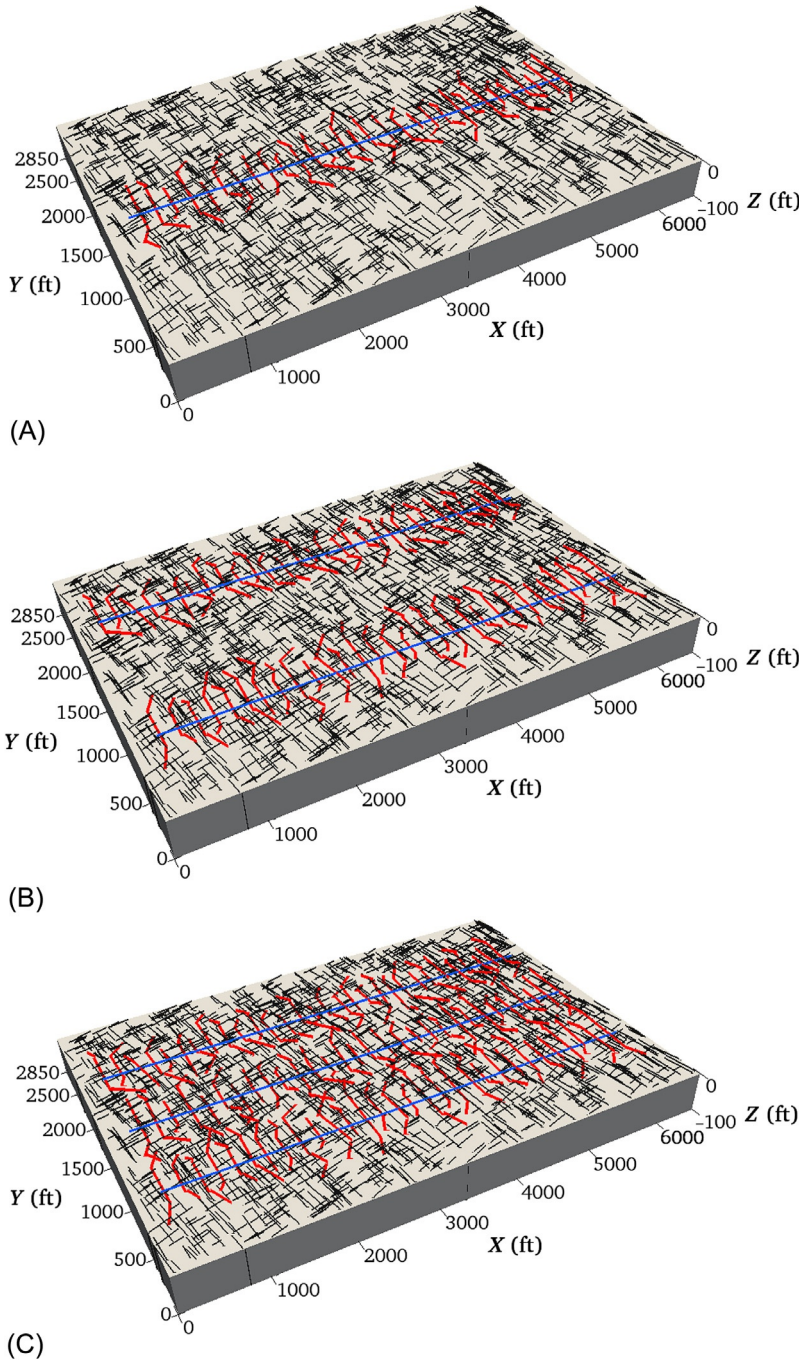

FIG. 5.39 Three cases with different number of horizontal wells (Yu et al., 2018b). (A) One well; (B) Two wells; (C) Three wells.

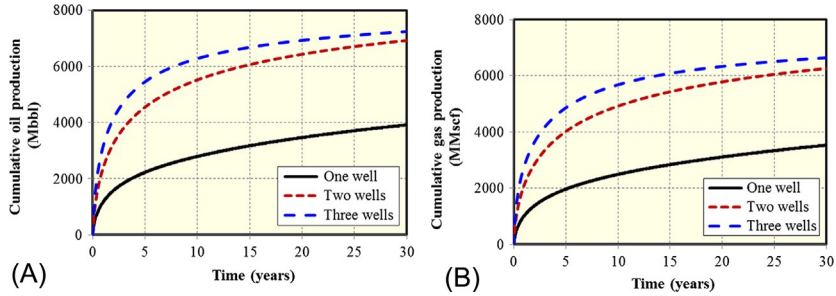

FIG. 5.40 Comparison of well performance between three cases with different well number at 30 years of production (Yu et al., 2017b). (A) Cumulative oil production; (B) Cumulative gas production.

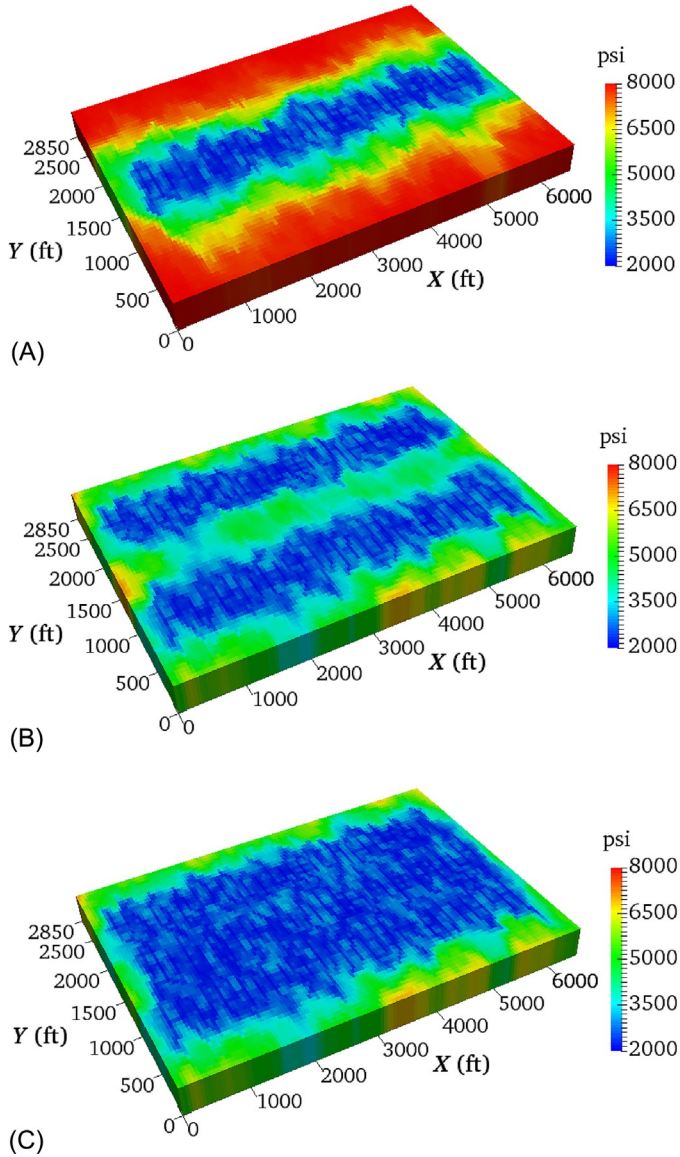

FIG. 5.41 Comparison of pressure distribution between three cases after 1000 days of production (Yu et al., 2017b). (A) One well; (B) Two wells; (C) Three wells.

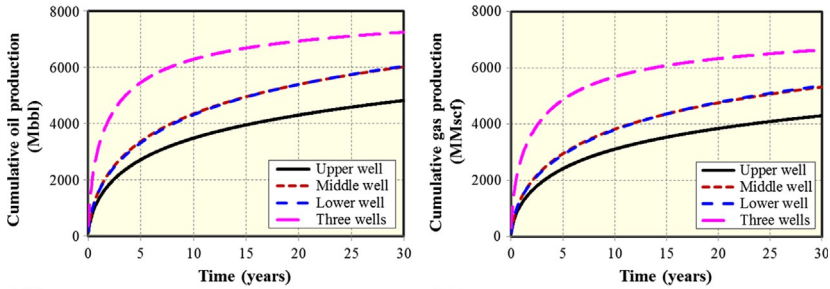

FIG. 5.42 Comparison of well performance between only opening one well while shutting in the other two wells and opening three wells at 30 years of production (Yu et al., 2017b).

produces about 83% as compared to production with all three wells open. The reason for better production performance by the lower wells again is that there is a stronger well-to-well connection between the middle well and the lower well. The pressure drawdown after 30 years of production (Fig. 5.43) shows reservoir depletion being the largest for production with all three wells open, and least with only the upper well open. Producing via either only the middle or only the lower well shows spatial depletion of the reservoir with similar areas.

5.11 DISCUSSION ABOUT WELL INTERFERENCE

It is important to mention that the impacts of natural fractures on well interference were less important than hydraulic fractures in the models of our current study because a small conductivity (1 md-ft) was assigned to natural fractures while a higher conductivity (100 md-ft) to hydraulic fractures. Results in the field may be different when naturally fractured reservoirs have higher fracture conductivities than assumed here. Future study will examine the impacts of propped and unpropped natural fractures, as well as natural and hydraulic fractures with varying fracture conductivities. Furthermore, pressure-dependent fracture conductivity and matrix permeability can be taken into account. In addition, it should be mentioned that the geomechanics effect related to stress changes and rock deformation plays an important role in production simulation of unconventional reservoirs, which has not been covered in the current numerical model and will be implemented in the future model development.

Note that a numerical compositional model is developed in this study to simulate well interference and well performance in tight-oil reservoirs. Although a black oil model is often used to handle multiphase flow in tight-oil reservoirs, the composition model has more other applications such as gas condensate shale/tight reservoirs and gas injection for enhanced oil recovery in shale/tight-oil reservoirs. Hence, the developed numerical compositional model

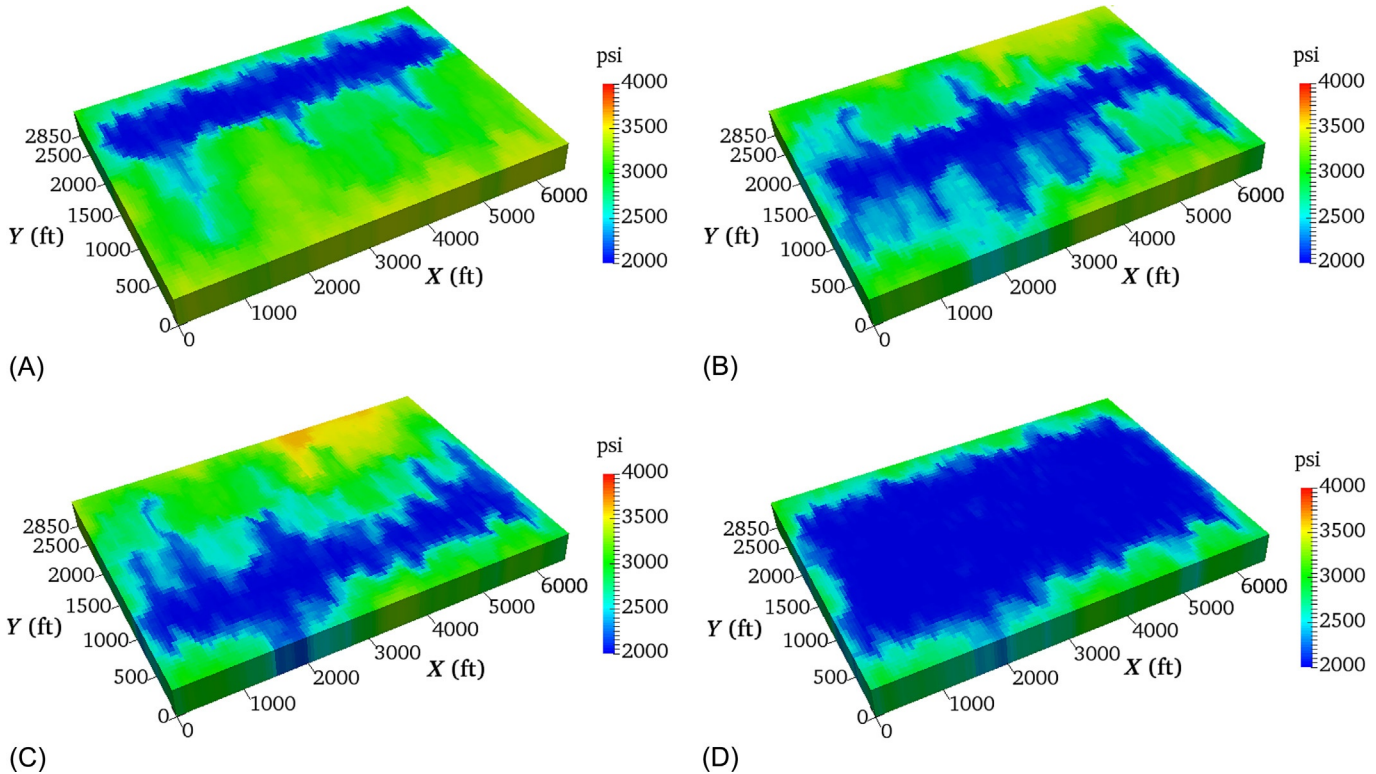

FIG. 5.43 Comparison of pressure distribution between four cases after 30 years of production (Yu et al., 2017b). (A) Only opening upper well; (B) Only opening middle well; (C) Only opening lower well; (D) Opening all three wells.

can handle well interference in gas condensate reservoirs. Furthermore, the compositional effects on dynamic behavior of the transient pressure of the shut-in well will be explored in the future work.

REFERENCES

Abass, H.H., Hedayati, S., Meadows, D.L., 1996. Nonplanar fracture propagation from a horizontal wellbore: experimental study. SPE Prod. Facil. 11 (3), 133–137.

Ajani, A., Kelkar, M., 2012. Interference study in shale plays. Paper SPE 151045, SPE Hydraulic Fracturing Technology Conference, The Woodlands, Texas.

Akkutlu, I.Y., Fathi, E., 2012. Multi-scale gas transport in shales with local kerogen heterogeneities. SPE J. 17 (4), 1002–1011.

Alramahi, B., Sundberg, M.I., 2012. Proppant embedment and conductivity of hydraulic fractures in shales. Paper ARMA 2012–291, 46th US Rock Mechanics/Geomechanics Symposium, Chicago, Illinois.

An, C., Fang, Y., Liu, S., Alfi, M., Yan, B., Wang, Y., Killough, J., 2017. Impacts of matrix shrinkage and stress changes on permeability and gas production of organic-rich shale reservoirs. Paper SPE 186029, SPE Reservoir Characterization and Simulation Conference and Exhibition, Abu Dhabi, UAE.

Awada, A., Santo, M., Lougheed, D., 2016. Is that interference? A work flow for identifying and analyzing communication through hydraulic fractures in a multi-well pad. SPE J. 21 (5), 1554–1566.

Brunauer, S., Emmett, P.H., Teller, E., 1938. Adsorption of gases in multimolecular layers. J. Am. Chem. Soc. 60, 309–319.

Cavalcante Filho, J.S.A., Shakiba, M., Moinfar, A., Sepehrnoori, K., 2015. Implementation of a preprocessor for embedded discrete fracture modeling in an IMPEC compositional reservoir simulator. Paper SPE 173289, SPE Reservoir Simulation Symposium, Houston, Texas.

Chang, Y., 1990. Development of a three-Dimensional, Equation-of-State Compositional Reservoir Simulator for Miscible Gas Flooding. PhD Dissertation, The University of Texas at Austin.

Chen, C.C., Raghavan, R., 1997. A multiply-fractured horizontal well in a rectangular drainage region. SPE J. 2 (4), 455–465.

Chen, Z., Liao, X., Zhao, X., Lyu, S., Zhu, L., 2017. A comprehensive productivity equation for multiple fractured vertical wells with non-linear effects under steady-state flow. J. Pet. Sci. Eng. 149, 9–24.

Chu, L., Ye, P., Harmawan, I.S., Du, L., Shepard, L.R., 2012. Characterizing and simulating the nonstationariness and nonlinearity in unconventional oil reservoirs: Bakken application. Paper SPE 161137, SPE Canadian Unconventional Resources Conference, Calgary, Alberta, Canada.

Cipolla, C.L., Wallace, J., 2014. Stimulated reservoir volume: a misapplied concept? Paper SPE 168596, SPE Hydraulic Fracturing Technology Conference, The Woodlands, Texas.

Cipolla, C.L., Lolon, E.P., Erdle, J.C., Rubin, B., 2010. Reservoir modeling in shale-gas reservoirs. SPE Reserv. Eval. Eng. 13 (4), 638–653.

Civan, F., 2010. Effective correlation of apparent gas permeability in tight porous media. Transp. Porous Media 82 (2), 375–384.

Civan, F., Rai, C.S., Sondergeld, C.H., 2011. Shale-gas permeability and diffusivity inferred by improved formulation of relevant retention and transport mechanisms. Transp. Porous Media 86 (3), 925–944.

Clarkson, C.R., Bustin, R.M., Levy, J.H., 1997. Application of the monolayer/multilayer and adsorption potential theories to coal methane adsorption isotherms at elevated temperature and pressure. Carbon 35 (12), 1689–1705.

CMG-GEM, 2012. GEM User's Guide. Computer Modeling Group Ltd.

Dershowitz, B., LaPointe, P., Eiben, T., Wei, L., 1998. Integration of discrete feature network methods with conventional simulator approaches. Paper SPE 49069, SPE Annual Technical Conference and Exhibition, New Orleans, Louisiana.

Du, S., Yoshida, N., Liang, B., Chen, J., 2016. Application of multi-segment well approach: dynamic modeling of hydraulic fractures. J. Nat. Gas Sci. Eng. 34, 886–897.

Edwards, D.A., Cheng, N., Dombrowsky, T.P., Bowen, G., Nasvik, H., 2013. Representing hydraulic fractures using a multilateral, multisegment well in simulation models. Paper SPE 163644, SPE Reservoir Simulation Symposium, The Woodlands, Texas.

Evans, R.D., Civan, F., 1994. Characterization of non-Darcy multiphase flow in petroleum bearing formations. Report, U.S. DOE Contract No. DE-AC22-90BC14659. School of Petroleum and Geological Engineering, University of Oklahoma.

Fan, L., Thompson, J.W., Robinson, J.R., 2010. Understanding gas production mechanism and effectiveness of well stimulation in the haynesville shale through reservoir simulation. Paper SPE 136696, Canadian Unconventional Resources and International Petroleum Conference, Calgary, Canada.

Florence, F.A., Rushing, J., Newsham, K.E., Blasingame, T.A., 2007. Improved permeability prediction relations for low permeability sands. Paper SPE 107954, SPE Rocky Mountain Oil & Gas Technology Symposium, Denver, Colorado.

Fung, L.S.K., Du, S., 2016. Parallel-simulator framework for multipermeability modeling with discrete fractures for unconventional and tight gas reservoirs. SPE J. 21 (4), 1370–1385.

Hao, S., Chu, W., Jiang, Q., Yu, X., 2014. Methane adsorption characteristics on coal surface above critical temperature through Dubinin-Astakhov model and Langmuir model. Colloids Surf. A Physicochem. Eng. Asp. 444, 104–113.

Heidemann, R.A., Jeje, A.A., Mohtadi, F., 1984. An Introduction to the Properties of Fluids and Solids. Canada, University of Calgary Press, Calgary.

Hui, M.H., Mallison, B.T., Fyrozjaee, M.H., Narr, W., 2013. The upscaling of discrete fracture models for faster, coarse-scale simulations of IOR and EOR processes for fractured reservoirs. Paper SPE 166075, SPE Annual Technical Conference and Exhibition, New Orleans, Louisiana.

Javadpour, F., Fisher, D., Unsworth, M., 2007. Nanoscale gas flow in shale gas sediments. J. Can. Pet. Technol. 46 (10), 55–61.

Jones, S.C., 1988. Two-point determinations of permeability and PV vs. net confining stress. SPE Form. Eval. 3 (1), 235–241.

Karniadakis, G.E., Beskok, A., 2002. Micro-Flows, Fundamentals and Simulation. Spriger-Verlag, New York.

King, G.E., Valencia, R.L., 2016. Well integrity for fracturing and re-fracturing: what is needed and why? Paper SPE 179120, SPE Hydraulic Fracturing Technology Conference, The Woodlands, Texas.

Kurtoglu, B., Salman, A., 2015. How to utilize hydraulic fracture interference to improve unconventional development. Paper SPE 177953, International Petroleum Exhibition and Conference, Abu Dhabi, UAE.

LaFollette, R.F., Carman, P.S., 2010. Proppant diagenesis: results so far. Paper SPE 131782, SPE Unconventional Gas Conference, Pittsburgh, Pennsylvania.

Lake, L.W., 1989. Enhanced Oil Recovery. Prentice Hall, Englewood Cliffs, New Jersey.

Langmuir, I., 1918. The adsorption of gases on plane surfaces of glass, mica and platinum. J. Am. Chem. Soc. 40, 1403–1461.

Lawal, H., Jackson, G., Abolo, N., Flores, C., 2013. A novel approach to modeling and forecasting frac hits in shale gas wells. Paper SPE 164898, EAGE Annual Conference & Exhibition, London, United Kingdom.

Li, X., Zhang, D., Li, S., 2015. A multi-continuum multiple flow mechanism simulator for unconventional oil and gas recovery. J. Nat. Gas Sci. Eng. 26, 652–669.

Lindner, P., Bello, H., 2015. Eagle Ford well spacing: a methodology to integrate, analyze, and visualize multisource data in solving a complex value-fouced problem. Paper URTeC 2174709, Unconventional Resources Technology Conference, San Antonio, Texas.

Lohrenz, J., Bray, B.G., Clark, C.R., 1964. Calculating viscosities of reservoir fluids from their compositions. J. Pet. Technol. 16 (10), 1171–1176.

Malpani, R., Sinha, S., Charry, L., Sinosic, B., Clark, B., Gakhar, K., 2015. Improving hydrocarbon recovery of horizontal shale wells through refracturing. Paper SPE 175920, SPE/CSUR Unconventional Resources Conference, Calgary, Alberta, Canada.

Marongiu-Porcu, M., Lee, D., Shan, D., Morales, A., 2016. Advanced modeling of interwell-fracturing interference: an Eagle Ford shale-oil study. SPE J. 21 (5), 1567–1582.

Mehra, R.K., Heidemann, R.A., Aziz, K., 1983. An accelerated successive substitution algorithm. Can. J. Chem. Eng. 61 (4), 590–596.

Mirzaei, M., Cipolla, C.L., 2012. A workflow for modeling and simulation of hydraulic fractures in unconventional gas reservoirs. Paper SPE 153022, SPE Middle East Unconventional Gas Conference and Exhibition, Abu Dhabi, UAE.

Moinfar, A., Varavei, A., Sepehrnoori, K., Johns, R.T., 2014. Development of an efficient embedded discrete fracture model for 3D compositional reservoir simulation in fractured reservoirs. SPE J. 19 (2), 289–303.

NIST, 2011. Thermophysical properties of fluid systems. http://webbook.nist.gov/chemistry/fluid/.

Olson, J.E., Wu, K., 2012. Sequential versus simultaneous multi-zone fracturing in horizontal wells: insights from a non-planar, multi-frac numerical model. Paper SPE 152602, SPE Hydraulic Fracturing Technology Conference, The Woodlands, Texas.

Orangi, A., Nagarajan, N.R., Hanapour, M.M., Rosenzweig, J., 2011. Unconventional shale oil and gas-condensate reservoir production, impact of rock, fluid, and hydraulic fractures. Paper SPE 140536, SPE Hydraulic Fracturing Technology Conference and Exhibition, The Woodlands, Texas.

Ozdemir, E., 2004. Chemistry of the Adsorption of Carbon Dioxide by Argonne Permium Coals and a Model to Simulate CO2 Sequestration in Coal Seams. PhD Dissertation, University of Pittsburgh.

Peng, D.Y., Robinson, D.B., 1976. A new two-constant equation of state. Ind. Eng. Chem. Fundam. 15, 59–64.

Perschke, D.R., Chang, Y., Pope, G.A., Sepehrnoori, K., 1989. Comparison of phase behavior algorithms for an equation-of-state compositional simulator. Paper SPE 19443.

Portis, D.H., Bello, H., Murray, M., Barzola, G., Clarke, P., Canan, K., 2013. Searching for the optimal well spacing in the Eagle Ford shale: a practical tool-kit. Paper SPE 168810, Unconventional Resources Technology Conference, Denver, Colorado.

Riewchotisakul, S., Akkutlu, I.Y., 2015. Adsorption enhanced transport of hydrocarbons in organic nanopores. Paper SPE 175107, SPE Annual Technical Conference and Exhibition, Houston, Texas.

Rubin, B., 2010. Accurate simulation of non-Darcy flow in stimulated fractured shale reservoirs. Paper SPE 132093, SPE Western Regional Meeting, Anaheim, California.

Sakhaee-Pour, A., Bryant, S.L., 2012. Gas permeability of shale. SPE Reserv. Eval. Eng. 15 (4), 401–409.

Sandve, T.H., Berre, I., Nordbotten, J.M., 2012. An efficient multi-point flux approximation method for discrete fracture-matrix simulations. J. Comput. Phys. 231 (9), 3784–3800.

Sani, A.M., Podhoretz, S.B., Chambers, B.D., 2015. The use of completion diagnostics in Haynesville shale horizontal wells to monitor fracture propagation, well communication, and production impact. Paper SPE 175917, SPE/CSUR Unconventional Resources Conference, Calgary, Alberta, Canada.

Sardinha, C., Petr, C., Lehmann, J., Pyecroft, J., 2014. Determining interwell connectivity and reservoir complexity through frac pressure hits and production interference analysis. Paper SPE 171628, SPE/CSUR Unconventional Resources Conference, Calgary, Alberta, Canada.

Scott, K.D., Chu, W.C., Flumerfelt, R.W., 2015. Application of real-time bottom-hole pressure to improve field development strategies in the Midland basin Wolfcamp shale. Paper URTeC 2154675, Unconventional Resources Technology Conference, San Antonio, Texas.

Shakiba, M., Sepehrnoori, K., 2015. Using embedded discrete fracture model (EDFM) and microseismic monitoring data to characterize the complex hydraulic fracture networks. Paper SPE 175142, SPE Annual Technical Conference and Exhibition, Houston, Texas.

Simpson, M.D., Patterson, R., Wu, K., 2016. Study of stress shadow effects in Eagle Ford shale: insight from field data analysis. Paper ARMA 2016-190, 50th U.S. Rock Mechanics/Geomechanics Symposium, Houston, Texas.

Sun, H., Chawathe, A., Hoteit, H., Shi, X., Li, L., 2015. Understanding shale gas flow behavior using numerical simulation. SPE J. 20 (1), 142–154.

U.S. Energy Information Administration, 2016. Shale gas production drives world natural gas production growth. http://www.eia.gov/todayinenergy/detail.cfm?id=27512.

Wang, F.P., Reed, R.M., 2009. Pore networks and fluid flow in gas shales. Paper SPE 124253, SPE Annual Technical Conference and Exhibition, New Orleans, Louisiana.

Wang, W., Yu, W., Hu, X., Liu, H., Chen, Y., Wu, K., Wu, B., 2018. A semianalytical model for simulating real gas transport in nanopores and complex fractures of shale gas reservoirs. AIChE J 64 (1), 326–337.

Warpinski, N.R., Kramm, R.C., Heinze, J.R., Waltman, C.K., 2005. Comparison of single and dual-array microseismic mapping techniques in the Barnett shale. Paper SPE 95568, SPE Annual Technical Conference and Exhibition, Dallas, Texas.

Warren, J.E., Root, P.J., 1963. The behavior of naturally fractured reservoirs. SPE J. 3 (3), 245–255.

Weijers, L., de Pater, C.J., 1992. Fracture reorientation in model tests. Paper SPE 23790, SPE Formation Damage Control Symposium, Lafayette, Louisiana, 1992.

Wu, K., Olson, J.E., 2013. Investigation of the impact of fracture spacing and fluid properties for interfering simultaneously or sequentially generated hydraulic fractures. SPE Prod. Oper. 28 (4), 427–436.

Wu, K., Olson, J.E., 2015. Simultaneous multifracture treatments: fully coupled fluid flow and fracture mechanics for horizontal wells. SPE J. 20 (2), 337–346.

Wu, K., Olson, J.E., 2016. Numerical investigation of complex fracture networks in naturally fractured reservoirs. SPE Prod. Oper. 31 (4), 300–309.

Wu, R., Kresse, O., Weng, X., Cohen, C., Gu, H., 2012. Modeling of interaction of hydraulic fractures in complex fracture networks. Paper SPE 152052, SPE Hydraulic Fracture Technology Conference, The Woodlands, Texas.

Wu, Y.S., Li, J., Ding, D., Wang, C., Di, Y., 2014. A generalized framework model for the simulation of gas production in unconventional gas reservoirs. SPE J. 19 (5), 845–857.

Wu, K., Li, X., Wang, C., Yu, W., Chen, Z., 2015. Model for surface diffusion of adsorbed gas in nanopores of shale gas reservoirs. Ind. Eng. Chem. Res. 54 (12), 3225–3236.

Wu, K., Chen, Z., Li, J., Li, X., Xu, J., Dong, X., 2017. Wettability effect on nanoconfined water flow. PNAS 114 (13), 3358–3363.

Xu, Y., 2015. Implementation and Application of the Embedded Discrete Fracture Model (EDFM) for Reservoir Simulation in Fractured Reservoirs. Master Thesis, The University of Texas at Austin, Austin, Texas.

Xu, G., Wong, S.W., 2013. Interaction of multiple non-planar hydraulic fractures in horizontal wells. Paper IPTC 17043, International Petroleum Technology Conference, Beijing, China.

Xu, Y., Cavalcante Filho, J.S.A., Yu, W., Sepehrnoori, K., 2017a. Discrete-fracture modeling of complex hydraulic-fracture geometries in reservoir simulators. SPE Reserv. Eval. Eng. 20 (2), 403–422.

Xu, Y., Yu, W., Sepehrnoori, K., 2017b. Modeling dynamic behaviors of complex fractures in conventional reservoir simulators. Paper URTeC 2670513, SPE/AAPG/SEG Unconventional Resources Technology Conference, Austin, Texas.

Yaich, E., Diaz de Souza, O.C., Foster, R.A., 2014. A methodology to quantify the impact of well interference and optimize well spacing in the Marcellus shale. Paper SPE 171578, SPE/CSUR Unconventional Resources Conference, Calgary, Alberta, Canada.

Yang, R., Huang, Z., Yu, W., Li, G., Ren, W., Zuo, L., Tan, X., Sepehrnoori, K., Tian, S., Sheng, M., 2016. A comprehensive model for real gas transport in shale formations with complex non-planar fracture networks. Sci. Rep. 6.

Yu, W., Sepehrnoori, K., 2014a. Simulation of gas desorption and geomechanics effects for unconventional gas reservoirs. Fuel 116, 455–464.

Yu, W., Sepehrnoori, K., 2014b. Optimization of well spacing for Bakken tight oil reservoirs. Paper URTeC 1922108, SPE/AAPG/SEG Unconventional Resources Technology Conference, Denver, Colorado.

Yu, W., Sepehrnoori, K., Patzek, T.W., 2016a. Modeling gas adsorption in Marcellus shale with Langmuir and BET isotherms. SPE J. 21 (2), 589–600.

Yu, W., Wu, K., Sepehrnoori, K., 2016b. A semianalytical model for production simulation from nonplanar hydraulic-fracture geometry in tight oil reservoirs. SPE J. 21 (3), 1028–1040.

Yu, W., Wu, K., Zuo, L., Tan, X., Weijermars, R., 2016c. Physical models for inter-well interference in shale reservoirs: relative impacts of fracture hits and matrix permeability. Paper URTeC 2457663, Unconventional Resources Technology Conference, San Antonio, Texas.

Yu, W., Wu, K., Sepehrnoori, K., Xu, W., 2017a. A comprehensive model for simulation of gas transport in shale formation with complex hydraulic-fracture geometry. SPE Reserv. Eval. Eng. 20 (3), 547–561.

Yu, W., Xu, Y., Weijermars, R., Wu, K., Sepehrnoori, K., 2017b. Impact of well interference on shale oil production performance: a numerical model for analyzing pressure response of fracture hits with complex geometries. Paper SPE 184825, SPE Hydraulic Fracturing Technology Conference and Exhibition, The Woodlands, Texas.

Yu, W., Xu, Y., Liu, M., Wu, K., Sepehrnoori, K., 2018a. Simulation of shale gas transport and production with complex fractures using embedded discrete fracture model. AIChE J 64 (6), 2251–2264.

Yu, W., Xu, Y., Weijermars, R., Wu, K., Sepehrnoori, K., 2018b. A numerical model for simulating pressure response of well interference and well performance in tight oil reservoirs with complex-fracture geometries using the fast embedded-discrete-fracture-model method. SPE Reserv. Eval. Eng. 21 (2), 489–502.

Zhang, Y., Yu, W., Sepehrnoori, K., Di, Y., 2017a. A comprehensive numerical model for simulating fluid transport in nanopores. Sci. Rep. 7.

Zhang, Y., Di, Y., Yu, W., Sepehrnoori, K., 2017b. A comprehensive model for investigation of CO2-EOR with nanopore confinement in the Bakken tight oil reservoir. Paper SPE 187211, SPE Annual Technical Conference and Exhibition, San Antonio, Texas.

Zhou, W., Banerjee, R., Poe, B.D., Spath, J., Thambynayagam, M., 2013. Semi-analytical production simulation of complex hydraulic-fracture networks. SPE J. 19 (1), 6–18.

Zuloaga-Molero, P., Yu, W., Xu, Y., Sepehrnoori, K., Li, B., 2016. Simulation study of CO2-EOR in tight oil reservoirs with complex fracture geometries. Sci. Rep. 6.

Chapter 6

An Integrated Framework for Sensitivity Analysis and Economic Optimization in Shale Reservoirs

Chapter Outline

6.1 INTRODUCTION

The combination of horizontal drilling and multistage fracturing technology has made possible the current flourishing gas and oil production from shale reservoirs in the United States, as well as the global fast growing investment in shale gas and tight oil exploration and development. However, there are high uncertainties in reservoir and fracture properties, which have significant effects on

Shale Gas and Tight Oil Reservoir Simulation. https://doi.org/10.1016/B978-0-12-813868-7.00006-7

well performance and economics. In reality, the ultralow permeability of shale ranges from 10 to 100 nano-Darcy. The operation cost of drilling and multistage fracturing is high, although it can make production from shale reservoirs that were previously recognized as caprock feasible economically. The optimization of hydraulic fracture parameters (e.g., number of fracture, fracture spacing, fracture half-length, and fracture conductivity) and well spacing is important to obtain the most economical scenario. In addition, with the development of unconventional resources, a large number of wells have been drilled and need to be evaluated efficiently. Therefore, the development of a method to quantify uncertainties, perform history matching, and optimize production in an efficient and practical manner is clearly desirable.

There have been a significant number of attempts in recent years to optimize the design of transverse fractures of horizontal wells for shale gas reservoirs (Britt and Smith, 2009; Marongiu-Porcu et al., 2009; Zhang et al., 2009; Bagherian et al., 2010; Meyer et al., 2010; Bhattacharya and Nikolaou, 2011; Gorucu and Ertekin, 2011). In most of the reviewed works, the optimum fracture design is identified by local sensitivity analysis and one variable is usually varied while keeping all the other variables fixed. These optimization methods do not provide sufficient insights for screening insignificant parameters and considering parameter interactions to obtain the optimal design. Additionally, most reservoir modeling works in the literature have ignored the combined impact of gas desorption and geomechanics on ultimate gas and oil recovery. If the factors playing an important role in shale gas and tight oil production are unknown, it is obviously important to perform a screening design to identify which factors are significant. Different approaches such as design of experiment (DoE) and response surface methodology (RSM) have been used to address the uncertainties (Damsleth et al., 1992; Dejean and Blanc, 1999). RSM is an efficient statistical method for evaluation and optimization of complex processes. Therefore, in this study, we developed an integrated reservoir simulation framework by combining numerical reservoir simulators, the semianalytical model developed in Chapter 3, an economic model, DoE and RSM with an efficient platform of ISPUR (integrated simulation platform for unconventional reservoirs) to perform a large number of reservoir simulation scenarios in order to optimize fracture design and multiple well placement for the economic development of shale gas and tight oil reservoirs.

6.2 DESIGN OF EXPERIMENT

DoE is a systematic method used to determine the relationship between uncertain factors affecting a process and the response of that process. It can be used to evaluate statistically the significance of different factors at the lowest experimental costs (Zhang et al., 2007).

Factorial designs are widely used in DoE to study several uncertain factors with the purpose of identifying both main effects and interactions. Two-level

factorial design is a special case of factorial designs in which each factor is only given two values to determine the range: the minimum value and the maximum value. The design for k factors requires 2^k experimental runs. Therefore, it is called 2^k factorial design (Myers et al., 2008). It can investigate not only the effect from a single parameter but also the effect from the interaction of parameters, compared with the traditional sensitivity analysis method such as changing one variable at a time.

When there are many factors involved, the full factorial design is not applicable in practice because an extensive number of factor combinations are required to be investigated. For example, 10 factors require 2^{10} (1024) combinations to be investigated. However, this problem can be solved by using the two-level fractional factorial design, which can offer fewer numbers of scenarios. For example, one-half fractional factorial design, called 2^{k-1} fractional factorial design, would reduce by half the total number of cases required for the 2^k design. The selection of two-level fractional factorial design with a minimum number of cases is primarily based on the smallest effect from aliasing (Peng and Gupta, 2003) and the highest possible resolution (Myers et al., 2008).

6.3 RESPONSE SURFACE METHODOLOGY

RSM is a group of statistical and mathematical techniques, which is used to optimize processes. It can generate an empirical model from observed data of the system to approximately represent the true response surface of the objective function over a region of interest specified by the range of variability of input factors. Net present value (NPV) is often used as the objective function to perform economic analysis of shale gas and tight oil wells. The generated empirical model can be represented in a form of the linear regression model as follows:

$$y = \beta_o + \beta_1 x_1 + \beta_2 x_2 + \cdots + \beta_k x_k + \varepsilon, \tag{6.1}$$

where y is the objective function, x_i, $i = 1, 2, \ldots, k$, are uncertain variables, β_i, $i = 0, 1, 2, \ldots, k$, are regression coefficients, k is the number of uncertain variables investigated and optimized in the study, and ε is the error term. This equation is called a multiple linear regression model with k regressors. It can also be modified by adding an interaction term as shown here:

$$y = \beta_o + \beta_1 x_1 + \beta_2 x_2 + \cdots + \beta_k x_k + \sum_{i<j}\sum_{=2}^{k} \beta_{ij} x_i x_j + \varepsilon. \tag{6.2}$$

Or it can be modified to form the second-degree polynomial equation as follows:

$$y = \beta_o + \beta_1 x_1 + \beta_2 x_2 + \cdots + \beta_k x_k + \sum_{i<j}\sum_{=2}^{k} \beta_{ij} x_i x_j + \sum_{i=1}^{k} \beta_{ii} {x_i}^2 + \varepsilon. \tag{6.3}$$

Two popular designs, central composite design (CCD) and D-optimal design, are often used to fit the second-degree surface model. More detailed mathematical and statistical theories of CCD and D-optimal design can be found in the work by Myers et al. (2008).

6.4 ECONOMIC MODEL

NPV is one of the most common methods used to evaluate the economic viability of investing in a project. The NPVs of shale gas and tight oil wells are calculated by use of the following expression:

$$NPV = \sum_{j=1}^{n} \frac{(V_F)_j}{(1+i)^j} - \sum_{j=1}^{n} \frac{(V_O)_j}{(1+i)^j} - \left[FC + \sum_{k=1}^{N} \left(C_{well} + C_{fracture} \right) \right], \tag{6.4}$$

where V_F is future value of production revenue for a fractured shale reservoir, V_o is future value of production revenue for an unfractured shale reservoir, FC is the total fixed cost, C_{well} is the cost of a single horizontal well, $C_{fracture}$ is the cost of hydraulic fracturing in a single horizontal well, N is the number of horizontal wells, i is the interest rate, and n is the number of periods.

6.5 INTEGRATED RESERVOIR SIMULATION FRAMEWORK

We present an integrated reservoir simulation framework for optimization of shale gas and tight oil production, as shown in Fig. 6.1. The framework combines numerical reservoir simulators, the semianalytical model, an economic model, DoE, and RSM to optimize hydraulic fracture treatment design for the economic development of shale gas and tight oil reservoirs. An efficient platform of ISPUR is developed to make this framework perform sensitivity studies, history matching, and economic optimization more effectively and more efficiently. In addition, this framework can be applied to investigate gas injection for enhanced oil recovery (EOR) in tight oil reservoirs and enhanced gas recovery (EGR) in shale gas reservoirs.

6.5.1 Reservoir Modeling Including Multiple Fractures

In this framework, four fracture geometries can be handled during building a reservoir model for shale gas and tight oil reservoirs. They are biwing fractures, orthogonal fracture networks, unstructured fracture networks, and nonplanar fractures. In addition, a three-dimensional fracture propagation model developed by Wu and Olson (2015), which fully couples elastic deformation of the rock and fluid flow to simulate complex hydraulic fracture propagation, is used to predict the nonplanar fractures, which are input into the reservoir models to simulate production from such fractures. Three numerical reservoir simulators including CMG (Computer Modeling Group Ltd., 2012), ECLIPSE

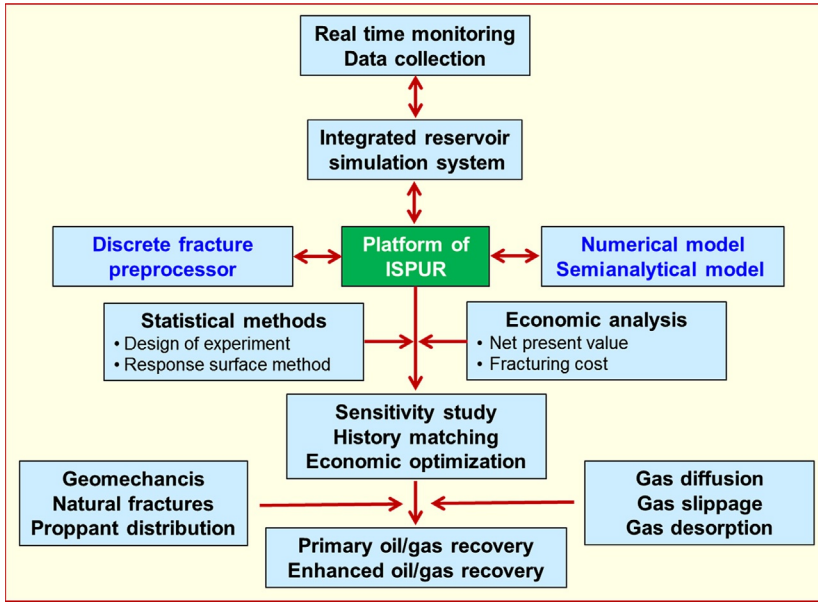

FIG. 6.1 An integrated simulation framework for the economic development of shale gas and tight oil reservoirs (Yu, 2015).

(Schlumberger, 2012), and UTCOMP (The University of Texas at Austin, 2014), and the semianalytical model developed in Chapter 3 are used to build reservoir model including multiple hydraulic fractures.

For shale gas simulation, the important gas transport mechanisms such as gas slippage, gas diffusion, and gas desorption can be simulated using the semi-analytical model. In addition, for gas flow in the fracture, the key effects of non-Darcy flow and geomechanics (pressure-dependent fracture conductivity) can be taken into account.

6.5.2 Sensitivity Study and Economic Optimization

A commercial software package of Design-Expert (Stat-Ease Incorporated, 2014) has been integrated in the framework to prepare multiple combinations based on investigated uncertain parameters, which are required by DoE and RSM. Also, it can be used for further results manipulation and graphical presentations. For sensitivity studies, the rank of important parameters and nonsignificant parameters can be quantified. For optimization, a response surface model describing the relationship between the objective function and important design variables can be obtained. Finally, the best case based on the response surface model can be determined.

A package based on Microsoft Excel is designed and has been implemented in this framework to calculate NPV using Eq. (6.4). The inputs mainly include gas price, oil price, well cost, well number, fracture cost, total fixed cost, interest rate, tax, cumulative gas production, and cumulative oil production. The fracture cost is related to fracture number, fracture area, and fracture conductivity. Fracture area is linked to liquid volume pumped and fracture conductivity is linked to proppant amount usage.

6.6 INTEGRATED SIMULATION PLATFORM FOR UNCONVENTIONAL RESERVOIRS

The approach of local grid refinement is often used to model hydraulic fractures and fracture networks, resulting in a complex gridding issue to prepare input files for reservoir simulators. In addition, a large number of simulation cases are required, based on two statistical methods of DoE and RSE to perform sensitivity studies, history matching, and economic optimization. If these input files are prepared manually, it will be very time consuming. Hence, an automated platform for simulation of unconventional reservoirs is necessary. In 2005, Zhang developed an integrated reservoir simulation platform (UT_IRSP) to prepare multiple reservoir simulation studies using different methodologies for the design and optimization of chemical flooding processes (Zhang, 2005). However, UT_IRSP is not designed for unconventional reservoirs with multiple hydraulic fractures. Consequently, in this work, we developed a new platform by borrowing the design principle of UT_IRSP, which is an ISPUR, to generate a large number of input files for reservoir simulators more easily and more efficiently, as shown in Fig. 6.2.

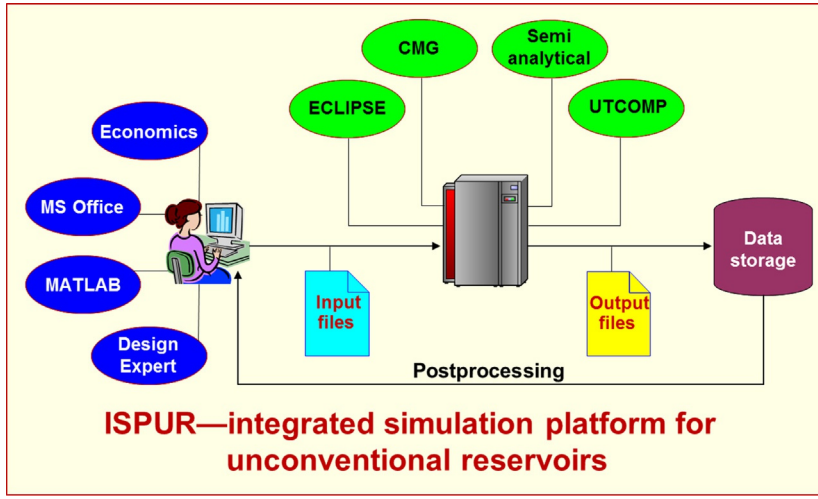

FIG. 6.2 An integrated simulation platform for unconventional reservoirs (ISPUR) (Yu, 2015).

Before launching ISPUR, the main program requires the user to provide the name of reservoir simulator, the name of excel file for multiple cases, the number of uncertain parameters, the name of uncertain parameters, and the base case. After providing these requirements, the ISPUR will generate multiple cases automatically. Subsequently, ISPUR will call the executable files of different simulators to run these simulation cases automatically in a sequential mode (one simulation at a time) or a distributed mode (multiple simulations at a time). After finishing all simulation cases, the output files will be saved in different folders, which are named, based on the simulation case number. Fig. 6.3 shows one example of illustrating the workflow of using ISPUR to prepare and run 100 different simulation cases.

6.6.1 Integration of Reservoir Simulators

In this platform, three numerical reservoir simulators including CMG (Computer Modeling Group Ltd., 2012), ECLIPSE (Schlumberger, 2012), and UTCOMP (The University of Texas at Austin, 2014), and the semianalytical model developed in Chapter 3 have been integrated in the system. The semianalytical model can be used to simulate shale gas and tight oil production from complex nonplanar hydraulic fractures. Specifically, for CMG software, CMG-IMEX (a black-oil simulator) (CMG-IMEX, 2012) and CMG-GEM (a compositional simulator)

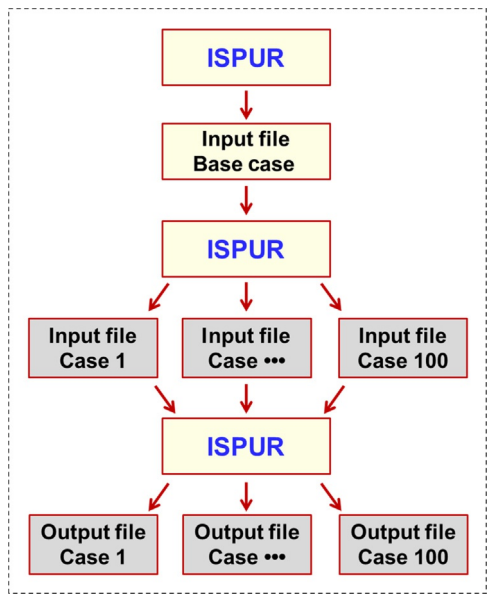

FIG. 6.3 One example of illustrating the workflow of using ISPUR to prepare and run 100 different simulation cases (Yu, 2015).

(CMG-GEM, 2012) are included. For ECLIPSE, E100 (a black-oil simulator) and E300 (a compositional simulator) are included. UTCOMP is an in-house compositional simulator, which can simulate shale gas and tight oil production with complex fracture networks using embedded discrete fracture model (EDFM) (Moinfar, 2013; Shakiba, 2014; Cavalcante Filho et al., 2015).

6.6.2 Base Case

For preparing the input files of base case for different reservoir simulators, we develop preprocessing programs to generate these input files in order to simulate shale gas and tight oil production. Gas desorption and geomechanics effects are also included in the preprocessing programs. The main inputs include reservoir, fracture, and well properties. After providing these properties, the programs will generate the input files of base case for different reservoir simulators automatically.

6.6.3 Multiple Cases

The number of multiple cases is dependent on the number of uncertain parameters investigated. The package of Design-Expert (Stat-Ease Incorporated, 2014) is used to generate the required multiple combinations of the uncertain parameters. Subsequently, all the combinations will be stored as an Excel file. In combination with input file for the base case, ISPUR automatically reads this Excel file and modifies the input file to generate multiple input files for reservoir simulators such as CMG, ECILIPSE, UTCOMP, and the semianalytical model. Specifically, using the keyword-matching method compared with the input file for the base case, ISPUR finds the keywords corresponding to the uncertain parameters and changes the values according to the Excel file automatically. The other keywords in the input file of the base case where no change is required will be just copied to the new input files.

6.6.4 Simulation Running Mode

After generating multiple input files for reservoir simulators, ISPUR will call the executable file of the reservoir simulator of interest to run these simulation cases automatically. Two running modes have been integrated in the ISPUR: one is in sequential mode, meaning that only one simulation case at a time; another is in distributed mode, meaning that multiple simulation cases at the same time. After finishing all simulation running, the simulation results for each case will be saved in different folders automatically in order to perform further data analysis and graphic presentations.

6.6.5 Postprocessing

The simulation results such as cumulative gas production or cumulative oil production are input into the package of Design-Expert to perform sensitivity studies with the purpose of quantifying the rank of important parameters and screening nonsignificant ones. In addition, the simulation results can be input into the package of Microsoft Excel designed for economic analysis to calculate the NPVs for each case. Then, the NPVs will be input into the package of Design-Expert to perform optimization with purpose of quantifying the relationship between the NPV and uncertain parameters and determining the best economic production scenario.

6.6.6 Flowchart for Sensitivity Study and Economic Optimization

The flowchart shown in Fig. 6.4 summarizes how to perform sensitivity studies and optimization using the DoE and RSM. The main steps are listed as follows:

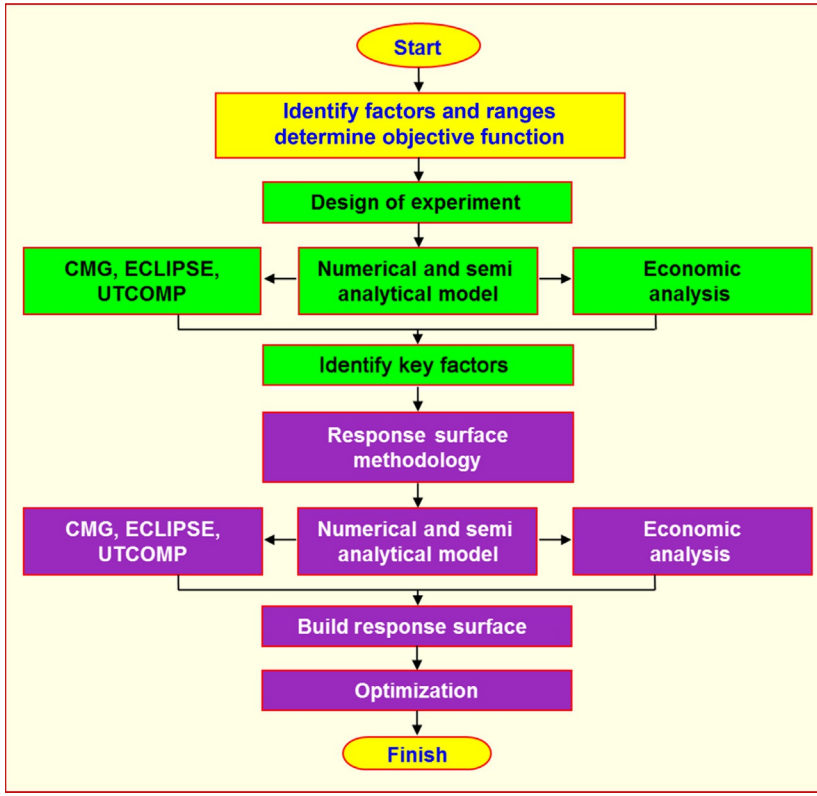

FIG. 6.4 Flowchart for sensitivity study and economic optimization for the development of unconventional oil and gas reservoirs (Yu, 2015).

(1) Determine the objective function, and identify the reasonable range for each uncertain factor based on the field data or published work.
(2) Select DoE to prepare multiple combinations and use ISPUR to generate multiple input files and run all simulations by use of a reservoir simulator or the semianalytical model.
(3) Export simulation results such as gas recovery and oil recovery and perform statistical analysis for obtaining the influence order of all factors and screening of insignificant factors.
(4) Select RSM to prepare multiple combinations again with the remaining significant factors and use ISPUR to generate multiple input files and run all simulations by use of a reservoir simulator or the semianalytical model.
(5) Export simulation results for calculating the NPVs, and perform statistical analysis for obtaining the response surface model.
(6) Perform further optimization to obtain the best economic production scenario.

6.7 APPLICATION OF FRAMEWORK IN MARCELLUS SHALE GAS RESERVOIRS

The framework is used to quantify the high uncertainties and perform optimization of fracture treatment design for the development of Marcellus shale. According to a recent report released by Energy Information Administration (EIA, 2014), Marcellus shale is one of six key tight oil and shale gas regions, as shown in Fig. 6.5. The Marcellus shale is located in the Appalachian basin

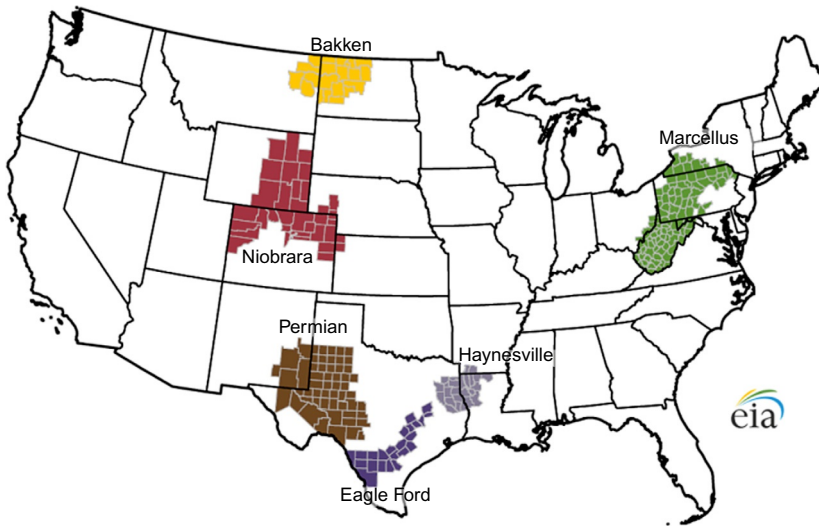

FIG. 6.5 Six key U.S. shale gas and shale oil regions (EIA, 2014).

across six states, including Pennsylvania, New York, West Virginia, Ohio, Virginia, and Maryland. Although there are many horizontal wells drilled along with multistage hydraulic fracturing in the Marcellus shale, the completion effectiveness is not completely understood and a lot of research is required to evaluate well performance and perform optimization of completion strategy.

The well performance is strongly related to permeability-thickness product ($k \cdot h$), initial reservoir pressure, total hydraulic fracture area, and the distribution of fracture conductivity (Cipolla et al., 2008; Mayerhofer et al., 2008). However, it is very challenging to exactly characterize the actual fracture geometry and the distribution of fracture conductivity, even with microseismic images, since microseismic images do not provide details about hydraulic fracture structure, total fracture area, and proppant distribution (Cipolla et al., 2012). Several authors stated that microseismic measurements represent only a small portion of the complete hydraulic fracture deformation (Maxwell et al., 2013; Cipolla and Wallace, 2014). History matching with field production data may provide an effective way to predict fracture properties. During hydraulic fracturing treatments, complex fracture networks are actually often generated and the interaction of hydraulic fractures and natural fractures significantly impacts the complexity, which is an important contributor to ultimate gas recovery (Daniels et al., 2007; Maxwell et al., 2013). The cost of hydraulic fracturing is expensive. The optimization of hydraulic fracture parameters, such as cluster spacing, fracture half-length, and fracture conductivity is important to obtain the most economical scenario. In addition, high uncertainties in shale gas reservoirs have resulted in the optimization of fracture design more challenging. Accordingly, the objective of this section is to use the framework to quantify the high uncertainties and investigate fracture properties through history matching with field production data. Six uncertain parameters including fracture height, fracture conductivity, fracture half-length, cluster spacing, permeability, and initial reservoir pressure were studied. We first used DoE to investigate the order of influence of each parameter and parameter interactions, and quantify which parameter significantly impacts the gas recovery and eliminates the variables that have little impact on the gas recovery. According to the rank of significant parameters, we performed history matching with one field production well. Additionally, a 30-year production forecasting was performed and its corresponding estimated ultimate recovery was quantified. Finally, we used RSM to build a response surface model in terms of NPV on the basis of the significant design variables to obtain the best economic production scenario. The proposed framework can provide a quantitative assessment of optimal horizontal well stimulations for shale gas production. Although the focus of this study is to guide completion evaluation and optimization of fracture design in the Marcellus shale, it can also be easily extended to the other shale gas reservoirs.

6.7.1 Sensitivity Study

In this case study, six uncertainty parameters were investigated including fracture height, fracture half-length, fracture conductivity, cluster spacing, permeability, and initial reservoir pressure. Each parameter was given a reasonable range with the actual maximum and minimum values or coded symbol of "+1" and "−1" based on the actual field data of the Marcellus shale, as listed in Table 6.1. The other reservoir and fracture properties are listed in Table 6.2.

A basic 3D numerical reservoir model using the numerical reservoir simulator of CMG-GEM (a compositional simulator) was built with dimensions of 5000 ft × 1500 ft × 135 ft, which corresponds to length, width, and thickness, respectively. The reservoir was divided into two layers. The top layer is with thickness of 95 ft and porosity of 9%. The bottom layer is with thickness of 40 ft and porosity of 13%. The horizontal well with length of 4500 ft was located in the bottom layer. Four clusters per stage are considered and each cluster is assumed to produce an effective hydraulic fracture. The number of stage corresponding to cluster spacing of 40 and 90 ft is 20 and 12, respectively. Constant flowing BHP of 200 psi is used for 30 years. In the simulation studies, single-phase gas flow was assumed and the effects of non-Darcy flow, gas desorption, and pressure-dependent fracture conductivity were considered. The non-Darcy Forchheimer coefficient proposed by Evans and Civan (1994) is used. The gas adsorption isotherm curve, as shown in Fig. 4.5A is used. The pressure-dependent fracture conductivity curves corresponding to different initial reservoir pressure in this study are shown in Fig. 6.6. As shown, the fracture

TABLE 6.1 Six Uncertainty Parameters Used for Sensitivity Study in the Marcellus Shale (Yu, 2015)

Parameter	Coded Symbol	Minimum (−1)	Maximum (+1)	Unit
Fracture height	A	40	135	ft
Fracture half-length	B	300	500	ft
Fracture conductivity	C	1	100	md-ft
Cluster spacing	D	40	90	ft
Permeability	E	100	1000	nD
Reservoir pressure	F	4000	5000	psi

TABLE 6.2 Parameters Used for Simulations in the Marcellus Shale (Yu, 2015)

Parameter	Value	Unit
Reservoir temperature	130	°F
Reservoir porosity (top layer)	9%	
Reservoir porosity (bottom layer)	13%	
Reservoir thickness (top layer)	95	ft
Reservoir thickness (bottom layer)	45	ft
Initial water saturation	10%	
Total compressibility	3×10^{-6}	psi^{-1}
Horizontal well length	4500	ft
Gas-specific gravity	0.58	

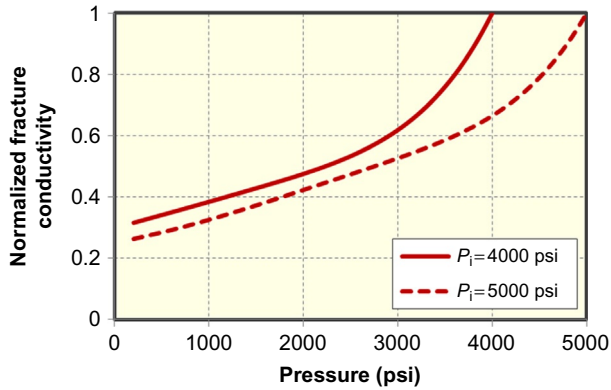

FIG. 6.6 Pressure-dependent fracture conductivity curves corresponding to initial reservoir pressure of 4000 and 5000 psi (Yu, 2015).

conductivity corresponding to the flowing BHP of 200 psi reduces to approximately 26%–32% of the original fracture conductivity.

In accordance to six variables, 32 simulation cases need to be prepared on the basis of two-level fractional factorial design, which can be generated automatically and efficiently using the ISPUR, as shown in Table 6.3.

After numerical simulation of each case, cumulative gas production was obtained and shown in Fig. 6.7. The figure clearly shows that there is a wide range of cumulative gas production ranging from 6.53 to 30.61 BCF at 30 years of production.

TABLE 6.3 32 Simulation Cases Based on Half Fractional Factorial Design for Six Uncertain Parameters in Marcellus Shale (Yu, 2015)

Run	A	B	C	D	E	F
1	40	300	1	90	1000	4000
2	40	500	100	90	100	5000
3	40	300	100	90	1000	5000
4	135	500	100	40	100	5000
5	40	500	100	40	100	4000
6	40	500	1	40	100	5000
7	40	300	1	40	1000	5000
8	40	300	100	40	100	5000
9	135	300	100	40	100	4000
10	40	500	1	90	1000	5000
11	135	300	1	40	100	5000
12	40	500	100	40	1000	5000
13	135	500	1	40	1000	5000
14	135	500	1	90	100	5000
15	135	300	1	90	1000	5000
16	40	300	100	40	1000	4000
17	135	500	1	90	1000	4000
18	135	500	100	90	100	4000
19	135	300	1	90	100	4000
20	135	300	1	40	1000	4000
21	40	500	100	90	1000	4000
22	40	500	1	90	100	4000
23	135	500	100	40	1000	4000
24	135	300	100	40	1000	5000
25	40	300	1	90	100	5000
26	135	500	1	40	100	4000
27	40	300	100	90	100	4000
28	135	300	100	90	100	5000
29	135	300	100	90	1000	4000
30	40	300	1	40	100	4000
31	40	500	1	40	1000	4000
32	135	500	100	90	1000	5000

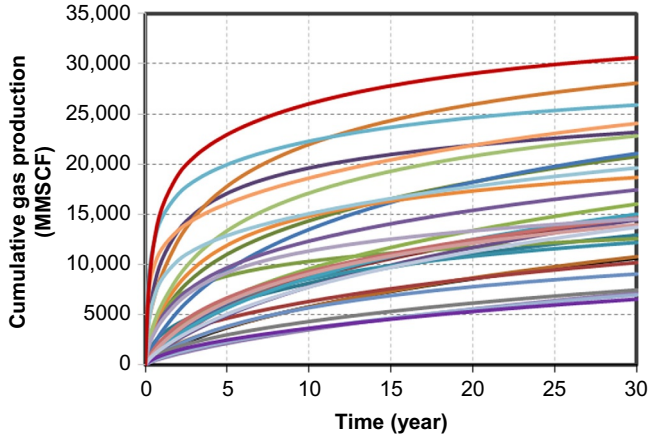

FIG. 6.7 Cumulative gas production of 32 cases for the Marcellus shale (Yu, 2015).

Results from Fig. 6.7 are then used to construct the half-normal plot, Pareto chart (Myers et al., 2008), and the analysis-of-variance (ANOVA) (Myers et al., 2008) table to identify the ranking of significant factors affecting the objective function of cumulative gas production. The half-normal plot and the corresponding Pareto chart at different period of production are presented in Figs. 6.8–6.11. Any parameters or two-parameter interaction highly deviating from the straight line are recognized as the parameters that affect the cumulative gas production significantly. At early time of production (5 years), as shown in Figs. 6.8 and 6.10, the following order in terms of influence of main parameter effects is fracture conductivity (C), permeability (E), fracture height (A), fracture half-length (B), reservoir pressure (F), and cluster spacing (D); while at late time of production (30 years), as shown in Figs. 6.9 and 6.11, the order of influence becomes permeability (E), fracture conductivity (C), fracture half-length (B), fracture height (A), reservoir pressure (F), and cluster spacing (D). This illustrates that fracture conductivity is significantly more important than permeability at the early time of production, while permeability will become more important than fracture conductivity at the late time of production.

The significant and insignificant model parameters were also determined by the ANOVA table, as shown in Tables 6.4 and 6.5. A parameter having value of "Prob $>$ F" (probability of a large F-value) <0.1 is called a significant model term. F means F-value in the ANOVA table, which is defined as the ratio of model mean square to the appropriate error mean square (Anderson and Whitcomb, 2007). Parameters not presented in Tables 6.4 and 6.5 are insignificant model terms. More details about the definitions of the terms in the ANOVA table can be found in the package of Design-Expert (Stat-Ease Incorporated, 2014).

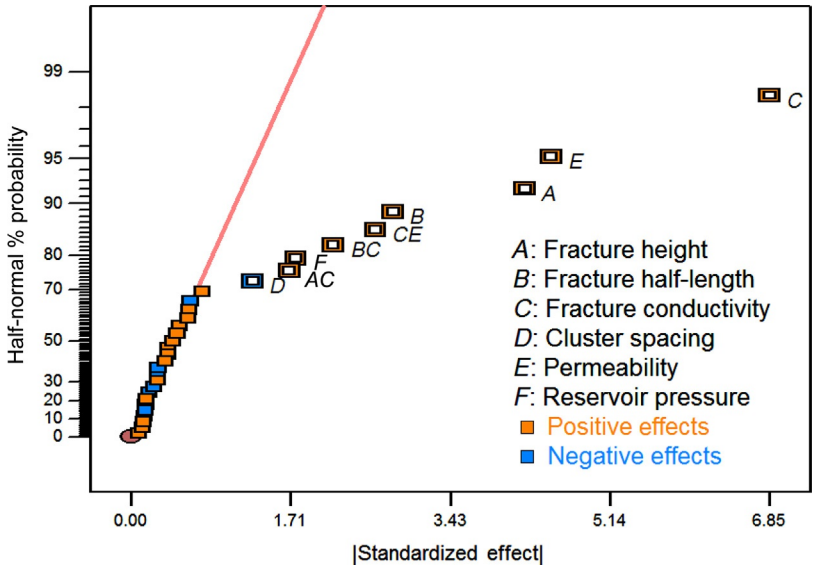

FIG. 6.8 The half normal plot at 5 years of gas production (Yu, 2015).

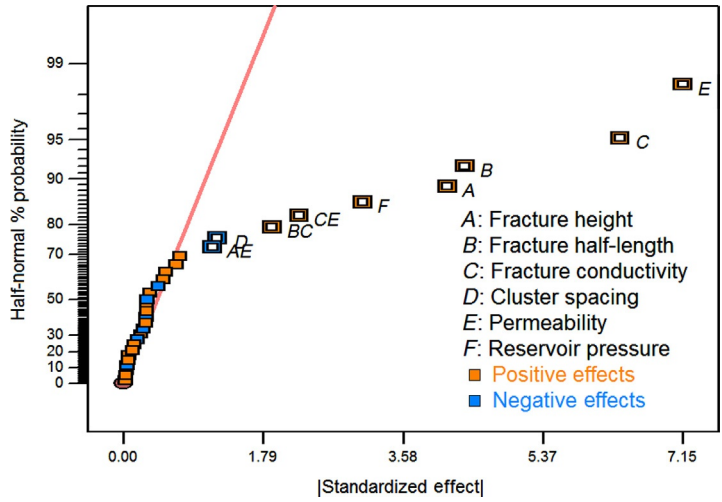

FIG. 6.9 The half normal plot at 30 years of gas production (Yu, 2015).

The detailed influences of all parameters on the well performance at a short-term period (5 years) and a long-term period (30 years) are shown in Fig. 6.12. It can be observed that impacts of some parameters on gas recovery decrease with time, including fracture conductivity (*C*), fracture height (*A*), and cluster spacing (*D*); while effects of some parameters increase with time, including

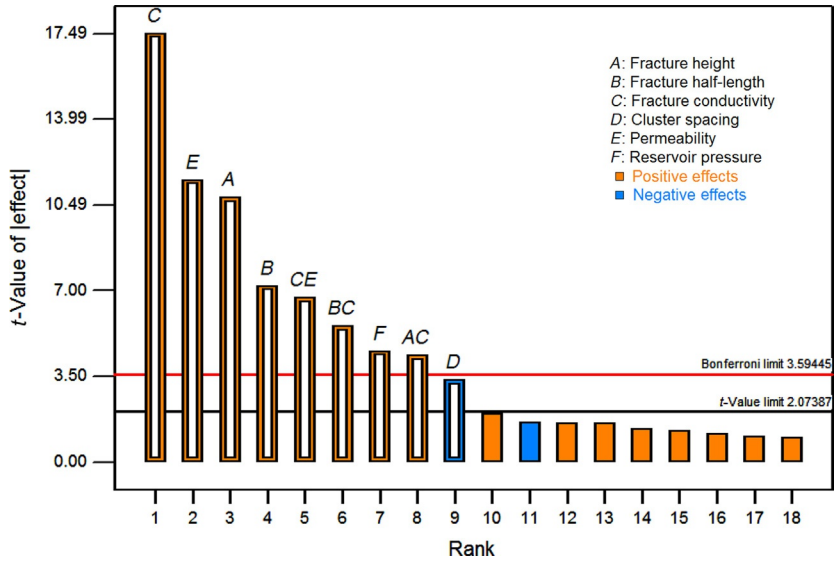

FIG. 6.10 Pareto chart of important parameters at 5 years of gas production (Yu, 2015).

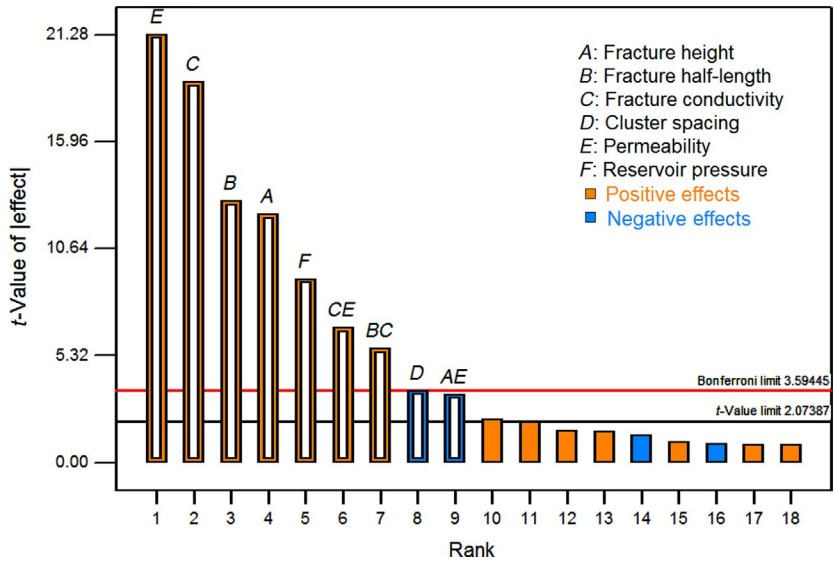

FIG. 6.11 Pareto chart of important parameters at 30 years of gas production (Yu, 2015).

TABLE 6.4 ANOVA Table for 5 Years of Gas Production (Yu, 2015)

Source	Sum of Squares	Degree of Freedom	Mean Square	*F*-Value	*P*-Value
Model	898.36	9	99.82	81.29	<0.0001
A	142.81	1	142.81	116.31	<0.0001
B	63.21	1	63.21	51.48	<0.0001
C	375.57	1	375.57	305.88	<0.0001
D	13.65	1	13.65	11.12	0.0030
E	162.48	1	162.48	132.33	<0.0001
F	25.00	1	25.00	20.36	0.0002
AC	23.06	1	23.06	18.78	0.0003
BC	37.61	1	37.61	30.63	<0.0001
CE	54.97	1	54.97	44.77	<0.0001
Residual	27.01	22	1.23		
Cor. total	925.37	31			

TABLE 6.5 ANOVA Table for 30 Years of Gas Production (Yu, 2015)

Source	Sum of Squares	Degree of Freedom	Mean Square	*F*-Value	*P*-Value
Model	1188.05	9	132.01	145.91	<0.0001
A	137.38	1	137.38	151.86	<0.0001
B	152.42	1	152.42	168.48	<0.0001
C	322.66	1	322.66	356.65	<0.0001
D	11.51	1	11.51	12.73	0.0017
E	409.48	1	409.48	452.63	<0.0001
F	74.94	1	74.94	82.84	<0.0001
AE	10.35	1	10.35	11.44	0.0027
BC	28.88	1	28.88	31.92	<0.0001
CE	40.43	1	40.43	44.69	<0.0001
Residual	19.90	22	0.90		
Cor. total	1207.95	31			

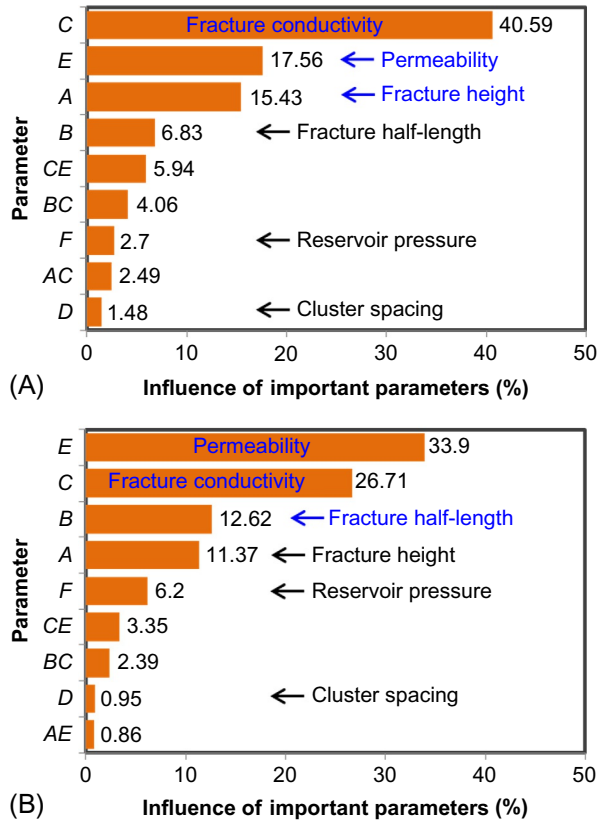

FIG. 6.12 Rank of the influences of uncertainty parameters on well performance (Yu, 2015). (A) At a short-term production (5 years). (B) At a long-term production (30 years).

permeability (E), fracture half-length (B), and reservoir pressure (F). The interactions between various parameters are defined as CE, BC, AC, and AE. As shown, the interaction parameter CE is more important that the other interaction parameters. The rank of important parameters can provide critical insights into performing history matching with field production data.

6.7.2 History Matching and Production Forecasting

One well, denoted as Well 1, from the Marcellus shale reservoir was selected to perform history matching and production forecasting. The primary purpose of history matching is to better understand the fracture properties such as fracture half-length, fracture height, and fracture conductivity. The reservoir has two different shale layers with high TOC. Porosity of top layer is 9%, and porosity of bottom layer is around 13.8%. Thickness of top layer is 94 ft, and thickness of

bottom layer is 43 ft. This well was drilled in the bottom layer and completed using a lateral length of 2605 ft, 10 fracturing stages, four perforation clusters per stage, and the cluster spacing is 52.2 ft. Almost 180 days of production data were available to perform history matching and evaluate the well performance.

We set up a basic 3D reservoir model with dimensions of 3105 ft × 1000 ft × 137 ft, which corresponds to length, width, and thickness, respectively, as shown in Fig. 6.13. As shown in this model, hydraulic fractures are assumed to completely penetrate the bottom layer and some part of top layer. Table 6.6 summarizes the detailed reservoir and fracture properties of the well required for simulation. Flowing bottomhole pressure in Fig. 6.14 is used to constrain the simulation and gas flow rate and cumulative gas production are the history-matching variables. Based on the sensitivity analysis, the top four key parameters such as fracture height, fracture conductivity, fracture half-length, and permeability were tuned to perform history matching.

The history-matching results for gas flow rate and cumulative gas production are shown in Fig. 6.15, illustrating that a good match between simulation results and field data is obtained with fracture conductivity of 5 md-ft, fracture height of 93 ft, fracture half-length of 330 ft, and permeability of 800 nD. It should be noted that history matching is not unique and the match obtained in this study is only one possible solution. The pressure distribution at end of field production is shown in Fig. 6.16, clearly showing the effective drainage volume of this well.

Incorporating the history match period, we performed a production forecasting for 30 years. After history-matching period, bottomhole pressure of 100 psi remained constant until 30 years of production. Fig. 6.17 shows the gas recovery at 30 years of production. It can be seen that the estimated ultimate recovery at

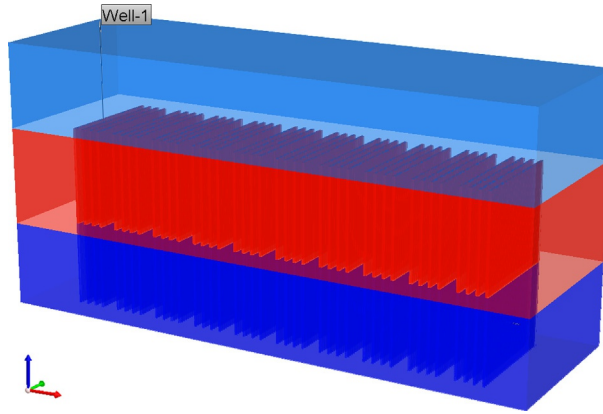

FIG. 6.13 A basic 3D reservoir model for the Well 1 (Yu, 2015).

TABLE 6.6 Reservoir and Fracture Parameters for Well 1 in Marcellus Shale (Yu, 2015)

Parameter	Value	Unit
Initial reservoir pressure	4300	psi
Reservoir temperature	130	°F
Reservoir permeability	800	nD
Reservoir porosity (top layer)	9%	
Reservoir porosity (bottom layer)	13.8%	
Reservoir thickness (top layer)	94	ft
Reservoir thickness (bottom layer)	43	ft
Initial water saturation	10%	
Total compressibility	3×10^{-6}	psi^{-1}
Horizontal well length	2605	ft
Number of stages	10	
Cluster spacing	52.2	ft
Total number of fractures	40	
Gas-specific gravity	0.58	

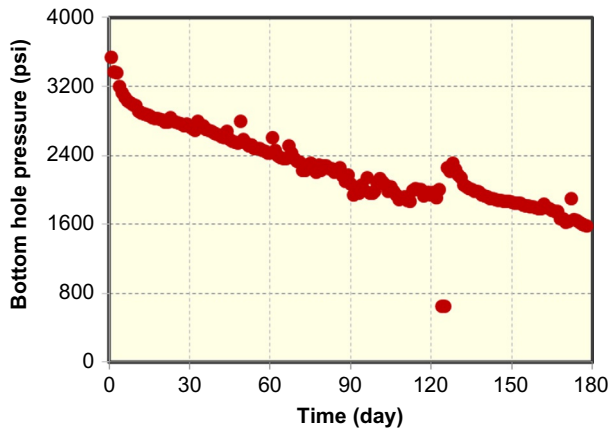

FIG. 6.14 Flowing bottomhole pressure of the Well 1 (Yu, 2015).

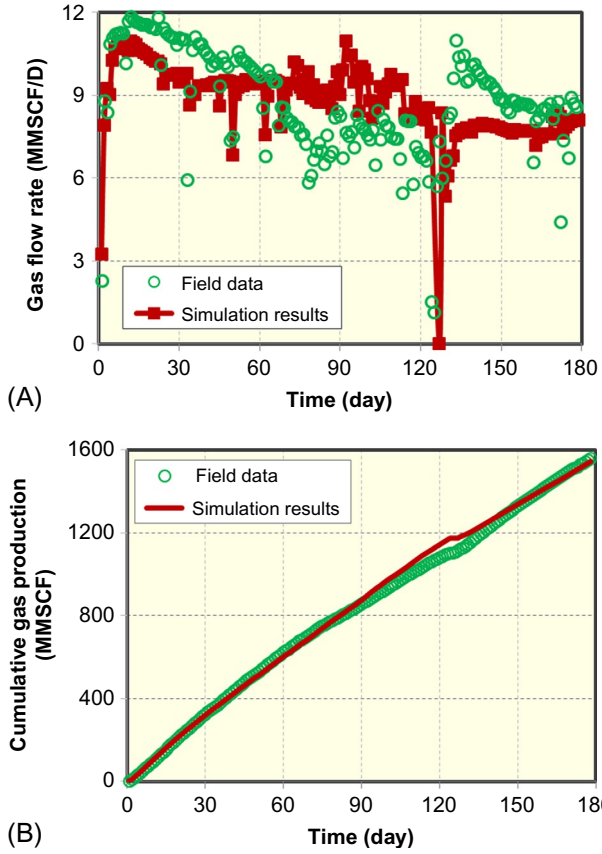

FIG. 6.15 History-matching results (Yu, 2015). (A) Gas flow rate. (B) Cumulative gas production.

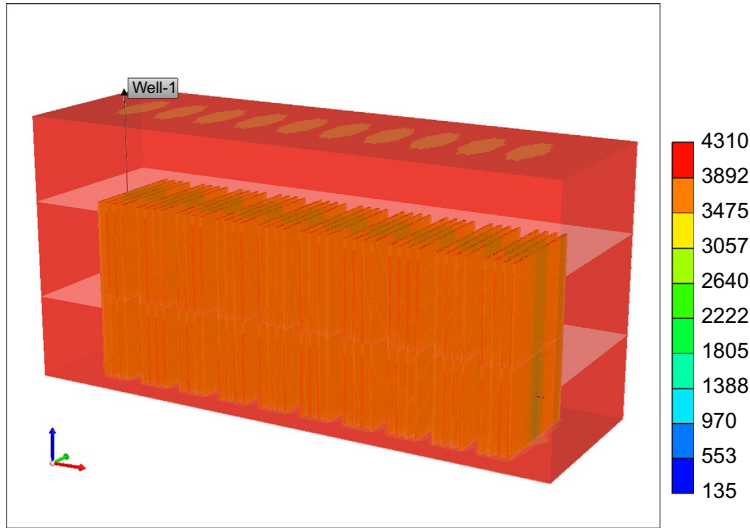

FIG. 6.16 Pressure distribution at end of field production (pressure unit: psi) (Yu, 2015).

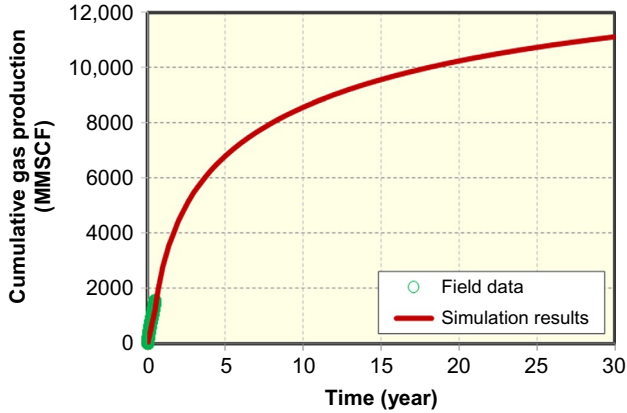

FIG. 6.17 Production forecasting for a 30-year period incorporating the history match period (Yu, 2015).

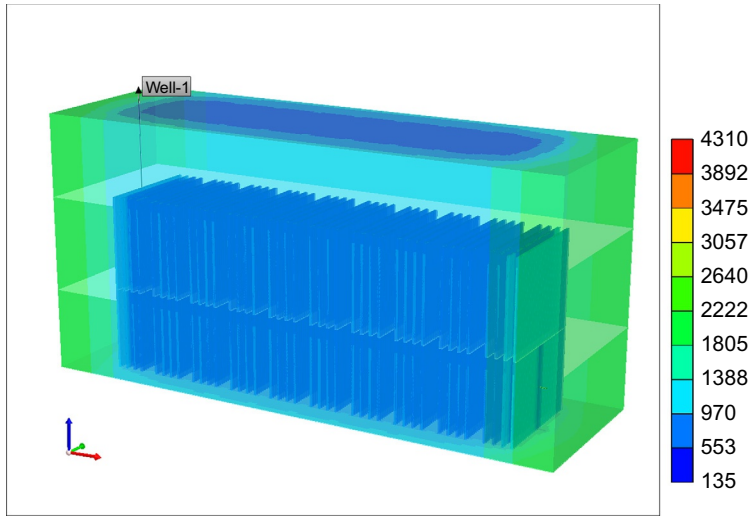

FIG. 6.18 Pressure distribution after 30 years of production (pressure unit: psi) (Yu, 2015).

30 years is quantified as 11.12 BCF for this well. The pressure distribution at 30 years of production is shown in Fig. 6.18, clearly illustrating the effective drainage volume of this well.

6.7.3 Fracture Treatment Cost

In order to perform economic optimization, the fracture treatment cost is an important part and it is determined based on the field data from Marcellus shale

in this section. The fracturing treatments cost is mainly divided into well drilling cost and completion cost. In this study, hydraulic fracture treatment data from four wells in Marcellus shale in combination with performing history matching with field production data are used to determine the fracture treatment cost. In general, the average well drilling cost is around $2.5 MM (MM refers to one million). The completion cost of single hydraulic fracture is strongly related to the volume of injected fluid and the amount of pumped proppants.

6.7.3.1 Reservoir and Operation Parameters

Table 6.7 summarizes the detailed reservoir properties and operation parameters of the four wells in Marcellus shale, which were provided by Chief Oil and

TABLE 6.7 Reservoir and Operation Parameters for Four Horizontal Wells in Marcellus Shale (Yu, 2015)

Parameter	Well 1	Well 2	Well 3	Well 4
True vertical depth (ft)	7050	7549	7120	7354
Reservoir temperature (°F)	130	130	130	130
Reservoir pressure (psi)	4500	4960	4300	4300
Porosity (top layer)	0.0857	0.08	0.09	0.09
Porosity (bottom layer)	0.134	0.13	0.138	0.138
Thickness (top layer) (ft)	90	88	94	94
Thickness (bottom layer) (ft)	40	51	43	43
Well length (ft)	5017	4046	2853	1904
Stage spacing (ft)	426	254	259	272
Number of stage	12	16	11	7
Number of cluster	60	63	44	21
Cluster spacing (ft)	80	53	52	68
Fracture design	2	3	4	5
Total sand (lbs)	6,655,920	6,007,757	4,797,713	3,079,918
Total liquid (bbls)	142,007	146,360	89,581	53,814
Sand per cluster (lbs)	110,932	95,361	109,039	146,663
Gas-specific gravity	0.58	0.58	0.58	0.58

Gas LLC. Four different hydraulic fracture treatment designs with various numbers of perforation clusters and injected amount of proppants per stage were investigated for these four wells as follows:

1. Fracture design 1: 5 clusters per stage with 554,660 lbs per stage;
2. Fracture design 2: 4 clusters per stage with 381,444 lbs per stage;
3. Fracture design 3: 4 clusters per stage with 436,156 lbs per stage;
4. Fracture design 4: 3 clusters per stage with 439,989 lbs per stage.

First, we set up a basic 3D numerical reservoir model including multiple hydraulic fractures to perform history matching. The reservoir model includes two layers with different thickness and porosity for each layer, as shown in Table 6.7. The horizontal well was drilled in the bottom layer. Fracture is assumed to completely penetrate the bottom layer and some part of the top layer, as shown in Fig. 6.19. For each well, flowing BHP is used to constrain the simulation and gas flow rate and cumulate gas production are the history-matching variables. A biwing fracture model is selected to perform history matching. Fracture half-length, fracture conductivity, fracture height, and reservoir permeability were the main tuning parameters to obtain a good history match. Gas desorption measurement data, as shown in Fig. 4.5A, is used to consider the gas desorption effect in the model.

6.7.3.2 *History Matching*

Fig. 6.20 shows the flowing BHP with different production time for these four horizontal wells. Comparisons between field production data and simulation results for gas flow rate and cumulative gas production are shown in Figs. 6.21 and 6.22, respectively. As shown, a good agreement for each well was obtained. Fig. 6.23 presents the pressure distribution of four wells at end of field production period, clearly illustrating the drainage area of each well.

Based on a good history match result, the key fracture properties and reservoir permeability were quantified (see Table 6.8). As shown, the range for fracture conductivity is 3–6 md-ft, for fracture half-length is 350–495 ft, and for fracture height is 80–111 ft. Reservoir permeability is 800 nD.

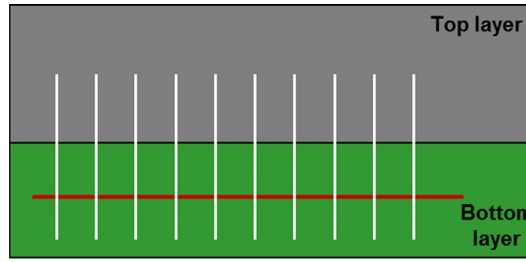

FIG. 6.19 Two layers with multiple hydraulic fractures and the horizontal well located in the bottom layer (Yu, 2015).

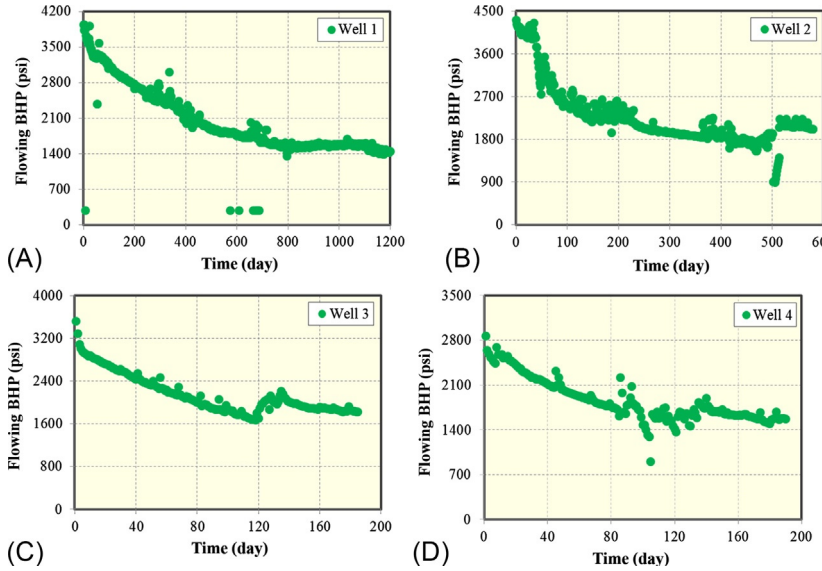

FIG. 6.20 Flowing bottomhole pressure of four wells in Marcellus shale (Yu, 2015). (A) Well 1. (B) Well 2. (C) Well 3. (D) Well 4.

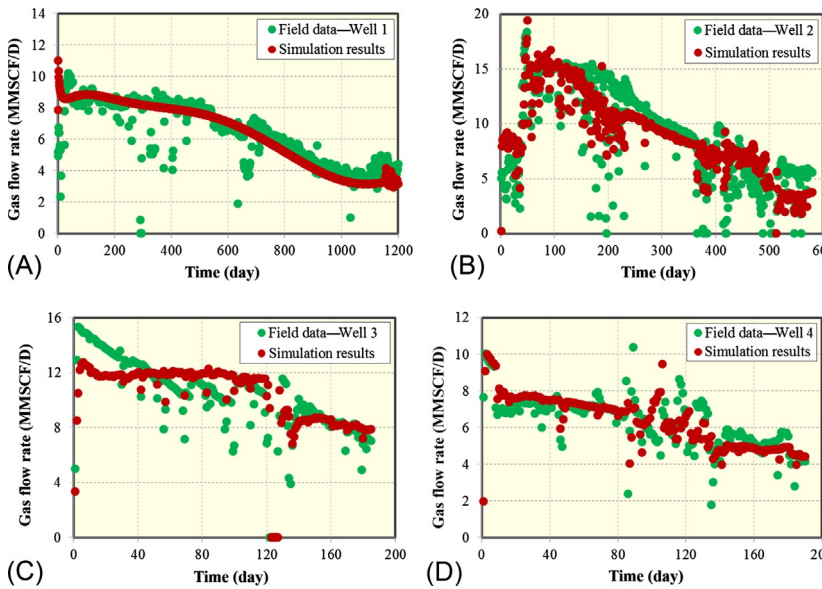

FIG. 6.21 History-matching results for gas flow rate of four wells in Marcellus shale (Yu, 2015). (A) Well 1. (B) Well 2. (C) Well 3. (D) Well 4.

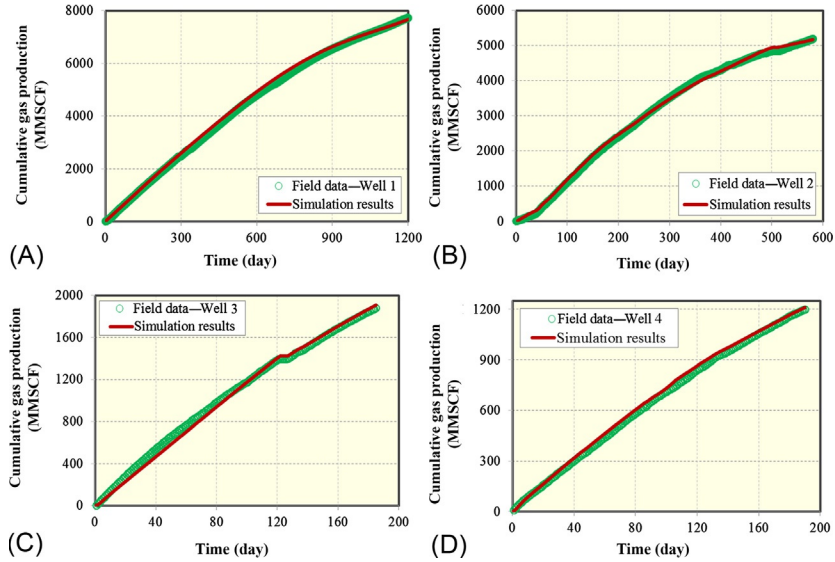

FIG. 6.22 History-matching results for cumulative gas production of four wells in Marcellus shale (Yu, 2015). (A) Well 1. (B) Well 2. (C) Well 3. (D) Well 4.

In order to determine the infinite fracture conductivity in the reservoir models for these wells, the effect of fracture conductivity with a range from 1 to 1000 md-ft on gas recovery of Well 3 at a 30-year period was studied and the simulation results are shown in Fig. 6.24. The flowing BHP of 200 psi is used in the simulation. It can be seen that there is a very small difference of gas recovery between fracture conductivity of 100 and 1000 md-ft, illustrating that 100 md-ft is very close to the infinite fracture conductivity. Hence, the current fracture treatment design for fracture conductivity based on the history-matching results is far away from the infinite fracture conductivity.

6.7.3.3 *Cost of Single Hydraulic Fracture*

Based on the history-matching results, the relationship between proppant amount pumped per cluster and fracture conductivity and the relationship between fluid injected per cluster and single fracture area is shown in Figs. 6.25 and 6.26, respectively. Single fracture area is defined as fracture length times fracture height in this work.

The cost of single hydraulic fracture corresponding to proppants pumped and fluid injected is shown in Figs. 6.27 and 6.28, respectively. Also, through fitting these values, the expressions were obtained as follows:

For fracture cost related to proppants pumped:

$$y = 4393.63 \times e^{2.097x}, \quad R^2 = 99\%, \tag{6.5}$$

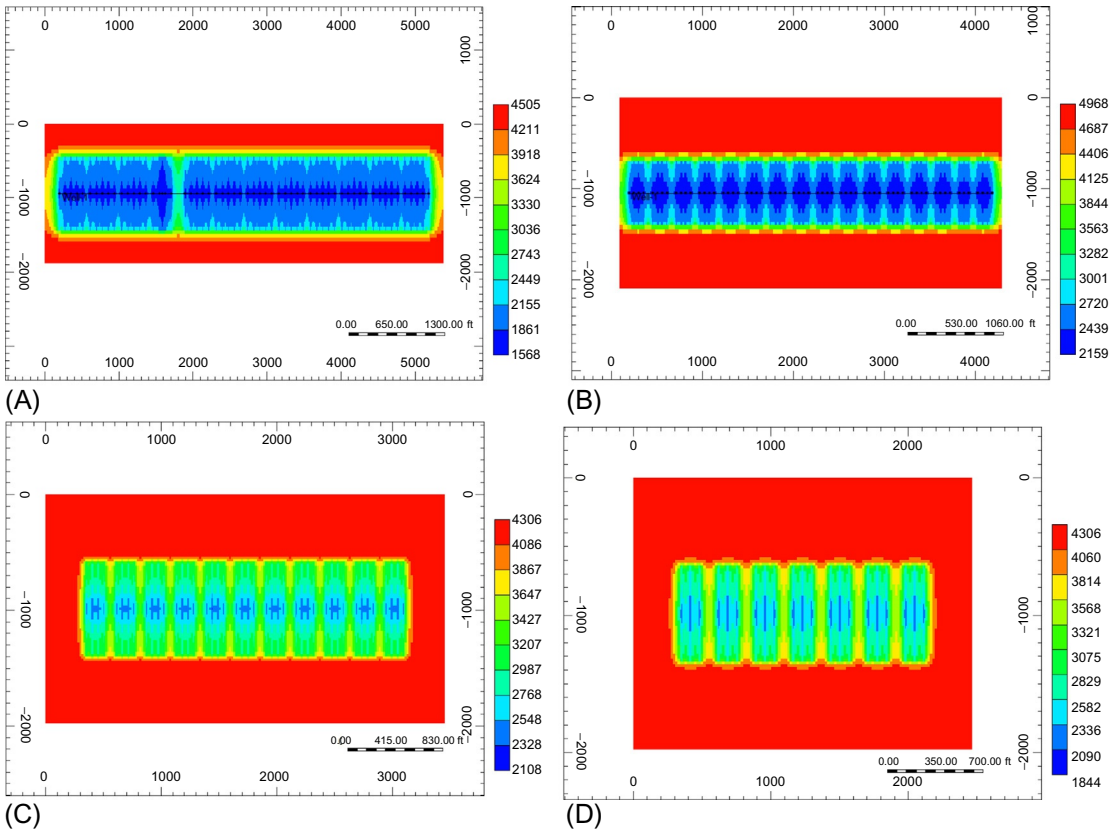

FIG. 6.23 Pressure distribution of four wells at end of different production times in Marcellus shale, respectively (pressure unit: psi) (Yu, 2015). (A) Well 1. (B) Well 2. (C) Well 3. (D) Well 4.

TABLE 6.8 History-Matching Results of Fracture Properties and Reservoir Permeability for Four Wells in Marcellus Shale (Yu, 2015)

Parameter	Well 1	Well 2	Well 3	Well 4
Fracture conductivity (md-ft)	5	3	4.5	6
Fracture half-length (ft)	495	350	410	410
Fracture height (ft)	80	111	98	96
Reservoir permeability (nD)	800	800	800	800

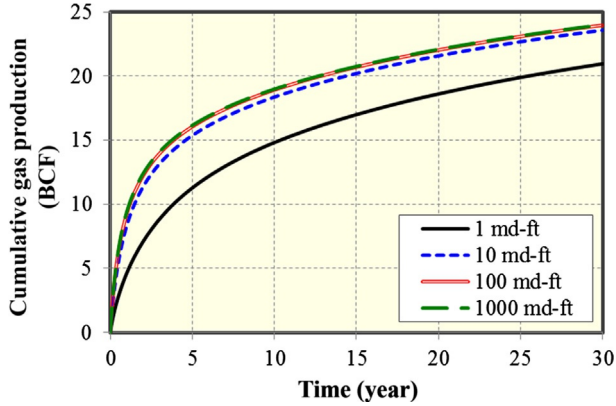

FIG. 6.24 Effect of fracture conductivity on gas recovery of Well 3 (Yu, 2015).

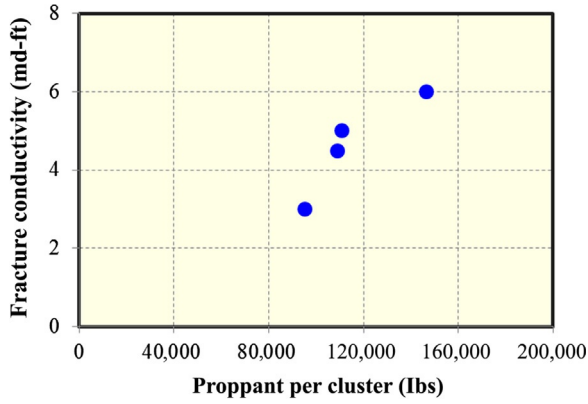

FIG. 6.25 Relationship between proppant amount pumped per cluster and fracture conductivity based on history-matching results for four wells (Yu, 2015).

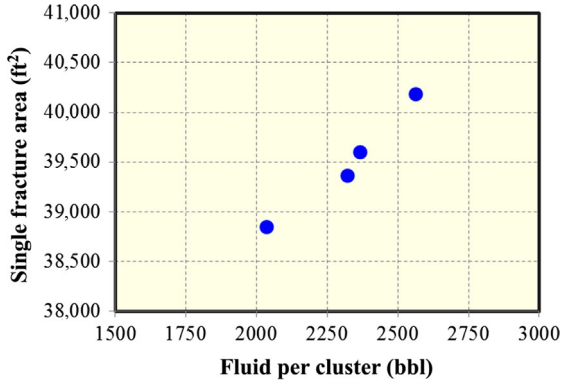

FIG. 6.26 Relationship between fluid injected per cluster and single fracture area based on history-matching results for four wells (Yu, 2015).

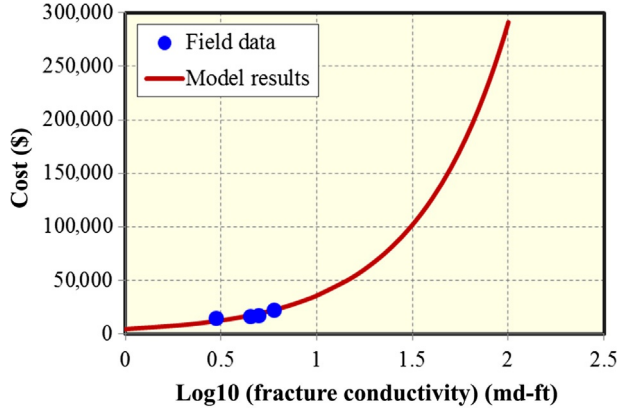

FIG. 6.27 Cost of single fracture corresponding to proppants pumped for four wells (Yu, 2015).

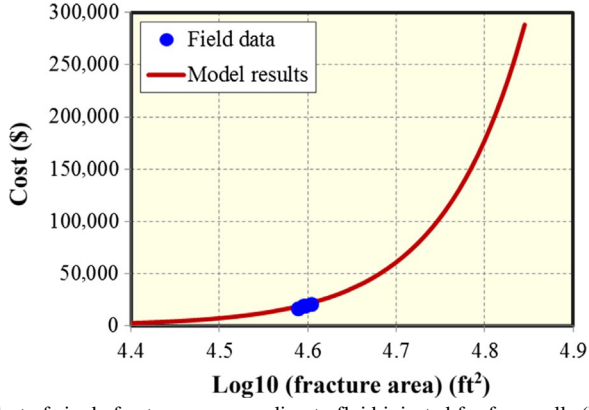

FIG. 6.28 Cost of single fracture corresponding to fluid injected for four wells (Yu, 2015).

where y is fracture cost and x is $\log_{10}$ (fracture conductivity).

For fracture cost related to fluid injected:

$$y = 8 \times 10^{-18} \times e^{10.72x}, \quad R^2 = 99\%, \tag{6.6}$$

where y is fracture cost and x is $\log_{10}$ (fracture area).

6.7.3.4 *Economic Evaluation of Four Fracture Designs*

In order to evaluate the economics of these four different fracture treatment designs, we set up a new 3D numerical reservoir model including multiple hydraulic fractures with a constant well length of 4500 ft. The reservoir also has two layers: the bottom layer is fixed at 43 ft and the top layer is fixed 92 ft. The total thickness is 135 ft. Hydraulic fractures are assumed to completely penetrate the bottom layer and some part of the top layer, as shown in Fig. 6.29. Fracture properties such as fracture spacing, fracture height, fracture half-length, and fracture conductivity are the same as the history-matching results for each well. The other parameters used for simulation are listed in Table 6.9.

Fig. 6.30 compares the cumulative gas production for four wells with different fracture designs. As shown, the rank of gas recovery at 30 years of production is Well 1, Well 3, Well 4, and Well 2, respectively.

The NPVs of four wells are calculated by assuming the gas price of \$3.5/MSCF, the interest rate of 10%, and the royalty tax of 12.5%, as shown in Fig. 6.31. It can be seen that the rank of NPV is Well 3, Well 1, Well 4, and Well 2, respectively. Hence, the fracture design 3 with 4 clusters per stage

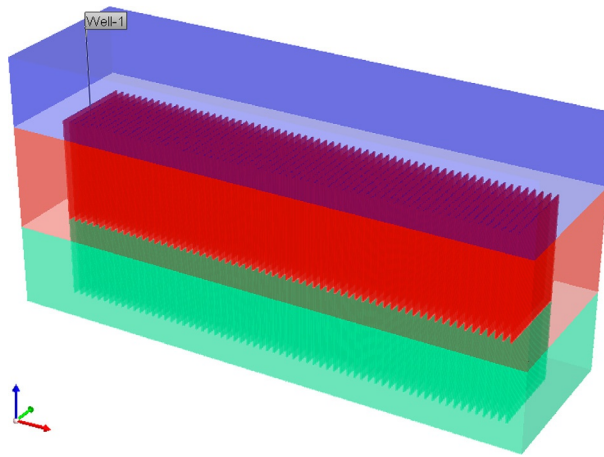

FIG. 6.29 A basic reservoir model with two layers for economic evaluation of four different fracture designs in Marcellus shale (Yu, 2015).

TABLE 6.9 Parameters Used Simulation to Perform Economic Evaluation of Four Different Fracture Designs in Marcellus Shale (Yu, 2015)

Parameter	Value
Reservoir pressure (psi)	4400
Porosity (bottom layer)	13%
Porosity (top layer)	9%
Reservoir permeability (nD)	800
Total compressibility (psi^{-1})	3×10^{-6}
Temperature (°F)	130
Flowing BHP (psi)	200
Initial gas saturation	90%
Gas-specific gravity	0.58
Production time (year)	30

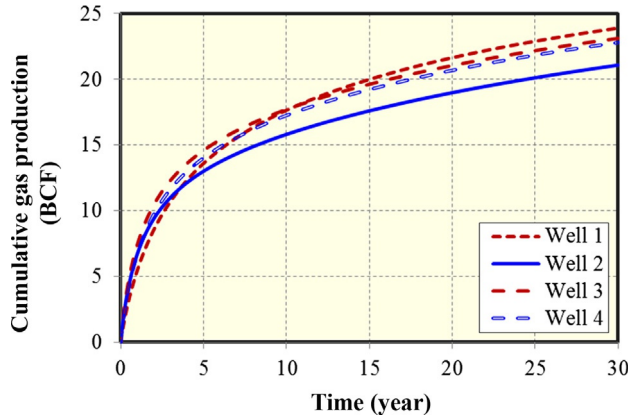

FIG. 6.30 Comparison of cumulative gas production for four wells with different fracture designs (Yu, 2015).

and 436,156 lbs of proppants per stage for Well 3 is the best design among these four different designs in Marcellus shale.

6.7.4 Economic Optimization

After the sensitivity analysis using the framework, the response surface of NPV based on the four design variables such as fracture height (A), fracture

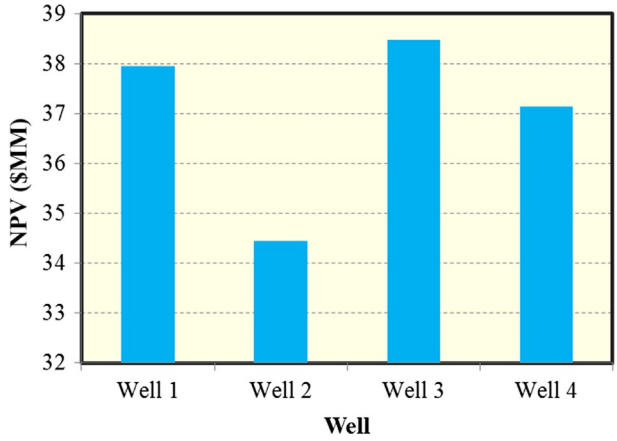

FIG. 6.31 Comparison of NPV for four wells with different fracture designs (Yu, 2015).

half-length (B), fracture conductivity (C), and cluster spacing (D) was built. The range for each parameter is the same as that in Table 6.1. The reservoir permeability is assumed to be 800 nD and the average reservoir pressure is assumed to be 4500 psi. According to four variables in this study, 25 simulation cases were generated based on the approach of D-optimal design, which was originated from the optimal design theory (Kiefer and Wolfowitz, 1959), as shown in Table 6.10. More details about the approach of D-optimal design can be found elsewhere (Myers et al., 2008). Similarly with sensitivity study, the ISPUR is used to generate 25 cases automatically and efficiently.

After numerical simulation of each case, cumulative gas production was obtained and shown in Fig. 6.32. It clearly shows that the cumulative gas production at 30 years of gas production has a large uncertainty. This means that further optimization is needed.

Once the cumulative gas production of 25 cases was obtained, the economic Excel spreadsheet is used to calculate the corresponding NPVs based on the price of natural gas of $3.5/MSCF, interest rate of 10%, and Royalty tax of 12.5%. The fracture cost related to single fracture conductivity and area, as shown in Figs. 6.27 and 6.28, respectively, is used. The single well drilling cost is around $2.5 MM in this case study. Fig. 6.33 presents NPVs of 25 simulation cases at 30 years of production.

Once NPVs of 25 simulation cases were obtained, the Design-Expert software package is used to build the NPV response surface model. To select the appropriate model, the statistical approach is used to determine which polynomial fits the equation among linear model, two-factor interaction model (2FI), quadratic model, and cubic model, as shown in Table 6.11. The criterion for selecting the appropriate model is choosing the highest polynomial model, where the additional terms are significant and the model is not aliased. Although

TABLE 6.10 25 Simulation Cases Based on D-Optimal Design (Yu, 2015)

Run	A	B	C	D
1	135	390	47	40
2	82	380	9	70
3	40	500	100	40
4	40	300	100	50
5	40	400	1	40
6	135	500	100	90
7	99	420	100	60
8	62	310	67	80
9	135	300	100	40
10	40	300	1	90
11	121	300	100	90
12	40	500	39	70
13	40	300	1	90
14	135	300	1	60
15	135	500	1	40
16	96	500	50	50
17	135	300	1	60
18	85	300	38	40
19	54	400	61	50
20	135	400	35	90
21	40	450	100	90
22	89	500	1	90
23	40	500	100	40
24	40	450	100	90
25	135	500	100	90

the cubic model is the highest polynomial model, it is not selected because it is aliased. Aliasing means some effects are confounded with each other, which is a result of reducing the number of experimental runs (Zhang, 2005). When it occurs, several groups of effects are combined into one group and the most

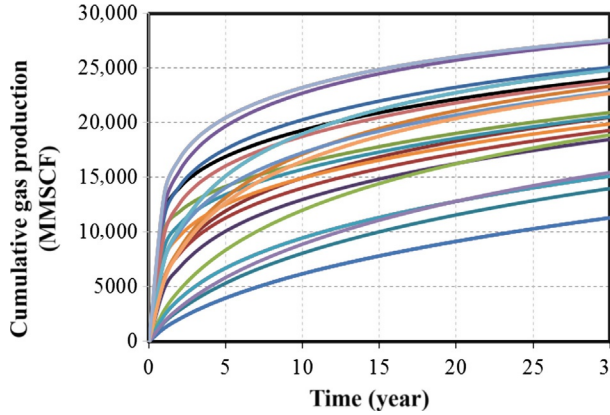

FIG. 6.32 Cumulative gas production of 25 simulation cases for a 30-year period (Yu, 2015).

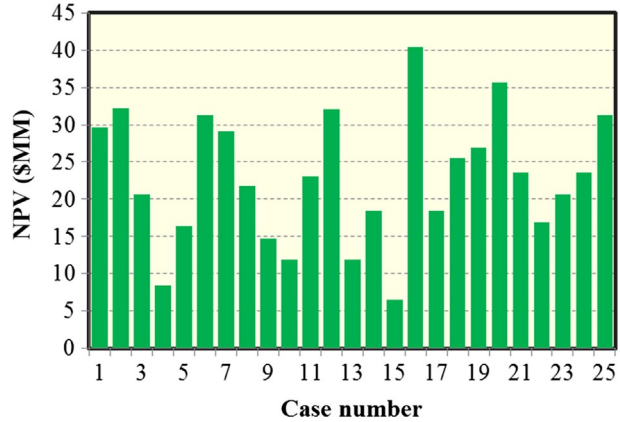

FIG. 6.33 NPVs of 25 cases at 30 years of gas production with the gas price of $3.5/MSCF (Yu, 2015).

significant effect in the group is used to represent the effect of the group. Essentially, it is important that the model is not aliased. In addition, other criteria are to select the model that has the maximum "Adjusted *R*-Squared" and "Predicted *R*-Squared." Thus, the fully quadratic model is selected to build the NPV response surface in the subsequent optimization process.

The equation fitted to the NPV response surface with the actual factors is presented as:

TABLE 6.11 25 Statistical Approach to Select the RSM Model With Gas Price of $3.5/MSCF (Yu, 2015)

Source	Std. Dev.	*R*-Squared	Adjusted *R*-Squared	Predicted *R*-Squared	Press	
Linear	0.19	0.21	0.052	−0.37	1.27	
2FI	0.19	0.47	0.088	−2.20	2.96	
Quadratic	0.050	0.97	0.936	0.62	0.35	Suggested
Cubic	0.00	1.00	1.00			Aliased

$$\begin{aligned} Log_{10}(NPV) = & -1.0544 + 0.01609 \times A + 7.9739 \times 10^{-3} \times B - 9.4093 \times 10^{-4} \\ & \times C + 5.6403 \times 10^{-3} \times D - 2.0868 \times 10^{-5} \times AB + 2.5452 \\ & \times 10^{-5} \times AC + 2.7032 \times 10^{-5} \times AD + 2.1057 \times 10^{-5} \times BC \\ & + 6.4429 \times 10^{-6} \times BD + 1.1089 \times 10^{-5} \times CD - 5.6609 \times 10^{-5} \\ & \times A^2 - 8.8926 \times 10^{-6} \times B^2 - 9.2179 \times 10^{-5} \times C^2 - 6.7692 \\ & \times 10^{-5} \times D^2, \end{aligned} \tag{6.7}$$

where A is fracture height, B is fracture half-length, C is fracture conductivity, and D is cluster spacing.

The normal plot of residuals, reflecting the distribution of the residuals, is shown in Fig. 6.34. All the points in the "normal plot of residuals" fall on the straight line, meaning the residuals are normally distributed. Fig. 6.35 shows the plot of "Predicted vs. Actual," illustrating whether the generated equation of NPV response surface accurately predicts the actual NPV values. It can be seen that generated NPV response surface models provide such reliable predicted values of NPV, as compared with the actual values of NPV. This means that the generated NPV response surface model is reliable.

Fig. 6.36 shows the 3D surface of NPV at varied values of fracture conductivity and fracture height with gas price of $3.5/MSCF. It shows that there is an optimal fracture design related to fracture conductivity and fracture height. Therefore, this methodology can provide some insights into optimization of fracturing treatment design to obtain the maximum economic viability of the field.

The objective function of NPV will be maximized by selecting the best combinations with uncertain parameters through the method of RSM. The best scenario is obtained based on the range of parameters investigated in this study for the Marcellus shale. The best case with the highest NPV value of $49.25 MM

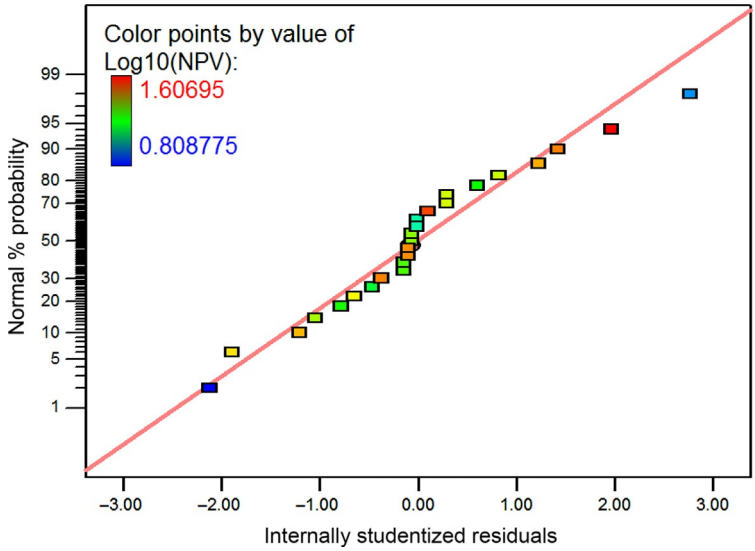

FIG. 6.34 Normal plot of residuals at gas price of $3.5/MSCF (Yu, 2015).

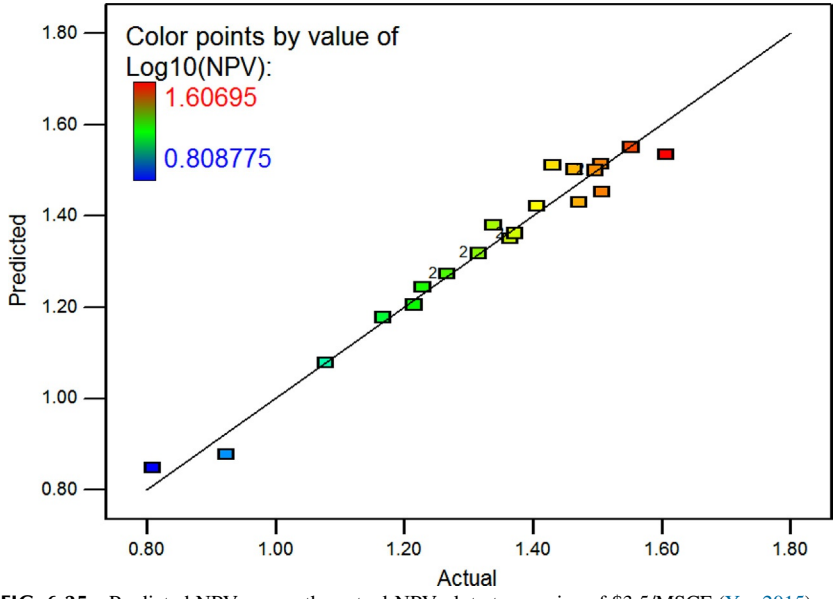

FIG. 6.35 Predicted NPV versus the actual NPV plot at gas price of $3.5/MSCF (Yu, 2015).

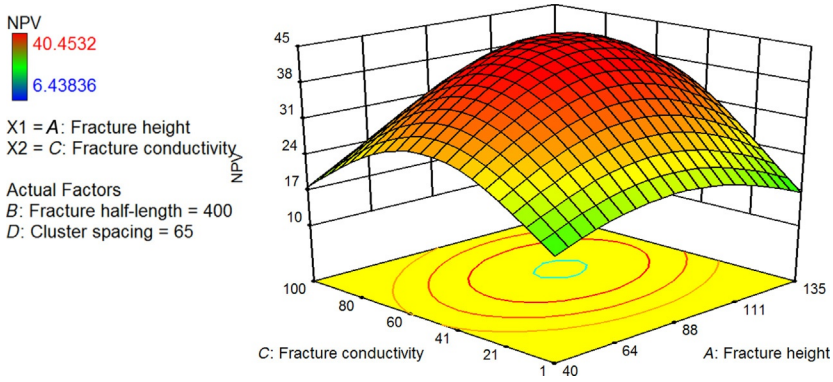

FIG. 6.36 3D surface of NPV at varied values of fracture conductivity and fracture height (Yu, 2015).

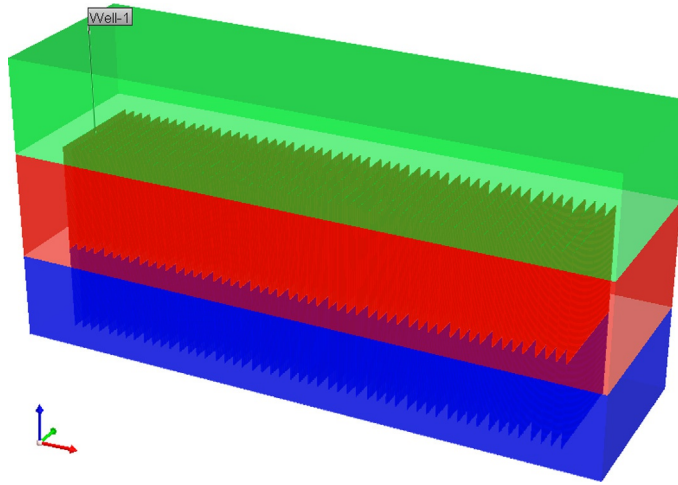

FIG. 6.37 The best case with fracture height of 90 ft, fracture half-length of 460 ft, fracture conductivity of 62 md-ft, and cluster spacing of 80 ft for the Marcellus shale (Yu, 2015).

corresponding to fracture height of 90 ft, fracture half-length of 460 ft, fracture conductivity of 62 md-ft, and cluster spacing of 80 ft, as shown in Fig. 6.37. Fig. 6.38 shows gas flow rate and cumulative gas production at 30 years of production. Fig. 6.39 presents pressure distribution for the best case at 30 years of gas production, illustrating the drainage volume clearly.

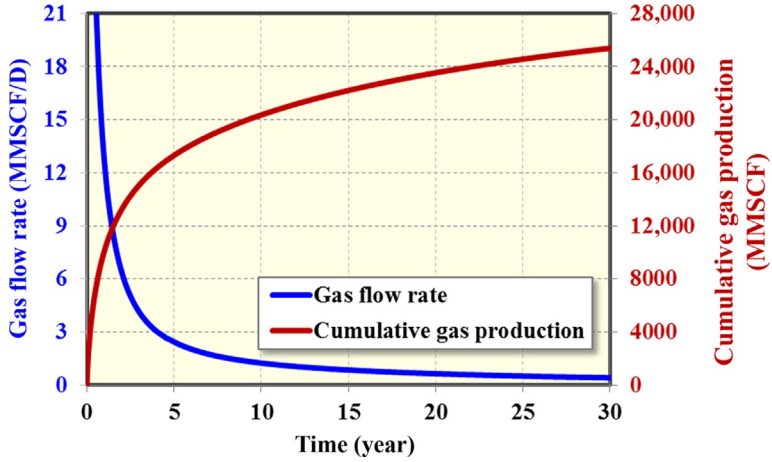

FIG. 6.38 Cumulative gas production and gas flow rate of the best case (Yu, 2015).

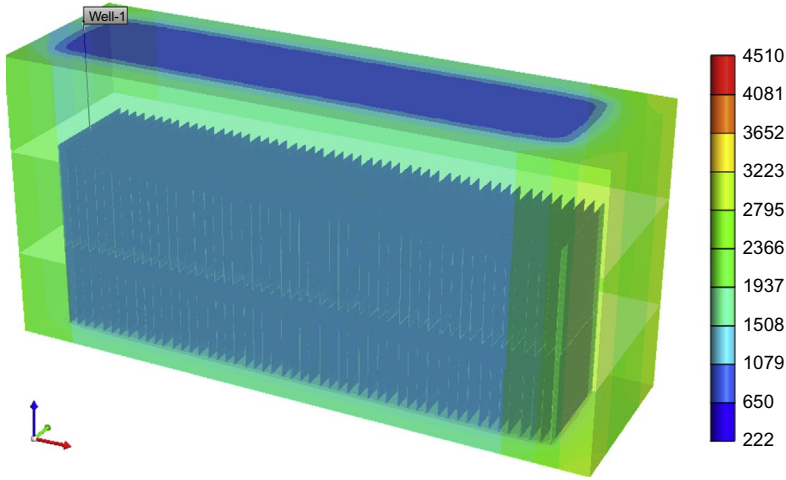

FIG. 6.39 Pressure distribution at 30 years of production for the best case (pressure unit: psi) (Yu, 2015).

6.8 APPLICATION OF FRAMEWORK IN BAKKEN TIGHT OIL RESERVOIRS

The framework is also used to quantify the high uncertainties and perform optimization of multiple well placement for the development of Bakken tight oil formation. The Bakken formation is one of the largest tight oil developments in North America, which consists of Upper and Lower Bakken shales, Middle

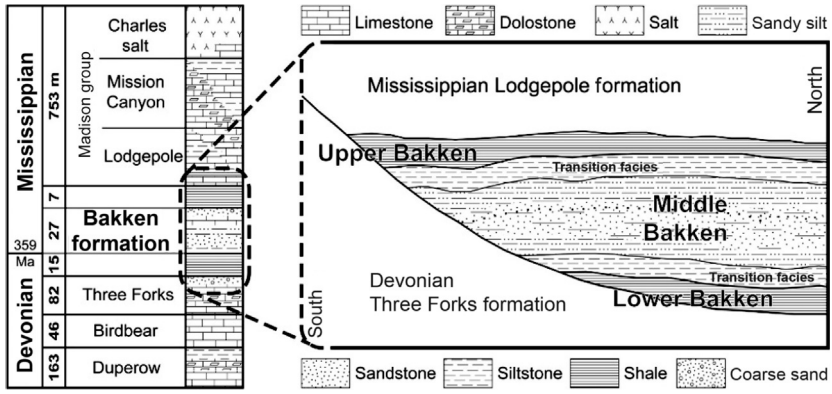

FIG. 6.40 A cross section of the Bakken formation (West et al., 2013).

Bakken, Sanish and Three Forks, as shown in Fig. 6.40. The Middle Bakken and Three Forks are two primary targets for the current field development. Recently, the United States Geological Survey (USGS) performed an assessment and reported that Middle Bakken has an estimated average oil resource of 3.65 billion barrels and Three Forks has an estimated average resource of 3.73 billion barrels (USGS, 2013).

Numerous horizontal wells along with hydraulic fracturing are required to make the economic development of the Bakken formation. Multiple created hydraulic fractures can generate a large contact area between the wellbore and formation with low or ultralow permeability. Fracture conductivity plays an important role in providing an adequate connection between the wellbore and the formation to transmit reservoir fluids. Also, it is a key parameter for evaluation of postfracture treatments and optimization of fracture design for new completion strategy. Most horizontal wells are drilled in the N-S orientation, which is the approximate direction of the minimum horizontal stress (Besler et al., 2007). The majority of wells are drilled in the depth between 10,500 and 11,000 ft true vertical depth (TVD) (Flowers et al., 2014). Lateral length in the Bakken in most cases has two scenarios, one is "short laterals" with approximately 1 mile long and spaced at 640 acres; the other is "long laterals" with approximately 2 miles long and spaced at 1280 acres (West et al., 2013). West et al. (2013) recommended the optimal stage spacing to be 325 ft with three clusters per single fracturing stage. An average of 30 perforation stages is used for each long lateral (Luo et al., 2011).

During hydraulic fracturing, a total of about 182,500 bbl of fluid and 2,555,000 lbs of proppant are pumped for each well in the Middle Bakken and 153,000 bbl of fluid and 2,454,000 lbs of proppant for each well in the Three Forks (Ganpule et al., 2013). The main goal of proppant is to keep the created hydraulic fractures open with enough fracture conductivity. There are many

proppant types used in the Bakken formation, such as sand, ceramic, resin-coated sand, or their combinations (Flowers et al., 2014). Ceramic proppant can provide not only a higher fracture conductivity but also a greater longevity and durability than sand or resin-coated sand (Handren and Palisch, 2007; Rankin et al., 2010). Retaining high fracture conductivity over the lifetime of a well is critical for the economic development of the Bakken formation. However, it is very challenging to maintain such high fracture conductivity for a long-term period due to proppant embedment, proppant crushing, proppant fines generation and migration, proppant flowback, and proppant diagenesis, resulting in the loss of fracture conductivity (Pope et al., 2009; LaFollette and Carman, 2010; Fan et al., 2010). Also, non-Darcy flow and multiphase flow in propped fractures will decrease fracture conductivity significantly (McDaniel et al., 2010).

In the Bakken formation, hydraulic fracturing is performed in the deeper depth with higher fracture closure pressure. The phenomenon of proppant embedment becomes an important issue in the loss of fracture conductivity. The deeper well depth leads to the pumped proppants being exposed to a high stress over 9450 psi based on the fracture gradient of 0.90 psi/ft. The Bakken is overpressured with pressure gradient up to 0.73 psi/ft in the central part of the Williston Basin (Meissner, 1978). Accordingly, if the initial reservoir pressure is around 7600 psi, then the effective stress of 1850 psi is generated on the proppants at the beginning of production. When the flowing bottomhole pressure declines to 1000 psi, the effective stress will increase to about 8450 psi. Propped fracture conductivity is a function of effective stress, and it decreases with the increasing effective stress. Additionally, mixing of various proppant sizes might reduce fracture conductivity due to proppants with small size invading and occupying pore space (McDaniel and Willingham, 1978; Schmidt et al., 2014). It is recognized in the industry that the actual fracture conductivity is often a small fraction of those measured by the American Petroleum Institute (API) conductivity test, and it is still less than the optimal fracture conductivity (McDaniel et al., 2010). Flowers et al. (2014) analyzed the field production data of 205 wells with production history of 325 days in the Bakken, and presented that the wells treated with proppant of ceramic only outperform the wells treated with proppant type of sand only by 40% and the wells treated with the mixture of ceramic and sand by 21%. Accordingly, the selection of proppant type and concentration to achieve high fracture conductivity for a long-term in the Bakken formation is still important to improve well productivity and profitability.

Similar to many shale gas reservoirs, there is a large uncertainty in reservoir and fracture properties in the Bakken formation. It was reported that porosity in the Middle Bakken is in the range of 4%–12%, and initial water saturation is 25%–60% (Cherian et al., 2013). The average porosity of the Middle Bakken is 6% and permeability is in the order of microdarcies (Nojabaei et al., 2013). Reservoir temperature is approximately 240°F (Rankin et al., 2010). Average oil gravity is about 42° API, indicating the crude oil is light with

low viscosity. Nojabaei et al. (2013) presented that the range of gas oil ratio (GOR) is from 507 to 1712 SCF/bbl and bubble point pressure varies from 1617 to 3403 psi. Cherian et al. (2013) reported that although fracture half-length in most cases in the Bakken exceeds 300 ft (300–900 ft), the proppants only transport 10%–30% of that distance because of fracture height growth. They found that an equivalent fracture half-length is in the range of 100–200 ft and fracture conductivity ranges between 4 and 7 md-ft based on history-matching results. The number of fractures in each stage plays a key role in controlling the fracture half-length and corresponding drainage area. It may have one fracture or multiple fractures in single perforation stage.

Although there are many attempts to optimize fracture design in the Bakken formation, the existence of high uncertainty in reservoir and fracture properties is still poorly understood. In addition, economic analysis is required for the optimal multiple well placement due to the high drilling and completion cost. In this work, we used the framework to first quantify the significant parameters and screen insignificant ones for single horizontal well. Six uncertain parameters including fracture spacing, fracture half-length, fracture conductivity, permeability, porosity, and initial water saturation were investigated, and each parameter was given a reasonable range based on the typical reservoir and fracture properties from the Middle Bakken. Then, based on the sensitivity analysis, we performed history matching with field production data from Middle Bakken. Subsequently, we performed production forecasting to predict long-term oil recovery. Finally, we optimized fracture design in combination with maximizing NPV for multiple well placement. This work is valuable for guiding fracture design and completion optimization for multiple well placement in the Bakken formation.

6.8.1 Numerical Modeling for Tight Oil Reservoirs

Reservoir simulation is an effective approach to simulate multiphase flow (gas-water-oil) in the Bakken formation, especially in the early stage of field developments. In this study, reservoir simulator of CMG-IMEX (a black-oil simulator) is used to model multiple hydraulic fractures and fluid flow in the Bakken tight oil reservoirs. For reservoir modeling including multiple fractures, local grid refinement (LGR) method is utilized to accurately model fluid flow from matrix to fractures.

For single horizontal well, we set up a basic 3D reservoir model with dimensions of 10,560 ft × 1320 ft × 40 ft, which corresponds to length, width, and thickness, respectively. For multiple horizontal wells, the width of basic reservoir model is extended to 5280 ft. A biwing fracture model is used in the basic reservoir model. The horizontal well length is set at 10,000 ft with 31 perforation stages. The number of effective fractures in each stage ranges from 1 to 4, as shown in Fig. 6.41. Fig. 6.41A assumes that there is only one effective fracture in each stage and the fractures are evenly spaced, so there are totally 31 effective hydraulic fractures along the horizontal well. Fig. 6.41B assumes that there are

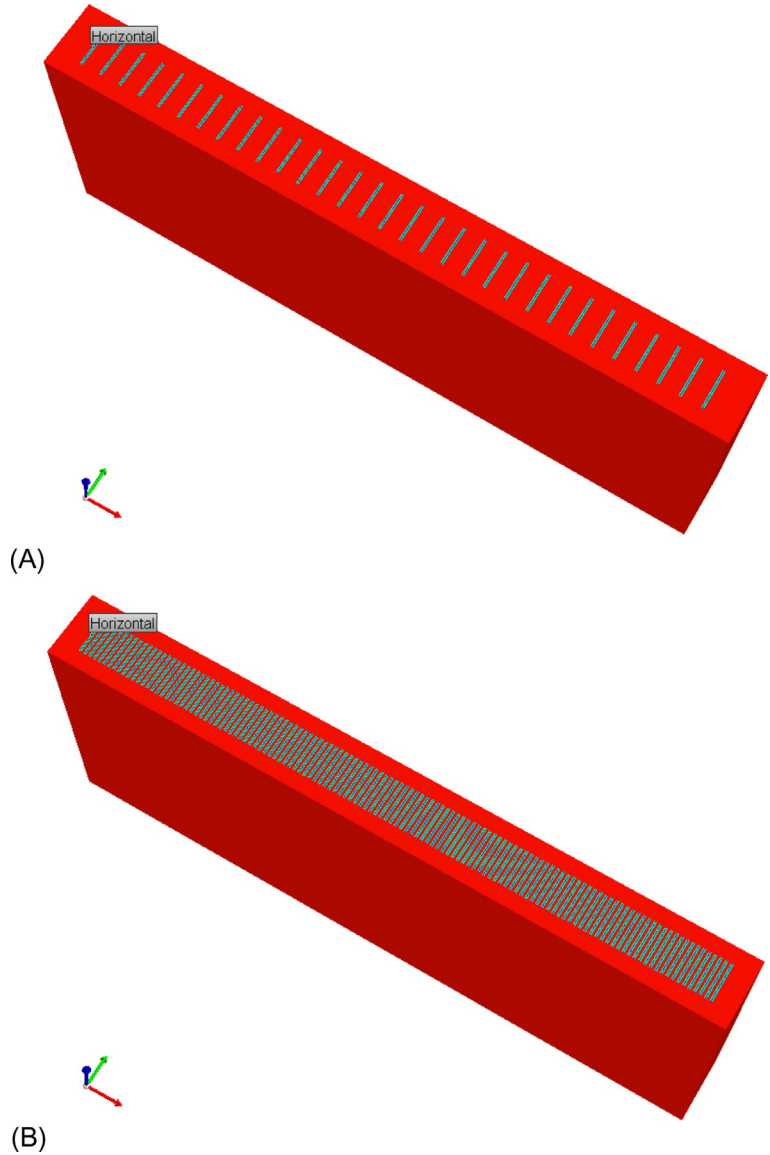

FIG. 6.41 A basic 3D reservoir model including 31 fracturing stages for Bakken tight oil reservoir (Yu, 2015). (A) One effective fracture per stage. (B) Four effective fractures per stage.

four effective fractures in each stage; hence, there are total 124 effective hydraulic fractures along the horizontal well. The stage spacing is 320 ft and the cluster spacing (the distance between two neighboring fractures) is 80 ft for the case with four fractures per stage.

TABLE 6.12 Parameters Used for Simulations in the Middle Bakken (Yu, 2015)

Parameter	Value	Unit
Initial reservoir pressure	7500	psi
Reservoir temperature	240	°F
Total compressibility	1×10^{-6}	psi^{-1}
Horizontal well length	10,000	ft
Reservoir thickness	40	ft
Gas-specific gravity	0.92	
Bubble point	2500	psi
Fracture spacing	80	ft
Fracture half-length	260	ft
Fracture conductivity	10	md-ft
Permeability	10	μD
Porosity	7%	
Water saturation	35%	

The typical fluid and rock properties from the Middle Bakken are used for the subsequent simulation study, as listed in Table 6.12. Six uncertainty parameters were investigated including fracture spacing, fracture half-length, fracture conductivity, permeability, porosity, and water saturation. Each parameter was given a reasonable range with the actual maximum and minimum values or coded symbol of "+1" and "−1" based on the actual field data of the Bakken formation, as listed in Table 6.13. The reservoir is assumed to be homogeneous. Fracture height is equal to the reservoir thickness. A synthetic flowing bottomhole pressure curve is used to represent the real pressure drawdown, as illustrated in Fig. 6.42.

The bottomhole pressure decreases from 7000 to 1000 psi at the early time of production (around 1 year); after that, it stabilizes until the end of production (30 years). The relative permeability curves, such as water-oil relative permeability and liquid-gas relative permeability (see Fig. 6.43), are used in the numerical model.

6.8.1.1 *Effect of Fracture Conductivity*

For the base case, effect of fracture conductivity on cumulative oil production is shown in Fig. 6.44. The range fracture conductivity is from 0.1 to 100 md-ft. As

TABLE 6.13 Six Uncertainty Parameters Investigated in This Study for the Bakken Formation (Yu, 2015)

Parameter	Coded Symbol	Minimum (−1)	Maximum (+1)	Unit
Fracture spacing	A	80	320	ft
Fracture half-length	B	140	380	ft
Fracture conductivity	C	1	100	md-ft
Permeability	D	1	100	μD
Porosity	E	4%	10%	
Water saturation	F	25%	45%	

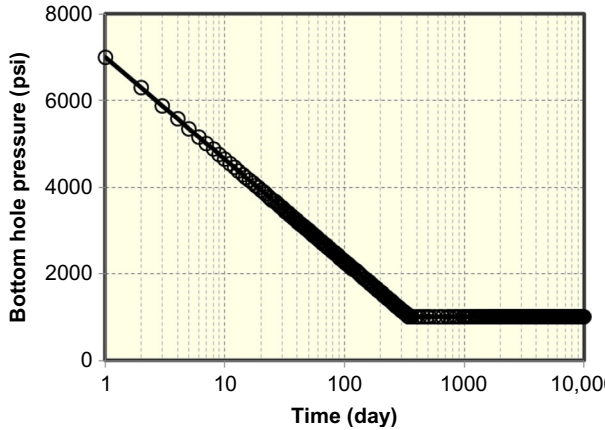

FIG. 6.42 Flowing bottomhole pressure used for simulation of the Bakken formation (Yu, 2015).

shown, there is no big difference of cumulative oil production between 100 and 1000 md-ft, illustrating that the fracture conductivity of 100 md-ft is very close to infinite fracture conductivity in this case study.

6.8.1.2 *Effect of Geomechanics*

For the geomechanics effect, the pressure-dependent fracture conductivity curve used in this case study is shown in Fig. 6.45. As shown, the fracture conductivity corresponding to bottomhole pressure of 1000 psi is about 22% of initial fracture conductivity corresponding to the initial reservoir pressure of

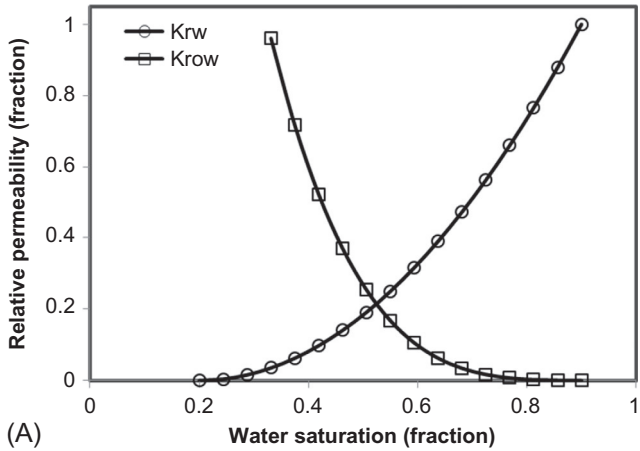

FIG. 6.43 Relative permeability curves for the Middle Bakken tight oil reservoirs (Yu, 2015). (A) Water-oil relative permeability curve. (B) Liquid-gas relative permeability curve.

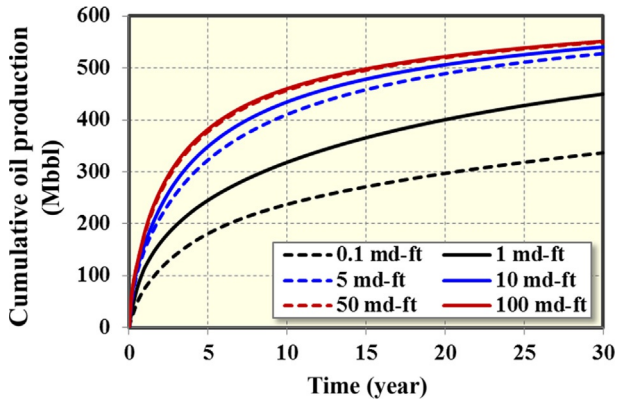

FIG. 6.44 Effect of fracture conductivity on well performance in Bakken (Yu, 2015).

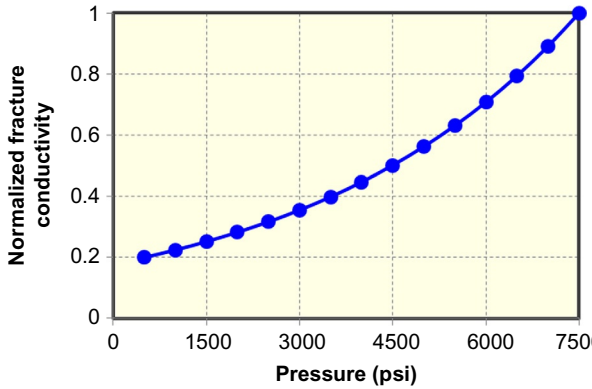

FIG. 6.45 The pressure-dependent fracture conductivity curve for the Middle Bakken (Yu, 2015).

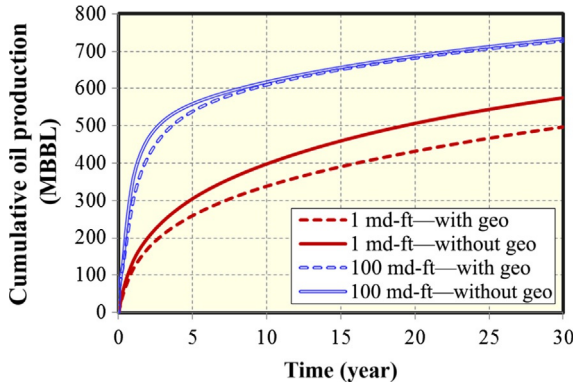

FIG. 6.46 The comparison of well performance with and without the geomechanics effect for two scenarios (Yu, 2015).

7500 psi. Two initial fracture conductivities of 1 and 100 md-ft are used to evaluate the effect of geomechanics. Fig. 6.46 shows the comparison of cumulative oil production with and without the geomechanics effect. It can be seen that the initial fracture conductivity has a significant effect on the contribution of geomechanics to the decline rate of oil recovery. Cumulative oil production at 30 years of production decreases by around 13.6% and 0.8% for initial fracture conductivity of 1 and 100 md-ft, respectively. Hence, consideration of the geomechanics effect is important for completion optimization.

6.8.2 Sensitivity Study

According to six parameters, 32 different simulation cases need to be prepared based on two-level fractional factorial design, as shown in Table 6.14. The

TABLE 6.14 32 Simulation Cases Based on Half Fractional Factorial Design for Six Parameters in the Middle Bakken (Yu, 2015)

Run	A	B	C	D	E	F
1	80	140	1	100	0.10	0.25
2	80	140	100	100	0.10	0.45
3	80	380	100	100	0.04	0.45
4	80	140	1	100	0.04	0.45
5	320	380	100	100	0.04	0.25
6	320	380	1	100	0.10	0.25
7	80	140	1	1	0.10	0.45
8	320	380	1	100	0.04	0.45
9	80	380	1	100	0.04	0.25
10	80	380	1	1	0.10	0.25
11	80	140	1	1	0.04	0.25
12	320	380	100	100	0.10	0.45
13	320	380	100	1	0.04	0.45
14	320	140	1	1	0.04	0.45
15	320	380	1	1	0.10	0.45
16	80	380	1	1	0.04	0.45
17	80	380	100	1	0.04	0.25
18	80	380	1	100	0.10	0.45
19	80	140	100	100	0.04	0.25
20	320	140	100	100	0.04	0.45
21	320	140	1	1	0.10	0.25
22	320	380	100	1	0.10	0.25
23	80	140	100	1	0.10	0.25
24	80	380	100	100	0.10	0.25
25	80	140	100	1	0.04	0.45
26	80	380	100	1	0.10	0.45
27	320	140	100	100	0.10	0.25
28	320	380	1	1	0.04	0.25
29	320	140	100	1	0.04	0.25
30	320	140	100	1	0.10	0.45
31	320	140	1	100	0.10	0.45
32	320	140	1	100	0.04	0.25

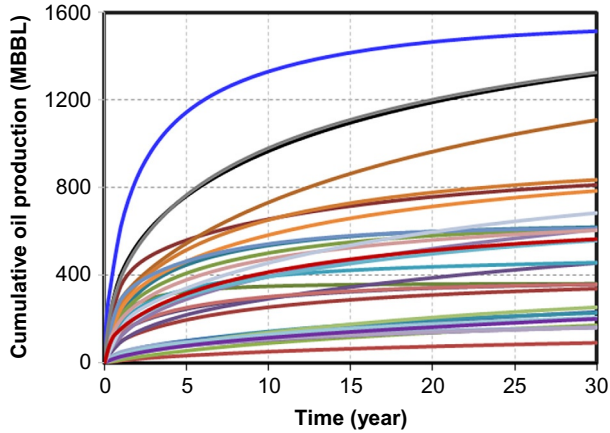

FIG. 6.47 Cumulative oil production of 32 cases for the Middle Bakken (Yu, 2015).

ISPUR is used to generate 32 input files automatically and efficiently for reservoir simulator of CMG-IMEX (CMG-IMEX, 2012). After performing numerical simulations for each case, cumulative oil production and oil recovery factor were obtained and are shown in Figs. 6.47 and 6.48, respectively. The figures clearly show that there is a wide range of cumulative oil production and oil recovery factor. The ranges for the cumulative oil production and oil recovery factor at a 30-year period are obtained as 91.6–1514.9 MBBL (10^3 BBL) and 4.3%–28.7%, respectively. The average cumulative oil production and oil recovery factor are 530.5 MBBL and 16.6%, respectively.

Simulation results from Fig. 6.47 are then used to construct the half-normal plot, Pareto chart, and the analysis-of-variance (ANOVA) table to identify the

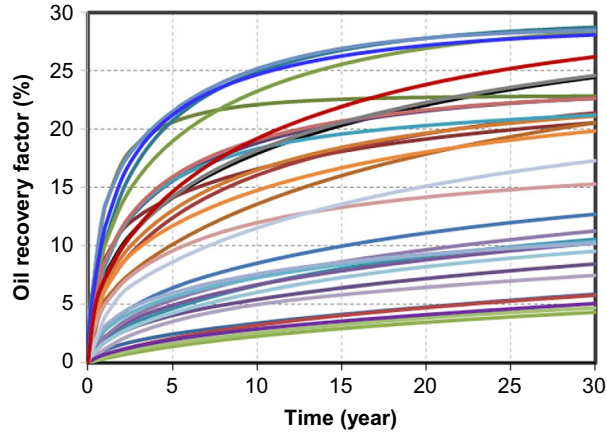

FIG. 6.48 Oil recovery factor of 32 cases for the Middle Bakken (Yu, 2015).

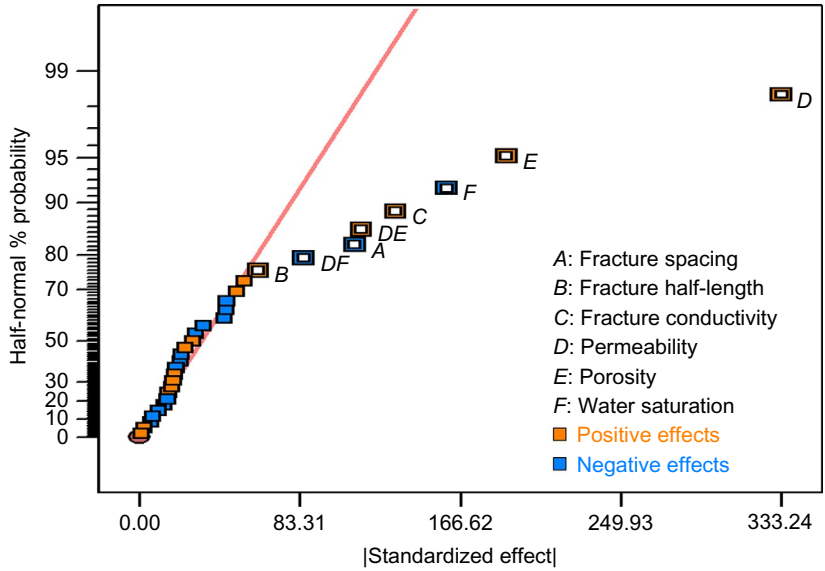

FIG. 6.49 The half normal plot for cumulative oil production at 5 years of production (Yu, 2015).

ranking of significant factors affecting cumulative oil production. The half-normal plot and the corresponding Pareto chart at different period of production for cumulative oil production are presented in Figs. 6.49–6.52. Any parameters or two-parameter interaction highly deviating from the straight line are recognized as the parameters that affect the oil production significantly. At early time of production (5 years) as shown in Figs. 6.49 and 6.51, the following order in terms of influence of main parameter effects is permeability (*D*), porosity (*E*), water saturation (*F*), fracture conductivity (*C*), fracture spacing (*A*), and fracture half-length (*B*); at late time of production (30 years) as shown in Figs. 6.50 and 6.52, the order of influence of main parameters remains the same.

The significant and insignificant model parameters are also determined by the ANOVA table, as shown in Tables 6.15 and 6.16. A parameter having value of "Prob > *F*" (probability of a large *F*-value) <0.1 is called a significant model term. Parameters not presented in Tables 6.15 and 6.16 are insignificant model terms.

The detailed influences of all parameters on the well performance in a short-term period (5 years) and a long-term period (30 years) are shown in Fig. 6.53. It can be observed that impacts of some parameters on cumulative oil production decrease with time, including permeability (*D*), fracture conductivity (*C*), fracture spacing (*A*), and fracture half-length (*B*); while effects of some parameters

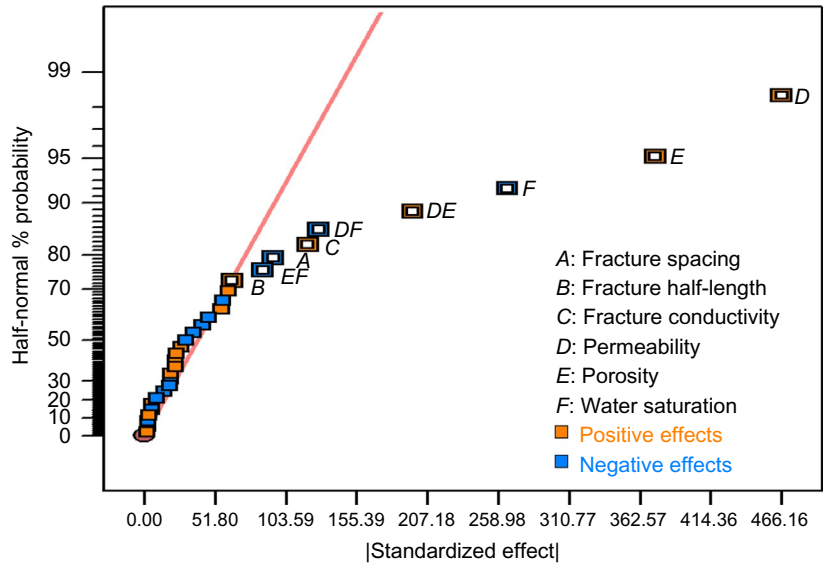

FIG. 6.50 The half normal plot for cumulative oil production at 30 years of production (Yu, 2015).

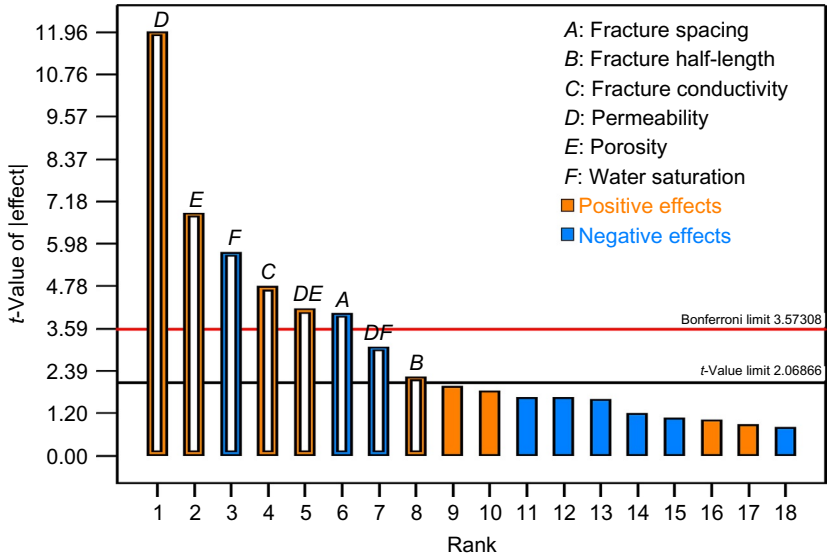

FIG. 6.51 Pareto chart for cumulative oil production at 5 years of production (Yu, 2015).

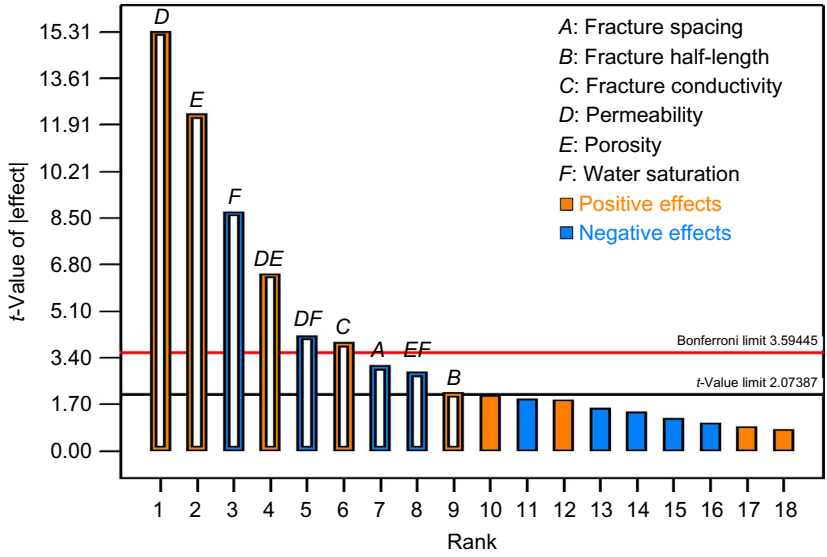

FIG. 6.52 Pareto chart for cumulative oil production at 30 years of production (Yu, 2015).

TABLE 6.15 ANOVA Table for 5 Years of Cumulative Oil Production (Yu, 2015)

Source	Sum of Squares	Degree of Freedom	Mean Square	*F*-Value	*P*-Value
Model	1.818E +006	8	2.272E +005	36.58	<0.0001
A	1.001E +005	1	1.001E +005	16.11	0.0005
B	30,455.12	1	30,455.12	4.90	0.0370
C	1.412E +005	1	1.412E +005	22.72	<0.0001
D	8.884E +005	1	8.884E +005	143.01	<0.0001
E	2.904E +005	1	2.904E +005	46.74	<0.0001
F	2.033E +005	1	2.033E +005	32.73	<0.0001
DE	1.059E +005	1	1.059E +005	17.05	0.0004

TABLE 6.15 ANOVA Table for 5 Years of Cumulative Oil Production (Yu, 2015)—cont'd

Source	Sum of Squares	Degree of Freedom	Mean Square	*F*-Value	*P*-Value
DF	58,055.28	1	58,055.28	9.35	0.0056
Residual	1.429E +005	23	6212.16		
Cor. total	1.961E +006	31			

TABLE 6.16 ANOVA Table for 30 Years of Cumulative Oil Production (Yu, 2015)

Source	Sum of Squares	Degree of Freedom	Mean Square	*F*-Value	*P*-Value
Model	4.138E +006	9	4.598E +005	61.99	<0.0001
A	70,998.54	1	70,998.54	9.57	0.0053
B	33,108.08	1	33,108.08	4.46	0.0462
C	1.148E +005	1	1.148E +005	15.48	0.0007
D	1.738E +006	1	1.738E +006	234.36	<0.0001
E	1.118E +006	1	1.118E +006	150.72	<0.0001
F	5.642E +005	1	5.642E +005	76.06	<0.0001
DE	3.087E +005	1	3.087E +005	41.62	<0.0001
DF	1.300E +005	1	1.300E +005	17.53	0.0004
EF	60,005.14	1	60,005.14	8.09	0.0094
Residual	1.632E +005	22	7417.67		
Cor. total	4.301E +006	31			

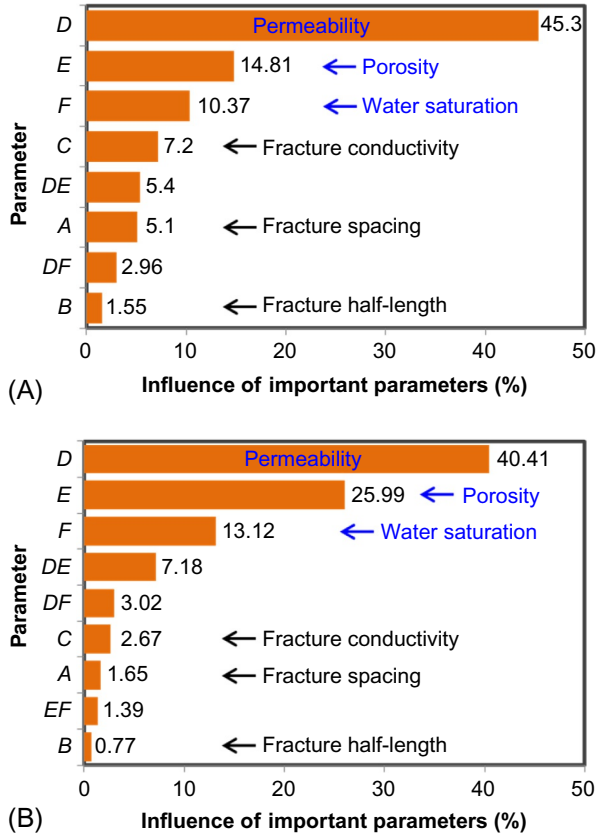

FIG. 6.53 Rank of the influences of uncertainty parameters on cumulative oil production (Yu, 2015). (A) A short-term of production (5 years). (B) A long-term production (30 years).

increase with time, including porosity (E) and water saturation (F). The interactions between various parameters are defined as DE, DF, and EF. As it can be seen, the interaction parameter DE (interaction of permeability and porosity) is more important that the other interaction parameters. The rank of important parameters can provide critical insights into performing history matching with field production data in a short-term period.

6.8.3 History Matching and Production Forecasting

In this study, the field production data of a hydraulically fractured horizontal well from the Middle Bakken in North Dakota is used to perform history matching and production forecasting (Kurtoglu and Kazemi, 2012). In this field case study, the horizontal well was stimulated with 15 hydraulic fracturing stages.

In the model, it is assumed that there are four effective fractures per single stage; so there are a total of 60 hydraulic fractures along the horizontal well. The fracture width is set at 0.001 ft. An area of about 326 acres was simulated by setting up a basic 3D reservoir model using reservoir simulator of CMG-IMEX (CMG-IMEX, 2012) with dimensions of 10,500 ft × 2640 ft × 50 ft, which corresponds to length, width, and thickness, respectively. The other detailed reservoir and fracture properties about this well are listed in Table 6.17. During history matching, bottomhole pressure measured from the field is used for a constraint input, as shown in *red line* in Fig. 6.54. Oil and gas flow rates are the targets for history matching. Permeability, initial water saturation, fracture conductivity, and fracture half-length are mainly tuned to obtain a good match.

The history-matching results for oil and gas flow rate are shown in Figs. 6.55 and 6.56, respectively. As shown, a reasonable match between the numerical simulation results and the actual field data is obtained for oil and gas flow rate, respectively. Based on a good history-matching result, we obtained matrix permeability of 5 μD, fracture half-length of 215 ft, fracture conductivity of 50 md-ft, and initial water saturation of 41%. Fig. 6.57 presents the pressure distribution in 2D view at 1.2 years of field production. It can be seen that the effective drainage area is clearly illustrated in the horizontal fractured Bakken well.

TABLE 6.17 Parameters Used for History Matching in the Middle Bakken (Yu et al., 2014)

Parameter	Value	Unit
Initial reservoir pressure	7800	psi
Reservoir temperature	245	°F
Total compressibility	1×10^{-6}	psi^{-1}
Horizontal well length	8828	ft
Reservoir thickness	50	ft
Gas-specific gravity	0.92	
Bubble point	2500	psi
Oil viscosity	0.32	cp
Fracture spacing	118	ft
Number of fracture	60	
Porosity	5.6%	

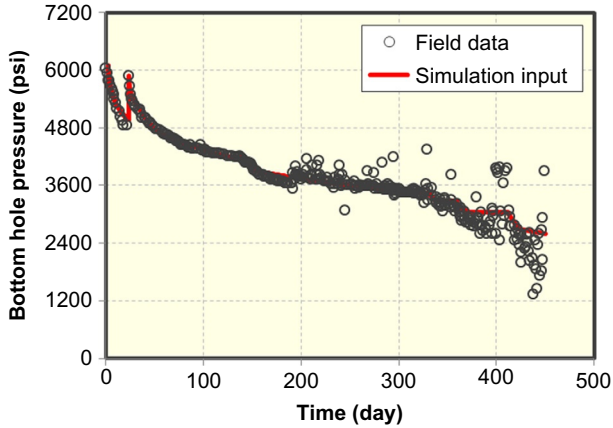

FIG. 6.54 Bottomhole pressure used as a constraint input for history matching (Yu et al., 2014).

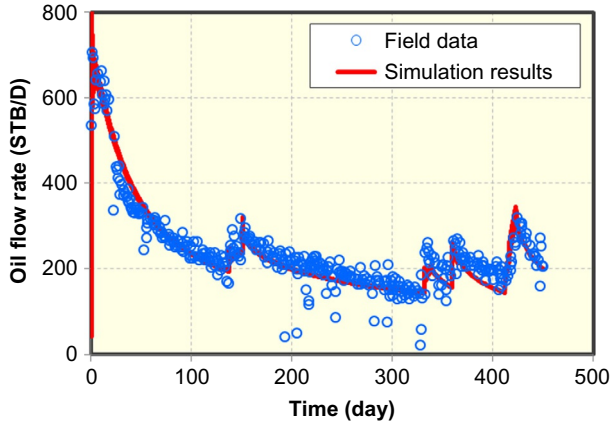

FIG. 6.55 History matching for oil flow rate in the Middle Bakken (Yu et al., 2014).

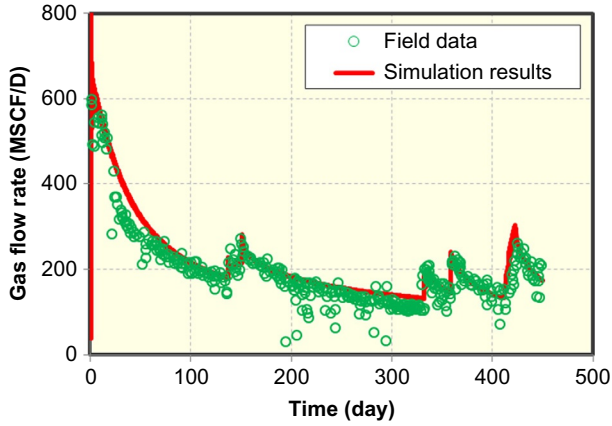

FIG. 6.56 History matching for gas flow rate in the Middle Bakken (Yu et al., 2014).

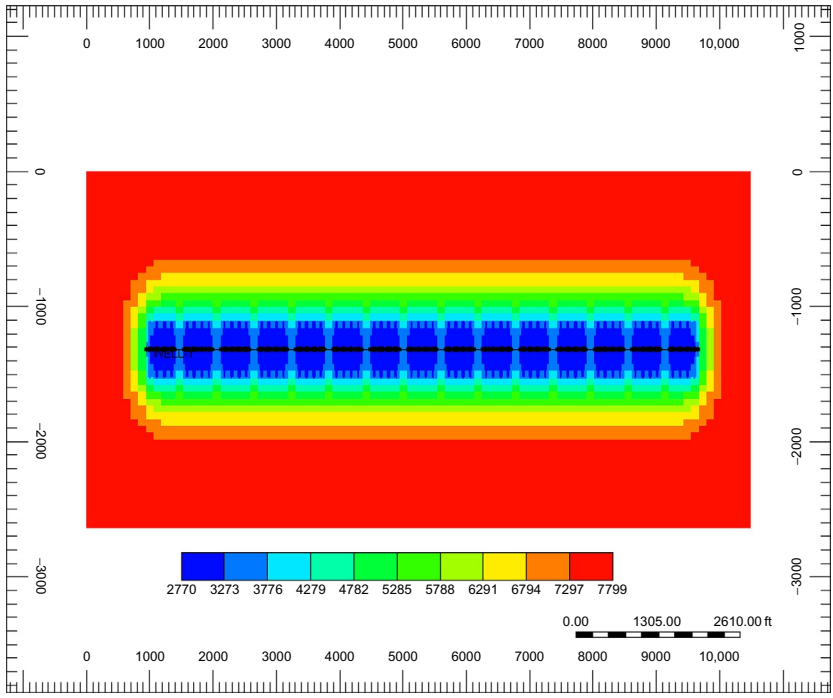

FIG. 6.57 Pressure distribution at end of field production (pressure unit: psi) (Yu et al., 2014).

Incorporating the history match period, we performed a production forecasting for 30 years. After history-matching period, bottomhole pressure of 1000 psi remains constant until 30 years of production. Cumulative oil production and oil recovery factor are shown in Figs. 6.58 and 6.59, respectively. It can be seen that the cumulative oil production and oil recovery factor at 30 years of production are determined as 627 MBBL and 11%, respectively.

6.8.4 Economic Optimization of Multiple Well Placement

After the sensitivity analysis, the response surface of NPV based on the key design variables was built to optimize multiple well placement in the Bakken formation. Totally, there are four uncertain parameters, as shown in Table 6.18. Fracture height is assumed to be equal to reservoir thickness. The matrix permeability was fixed at 5 μD based on history-matching results. The other reservoir and fracture properties are the same as those shown in Table 6.12. The well number in the model ranges from 4 to 8. According to four variables in this study, 25 simulation cases were generated based on the approach of D-optimal design, as shown in Table 6.19. Similarly with

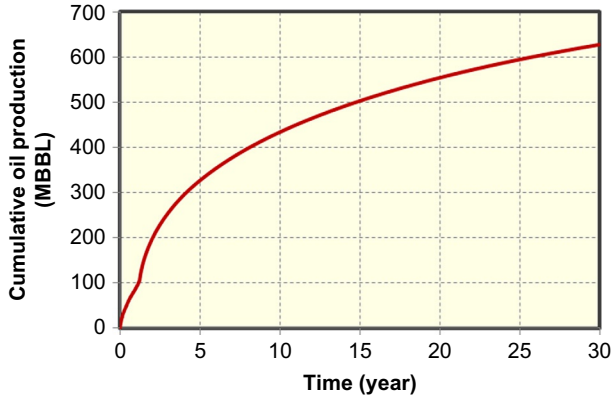

FIG. 6.58 Production forecasting for cumulative oil production at a 30-year period (Yu, 2015).

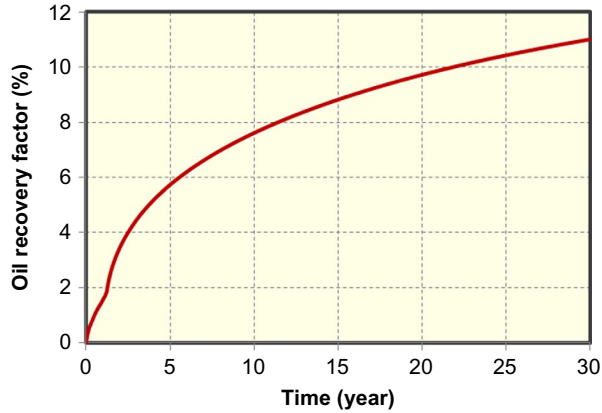

FIG. 6.59 Production forecasting for oil recover factor at a 30-year period (Yu, 2015).

TABLE 6.18 Four Uncertainty Parameters Investigated in This Study for the Bakken Formation (Yu, 2015)

Parameter	Coded Symbol	Minimum (−1)	Maximum (+1)	Unit
Fracture spacing	A	80	320	ft
Fracture half-length	B	140	380	ft
Fracture conductivity	C	1	100	md-ft
Well number	B	4	8	

TABLE 6.19 25 Simulation Cases Based on D-Optimal Design (Yu, 2015)

Run	A	B	C	D
1	320	300	1	4
2	80	140	68	4
3	320	140	100	8
4	320	380	100	4
5	80	380	1	6
6	80	140	55	8
7	160	140	100	6
8	160	380	46	4
9	160	140	100	6
10	160	220	1	8
11	320	140	100	8
12	320	140	85	4
13	160	380	38	8
14	320	380	1	8
15	320	380	100	4
16	320	140	1	7
17	80	140	55	8
18	80	380	100	8
19	80	380	100	8
20	80	300	100	4
21	80	300	57	6
22	80	300	8	4
23	320	140	16	4
24	80	140	1	4
25	320	300	65	7

sensitivity study, the ISPUR of the framework is used to generate 25 cases automatically and efficiently.

After numerical simulation of each case, cumulative oil production was obtained and shown in Fig. 6.60. It clearly shows that the cumulative oil production at 30 years of production has a large uncertainty. This means that further optimization is required.

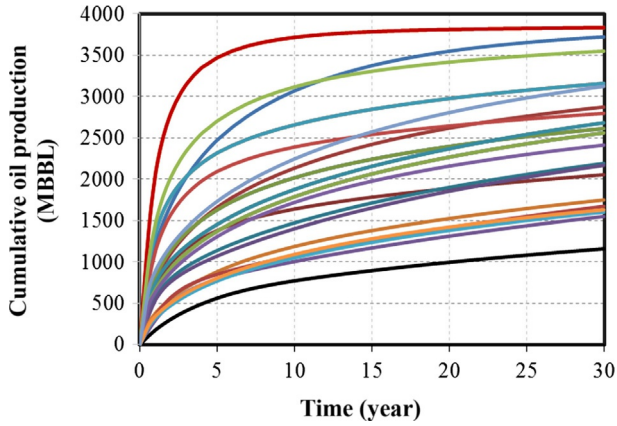

FIG. 6.60 Cumulative oil production of 25 cases for a 30-year period (Yu, 2015).

Once the cumulative oil production of 25 cases was obtained, the economic EXCEL spreadsheet is used to calculate the corresponding NPVs based on the price of oil of $90/BBL, interest rate of 10%, and royalty tax of 12.5%. The fracturing treatments cost includes two parts: drilling cost and completion cost, as shown in Fig. 6.61. It can be seen that the current total drilling and completion cost of Hess Corporation is about $8.4 MM. In this study, the well drilling cost of $5.0 MM is assumed. The completion cost related to fracture area and fracture conductivity, as shown in Figs. 6.27 and 6.28, is used in this study. Fig. 6.62 presents NPVs of 25 simulation cases at 30 years of production.

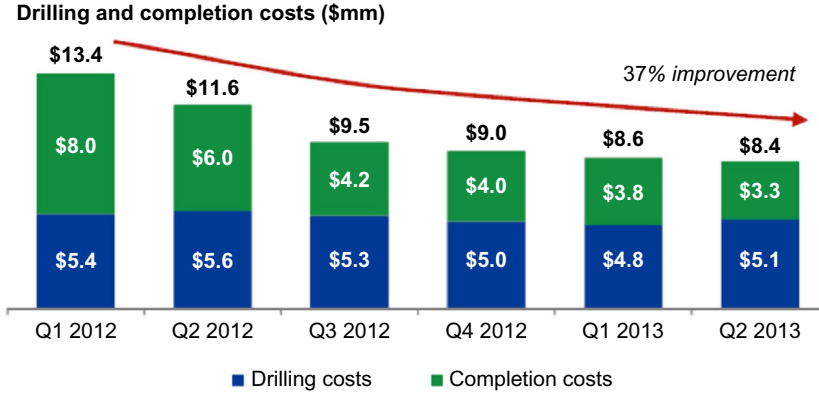

FIG. 6.61 Drilling and completion costs of Hess Corporation in the Bakken formation (Drillinginfo, 2013).

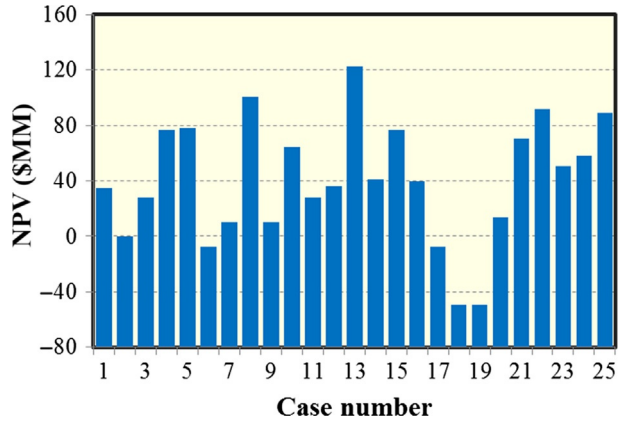

FIG. 6.62 NPVs of 25 cases at 30 years of oil production with the oil price of $90/BBL (Yu, 2015).

TABLE 6.20 Statistical Approach to Select the RSM Model With Oil Price of $90/BBL (Yu, 2015)

Source	Std. Dev.	*R*-Squared	Adjusted *R*-Squared	Predicted *R*-Squared	Press	
Linear	36.33	0.43	0.32	0.104	41,724	
2FI	29.53	0.74	0.74	0.088	42,470	
Quadratic	15.25	0.95	0.95	0.439	26,115	Suggested
Cubic	0.00	1.00	1.00			Aliased

Once NPVs of 25 simulation cases were obtained, the Design-Expert Software package is used to build the NPV response surface model. To select the appropriate model, the statistical approach is used to determine which polynomial fits the equation among linear model, two-factor interaction model (2FI), quadratic model, and cubic model, as shown in Table 6.20. The criterion for selecting the appropriate model is choosing the highest polynomial model, where the additional terms are significant and the model is not aliased. In addition, other criteria are to select the model that has the maximum "Adjusted *R*-Squared" and "Predicted *R*-Squared." Thus, the fully quadratic model is selected to build the NPV response surface in the subsequent optimization process.

The equation fitted to the NPV response surface with the actual factors is presented as:

$$\begin{aligned} NPV = & -132.77 + 0.79205 \times A + 0.55511 \times B - 0.053947 \times C + 31.36357 \times D \\ & - 3.25027 \times 10^{-4} \times AB + 4.94319 \times 10^{-3} \times AC + 0.047027 \times AD \\ & + 1.37909 \times 10^{-3} \times BC - 1.54091 \times 10^{-3} \times BD - 0.048211 \times CD \\ & - 2.72371 \times 10^{-3} \times A^2 - 7.80724 \times 10^{-4} \times B^2 - 0.013985 \times C^2 \\ & - 3.54896 \times D^2, \end{aligned} \tag{6.8}$$

where A is fracture spacing, B is fracture half-length, C is fracture conductivity, and D is well number.

The normal plot of residuals, reflecting the distribution of the residuals, is shown in Fig. 6.63. All the points in the "normal plot of residuals" fall on the straight line, meaning the residuals are normally distributed. Fig. 6.64 shows the plot of "Predicted vs. Actual," illustrating whether the generated equation of NPV response surface accurately predicts the actual NPV values. It can be seen that generated NPV response surface models provide such reliable predicted values of NPV, as compared with the actual values of NPV. This means that the generated NPV response surface model is reliable.

Fig. 6.65 shows the 3D surface of NPV at varied values of fracture conductivity and fracture spacing. It shows that there is an optimal fracture design related to fracture conductivity and fracture spacing. Therefore, this

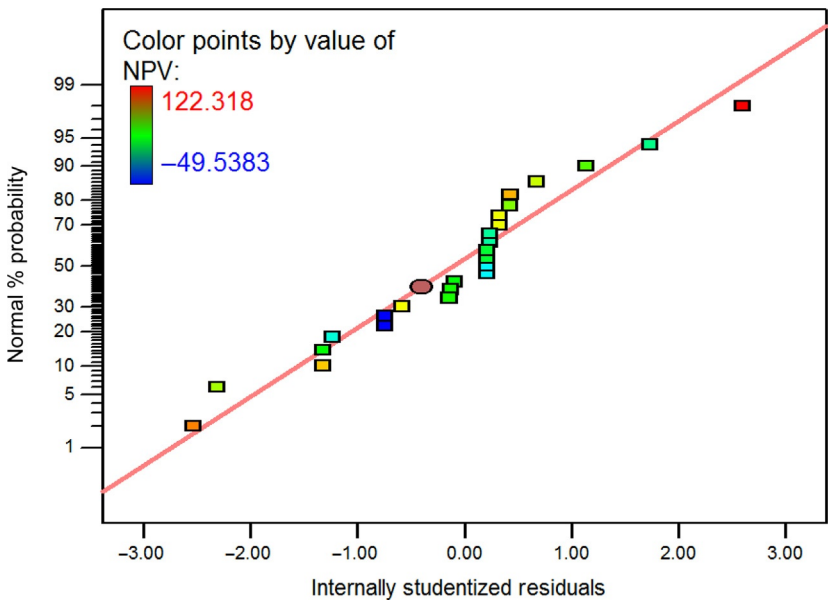

FIG. 6.63 Normal plot of residuals at oil price of $90/BBL (Yu, 2015).

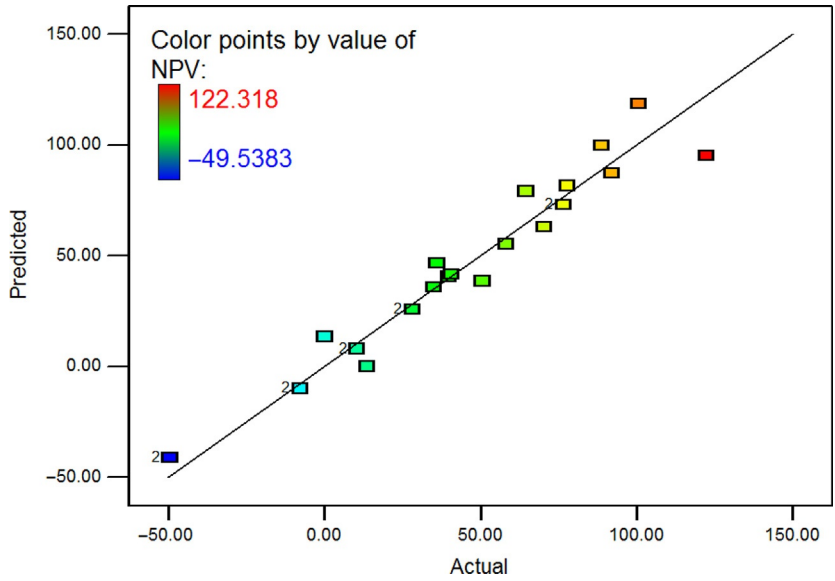

FIG. 6.64 Predicted NPV versus the actual NPV plot at oil price of $90/BBL (Yu, 2015).

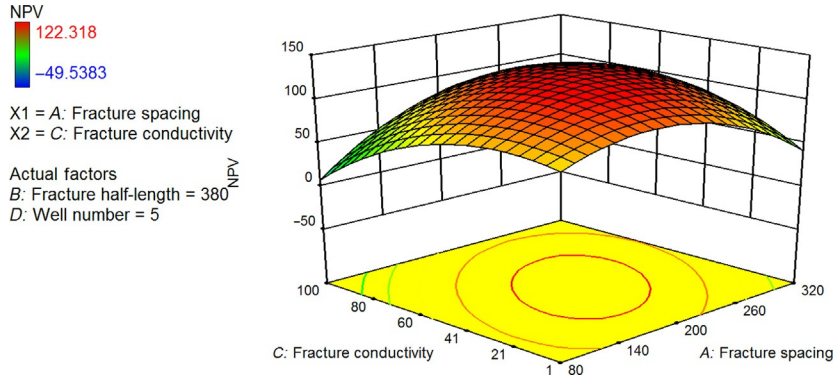

FIG. 6.65 3D surface of NPV at varied values of fracture conductivity and fracture spacing (Yu, 2015).

methodology can provide some insights into optimization of fracturing treatment design to obtain the maximum economic viability of the field.

The objective function of NPV will be maximized by selecting the best combinations with uncertain parameters through the method of RSM. The best case is obtained based on the range of parameters investigated in this study for the Bakken formation. The best case with the highest NPV value of $124.77 MM ($10^6$) corresponding to fracture spacing of 160 ft, fracture half-length of 340 ft, fracture conductivity of 35 md-ft, and well number of 5, as shown in Figs. 6.66 and 6.67.

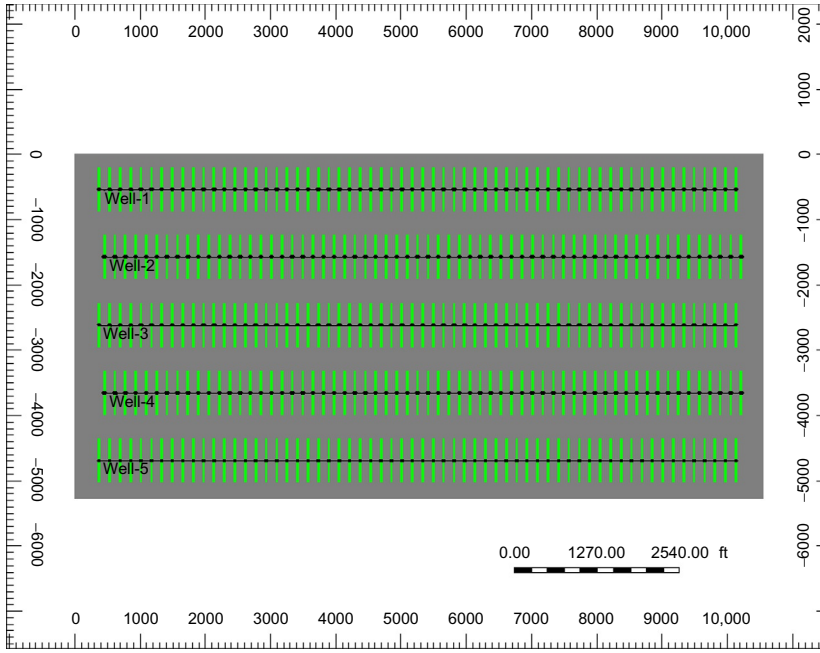

FIG. 6.66 The best case in 2 dimensions with fracture spacing of 160 ft, fracture half-length of 340 ft, fracture conductivity of 35 md-ft, and well number of 5 for the Middle Bakken (Yu, 2015).

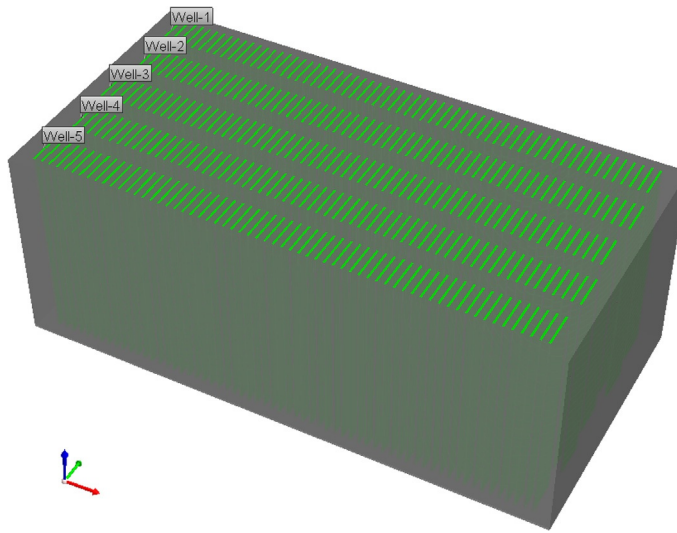

FIG. 6.67 The best case in 3 dimensions with fracture spacing of 160 ft, fracture half-length of 340 ft, fracture conductivity of 35 md-ft, and well number of 5 for the Middle Bakken (Yu, 2015).

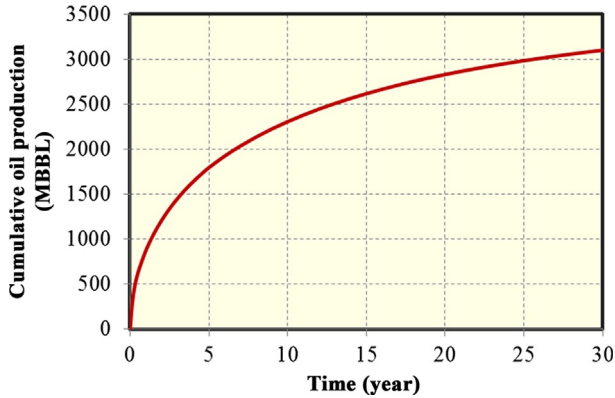

FIG. 6.68 Production forecasting for cumulative oil production at a 30-year period (Yu, 2015).

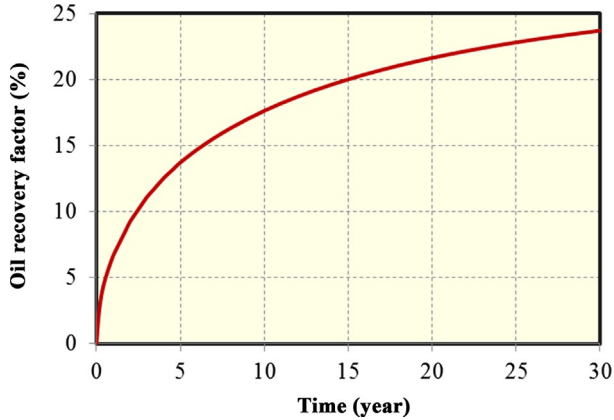

FIG. 6.69 Production forecasting for oil recover factor at a 30-year period (Yu, 2015).

Cumulative oil production and oil recovery factor are shown in Figs. 6.68 and 6.69, respectively. It can be seen that the cumulative oil production and oil recovery factor at 30 years of production are determined as 3101 MBBL and 23.7%, respectively.

Figs. 6.70 and 6.71 present pressure distribution for the best case at 1 month and 30 years of oil production, respectively, illustrating the drainage volume clearly.

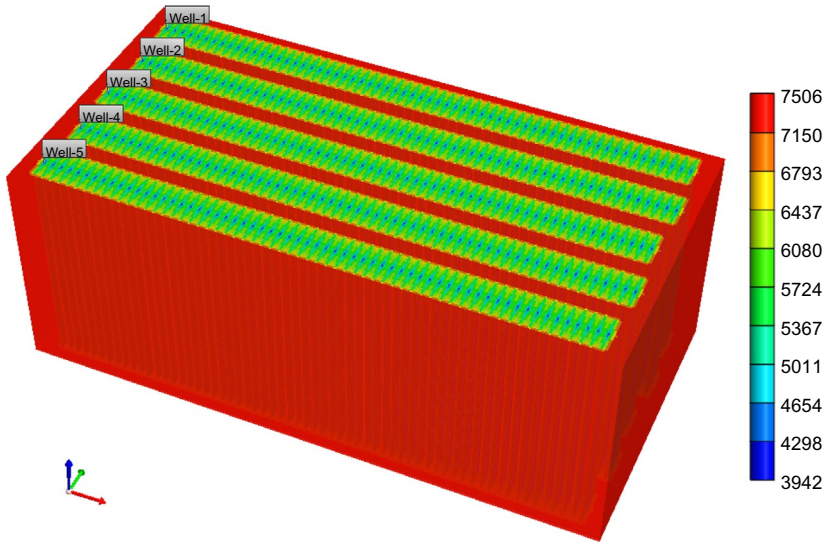

FIG. 6.70 Pressure distribution at 1 month of production for the best case (pressure unit: psi) (Yu, 2015).

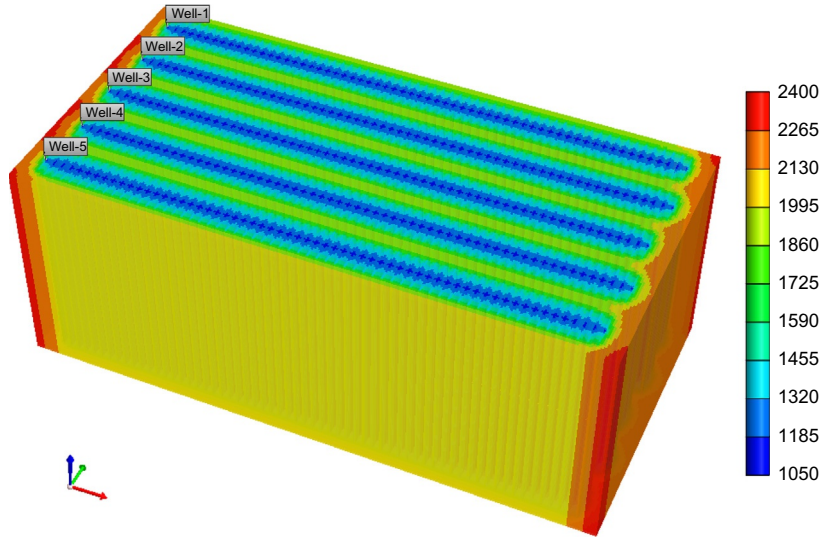

FIG. 6.71 Pressure distribution at 30 years of production for the best case (pressure unit: psi) (Yu, 2015).

REFERENCES

Anderson, M.J., Whitcomb, P.J., 2007. DOE Simplified: Practical Tools for Effective Experimentation, second ed. Productivity Press, New York.

Bagherian, B., Sarmadivaleh, M., Ghalambor, A., Nabipour, A., Rasouli, V., Mahmoudi, M., 2010. In: Optimization of multiple-fractured horizontal tight gas well. Paper SPE 127899, SPE International Symposium and Exhibition on Formation Damage Control, Lafayette, LA.

Besler, M.R., Steele, J.W., Egan, T., Wagner, J., 2007. In: Improving well productivity and profitability in the Bakken—a summary of our experiences drilling, stimulating, and operating horizontal wells. Paper SPE 110679, SPE Annual Technical Conference and Exhibition, Anaheim, CA.

Bhattacharya, S., Nikolaou, M., 2011. In: Optimal fracture spacing and stimulation design for horizontal wells in unconventional gas reservoirs. Paper SPE 147622, SPE Annual Technical Conference and Exhibition, Denver, CO.

Britt, L.K., Smith, M.B., 2009. In: Horizontal well completion, stimulation optimization, and risk mitigation. Paper SPE 125526, SPE Eastern Regional Meeting, Charleston, WV.

Cavalcante Filho, J.S.A., Shakiba, M., Moinfar, A., Sepehrnoori, K., 2015. In: Implementation of a preprocessor for embedded discrete fracture modeling in an IMPEC compositional reservoir simulator. Paper SPE 173289, SPE Reservoir Simulation Symposium, Houston, TX.

Cherian, B.V., Nichols, C.M., Panjaitan, M.L., Krishnamurthy, J.K., Sitchler, J., 2013. In: Asset development drivers in the Bakken and Three Forks. Paper SPE 163855, SPE Hydraulic Fracturing Technology Conference, The Woodlands, TX.

Cipolla, C.L., Maxwell, S., Mack, M., 2012. In: Engineering guide to the application of microseismic interpretations. Paper SPE 152165, SPE Hydraulic Fracturing Technology Conference, The Woodlands, TX.

Cipolla, C.L., Wallace, J., 2014. In: Stimulated reservoir volume: a misapplied concept?. Paper SPE 168596, SPE Hydraulic Fracturing Technology Conference, The Woodlands, TX.

Cipolla, C.L., Warpinski, N.R., Mayerhofer, M.J., Lolon, E.P., 2008. In: The relationship between fracture complexity, reservoir properties, and fracture treatment design. Paper SPE 115769, SPE Annual Technical Conference and Exhibition, Denver, CO.

CMG-GEM, 2012. GEM User's Guide. Computer Modeling Group Ltd.

CMG-IMEX, 2012. IMEX User's Guide. Computer Modeling Group Ltd.

Computer Modeling Group Ltd., 2012. CMG Reservoir Simulator. http://www.cmgl.ca/.

Damsleth, E., Hage, A., Volden, R., 1992. Maximum information at minimum cost: a north sea field development study with an experimental design. J. Pet. Technol. 44, 1350–1356.

Daniels, J., Waters, G., LeCalvez, J., Lassek, J., Bentley, D., 2007. In: Contacting more of the Barnett shale through an integration of real-time microseismic monitoring, petrophysics, and hydraulic fracture design. Paper SPE 110562, SPE Annual Technical Conference and Exhibition, Anaheim, CA.

Dejean, J.P., Blanc, G., 1999. In: Managing uncertainties on production predictions using integrated statistical methods. Paper SPE 56696, SPE Annual Technical Conference and Exhibition Proceedings, Houston, TX.

Drillinginfo, 2013. 5 Top Bakken Shale Producers—What's Their Secret? http://infodrillinginfo.com/5-top-bakken-shale.

Evans, R.D., Civan, F., 1994. Characterization of Non-Darcy Multiphase Flow in Petroleum Bearing Formations. Report, U.S. DOE Contract No. DE-AC22-90BC14659, School of Petroleum and Geological Engineering, University of Oklahoma.

Fan, L., Thompson, J.W., Robinson, J.R., 2010. In: Understanding gas production mechanism and effectiveness of well stimulation in the Haynesville shale through reservoir simulation. Paper

SPE 136696, Canadian Unconventional Resources and International Petroleum Conference, Calgary, Canada.

Flowers, J.R., Guetta, D.R., Stephenson, C.J., Jeremie, P., d'Arco, N., 2014. In: A statistical study of proppant type vs. well performance in the Bakken central basin. Paper SPE 168618, SPE Hydraulic Fracturing Technology Conference, The Woodlands, TX.

Ganpule, S., Cherian, B., Gonzales, V., Hudgens, P., Aguirre, P.R., Mata, D., Olarte, D.P., Yunuskhojayev, A., Moore, W.R., 2013. In: Impact of well completion on the uncertainty in technically recoverable resource estimation in Bakken and Three Forks. Paper SPE 167131, SPE Unconventional Resource Conference, Calgary, Canada.

Gorucu, S.E., Ertekin, T., 2011. In: Optimization of the design of transverse hydraulic fractures in horizontal wells placed in dual porosity tight gas reservoirs. Paper SPE 142040, SPE Middle East Unconventional Gas Conference and Exhibition, Muscat, Oman.

Handren, P., Palisch, T., 2007. In: Successful hybrid slickwater fracture design evolution—an east Texas cotton valley taylor case history. Paper SPE 110451, SPE Annual Technical Conference and Exhibition, Anaheim, CA.

Kiefer, J., Wolfowitz, J., 1959. Optimum designs in regression problems. Ann. Math. Stat. 30 (2), 271–294.

Kurtoglu, B., Kazemi, H., 2012. In: Evaluation of Bakken performance using coreflooding, well testing, and reservoir simulation. Paper SPE 155655, SPE Annual Technical Conference and Exhibition, San Antonio, TX.

LaFollette, R.F., Carman, P.S., 2010. In: Proppant diagenesis: results so far. Paper SPE 131782, SPE Unconventional Gas Conference, Pittsburgh, Pennsylvania.

Luo, S., Wolff, M., Ciosek, J., Rasdi, F., Neal, L., Arulampalam, R., Willis, S., 2011. In: Probabilistic reservoir simulation workflow for unconventional resource play: Bakken case study. Paper SPE 142896, SPE EUROPEC/EAGE Annual Conference and Exhibition, Vienna, Austria.

Marongiu-Porcu, M., Wang, X., Economides, M.J., 2009. In: Delineation of application: physical and economic optimization of fractured gas wells. Paper SPE 120114, SPE Production and Operations Symposium, Oklahoma City, OK.

Maxwell, S.C., Weng, X., Kresse, O., Rutledge, J., 2013. In: Modeling microseismic hydraulic fracture deformation. Paper SPE 166312, SPE Annual Technical Conference and Exhibition, New Orleans, LA.

Mayerhofer, M.J., Lolon, E.P., Warpinski, N.R., Cipolla, C.L., Walser, D., Rightmire, C.M., 2008. In: What is stimulated reservoir volume (SRV)?. Paper SPE 119890, SPE Shale Gas Production Conference, Fort Worth, TX.

McDaniel, G.A., Abbott, J., Mueller, F.A., Mueller, F., Mokhtar, A., Pavlova, S., Nevvonen, O., Parias, T., Alary, J.A., 2010. In: Changing the shape of fracturing: new proppant improves fracture conductivity. Paper SPE 135360, SPE Annual Technical Conference and Exhibition, Florence, Italy.

McDaniel, R.R., Willingham, J.R., 1978. In: The effects of various proppants and proppant mixtures on fracture permeability. Paper SPE 7573, The 53rd Annual Fall Technical Conference and Exhibition, Houston, TX.

Meissner, F.F., 1978. In: Estelle, D., Miller, R. (Eds.), Petroleum geology of the Bakken formation, Williston Basin, North Dakota and Montana. The Economic Geology of the Williston Basin, 1978 Williston Basin Symposium, Billings, Montana. Montana Geological Society, pp. 207–230.

Meyer, B.R., Bazan, L.W., Jacot, R.H., Lattibeaudiere, M.G., 2010. In: Optimization of multiple transverse hydraulic fractures in horizontal wellbores. Paper SPE 131732, SPE Unconventional Gas Conference, Pittsburgh, PA.

Moinfar, A., 2013. Development of an Efficient Embedded Discrete Fracture Model for 3D Compositional Reservoir Simulation in Fractured Reservoirs. (PhD Dissertation), The University of Texas at Austin.

Myers, R.H., Montgomery, D.C., Anderson-Cook, C., 2008. Response Surface Methodology: Process and Product Optimization Using Designed Experiments, third ed. New York, John Wiley and Sons.

Nojabaei, B., Johns, R.T., Chu, L., 2013. Effect of capillary pressure on phase behavior in tight rocks and shales. SPE Reserv. Eval. Eng. 16 (3), 281–289.

Peng, C.Y., Gupta, R., 2003. In: Experimental design in determining modeling: assessing significant uncertainties. Paper SPE 80537, SPE Asia Pacific Oil and Gas Conference and Exhibition, Jakarta, Indonesia.

Pope, C., Benton, T., Palisch, T., 2009. In: Haynesville shale—one operator's approach to well completions in this evolving play. Paper SPE 125079, SPE Annual Technical Conference and Exhibition, New Orleans, LA.

Rankin, R., Thibodeau, M., Vincent, M.C., Palisch, T.T., 2010. In: Improved production and profitability achieved with superior completions in horizontal wells: a Bakken/Three Forks case history. Paper SPE 134595, SPE Annual Technical Conference and Exhibition, Florence, Italy.

Schlumberger, 2012. ECLIPSE Reservoir Engineering Software. http://www.softwareslb.com/products/domains/Pages/reservoir-engineering.aspx.

Schmidt, D., Rankin, P.E.R., Williams, B., Palisch, T., Kullman, J., 2014. In: Performance of mixed proppant sizes. Paper SPE 168629, SPE Hydraulic Fracturing Technology Conference, The Woodlands, TX.

Shakiba, M., 2014. Modeling and Simulation of Fluid Flow in Naturally and Hydraulically Fractured Reservoirs Using Embedded Discrete Fracture Model (EDFM). (Master Thesis)The University of Texas at Austin.

Stat-Ease, Inc., 2014. Design-Expert® 8 User's Guide. .

U.S Energy Information Administration, 2014. Drilling Productivity Report. http://www.eia.gov/petroleum/drilling/#tabs-summary-1.

United States Geological Survey (USGS), 2013. USGS Releases New Oil and Gas Assessment for Bakken and Three Forks Formations. USGS Webpost. http://www.usgs.gov/blogs/features/usgs_top_story/usgs-releases-new-oil-and-gas-assessment-for-bakken-and-three-forks-formations/.

UTCOMP, 2014. The University of Texas at Austin.

West, D.R.M., Harkrider, J., Besler, M.R., Barham, M., Mahrer, K.D., 2013. In: Optimized production in the Bakken shale: south antelope case study. Paper SPE 167168, SPE Unconventional Resources Conference, Calgary, Canada.

Wu, K., Olson, J.E., 2015. Simultaneous multi-frac treatments: fully coupled fluid flow and fracture mechanics for horizontal wells. SPE J. 20 (2), 337–346.

Yu, W., 2015. Developments in Modeling and Optimization of Production in Unconventional Oil and Gas Reservoirs. (PhD Dissertation), The University of Texas at Austin.

Yu, W., Lashgari, H.R., Sepehrnoori, K., 2014. In: Simulation study of CO_2 huff-n-puff process in Bakken tight oil reservoirs. Paper SPE 169575, SPE Western North American and Rocky Mountain Joint Meeting, Denver, CO.

Zhang, J., 2005. IRSS: An Integrated Reservoir Simulation System. (PhD Dissertation), The University of Texas at Austin.

Zhang, J., Delshad, M., Sepehrnoori, K., 2007. Development of a framework for optimization of reservoir simulation studies. J. Pet. Sci. Eng. 59, 135–146.

Zhang, X., Du, C., Deimbacher, F., Crick, M., Harikesavanallur, A., 2009. In: Sensitivity studies of horizontal wells with hydraulic fractures in shale gas reservoirs. Paper IPTC 13338, International Petroleum Technology Conference, Doha, Qatar.

Chapter 7

An Assisted History-Matching Workflow Using a Proxy-Based Approach for Shale Reservoirs

Chapter Outline

7.1 INTRODUCTION

A large number of horizontal wells have been extensively drilled to explore unconventional resources, such as shale gas and tight oil. Each well behaves differently, highly dependent on effective fracture networks generated underground. The existing large uncertainty in both reservoir and fracture information enlarges the nonunique feature of history matching. The conventional method of manually adjusting uncertain parameters to achieve a good match with production data is very time consuming and generally unreliable to perform long-term production forecasting. Hence, an assisted history-matching workflow to automatically tune uncertain parameters to obtain multiple history-matching solutions in a probabilistic manner is necessary.

Shale Gas and Tight Oil Reservoir Simulation. https://doi.org/10.1016/B978-0-12-813868-7.00007-9

There are various uncertainties in reservoir characterization of unconventional tight reservoirs, which pose big challenges in reservoir simulation. The shale matrix permeability could vary from a few hundred nanodarcies to a few millidarcies (EIA, 2013). It is difficult to accurately measure and estimate in both experimental and theoretical investigations due to the complex flow behavior through nanoscale pore throats (Sakhaee-Pour and Bryant, 2012). In addition, accurate calibration of fracture properties such as fracture length, fracture height, fracture conductivity, and fracture distribution is very difficult. It is also challenging to efficiently perform production simulation for shale reservoir with complex fracture geometry. Hence, a systematic and effective approach is needed to perform history-matching process by considering all of these uncertainties. Many history-matching studies for shale reservoirs in the literature are mainly focused on one possible match without resolving the nonunique issue, which is classified as deterministic approach (Li et al., 2011; Feng et al., 2012; Kurtoglu and Kazemi, 2012; Yu et al., 2014; Siddiqui et al., 2015). The uncertainty in long-term production prediction cannot be captured.

Various assisted history-matching techniques have been developed to capture the uncertainty in unknown variables and prediction, which can be widely categorized as optimization-based and proxy-based approaches (Maschio and Schiozer, 2013; Bhark and Dehghani, 2014; Goodwin, 2015). The optimization-based approach will efficiently locate the global minimum history-matching error region through optimization algorithms to explore a predefined parameter space of all uncertain parameters. Genetic algorithms and particle-swarm optimization are examples of the optimization-based approach. However, the probabilistic relationship of uncertain reservoir and fracture properties cannot be exemplified. On the other hand, the proxy-based approach can systematically quantify the probability relationship between uncertain parameters and history-matching misfit, which is the discrepancy of observed field data and simulation data. Response surface methodology (RSM), Kriging, and artificial neural network are examples and are widely used to construct the proxy models, which can approximate the full numerical reservoir simulation to predict the history-matching misfit. Due to its simplicity and efficiency, the proxy model can facilitate the history-matching process to locate the history-matching solutions within the predefined parameter space of all uncertain parameters. However, the proxy-based approach has not yet been widely used in unconventional oil and gas reservoirs, which is the main focus of this study.

During the history-matching process using the proxy-based approach, the design of experiment (DoE) is often used to do screening of significant uncertain parameters and the RSM is often applied to do solving for probabilistic history-matching solutions. Both numerical and categorical variables can be treated as uncertain parameters. For example, different relative

permeability curves can be considered. In addition, the proxy modeling process (e.g., polynomial regression) is faster compared to the numerical reservoir simulation process. It benefits the history-matching process. However, building an accurate proxy model to adequately approximate actual reservoir simulation is not an easy task. First, the number of uncertain parameters significantly affects the complexity of the proxy modeling. More parameters will enlarge the design space of unknowns, leading to additional regression errors of the proxy models. The number of significant uncertain parameters must be determined to sufficiently explain the variations of the proxy model response. Second, the number of simulation cases generated based on a RSM design may not be sufficient to construct proxy models with satisfactory accuracy. In general, the scattered points are generated over the design space using the RSM. There are not enough points generated in the region of interest with low history-matching errors, resulting in the low accuracy of the proxy models. It has been reported in the literature that an iteration proxy modeling process is required to improve the accuracy of the proxy models to satisfy given criteria (Peake et al., 2005; Billiter et al., 2008; Slotte and Smorgrav, 2008; Kassenov et al., 2014). Third, the proxy models might reduce the precision due to smoothing out the predicted response surface (Zubarev, 2009). Hence, it is important to validate the proxy model results against the actual reservoir simulation results to improve both accuracy and precision of the proxy model. An additional filtering step is recommended by some literatures to ensure that the predicted history-matching error is acceptable (Billiter et al., 2008; Kassenov et al., 2014).

After obtaining multiple simulation cases with good history match results, they are generally used to perform long-term production forecasting (Gupta et al., 2008; Vink et al., 2015; Yang et al., 2015). Then, a cumulative distribution function (CDF) of estimated ultimate recovery (EUR) is given based on a statistic confidence level such as P10, P50, and P90. In addition, a proxy model of EUR at certain time of long-term production is built to provide a large number of samples to predict the EUR distribution (Fillacier et al., 2014; Collins et al., 2015). It should be mentioned that the generated CDF is an empirical function to approximate the true CDF. The quality of approximation highly depends on its accuracy. Through multiple iterations, the accuracy of the proxy models can be improved significantly. During the iteration process, sampling algorithms such as Monte Carlo or Markov chain Monte Carlo (MCMC) can be used to generate points at the region with low history-matching errors. Nonetheless, it is important point out that even though the final proxy model is strictly rigorous, it is still an approximation of the actual simulation.

In this chapter, we introduce an iterative history-matching workflow through integrating multiple techniques such as DoE, RSM, Monte Carlo, MCMC, and reservoir simulator to perform automatic history matching, production forecasting, and uncertainty quantification in shale reservoirs.

7.2 METHODOLOGY

History matching is the experiment to find the acceptable scenarios of uncertain parameters that minimize the discrepancies between the actual and simulated reservoir behavior. In this study, the DoE is used to analyze how these uncertain parameters relate to the discrepancies known as response parameters. Generally, DoE creates a strategy for proxy models—specifying the design points within the predefined ranges of uncertain parameters to be regressed. Then, the value of response parameters can be approximated quickly from proxy models. The method is easy to use and compatible with both numerical and categorical uncertain parameters. In the whole, the benefits from DoE's ability are to reduce the required simulation cases (the size of experiment), while yielding sufficient response parameters information.

One basic type of DoE is a two-level factorial design, which applies to linear polynomial models. The two-level factorial design requires only the maximum and minimum of the input factors. Therefore, the design generates 2^k cases from k input factors. Even though the linear models normally have the limitation of prediction accuracy, they still give us useful information about the relative effects of each uncertain parameter (at minimum and maximum) on response parameters. With this information, screening study is performed to determine which uncertain parameters have significant impacts on response parameters. However, poor fitting quality sometimes occurs in linear model as two-level factorial design, specifically when actual data suggest curvature in response parameters. Therefore, in this case, more complex model, such as a full quadratic polynomial model, is required (Myers et al., 2009; Wass, 2011).

RSM is another term to describe the process in DoE that builds proxy models by using high-degree polynomial. Although the high-degree polynomial model requires more number of design points and more computational resources, it provides more flexibility to bend and curve along the highly complex responses. The more number of design points are, the more information the response parameters provide and then strengthen the decision what an appropriate polynomial model should be used.

To create RSM optimally for a highly nonlinear problem, optimal design, e.g., D-optimal and I-optimal designs, has been widely used. Optimal design adopts statistic optimal criteria to reduce the number of required design points while maintaining the same accuracy. D-optimal design aims to identify significant input factors while I-optimal design is recommended for prediction because it automatically selects the points that minimizes the integral of the prediction variance across the design space (Jones and Goos, 2012).

Regardless of regressed polynomial models, the regression coefficients that are estimated from linear least-square method depend on the design points in the parameter space—how many design points are there and how they are distributed in the parameter space. In order to retrieve a better proxy model—the observed data building an accurate proxy model in the region of interest—the

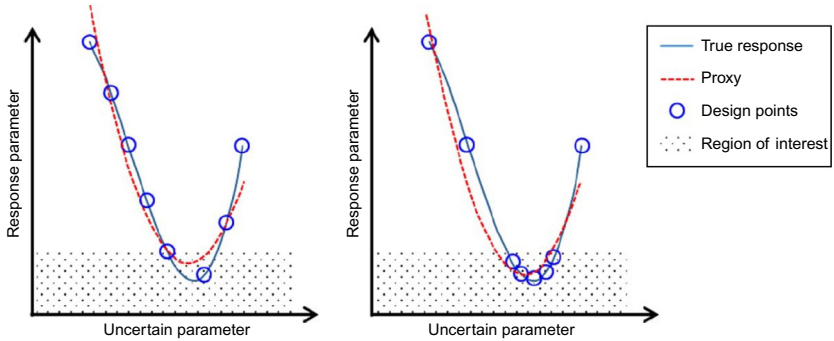

FIG. 7.1 Comparison of true response and the proxy model under different design points distributed in the region of interest (Wantawin et al., 2017).

proxy model should be reconstructed by adding new design points and/or considering alternative regression equations. To illustrate, Fig. 7.1 shows two proxy model examples with equal number of design points. As one can see, the true response in the shaded area or the region of interest is approximated better when the number of design points inside the region of interest is larger. Therefore, proxy models should be refined in the region of interest by allocating more design points.

In this study, an assisted history-matching workflow will identify the regions of interest by starting with the low-degree proxy model, and then through iteration process, the workflow adds more points inside the region of interest and considers whether it should progressively increase the degree of polynomial for better response parameters. In addition to the history-matching process, the workflow will create another proxy model simultaneously for forecasting the ultimate recovery of hydrocarbon. This proxy model will assist finding the probabilistic distribution of hydrocarbon recovery.

7.3 AN ASSISTED HISTORY-MATCHING WORKFLOW

Generally, the concept of this workflow is to build an integrated analysis of history matching and production forecasting. For any simulation study, if we identify indefinite number of cases to cover all possible and reasonable uncertain parameters, then the knowledge on these subsurface parameters can be quantified through the process of history matching and production forecasting. However, this is a tedious task requiring huge amount of computational effort and is almost impossible to run for the complex cases. Therefore, if we have a comprehensive data-handling strategy, it will alleviate the problem significantly.

The petroleum industry often uses assisted history-matching technique as the solution for the too extensive computational resources problems by screening for good candidates and conducting simulations accordingly. Proxy modeling, one of assisted history-matching technique, normally initiates with simpler

model as linear or quadratic response-surface models, which require fewer design points from simulation cases. Then, when the workflow progresses, more cases are created to add more design points; hence, the prediction quality is improved. Similarly, when progressing through higher iteration cycles, workflow produces more history-matching solutions. And the iteration cycles are terminated when the history-matching solutions collected gradually from each iteration can comprehensively describe the uncertainty range of prediction.

Fig. 7.2 emphasizes the fundamental concept of the assisted history-matching (HM) workflow. First, the HM proxy model is initially created by RSM regression on the initial design points in the parameters space. Then, the Monte Carlo sampling selects HM-solution candidates by filtering the proxy model response parameters that are lower than the tolerance. After that, these possible HM-solution candidates will be run on the actual simulation. The candidates will be HM solutions if their response parameters from actual simulation are also lower than the tolerance. Next step, these solutions are used to construct the prediction proxy model, and will be later used for generating a probabilistic distribution of prediction parameter. Then, the workflow progresses to the next iteration by using all candidates from previous iteration (not limited to only HM solutions) as new points in the HM proxy model. For prediction proxy, only HM solutions from previous iterations are used to build the prediction proxy model in the following iteration. The iteration continues until the probabilistic distribution is converged. The workflow compares two distribution by adopting a two-sample Kolmogorov Smirnov test (K-S test) (Chakravarti et al., 1967) as the convergence criteria. To emphasize about K-S test, the null hypothesis of K-S test is the two distributions coming from the same reference. The K-S test will reject the null hypothesis when two distributions are different and fail to reject the null hypothesis when they are similar. Therefore, the iteration will be terminated when the probabilistic distribution of prediction parameters in current iteration is similar to ones in the previous iteration; in other words, the K-S test fails to reject the null hypothesis. In conclusion, the workflow performs a full cycle of uncertainty analysis, starting from HM process until the forecasting period.

Besides, in this study, we developed additional script files as a supplementary preprocessing framework for the assisted HM workflow. Fig. 7.3 shows the integration of four platforms to run the HM workflow. As mentioned earlier, as there are many simulation cases to be created throughout the HM workflow in each iteration, the preprocessing script can handle all combinations of uncertain parameters (both numerical and categorical variables) from the sampling algorithm and create inputs files for the reservoir simulator. Then, the calculated history-matching errors are transferred to RSM as new design points. Next, a new proxy model is reconstructed including new design points. Afterwards, the sampling algorithm works on the new proxy model and the framework continues. In sum, the developed framework connects each platform and supports the workflow to run efficiently regardless of number of simulation cases.

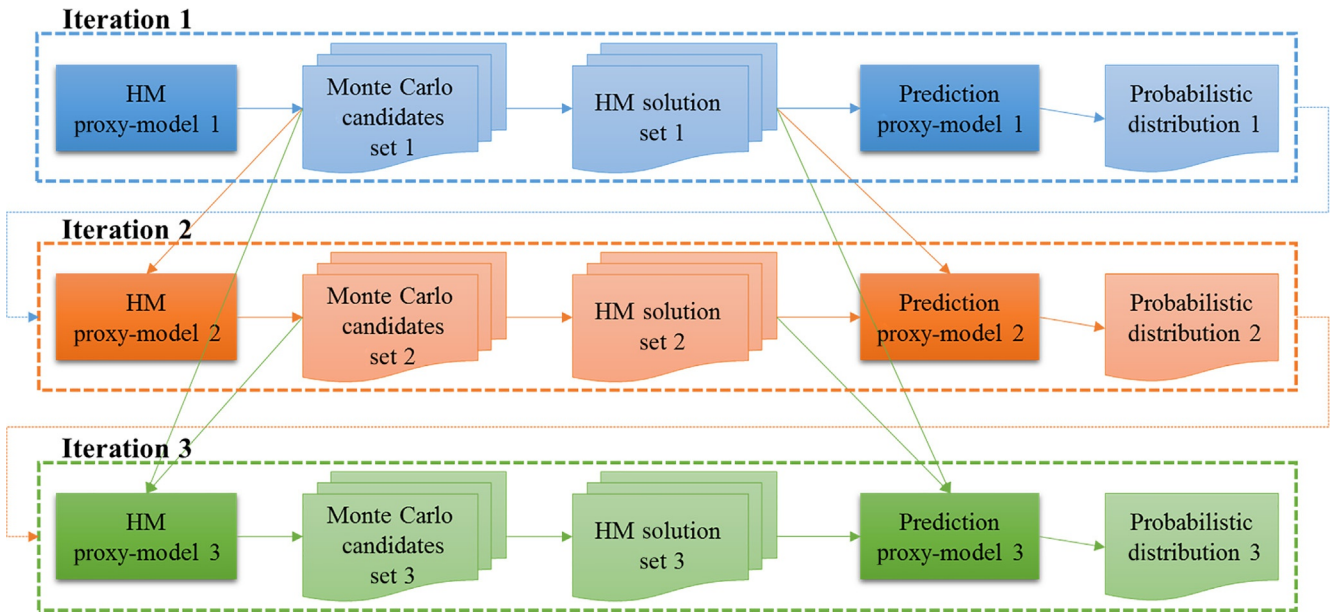

FIG. 7.2 Demonstration of the fundamental concept of the assisted history-matching (HM) workflow (Wantawin et al., 2017).

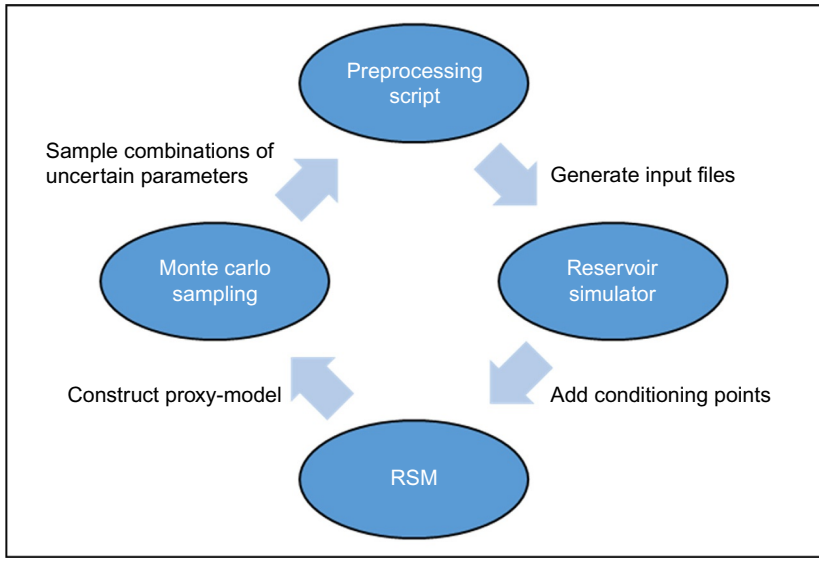

FIG. 7.3 A framework through integrating four platforms for the assisted history-matching (HM) workflow (Wantawin et al., 2017).

In this study, there are two workflows with different sampling algorithm, which consist of workflow with Monte Carlo (MC) sampling algorithm and with MCMC sampling algorithm.

7.3.1 Workflow With MC Sampling Algorithm

The first workflow presented in this study is workflow with MC sampling algorithm. Fig. 7.4 illustrates the complete workflow of integrated proxy-based HM and probabilistic forecasting with MC sampling algorithm. There are three main sections: parameters identification and screening, history matching, and production forecasting.

7.3.1.1 Parameter Identification and Screening

There are two types of parameters: uncertain parameters and response parameters. Identifying these two parameters is the first important step of the HM workflow. Firstly, we identify uncertain parameters. Uncertain parameters are reservoir and fracture properties that contain uncertainty or may be unknown due to no sufficient measurements conducted or could have been conducted but difficult to be conducted accurately. These uncertain parameters such as reservoir properties and fracture properties are normally adjusted in the simulation model to obtain good HM results. As HM problem always gives nonunique solutions, the question is how many adjustments we should perform for each uncertain parameters? The answer can be determined from this

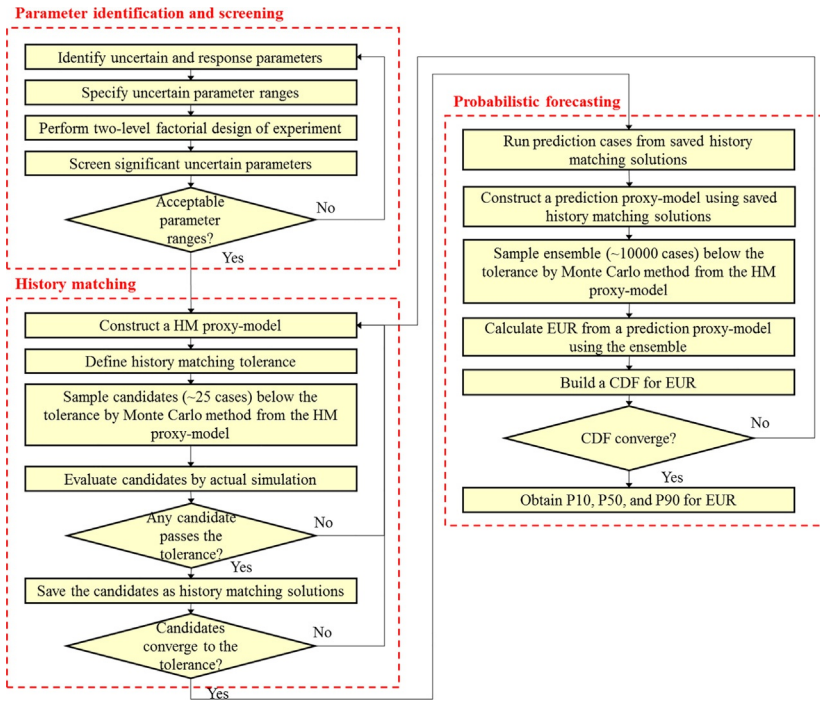

FIG. 7.4 The complete workflow of integrated proxy-based HM and probabilistic forecasting with MC sampling algorithm (Wantawin et al., 2017).

workflow when we integrate the HM results with probabilistic forecasting. Secondly, we identify response parameters. In this workflow, they consist of the HM-response parameter and the prediction-response parameter. Basically, the HM-response parameter is a parameter calculated from the misfit between the actual data and simulated data. For example, a root-mean-square error (RMSE) of cumulative gas production is an HM-response parameter. The RMSE can be calculated as:

$$RMSE\left(d^{sim}\right) = \sqrt{\frac{1}{N}\sum_{i=1}^{N} w_i \left(d_i^{sim} - d_i^{obs}\right)^2}, \tag{7.1}$$

where $RMSE(d^{sim})$ is an RMSE of a simulated reservoir parameter d, N is the number of data points, d_i^{sim} and d_i^{obs} represent the ith point of simulated and observed data, respectively, and w_i is the weighted factor of the ith data points, which is directly related to the measurement errors. If the measured data points contain high measurement errors, which should be considered less important, a lower value of w_i should be assigned. Accordingly, the lower the RMSE, the better the history-matching results are.

The prediction-response parameter is a prediction variable obtaining from running the HM-solution cases to forecasting period; for example, cumulative gas production after 30 years. The HM workflow will create separate proxy models for both HM-response and prediction-response parameters.

After identifying uncertain parameters and response parameters, we specify the range of uncertain parameters with the minimum and maximum values. We use these ranges as the boundary of the parameter space, and more importantly, use them as the input for the two-level factorial experiment. Then, we run numerical reservoir simulator for the cases generated based on factorial combination of uncertain parameters to retrieve the HM response.

Then, we should ensure that HM solution exists within the predefined ranges of uncertain parameters. In other words, the simulated production data from all cases of uncertain parameter sets should cover the actual data. This is a fundamental requirement of DoE that solutions must exist within the predefined parameter space because the proxy model fails to be validated if solutions are outside the parameter boundary. In case the simulated production data fail to cover the actual data, we should recheck the previous step of specifying the ranges of uncertain parameters; for example, the ranges may be too narrow or too few uncertain parameters are assumed in the experiment. This simple check is a hint to confirm that prior knowledge is acceptable before proceeding into the next step. Even though this hint is imperfect information, it is still useful and cheaper to correct the prior knowledge before running the whole HM workflow and failing to find the solutions at the end because of an incorrect prior knowledge. However, this is not always the stopper because the failure may be due to the limited number of simulation cases in this step.

After that, we screen and rank what uncertain parameters have more profound effects on the HM response. In this study, we use the software of Design-Expert (Stat-Ease, 2015) to perform sensitivity analysis. In the software, there is statistical tool for two-level factorial design such as half-normal plot. The half-normal plot will help evaluate what uncertain parameters affect more on the HM-response parameter, what interaction or combination of what uncertain parameters affect considerably on the HM-response parameter. Finally, we retrieve what uncertain parameters significantly affect the HM process and meanwhile screen out the immaterial ones. So, we can only carry over the necessary uncertain parameters into the next step of proxy modeling.

However, the two-level factorial design is the linear model with two-factor interaction terms. The design uses only the corner points of the design space so that it lacks the predictive capability to accurately represent proxy model for finding HM solutions. As a result, the two-level factorial design is only appropriate to be used in the screening steps. But when the workflow progresses to HM section, we will adopt a higher-degree polynomial as RSM. Again, this parameter identification and screening step is separated from the following steps—history matching and probabilistic forecasting; therefore, we should complete this step before moving on.

7.3.1.2 History Matching

After we establish the set of significant parameters, we will use them to build an RSM design for constructing a proxy model for HM response. The objective is to use a proxy model as an assisting predictive tool for finding the potential HM solutions (scenarios of uncertain parameters) at reasonable accuracy. For this purpose, the proxy model has no need to perfectly represent the true response for the entire space. Instead, the proxy model that is accurate on low RMSE regions is adequate. Basically, if the proxy model is constructed from only one set of data points, the proxy model will be deficient for the purpose of finding HM solutions. The reason is that the data points are randomly scattered over the entire parameter space regardless of high or low RMSE values. However, the iterative process of this HM workflow, which will be discussed later, will gradually add data points and also increase the degree of polynomial until the solution passes the set tolerance. The sampling algorithm will draw more design points in low-RMSE regions as iterations progress. Therefore, the resulting proxy model will be accurate in the low-RMSE regions or the region of interest.

Basically, the degree of polynomial to fit the HM-response parameter is an unknown at the beginning. Also, more regression coefficients in higher-degree polynomial models provide more flexibility to fit more nonlinear response. However, the tradeoff is that we require more design points or more simulation cases to build higher-degree polynomial model. As a result, this workflow will start the model with the simple model as quadratic terms and then progress to higher degree later, which depends on number of acceptable HM solutions and numbers of affordable runs. In this study, we consider only "complete" polynomials—including all the terms and allowing to remove any individual term. Also, the maximum degree of the polynomial depends on the number of level defined. If there is any discrete uncertain parameter, the degree of polynomial must be less than the discretized levels in order to find all the regression coefficients. To exemplify, if fracture half-length has five discretized levels, the polynomial degree will be limited at a quartic equation.

Normally, the information about the HM response is unavailable at the initial stage, so we should use the initial design strategy to keep the minimum variance unbiased estimator for the parameter, and minimize the number of simulation runs. Therefore, in this study, we select the optimal design—a class of RSM that adopts the optimal statistic criterion to decrease the run requirement—as the initial design strategy. The optimal design is suitable for the HM problem because it can accommodate both numerical and categorical uncertain parameters. Then, a proxy model is built by using the best polynomial model based on fitting quality measured by statistical parameters.

Next step is to define HM tolerance for HM solutions. The HM tolerance is the maximum limit of the HM-response parameter. Then, the workflow performs Monte Carlo sampling on the proxy model where the HM-response parameters are lower than the tolerance. However, the predicted HM response

from proxy model will always be different from the HM response given by simulation results from numerical reservoir simulator. Thus, we will run simulation cases for all candidates. If the HM-response parameter from simulation run is also lower than the tolerance, then the case is saved as a HM solution.

For the subsequent iterations, all candidates from previous iteration are used as additional design points for the proxy model. Thus, proxy model will be improved and give a better prediction quality as the iteration progresses because more data weighted in the low-RMSE region are used for proxy model regression. Fig. 7.5 emphasizes the proxy model improvement when there are more design points in the region of low response—creating a more accurate proxy model. Before progressing to the probabilistic forecasting, the HM proxy model must be reasonably accurate. The criterion is the average value of the actual HM response from the candidates should converge to the HM tolerance so we can ensure that the proxy model is acceptable and ready to be used for the next step—probabilistic forecasting.

7.3.1.3 Probabilistic Forecasting

The workflow proceeds here when the actual HM response from candidates converges to the tolerance value. In other words, this implies HM proxy model accuracy is acceptable because most of the candidates yield HM solutions. Although any proxy model accuracy is imperfect, this is sufficient for the purpose of the study. Next step is that we build the cumulative density function of prediction parameters from HM solutions. However, one thing to be aware is that using few discretized solutions could possibly end up with erroneous probabilistic forecasts—leading to underestimate or overestimate the recoverable volume. Therefore, to avoid this error, this workflow aims to generate the continuous probabilistic distribution of prediction parameters by creating another proxy model—prediction proxy model.

Firstly, we run all saved HM solutions extending to the prediction period, i.e., production forecasting for 30 years. Then, we calculate the identified prediction-

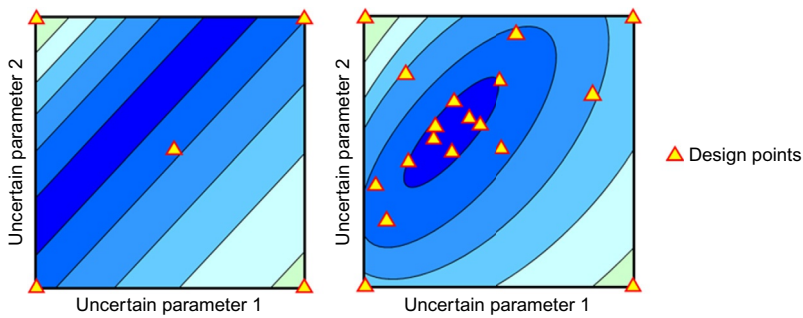

FIG. 7.5 Schematic for demonstration of improvement of proxy models with more design points in the region of low response (Wantawin et al., 2017).

response parameters for each HM solution as the input for proxy modeling. After that, we build a proxy model of prediction-response parameter from those inputs of each HM solution. In other words, HM solutions are used as design points in the parameter space for the prediction proxy model. Besides, we should ensure that the number of HM solutions is above the minimum requirement to build the selected polynomial model. To illustrate, the prediction proxy model is a quadratic based model with four uncertain parameters, 15 HM solutions as design points are the minimum to calculate regression coefficients (Stat-Ease, 2015).

After the prediction proxy model is built, the workflow will create a probabilistic distribution of the prediction-response parameters. Many sampled data points are needed for a smooth empirical CDF (ECDF), which is an approximation of true CDF. Fig. 7.6 shows the sampling process for constructing ECDF. We will take many sampled data points from the region of interest *(red dotted area)*—the HM solutions area. In this study, we take 10,000 samples from region of interest in HM proxy model, where the HM response is lower than the tolerance. Then, we calculate the prediction-response parameters based on these 10,000 combinations of uncertain parameters. Eventually, we have an ECDF of a particular iteration for further evaluation.

Afterwards, the probabilistic forecasting has an additional step to validate whether the estimated uncertainty or ECDF is stable. The ECDF built from the early iteration step can have limited information for proxy modeling. In other words, few design points controls the proxy model to low-degree polynomial. This means the early proxy model can ignore some other potential solution regions and lead to too narrow range of probabilistic results. Hence, the iteration process forces the proxy models to rebuild when there are more design points through iteration. Next, the ECDF of the latest iteration is compared with the previous ECDF. If ECDF has converged, this means the distribution of prediction-response parameters or ECDF is stable. As a result, we have a final distribution of prediction-response parameters and the workflow is terminated. Additionally, as illustrated in Fig. 7.7, when proxy models adopt the higher-

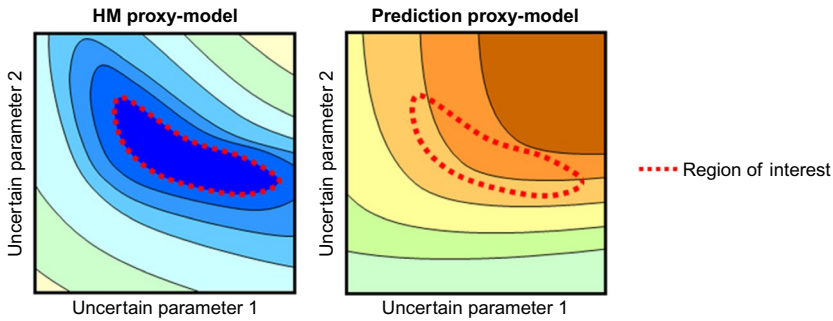

FIG. 7.6 Schematic of the sampling process from the HM proxy model for constructing ECDF using the prediction proxy model (Wantawin et al., 2017).

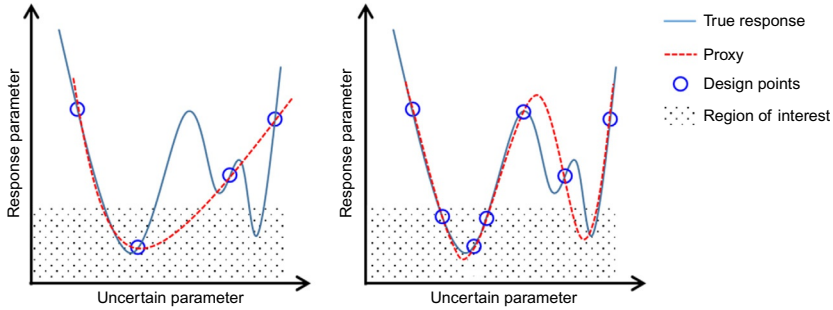

FIG. 7.7 Comparison of low-degree polynomial (left) and high-degree polynomial (right) for building proxy models (Wantawin et al., 2017).

degree polynomial, it is possible that new potential solution regions occur, leading to a broader uncertainty range of the prediction parameter. Thus, the workflow also assists determining whether the degree of polynomial is sufficient to predict the stable probabilistic forecasting.

7.3.2 Workflow With MCMC Sampling Algorithm

The workflow with MCMC sampling algorithm is similar to the workflow with MC in the previous section consisting of parameter identification and screening, history matching, and probabilistic forecasting. After the proxy model is built, the only different step is the algorithm to select or sample the design points from uncertain parameter space for the actual simulation run. So in this section, we will highlight how the MCMC sampling algorithm works.

In this study, we use a Metropolis-Hasting (MH) algorithm (Metropolis et al., 1953; Hastings, 1970), a subclass of MCMC methods. To start the Markov chains for the algorithm, we assign arbitrary points in parameter space that have model responses (e.g., RMSEs) lower than the tolerance as initial guesses. Then, the proposed uncertain parameters, θ^*, for the next step of the chain is calculated by

$$\theta^* = \theta + \delta, \tag{7.2}$$

where θ is the uncertain parameter at the current step of the chain and δ is the maximum step size that the chain will move within the space. The acceptance probability of MH algorithm, α^*, is then defined by

$$\alpha^* = \min\left\{1, \frac{p(\theta^*|\, y)}{p(\theta|\, y)}\right\}, \tag{7.3}$$

where $p(\theta|\, y)$ is the posterior distribution of the uncertain parameters, θ, given the measured production history, y. Gaussian distribution and variances, σ^2,

are assumed for this study. The algorithm will accept the proposed θ^* with acceptance probability, α^*, and reject it with probability $1-\alpha^*$. In this study, the MH algorithm is applied with a modification to the acceptance condition in order to obtain the samples from multiple model responses. The algorithm will more frequently search the region that all model responses share low magnitude. The acceptance probability of all model responses is calculated simultaneously and all must be satisfied in order to accept the proposed θ^*. This acceptance condition is treated according to the combined acceptance probability:

$$\alpha^*_{combined} = \prod_{i=1}^{N} \min\left\{1, \frac{p(\theta^*|y)_i}{p(\theta|y)_i}\right\}, \tag{7.4}$$

where $p(\theta|y)_i$ is the posterior distribution of the ith model response and N is the total number of model responses. Nevertheless, the combined criteria result in lower acceptance probability, thus decreasing the accepted solutions from the Markov chains. Therefore, the number of proposed samples for each chain should be sufficient. In addition, variances should be adjusted so that they yield adequate acceptance rate and converge to target distribution. Then, the HM workflow continues to the next step of running the numerical simulation for ensemble to calculate the actual RMSE from simulation. The detailed HM workflow with MCMC sampling algorithm is listed in Fig. 7.8.

7.4 FIELD APPLICATION IN MARCELLUS SHALE GAS RESERVOIR

In this section, an actual field case in Marcellus Shale gas reservoir was shown as an application of this designed workflow. A multifractured horizontal well is producing in a shale formation that has extremely low permeability. At the start of the production, the well was stimulated by multistage hydraulic fracturing in order to enable economic development. Some reservoir properties of shale were not measured accurately. In addition, it is difficult to measure fracture properties directly by use of the current fracture diagnostic technologies. The reservoir model needs to be calibrated with the observed well performance through history matching to deal with the uncertainty of fracture properties, so that reliable forecasts can be determined by the calibrated model. However, it might have incomplete understanding of the particular well performance based on the solution from a single history-matching model without comprehensively exploring multiple solutions. So, the object of this section is to show the workflow that is capable of examining the uncertainty involved in the history-matching process to perform production forecasting and uncertainty quantification in Marcellus Shale gas reservoir.

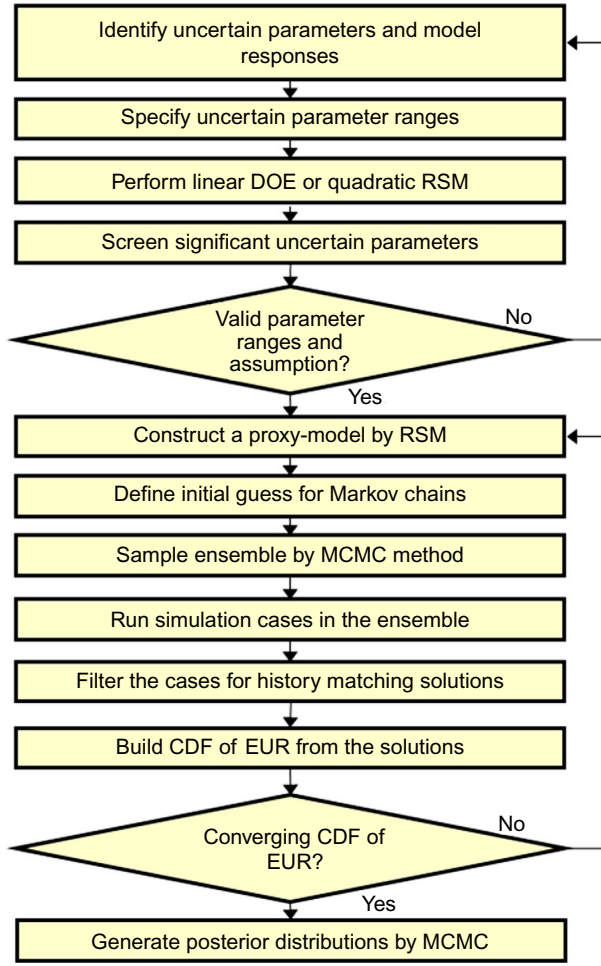

FIG. 7.8 The complete workflow of integrated proxy-based HM and probabilistic forecasting with MC sampling algorithm (Wantawin et al., 2017).

7.4.1 Basic Reservoir Model

We built a black-oil reservoir model to simulate shale gas production with modified fluid properties to accurately capture gas desorption effect, which can significantly improve computational time (CMG-IMEX, 2015). The reservoir model dimension is 6000 ft long and 1500 ft wide. There are two layers with different matrix porosities, as shown in Fig. 7.9. The thickness of the bottom layer and the top layer is 40 and 95 ft, respectively. The horizontal well is located at the center of the bottom layer. There are 16 hydraulic fracturing stages along the lateral and it is assumed that 64 effective hydraulic fractures are generated (four perforation clusters per state). The approach of local grid

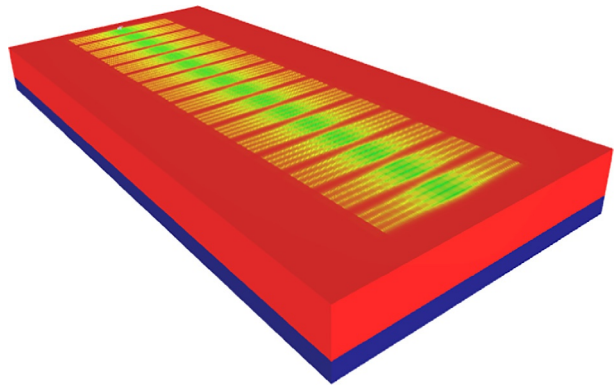

FIG. 7.9 Reservoir model used in this study including a horizontal well with multiple fractures in Marcellus Shale gas reservoir (Wantawin et al., 2017).

TABLE 7.1 Basic Input Parameters Used for Marcellus Shale Gas Reservoir (Wantawin et al., 2017)

Parameter	Value	Unit
Model dimension ($x \times y \times z$)	$5000 \times 2000 \times 135$	ft
Number of grid blocks ($x \times y \times z$)	$500 \times 41 \times 2$	
Initial reservoir pressure	5100	psi
Reservoir temperature	130	°F
Total compressibility	3×10^{-6}	psi^{-1}
Matrix porosity (upper layer)	7.1%	
Matrix porosity (bottom layer)	14.2%	
Horizontal well length	3921	ft
Number of stages	16	
Cluster spacing	50	ft
Total number of fractures	64	
Fracture width	0.01	ft
Gas-specific gravity	0.58	

refinement (LGR) is used to explicitly handle these hydraulic fractures. Also, a dry gas reservoir with single phase is simulated by setting the model above the dew point pressure initially. The basic input parameters used for the reservoir model are summarized in Table 7.1 (Yu et al., 2014). The measured 190-day gas production data were used. The peak of gas flow rate is about 25 MMSCF/d. In

this model, the flowing bottomhole pressure (BHP) was used as simulation constraint. The measured gas flow rates were used to calibrate uncertain parameters in the reservoir model during the history-matching process.

7.4.2 Parameter Identification and Screening

Reservoir and fracture properties that possess great deal of uncertainty were selected as uncertain parameters. Laboratory measurements for matrix permeability in shale gas reservoirs may have a considerable range of uncertainty due to its extremely low value; based on previous work, it could vary from 100 to 1000 nD (Ajayi et al., 2011; Mayerhofer et al., 2011; Izadi et al., 2014; Nelson et al., 2014; Yu et al., 2014).

In this study, uncertain parameters include three fracture properties, such as fracture half-length, fracture conductivity, and fracture height. Their average values are referred to the work by Yu et al. (2014). Firstly, fracture half-length measures the perpendicular distance from the wellbore to the tip of a hydraulic fracture, which was categorized as a discrete numerical parameter so that it could facilitate reservoir modeling process using similar grid dimension (50 ft in y-direction). Secondly, fracture conductivity is the product of fracture permeability and fracture width. Its range basically describes the uncertainty of propped fracture width and fracture permeability. The geomechanics effect is not considered in the reservoir model. Finally, fracture height measures the height of the hydraulic fractures extending from the bottom layer to the upper layer of the formation. The entire thickness of the bottom layer is fully penetrated while the thickness of the upper layer is partially or fully penetrated. It is assumed that the longer vertical distance of hydraulic fractures will access more volume of gas in the upper layer; hence, the thickness of the upper layer will vary continuously according to the value of fracture height. For this case study, uniform distribution is assumed for the uncertain parameters because there were no prior information about the distribution of matrix permeability, fracture half-length, fracture conductivity, and fracture height. However, cores, logs, microseismic data, and other additional evidence can be used to show how the uncertain parameters are distributed and define their distributions for Monte Carlo sampling purpose.

Proxy models are used to approximate the actual response parameters. A misfit function of cumulative gas production during the first 190 days of production period was used as history-matching response parameter, which basically quantified the discrepancies between the observed data and the simulated data. In this study, RMSE was used to define the misfit function:

$$RMSE\left(G_p\right) = \sqrt{\frac{1}{N}\sum_{i=1}^{N} w_i \left(G_{p,i}^{obs} - G_{p,i}^{sim}\right)^2}, \tag{7.5}$$

where $RMSE(G_p)$ is an RMSE of cumulative gas production, N is the number of observations during 190 days, w_i is the weighting factor for the ith observation,

$G_{p,i}^{obs}$ and $G_{p,i}^{sim}$ are the observed and simulated cumulative gas production at the time of the ith observation, respectively. In this study, the weighting factor is fixed at one for all observations. The calculated RMSE will always be positive according to the equation. Better match of simulated data to the observations will be gained when the value of objective function is closer to zero. In the later section, a tolerance will be set to RMSE to filter the cases as history-matching solutions. In addition, the EUR of gas production after 30 years was used as the prediction response parameter. Two-level full factorial design was used to analyze the relationship between uncertain parameters and the history-matching response parameter.

7.4.3 Two-Level Full Factorial Design

We performed 16 simulation cases based on the two-level full factorial design. The half normal plots from the design are shown in Fig. 7.10. The terms with highest effect are on the right side of the plot. It can be seen that the large effects came from the two-way and three-way interaction terms between matrix permeability, fracture conductivity, and fracture height, which were selected in Fig. 7.10A (highlighted points). The effect of fracture half-length is not as important as others, which can be approximated by normal distribution line (orange line in the plot) along with others with small effect. The Shapiro-Wilk test (Shapiro and Wilk, 1965) is used to evaluate if the selected parameters are relatively important through rejection of null hypothesis, which means that the effects of unselected parameters are normally distributed. We also need to compare the Shapiro-Wilk test when no selection is made and make sure that the effects of selected parameters are indeed significant and cannot be approximated by normal distribution.

The Shapiro-Wilk P-value is determined as 0.107 when significant effects listed earlier are selected. The null hypothesis cannot be rejected since the value was slightly higher than an assumed alpha level of 0.10. However, when no terms were selected in Fig. 7.10B, the Shapiro-Wilk P-value is 0.108, which is still larger than the assumed alpha level of 0.10, indicating that no individual effect in the design is statistically insignificant (Stat-Ease, 2015); in other words, the null hypothesis cannot be rejected. Hence, we cannot drop any parameters to reduce uncertainties. Table 7.2 presents the summary of every uncertain parameter with the minimum and maximum value and response parameters. The comparison of gas flow rate and cumulative gas production between 16 simulation cases and actual production data is shown in Fig. 7.11. It can be observed that the simulation results under the given range of uncertain parameters have expanded throughout the actual data. Hence, it is guaranteed that the history-matching solutions will be within the design space of uncertain parameters.

7.4.4 History-Matching Results From Iterative Proxy Model

Next, the iterative workflow proceeds to history matching and production forecasting. An I-optimal design with a quadratic base model is initially set as a

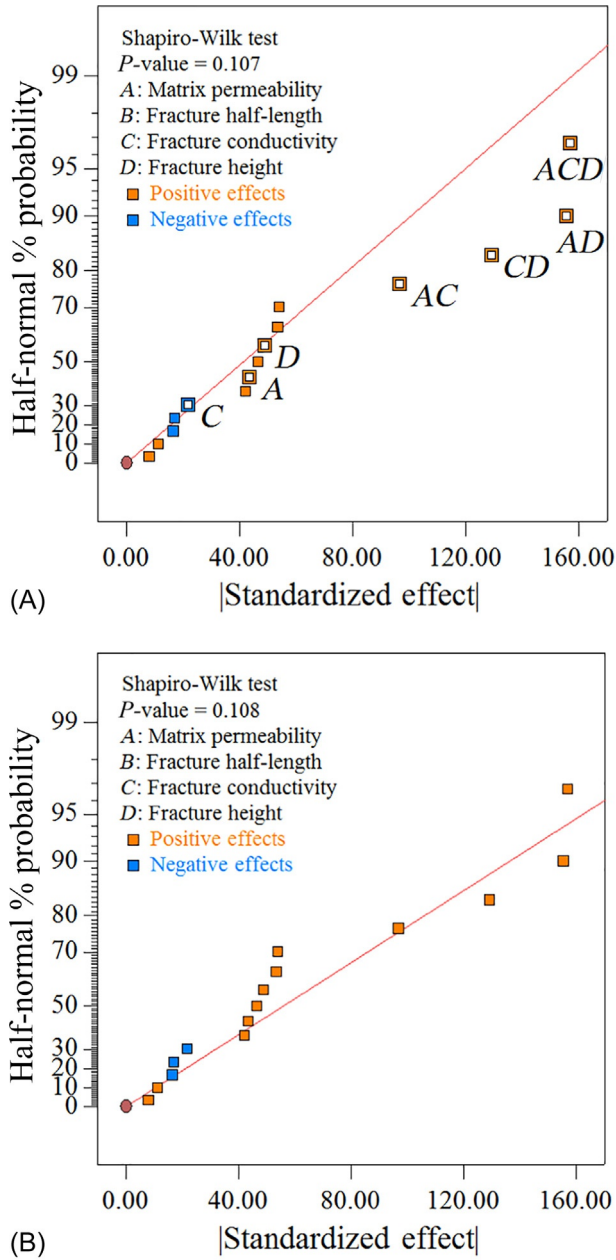

FIG. 7.10 Half-normal plots of the two-level full factorial design (Wantawin et al., 2017). (A) Significant parameters are selected and highlighted; (B) no significant parameters are selected.

TABLE 7.2 Uncertain and Response Parameters Considered in This Study (Wantawin et al., 2017)

Uncertain Parameter	Unit	Type	Distribution	Low				High
Matrix permeability	nD	Continuous	Uniform	100		–		1000
Fracture half-length	Ft	Discrete	Uniform	300	350	400	450	500
Fracture conductivity	mD-ft	Continuous	Uniform	1		–		10
Fracture height	Ft	Continuous	Uniform	40		–		135

HM Response Parameter	Unit	Type
RMSE of cumulative gas production	MMSCF	Continuous
Prediction Response Parameter	**Unit**	**Type**
EUR of gas after 30 years	MMSCF	Continuous

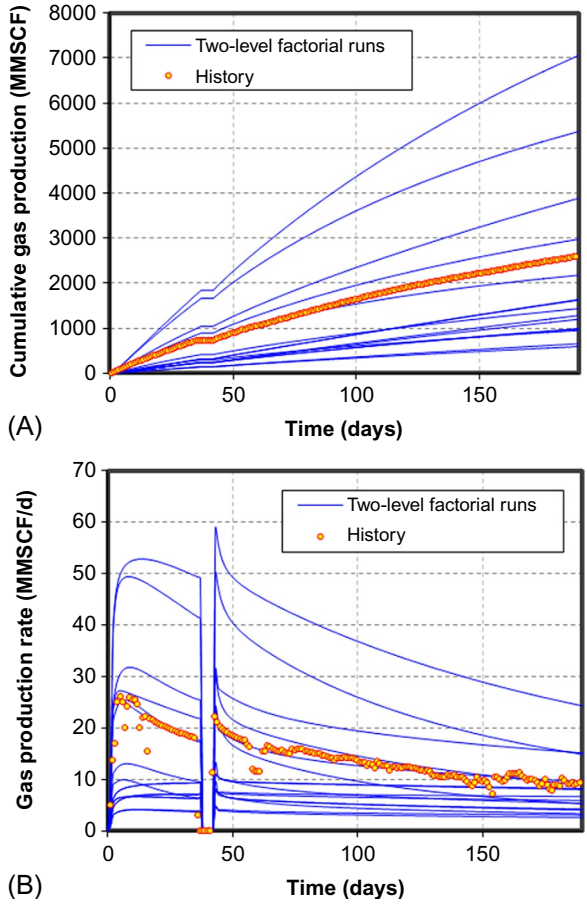

FIG. 7.11 Comparison of well performance between simulation results from the two-level full factorial design and actual filed data (Wantawin et al., 2017). (A) Gas flow rate; (B) cumulative gas production.

history-matching proxy model. The I-optimal design reduces the number of required simulation runs because the design points will be chosen automatically to minimize the integral of prediction variance (Jones and Goos, 2012; Stat-Ease, 2015). The initial regression terms can be minimized using the quadratic base model. As a result, 25 simulation cases were generated for the selected design, which include 15 model points required to determine the regression coefficients, 5 lack-of-fit points to additionally fill in parameter space, and 5 replicate points to support optimality. Subsequently, 14 iteration cycles were finished to achieve stable probabilistic production forecasts. Finally, 165 history-matching solutions were collected from a total of 400 simulation cases.

The summary of the workflow starting from the initial design to the end of 14th iteration is presented in Table 7.3. The table provides detailed

TABLE 7.3 Summary of Application of Assisted History-Matching Workflow in Marcellus Shale Gas Reservoir (Wantawin et al., 2017)

Iterations	HM Design Points	HM Proxy Model	HM Tolerance (MMSCF)	Total Runs	HM Solutions	Prediction Design Points	Prediction Proxy model	K-S Test
Initial	25	Quadratic	200	50	12	12	Linear	–
1	50	Quadratic	100	75	–	12	–	–
2	75	Cubic	50	100	5	17	–	–
3	100	Cubic	50	125	3	20	–	–
4	125	Cubic	50	150	9	29	Quadratic	Rejected
5	150	Cubic	50	175	10	39	Quadratic	Rejected
6	175	Cubic	50	200	15	54	Cubic	Rejected
7	200	Quartic	50	225	11	65	Cubic	Rejected
8	225	Quartic	50	250	13	78	Quadratic	Rejected
9	250	Quartic	50	275	12	90	Quadratic	Rejected
10	275	Quartic	50	300	14	104	Cubic	Rejected
11	300	Quartic	50	325	13	117	Cubic	Rejected
12	325	Quartic	50	350	13	130	Cubic	Rejected
13	350	Quartic	50	375	16	146	Cubic	Rejected
14	375	Quartic	50	400	19	165	Cubic	Failed to Reject

information about the number of design points that were used to build proxy models, the degree of regressed polynomial equations, the value of history-matching tolerance, the number of collected history-matching solutions used to construct prediction proxy model, and the convergence criteria of the probability distribution for EUR by the rejection of null hypothesis from the K-S test. New 25 points were produced for each iteration, which were filtered from the Monte Carlo sampling on the proxy model based on the given tolerance at the iteration. Some of these points will also be added to the design points for prediction if they are collected as history-matching solutions. We sequentially decreased the value for the tolerance that classified the sampled points as history-matching solutions from 200 to 50 MMSCF after the 2nd iteration. The proxy model of the next iteration was updated using all of the points for achieving better predictability.

After each iteration, the history-matching proxy model was used to obtain new design points for simulation. The actual response parameter of these new points was determined, based on the simulation results. The actual RMSE of the cumulative gas production during the history-matching process is shown in Fig. 7.12. As shown, the *dashed black line* represents the final history-matching tolerance of 50 MMSCF. We can notice that the trend of RMSE is gradually decreasing, clearly indicating that the prediction performance of proxy models is improved. At the 1st iteration, the quadratic proxy model identified the region of interest where the RMSE is low and 12 history-matching solutions were collected. However, these solutions were restricted into a single region and the model did not explore the global uncertain parameter space thoroughly. Fig. 7.13 shows the progression of four uncertain parameters with all the 165 history-matching solutions. It can be seen that

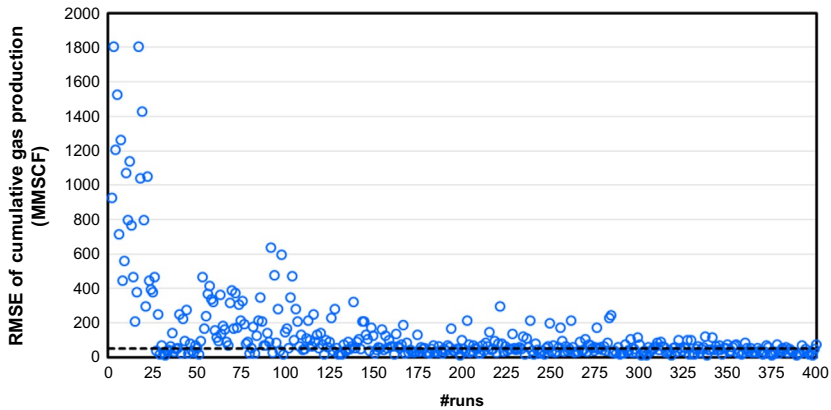

FIG. 7.12 RMSE of cumulative gas production of vs. the number of simulation runs (Wantawin et al., 2017).

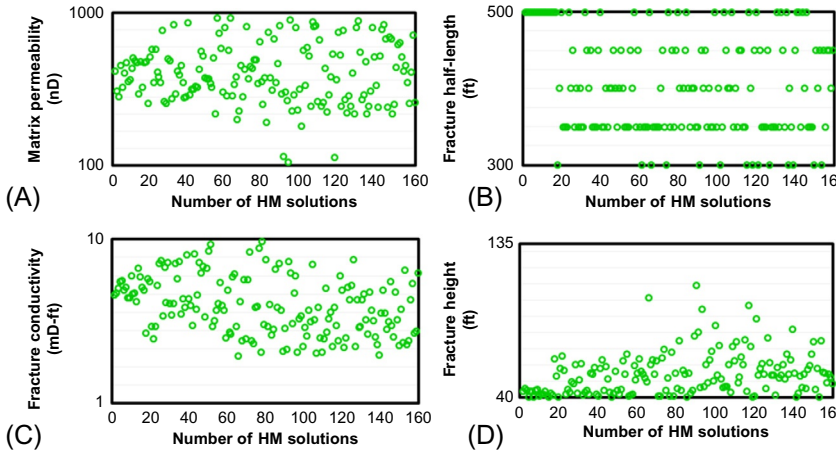

FIG. 7.13 Progression of uncertain parameters with all the history-matching solutions (Wantawin et al., 2017). (A) Matrix permeability; (B) fracture half-length; (C) fracture conductivity; (D) fracture height.

the solutions from early iterations have relatively narrow range of uncertain parameters. For example, the matrix permeability ranges from 500 to 700 nD for the first 12 solutions generated from the quadratic proxy model. However, when the proxy model achieves higher order with iteration process, the matrix permeability of later solutions actually changes from 100 to 1000 nD. This suggests that a wider range of uncertain parameters can be captured with updating the proxy model through iterations. The similar behavior can be found for the other three uncertain parameters, such as fracture half-length, fracture conductivity, and fracture height.

Fig. 7.14 compares the predicted RMSE and the actual RMSE at different iterations. As shown, there exists a large discrepancy between the predicted and the actual RMSE at the 1st iteration. Hence, the workflow needs to proceed to the next iteration process. In addition, it can be clearly seen that the accuracy of proxy models was improved correspondingly with the iteration continuing. It can be observed from Table 7.3 that the accepted history-matching solutions at each iteration increased through the iteration process. Finally, the acceptance ratio is about 76% at the 14th iteration.

The proxy model progressed to higher-degree polynomial equations after more information were obtained from the increasing design points, resulting in more regression terms and better fitting to the curvature. The criteria to increase the regression terms are dependent on the number of design points and the regression quality. The following equations are the proxy models from the initial design, the 6th iteration, and the 14th iteration, which are quadratic, cubic, and quartic polynomial, respectively:

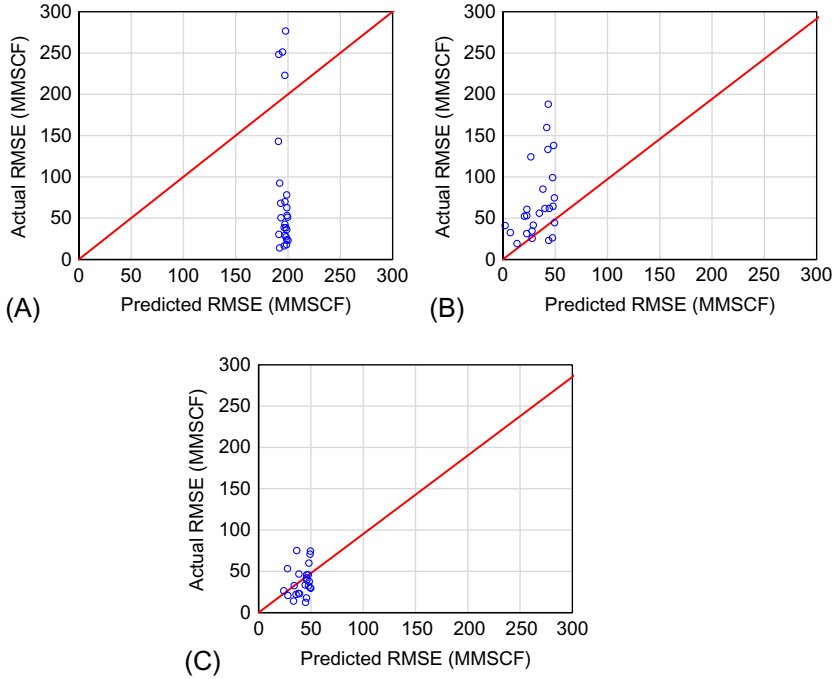

FIG. 7.14 Effects of different iterations on comparison of predicted RMSE from the proxy model and actual RMSE from the simulation (Wantawin et al., 2017). (A) Initial design; (B) 6th iteration; (C) 14th iteration.

$$\begin{aligned}\left[RMSE\left(G_p\right)\right]^{0.22} = {} & 3.93 + 0.097A - 2.599\left(10^{-3}\right)B - 0.025C + 0.32D \\ & + 0.23AB + 0.023AC + 0.37AD - 0.12BC + 0.14BD \\ & + 0.40CD + 0.12A^2 - 0.37B^2 + 0.64C^2 + 0.19D^2,\end{aligned} \tag{7.6}$$

$$\begin{aligned}\left[RMSE\left(G_p\right)\right]^{1.59} = {} & 23341 + 24293A + 12802B + 23977C + 58298D \\ & + 11550AB + 27835AC + 33532AD + 14235BC \\ & + 15099BD + 32593CD - 4384A^2 + 3221B^2 + 28259C^2 \\ & + 18221D^2 + 5922ABC + 6878ABD + 29350ACD \\ & + 13474BCD - 5006A^2B - 4899A^2C - 30572A^2D \\ & - 341.78AB^2 + 12382AC^2 - 5407AD^2 + 5908B^2C \\ & + 2898B^2D + 1606BC^2 - 2810BD^2 + 12725C^2D \\ & - 13797CD^2 - 14093A^3 - 1326B^3 - 5859C^3 - 27432D^3,\end{aligned} \tag{7.7}$$

$$
\begin{aligned}
\left[RMSE\left(G_p\right)\right]^{1.55} = {} & 16409 + 29136A + 13719B + 38074C + 41320D \\
& + 12804AB + 41868AC + 44212AD + 19833BC \\
& + 24363BD + 59068CD - 1340A^2 + 4526B^2 + 14643C^2 \\
& + 12619D^2 + 14827ABC + 5837ABD + 24229ACD \\
& + 15062BCD - 7908A^2B - 11644A^2C - 23093A^2D \\
& - 2976AB^2 - 8.35AC^2 - 11718AD^2 + 5108B^2C \\
& + 12902B^2D + 3772BC^2 - 2554BD^2 - 3546C^2D \\
& - 9113CD^2 - 13304A^3 - 3416B^3 - 19930C^3 - 18095D^3 \\
& + 13987ABCD - 1398A^2B^2 - 1993A^2BC - 11683A^2BD \\
& + 884A^2C^2 - 17831A^2CD - 16612A^2D^2 - 2051AB^2C \\
& - 6153AB^2D + 6381ABC^2 - 8104ABD^2 - 4340AC^2D \\
& - 8786ACD^2 + 5821B^2C^2 + 7597B^2CD + 7679B^2D^2 \\
& + 1436BC^2D - 2191BCD^2 - 6659C^2D^2 - 1163A^3B \\
& - 5040A^3C - 7324A^3D - 142AB^3 - 7978AC^3 - 14513AD^3 \\
& + 800B^3C + 5419B^3D - 5041BC^3 - 9577BD^3 - 18724C^3D \\
& - 9617CD^3 + 5437A^4 + 1967B^4 + 873C^4 + 5187D^4.
\end{aligned}
\tag{7.8}
$$

where A is the coded matrix permeability, B is the coded fracture half-length, C is the coded fracture conductivity, and D is the coded fracture height.

Fig. 7.15 presents the contour plots between fracture conductivity and matrix permeability using different proxy models at different iterations. Fracture half-length is 500 ft and fracture height is 50 ft. As can be seen, the surface becomes increasingly complicated when the proxy models incorporate more higher-degree terms. The surface from the quadratic model at the initial design shows a bowl-shaped region of interest; however, the quartic model at the 14th iteration changes the surface to an irregular shape, which has better accuracy. Comparison of cumulative gas production and gas flow rate during 192 days of production period between the 165 history-matching solutions and field data is illustrated in Fig. 7.16. These history-matching solutions had the RMSE below 50 MMSCF, which provide reasonable match with the measured field data.

In this case study, it takes 14 iterations to achieve a stable probabilistic estimate of gas recovery. We start to perform the prediction when the actual RMSE in Fig. 7.12 decreases to the given tolerance. Even though the accuracy of the history-matching proxy model can be improved with the subsequent iterations, the prediction can be performed at any point in the workflow when the number of history-matching solutions is sufficient to build the prediction proxy model. After collecting history-matching solutions at each iteration, we continued to

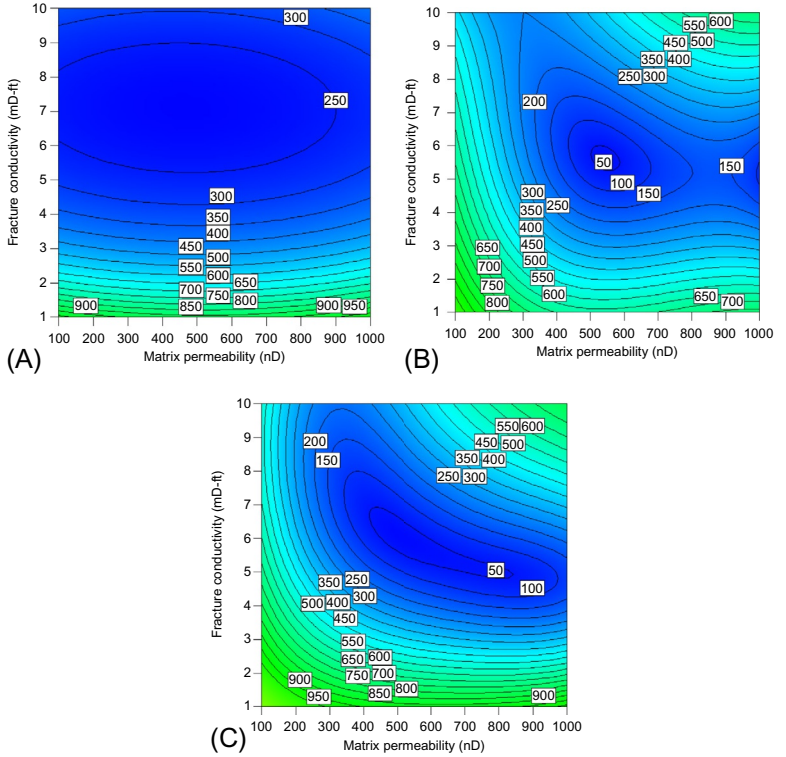

FIG. 7.15 Effects of different iterations on the contour plots of the proxy models of RMSE of cumulative gas production (Wantawin et al., 2017). (A) Initial design; (B) 6th iteration; (C) 14th iteration.

perform production forecasting simulation for these history-matching cases in a 30-year period. In the end, their EURs at 30 years were calculated. Fig. 7.17 shows cumulative gas production from 165 history-matching solutions in both history-matching and production forecasting periods after the 14th iteration. We used the calculated EUR values as design points to build the prediction proxy model. Now, the EUR becomes a prediction-response parameter and its relationship with the same four uncertain parameters will be regressed and improved after each iteration. Fig. 7.18 compares the contour plot of prediction proxy models that were constructed at the 6th and the 14th iterations. The contour plot demonstrates the effects of matrix permeability and fracture conductivity on the EUR at 30 years at fracture half-length of 500 ft and fracture height of 50 ft. Although we used a cubic equation at both iterations, the surface of the 14th iteration indicates more curvature than that of the 6th iteration. This is because more design points (165 points) introduced in the 14th iteration than that (54 points) in the 6th iteration. In addition, it can be observed that the

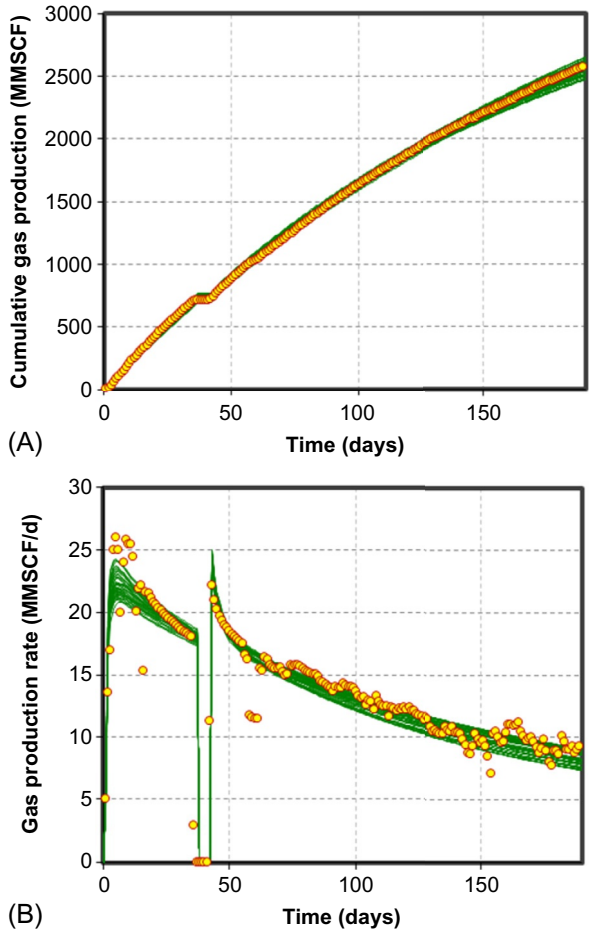

FIG. 7.16 Comparison of simulation results from all 165 history-matching solitons and field production data (Wantawin et al., 2017). (A) Cumulative gas production; (B) gas flow rate.

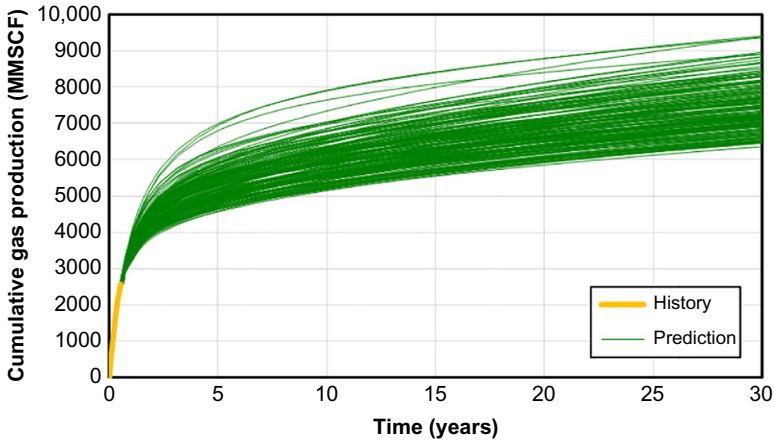

FIG. 7.17 Production forecasting for 30 years of all history-matching solutions (Wantawin et al., 2017).

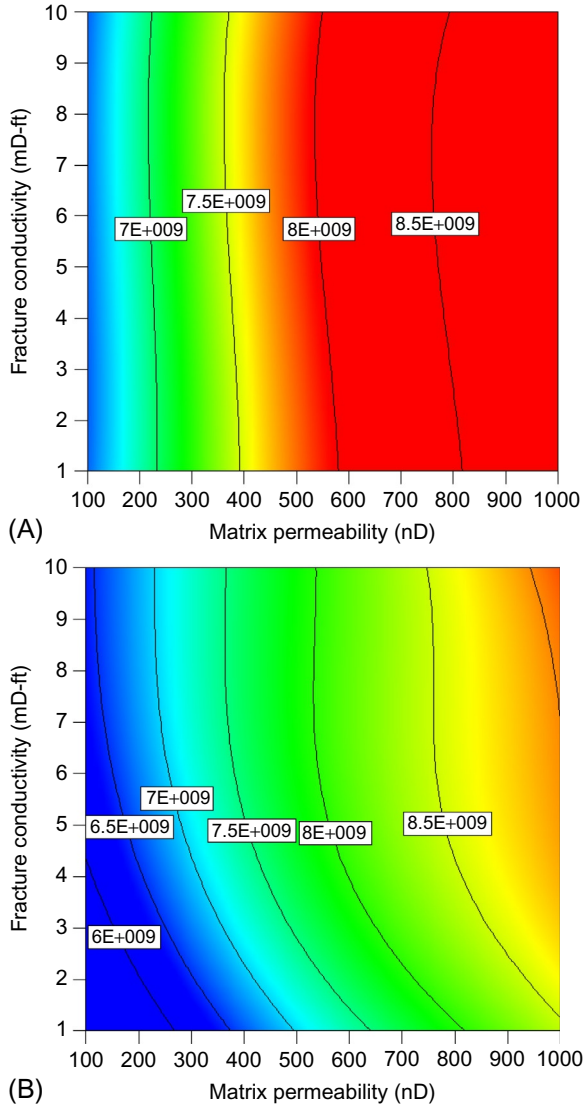

FIG. 7.18 Effects of different iterations on contour plots of the proxy models of EUR after 30 years between fracture conductivity and matrix permeability (Wantawin et al., 2017). (A) 6th Iteration with 54 design points; (B) 14th iteration with 165 design points.

nonlinearity of the prediction proxy model is not as complicated as the history-matching proxy model. Hence, the accuracy of the prediction proxy model can be improved favorably through regression from the quadratic to the cubic polynomial equations.

After each iteration, we draw 10,000 Monte Carlo samples based on the built history-matching proxy model. The acceptance criteria for the sampling process remain the same as the history-matching tolerance; i.e., the sample will be accepted if the calculated RMSE using the sampled uncertain parameters is less than 50 MMSCF. Correspondingly, these 10,000 samples with different combinations of four uncertain parameters were used to predict EUR from the built prediction proxy model and simultaneously build an ECDF. It should be mentioned that the number of 10,000 samples is assumed to be sufficiently large so that the ECDF approximately converges to the true CDF. Consequently, we can evaluate the continuous EUR distribution at the end of each iteration. In this case study, 14 ECDFs from the assisted history-matching workflow are plotted in Fig. 7.19. As can be seen, the uncertainty range of ECDF increases with the increasing iteration steps. This is because the degree of the proxy models becomes higher with more iterations and more history-matching solutions are discovered. Specifically, the quadratic proxy model (in *blue color*) was fitted for the initial design and an enclosed region of EUR distribution was captured. Afterwards, the cubic proxy model (in *green color*) was updated and fitted for the 6th iteration and the range of EUR distribution spreads out toward the low estimates. Eventually, the quartic proxy model (in *red color*) was determined for the 14th iteration to provide better approximation to the true response and wider regions of EUR distribution were uncovered. It can be implied that the initial quadratic proxy model may not fully generate the probabilistic range of EUR distribution and updating proxy models with more regression terms improves the prediction accuracy. Although the degree of improved proxy model is quartic polynomial equation, the ECDF generated from the updated

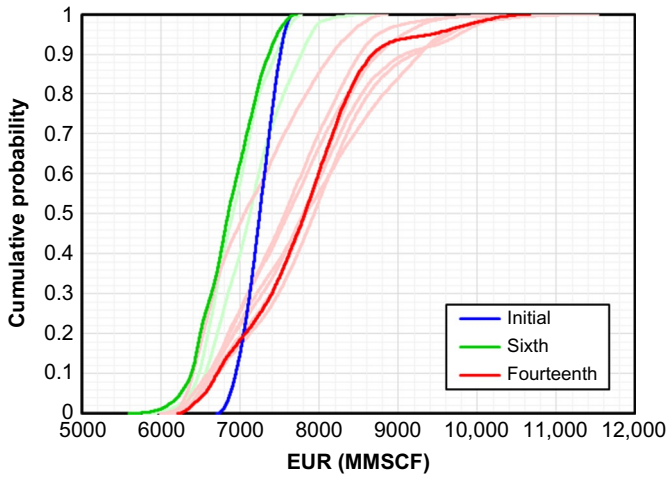

FIG. 7.19 ECDFs of EUR after 30 years vs. iterations during the history-matching process (Wantawin et al., 2017).

proxy model has converged, which also serves as the criteria for stopping the history-matching workflow. For this reason, we use a two-sample K-S test to evaluate the difference of two ECDFs from the last iteration and the preceding iteration. The absolute distance between two ECDFs was tested against the null hypothesis. If the absolute distance is larger than the critical value, then the null hypothesis will be rejected, indicating that the samples generated for these two iterations were not taken from the same reference distributions. The alpha value is used to calculate the critical absolute distance. Based on the alpha value of 5%, the K-S test failed to reject the null hypothesis when evaluating two ECDFs from the 13th and the 14th iterations. All the test results for the previous iterations are listed in the last column of Table 7.3. Hence, the history-matching workflow was terminated after the 14th iteration with 165 collected history-matching solutions, which are sufficient to produce stable probabilistic EUR forecasts. Finally, the P10, P50, and P90 of EUR at the end of 30 years were determined as 6.71, 7.82, and 8.67 BSCF respectively. Next, we compared these results with the EUR predicted from the direct MCMC method.

7.4.5 History-Matching Results From Direct MCMC Method

We also used the direct MCMC method to generate exhaustive history-matching solutions and the EUR distribution using reservoir-simulation models within the designed parameter space. This method can build ECDF of EUR distribution from actual simulation solutions without from the proxy models. The Metropolis-Hastings (MH) algorithm (Metropolis et al., 1953; Hastings, 1970), one of the classic MCMC methods, was applied to make samples in this study. The initial sample was provided for the Metropolis-Hastings algorithm based on the best history-matched model from the two-level full-factorial design. This sample has matrix permeability of 100 nD, fracture half-length of 300 ft, fracture conductivity of 10 mD-ft, and fracture height of 135 ft. The RMSE of cumulative gas production for this initial sample is 42.7 MMSCF. The step size of one-sixth and the variance of 100,000 $MMSCF^2$ was assumed to generate the next step of the chain and calculate the acceptance ratio. The total 10,000 samples were proposed for this workflow. The convergence of the MCMC is validated through monitoring the mean and the coefficient of variance (CV) of all the uncertain parameters. The CV is a dimensionless statistical parameter suitable to measure variation for the data set with different units or widely different means, which is calculated by (Everitt, 1998):

$$C_v = \frac{\sigma}{\mu}, \tag{7.9}$$

where C_v is the coefficient of variation, σ is the standard deviation, and μ is the mean.

Fig. 7.20 displays the means and the CVs for the four uncertain parameters against the number of MCMC proposed samples. As shown, the means and CVs

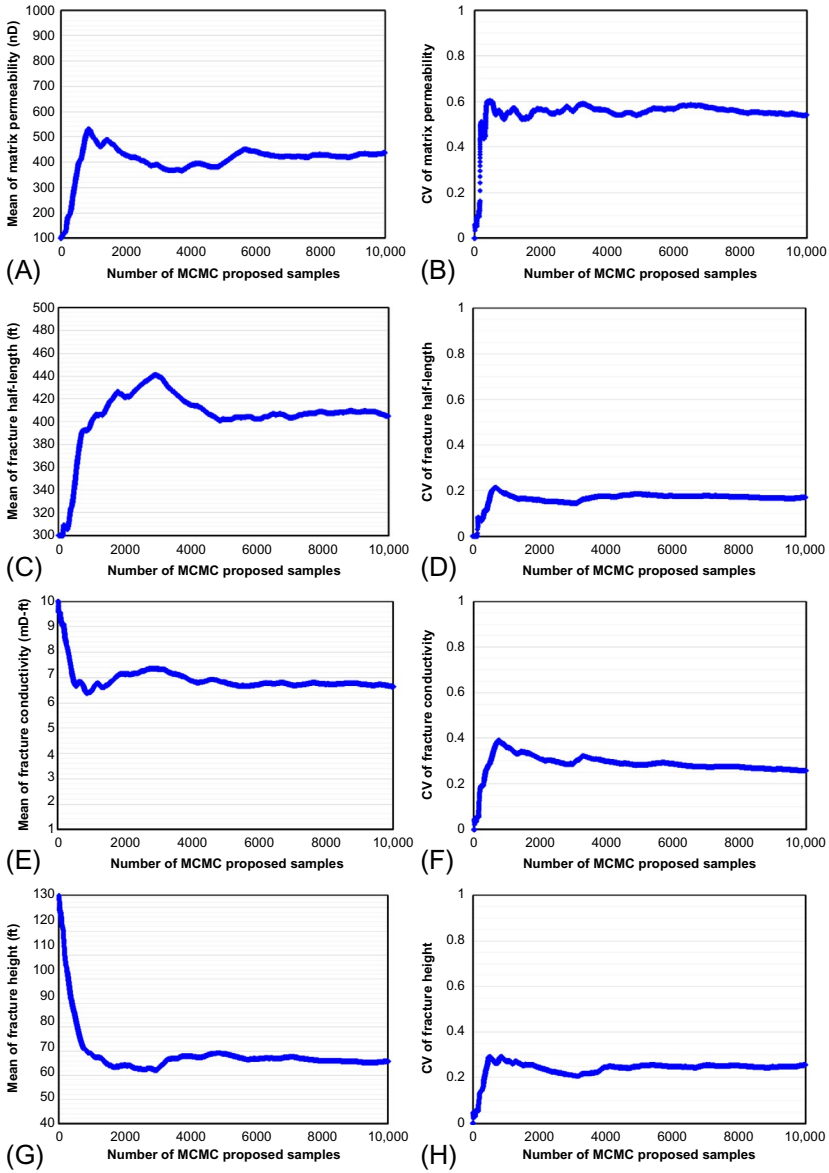

FIG. 7.20 Mean and coefficient of variance for the four uncertain parameters vs. number of MCMC proposed samples (Wantawin et al., 2017). (A) Mean of matrix permeability; (B) CV of matrix permeability; (C) mean of fracture half-length; (D) CV of fracture half-length; (E) mean of fracture conductivity; (f) CV of fracture conductivity; (G) mean of fracture height; (H) CV of fracture height.

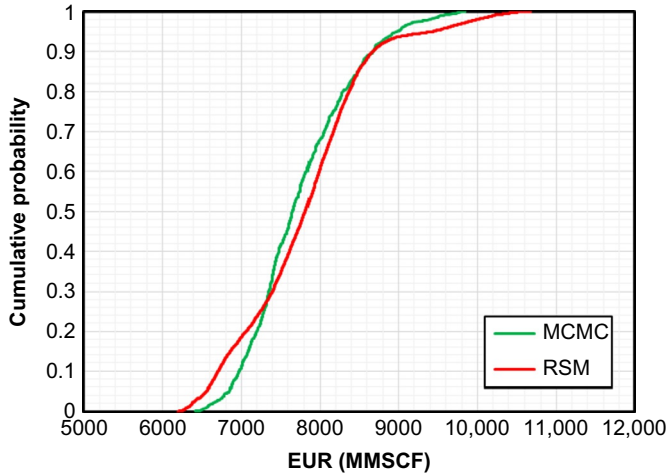

FIG. 7.21 Comparison of ECDF of EUR after 30 years from the proxy model after iteration and direct MCMC method (Wantawin et al., 2017).

seem fairly stabilized at the late parts of the MCMC chains, which convince us that the convergence of the MCMC is acceptable after 10,000 samples. There are 855 different samples from these 10,000 samples satisfying the history-matching tolerance at RMSE of 50 MMSCF.

We compared the ECDF generated from the direct MCMC method (in *green color*) with the ECDF from the iterative RSM method (in *red color*) in Fig. 7.21. A large number of proposed samples are needed to refine the ECDF for the direct MCMC method. However, the continuous functions of proxy models are used to build ECDF for the iterative RSM method, which reduces the cost of computation significantly. It can be seen that the probabilistic EUR distribution generated using the quartic proxy model at the 14th iteration of iterative RSM method reasonably agrees with that created from the direct MCMC method. On the other hand, both quadratic and cubic proxy models underestimate the probabilistic range of EUR distribution even though the history-matching solutions may arrive within early several iterations. The comparison of P10, P50, and P90 of EUR between the direct MCMC method and the iterative RSM method along with their computational requirement are presented in Table 7.4. It can be noticed that the difference of EURs from both methods is negligible. Besides different sample sizes, the assumption of the initial sample for the Markov chain also affects this dissimilarity. In addition, the total number of simulation runs performed by the iterative RSM method is significantly lower than that of the direct MCMC method. Correspondingly, a higher overall acceptance ratio (a percentage of history-matching solutions over total number of runs) of 41.25% for the iterative RSM method is obtained, which is a substantial improvement. In conclusion, the iterative RSM method with the history-matching solutions can sufficiently approximate the true distribution of prediction parameters while maintaining high computational efficiency.

TABLE 7.4 Comparison of EUR After 30 Years and Number of Simulation Runs Between the Iterative Response Surface Methodology and Direct MCMC Method (Wantawin et al., 2017)

	Iterative RSM Method	Direct MCMC Method	% of Difference
P10 of EUR after 30 years (BSCF)	6.71	6.98	4.01%
P50 of EUR after 30 years (BSCF)	7.82	7.66	−2.01%
P90 of EUR after 30 years (BSCF)	8.67	8.68	−0.02%
Total simulation runs	400	10,000	–
History-matching solutions	165	855	–

7.4.6 Discussions About Overfitting Issue

In this study, we used the cubic and quartic polynomial equations to fit some of the history-matching proxy models and the prediction proxy models. These high-order polynomials with more number of regression coefficients can fit a training data set more closely than the low-order polynomials. However, these higher-order polynomials are more prone to have the overfitting issue, which means that the proxy model may have poor prediction for a new data set despite a good fitting with the training data set. This explains why statisticians or reservoir engineers commonly use the quadratic or lower-order polynomials to fit data set, except that there are physical theories or validation tests to support using the higher-order polynomials. In our workflow, we chose the degree of polynomials based on two criteria: (1) high adjusted R^2, and (2) high predicted R^2. The highest adjusted R^2 and/or the highest predicted R^2 should be achieved for the appropriate polynomials when compared to the other polynomials. The adjusted R^2 is calculated for the total design points using the following equation:

$$\overline{R}^2 = 1 - \left[\frac{\sum_{i=1}^{n}\left(y_{proxy,i} - y_{simulator,i}\right)^2}{\sum_{i=1}^{n}\left(y_{simulator,i} - \overline{y_{simulator}}\right)^2}\right] \times \frac{(n-1)}{(n-m-1)}, \tag{7.10}$$

where $\overline{R}^2$ is the adjusted R^2, y_{proxy} is the response parameter using the proxy model, $y_{simulator}$ is the response parameter using the reservoir simulator, m is the total number of regression coefficients excluding the constant terms, and n is the number of the total design points. As can be seen from the formula,

the adjusted R^2 can be considered as a modified version of the standard R^2 through adjusting the number of predictors in the model. The higher m will decrease the $\overline{R^2}$ value if the other terms on the right-hand size remain the same. That is to say, the adjusted R^2 will promote using higher degree polynomials only when the model is improved to a certain extent.

Our second criterion, the predicted R^2, is calculated using the procedure called the training-and-testing method. Firstly, 80% of the total design points were randomly picked up and held as the training data. The same training data were used to evaluate every proxy. The polynomials are fitted with the training data. After that, we used the fitted proxy to predict the remaining 20% data that are typically called the testing data. Lastly, the predicted R^2 within proxy vs. actual responses of the testing data is evaluated using the equation:

$$R^2 = 1 - \left[\frac{\sum_{i=1}^{n'} \left(y_{proxy,i} - y_{simulator,i} \right)^2}{\sum_{i=1}^{n'} \left(y_{simulator,i} - \overline{y_{simulator}} \right)^2} \right], \tag{7.11}$$

where n' is the number of the testing data. Taking the predicted R^2 as an example, we evaluate the appropriate proxy model through fitting the 375 history-matching design points in the 14th iteration of the workflow. We randomly picked 300 points from the 375 points as the training data for the four polynomials proxies: (1) linear, (2) quadratic, (3) cubic, and (4) quartic. Then, we used the fitted four proxy models to predict the other 75 points. The comparisons between RMSE from the four proxy models vs. simulated RMSE along with their predicted R^2 are presented in Fig. 7.22. We can see that the best predicted R^2 is achieved by the quartic proxy model. Thus, we are convinced that the quartic proxy model is suitable and not overfitted for this case study.

7.5 FIELD APPLICATION IN BAKKEN TIGHT OIL RESERVOIR

In this section, we applied the assisted HM workflow with a field case study from the Middle Bakken Formation in North Dakota. The Bakken Formation is one of the main contributions to the tight oil production in North America. The lithology of Bakken Formation is complex and mixed between carbonate and clastic petroleum systems with low porosity and permeability, consisting of Upper and Lower Bakken Shales, Middle Bakken, Sanish, and Three Forks. To develop the Bakken Formation economically, it requires many horizontal wells with multistage hydraulic fracturing (Yu et al., 2014).

In this study, we performed history matching for one horizontal well with 15-month production data (Kurtoglu and Kazemi, 2012). We applied the introduced workflow to identify uncertain parameter ranges, both reservoir and fracture properties, and to find the possible history-matching solutions over the

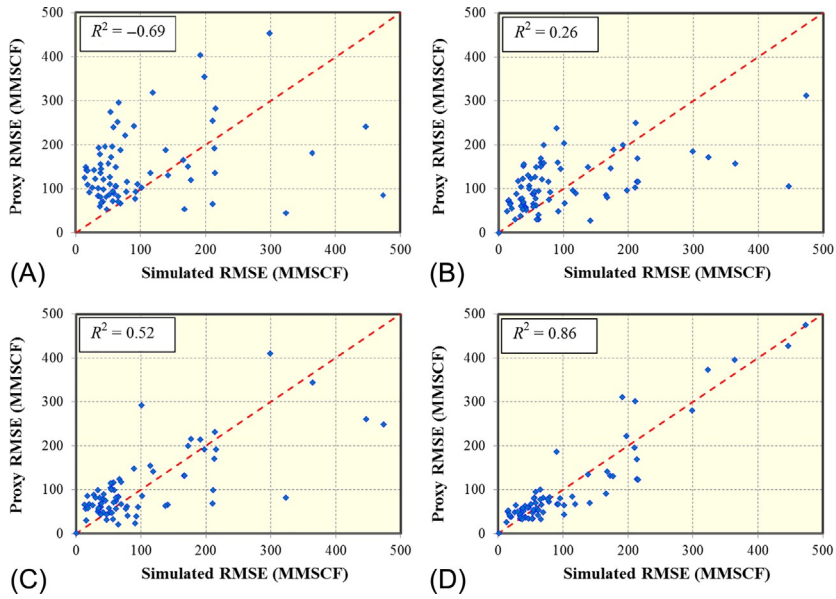

FIG. 7.22 Comparisons between proxy RMSE and simulated RMSE for different proxy models (Wantawin et al., 2017). (A) Linear proxy; (b) quadratic proxy; (C) cubic proxy; (D) quartic proxy.

parameter space. In other words, we calibrated the numerical model with historical-production data during early natural depletion. By using the assisted HM workflow, we were allowed to evaluate multiple realizations of reservoir properties and hydraulic fracture configuration.

7.5.1 Reservoir Model

We modeled a single horizontal well with multiple hydraulic fractures by numerical-reservoir simulator (CMG-IMEX, 2015). Fig. 7.23 shows the top view of the reservoir model including a horizontal well with multiple planar hydraulic fractures. The model dimension is of 10,500-ft length, 2640-ft width, and 50-ft height, covering the total area of 326 acres. We summarized the reservoir and fracture parameters used in the model in Table 7.5.

We modeled hydraulic fractures by using the LGR approach, which has been widely adopted to effectively model transient flow in hydraulically fractured reservoirs (Cipolla et al., 2009; Yu and Sepehrnoori, 2014). Then we calculated fracture permeability from fracture conductivity divided by fracture width. We assumed the hydraulic fractures fully penetrate the whole reservoir thickness. From production data, producing gas-oil ratio (GOR) is constant, so we adjusted the pressure-volume-temperature (PVT) fluid model to match the producing GOR. For water production, there were no published data; therefore, we assumed constant 25% water cut for history matching.

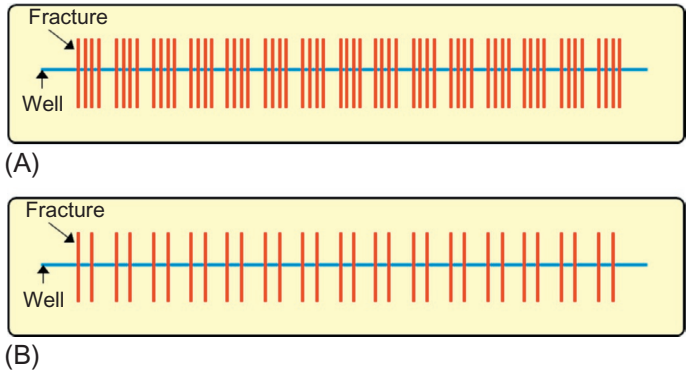

FIG. 7.23 Schematic of a reservoir model inclding a horizontal well with multiple hydrualic fractures (Wantawin et al., 2017). (A) Four effective fractures per stage; (B) two effective fractures per stage.

TABLE 7.5 Reservoir and Fracture Parameters of Middle Bakken Used for This Study (Wantawin et al., 2017)

Parameter	Value	Unit
Model dimension ($x \times y \times z$)	$10{,}502 \times 2640 \times 50$	ft
Number of grid blocks ($x \times y \times z$)	$178 \times 43 \times 1$	
Initial reservoir pressure	7800	psi
Reservoir temperature	245	°F
Total compressibility	1×10^{-6}	psi^{-1}
Bubble point pressure	2500	psi
Oil density	50.86	lb/ft^3
Gas density	0.92	
Matrix porosity	5.6%	
Horizontal well length	8828	ft
Number of stages	15	
Cluster spacing	118	ft
Fracture width	0.01	ft

7.5.2 Parameter Identification and Screening

We identified uncertain parameters from reservoir properties that have high uncertainty. Then we specified the typical range of each reservoir property for the history-matching process. Table 7.6 summarizes the minimum and maximum of six uncertain parameters, which will later be used for two-level full factorial design. According to the literature, the average porosity of Middle Bakken is 6% with low variance. In contrast, matrix permeability varies extensively from 1 to 50 μD (Dechongkit and Prasad, 2011; Pilcher et al., 2011; Kumar et al., 2013; Yu et al., 2014). The initial water saturation is between 25% and 50% in the Middle Bakken (Cherian et al., 2012). We had no direct measurement information of fracture conductivity, so we specified a wide estimated range for fracture conductivity. We identified these three parameters—matrix permeability, initial water saturation, and fracture conductivity—as numerical continuous variables.

Although the number of fracturing stages is certain, the number of effective hydraulic fractures per stage is still uncertain. Thus, we specified the effective hydraulic fractures per stage range of two to four fractures as minimum and maximum. In other words, the total number of fractures in the model varies from 30 to 60 as shown in Fig. 7.23. We identified the fracture number as discrete parameter including six discretized levels of 30, 36, 42, 48, 54, and 60 hydraulic fractures, so they distributed evenly and can serve a high-degree polynomial regression if necessary. Furthermore, we assumed each hydraulic fracture has equal fracture half-length. In reality, there is no direct way to measure fracture

TABLE 7.6 Six Uncertain Parameters for the Middle Bakken Horizontal Well (Wantawin et al., 2017)

Uncertain Parameter	Unit	Type	Minimum	Maximum
Matrix permeability	μD	Numerical, continuous	1	50
Initial water saturation	%	Numerical, continuous	25	50
Total fracture number		Numerical, discrete	30	60
Fracture conductivity	mD-ft	Numerical, continuous	5	500
Fracture half-length	ft	Numerical, discrete	92.1	399.1
Relative permeability	type	Categorical	Oil wet (0)	Water wet (1)

half-length; hence, we also assumed the hydraulic fracture propagating between 1.5 and 6.5 grid cells away from the wellbore as minimum and maximum, respectively. We specified six discretized levels of fracture half-length of 92.1, 153.5, 214.9, 276.3, 337.7–399.1 ft because the parameter depends on grid cell size.

Formation wettability affects the relative permeability curve—controlling the multiphase flow in reservoir. Relative permeability in tight reservoir, unlike a conventional reservoir, is cumbersome to be measured directly. In this study, we obtained relative permeability curve from the work by Yu and Sepehrnoori (2014). Then, we modified relative permeability curve toward water-wet condition—the intersection of oil and water relative permeability is higher than water saturation of 50%, as shown in Fig. 7.24. We classified relative permeability as categorical parameter. Lastly, after we completed identifying uncertain parameter, we identified model response parameters by an RMSE of BHP, gas production rate, and water production rate.

In this step, we had six uncertain parameters and three model responses for the screening process. We used two-level factorial design to evaluate the effect of each uncertain parameter upon each model response. Owing to six uncertain parameters, the design required 2^6 or 64 numerical simulation runs.

After completing all runs, we should ensure that the simulated data from all runs covered the entire interval of the actual data, so we could guarantee there was a history-matching solution in the ranges of uncertain parameters. To illustrate, Fig. 7.25 shows the BHP vs. time of 64 simulated cases (*blue lines*) compared with the actual data (*yellow circles*). As shown, all the actual data points lie within the simulated cases and they have similar decreasing trends. As a result, we were confident before continuing to the next step that we could search for the combinations of uncertain parameters within the specified parameter space to minimize the RMSE of BHP, gas, and water-production rate.

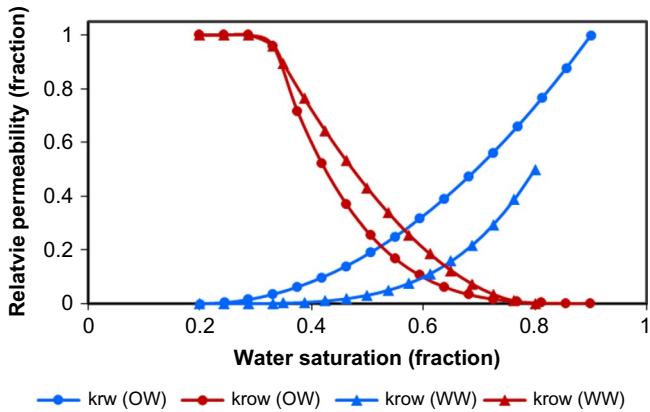

FIG. 7.24 Relative permeability curves from oil-wet (OW) to water-wet (WW) used in this study for the Middle Bakken well (Wantawin et al., 2017).

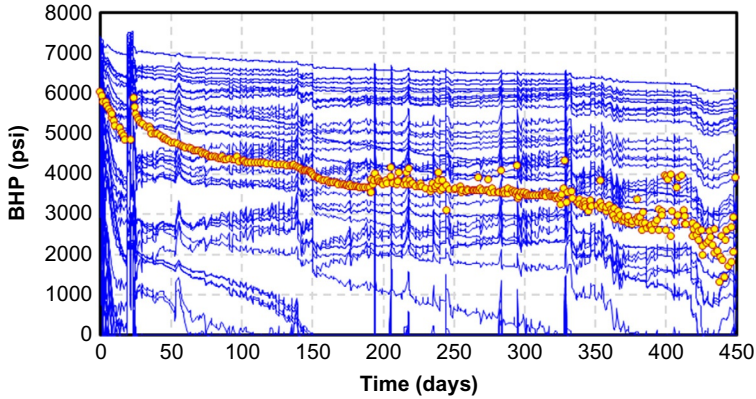

FIG. 7.25 Comparison between simulated BHP of 64 cases and observed BHP (Wantawin et al., 2017).

Then, we performed the analysis by selecting the significant modeling terms and by applying the recommended data transformation in order to improve the proxy-model regression quality. We selected significant model terms from the half-normal plots. Moreover, we used power transformation of the model response to better differentiate the terms with large effects.

Fig. 7.26 shows the half-normal plots of three model responses. The half normal plot compares the absolute value of the effect from each term (including interactions) on the probability scale. High-effect terms would fall near the right side and deviate from the rest of the terms. In other words, if they are out of normal distribution, these terms affect significantly on model response. As shown, each model response has different significant terms. Terms that yield significant effects on RMSE of BHP and gas-production rate are matrix permeability, initial water saturation, fracture half-length, and their interaction terms. Whereas the significant terms for RMSE of water-production rate are initial water saturation, relative permeability and matrix permeability. On the other hand, fracture conductivity and fracture number do not affect significantly as the other terms. Thus, the later process would exclude both parameters' range to build the proxy models. The proxy models from two-level factorial design are presented in the following equations:

$$[RMSE(BHP)]^{1.22} = 1.34(10)^4 - 3.33(10)^3 A - 3.85(10)^2 B - 2.27(10)^3 E - 3.76(10)^3 AB + 3.81(10)^3 AE + 1.71(10)^3 BE, \tag{7.12}$$

$$[RMSE(Gas)]^{1} = 5.72(10)^4 - 2.75(10)^4 A + 1.25(10)^4 B - 1.52(10)^4 E - 1.25(10)^4 AB + 1.53(10)^4 AE, \tag{7.13}$$

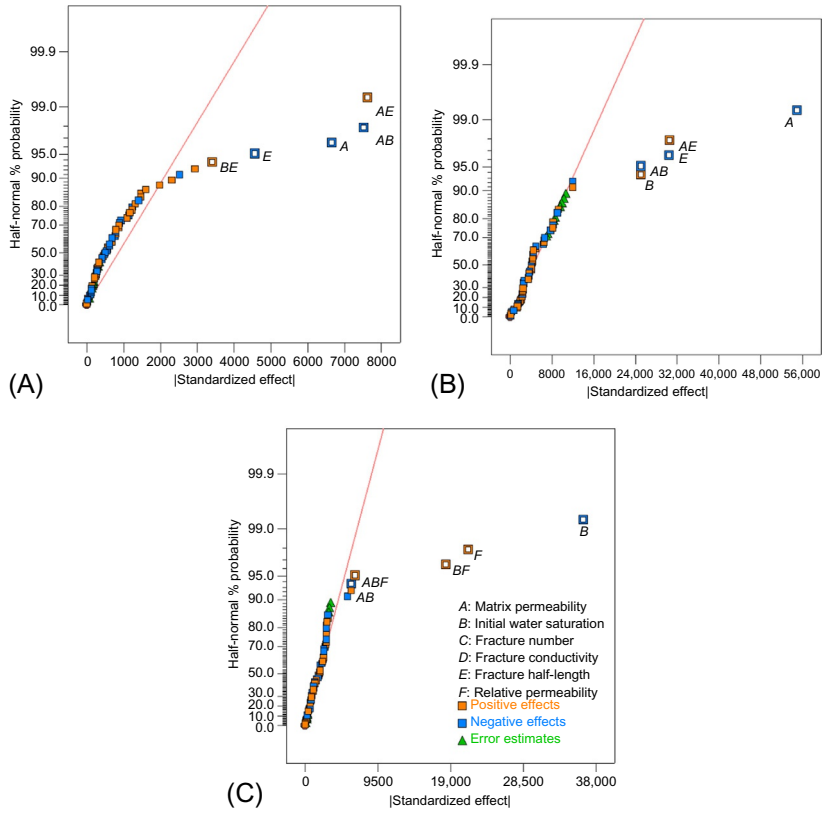

FIG. 7.26 Half-normal plots for screening important uncertain parameters affecting response parameters (Wantawin et al., 2017). (A) RMSE of BHP; (B) RMSE of gas production rate; (C) RMSE of water production rate.

$$[RMSE(Water)]^3 = 4.64(10)^5 - 2.20(10)^4 A - 1.79(10)^5 B + 9.37(10)^4 F - 2.50(10)^4 AB + 2.44(10)^4 AF + 8.23(10)^4 BF + 2.72(10)^4 ABF, \quad (7.14)$$

where $RMSE(BHP)$, $RMSE(Gas)$, and $RMSE(Water)$ represent predicted RMSE of BHP, RMSE of gas production rate, RMSE of water production rate, respectively. A, B, E, and F represent coded factors for matrix permeability, initial water saturation, fracture half-length, and relative permeability, respectively. The coded factors transformed the original uncertain parameters to dimensionless factor, where the high levels of uncertain parameters are coded as +1 and the low levels of the uncertain parameters are coded as -1.

To validate the linear assumption of the two-level factorial design, we used eight center points. These center points have the uncertain parameters between the maximum and minimum values. The estimated errors of center points, shown by *green triangle* in Fig. 7.26, are the residuals of proxy-estimated

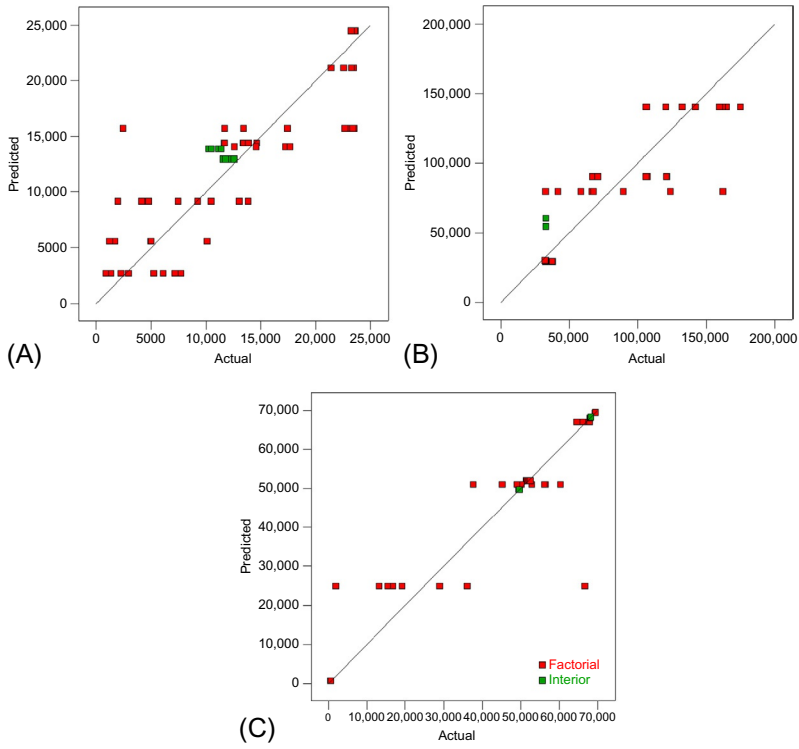

FIG. 7.27 Comparison of proxy model results against the actual simulation results (Wantawin et al., 2017). (A) RMSE of BHP; (B) RMSE of gas production rate; (C) RMSE of water production rate.

and actual value. In this case, the triangles appear to align with the normal line; hence, this means they behave as a normal distribution and their error estimates of linear model may be statistically insignificant. Additionally, Fig. 7.27 illustrates the validation of these center points—the comparison between the predicted responses from proxy models and the actual simulation results. The plots show that the residuals of all center points are in line with the fitted model and take on a normal distribution. It should be noted that a linear model with interaction terms is a coarse approximation of the actual response and barely to be used for the prediction purposes; however, for the screening purpose, using linear model was sufficient for the analysis in this step.

In case the validation process suggests linear model as two-level factorial, design fails. That means we should consider the higher class of DoE/RSM. This study also briefly illustrated the application of D-optimal design as an alternative preliminary screening tool. The design is suitable for identifying critical variables as it automatically selects design points that maximize the information regarding the polynomial coefficients (Stat-Ease, 2015). We used the quadratic model as a base model. Fig. 7.28 shows the ranking of F-value of the selected

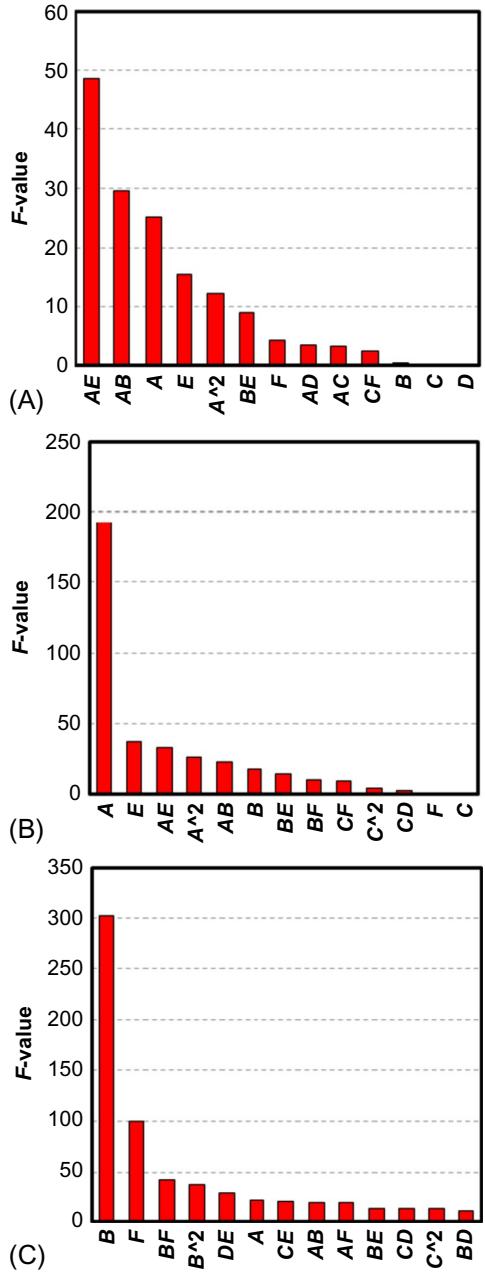

FIG. 7.28 Ranking uncertain parameters based on *F*-vales from the D-optimal design (Wantawin et al., 2017). (A) RMSE of BHP; (B) RMSE of gas production rate; (C) RMSE of water production rate.

model terms from D-optimal design. F-value compares the variance of the term over that of the residual; therefore, terms with higher F-value are likely to have more effect on the response. However, one disadvantage of D-optimal design is that it does not detect three-way interaction while the two-level factorial design does. From the plot, we concluded that the significant parameters are similar to the ones from half-normal plots of two-level factorial design in Fig. 7.26.

In summary, we determined significant parameters from the half-normal plot of two-level factorial design. We selected those significant parameters from ones that deviate more from a normal population of all effective terms. In addition, we could investigate the significant parameters with D-optimal design, using the calculated F-value. The higher F-value was, the more effect those parameters had on the model response. The set of significant parameters may be different for different model responses. We should select all important ones for the subsequent proxy modeling. In this case study, from both analyses, we screened from all six terms reducing to four significant terms including matrix permeability, initial water saturation, fracture half-length, and relative permeability.

7.5.3 History Matching and Probabilistic Forecasting

In this step, we regressed the proxy model based on four uncertain parameters screening from previous step: matrix permeability, initial water saturation, fracture half-length, and relative permeability. And we used the constant value for the other two insignificant parameters—30 hydraulic fractures and fracture conductivity of 500 md-ft, based on the case with the lowest RMSE of BHP, gas production rate, and water production rate by two-level factorial design. In this study, we initially used the I-optimal design with a quadratic base model for RSM design. We started with total 25 simulation cases to estimate the coefficient of the quadratic polynomial terms, providing extra points to fill the parameter space and supporting the optimality.

Then, we used the MH algorithm for sampling the points for simulation runs. We assigned a priori uniform distribution for all four uncertain parameters and specifically assigned for fracture half-length and relative permeability type as discrete uniform distribution. Next, in this study, the workflow initiated 10 Markov chains and 10,000 proposed samples assigned to each chain. After that, the workflow filtered the accepted samples from the MH algorithm to find the HM solutions—comparing the value of model response whether they were lower than the predefined HM tolerance. The tolerances/thresholds of RMSE of BHP, gas production rate, and water production rate are 350 psi, 33 MMSCF/D, and 20 STB/D, respectively. From the runs performed during preliminary screening step, we found that these threshold values delivered the acceptable history-matching quality for this study. Finally, at the end of 7th iteration, the proxy models have evolved to the following equations:

$$[RMSE(BHP)]^{-0.34} = 8.34(10)^{-2} + 2.32(10)^{-3}A + 5.09(10)^{-3}B + 2.73(10)^{-5}E - 5.96(10)^{-3}F + 1.62(10)^{-2}AB - 1.92(10)^{-2}AE - 6.57(10)^{-3}AF - 7.26(10)^{-3}BE - 7.21(10)^{-3}BF - 1.57(10)^{-2}A^2 + 1.22(10)^{-2}B^2, \tag{7.15}$$

$$[RMSE(Gas)]^{-1} = 3.30(10)^{-5} + 7.06(10)^{-6}A - 2.41(10)^{-6}B + 2.23(10)^{-6}E + 4.82(10)^{-7}F + 2.31(10)^{-6}AB - 2.40(10)^{-6}AE - 7.3(10)^{-7}BE + 1.56(10)^{-6}BF + 1.34(10)^{-6}EF - 9.12(10)^{-6}A^2 - 1.26(10)^{-6}E^2, \tag{7.16}$$

$$[RMSE(Water)]^{0.17} = 2.11 - 2.20(10)^{-2}A - 1.43(10)^{-1}B - 5.35(10)^{-3}E + 9.28(10)^{-2}F - 3.51(10)^{-2}AB + 6.97(10)^{-2}AE + 4.09(10)^{-2}AF - 2.47(10)^{-2}BE + 1.04(10)^{-1}BF + 3.12(10)^{-2}EF + 1.01(10)^{-1}A^2 - 2.01(10)^{-1}B^2. \tag{7.17}$$

At the end of 7th iteration, there were 121 numerical-simulation runs conducted in total, and the workflow collected 63 history-matching solutions. As mentioned earlier, the workflow developed the framework by sampling the combination of uncertain parameters from prior proxy model, and then ran the numerical simulation, and later used the simulation results as the input for the subsequent iterations. Fig. 7.29 shows contour plots of the proxy models from the 7th iteration. The plot shows RMSE of BHP, gas production rate and water production rate across matrix permeability, and initial water saturation under a given fracture half-length of 92.1 ft and water-wet wettability condition. For this case, the minimum region from every proxy model is coincidently located near the maximum permeability and initial water saturation—the region all three model responses mutually yield low value. As shown, the accepted samples from MCMC algorithm, illustrated by *yellow circles* in Fig. 7.29, accumulated densely in the region of low-model responses. Besides, we monitored the performance of proxy models with the increasing number of simulation runs as shown in Fig. 7.30. The figures display the actual RMSE of BHP, gas production rate, and water production rate from the first simulation case to the last one. The RMSE for each model response was developed quickly and simultaneously to low value according to the modified MH algorithm. The algorithm automatically rejected the combination of uncertain parameters that would not move the Markov chains to the target posterior distribution. Despite low and stable actual RMSE, the later stage of runs in Fig. 7.30 was the fine-tuning process for proxy models accuracy. Eventually, we discovered the region that shares minimum of three model responses.

To validate the improvement accuracy of the proxy models, Fig. 7.31 compares the actual simulated and proxy-model predicted RMSE of BHP, gas production rate, and water production rate of the ensemble in the 1st, the 3rd, and the 7th iterations. Accordingly, the data points became less scattered

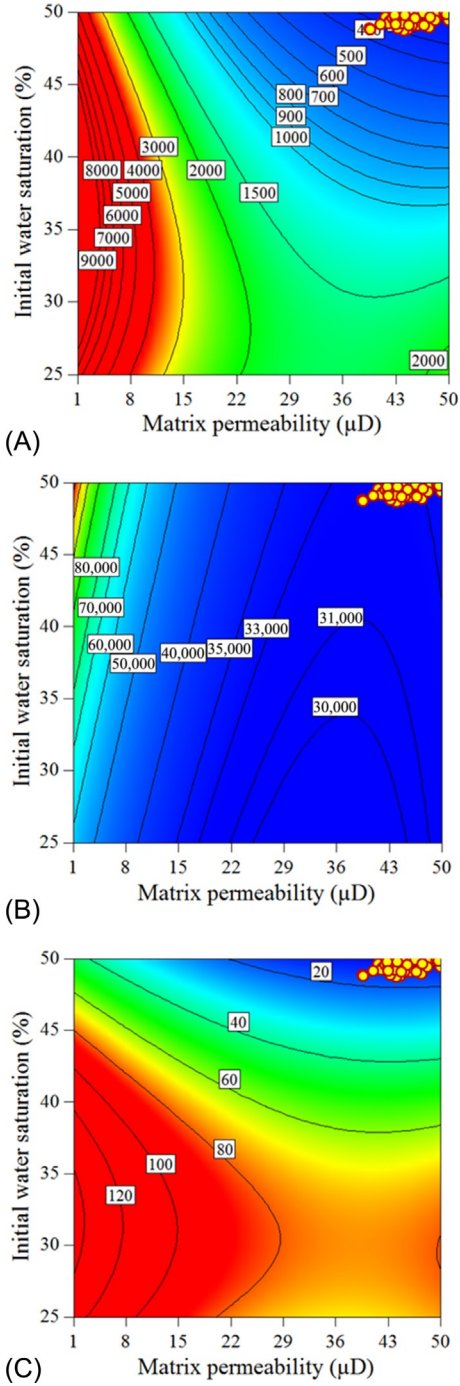

FIG. 7.29 Contour plots of the proxy models after the 7th iteration process (Wantawin et al., 2017). (A) RMSE of BHP (psi); (B) RMSE of gas production rate (MSCF/D); (C) RMSE of water production rate (STB/D).

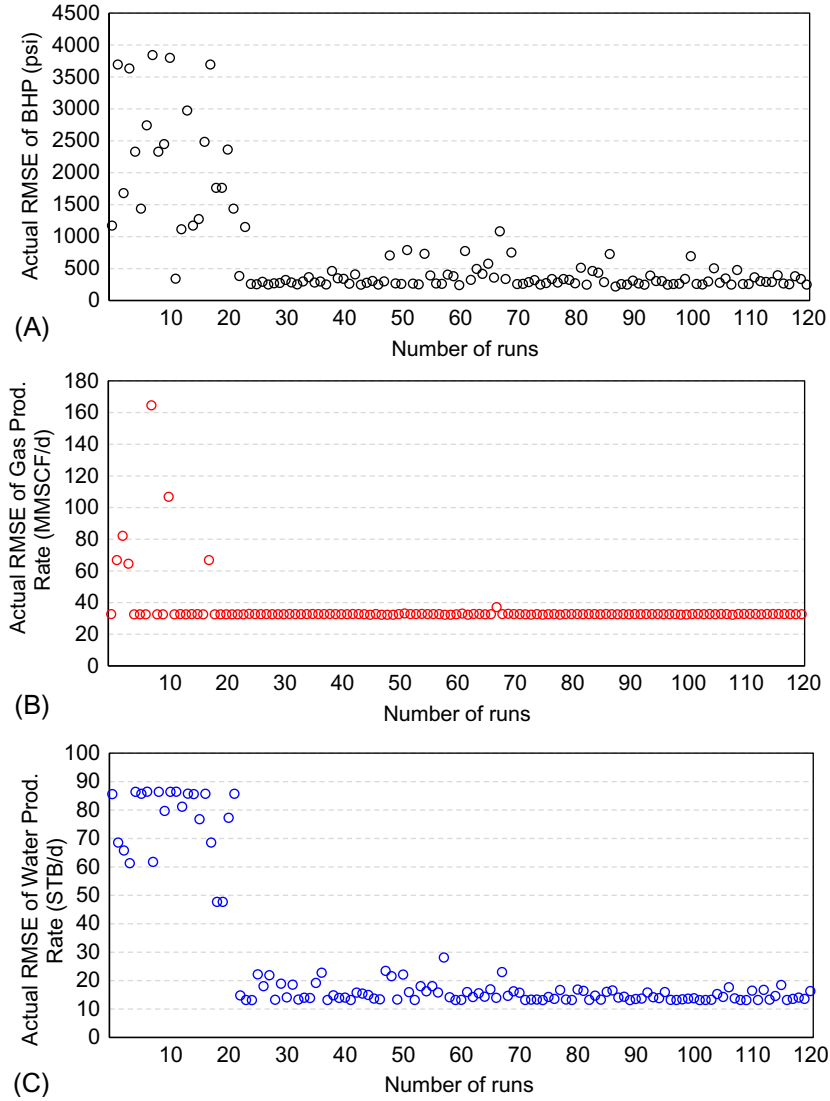

FIG. 7.30 The performance of proxy models with the increasing number of simulation runs during the HM process (Wantawin et al., 2017). (A) RMSE of BHP; (B) RMSE of gas production rate; (C) RMSE of water production rate.

and approach the unit slope line when progressing to later iterations. This suggested that the variances of model responses in the ensemble were getting lower; in other words, the proxy models had a better accuracy. Although the accuracy of polynomial proxy models might not be smoothed, they were still

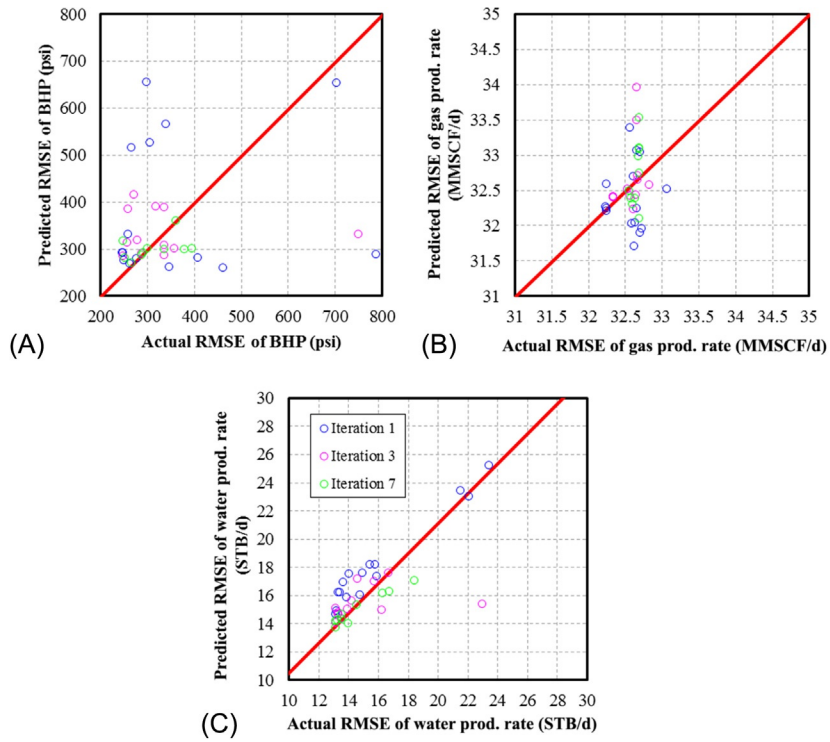

FIG. 7.31 Comparison of actual and predicated RMSEs at the 1st, the 3rd, and the 7th iterations (Wantawin et al., 2017). (A) RMSE of BHP; (B) RMSE of gas production rate; (C) RMSE of water production rate.

able to approximate the HM solutions and later to be used for probabilistic EUR prediction.

As mentioned earlier, the HM workflow gradually collected the HM solutions through each iteration. If the RMSE from the numerical-simulation result was lower than the HM tolerance (RMSE of BHP of 350 psi, RMSE of gas production rate of 33 MMSCF/D, and RMSE of water production rate of 20 STB/D), the workflow would save those cases as HM solutions. Fig. 7.32 presents 63 HM solutions at the end of the 7th iteration. We controlled all reservoir simulation cases with the observed oil production rate so they were exactly matched with the observed data. As shown, although the solutions had some error contributed by noise during the later-time production period, they still yielded the reasonable match with the observed data.

After each iteration, we ran the history-matching solutions to perform a 30-year production forecasting by constraining the minimum BHP of 500 psi. Fig. 7.33 presents the predicted cumulative oil production from 63 HM solutions. Despite similar values of cumulative oil production at the end of

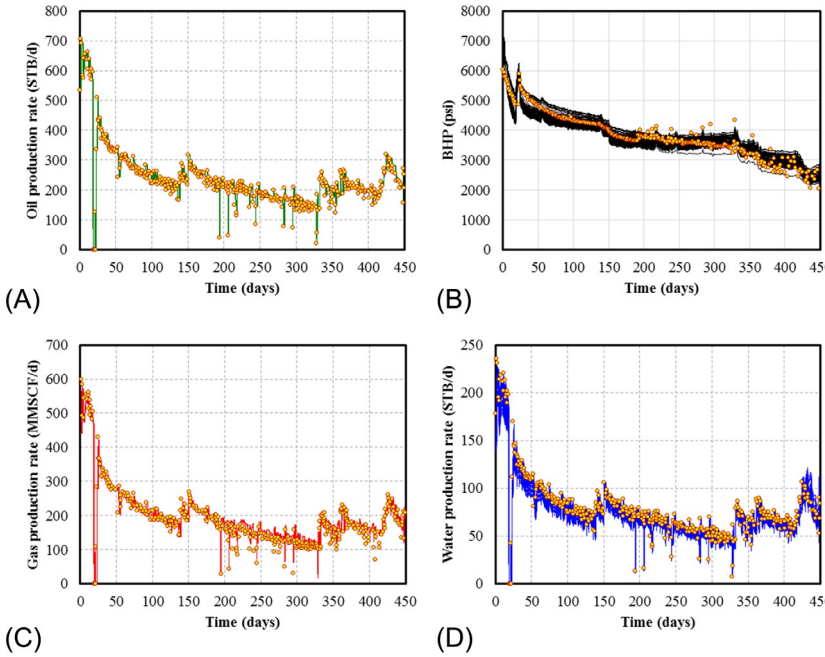

FIG. 7.32 Comparison of HM solutions with observed data (Wantawin et al., 2017). (A) Oil production rate; (B) BHP; (C) Gas production rate; (D) Water production rate.

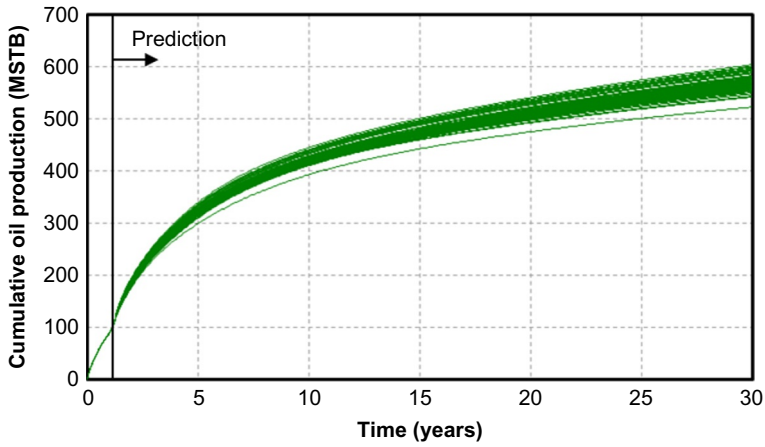

FIG. 7.33 Cumulative oil production of 63 HM solutions for a 30-year period (Wantawin et al., 2017).

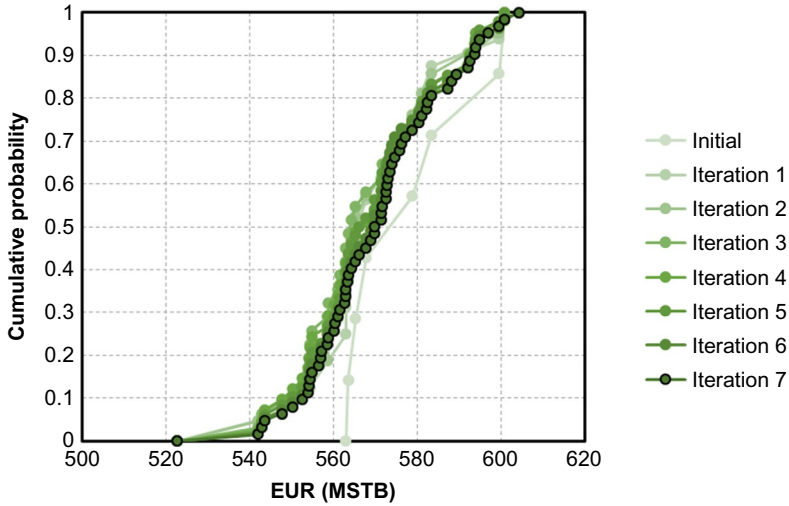

FIG. 7.34 Comparison of CDFs of EUR after 30 years of production between different iterations (Wantawin et al., 2017).

history-matching period, the different combination of uncertain parameters caused considerable discrepancies of the EUR magnitude after 30 years. Then, the workflow should ensure that the number of HM solutions was enough to generate a realistic ECDF of ultimate recovery, not underestimating the range of EUR.

Next, the workflow would be terminated if the ECDF of current iteration was similar to the previous iteration evaluated by the K-S test. Fig. 7.34 displays the ECDFs of EUR from the HM workflow. The distribution was stable after seven iterations and consisted of 63 HM solutions. Then, we evaluated P10, P50, and P90 of EUR. In this study, we defined probabilistic estimates as cumulative probabilities, i.e., P10 is defined as 10% of estimates less than P10. Thus, P10 is a low estimate; on the other hand, P90 is a high estimate. The P10, P50, and P90 of EUR after 30 years of prediction period were 552.59, 569.80, and 593.74 MSTB, respectively. To further reduce the uncertainty of EUR, we required longer historical data or additional model responses.

Finally, we generated the posterior distributions of uncertain parameters by using modified MH algorithm. The algorithm increases the proposed samples until we had 10,000 accepted solutions instead of keeping constant proposed samples. Besides, we analyzed all accepted samples without a thinning process and we treated the discrete parameters, i.e., fracture half-length and relative permeability, as numerical continuous parameters for visualization purposes. Also, we kept calculating the combined acceptance probability with the same formula.

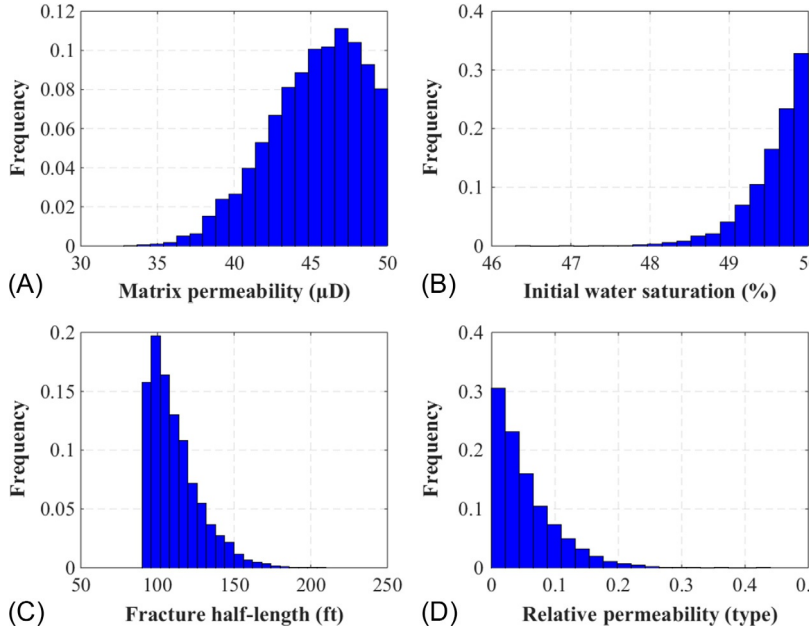

FIG. 7.35 Posterior distribution of four uncertain parameters (Wantawin et al., 2017). (A) Matrix permeability; (B) Initial water saturation; (C) Fracture half-length; (D) Relative permeability.

Fig. 7.35 illustrates the posterior distribution of matrix permeability, initial water saturation, fracture half-length, and relative permeability. As shown, the ranges of posterior distribution are narrower compared to the ranges of a priori uniform distribution in Table 7.6. In other words, the assisted HM workflow reduced the uncertainty of four parameters. Matrix permeability and initial water saturation appear to be skewed left while the fracture half-length appears to be skewed right. For fracture half-length, it matches with actual production data most frequent at 92.1 ft. For relative permeability, oil-wet condition provides more favorable results because the peak of distribution is near zero—the category of oil-wet relative permeability. Furthermore, Fig. 7.36 emphasizes the probability distribution of RMSE of BHP, gas production rate, and water production rate. The plots confirm that the posterior distribution of uncertain parameters is sampled more frequently in low RMSE regions. Lastly, the assisted HM workflow works efficiently to identify the effective ranges of uncertain parameters as history-matching solutions and probabilistic distribution of EUR.

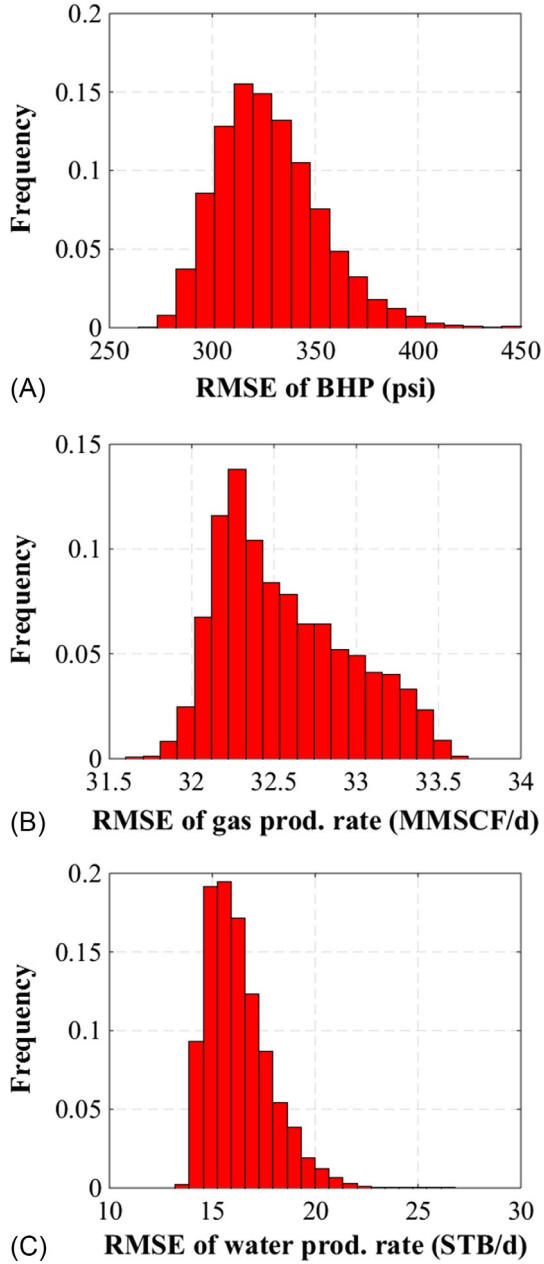

FIG. 7.36 Probability distribution of RMSEs (Wantawin et al., 2017). (A) RMSE of BHP; (B) RMSE of gas production rate; (C) RMSE of water production rate.

REFERENCES

Ajayi, B.T., Walker, K.J., Wutherich, K., Sink, J., 2011. In: Channel hydraulic fracturing and its applicability in the Marcellus shale. Paper SPE 149426, SPE Eastern Regional Meeting, Columbus, OH.

Bhark, E., Dehghani, K., 2014. In: Assisted history matching benchmarking: design of experiments-based techniques. Paper SPE 170690, SPE Annual Technical Conference and Exhibition, Amsterdam, The Netherlands.

Billiter, C., Dagistanova, K., King, G., 2008. In: Application of Brown-field experimental design techniques to a super giant carbonate reservoir. Paper SPE 115422, SPE Russian Oil & Gas Technical Conference and Exhibition, Moscow, Russia.

Chakravarti, I.M., Laha, R.G., Roy, J., 1967. Handbook of Methods of Applied Statistics. John Wiley and Sons, New York.

Cherian, B.V., Stacey, E.S., Lewis, R., Iwere, F.O., Heim, R.N., Higgins, S.M., 2012. In: Evaluating horizontal well completion effectiveness in a field development program. Paper SPE 152177, SPE Hydraulic Fracturing Technology Conference, The Woodlands, TX.

Cipolla, C.L., Lolon, E.P., Erdle, J.C., Rubin, B., 2009. In: Reservoir modeling in shale-gas reservoirs. Paper SPE 125530, SPE Eastern Regional Meeting, Charleston, WV.

CMG-IMEX, 2015. IMEX User's Guide. Computer Modeling Group Ltd.

Collins, P.W., Badessich, M.F., Ilk, D., 2015. In: Addressing forecasting non-uniqueness and uncertainty in unconventional reservoir systems using experimental design. Paper SPE 175139, SPE Annual Technical Conference and Exhibition, Houston, TX.

Dechongkit, P., Prasad, M., 2011. In: Recovery factor and reserves estimation in the Bakken petroleum system (analysis of the Antelope, Sanish and Parshall fields). Paper CSUG/SPE 149471, Canadian Unconventional Resources Conference, Calgary, Alberta, Canada.

Everitt, B., 1998. The Cambridge Dictionary of Statistics. Cambridge University Press, Cambridge, UK.

Feng, Y., Ning, Z., Liao, X., Liu, H., Liao, H., 2012. In: Case study: numerical simulation of a tight gas reservoir with multifractured horizontal wells. Paper SPE 160903, Nigeria Annual International Conference and Exhibition, Abuja, Nigeria.

Fillacier, S., Fincham, A.E., Hammersley, R.P., Heritage, J.R., Kolbikova, I., Peacock, G., Soloviev, V.Y., 2014. In: Calculating prediction uncertainty using posterior ensembles generated from proxy models. Paper SPE 171237, SPE Russian Oil and Gas Exploration & Production Technical Conference and Exhibition, Moscow, Russia.

Goodwin, N., 2015. In: Bridging the gap between deterministic and probabilistic uncertainty quantification using advanced proxy based methods. Paper SPE 173301, SPE Reservoir Simulation Symposium, Houston, TX.

Gupta, R., Collinson, R., Smith, G.C., Ryan, S.A., Louis, J.P., 2008. In: History matching of field production using design of experiments. Paper SPE 115685, SPE Asia Pacific Oil and Gas Conference and Exhibition, Perth, Australia.

Hastings, W., 1970. Monte Carlo sampling methods using Markov chains and their applications. Biometrika 57 (1), 97–109.

Izadi, G., Junca, J.P., Cade, R., Rowan, T., 2014. In: Multidisciplinary study of hydraulic fracturing in the Marcellus shale. Paper ARMA 2014-6975, 48th US Rock Mechanics/Geomechanics Symposium, Minneapolis, MN.

Jones, B., Goos, P., 2012. I-Optimal Versus D-Optimal Split-Plot Response Surface Designs. (Research Paper), University of Antwerp, Antwerp, Belgium.

Kassenov, B., King, G., Chaudhri, M., Abdrakhmanova, A., Jenkins, S., Bateman, P., Iskakov, E., 2014. In: Efficient workflow for assisted history matching and Brownfield design of experiment

for the Tengiz field. Paper SPE 172329, SPE Annual Caspian Technical Conference and Exhibition, Astana, Kazakhstan.

Kumar, S., Hoffman, T., Prasad, M., 2013. In: Upper and lower Bakken shale production contribution to the middle bakken reservoir. Paper SPE 168797, Unconventional Resources Technology Conference, Denver, CO.

Kurtoglu, B., Kazemi, H., 2012. In: Evaluation of Bakken performance using coreflooding, well testing, and reservoir simulation. Paper SPE 155655, SPE Annual Technical Conference and Exhibition, San Antonio, TX.

Li, J., Du, C.M., Zhang, X., 2011. In: Critical evaluation of shale gas reservoir simulation approaches: single-porosity and dual-porosity modeling. Paper SPE 141756, SPE Middle East Unconventional Gas Conference and Exhibition, Muscat, Oman.

Maschio, C., Schiozer, D.J., 2013. A new procedure to reduce uncertainties in reservoir models using statistical inference and observed data. J. Pet. Sci. Eng. 110, 7–21.

Mayerhofer, M.J., Stegent, N.A., Barth, J.O., Ryan, K.M., 2011. In: Integrating fracture diagnostics and engineering data in the Marcellus shale. Paper SPE 145463, SPE Annual Technical Conference and Exhibition, Denver, CO.

Metropolis, N., Rosenbluth, A.W., Rosenbluth, M.N., Teller, A.H., 1953. Equation of state calculations by fast computer machines. J. Chem. Phys. 21 (6), 1087–1092.

Myers, R.H., Montgomery, D.C., Anderson-Cook, C.M., 2009. Response Surface Methodology: Process and Product Optimization Using Designed Experiments, third ed. Wiley, Hoboken.

Nelson, B., Belyadi, F., Mashayekhi, A., Aminian, K., Ameri, S., 2014. In: Predicting long-term production behavior of the Marcellus shale. Paper SPE 169489, SPE Western North American and Rocky Mountain Joint Meeting, Denver, CO.

Peake, W.T., Abadah, M., Skander, L., 2005. In: Uncertainty assessment using experimental design: Minagish Oolite reservoir. Paper SPE 91820, SPE Reservoir Simulation Symposium, The Woodlands, TX.

Pilcher, R., Ciosek, J.M., McArthur, K., Hohman, J., Schmitz, P., 2011. In: Ranking production potential based on key geological drivers—Bakken case study. Paper IPTC 14733, International Petroleum Technology Conference, Bangkok, Thailand.

Sakhaee-Pour, A., Bryant, S., 2012. Gas permeability of shale. SPE Reserv. Eval. Eng. 15 (4), 401–409.

Shapiro, S.S., Wilk, M.B., 1965. An analysis of variance test for normality (complete samples). Biometrika 52 (3–4), 591–611.

Siddiqui, S., Dhuldhoya, K., Taylor, R., Dusterhoft, R., Hards, E., Niebergall, G., Stobo, B., 2015. In: An improved workflow for evaluating the performance of hydraulically fractured wells in unconventional reservoirs through production history matching using unstructured grid-based reservoir simulation. Paper SPE 174375, EUROPEC, Madrid, Spain.

Slotte, P.A., Smorgrav, E., 2008. In: Response surface methodology approach for history matching and uncertainty assessment of reservoir simulation models. Paper SPE 113390, SPE Europec/EAGE Annual Conference and Exhibition, Rome, Italy.

Stat-Ease, I., 2015. Design Expert Software (DX9). Stat-Ease, Inc., Minneapolis, MN

Energy Information Administration, U.S., 2013. Technically Recoverable Shale Oil and Shale Gas Resources: An Assessment of 137 Shale Formation in 41 Countries outside the United States. EIA, Washington, DC.

Vink, J.C., Gao, G., Chen, C., 2015. In: Bayesian style history matching: another way to underestimate forecast uncertainty?. Paper SPE 175121, SPE Annual Technical Conference and Exhibition, Houston, TX.

Wantawin, M., Yu, W., Dachanuwattana, S., Sepehrnoori, K., 2017. An iterative response-surface methodology by use of high-degree-polynomial proxy models for integrated history matching and probabilistic forecasting applied to shale-gas reservoirs. SPE J. 22 (6), 2012–2031.

Wantawin, M., Yu, W., Sepehrnoori, K., 2017. An iterative work flow for history matching by use of design of experiment, response-surface methodology, and Markov chain Monte Carlo algorithm applied to tight oil reservoirs. SPE Reserv. Eval. Eng. 20 (3), 613–626.

Wass, J.A., 2011. First steps in experimental design II: more on screening experiments. J. Valid. Technol. 17 (1), 12–20.

Yang, C., Nghiem, L., Erdle, J., Moinfar, A., Fedutenko, E., Li, H., Mirzabozorg, A., Card, C., 2015. In: An efficient and practical workflow for probabilistic forecasting of Brown fields constrained by historical data. Paper SPE 175122, SPE Annual Technical Conference and Exhibition, Houston, TX.

Yu, W., Lashgari, H., Sepehrnoori, K., 2014. In: Simulation study of CO_2 huff-n-puff process in Bakken tight oil reservoirs. Paper SPE 169575, SPE Western North American and Rocky Mountain Joint Regional Meeting, Denver, CO.

Yu, W., Sepehrnoori, K., 2014. In: Optimization of well spacing for Bakken tight oil reservoirs. Paper URTeC 1922108, Unconventional Resources Technology Conference, Denver, CO.

Yu, W., Sepehrnoori, K., Patzek, T.W., 2014. In: Evaluation of gas adsorption in Marcellus shale. Paper SPE 170801, SPE Annual Technical Conference and Exhibition, Amsterdam, The Netherlands.

Zubarev, D.I., 2009. In: Pros and cons of applying proxy-models as a substitute for full reservoir simulations. Paper SPE 124815, SPE Annual Technical Conference and Exhibition, New Orleans, LA.

Chapter 8

CO_2 Injection for Enhanced Oil Recovery in Tight Oil Reservoirs

Chapter Outline

8.1 INTRODUCTION

The Bakken formation with multiple oil-bearing layers is one of major productive tight oil reservoirs in North America (West et al., 2013), where Middle Bakken and Three Forks are the two primary layers for oil production since they have the best reservoir qualities, such as porosity and oil saturation (Iwere et al., 2012). It has been reported that the Middle Bakken has an estimated average oil resource of 3.65 billion barrels and Three Forks has an estimated average resource of 3.73 billion barrels (United States Geological Survey, 2013). Horizontal drilling and multistage hydraulic fracturing are the two key enabling technologies to make tight oil production commercial from the Bakken formation with low or ultralow permeability. The key dominant mechanisms for the primary recovery are depressurization and solution gas drive. Although with the advanced technologies, most estimates for primary oil recovery factor remain very low due to tight nature of the Bakken formation (Cherian et al., 2012; Hoffman, 2012). Hence, there are still substantial volumes of oil remaining in the reservoir, resulting in a strong motivation of applying enhanced oil recovery (EOR) methods to improve oil recovery in tight oil reservoirs. It has been

Shale Gas and Tight Oil Reservoir Simulation. https://doi.org/10.1016/B978-0-12-813868-7.00008-0

reported that a minor improvement in oil recovery factor such as 1% could yield 1.6 to 9 billion barrels of additional oil (Hawthorne et al., 2013). The 1% additional oil recovery factor could bring revenue of $128 to $720 billion with an assumption of crude oil price of $80 per barrel. Accordingly, it is important to investigate the potential of applying enhanced oil recovery methods to improve long-term oil productivity in the Bakken formation.

Although water flooding has been widely used in conventional oil reservoirs, it is challenging to be applied to unconventional oil reservoirs with low permeability because of low injectivity, poor sweep efficiency with fracture networks, and clay swelling problems. Nevertheless, it is believed that gas injection is more suitable due to lower viscosity and larger injectivity than water injection. Additionally, the depth of the Bakken formation (average of 10,000 ft) and high oil saturation are beneficial to gas injection (Iwere et al., 2012). Most gases used for injection include carbon dioxide (CO_2), nitrogen (N_2), natural gas, or the mixture of them. Among these gases, CO_2 has received much more attention for enhanced oil recovery in the Bakken formation (Kurtoglu et al., 2013; Song and Yang, 2013; Adekunle and Hoffman, 2014). CO_2 has a considerably lower minimum miscibility pressure (MMP) than that of the other gases, such as N_2 and CH_4 (Stalkup, 1987; Holm, 1987). The so-called MMP refers to the lowest pressure required to recover about 95% of the contacted oil at a given temperature, which highly depends on the reservoir temperature and crude oil composition (Holm, 1986, 1987). A high percentage of intermediate hydrocarbons (especially C_5-through-C_{12}) have a significantly larger impact on the MMP (Holm, 1987; Orr Jr. and Silva, 1987).

CO_2 injection is one of the most effective methods for enhanced oil recovery in conventional oil reservoirs, which has been well understood (Jarrell et al., 2002; Kong et al., 2015). The main mechanisms generally include oil swelling, oil viscosity reduction, oil density increasing, highly soluble in water, vaporization and extraction of crude oil, exerting an acid effect on rock (Holm and Josendal, 1974). CO_2-EOR process is generally classified as miscible or immiscible. For achieving a miscible oil-recovery process, the reservoir pressure is necessary to be maintained above the MMP. CO_2 and trapped oil will become completely miscible and CO_2 will extract light and intermediate hydrocarbons from the oil phase, and the interfacial tension will become zero and capillary pressure disappears, resulting in the oil phase and CO_2 phase, which contains some extracted hydrocarbon components, flowing together more easily through the porous media (Taber and Martin, 1983; Lambert et al., 1996; Martin and Taber, 1992). Fai-Yengo et al. (2014) showed that the effect of capillary pressure has negligible effect on oil recovery in the Bakken formation. The extraction of hydrocarbons is highly dependent on the density of the CO_2, and the CO_2 will extract more and heavier hydrocarbons with the increasing CO_2 density (Holm and Josendal, 1982; Orr Jr. et al., 1983; Sigmund et al., 1984). The CO_2 density varies from 0.1 to 0.8 g/cm^3 at pressure from 1000 to 4000 psi when the temperature is above its critical temperature of 87.9°F (Holm and Josendal, 1982). Holm and Josendal (1982) found that sufficient

hydrocarbon extraction occurs when the CO_2 density is about 0.42 g/cm^3, which is close to the CO_2 critical density of 0.468 g/cm^3. In practice, CO_2 injection is typically a multiple contact process since it is hard for the injected gas to be miscible with the in situ oil at the beginning, especially for the light and medium oil reservoirs (Wang et al., 2010). In the Bakken formation, the average reservoir pressure is between 7500 and 8000 psi and reservoir temperature is about 240°F (Kurtoglu et al., 2014). Under these conditions, the injected CO_2 is actually at super critical condition. The density of the super critical CO_2 is more like liquid, but the viscosity is like gas. Thus, the miscible process generally improves the oil recovery more effectively than that of immiscible process when injection pressure is below the MMP (Lambert et al., 1996).

Although CO_2-EOR in conventional reservoirs is well understood, it is still a new subject in unconventional oil reservoirs such as the Bakken formation with low permeability and multiple hydraulic fractures. Hawthorne et al. (2013) proposed five conceptual steps for CO_2 injection in the Bakken formation: (1) CO_2 flows into and through the fractures, (2) unfractured rock matrix is exposed to CO_2 at fracture surfaces, (3) CO_2 permeates the rock driven by pressure, carrying some hydrocarbon inward; however, the oil is also swelling and extruding some oil out of the pores, (4) oil migrates to the bulk CO_2 in the fractures via swelling and reduced viscosity, and (5) as the CO_2 pressure gradient gets smaller, oil production is slowly driven by concentration gradient diffusion from pores into the bulk CO_2 in the fractures. Also, they demonstrated that CO_2 is effective to improve oil recovery based on CO_2-exposure experiments with some rock samples from the Bakken formation. The main mechanisms for gas-EOR in naturally fractured reservoirs include viscous forces, gravity drainage, and molecular diffusion (Hoteit, 2013). However, in tight oil reservoirs with low permeability, the viscous forces and gravity drainage become less important while molecular diffusion will be dominant (Hoteit and Firoozabadi, 2006). Although there are many attempts to evaluate CO_2 injection in the tight oil reservoirs (Wang et al., 2010; Ren et al., 2011; Shoaib and Hoffman, 2009; Chen et al., 2014; Sheng, 2015), the effect of CO_2 molecule diffusion on well performance of the CO_2 injection is still poorly understood. Furthermore, the impacts of key reservoir and fracture properties such as permeability, fracture half-length, complex nonplanar fractures, natural fractures, and reservoir heterogeneity on the effectiveness of CO_2-EOR have not been evaluated quantitatively. Accordingly, a detailed study of investigation of the key parameters affecting the CO_2-EOR in the Bakken formation is necessary.

This chapter was mainly focused on numerical simulation of the CO_2-EOR process with typical reservoir and fracture properties from the Bakken formation. The comparison of two scenarios was investigated including CO_2 Huff-n-Puff and CO_2 flooding. The CO_2 Huff-n-Puff scenario consists of three stages such as CO_2 injection, CO_2 soaking, and production, as shown in Fig. 8.1. Effect of CO_2 molecular diffusion on the effectiveness of CO_2 injection was discussed in detail. Furthermore, a comprehensive sensitivity study was performed to investigate the effects of number of cycle, fracture half-length, permeability,

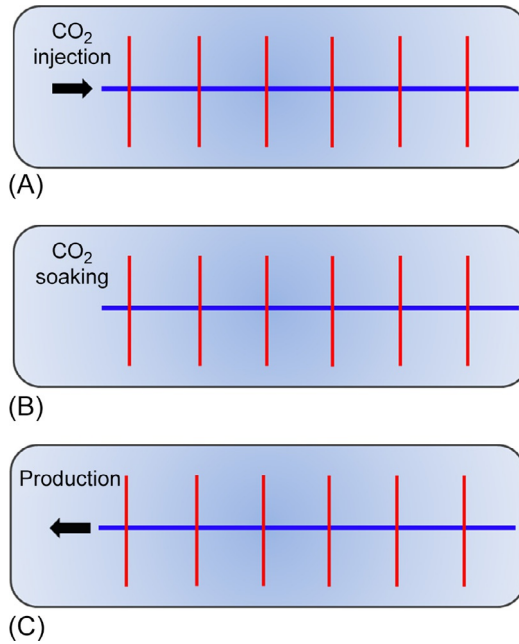

FIG. 8.1 The CO_2 Huff-n-Puff process in a horizontal well with multiple fractures (Yu et al., 2014). (A) Stage 1: CO_2 injection. (B) Stage 2: CO_2 soaking. (C) Stage 3: production.

and reservoir heterogeneity on the well performance of CO_2 Huff-n-Puff. This work can provide a better understanding of the effectiveness of CO_2 Huff-n-Puff process in the Bakken formation, which can be easily extended to evaluate CO_2 injection in the other tight oil reservoirs in North America, such as Eagle Ford shale in the Western Gulf Basin and Permian Basin in West Texas.

8.2 METHODOLOGY

8.2.1 Reservoir Simulation Model

The governing equation that describes the total mass balance for component i in the oil and gas phases is expressed by the following continuity equation, including accumulation term of component i in rock and fluid phases as well as convection, dispersion, and molecular diffusion terms of component i in phase (oil and gas phases) (Lashgari, 2014).

$$\frac{\partial}{\partial t}\left((1-\phi)\rho_s w_{is}+\phi\sum_{\ell=1}^{N_p}\rho_\ell S_\ell w_{i\ell}\right) + \vec{\nabla}\cdot\left(\sum_{\ell=1}^{N_p}\rho_\ell w_{i\ell}u_\ell-\phi\rho_\ell S_\ell\overline{\overline{K}}_{i\ell}\nabla w_{i\ell}\right)-r_i=0 \quad i=1,\ldots,N_c, \tag{8.1}$$

where ϕ is matrix porosity, ρ_s is matrix density, ρ_ℓ is density of phase ℓ, S_ℓ is saturation of phase ℓ, r_i is mass rate injection or production as source or sink term, N_p is number of phase, N_c is number of component, w_{is} is mass fraction of component i that precipitates on the matrix rock per unit volume, $w_{i\ell}$ is mass fraction of component i in the phase per unit volume, u_ℓ is Darcy's flow velocity, which is defined as

$$\frac{\overline{u}_\ell = -\overline{\overline{k}} k_{r\ell}}{\mu_\ell \left(\overline{\nabla} p_\ell - \rho_\ell \overline{g}\right),} \tag{8.2}$$

where $\overline{\overline{k}}$ is the formation permeability tensor, $k_{r\ell}$ is the relative permeability of phase ℓ, p_ℓ is pressure of phase ℓ, and μ_ℓ is viscosity of phase ℓ.

The dispersivity coefficient of component i in the phase ℓ ($\overline{\overline{K}}_{i\ell}$) is defined as

$$\frac{\overline{\overline{K}}_{i\ell} = \overline{\overline{D}}_{i\ell}}{\tau + \frac{\overline{\alpha}_\ell |\overline{u}_\ell|}{\phi S_\ell},} \tag{8.3}$$

where $\overline{\alpha}_\ell$ is the dispersivity coefficient of fluid ℓ in the longitudinal direction and two transverse directions, τ is tortuosity of the matrix, $\overline{\overline{D}}_{i\ell}$ is the diffusion coefficient of component i in phase phase ℓ. The Sigmund correlation (Sigmund, 1976) is often used to calculate the oil and gas diffusion coefficients (unit is cm^2/s) since it is valid for both oil and gas phases (Nghiem et al., 2000). The binary diffusion coefficient between component i and j is calculated by (Sigmund, 1976; Nghiem et al., 2000)

$$D_{ij} = \frac{\rho_\ell^0 D_{ij}^0}{\rho_\ell} \cdot \left(0.99589 + 0.096016\rho_{\ell r} - 0.22035{\rho_{\ell r}}^2 + 0.032874{\rho_{\ell r}}^3\right), \tag{8.4}$$

where $\rho_\ell^0 D_{ij}^0$ is the zero pressure limit of the product of density and diffusivity, which can be calculated by

$$\rho_\ell^0 D_{ij}^0 = \frac{0.0018583 T^{1/2}}{\sigma_{ij}^2 \Omega_{ij} R} \left(\frac{1}{M_i} + \frac{1}{M_j}\right)^{1/2}, \tag{8.5}$$

where $\rho_{\ell r}$ is the reduced density, which can be calculated from the following form:

$$\rho_{\ell r} = \rho_\ell \cdot \left(\frac{\sum_{i=1}^{n_c} y_{i\ell} v_{ci}^{5/3}}{\sum_{i=1}^{n_c} y_{i\ell} v_{ci}^{2/3}} \right), \tag{8.6}$$

where M_i is molecular weight of component i, R is universal gas constant, T is absolute temperature (K), v_{ci} is critical volume of component i, $y_{i\ell}$ is mole fraction of component i in phase ℓ, n_c is number of hydrocarbon components, σ_{ij} is

the collision diameter (Å), and Ω_{ij} is the collision integral of the Lennard-Jones potential (dimensionless). The diffusion of component i in the mixture is defined as

$$D_{i\ell} = \frac{1 - y_{i\ell}}{\sum_{j \neq i} \frac{y_{i\ell}}{D_{ij}}}. \tag{8.7}$$

Eq. (8.7) is used to calculate the amount of molecular diffusivity for Eq. (8.3). The collision diameter (σ_{ij}) and the collision integral of the Lennard-Jones potential (Ω_{ij}) can be calculated based on the component critical properties as follows (Nghiem et al., 2000; Reid et al., 1977):

$$\sigma_i = (2.3551 - 0.087\omega_i) \cdot \left(\frac{T_{ci}}{p_{ci}}\right)^{1/3}, \tag{8.8}$$

$$\varepsilon_i = k_B(0.7915 + 0.1963\omega_i) \cdot T_{ci}, \tag{8.9}$$

$$\sigma_{ij} = \frac{\sigma_i + \sigma_j}{2}, \tag{8.10}$$

$$\varepsilon_{ij} = \sqrt{\varepsilon_i \varepsilon_j}, \tag{8.11}$$

$$T^*_{ij} = \frac{k_B T}{\varepsilon_{ij}}, \tag{8.12}$$

$$\Omega_{ij} = \frac{1.06036}{\left(T^*_{ij}\right)^{-0.15610}} + \frac{0.19300}{\exp\left(-0.47635 T^*_{ij}\right)} + \frac{1.03587}{\exp\left(-1.52996 T^*_{ij}\right)} + \frac{1.76474}{\exp\left(-3.89411 T^*_{ij}\right)}, \tag{8.13}$$

where ω is acentric factor, p_c is critical pressure (atm), T_c is critical temperature (K), ε is the characteristic Lennard-Jones energy (ergs), and k_B is Boltzmann's constant (1.3805×10^{-16} ergs/K).

The system of partial differential equations (PDE) of Eq. (8.1) represents a reservoir simulation model. In this chapter, CMG-GEM (CMG-GEM, 2012), which is a numerical reservoir simulator, is used to solve Eqs. (8.1)–(8.7).

8.2.2 Reservoir Model Including Multiple Hydraulic Fractures

In our simulation model, a local grid refinement (LGR) with logarithmic cell spacing is utilized to model multiple hydraulic fractures explicitly. The fracture width is set at a small value (0.01 ft) but a large permeability. A no-flow boundary condition is used. This approach has been extensively used to model transient fluid flow in hydraulically fractured shale gas and tight oil reservoirs.

8.3 FLUID CHARACTERIZATION OF BAKKEN

Typical fluid properties of the Bakken formation are used to simulate the CO_2 injection for enhanced oil recovery. The average oil gravity of the Bakken formation is around 42 °API, indicating that the crude oil is light. Nojabaei et al. (2013) reported that the range for gas oil ratio (GOR) is from 507 to 1712 SCF/bbl and bubble point pressure varies from 1617 to 3403 psi based on the field production data from different location in the Bakken formation. Kurtoglu et al. (2014) conducted laboratory measurements of oil properties of eight fluid samples from the Middle Bakken and Three Forks, and presented that the bubble point is 1389–2674 psi, oil formation factor is 1.34–1.68 RB/STB, oil viscosity is 0.184–0.4883 cp, and GOR is 455–1062 psi. In this study, the crude oil of the Bakken is carefully divided into seven different pseudocomponents, i.e., CO_2, N_2, CH_4, C_2-C_4, C_5-C_7, C_8-C_9, C_{10+}, and their corresponding molar fractions are 0.02%, 0.04%, 25%, 22%, 20%, 13%, and 19.94%, respectively. In addition, these components are convenient to investigate different gas injection (CO_2, N_2, CH_4, or mixture) in the future study. The key oil properties are calculated, based on these components using CMG-WinProp (CMG-WinProp, 2012): oil gravity is 42 °API, GOR is 1000 SCF/bbl, bubble point is 2000 psi, oil formation factor is 1.6, which are within the reasonable range of typical values for the Bakken formation. The MMP is calculated as 3334 psi, which has a great match with the measured data of 3300 psi by Kurtoglu et al. (2014) using a rising-bubble apparatus (RBA). The other input data required for the Peng-Robinson equation-of-state (EOS) are listed in Table 8.1. The binary coefficient used for flash calculation is listed in Table 8.2.

8.4 SIMULATION OF CO_2 HUFF-N-PUFF

8.4.1 Base Case

For the base case, we set up a basic reservoir model with four effective hydraulic fractures within one stage because of the expensive computational time for the entire well with multiple fractures, as shown in Fig. 8.2. The dimensions for this segment are 340 ft × 1300 ft × 40 ft, which correspond to length, width, and thickness, respectively. The grid block size is set to 20 ft × 20 ft × 40 ft in x, y, z directions, respectively. Fracture half-length is 210 ft, fracture height is 40 ft, fracture conductivity is 50 md-ft, fracture width is 0.001 ft, and fracture spacing is 80 ft. The LGR for each grid with fracture is set as 7 × 1 × 1 to reduce the numerical dispersion effect. The air permeability of the Middle Bakken is on the order of microdarcies (Nojabaei et al., 2013). Water saturation ranges between 25% and 50% in the Middle Bakken (Cherian et al., 2012). In this study, matrix permeability of 10 μD and initial water saturation of 25% are used. Table 8.3 summarizes all the parameters used for simulation study based on the typical values of the Middle Bakken. The relative permeability curves from the work by Yu et al. (2014) are used. The reservoir is assumed to be homogeneous

TABLE 8.1 Compositional Data for the Peng-Robinson EOS in the Bakken Formation (Yu et al., 2015)

Component	Molar Fraction	Critical Pressure (atm)	Critical Temperature (K)	Critical Volume (L/mol)	Molar Weight (g/gmol)	Acentric Factor	Parachor Coefficient
CO_2	0.0002	72.80	304.20	0.0940	44.01	0.2250	78.0
N_2	0.0004	33.50	126.20	0.0895	28.01	0.0400	41.0
CH_4	0.25	45.40	190.60	0.0990	16.04	0.0080	77.0
C_2-C_4	0.22	42.54	363.30	0.1970	42.82	0.1432	145.2
C_5-C_7	0.20	33.76	511.56	0.3338	83.74	0.2474	250.0
C_8-C_9	0.13	30.91	579.34	0.4062	105.91	0.2861	306.0
C_{10+}	0.1994	21.58	788.74	0.9208	200.00	0.6869	686.3

TABLE 8.2 Binary Interaction Parameters for Oil Components From the Bakken Formation (Yu et al., 2015)

Component	CO_2	N_2	CH_4	C_2-C_4	C_5-C_7	C_8-C_9	C_{10+}
CO_2	0	−0.0200	0.1030	0.1327	0.1413	0.1500	0.1500
N_2	−0.0200	0	0.0130	0.0784	0.1113	0.1200	0.1200
CH_4	0.1030	0.0310	0	0.0078	0.0242	0.0324	0.0779
C_2-C_4	0.1327	0.0784	0.0078	0	0.0046	0.0087	0.0384
C_5-C_7	0.1413	0.1113	0.0242	0.0046	0	0.0006	0.0169
C_8-C_9	0.1500	0.1200	0.0324	0.0087	0.0006	0	0.0111
C_{10+}	0.1500	0.1200	0.0779	0.0384	0.0169	0.0111	0

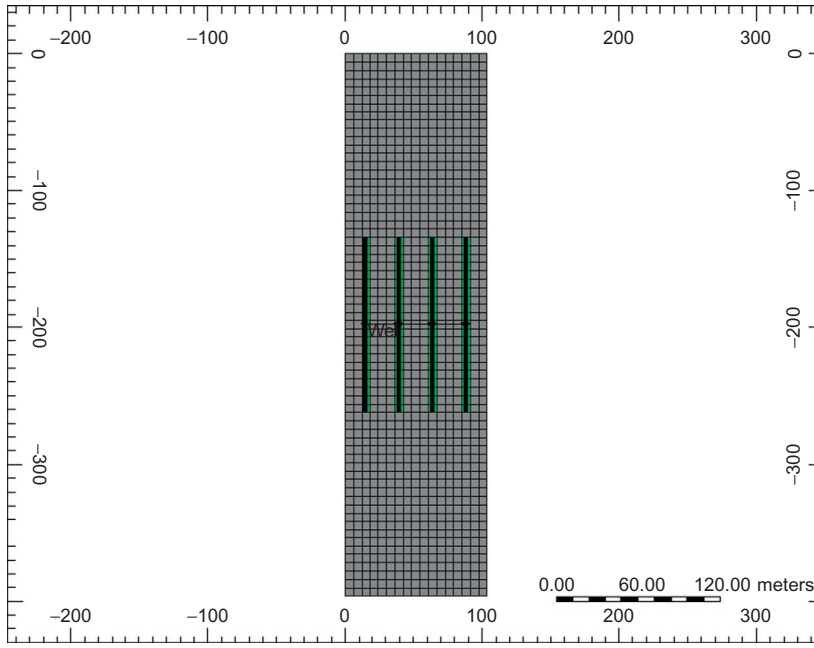

FIG. 8.2 A basic 3D model with four effective hydraulic fractures within one stage (Yu et al., 2015).

TABLE 8.3 Basic Reservoir and Fracture Properties From Middle Bakken for Simulation Study (Yu et al., 2015)

Parameter	Value	Unit
Initial reservoir pressure	8000	psi
Reservoir temperature	240	°F
Initial water saturation	0.25	–
Total compressibility	1×10^{-6}	psi^{-1}
Matrix permeability	10	μD
Matrix porosity	0.07	–
Stage spacing	340	ft
Fracture conductivity	50	md-ft
Fracture half-length	210	ft
Fracture height	40	ft

and the fractures are with stress-independent porosity and permeability. Flowing bottomhole pressure (BHP) of 1000 psi is used for simulation constraint.

The CO_2 diffusion coefficient in oil and gas phases can be determined, based on the published laboratory measurements (Grogan et al., 1988; Renner, 1988). Grogan et al. (1988) conducted experimental measurements of the CO_2 diffusion coefficients in pentane, decane, and hexadecane at temperature of 77°F and pressure up to 870 psi and presented that the CO_2 diffusion coefficients are in the range of 1.80×10^{-5} cm^2/s to 7.59×10^{-5} cm^2/s. Renner (1988) measured the CO_2 diffusion coefficients in decane at temperature of 100°F and pressure up to 850 psi and reported that the CO_2 diffusion coefficients range from 1.97×10^{-5} cm^2/s to 12.6×10^{-5} cm^2/s. It is worth noting that the CO_2 diffusion coefficients in oil phase at reservoir condition are 5–10 times higher than those measured at ambient conditions (Denoyelle and Bardon, 1983). More importantly, the diffusion coefficient for the super critical CO_2 is 10–100 times of that for liquid (Kumar and Mittal, 1999). Thus, the range of CO_2 diffusion coefficient of 0.0001–0.01 cm^2/s is selected and investigated in this study. For the base case, CO_2 diffusion coefficient in both oil phase and gas phase is assumed to be 0.001 cm^2/s and the diffusion coefficient of the other components is assumed to be zero. For the CO_2 Huff-n-Puff process, initially the horizontal well produces for 3 years, and then it is converted to a CO_2 injector with constraints of the maximum injection rate of 500 MSCF/day and the maximum bottomhole pressure of 8000 psi. After 1 year of CO_2 injection, the well is shut-in and soaked for 3 months. Finally, the well is put back into production. This is defined as one cycle of CO_2 Huff-n-Puff process. After 1 year of production of this cycle, another cycle of CO_2 Huff-n-Puff continues. The total production period of the well is 30 years. In order to compare the well performance of the base case with CO_2 injection and CO_2 diffusion, the case without CO_2 injection is simulated, which means that the well is only under shut in corresponding to the well is under CO_2 injection and soaking for the case with CO_2 injection, and another case with CO_2 injection while without considering CO_2 diffusion effect is also simulated.

Fig. 8.3 compares the oil recovery factor with and without CO_2 injection and CO_2 diffusion and only with primary production. As shown, the oil recovery factor at 30 years of production for the case with CO_2 injection and diffusion is the highest. Also, the oil recovery factor is almost the same for the case without CO_2 injection and the case only with primary production. In addition, the recovery factor of the case with CO_2 injection while without CO_2 diffusion is the lowest, illustrating that CO_2 diffusion plays an important role in simulating CO_2 injection for enhanced oil recovery. Figs. 8.4 and 8.5 compare CO_2 gas mole fraction distribution for the CO_2 injection cases with and without considering CO_2 diffusion. As shown, without CO_2 diffusion, most CO_2 molecules are mainly concentrated around hydraulic fractures due to the low permeability of shale matrix; however, with CO_2 diffusion, the CO_2 molecules can diffuse into the shale matrix to mix with the oil phase, leading to a higher oil recovery. Thus,

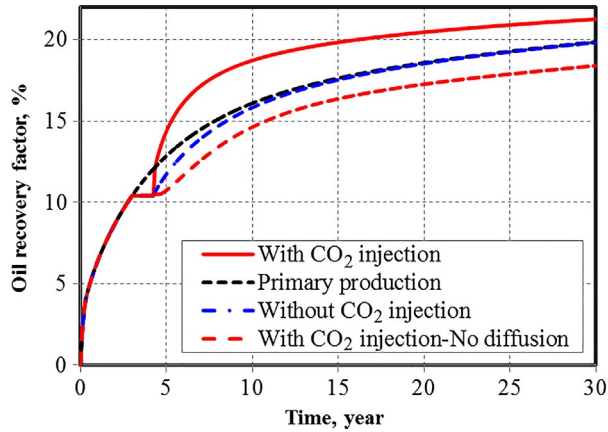

FIG. 8.3 Comparison of oil recovery factor with and without CO_2 injection and CO_2 diffusion and only with primary production (Yu et al., 2015).

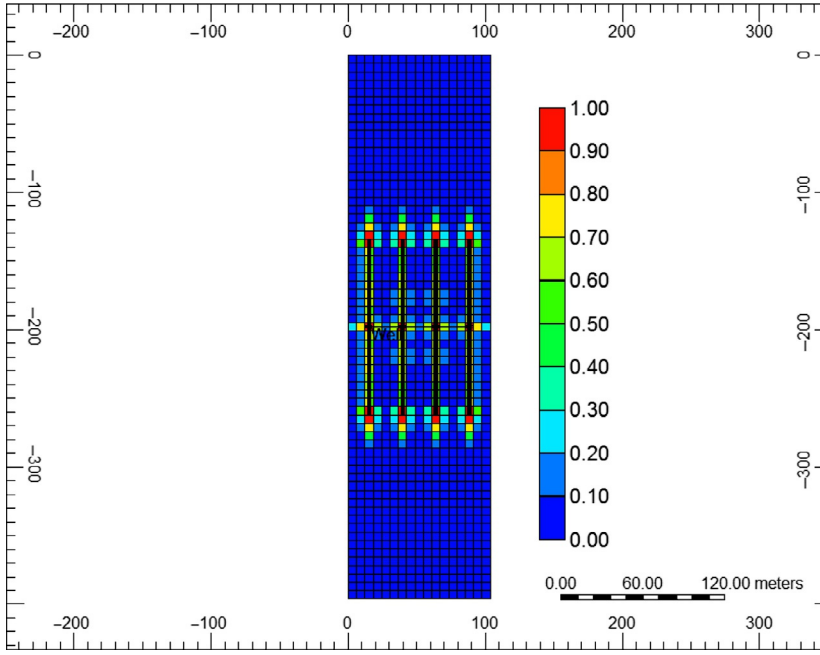

FIG. 8.4 CO_2 gas mole fraction distribution without considering CO_2 diffusion (Yu et al., 2015).

the CO_2 diffusion term should be considered in order to accurately model CO_2 injection for enhanced oil recovery in reservoir simulation model. Without considering CO_2 diffusion term, large amount of CO_2 will backflow to the surface after the end of soaking time and impede oil production, as shown in Fig. 8.6.

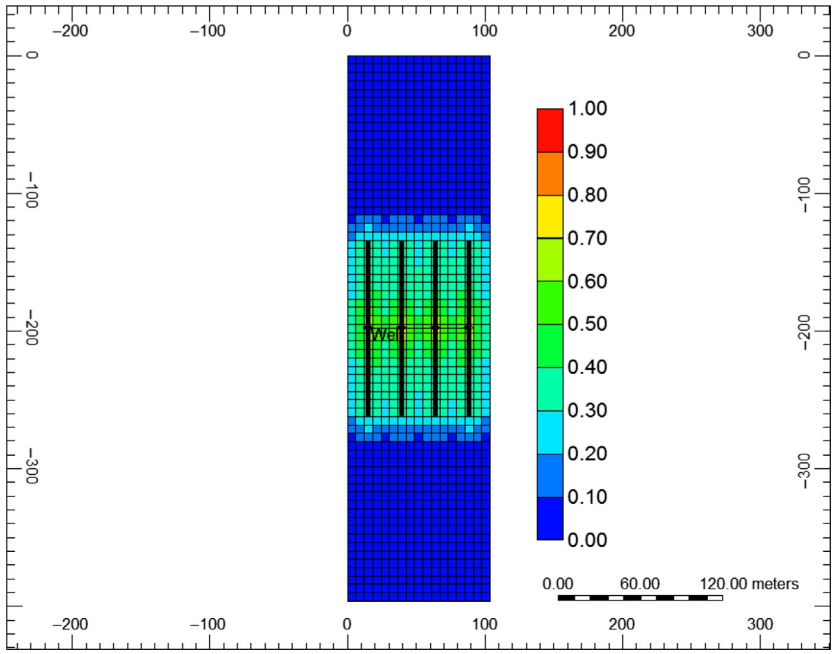

FIG. 8.5 CO_2 gas mole fraction distribution with considering CO_2 diffusion (Yu et al., 2015).

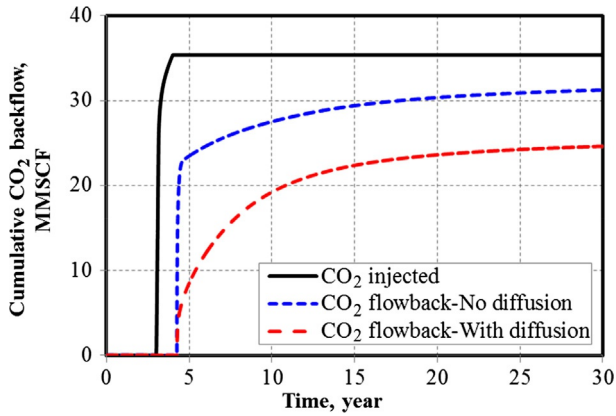

FIG. 8.6 Comparison of total volume of CO_2 injected and volume of CO_2 backflow to the surface with and without considering CO_2 diffusion (Yu et al., 2015).

The results show that about 88% of CO_2 injected is produced back at the end of production period without considering CO_2 diffusivity, while 69% of CO_2 injected is produced back with considering CO_2 diffusivity. For the base case, the oil recovery factor is increased by 2.90%, 1.93%, and 1.40% through CO_2

injection when compared to the case without CO_2 injection at 10, 20, and 30 years of production, respectively.

8.4.2 Effect of CO_2 Diffusion Coefficient

The effect of CO_2 diffusion coefficient for the comparison of well performance with and without CO_2 injection is shown in Fig. 8.7, while keeping the other parameters same as those in the base case. The case without CO_2 injection represents the primary production. As shown, the incremental oil recovery factor at 30 years of production is 0.10%, 1.40%, and 3.25% corresponding to the CO_2 diffusion coefficient of 0.0001, 0.001, and 0.01 cm^2/s, respectively, illustrating that the CO_2 diffusion plays an important role in improving oil recovery during the process of CO_2 Huff-n-Puff.

8.4.3 Effect of Number of Cycle

Fig. 8.8 shows the impact of number of cycle of CO_2 Huff-n-Puff on the comparison of well performance with and without CO_2 injection, while keeping the other parameters same as those in the base case. It can be seen that oil recovery factor increases with an increase in the number of cycle and the incremental oil recovery factor at 30 years of production is 1.40%, 2.12%, and 2.43% corresponding to the number of cycle of 1, 2, and 3, respectively.

8.4.4 Effect of Fracture Half-Length

In practice, fracture half-length is uncertain, which is hard to characterize exactly. The typical range of 110–310 ft is investigated. Fig. 8.9 presents the

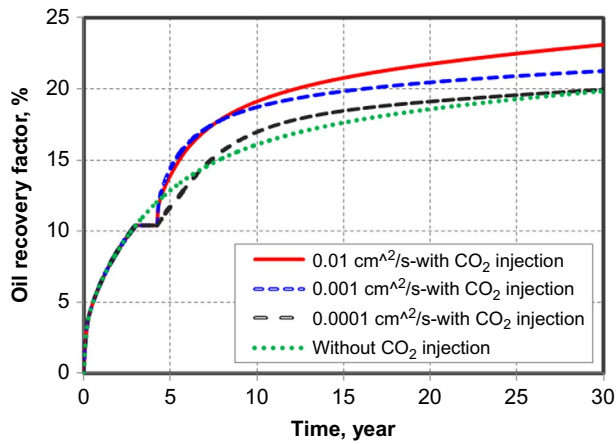

FIG. 8.7 Effect of CO_2 diffusion coefficient on comparison of oil recovery factor with and without CO_2 injection (Yu et al., 2015).

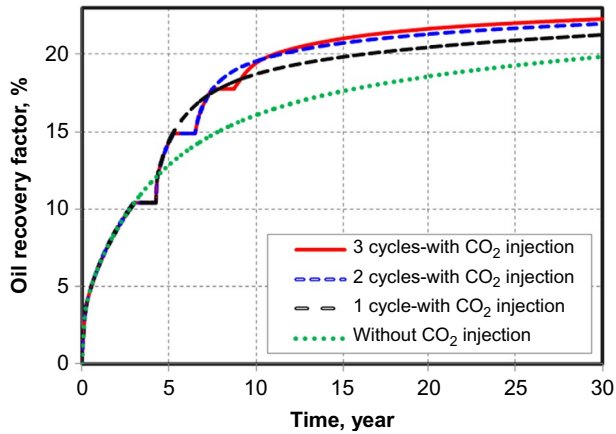

FIG. 8.8 Effect of number of cycle on comparison of oil recovery factor with and without CO_2 injection (Yu et al., 2015).

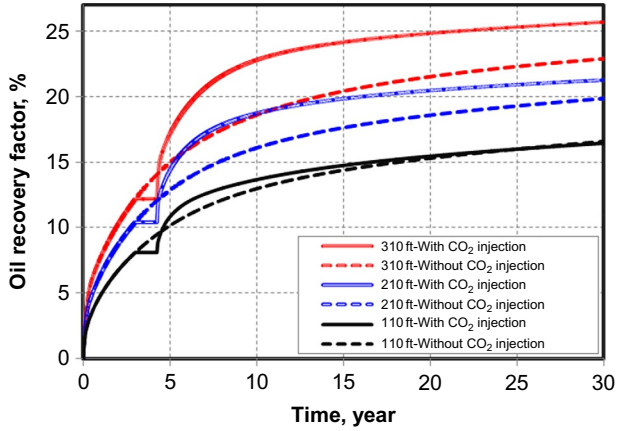

FIG. 8.9 Effect of fracture half-length on comparison of oil recovery factor with and without CO_2 injection (Yu et al., 2015).

impact of fracture half-length on the comparison of well performance with and without CO_2 injection, while keeping the other parameters same as those in the base case. It can be observed that the incremental oil recovery factor at 30 years of production is −0.13%, 1.40%, and 2.79% for the fracture half-length of 110, 210, and 310 ft, respectively, illustrating that longer fracture half-length is more favorable for the CO_2 Huff-n-Puff process. This is because longer fracture has more contact area with the reservoir, resulting in CO_2 diffusing in larger portion of the reservoir and leading to a higher recovery factor.

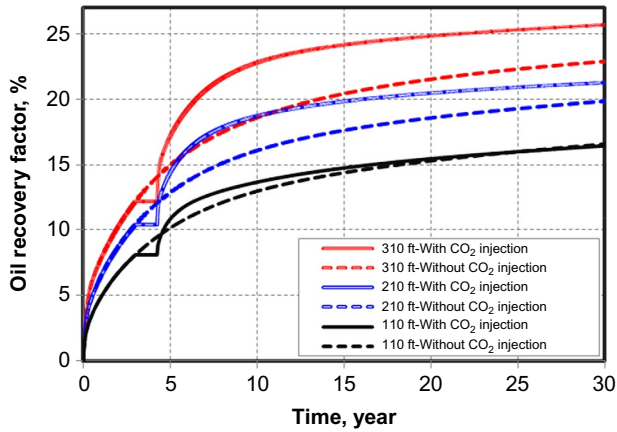

FIG. 8.10 Effect of reservoir permeability on comparison of oil recovery factor with and without CO_2 injection (Yu et al., 2015).

8.4.5 Effect of Reservoir Permeability

The typical reservoir permeability range of 0.001 md (1 μD) to 0.1 md (100 μD) is considered. Fig. 8.10 shows the effect of reservoir permeability on the comparison of well performance with and without CO_2 injection, while keeping the other parameters same as those in the base case. It can be seen that the incremental oil recovery factor at 30 years of production is 2.35%, 1.40%, and −0.70% for the permeability of 0.001, 0.01, and 0.1 md, respectively, illustrating that lower permeability is more beneficial for the CO_2 Huff-n-Puff process. This is because the reservoir with lower permeability at the end of primary production has larger residual oil saturation and the diffusion mechanism is more dominant than the convection mechanism compared to the larger permeability.

8.4.6 Effect of Reservoir Heterogeneity

In order to evaluate the reservoir heterogeneity effect, we used the geostatistical approach to generate stochastically multiple realizations of the permeability. The stochastic method uses and honors the mean and variances of observed static data in the presence of correlation lengths, which represent anisotropy of model in different dimensions and provide a relationship between data in space. This approach can give a better representation of the natural variability of the property. It is also a useful tool to quantify the uncertainty in the reservoir description. In order to generate heterogeneity, the spherical variogram type is used. We set up the correlation length of 1000 and 170 ft in the x and y direction, respectively. The nugget effect is used to generate discontinuity between data in reservoir. Larger nugget value causes more discontinuity and more heterogeneity. In this work, three different nugget values such as 0.0001, 0.2, and 0.7 are

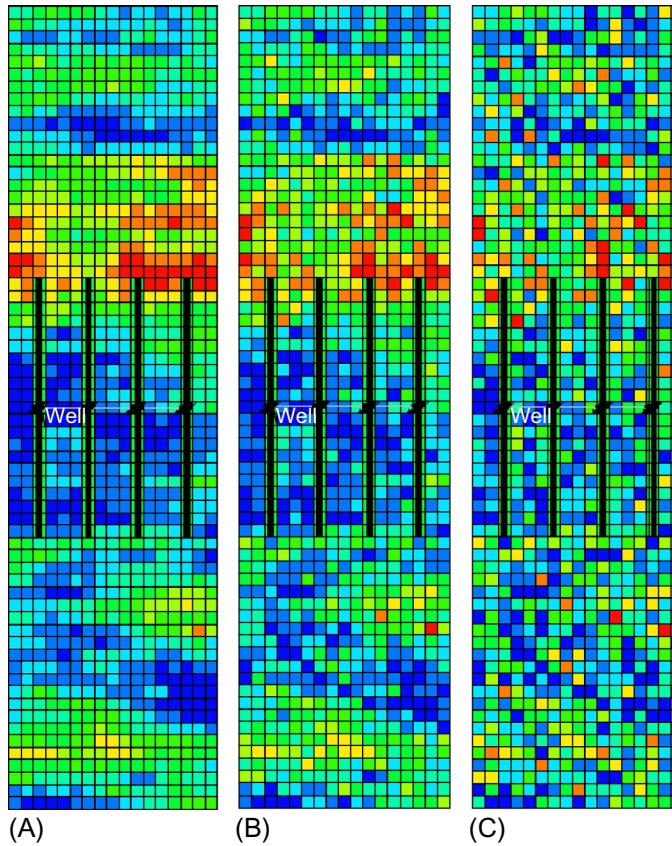

FIG. 8.11 Three cases of reservoir heterogeneity (Yu et al., 2015). (A) The minimum heterogeneity. (B) The medium heterogeneity. (C) The maximum heterogeneity.

used to represent the minimum heterogeneity, the medium heterogeneity, and the maximum heterogeneity, respectively, as shown in Fig. 8.11. The average permeability of these three cases remains the same as the base case of 0.01 md. The other parameters are the same as the base case.

Comparison of oil recovery factor with and without CO_2 injection for the homogeneous and heterogeneous cases is shown in Fig. 8.12. As shown, the incremental oil recovery factor at 30 years of production is 1.96%, 1.97%, and 2.02% for the minimum heterogeneity, the medium heterogeneity, and the maximum heterogeneity, respectively, which are larger than the homogeneous case (the base case) of 1.40%, illustrating that the more heterogeneous reservoir is more beneficial for the CO_2 Huff-n-Puff process in tight oil reservoirs. The reason is that the more heterogeneous reservoir has larger portion of lower permeability and higher residual oil saturation, resulting in the CO_2 diffusion process to be more pronounced.

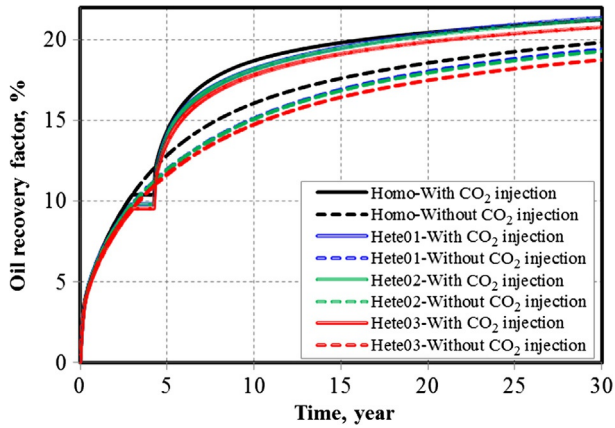

FIG. 8.12 Effect of reservoir heterogeneity on comparison of oil recovery factor with and without CO_2 injection (Hete01: minimum heterogeneity, Hete02: medium heterogeneity, Hete03: maximum heterogeneity) (Yu et al., 2015).

8.5 COMPARISON OF CO_2 HUFF-N-PUFF AND CO_2 FLOODING

We built a field-scale reservoir model with dimensions of 5240 ft × 5240 ft × 40 ft, which corresponds to length, width, and thickness, respectively. The grid block size is set to 20 ft × 20 ft × 40 ft in x, y, z directions, respectively. Multiple horizontal wells ranging from 4 to 8 are modeled. Each well was completed with four fracture stages and each stage includes four perforation clusters. In total, each well has 24 effective hydraulic fractures. For each well, the cluster spacing is 80 ft and lateral length is 4140 ft. The other key reservoir properties remain the same as those in Table 8.3. Based on the molar fraction for seven components as listed in Table 8.1, the primary oil properties were calculated again using CMG-WinProp (CMG-WinProp, 2012) and summarized in Table 8.4. The LGR is utilized to handle hydraulic fractures. Fracture height is 40 ft and fracture conductivity is 50 md-ft. The flowing BHP of 1800 psi was used for simulation constant. The CO_2 diffusion coefficient of 0.001 cm^2/s was used. The response surface methodology was used to systematically compare the well performance between CO_2 Huff-n-Puff and CO_2 flooding. Four uncertain parameters were considered including matrix permeability, number of wells, well pattern, and fracture half-length. Each one with the minimum and the maximum values is listed in Table 8.5. An aligned well pattern and a zipper well pattern are considered for well placement, as shown in Fig. 8.13. Fig. 8.14 displays the minimum and the maximum well number with different well spacing considered in this study.

In the following simulation study, CO_2 flooding scenario refers to half number of wells in an alternating manner are treated as CO_2 injectors after 3 years of primary production while the others remain as producers until the end of

TABLE 8.4 Primary Oil Properties for the Middle Bakken Formation (Zuloaga et al., 2017)

Parameter	Value	Unit
MMP	2400	psi
Bubble point pressure	2968	psi
Oil gravity	42	°API
Oil viscosity at 8000 psi	1.4	cp
Oil viscosity at bubble point	0.36	cp
Oil density at bubble point	42.7	lb/ft3
Oil formation factor at bubble point	1.33	bbl/STB

TABLE 8.5 Four Uncertain Parameters With the Minimum and the Maximum Values (Zuloaga et al., 2017)

Parameter	Units	Type	Subtype	Minimum	Maximum
Permeability	md	Numeric	Continuous	0.001	0.1
Fracture half-length	ft	Numeric	Continuous	210	410
Number of wells	–	Numeric	Discrete	4	8
Well pattern	–	Categorical	Nominal	Zipper	Aligned

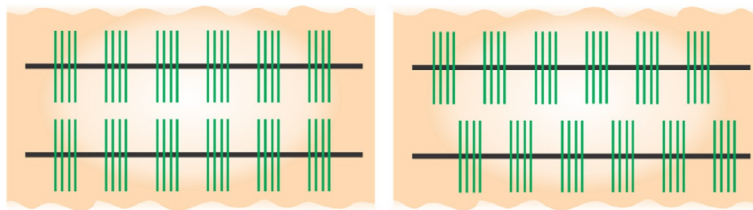

FIG. 8.13 Two different well patterns for well placement. (A) An aligned well pattern. (B) A zipper well pattern (Zuloaga et al., 2017).

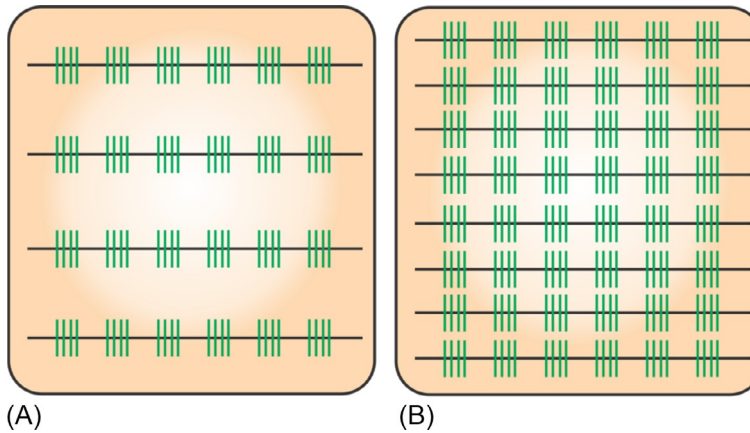

FIG. 8.14 Schematic of the minimum and maximum well number with different well spacing for the aligned well pattern (Zuloaga et al., 2017). (A) 4 wells with well spacing of 1320 ft. (B) 8 wells with well spacing of 610 ft.

simulation. CO_2 Huff-n-Puff scenario refers to all wells experience three cycles of Huff-n-Puff after 3 years of primary production. Each cycle consists of 1 year of CO_2 injection, 1 month of CO_2 soaking, and 47 months of back production. The total period of each cycle is 5 years. For the soaking time, there is no additional improvement of oil recovery when the time is longer than 1 month. A total simulation time of 18 years is considered. In order to fairly compare the effectiveness of both CO_2 injection scenarios, the total volume of CO_2 injection remains the same, which is 5475 MMSCF. Additionally, different CO_2 injection rates are needed for different CO_2 injection scenarios. 1000 MSCF/day is for CO_2 flooding and 5000 MSCF/day is for CO_2 Huff-n-Puff. Fig. 8.15 presents the path of cumulative CO_2 injection for different scenarios. As shown, the cumulative CO_2 injection volume after 18 years is the same.

Table 8.5 lists 24 cases with different combinations of four uncertain parameters using the approach of D-optimal design. The incremental oil recovery factor is used to compare CO_2 injection effectiveness for CO_2 Huff-n-Puff and CO_2 flooding scenarios. In order to calculate the incremental oil recovery factor, another additional 24 cases without CO_2 injection were needed to run. After simulation of all cases, the results of incremental oil recovery factor for both CO_2 injection scenarios are summarized in Table 8.6. As can be seen, the incremental oil recovery factor ranges from 2.56% to 14.34% for CO_2 Huff-n-Puff and from −1.79% to 30.06% for CO_2 flooding. The average value is obtained as 7.67% and 14.13% for CO_2 Huff-n-Puff and CO_2 flooding, respectively. The Design-Expert software was utilized to generate the Pareto plot, which can be used to identify the rank of important parameters affecting the difference of oil recovery factor between these two CO_2 injection scenarios, as shown in Fig. 8.16. It can be

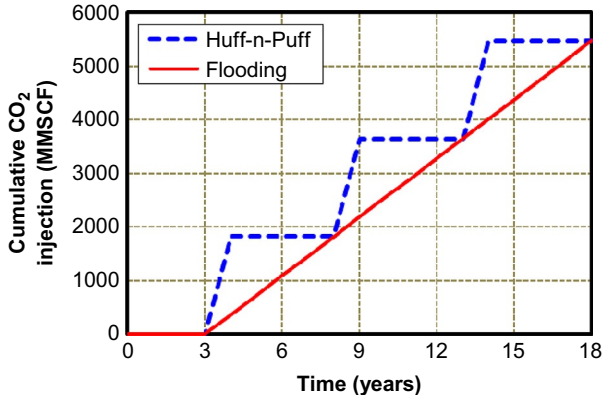

FIG. 8.15 Comparison of the path of cumulative CO_2 injection volume for CO_2 Huff-n-Puff and CO_2 flooding (Zuloaga et al., 2017).

observed that matrix permeability is the most important parameter, followed by well pattern, the interaction between fracture half-length and number of wells, fracture half-length, and number of wells.

The comparisons of contour plot of incremental oil recovery factor between the zipper well pattern and the aligned well pattern with 8 horizontal wells for CO_2 Huff-n-Puff and CO_2 flooding are shown in Figs. 8.17 and 8.18, respectively. As shown, the values in the contour lines represent the percentage of incremental oil recovery factor and the red color zones represent larger values. It is important to notice that the zipper well pattern always produces higher incremental oil recovery factor than the aligned well patter for both CO_2 injection scenarios. In addition, a small difference between two well patterns of about 2% is obtained for CO_2 Huff-n-Puff scenario, while a big difference of about 10% is achieved for CO_2 flooding scenarios. The reason can be explained through examining the comparison of CO_2 global mole fraction distribution between different scenarios after CO_2 injection, as shown in Fig. 8.19. For CO_2 Huff-n-Puff scenario in Fig. 8.19A, most of injected CO_2 molecules are primarily concentrated nearby the hydraulic fractures, resulting in the similar contact area between CO_2 molecules and reservoir for both well patterns. However, for CO_2 flooding scenario in Fig. 8.19B, the zipper well pattern generates a larger contact area and longer CO_2 breakthrough time than the aligned well pattern, significantly improving the CO_2 sweep efficiency. Hence, it implies that the zipper well pattern is a better candidate for implementing CO_2-EOR field project in tight oil reservoirs.

Next, the response surface model using the fully quadratic polynomial equation is determined for both CO_2 injection scenarios with the zipper well pattern. For the CO_2 Huff-n-Puff scenario, the relationship between the incremental oil recovery factors with three uncertain parameters is

TABLE 8.6 24 Cases With Different Combinations of Four Uncertain Parameters Based on the D-Optimal Design for Both CO_2 Injection Scenarios (Zuloaga et al., 2017)

Case	Permeability (md)	Fracture half-Length (ft)	Number of Wells	Well Pattern	Incremental Oil Recovery Factor (Huff-n-Puff)	Incremental Oil Recovery Factor (Flooding)
1	0.1	410	6	Zipper	12.47	28.97
2	0.001	290	8	Zipper	8.30	−1.16
3	0.0505	310	6	Aligned	9.31	22.00
4	0.1	210	8	Aligned	9.67	25.07
5	0.1	210	8	Aligned	9.67	25.07
6	0.01882	350	6	Zipper	9.89	21.65
7	0.001	210	8	Aligned	5.78	−1.50
8	0.001	270	6	Aligned	5.22	−1.79
9	0.001	410	4	Aligned	5.11	−1.77
10	0.001	410	8	Zipper	12.22	0.89
11	0.03763	210	4	Aligned	2.69	6.63
12	0.04948	410	4	Zipper	7.08	21.57
13	0.06337	410	8	Aligned	11.85	14.61
14	0.03763	210	4	Aligned	2.69	6.63
15	0.1	210	4	Zipper	3.02	27.91

16	0.0505	210	8	Zipper	9.40	28.54
17	0.1	330	8	Zipper	14.34	30.06
18	0.1	410	4	Aligned	6.93	25.25
19	0.06337	410	8	Aligned	11.85	14.61
20	0.001	210	4	Zipper	2.56	−1.28
21	0.1	370	6	Aligned	10.96	21.63
22	0.001	210	4	Zipper	2.56	−1.28
23	0.001	410	4	Aligned	5.11	−1.77
24	0.1	330	4	Zipper	5.32	28.55

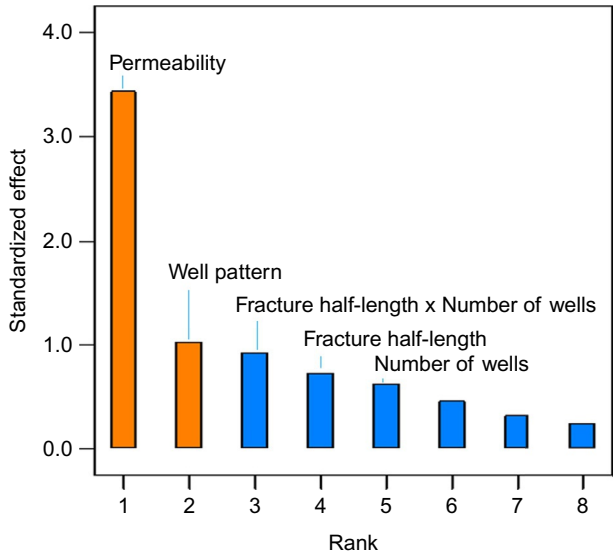

FIG. 8.16 Pareto plot for identifying the rank of key parameters affecting the difference of oil recovery factor between CO_2 Huff-n-Puff and CO_2 flooding (Zuloaga et al., 2017).

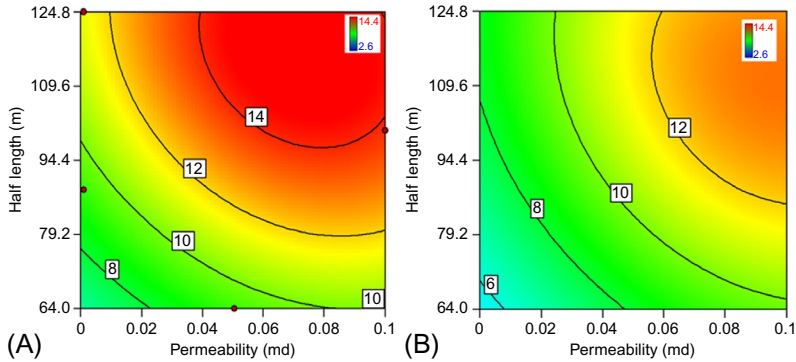

FIG. 8.17 Comparison of contour plot of incremental oil recovery factor between different well patterns for CO_2 Huff-n-Puff with 8 wells (Zuloaga et al., 2017). (A) Zipper well pattern. (B) Aligned well pattern.

$$\begin{aligned}\text{Incremental oil recover fractor} = (1/(&1.7988 - 1.6798\,k - 3.0608 \times 10^{-3} X_f \\ &- 0.2364\,N_W + 1.7849 \times 10^{-3}\,k\,X_f \\ &- 2.1357 \times 10^{-2}\,k\,N_W + 1.7885 \times 10^{-4} X_f\,N_W \\ &+ 8.1129\,k^2 + 1.9481 \times 10^{-6} {X_f}^2 \\ &+ 1.144 \times 10^{-2} N_W^2))^2,\end{aligned} \tag{8.14}$$

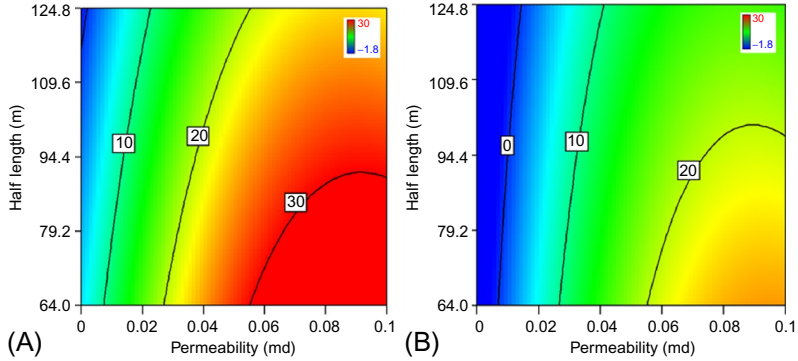

FIG. 8.18 Comparison of contour plot of incremental oil recovery factor between different well patterns for CO_2 flooding with 8 wells (Zuloaga et al., 2017). (A) Zipper well pattern. (B) Aligned well pattern.

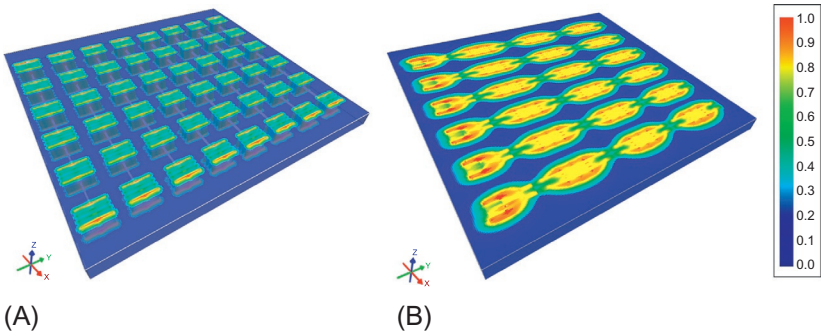

FIG. 8.19 Comparison of CO_2 global mole fraction distribution between different scenarios after CO_2 injection for the zipper well pattern with fracture half-length of 210 ft and matrix permeability of 0.1 mD (Zuloaga et al., 2017). (A) CO_2 Huff-n-Puff. (B) CO_2 flooding.

For the CO_2 flooding scenario, the relationship between the incremental oil recovery factors with four uncertain parameters is

$$\begin{aligned}\text{Incremental oil recover fractor} = &-75.1742 + 702.08\,k + 0.1064\,X_f + 21.587 N_W \\ &- 0.3126\,k\,X_f - 1.8965\,k\,N_W - 1.6133 \times 10^{-2}\,X_f\,N_W \\ &- 3235.7\,k^2 - 1.6839 \times 10^{-5}\,{X_f}^2 - 1.35\,N_W^2,\end{aligned} \tag{8.15}$$

where k is permeability in md, X_f is fracture half-length in ft, and N_W is number of wells.

The plot of "predicted vs. actual," which is often used to validate these response surface models for both CO_2 injection scenarios, is shown in Fig. 8.20. As can be seen, a reasonable match between the calculated values

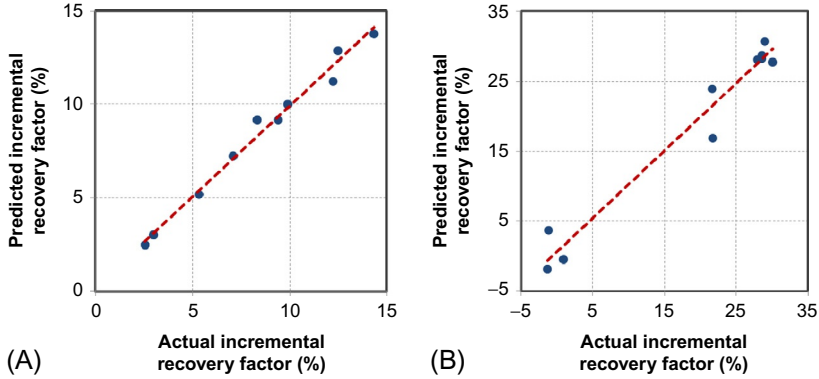

FIG. 8.20 Validation of two response surface models for both CO_2 injection scenarios using the plot of "predicted vs. actual"(Zuloaga et al., 2017). (A) CO_2 Huff-n-Puff. (B) CO_2 flooding.

and the actual values is obtained for each scenario, illustrating that the generated two response surface models are reliable to perform prediction.

The impacts of fracture half-length and permeability on the comparison of well performance between two CO_2 injection scenarios in 3D using the zipper well pattern with 8 horizontal wells are presented in Fig. 8.21. The intersection black line between two response surfaces represents the same well performance between two CO_2 injection scenarios. In addition, it clearly shows that CO_2 Huff-n-Puff performs better than CO_2 flooding under the condition of smaller permeability and longer fracture half-length. The corresponding 2D contour

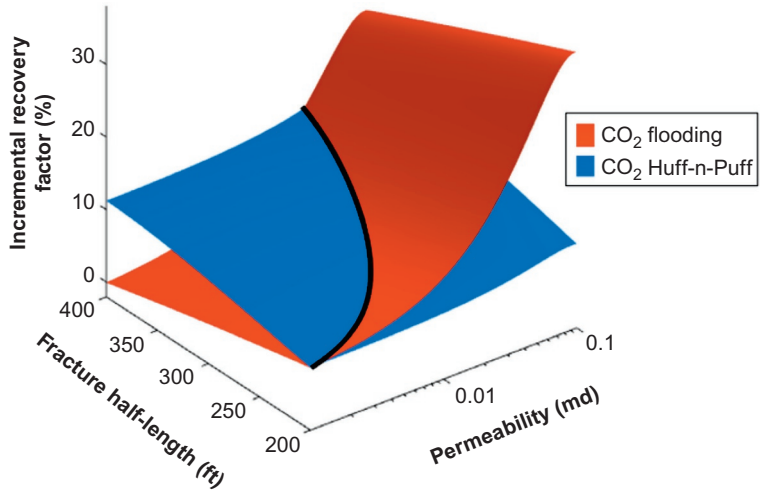

FIG. 8.21 Impacts of fracture half-length and permeability on the comparison of well performance between CO_2 Huff-n-Puff and CO_2 flooding scenarios (Zuloaga et al., 2017).

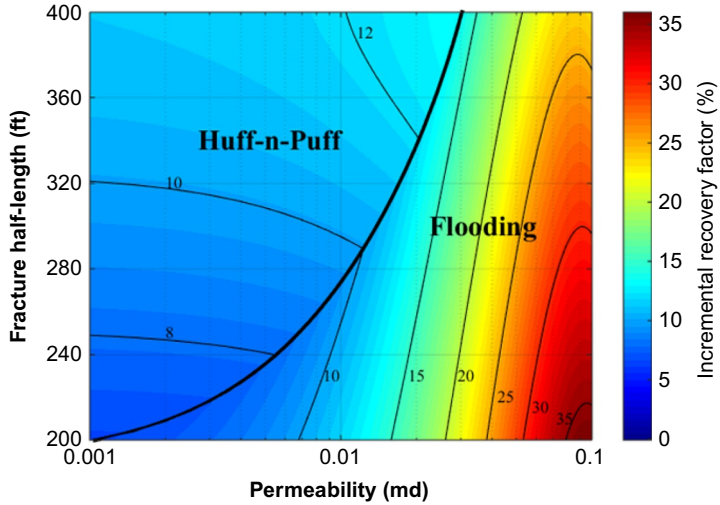

FIG. 8.22 2D contour plot of the comparison of well performance between different CO_2 injection scenarios with 8 horizontal wells (Zuloaga et al., 2017).

plot is illustrated in Fig. 8.22, clearly distinguishing different regions with larger incremental oil recovery factor for different CO_2 injection scenarios.

Similarly, when the well number is reduced from 8 to 6, the diagnostic contour plot is shown in Fig. 8.23. As can be seen, the region with better well performance for CO_2 flooding scenario increases significantly. This is because the increasing well spacing from 8 wells to 6 wells materially decreases the CO_2

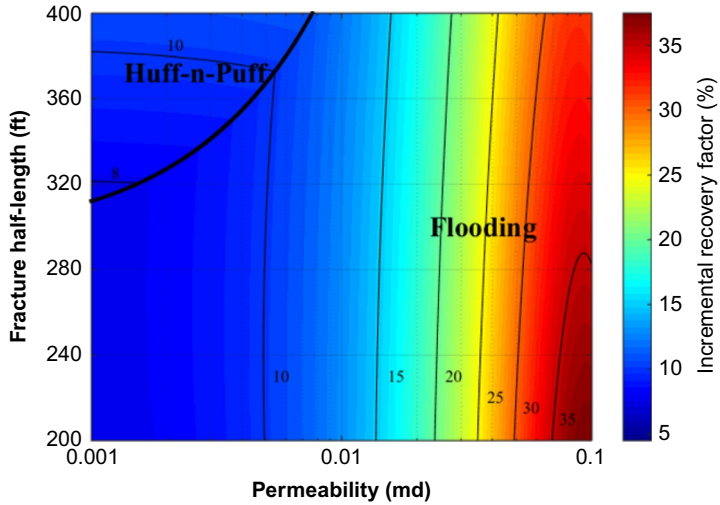

FIG. 8.23 2D contour plot of the comparison of well performance between different CO_2 injection scenarios with 6 horizontal wells (Zuloaga et al., 2017).

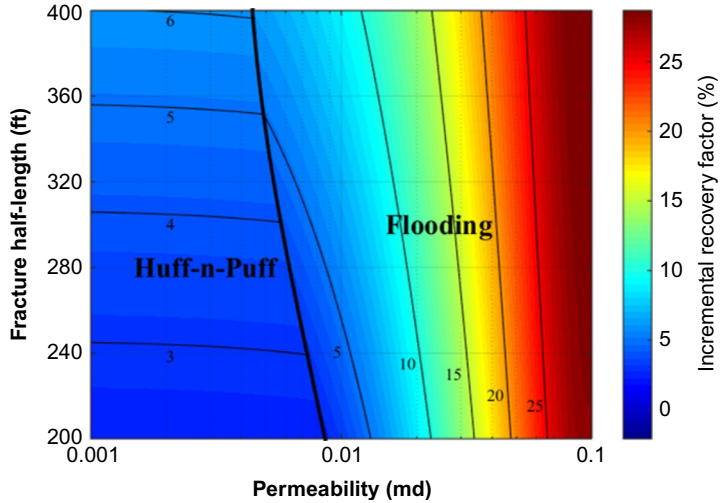

FIG. 8.24 2D contour plot of the comparison of well performance between different CO_2 injection scenarios with 4 horizontal wells (Zuloaga et al., 2017).

breakthrough time, resulting in larger CO_2 sweep efficiency and higher oil recovery factor. However, when the well number is continuously decreased from 6 to 4, the region for CO_2 flooding scenario did not increase further and the region for CO_2 Huff-n-Puff increases, as shown in Fig. 8.24. The reason is that CO_2 is difficult to transport to the producers due to larger well spacing between the injectors and the producers, especially for the lower values of permeability. Accordingly, well spacing plays an important role in the comparison of CO_2-EOR effectiveness between CO_2 Huff-n-Puff and CO_2 flooding, which should be carefully examined in the field project.

Based on these simulation results analysis, it can be concluded that CO_2 Huff-n-Puff performs better than CO_2 flooding for the lower permeability (0.001–0.01 md) and longer fracture half-length. The incremental oil recovery factor increases with the increasing well number and fracture half-length due to an increase in contact area between CO_2 molecules and reservoir. The highest incremental recovery factor of 13% is obtained for the CO_2 Huff-n-Puff under the conditions of permeability of 0.02 mD, 8 wells, and fracture half-length of 400 ft. On the other hand, CO_2 flooding performs better than CO_2 Huff-n-Puff for the larger permeability ranging from 0.01 to 0.1 mD, especially when the well number is 6. The highest incremental oil recovery factor of 37% was achieved for the CO2 flooding under the conditions of permeability of 0.1 mD, 6 wells, and fracture half-length of 210 ft.

In addition, we examined the impact of well production lifetime on the comparison of two CO_2 injection scenarios. A shorter well production lifetime with 8 years was considered. There is only one cycle for CO_2 Huff-n-Puff. The similar 2D contour plots with longer well production lifetime of 18 years for 8, 6,

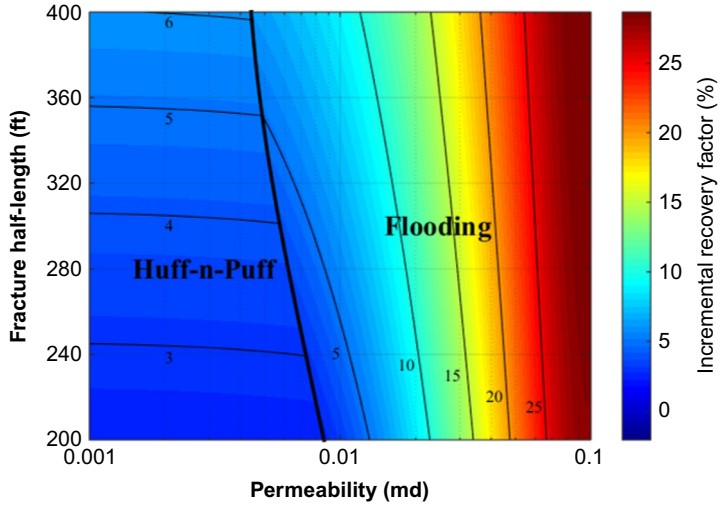

FIG. 8.25 2D contour plot of the comparison of well performance between different CO_2 injection scenarios with 8 horizontal wells and 8 years of well production lifetime (Zuloaga, 2016).

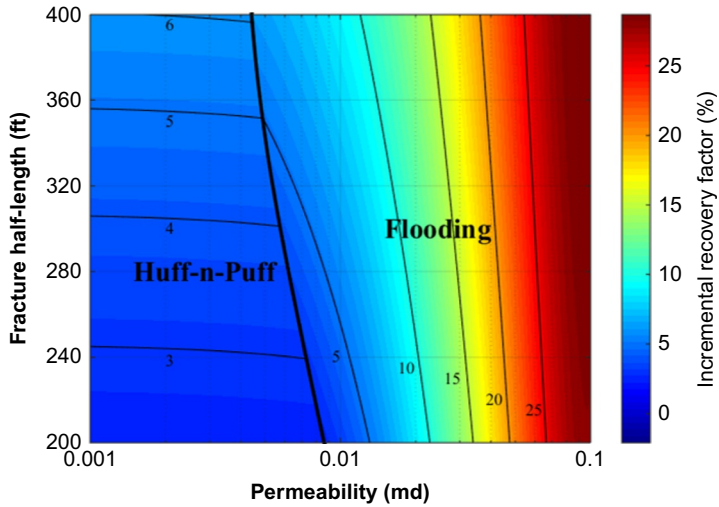

FIG. 8.26 2D contour plot of the comparison of well performance between different CO_2 injection scenarios with 6 horizontal wells and 8 years of well production lifetime (Zuloaga, 2016).

and 4 horizontal wells are shown in Figs. 8.25, 8.26, and 8.27, respectively. It can be clearly shown that the well production lifetime significantly impacts the comparison results. The region of CO_2 Huff-n-Puff has a larger expansion when compared to longer well production lifetime.

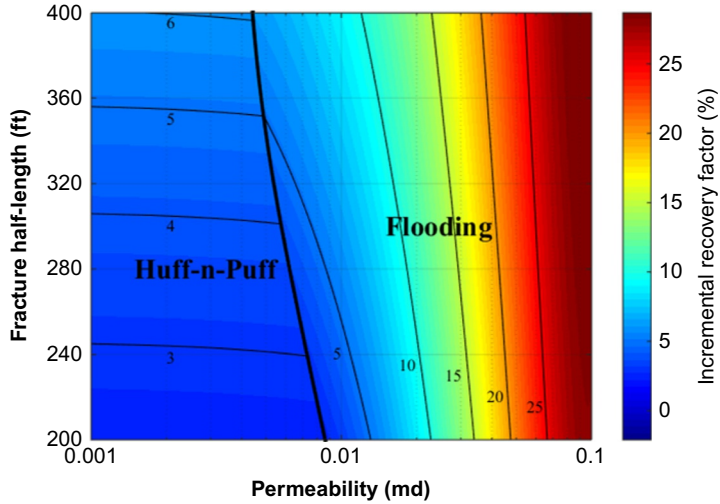

FIG. 8.27 2D contour plot of the comparison of well performance between different CO_2 injection scenarios with 4 horizontal wells and 8 years of well production lifetime (Zuloaga, 2016).

8.6 IMPACTS OF COMPLEX FRACTURE GEOMETRIES USING EDFM

The EDFM method was used to investigate the impacts of complex hydraulic and natural fractures on well performance of CO_2 Huff-n-Puff and CO_2 flooding. First, we built a basic reservoir model with four simple planar hydraulic fractures to validate the EDFM method against the LGR method. The model dimension is $1400\,\text{ft} \times 1020\,\text{ft} \times 40\,\text{ft}$, which corresponds to length, width, and thickness, respectively. The grid block size is set to $20\,\text{ft} \times 20\,\text{ft} \times 40\,\text{ft}$ in x, y, z directions, respectively. Fracture half-length is 210 ft, fracture height is 40 ft, fracture conductivity is 50 md-ft, and fracture spacing is 140 ft. Matrix permeability is 0.1 mD. The flowing BHP is 1800 psi. Constant CO_2 injection rate of 1000 MSCF/day is used for CO_2 Huff-n-Puff with three cycles (one cycle consists of 1 year of injection, 1 month of soaking, and 4 years of production) after 4 years of primary production. The CO_2 molecular diffusion coefficient in the oil phase was $0.001\,\text{cm}^2/\text{s}$. The other key reservoir and fluid properties remain the same as those in Tables 8.3–8.4. The comparison of grid blocks to handle hydraulic fractures between the EDFM method and the LGR method is demonstrated in Fig. 8.28. As shown, no grid refinement nearby fractures is needed for the EDMF approach compared to the LGR approach, resulting in less number of grid blocks and higher computational efficiency for the EDFM method to simulate production with multiple fractures. Fig. 8.29 shows the comparison of oil recovery factor between the EDFM method and the LGR method, illustrating a good agreement was obtained. Hence, the EDMF approach is reliable to efficiently simulate CO_2-EOR process in tight oil reservoir with multiple fractures.

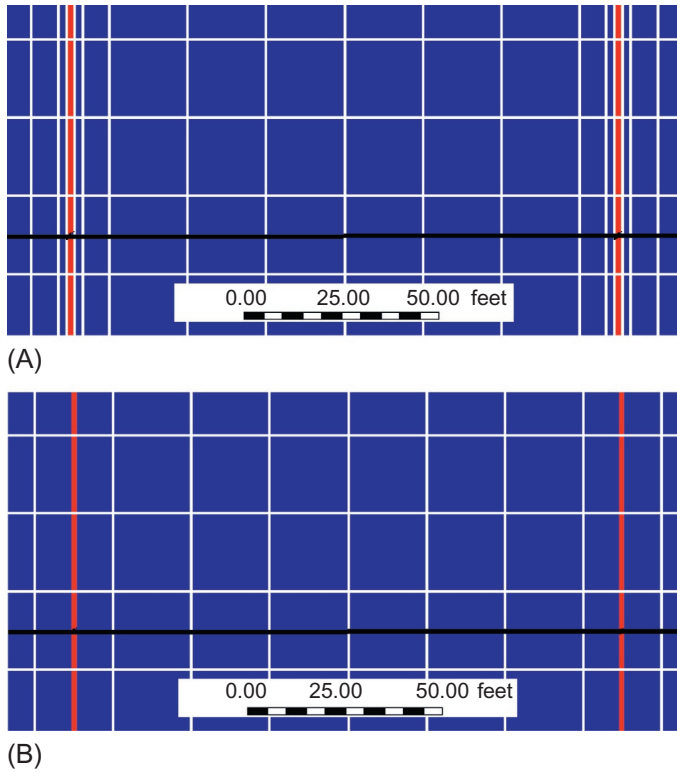

FIG. 8.28 Comparison of gird blocks to handle hydraulic fractures between different methods (Zuloaga et al., 2016). (A) The LGR method. (B) The EDFM method.

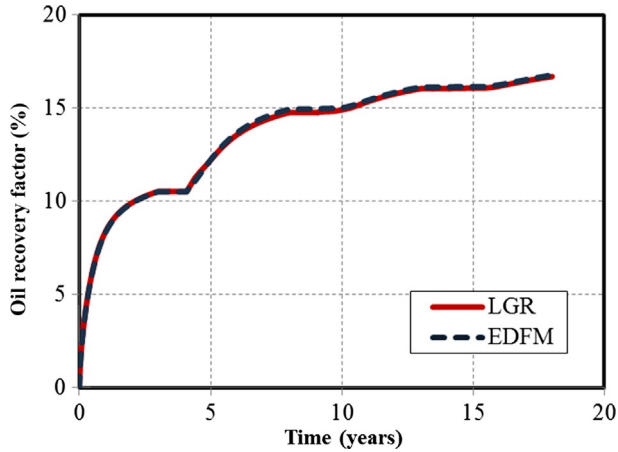

FIG. 8.29 Comparison of oil recovery factor between the EDFM method and the LGR method (Zuloaga et al., 2016).

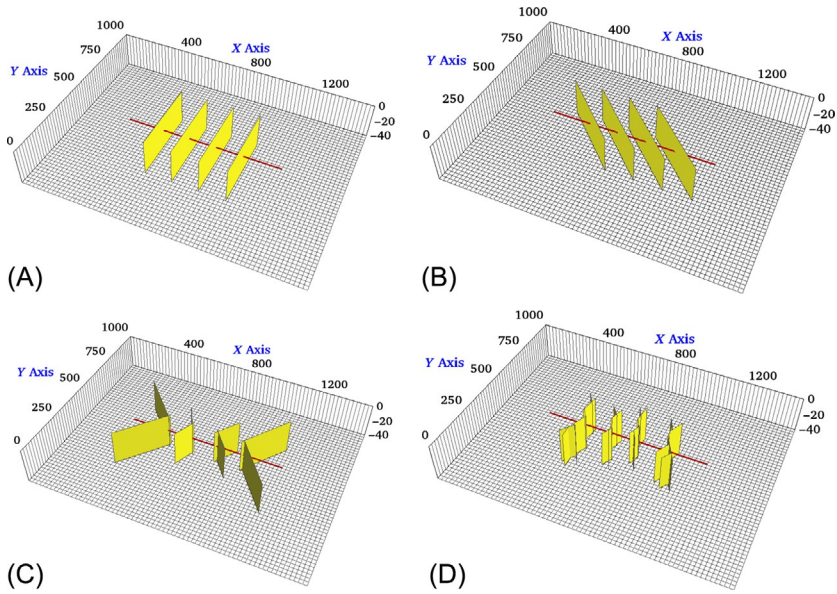

FIG. 8.30 Four case studies with different fracture geometries for CO_2 Huff-n-Puff scenario (Zuloaga et al., 2016). (A) Case 1: Planar fractures. (B) Case 2: Diagonal fractures. (C) Case 3: Reoriented fractures. (D) Case 4: Fracture networks.

Next, four case studies with different fracture geometries were designed to investigate the impact of different fracture complexities on well performance of CO_2 Huff-n-Puff, as shown in Fig. 8.30.

- Case 1: Planar fractures, which is considered as reference case. In this case, four simple planar hydraulic fractures are oriented orthogonal to the horizontal wellbore with the same fracture properties.
- Case 2: Diagonal fractures. In this case, four hydraulic fractures are oriented at an angle of 45° with respect to the horizontal wellbore. The perforation cluster spacing remains the same as case 1; however, the orthogonal distance between two neighboring fractures was decreased from 140 to 99 ft.
- Case 3: Reoriented fractures. This case represents the nonplanar fracture geometry with two longer outer fractures and two shorter inner fractures. Both upper and lower parts of each fracture are oriented at 45° and 135° or 135° and 45°, respectively. The fracture half-length for two outer and inner fractures is 295 and 125 ft, respectively. It should be mentioned that the total fracture length remains the same as that of cases 1 and 2.
- Case 4: Fracture networks. This case represents a more realistic fracture geometry. Several fracture segments interact each other to form fracture networks for each hydraulic fracture. In addition, the total fracture length remains the same as that of these three cases.

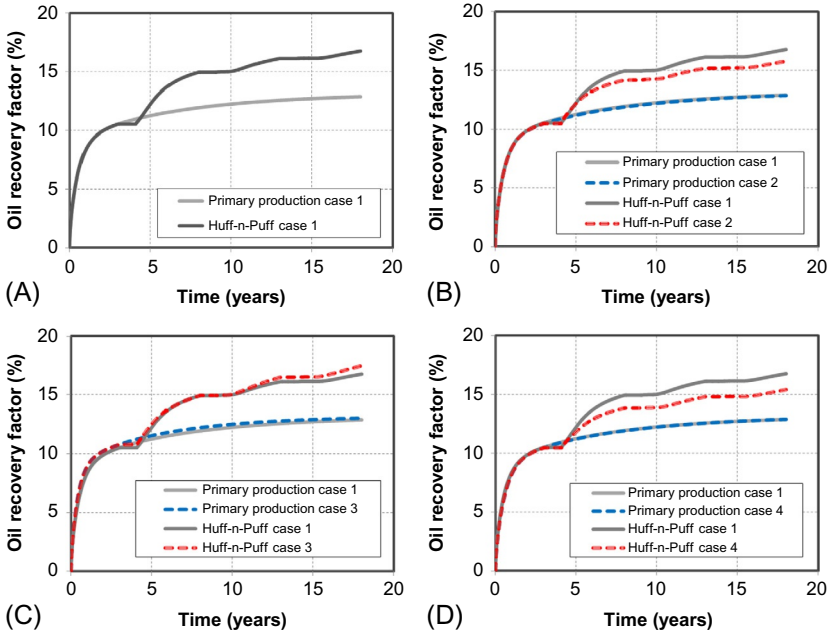

FIG. 8.31 Comparison of incremental oil recovery factor for different cases (Zuloaga et al., 2016). (A) CO_2 Huff-n-Puff vs. primary production for case 1. (B) Case 2 vs. case 1. (C) Case 3 vs. case 1. (D) Case 4 vs. case 1.

Fig. 8.31 presents the comparison of oil recovery factor between CO_2 Huff-n-Puff and primary production for different cases. For case 1 as shown in Fig. 8.31A, the incremental oil recovery factor at end of simulation is about 3.9%. For case 2 in Fig. 8.31B, the oil recovery factor of primary production between cases 1 and 2 is almost the same. However, the incremental oil recovery factor at end of simulation for case 2 is about 2.9%, which is less than that of case 1. The reason can be explained through examining the comparison of global CO_2 molecule distribution after 1 year of CO_2 injection, as shown in Fig. 8.32A and B. It can be seen that case 2 has a larger production interference than case 1, resulting in CO_2 Huff-n-Puff is less effective for case 2. In Fig. 8.32C, the incremental oil recovery factor of case 3 is 4.5%, which is larger than that of case 1. The reason is that two outer longer fractures have a less production interference with two inner shorter fractures when compared to case 1, resulting in larger contact area between CO_2 molecules and reservoir, as displayed in Fig. 8.32C. For case 4, the incremental oil recovery factor is only about 2.6%, which is lower than the other three cases. As can be seen in Fig. 8.32D, more serious interference between fractures is observed, leading to smaller contact area between CO_2 molecules and reservoir. In order to quantitatively evaluate the degree of production interference for different cases, the CO_2-contact area was calculated based on the global CO_2 molecule distribution

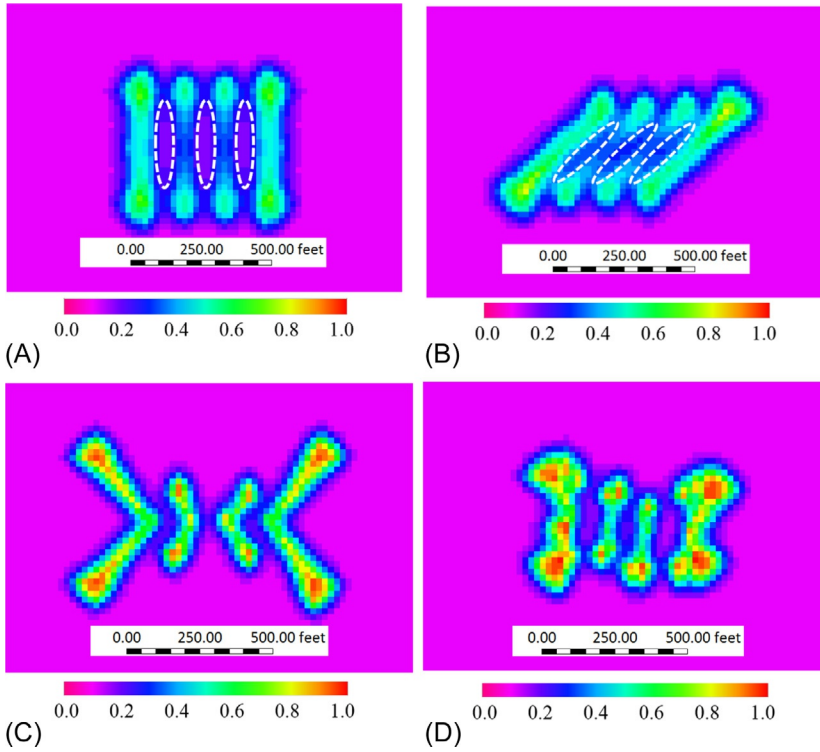

FIG. 8.32 Comparison of global CO_2 molecule distribution after 1 year of CO_2 injection between different cases (Zuloaga, 2016). (A) Case 1. (B) Case 2. (C) Case 3. (D) Case 4.

maps, which refers to the area with a CO_2 mole fraction larger than 5% in this study. The calculation results for different cases are summarized in Table 8.7. In addition, the oil recovery factor (RF) after primary production and CO_2 Huff-n-Puff is included. As shown, there are small differences of primary oil recovery factor. However, the incremental oil recovery factor decreases as the fractures become closer and shorter to each other under the same total fracture length. Simultaneously, the CO_2-contact area decreases with the increasing fracture interference. Hence, it is important to accurately characterize and model complex fracture geometry in order to better evaluate the effectiveness of CO_2 Huff-n-Puff in tight oil reservoirs.

In order to evaluate the impacts of complex fracture geometries on well performance of CO_2 flooding, we expanded the model size of CO_2 Huff-n-Puff to $1400\,\text{ft} \times 2040\,\text{ft} \times 40\,\text{ft}$, which corresponds to length, width, and thickness, respectively. Two horizontal wells were included with identical fracture geometries as CO_2 Huff-n-Puff, as shown in Fig. 8.33. Well spacing is given by 1020 ft. After 3 years of primary production, one well is converted to CO_2 injector and another well continues to produce until the end of production time (18 years in total). In order to maintain similar amount of CO_2 injected with CO_2 Huff-n-Puff,

TABLE 8.7 Comparison of RF of Primary Production, After CO_2 Huff-n-Puff and CO_2-Contact Area Between Different Cases (Zuloaga, 2016)

Case Number	RF Primary Production (%)	RF Huff-n-Puff (%)	Incremental RF (%)	CO_2-Contacted Area ($\times 1000\,ft^2$)
Case 1	12.9	16.8	3.9	170.9
Case 2	12.8	15.7	2.9	160.9
Case 3	12.9	17.4	4.5	180.2
Case 4	12.8	15.4	2.6	152.6

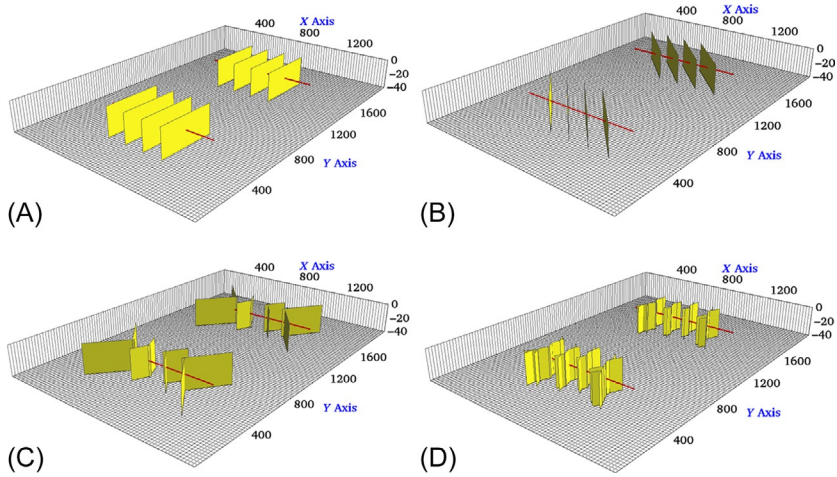

FIG. 8.33 Four case studies with different fracture geometries for CO_2 flooding scenario (Zuloaga et al., 2016). (A) Case 1: Planar fractures. (B) Case 2: Diagonal fractures. (C) Case 3: Reoriented fractures. (D) Case 4: Fracture networks.

a constant CO_2 injection rate of 2500 MSCF/day and a maximum BHP of 8000 psi are used as simulation constraints. The oil recovery factor of primary production is used to calculate the incremental oil recovery factor. The comparison of oil recovery factor between different cases for CO_2 flooding scenario is presented in Fig. 8.34. Similarly, the primary oil RF, oil RF after CO_2 flooding, incremental oil RF, and CO_2-contact area were listed in Table 8.8. As shown, the incremental RF of cases 1 and 4 is lower than that of cases 2 and 3. In addition, there is no clear trend between the increasing fracture complexity and CO_2 flooding effectiveness. It is important to notice that the dimension size of cross-sectional area covered by fractures between injector and producer plays an important role in improving CO_2-EOR effectiveness. Cases 2 and 3 have a

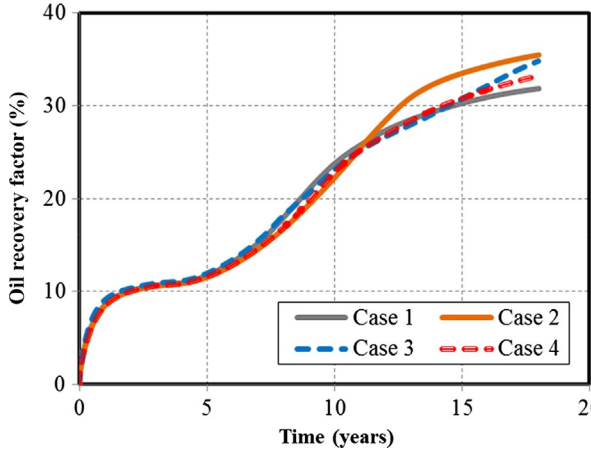

FIG. 8.34 Comparison of oil recovery factor between different cases for CO_2 flooding scenario (Zuloaga et al., 2016).

TABLE 8.8 Comparison of RF of Primary Production, After CO_2 Flooding and CO_2-Contact Area Between Different Cases (Zuloaga et al., 2016)

Fracture Geometry	RF Primary Production (%)	RF Flooding (%)	Incremental RF (%)	CO_2-Contacted Area (M ft^2)
Case 1	12.93	31.81	18.88	1054.9
Case 2	12.92	35.43	22.51	1151.4
Case 3	13.04	34.79	21.75	1187.2
Case 4	12.91	32.91	20.00	1095.5

larger extension size in the x-axis direction (717 and 572 ft, respectively) than cases 1 and 4 (420 and 529 ft, respectively), leading to a larger CO_2-contacted area and therefore a higher incremental oil recovery factor.

Next, in order to examine the impacts of complex nonplanar hydraulic fractures and natural fractures on CO_2-EOR effectiveness, we built a field-scale reservoir model with dimension of 5240 ft × 2680 ft × 40 ft, which represents length, width, and thickness, respectively. Two horizontal wells were considered with lateral length of 4640 ft and well spacing of 1340 ft. Each well consists of 15 effective hydraulic fractures and fracture spacing is 290 ft. Two permeabilities of 0.01 and 0.1 md were studied, which represent low and high permeability in the Bakken formation. The other reservoir, fracture, and fluid properties remain the same as those in Tables 8.3–8.4. Four fracture geometries were designed and shown in Fig. 8.35. The first geometry in Fig. 8.35A only

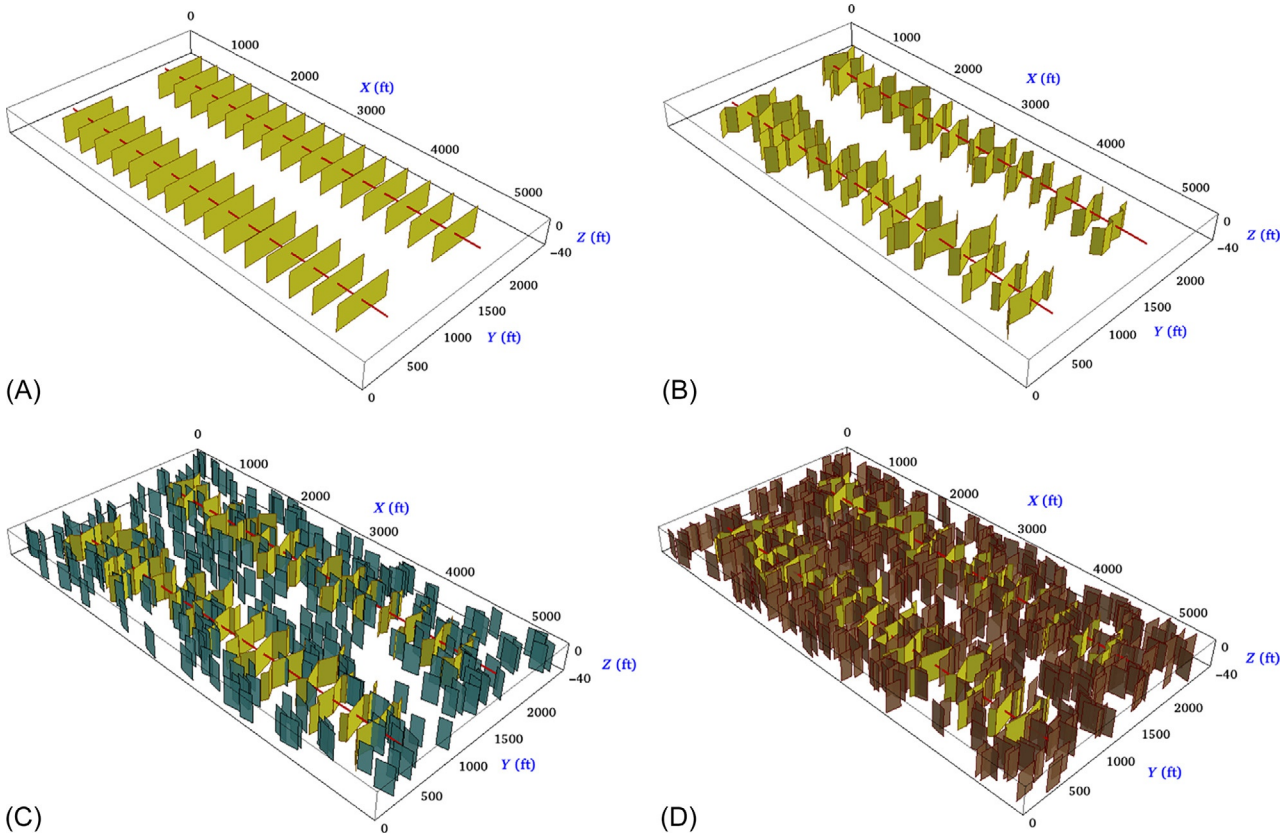

FIG. 8.35 Schematic of four fracture geometries used for the field-scale simulation (Zuloaga, 2016). (A) Planar fractures. (B) Nonplanar fractures. (C) Nonplanar fractures with one set of 300 natural fractures. (D) Nonplanar fractures with two sets of 600 natural fractures.

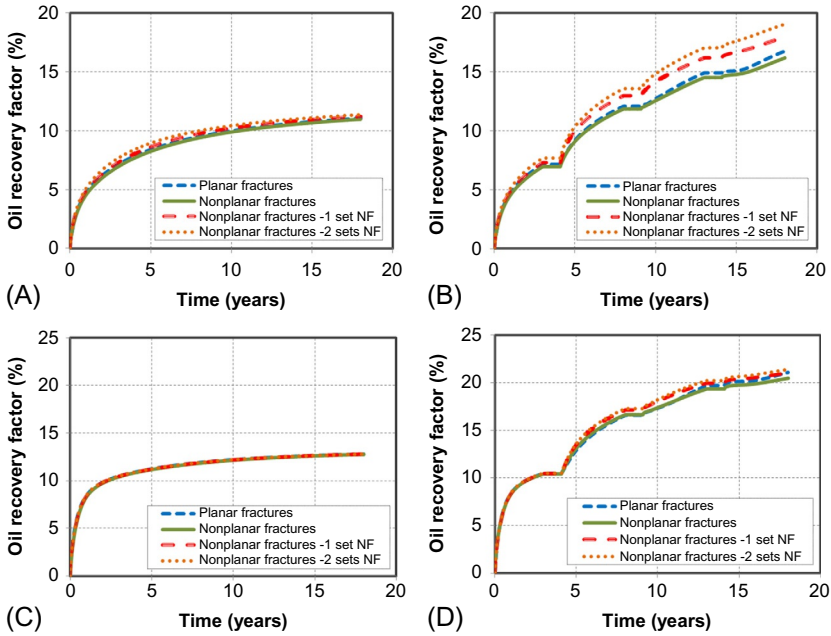

FIG. 8.36 Comparison of oil recovery factor for primary production and CO_2 Huff-n-Puff between different fracture geometries (Zuloaga, 2016). (A) Primary production under permeability of 0.01 md. (B) CO_2 Huff-n-Puff under permeability of 0.01 md. (C) Primary production under permeability of 0.1 md. (D) CO_2 Huff-n-Puff under permeability of 0.1 md.

assumes planar fractures and all fractures have the same half-length of 334 ft. The second geometry in Fig. 8.35B represents nonplanar fractures varying fracture half-length from 194 to 445 ft. It should be mentioned that the total fracture length for the first fracture geometries is kept the same. Based on the second geometry, we added one set of 300 natural fracture and two sets of 600 natural fractures for the third and fourth geometry in Fig. 8.35C and D, respectively. All natural fractures are randomly distributed with length ranging from 100 to 200 ft fracture height of 40 ft, and fracture conductivity of 5 md-ft. The orientation of one set of natural fractures is almost parallel to the horizontal wellbore and another set is oriented perpendicular to the horizontal wellbore.

First, we performed CO_2 Huff-n-Puff and presented the comparison of oil recovery factor between different fracture geometries under low permeability of 0.01 md and high permeability of 0.1 md in Fig. 8.36. As shown, a small difference of oil recovery factor between four fracture geometries during primary production is observed for low permeability of 0.01 md in Fig. 8.36A, while there is almost no difference for high permeability of 0.1 md in Fig. 8.36C. The maximum difference of oil recovery factor at end of simulation is about 0.4% and 0.05% for permeabilities of 0.01 md and 0.1 md, respectively. When considering CO_2 Huff-n-Puff, the difference of incremental oil recovery factor between planar fractures and nonplanar fractures without natural fractures is about the same (0.6%) regardless of low or

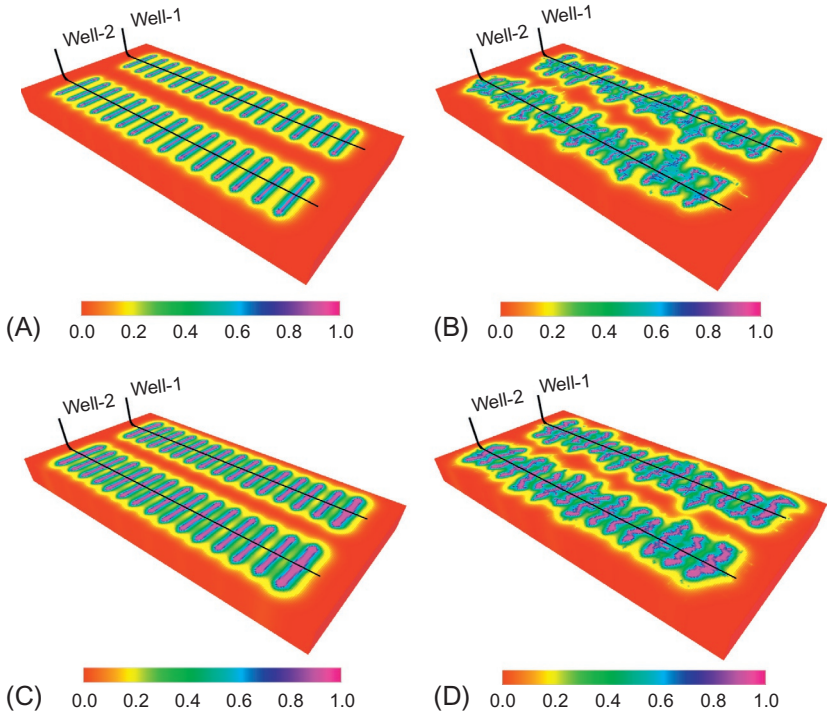

FIG. 8.37 Comparison of global CO_2 molecule distribution for CO_2 Huff-n-Puff between planar fractures and nonplanar fractures with 2 sets of natural fractures (Zuloaga, 2016). (A) Planar fractures under permeability of 0.01 md. (B) Nonplanar fractures with 2 sets of natural fractures under permeability of 0.01 md. (C) Planar fractures under permeability of 0.1 md. (D) Nonplanar fractures with 2 sets of natural fractures under permeability of 0.1 md.

high permeability in Fig. 8.36B and D. This is because less fracture interference with larger fracture spacing of 290 ft under the same total fracture length between planar and nonplanar fracture geometries. When compared to nonplanar fracture geometry without natural fractures under low permeability of 0.01 md, the incremental oil recovery factor increases from 5.2% to 6.8% and 7.7% for planar fractures with one set and two sets of natural fractures, respectively. However, when compared to nonplanar fracture geometry without natural fractures under high permeability of 0.1 md, the incremental oil recovery factor has a small increase from 7.7% to 8.2% and 8.8% for planar fractures with one set and two sets of natural fractures, respectively. Hence, the presence of natural fractures plays an important role in affecting well performance of CO_2 Huff-n-Puff under the conditions of lower permeability and higher density of natural fractures.

Comparison of global CO_2 molecule distribution for CO_2 Huff-n-Puff between planar fractures and nonplanar fractures with 2 sets of natural fractures under different permeabilities is shown in Fig. 8.37. It can be seen that the nonplanar fracture geometry with 2 sets of natural fractures has a higher CO_2

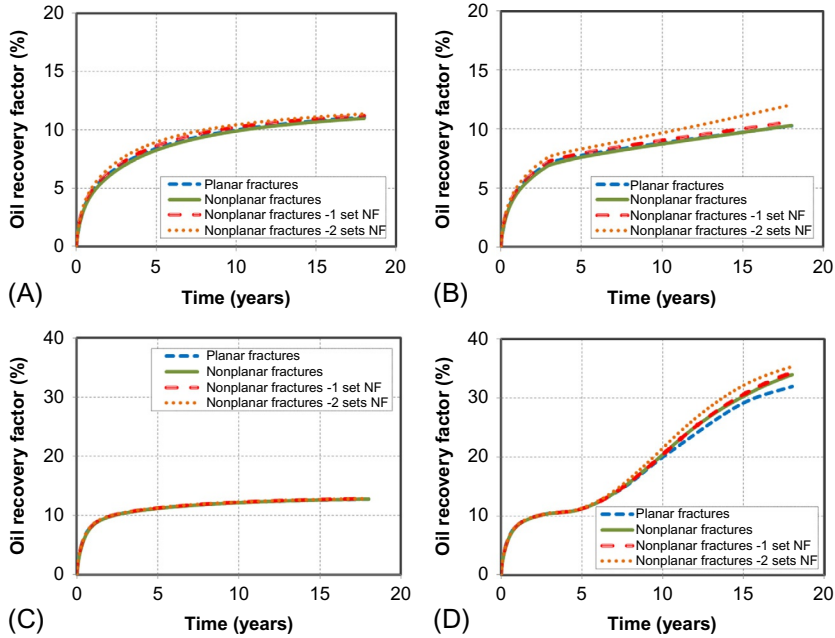

FIG. 8.38 Comparison of oil recovery factor for primary production and CO_2 flooding between different fracture geometries (Zuloaga, 2016). (A) Primary production under permeability of 0.01 md. (B) CO_2 Huff-n-Puff under permeability of 0.01 md. (C) Primary production under permeability of 0.1 md. (D) CO_2 Huff-n-Puff under permeability of 0.1 md.

molecule concentration than the planar fracture geometry under the low permeability of 0.01 md in Fig. 8.37A and B. However, a similar CO_2 molecule concentration is observed between these two fracture geometries under the high permeability of 0.1 md in Fig. 8.37C and D. Hence, the CO_2 molecule distribution confirms that the effectiveness of CO_2 Huff-n-Puff is more sensitive to the presence of natural fractures under the lower permeability.

Second, we performed CO_2 flooding and presented the comparison of oil recovery factor between different fracture geometries under low permeability of 0.01 md and high permeability of 0.1 md in Fig. 8.38. As shown, a small difference of oil recovery factor between four fracture geometries during primary production is observed regardless of low or high permeability in Fig. 8.38A and C. When considering CO_2 flooding under low permeability of 0.01 md in Fig. 8.38B, it can be seen that the final recovery factor is less than the primary oil recovery factor except the nonplanar fracture geometry with 2 sets of natural fractures. This is because the injected CO_2 has difficulty to reach the producer due to lower permeability and poor connectivity. The nonplanar fracture geometry with 2 sets of natural fractures improves the connectivity and sweep

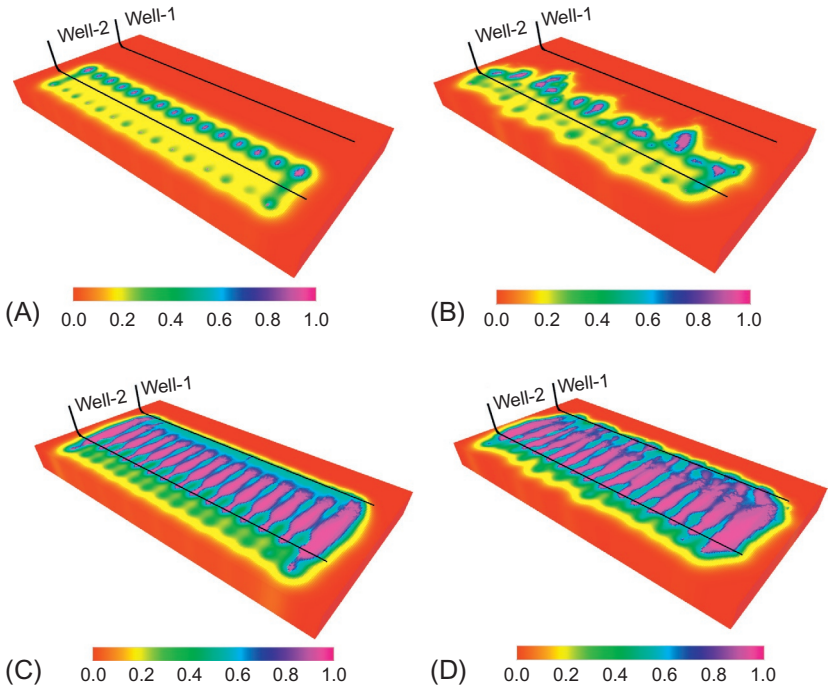

FIG. 8.39 Comparison of global CO_2 molecule distribution for CO_2 flooding between planar fractures and nonplanar fractures with 2 sets of natural fractures (Zuloaga, 2016). (A) Planar fractures under permeability of 0.01 md. (B) Nonplanar fractures with 2 sets of natural fractures under permeability of 0.01 md. (C) Planar fractures under permeability of 0.1 md. (D) Nonplanar fractures with 2 sets of natural fractures under permeability of 0.1 md.

efficiency between two wells, which can be clearly illustrated based on global CO_2 molecule distribution in Fig. 8.39A and B. The final oil recovery factor for this fracture geometry is about 12%, while it is around 10.3% for the other three fracture geometries.

However, under the high permeability of 0.1 md, all fracture geometries generate larger incremental oil recovery factor when compared to low permeability of 0.01 md. The incremental oil recovery factor at end of simulation is about 19.1%, 21.2%, 21.5%, and 22.5% for planar fractures, nonplanar fractures, nonplanar fractures with one set of natural fractures, and nonplanar fractures with two sets of natural fractures, respectively. Hence, more sets of natural fractures significantly improve sweep efficiency in Fig. 8.39C and D, resulting in larger incremental oil recovery factor.

REFERENCES

Adekunle, O., Hoffman, B.T., 2014. In: Minimum miscibility pressure studies in the Bakken. Paper SPE 169077, SPE Improved Oil Recovery Symposium, Tulsa, Oklahoma.

Chen, C., Balhoff, M., Mohanty, K.K., 2014. Effect of reservoir heterogeneity on primary recovery and CO2 huff 'n' puff recovery in shale-oil reservoirs. SPE Reserv. Eval. Eng. 17 (3), 404–413.

Cherian, B.V., Stacey, E.S., Lewis, R., Iwere, F.O., Heim, R.N., Higgins, S.M., 2012. In: Evaluating horizontal well completion effectiveness in a field development program. Paper SPE 152177, SPE Hydraulic Fracturing Technology Conference, The Woodlands, Texas.

CMG-GEM, 2012. GEM User's Guide. Computer Modeling Group Ltd.

CMG-WinProp, 2012. WinProp User's Guide. In: Computer Modeling Group Ltd..

Denoyelle, L., Bardon, C., 1983. In: Influence of diffusion on enhanced oil recovery by CO_2 injection. International Symposium on CO_2 Enhanced Oil Recovery, Budapest, Hungary.

Fai-Yengo, V., Rahnema, H., Alfi, M., 2014. In: Impact of light component stripping during CO_2 injection in Bakken formation. Paper URTeC 1922932, Unconventional Resources Technology Conference, Denver, Colorado.

Grogan, A.T., Pinczewski, V.W., Ruskauff, G.J., Orr Jr., F.M., 1988. Diffusion of CO_2 at reservoir conditions: models and measurements. SPE Reserv. Eng. 3 (1), 93–102.

Hawthorne, S.B., Gorecki, C.D., Sorensen, J.A., Steadman, E.N., Harju, J.A., Melzer, S., 2013. In: Hydrocarbon mobilization mechanisms from upper, middle, and lower Bakken reservoir rocks exposed to CO_2. Paper SPE 167200, SPE Unconventional Resources Conference, Calgary, Canada.

Hoffman, B.T., 2012. In: Comparison of various gases for enhanced recovery from shale oil reservoirs. Paper SPE 154329, SPE Improved Oil Recovery Symposium, Tulsa, Oklahoma.

Holm, L.W., 1986. Miscibility and miscible displacement. J. Pet. Technol. 38 (8), 817–818.

Holm, L.W., 1987. Evolution of the carbon dioxide flooding processes. J. Pet. Technol. 39 (11), 1337–1342.

Holm, L.W., Josendal, V.A., 1974. Mechanisms of oil displacement by carbon dioxide. J. Pet. Technol. 26 (12), 1427–1438.

Holm, L.W., Josendal, V.A., 1982. Effect of oil composition on miscible-type displacement by carbon dioxide. SPE J. 22 (1), 87–98.

Hoteit, H., 2013. Modeling diffusion and gas-oil mass transfer in fractured reservoirs. J. Pet. Sci. Eng. 105, 1–17.

Hoteit, H., Firoozabadi, A., 2006. Compositional modeling by the combined discontinuous Galerkin and mixed method. SPE J. 11 (1), 19–34.

Iwere, F.O., Heim, R.N., Cherian, B.V., 2012. In: Numerical simulation of enhanced oil recovery in the middle Bakken and upper Three Forks tight oil reservoirs of the Williston basin. Paper SPE 154937, SPE Americas Unconventional Resources Conference, Pittsburgh, Pennsylvania.

Jarrell, P.M., Fox, C.E., Stein, M.H., Webb, S.L., 2002. In: Practical aspects of CO_2 flooding. SPE Monograph, vol. 22, Henry L. Doherty Series, Richardson, Texas, USA.

Kong, X., Delshad, M., Wheeler, M.F., 2015. In: A numerical study of benefits of adding polymer to WAG processes for a pilot case. Paper SPE 173230, SPE Reservoir Simulation Symposium, Houston, Texas.

Kumar, P., Mittal, K.L. (Eds.), 1999. Handbook of Microemulsion Science and Technology. Marcel Dekker, New York.

Kurtoglu, B., Sorensen, J.A., Braunberger, J., Smith, S., Kazemi, H., 2013. In: Geologic characterization of a Bakken reservoir for potential CO2 EOR. Paper SPE 168915, Unconventional Resources Technology Conference, Denver, Colorado.

Kurtoglu, B., Kazemi, H., Rosen, R., Michelson, W., Kosanke, T., 2014. In: A rock and fluid study of middle Bakken formation: key to enhanced oil recovery. Paper SPE 171668, SPE Unconventional Resources Conference, Calgary, Canada.

Lambert, M.R., Marino, S.D., Anthony, T.L., Calvin, M.W., Gutierrez, S., Smith, D.P., 1996. In: Implementing CO_2 floods: no more delays!. Paper SPE 35187, Permian Basin Oil and Gas Recovery Conference, Midland, Texas.

Lashgari, H.R., 2014. Development of a four-Phase Thermal-Chemical Reservoir Simulator for Heavy Oil. PhD dissertationThe University of Texas at Austin.

Martin, F.D., Taber, J.J., 1992. Carbon dioxide flooding. J. Pet. Technol. 44 (4), 396–400.

Nghiem, L.X., Kohse, B.F., Sammon, P.H., 2000. In: Compositional simulation of the vapex process. Paper PETSOC 2000–034, Canadian International Petroleum Conference, Calgary, Canada.

Nojabaei, B., Johns, R.T., Chu, L., 2013. Effect of capillary pressure on phase behavior in tight rocks and shales. SPE Reserv. Eval. Eng. 16 (3), 281–289.

Orr Jr., F.M., Silva, M.K., 1987. Effect of oil composition on minimum miscibility pressure-part 2: Correlation. SPE Reserv. Eng. 2 (4), 479–491.

Orr Jr., F.M., Silva, M.K., Lien, C.L., 1983. Equilibrium phase compositions of CO_2/crude oil mixtures-part 2: Comparison of continuous multiple-contact and slim-tube displacement tests. SPE J. 23 (2), 281–291.

Reid, R.C., Frautsnitz, J.M., Sherwood, T.K., 1977. The Properties of Gases and Liquids, third ed. McGraw-Hill, New York.

Ren, B., Xu, Y., Niu, B., Ren, S., Li, X., Guo, P., Song, X., 2011. In: Laboratory assessment and field pilot of near miscible CO_2 injection for IOR and storage in a tight oil reservoir of ShengLi oilfield China. Paper SPE 144108, SPE Enhanced Oil Recovery Conference, Kuala Lumpur, Malaysia.

Renner, T.A., 1988. Measurement and correlation of diffusion coefficients for CO_2 and rich-gas applications. SPE Reserv. Eng. 3 (2), 517–523.

Sheng, J.J., 2015. Enhanced oil recovery in shale reservoirs by gas injection. J. Nat. Gas Sci. Eng. 22, 252–259.

Shoaib, S., Hoffman, B.T., 2009. In: CO_2 flooding the Elm Coulee field. Paper SPE 123176, SPE Rocky Mountain Petroleum Technology Conference, Denver, Colorado.

Sigmund, P.M., 1976. Prediction of molecular diffusion at reservoir conditions. Part II-estimating the effects of molecular diffusion and convective mixing in multicomponent systems. J. Can. Pet. Technol. 15 (3), 53–62.

Sigmund, P.M., Kerr, W., MacPherson, R.E., 1984. In: A laboratory and computer model evaluation of immiscible CO_2 flooding in a low-temperature reservoir. Paper SPE 12703, SPE Enhanced Oil Recovery Symposium, Tulsa, Oklahoma.

Song, C., Yang, D., 2013. In: Performance evaluation of CO_2 huff-n-puff processes in tight oil formations. Paper SPE 167217, SPE Unconventional Resources Conference, Alberta, Canada.

Stalkup, F.I., 1987. In: Displacement behavior of the condensing/vaporizing gas drive process. Paper SPE 16715, SPE Annual Technical Conference and Exhibition, Dallas, Texas.

Taber, J.J., Martin, F.D., 1983. In: Technical screening guides for the enhanced recovery of oil. Paper SPE 12069, SPE Annual Technical Conference and Exhibition, San Francisco, California.

United States Geological Survey (USGS), 2013. USGS Releases New Oil and Gas Assessment for Bakken and Three Forks Formations. USGS Webpost.http://www.usgs.gov/blogs/features/usgs_top_story/usgs-releases-new-oil-and-gas-assessment-for-bakken-and-three-forks-formations/.

Wang, X., Luo, P., Er, V., Huang, S., 2010. In: Assessment of CO_2 flooding potential for Bakken formation, Saskatchewan. Paper SPE 137728, Canadian Unconventional Resources and International Petroleum Conference, Calgary, Canada.

West, D.R.M., Harkrider, J., Besler, M.R., Barham, M., Mahrer, K.D., 2013. In: Optimized production in the Bakken shale: south Antelope case study. Paper SPE 167168, SPE Unconventional Resources Conference, Calgary, Canada.

Yu, W., Lashgari, H.R., Sepehrnoori, K., 2014. In: Simulation study of CO2 Huff-n-Puff process in Bakken tight oil reservoirs. Paper SPE 169575, SPE Western North American and Rocky Mountain Joint Meeting, Denver, Colorado.

Yu, W., Lashgari, H.R., Wu, K., Sepehrnoori, K., 2015. CO_2 injection for enhanced oil recovery in Bakken tight oil reservoirs. Fuel 159, 354–363.

Zuloaga, P., 2016. Performance Evaluation of CO_2 EOR in Tight Oil Formations with Complex Fracture Geometries. MS Thesis, The University of Texas at Austin.

Zuloaga, P., Yu, W., Xu, Y., Sepehrnoori, K., Li, B., 2016. Simulation study of CO_2-EOR in tight oil reservoirs with complex fracture geometries. Sci. Rep. 33445, 1–15.

Zuloaga, P., Yu, W., Miao, J., Sepehrnoori, K., 2017. Performance evaluation of CO_2 Huff-n-Puff and continuous CO_2 injection in tight oil reservoirs. Energy 134, 181–192.

Chapter 9

Phase Behavior Modeling by Considering Nanopore Confinement

Chapter Outline

9.1 INTRODUCTION

Understanding the fluid properties based on phase equilibria calculation plays an important role in development of unconventional oil and gas reservoirs. In unconventional reservoirs, the presence of a large amount of nanopores often leads to high capillary pressure values, which significantly impact phase behavior and fluid properties (Zhang et al., 2016; Zhang et al., 2017b,c). In conventional reservoirs, the capillary pressure value is small, which is often ignored in phase-equilibria calculation. Although Tarek (2007) provided a systematic summary about methods for calculation of phase equilibrium and fluid properties, the assumption of the equal phase pressures is not suitable for the unconventional reservoirs. Hence, a new equation of state is still needed to calculate the phase behavior and fluid properties when considering the capillary pressure effect.

Sigmund et al. (1973) investigated the effect of porous media on phase behavior of binary hydrocarbon mixtures, such as methane-n-butane and methane-n-pentane experimentally and theoretically. They found that the only very high

Shale Gas and Tight Oil Reservoir Simulation. https://doi.org/10.1016/B978-0-12-813868-7.00009-2

surface curvatures significantly affect equilibrium composition and pressures. Brusilovsky (1992) proposed a new general cubic equation of state (EOS) to predict phase behavior of natural multicomponent systems considering the capillary pressure effect, especially at high pressures. The simulation results indicate that the bubble point pressure decreases and the dew point pressure increases with the increasing surface curvature or the decreasing principle radius. It can be seen that the bubble point will be achieved first in larger pores while the dew point will be obtained first in small pores in porous media with varying pore sizes. Shapiro and Stenby (2001) applied the multicomponent Kelvin equation to perform thermodynamic behavior calculation of the vapor-liquid equilibrium under the capillary pressure condition. Zarragoicoechea and Kuz (2004) derived an equation for the critical temperature and pressure shift to properly account for the phase behavior of confined fluids in nanopores. The derivation is based on a generalized van der Waals equation of state. Qi et al. (2007) proposed a thermodynamic model to calculate phase equilibrium in deep low-permeability gas condensate reservoirs by considering adsorption, capillary pressure, and reservoir deformation effects. The radius of capillary tube of porous media changes with pressure during reservoir depletion. They found that the dew point pressure is increased due to the interfacial phenomena and reservoir deformation, resulting in the earlier occurrence of retrograde condensation.

Pang et al. (2012) applied the Peng-Robinson equation of state with conventional mixing rules to investigate the effect of capillary pressure on dew point and bubble point pressures in shale (tight) gas and shale (tight) oil reservoirs. They noted that the bubble point always decreases and the dew point in the upper dew point interval increases while it decreases in the lower dew point interval when considering the capillary pressure effect. In addition, the capillary pressure effect will become prominent when the radius of curvature is $<10^{-8}$ m. Honarpour et al. (2012) pointed out that the high capillary pressures encountered in unconventional shale reservoirs decrease bubble point pressure and oil viscosity and increase formation volume factor, resulting in a longer time of constant gas-oil ratio (GOR), as shown in Fig. 9.1. Chu et al. (2012) mentioned that changes of confined PVT properties are process dependent due to the dynamic pore size reduction caused by reservoir compaction, which is difficult to model accurately by the existing commercial reservoir simulators. In addition, a high uncertainty of long-term estimated ultimate recovery (EUR) forecasting with and without considering the capillary pressure effect is observed based on one typical Bakken tight oil well, which highly depends on the degree of reservoir compaction. Nojabaei et al. (2013) highlighted that it is important to accurately measure interfacial tension and pore size reductions with pressure, which significantly affect saturation pressures, phase densities, and viscosities. In addition, they explained that no increase in producing GOR for the Bakken shale oil wells is caused by the reduction of bubble point pressure due to small pores and high critical gas saturation.

Fig. 9.2 compared the conceptual pore network model during reservoir depletion with and without considering the nanopore confinement effect.

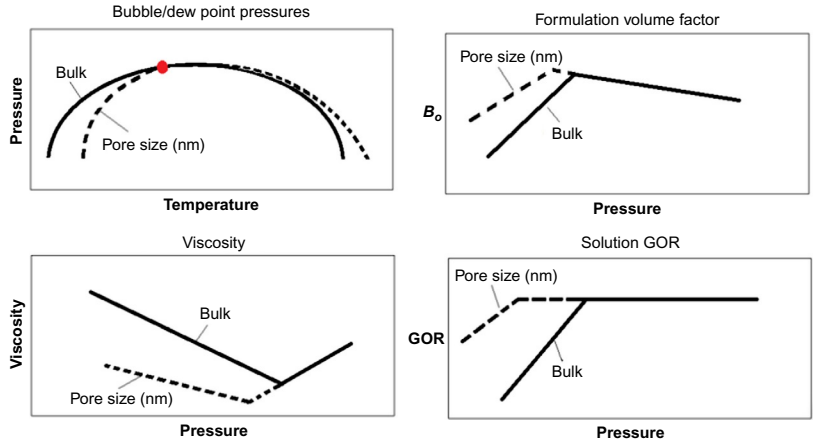

FIG. 9.1 Schematic of the effect of capillary pressure on phase behavior in nanopores (Honarpour et al., 2012).

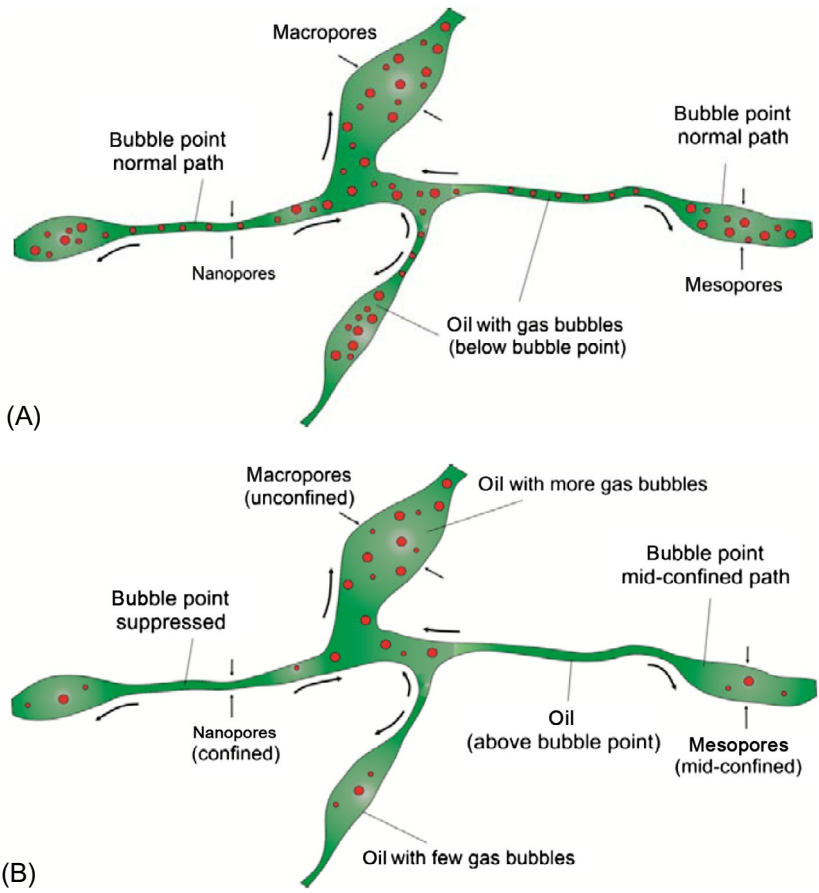

FIG. 9.2 Phase behavior in different pore sizes for a bubble point system during reservoir depletion (Alharthy et al., 2013). (A) Without the phase envelope shift. (B) With the phase envelope shift.

As shown in Fig. 9.2A, the bubble point is reached normally in the nanopores, mesopores, and macropores and oil and gas bubbles are formed. The gas becomes mobile after critical saturation and earlier gas breakthrough occurs, which is not favorable for hydrocarbon recovery since the oil is bypassed leading to higher GOR (Alharthy et al., 2013). As shown in Fig. 9.2B, the bubble point is suppressed in the nanopores, which delays the occurrence of gas in solution. However, the phase behavior is normal in macropores and oil and gas bubbles form as the unconfined bubble point is achieved, which is favorable for pushing oil out of the nanopores and mesopores (Alharthy et al., 2013). Nojabaei et al. (2014) used a compositionally extended black-oil model to incorporate the capillarity effect on phase behavior. Rezaveisi et al. (2015) discussed the implementation of capillary equilibrium in an in-house compositional reservoir simulator and illustrated the influence of capillary pressure on unconventional reservoir production. The simulation results show that the capillary pressure effect significantly influences the hydrocarbon production.

In this chapter, we will introduce the methodology for phase equilibrium calculation considering the capillary pressure effect due to nanopore confinement. In addition, the impact of capillary pressure effect on history matching and production forecasting of Bakken shale oil reservoirs will be examined. Also, the nanopore size distribution is considered in the simulation.

9.2 METHODOLOGY

9.2.1 Phase Equilibrium Calculation Considering Nanopore Confinement

The fluid properties and phase behavior will be altered when the nanopore radius is 10 nm or less in shale reservoirs. This is because of the strong interactions between surface walls and fluid molecules, especially the critical temperatures and pressures (Zarragoicoechea and Kuz, 2004; Diaz Campos et al., 2009; Devegowda et al., 2012; Zhang et al., 2016). The correlations for the shifts in these critical properties are described here:

$$\Delta T_c^* = \frac{T_{cb} - T_{cp}}{T_{cb}} = 0.9409\frac{\sigma_{LJ}}{r_p} - 0.2415\left(\frac{\sigma_{LJ}}{r_p}\right)^2, \tag{9.1}$$

$$\Delta P_c^* = \frac{P_{cb} - P_{cp}}{P_{cb}} = 0.9409\frac{\sigma_{LJ}}{r_p} - 0.2415\left(\frac{\sigma_{LJ}}{r_p}\right)^2, \tag{9.2}$$

$$\sigma_{LJ} = 0.244\sqrt[3]{\frac{T_{cb}}{P_{cb}}}, \tag{9.3}$$

where r_p is the pore-throat radius, ΔT_c^* and ΔP_c^* are the relative critical temperature and pressure shift due to nanopore confinement, respectively, T_{cb} is the bulk critical temperature, T_{cp} is the pore critical temperature, P_{cb} is the bulk

critical pressure, P_{cp} is the pore critical pressure, and σ_{LJ} is the Lennard-Jones size parameter. The critical properties for each component can be found from the work by Reid et al. (1987). In our previous study, we have described the phase equilibrium calculation (Zhang et al., 2016; Zhang et al., 2017b,c). The fugacities of components in the liquid and vapor phases are equal at equilibrium, which can be expressed by

$$f_L^i(T, P_L, x_i) = f_V^i(T, P_V, y_i), \quad i = 1, \ldots, N_c, \tag{9.4}$$

where f_L^i and f_V^i are the fugacity of component i in the liquid and vapor phases, respectively, T is the reservoir temperature, P_L and P_V represent the pressures in the liquid and vapor phases, respectively.

The following mass balance equation and Rachford-Rice equation (Rachford and Rice, 1952) are used in this study:

$$\sum_{i=1}^{N} x_i = \sum_{i=1}^{Nc} y_i = 1, \tag{9.5}$$

$$Fz_i = x_i L + y_i V, \quad i = 1, \ldots, N_c, \tag{9.6}$$

$$\sum_{i=1}^{Nc} \frac{\left(K_c^i - 1\right) z_i}{1 + (V/F)\left(K_c^i - 1\right)} = 0, \tag{9.7}$$

where F is the number of moles of original fluid feed, L and V are the number of moles of liquid and vapor phases, respectively, z_i is the overall mole fraction of component i, x_i and y_i are the mole fractions of component i in the liquid and vapor phases, respectively, N_c is the number of components, and K_c^i is the equilibrium ratio between gas phase and liquid phase by considering the capillary pressure, which is calculated through modifying the traditional equilibrium ration (K^i) without considering the capillary pressure effect (Zhang et al., 2017c):

$$K_c^i = \left(1 - \frac{P_c}{P_V}\right) K^i = \left(\frac{P_L}{P_V}\right) K^i, \quad i = 1, \ldots, N_c, \tag{9.8}$$

$$K^i = \frac{\varphi_L^i}{\varphi_V^i}, \quad i = 1, \ldots, N_c, \tag{9.9}$$

where φ_V^i and φ_L^i are fugacity coefficient of component i in vapor and liquid phases, respectively.

Capillary pressure refers to the difference of pressure between vapor and liquid phases. We use the following Young-Laplace equation (Adamson, 1990) to calculate the capillary pressure:

$$P_V - P_L = P_{cap}, \tag{9.10}$$

$$P_{cap} = \frac{2\sigma \cos\theta}{r_p}, \tag{9.11}$$

where P_{cap} is the capillary pressure, θ is the contact angle, σ is the interfacial tension at the interface between the vapor and liquid phases, which is calculated using the parachor model (Adamson, 1990):

$$\sigma = \left[\sum_{i}^{N_C} \left(\overline{\rho}_L [P]_i x_i - \overline{\rho}_V [P]_i y_i\right)\right]^{\upsilon}, \tag{9.12}$$

where $\overline{\rho}_L$ and $\overline{\rho}_V$ are densities of the bulk liquid and vapor phases, respectively, υ is the scaling exponent, which is generally 3.6 or 4.0. We used 4.0 in this study, $[P]_i$ is the parachor of component i in the liquid or gas phase. The parachor of pure component can be found from the work by Reid et al. (1987).

In this study, the Peng-Robinson equation of state is used in the phase equilibrium calculation (Peng and Robinson, 1976):

$$P = \frac{RT}{V_m - b} - \frac{a\alpha}{V_m^2 + 2bV_m - b^2}, \tag{9.13}$$

where V_m is the mole volume of component i, R is the universal gas constant, a and b are the parameters calculated using van der Waals mixing rules:

$$a = \sum_{i=1}^{N_C}\sum_{j=1}^{N_C} x_i x_j \left[\left(1 - k_{ij}\right)\sqrt{a_i a_j}\right], \tag{9.14}$$

$$b = \sum_{i=1}^{N_C} x_i b_i, \tag{9.15}$$

where k_{ij} is the binary interaction coefficient between component i and j.

Considering the difference between vapor and liquid pressures, Eq. (9.13) is modified for liquid and vapor phases, respectively:

$$(Z_L)^3 - (1 - B_L)(Z_L)^2 + \left(A_L - 2B_L - 3(B_L)^2\right)Z_L - \left(A_L B_L - (B_L)^2 - (B_L)^3\right) = 0, \tag{9.16}$$

$$(Z_V)^3 - (1 - B_V)(Z_V)^2 + \left(A_V - 2B_V - 3(B_V)^2\right)Z_V - \left(A_V B_V - (B_V)^2 - (B_V)^3\right) = 0, \tag{9.17}$$

where $A_L = \dfrac{a_L \alpha P_L}{R^2 T^2}$, $B_L = \dfrac{b_L P_L}{RT}$, $A_V = \dfrac{a_V \alpha P_V}{R^2 T^2}$, $B_V = \dfrac{b_V P_V}{RT}$. Z_L and Z_V are the compressibility of liquid and vapor phases, respectively. The roots of compressibility factor for liquid and vapor phases are determined through satisfying the criteria of Gibbs free energy for liquid and vapor. The Newton-Raphson method is used for solving the above nonlinear equations (Stiel and Thodos, 1961). The flowchart of calculation procedure is shown in Fig. 9.3. More details can be found in the work by Zhang et al. (2016).

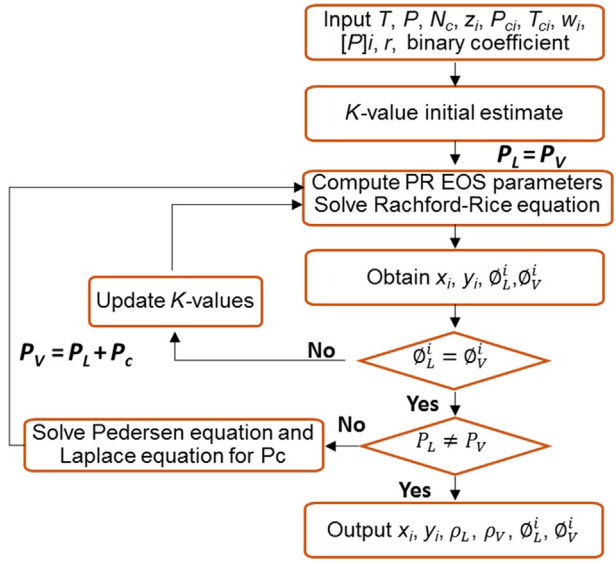

FIG. 9.3 Flowchart for phase equilibrium calculation considering the capillary pressure effect due to nanopore confinement (Zhang et al., 2016).

The following equations are used to calculate the fugacity coefficients of liquid and vapor phases:

$$\ln\varphi_L^i = \frac{b_{iL}}{b_L}(Z_L-1) - \ln(Z_L-B_L) - \frac{A_L}{2\sqrt{2}B_L}\left(\frac{2\sum_{i=1}^{Nc}x_{jL}\left(1-k_{ij}\right)\sqrt{a_{iL}a_{jL}}}{a_L} - \frac{b_{iL}}{b_L}\right)\ln\left(\frac{Z_L+\left(\sqrt{2}+1\right)B_L}{Z_L-\left(\sqrt{2}-1\right)B_L}\right). \tag{9.18}$$

$$\ln\varphi_V^i = \frac{b_{iV}}{b_V}(Z_V-1) - \ln(Z_V-B_V) - \frac{A_V}{2\sqrt{2}B_V}\left(\frac{2\sum_{i=1}^{Nc}x_{jV}\left(1-k_{ij}\right)\sqrt{a_{iV}a_{jV}}}{a_V} - \frac{b_{iV}}{b_V}\right)\ln\left(\frac{Z_V+\left(\sqrt{2}+1\right)B_V}{Z_V-\left(\sqrt{2}-1\right)B_V}\right). \tag{9.19}$$

9.2.2 Black-Oil Properties Calculation

Based on the foregoing phase equilibrium calculation, the black-oil fluid properties such as viscosities, solution gas-oil ratio (R_s), and formation volume factor (B_o) can be determined. When the equilibrium liquid composition is flashed at the standard condition, the solution gas-oil ratio is calculated as:

$$R_s = \frac{(n_V V_{mV})_{SC}}{(n_L V_{mL})_{SC}}, \tag{9.20}$$

where n_V and n_L are the vapor and liquid phase molar fraction, respectively, V_{mV} and V_{mL} are the vapor and liquid molar volume, respectively, and the subscript SC represents the standard condition.

The oil formation volume factor is calculated by the following equation:

$$B_o = \frac{(n_L V_{mL})_{RC}}{(n_L V_{mL})_{SC}}, \tag{9.21}$$

where the subscript RC represents reservoir condition.

The oil viscosity is calculated by the following equation (Jossi et al., 1962; Fong and Nghiem, 1980)

$$\left[(\mu - \mu^*)\xi + 10^{-4}\right]^{1/4} = a_0 + a_1\rho_r + a_2\rho_r^2 + a_3\rho_r^3 + a_4\rho_r^4, \tag{9.22}$$

where μ is oil viscosity at reservoir condition, μ^* is oil viscosity at low pressure, ξ is viscosity reducing parameter, a_0, a_1, a_2, a_3, and a_4 are 0.1023, 0.023364, 0.058533, −0.040758, and 0.0093324, respectively, and ρ_r is the reduced density, which is calculated by

$$\rho_r = \rho_L \left[\sum_{i=1}^{Nc} x_i v_{ci}\right]^{1/\alpha}, \tag{9.23}$$

where v_{ci} is the critical volume of component i, the parameter α is equal to 1.

The viscosity reducing parameter ξ in Eq. (9.22) is computed by

$$\xi = \left(\sum_{i=1}^{Nc} x_i T_{ci}\right)^{1/6} \left(\sum_{i=1}^{Nc} x_i M_i\right)^{-1/2} \left(\sum_{i=1}^{Nc} x_i P_{ci}\right)^{-2/3}, \tag{9.24}$$

where M_i represents the molecular weight of component i.

The low-pressure viscosity of the mixture in Eq. (9.22) is described by (Lohrenz et al., 1964)

$$\mu^* = \frac{\sum_{i=1}^{Nc}\left(x_i \mu_i^* M_i^{1/2}\right)}{\sum_{i=1}^{Nc}\left(x_i M_i^{1/2}\right)}, \tag{9.25}$$

where μ_i^* is the low-pressure viscosities for pure components and calculated using the following equation (Stiel and Thodos, 1961):

$$\mu_i^* \xi_i = \left[4.610 T_{ri}^{0.618} - 2.04 \exp(-0.449 T_{ri}) + 1.94 \exp(-4.058 T_{ri}) + 0.1\right] \times 10^{-4}, \tag{9.26}$$

where $\xi_i = T_{ci}^{1/6} M_i^{1/2} P_{ci}^{2/3}$ and $T_{ri} = T/T_{ci}$.

Similarly, the approach of calculating the oil viscosity can also be used in gas viscosity calculation. In addition, these methods for fluid properties calculation can be applied to both scenarios with and without considering the capillary pressure effect. Once the fluid properties are obtained, they can be input into a standard black-oil reservoir simulator to predict hydrocarbon recovery in unconventional reservoirs with and without considering the capillary pressure effect.

9.3 VALIDATION FOR PHASE EQUILIBRIUM CALCULATION

In this section, the phase equilibrium model was validated against several experimental measurements (Zhang et al., 2016).

9.3.1 *K*-Values for Bulk Fluid

The proposed model was first validated against the experimental data, which is taken from the work by Wang et al. (2014). Comparison of experimental *K*-values and simulated *K*-values is listed in Table 9.1. It can be seen that the simulated *K*-values are in close agreement with the experimental results at given temperature and pressure. The average relative error is about 2.45%, which indicates that the model can accurately predict the vapor-liquid phase equilibrium of hydrocarbon systems.

TABLE 9.1 Comparison Between Experimental and Simulated *K*-Values (Zhang et al., 2016)

Component	Mole Fraction (%)	Experimental *K*-Values	Simulated *K*-Values	Relative Error (%)
iC_4	61.89	2.652	2.816	6.2
nC_4	18.11	1.885	1.904	1.0
C_8	20.00	0.0524	0.053	0.2

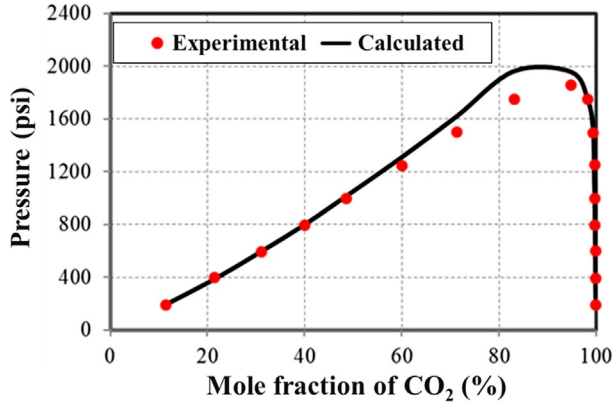

FIG. 9.4 Comparison of experimental and simulated phase behavior considering capillary pressure for CO_2-C_{10} mixture (Zhang et al., 2016).

9.3.2 Binary Mixture of CO_2/C_{10}

An early work about the phase behavior of binary mixture CO_2/C_{10} is used to validate the proposed model (Reamer and Sage, 1963) and the comparison result is shown in Fig. 9.4. It shows that a good match between the simulated and experimental phase envelope is obtained.

9.3.3 Binary Mixture of C_1/C_6

We selected the binary mixture of C_1/C_6 to better understand the difference of phase envelope with and without considering the capillary pressure effect. Fig. 9.5 shows the comparison of pressure-temperature phase envelopes for different C_1/C_6 mixtures at the pore radius of 20 nm. As shown, the bubble point

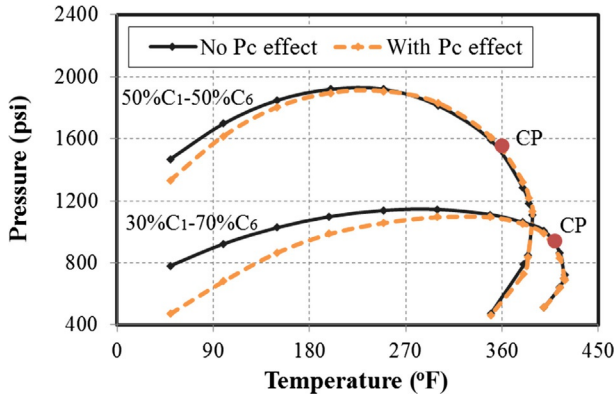

FIG. 9.5 Comparison of pressure-temperature phase envelopes for different C_1/C_6 mixtures with and without the capillary pressure effect (Zhang et al., 2016).

pressure decreases when considering the capillary pressure effect. In addition, the capillary pressure effect is more prominent for the mixture with more C_6 component, resulting in a smaller region of two-phase envelop. However, there is no change for the dew point pressure near the critical point. This is because the interfacial tension at critical point is zero. The symbols in the figure represent the results reported by Nojabaei et al. (2014). As can be seen, a good match between these results is obtained.

9.4 EFFECT OF NANOPORES ON PHASE BEHAVIOR OF BAKKEN SHALE OIL

The typical fluid properties of the Bakken shale oil are used to examine the effect of nanopores on phase behavior. The crude oil is divided into five different pseudocomponents, i.e., CH_4, C_2-C_4, C_5-C_7, C_8-C_9, C_{10+}, and their corresponding molar fractions are 25.06%, 22%, 20%, 13%, and 19.94%, respectively. The reservoir temperature is 240°F. The other parameters are listed in Table 9.2. The binary coefficient used for equilibrium calculation is listed in Table 9.3. Fig. 9.6 shows the effect of different pore sizes on bubble point pressure. It can be seen that the capillary pressure effect is more obvious when the pore size is smaller than 50 nm.

Fig. 9.7 compares formation volume factor, solution gas-oil ratio, and oil viscosity with and without considering the capillary pressure effect. Different nanopore sizes of 10, 30, and 50 nm are considered. As shown, there is deviation of confined fluid properties from bulk fluid properties when the pressure is less than the bulk bubble point pressure. The deviation becomes larger when the pore size is smaller. In addition, a reduction of 200 psi of bubble point pressure occurs when the pore size reduces to 10 nm. The reduction of bubble point results in longer single-phase flow during reservoir depletion. The formation volume factor and solution gas-oil ratio increase and the oil viscosity decreases in the gas-liquid region when considering the capillary pressure effect.

9.5 EFFECT OF NANOPORES ON PHASE BEHAVIOR OF EAGLE FORD SHALE OIL

Six pseudocomponents were assumed for the Eagle Ford shale oil, i.e., CO_2, N_2, C_1, C_2-C_5, C_6-C_{10}, and C_{11+}. The corresponding molar fractions are 0.01183, 0.00161, 0.11541, 0.26438, 0.38089, and 0.22588, respectively. Tables 9.4 and 9.5 list the critical properties of these pseudocomponents and their binary interaction parameters, which were used for phase behavior calculation. Reservoir temperature is 270°F. Fig. 9.8 shows the bubble-point pressure under different pore sizes. The nanopore confinement leads to the suppression of the bubble point pressure. The smaller the pore size, the larger reduction it will be. The reduction of bubble point pressure is about 218 psi when the nanopore size is 10 nm.

TABLE 9.2 Compositional Data for the Peng-Robinson EOS in the Bakken Formation (Yu et al., 2015)

Component	Molar Fraction	Critical Pressure (atm)	Critical Temperature (K)	Critical Volume (L/mol)	Molar Weight (g/gmol)	Acentric Factor	Parachor Coefficient
CH_4	0.2506	45.40	190.60	0.0990	16.04	0.0080	77.0
C_2-C_4	0.22	42.54	363.30	0.1970	42.82	0.1432	145.2
C_5-C_7	0.20	33.76	511.56	0.3338	83.74	0.2474	250.0
C_8-C_9	0.13	30.91	579.34	0.4062	105.91	0.2861	306.0
C_{10+}	0.1994	21.58	788.74	0.9208	200.00	0.6869	686.3

TABLE 9.3 Binary Interaction Parameters for Oil Components From the Bakken Formation (Yu et al., 2015)

Component	CH_4	C_2-C_4	C_5-C_7	C_8-C_9	C_{10+}
CH_4	0	0.0078	0.0242	0.0324	0.0779
C_2-C_4	0.0078	0	0.0046	0.0087	0.0384
C_5-C_7	0.0242	0.0046	0	0.0006	0.0169
C_8-C_9	0.0324	0.0087	0.0006	0	0.0111
C_{10+}	0.0779	0.0384	0.0169	0.0111	0

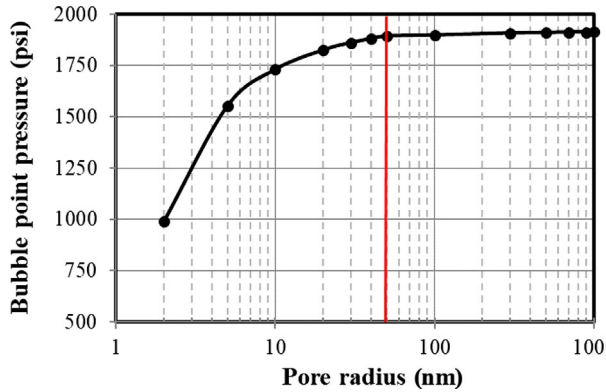

FIG. 9.6 Effect of pore size on bubble point pressure of Bakken shale oil (Zhang et al., 2017c).

9.6 CASE STUDIES

9.6.1 Middle Bakken Shale Oil

An actual shale-oil well from Middle Bakken formation with 450 days of production data was used to perform history matching and production forecasting (Yu et al., 2015). We built a reservoir model with dimension of 10,500 ft × 2600 ft × 50 ft, which represents length, width and thickness, respectively. A numerical reservoir simulator is used (CMG-IMEX, 2012). Thirty hydraulic fractures were explicitly modeled using local grid refinement approach. Fracture height is equal to reservoir thickness. The initial reservoir pressure is 7800 psi, water saturation is 0.49, reservoir porosity is 5.6%, compressibility is 1×10^{-6} psi^{-1}, and reservoir temperature is 240°F. Relative permeability curves from the work by Yu et al. (2015) were used. The fluid properties are listed in Tables 9.2 and 9.3. The nanopore size distribution from the Middle Bakken formation (see Figs. 9.9 and 9.10) is considered to investigate the effect of capillary pressure on well performance. Five regions with

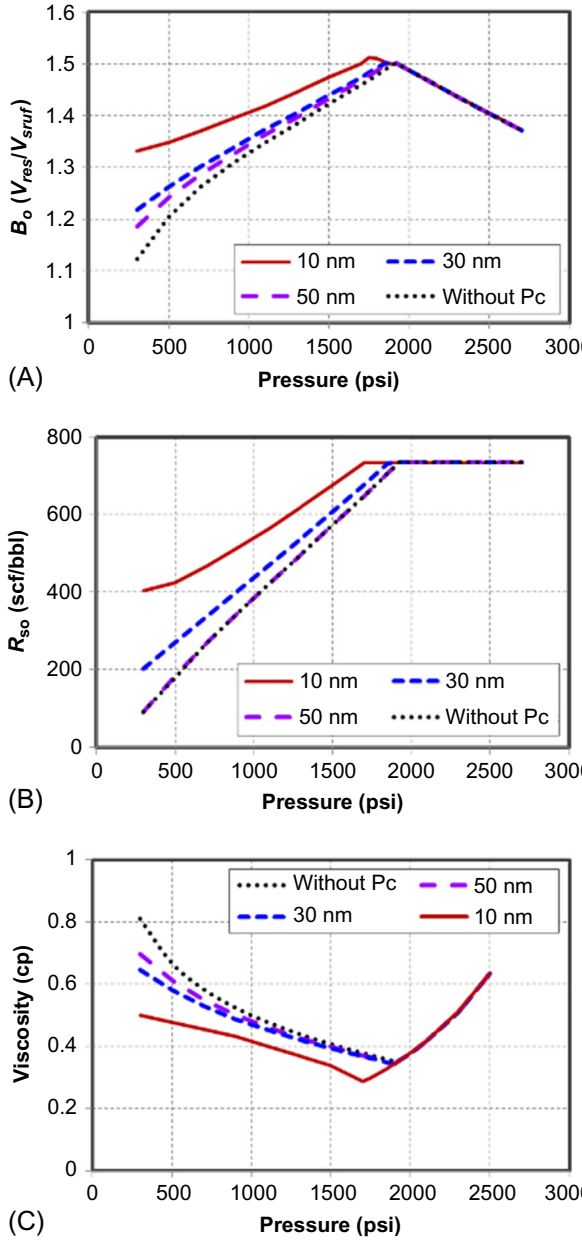

FIG. 9.7 Effect of different nanopore sizes on fluid properties of Bakken shale oil (Zhang et al., 2017c). (A) Formation volume factor; (B) solution gas-oil ratio; (C) oil viscosity.

TABLE 9.4 Compositional Data for the Peng-Robinson EOS in the Eagle Ford Shale Oil (Yu et al., 2018)

Component	Molar Fraction	Critical Pressure (atm)	Critical Temperature (K)	Critical Volume (L/mol)	Molar Weight (g/gmol)	Acentric Factor	Parachor Coefficient
CO_2	0.01183	72.80	304.20	0.0940	44.01	0.2250	78.00
N_2	0.00161	33.50	126.20	0.0895	28.01	0.0400	41.00
C_1	0.11541	45.40	190.60	0.0990	16.04	0.0080	77.00
C_2-C_5	0.26438	36.50	274.74	0.2293	52.02	0.1723	171.07
C_6-C_{10}	0.38089	25.08	438.68	0.3943	103.01	0.2839	297.42
C_{11+}	0.22588	17.55	740.29	0.8870	267.15	0.6716	661.45

TABLE 9.5 Binary Interaction Parameters for Oil Components From the Eagle Ford Shale Oil (Yu et al., 2018)

Component	CO_2	N_2	C_1	C_2-C_5	C_6-C_{10}	C_{11+}
CO_2	0	0.0200	0.1030	0.1299	0.1500	0.1500
N_2	0.0200	0	0.0310	0.0820	0.1200	0.1200
C_1	0.1030	0.0310	0	0.0174	0.0462	0.1110
C_2-C_5	0.1299	0.0820	0.0174	0	0.0073	0.0444
C_6-C_{10}	0.1500	0.1200	0.0462	0.0073	0	0.0162
C_{11+}	0.1500	0.1200	0.1110	0.0444	0.0162	0

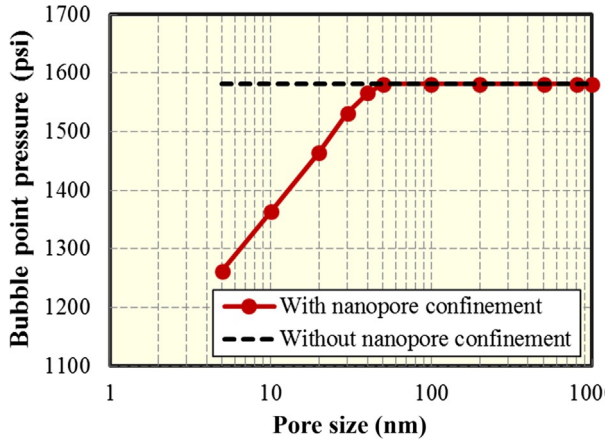

FIG. 9.8 Effect of pore size on bubble point pressure of Eagle Ford shale oil (Yu et al., 2018).

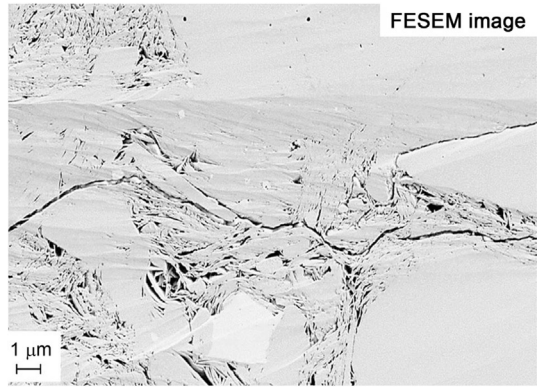

FIG. 9.9 SEM pore image of one example in the Middle Bakken formation (Jin et al., 2017).

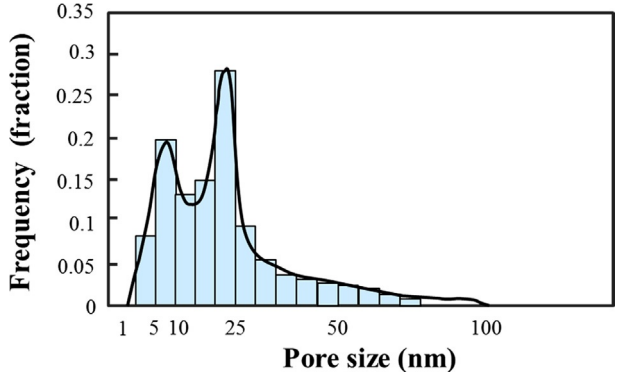

FIG. 9.10 Pore size distribution of one example in the Middle Bakken formation (Zhang et al., 2017c).

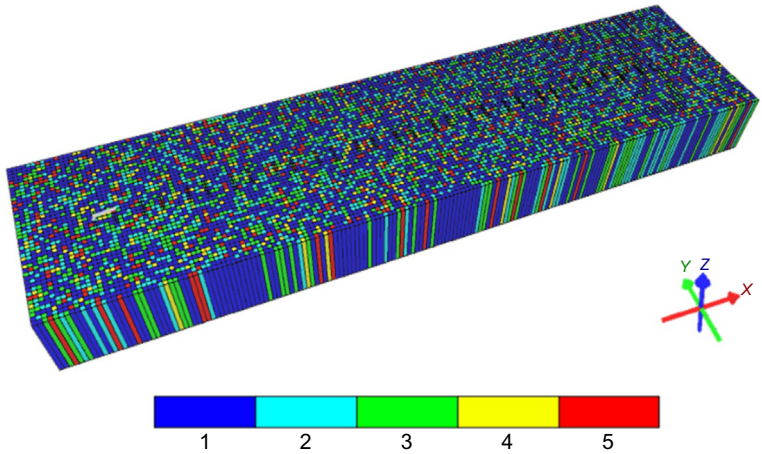

FIG. 9.11 Distribution of five different PVT regions in the reservoir model (color bar of 1–5 represents five pore sizes: 10 nm, 15 nm, 25 nm, 40 nm, and larger than 50 nm) (Zhang et al., 2017c).

different pore sizes were applied to represent the pore size distribution: <10 nm (27%), 10–20 nm (26%), 20–30 nm (30%), 30–50 nm (13%), and bulk [pore sizes more than 50 nm (4%)]. The percentage for each region is determined through the summation of the frequency for each pore size, as shown in Fig. 9.10. Correspondingly, five different PVT regions are calculated, based on five pore sizes such as 10 nm, 15 nm, 25 nm, 40 nm, and larger than 50 nm and assigned in the reservoir model randomly, as displayed in Fig. 9.11.

Next, we performed history matching with field data with and without considering the capillary pressure effect. Oil flow rate was treated as simulation constraint and gas flow rate and flowing bottomhole pressure (BHP) were history-matching objective functions. Matrix permeability, fracture half-length, and fracture conductivity are tuning parameters during the history-matching process. The history-matching results with and without considering the capillary pressure effect are shown in Fig. 9.12. It can be observed that good matching results between field data and simulation data are achieved. After history matching, matrix permeability is 0.032 and 0.037 mD, fracture half-length is 120 and 120 ft, fracture conductivity is 48 and 50 mD-ft for both scenarios with and without considering the capillary pressure effect.

In addition, we performed production forecasting for this well in a 30-year period. The constant BHP of 1000 psi is used for the simulation constraint after the history matching period. Comparisons of well performance with and without considering the capillary pressure effect are shown in Fig. 9.13. The differences of the cumulative oil and gas production and oil recovery factor after 30 years with and without the capillary pressure effect are 7%, 8%, and 6%, respectively. The confined phase behavior and the suppression of the bubble point pressure result in longer time of single-phase oil production when

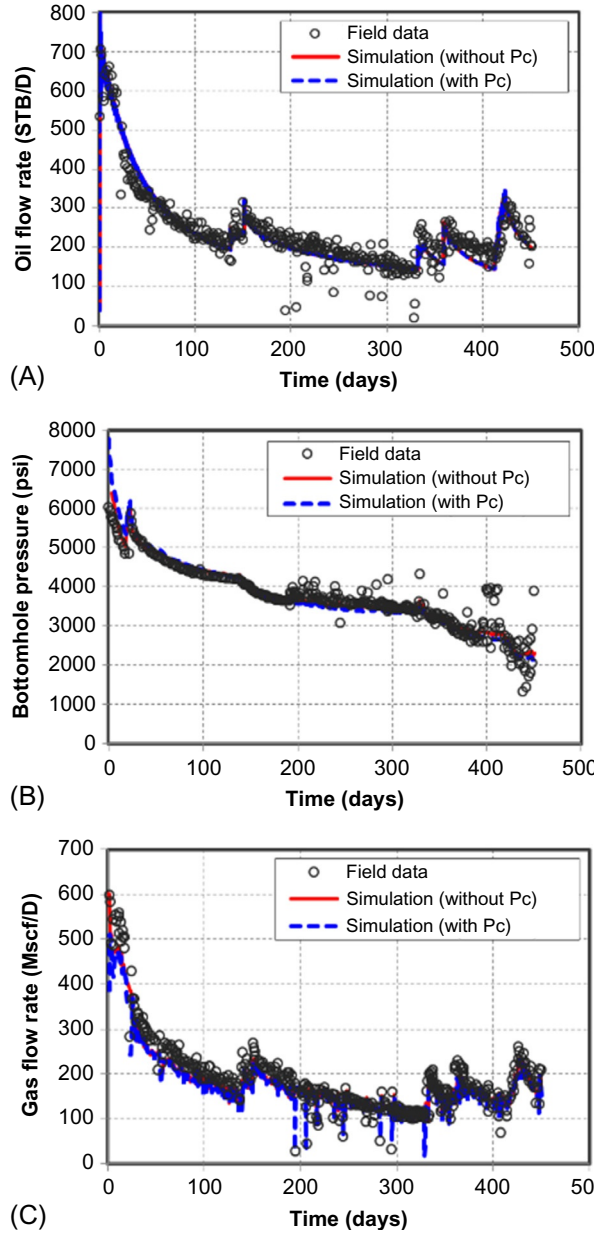

FIG. 9.12 History-matching results with and without considering the capillary pressure effect (Zhang et al., 2017c). (A) Oil flow rate; (B) bottomhole pressure; (C) gas flow rate.

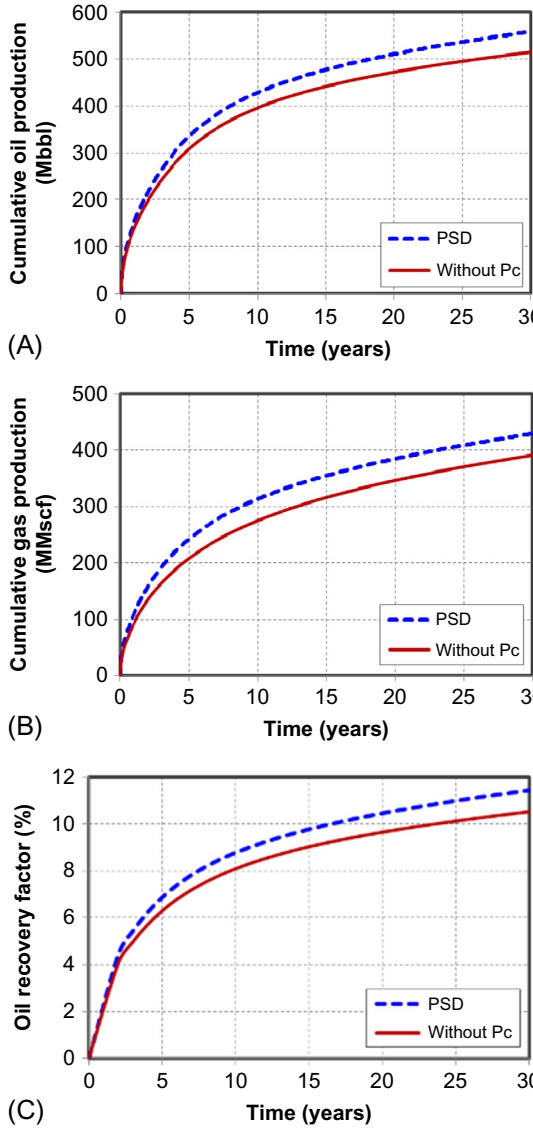

FIG. 9.13 Comparisons of well performance in a 30-year period with and without considering the capillary pressure effect for the Middle Bakken shale oil well (Zhang et al., 2017c). (A) Cumulative oil production; (B) cumulative gas production; (C) oil recovery factor.

considering the capillary pressure effect. In addition, the oil viscosity decreases with the capillary pressure effect, resulting in better well performance.

Comparison of pressure distribution after 30 years of production with and without considering the capillary pressure effect is presented in Fig. 9.14. It can be clearly seen that a larger pressure drop occurs for the scenario with the capillary pressure effect than the scenario without the capillary pressure effect.

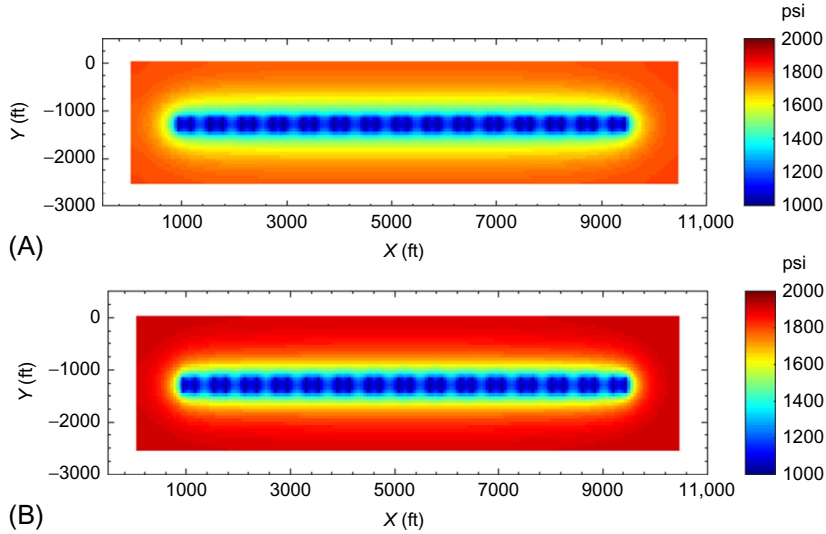

FIG. 9.14 Comparison of pressure distribution after 30 years for the Middle Bakken shale oil well (Zhang et al., 2017c). (A) With the capillary pressure effect; (B) without the capillary pressure effect.

9.6.2 Eagle Ford Shale Oil

The nanopore size distribution for one example in the Lower Eagle Ford formation is shown in Fig. 9.15. For oil-bearing samples, the pore volume significantly increases after removal of residual oil by solvent extraction, showing that oil is mainly stored in pores with widths larger than 5 nm. The contribution of <5 nm, 5–10 nm, 10–20 nm, 20–40 nm, and >40 nm pores to the total porosity is 42%, 27%, 13%, 4%, and 14%, respectively. And the pores smaller than 10 nm take almost 80% of total porosity; therefore, nanopore confinement is needed to be considered in reservoir modeling.

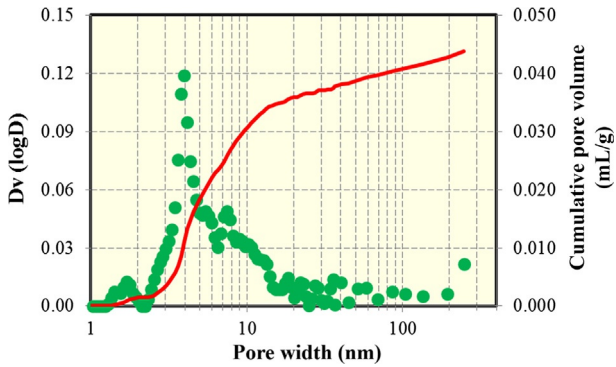

FIG. 9.15 Pore size distribution of one example in the Lower Eagle Ford formation (Yu et al., 2018).

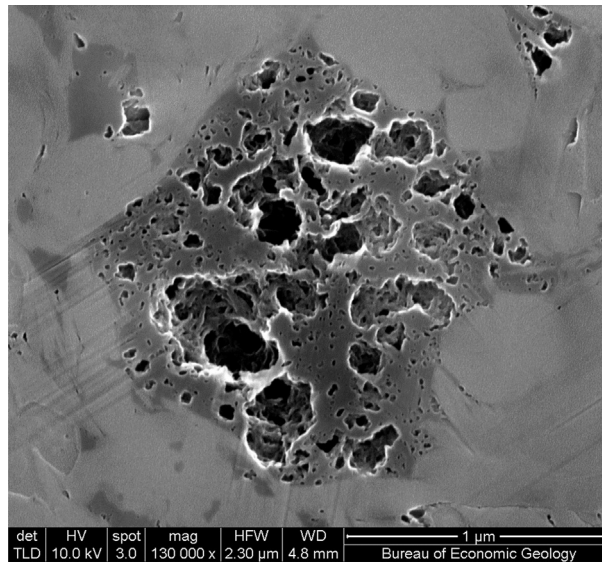

FIG. 9.16 SEM pore image of one example in the Lower Eagle Ford formation (Yu et al., 2018).

Thermal maturity also plays an important role to organic matter hosted nanopore development and the variation of oil and gas chemical properties (Zhang et al., 2017a). With an increase of thermal maturity, pores with widths <10 nm increase and pores with widths >40 nm are diminished (Ko et al., 2017). The development of smaller pores is associated with high thermal maturity, and the reduction larger pores may result from burial-related compaction and cementation. Thermal maturity greatly affects pore size distribution, in particular for pores with width <10 nm. Integrated studies that include SEM pore imaging are required to adequately define the genetic relationships between pore sizes, pore types, mineralogy, and rock texture. As shown in Fig. 9.16, organic-matter hosted pores, the size of organic matter hosted pores ranges from a few nanometers to a few hundred nanometers.

The nanopore size significantly affects the critical properties of different components. Table 9.6 compares the difference of critical temperature and pressure of six components between 10 nm, 20 nm, and bulk pore size. The fluid properties of six components are listed in Tables 9.4 and 9.5. It can be clearly seen that both critical temperature and critical pressure decrease when the pore size decreases. In the following production simulation, the PVT data corresponding to 10 nm of pore size are updated and utilized.

We built a 3D reservoir model with a horizontal well and multiple hydraulic fractures using a numerical reservoir simulator (CMG-GEM, 2016). The model dimension is 7785 ft $\times$ 1300 ft $\times$ 100 ft, which corresponds to length, width, and height, respectively, as shown in Fig. 9.17A. Three layers were modeled and the

TABLE 9.6 Effect of Pore Size on the Critical Temperature and Pressure of Six Components (Yu et al., 2018)

Component	Critical Temperature (K)			Critical Pressure (atm)		
	10 nm	*20 nm*	*Bulk*	*10 nm*	*20 nm*	*Bulk*
CO_2	293.06	298.6	304.20	70.1	71.5	72.8
N_2	121.74	123.96	126.20	32.3	32.9	33.5
C_1	183.61	187.09	190.60	43.7	44.6	45.4
C_2-C_5	262.53	268.6	274.74	34.9	35.7	36.5
C_6-C_{10}	412.97	425.72	438.68	23.6	24.4	25.1
C_{11+}	682.36	711.00	740.29	16.1	16.8	17.5

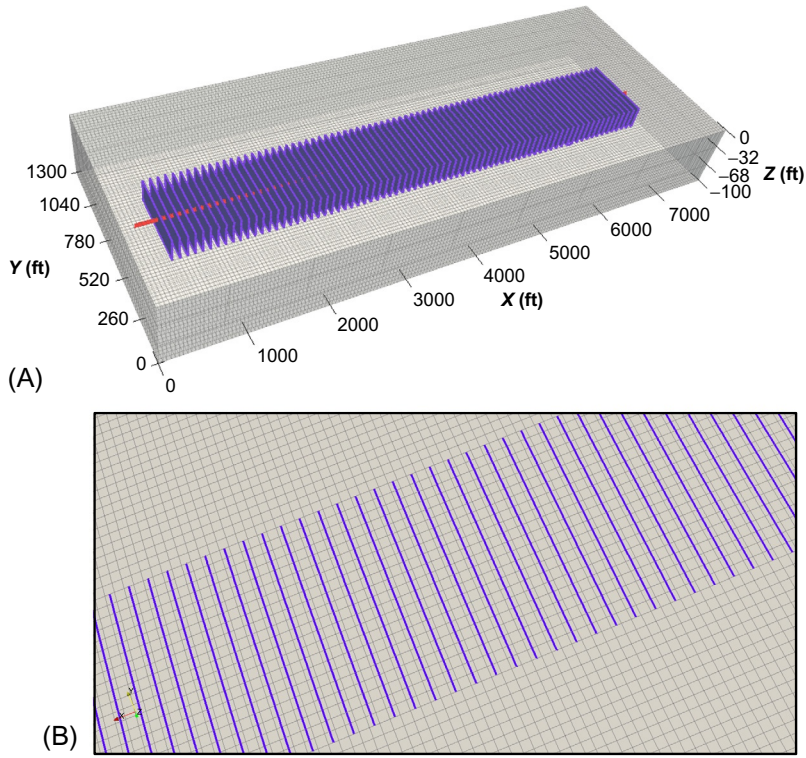

FIG. 9.17 A 3D reservoir model with a horizontal well and 76 biwing hydraulic fractures (Yu et al., 2018). (A) A three-layer reservoir model with multiple hydraulic fractures; (B) a small portion of the third layer model with multiple hydraulic fractures.

middle layer is fully penetrated by hydraulic fractures. The thickness of the middle layer is 36 ft and the thickness of the top and bottom layers is 32 ft. A horizontal well with 6913 ft length was placed in the middle layer. First, the embedded discrete fracture model (EDFM) method is applied to model multiple biwing hydraulic fractures in the numerical reservoir simulator. A small portion of the third layer with multiple fractures is shown in Fig. 9.17B. It can be clearly seen that no local grid refinement of nearby fractures is needed for the EDFM method. Table 9.7 lists the basic reservoir and fracture properties used in the simulation. The constant BHP of 1000 psi is used for simulation constraint. The relative permeability curves, such as water-oil relative permeability and liquid-gas relative permeability, were given in Fig. 9.18.

TABLE 9.7 Basic Reservoir and Fracture Properties Used in This Study (Yu et al., 2018)

Parameter	Value	Unit
Model dimension ($x \times y \times z$)	$7785 \times 1300 \times 100$	ft
Number of gridblocks ($x \times y \times z$)	$173 \times 65 \times 3$	–
Initial reservoir pressure	8125	psi
Reservoir temperature	270	°F
Reservoir permeability	900	nD
Reservoir porosity	12%	–
Initial water saturation	17%	–
Total compressibility	1×10^{-6}	psi^{-1}
Reservoir thickness	100	ft
Reservoir depth	11,109	ft
Well length	6913	ft
Number of stage	19	–
Clusters per stage	4	–
Cluster spacing	90	ft
K_v/K_H	0.06	–
Water saturation inside SRV	33%	–
Fracture half-length	210	ft
Fracture height	36	ft
Fracture conductivity	200	md-ft

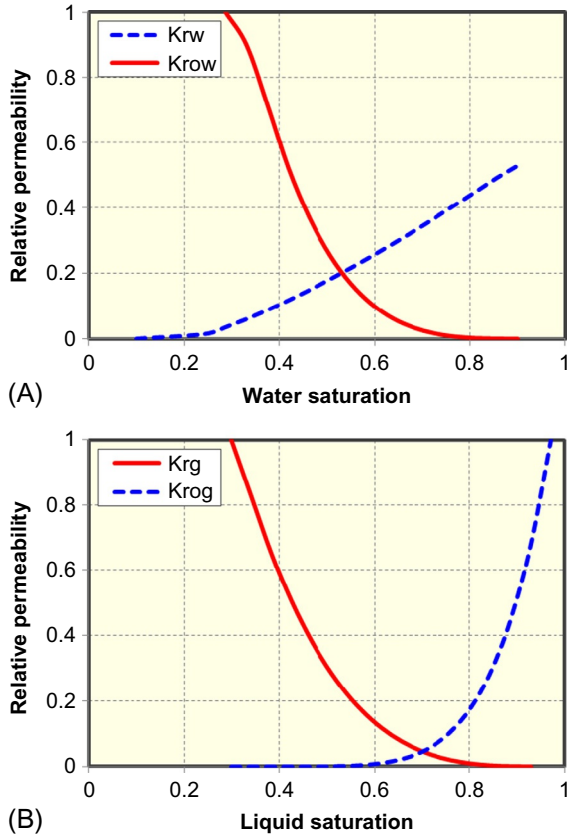

FIG. 9.18 Relative permeability curves used in this study (Yu et al., 2018). (A) Water-oil relative permeability curve; (B) liquid-gas relative permeability curve.

Comparisons of well performance with and without considering the capillary pressure effect are shown in Fig. 9.19. The differences of the cumulative oil and gas production and oil recovery factor after 30 years with and without the capillary pressure effect are 11.4%, 38.2%, and 27.2%, respectively. Comparison of pressure distribution after 30 years of production with and without considering the capillary pressure effect is presented in Fig. 9.20. It can be clearly seen that a larger pressure drop occurs for the scenario with the capillary pressure effect than the scenario without the capillary pressure effect.

In addition to 76 hydraulic fractures, a total number of natural fractures of 1800 are assumed in the reservoir volume studied and each layer contains 600 natural fractures, as shown in Fig. 9.21A. Fig. 9.21B displays a small portion of the third layer with multiple hydraulic fractures in blue color and natural fractures in black color. As shown, the complex fracture geometry is exactly captured through the EDFM method without the need for grid refinements.

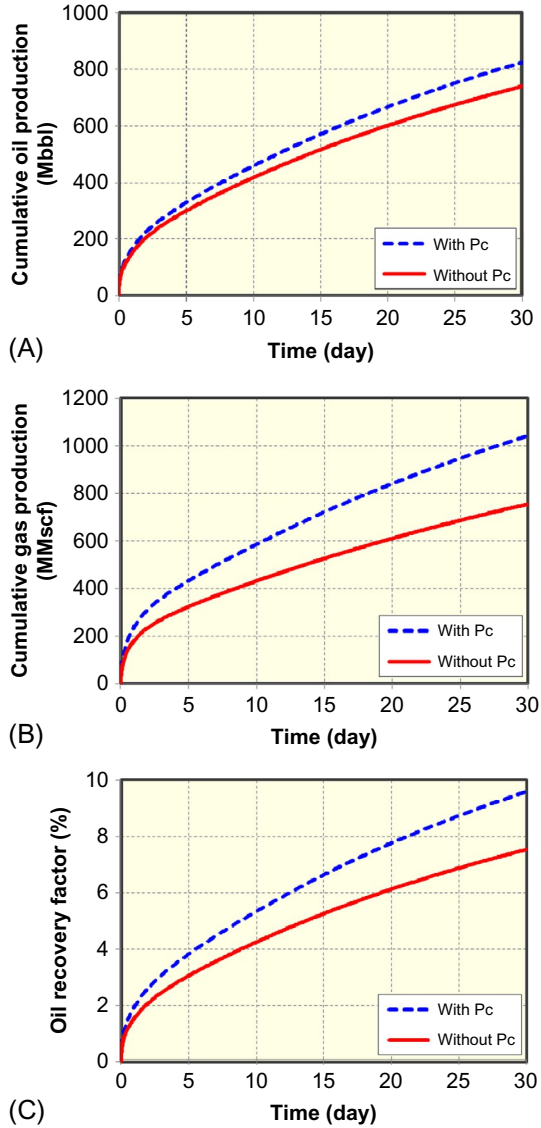

FIG. 9.19 Comparisons of well performance in a 30-year period with and without considering the capillary pressure effect for the Eagle Ford shale oil well. (A) Cumulative oil production; (B) cumulative gas production; (C) oil recovery factor.

In this study, we used a statistical method to generate the two sets of natural fractures. The angle with respect to the x axis for one set ranges from 0 to 20 degree and the other set ranges from 90 to 110 degree. The length of natural fractures varies between 100 and 300 ft. The conductivity of the natural

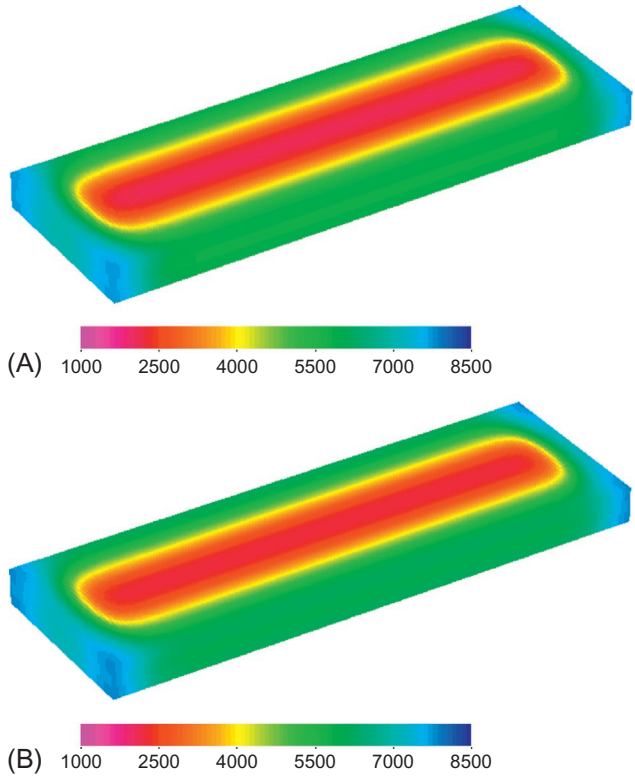

FIG. 9.20 Comparison of pressure distribution after 30 years for the Eagle Ford shale oil well. (A) With the capillary pressure effect; (B) without the capillary pressure effect.

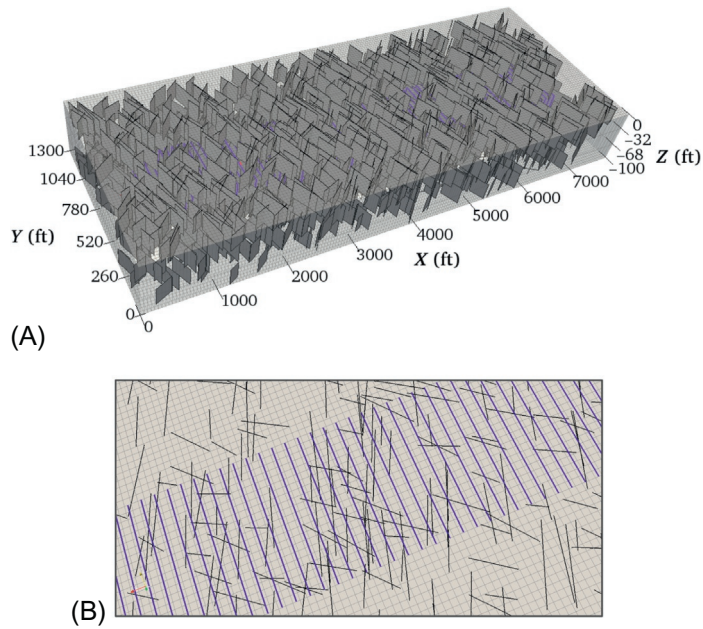

FIG. 9.21 A 3D reservoir model with a horizontal well and 76 biwing hydraulic fractures and 1800 natural fractures (Yu et al., 2018). (A) A three-layer reservoir model with multiple hydraulic and natural fractures; (B) a small portion of the third layer model with multiple hydraulic and natural fractures.

fractures is given by 10 md-ft. It is assumed that the height of natural fractures in each layer is equal to the reservoir thickness of the corresponding layer.

Comparisons of well performance with and without considering the capillary pressure effect are shown in Fig. 9.22. The differences of the cumulative

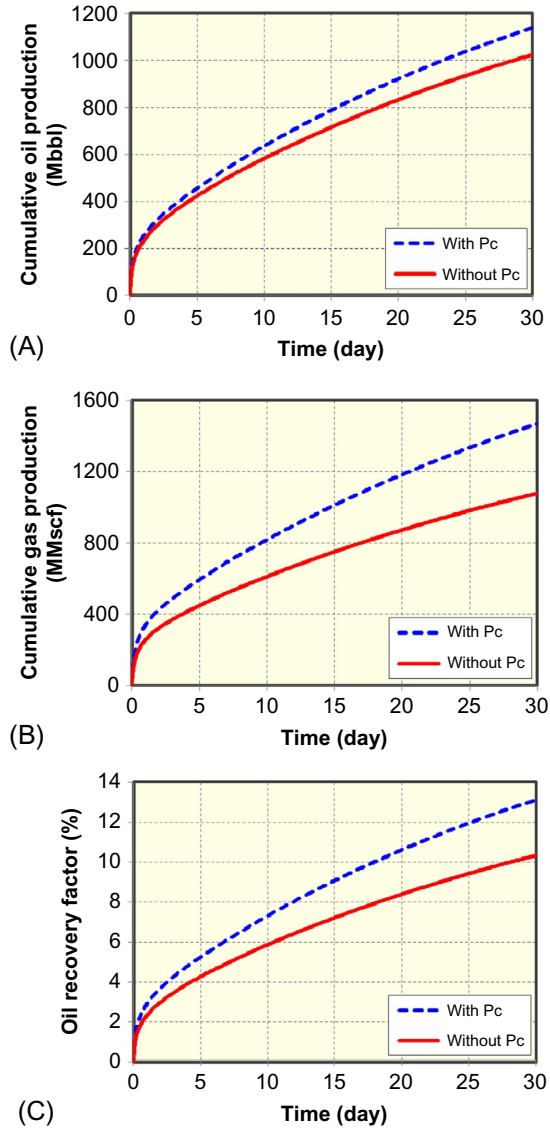

FIG. 9.22 Comparisons of well performance in a 30-year period with and without considering the capillary pressure effect for the Eagle Ford shale oil well with natural fractures. (A) Cumulative oil production; (B) cumulative gas production; (C) oil recovery factor.

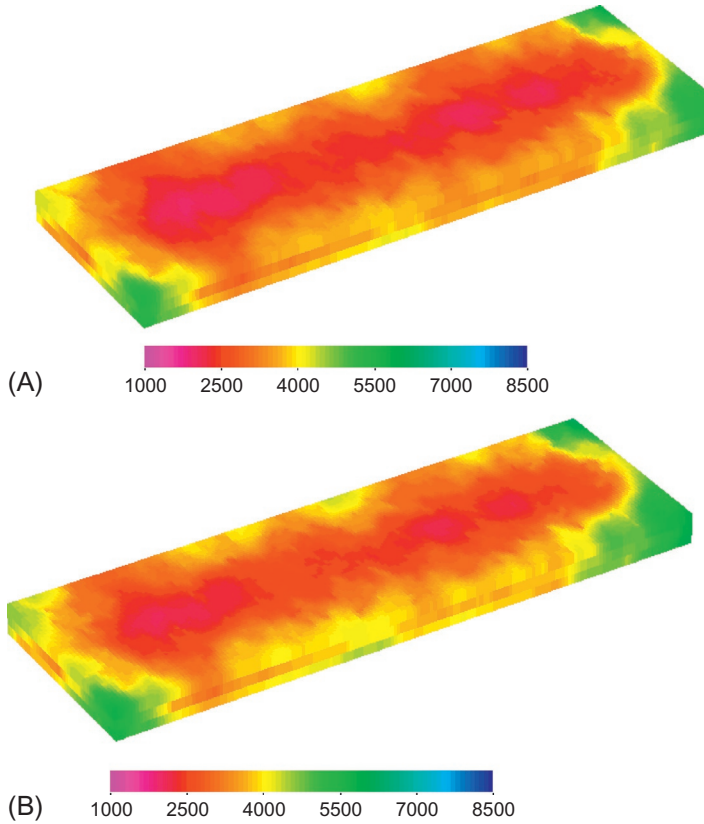

FIG. 9.23 Comparison of pressure distribution after 30 years for the Eagle Ford shale oil well with natural fractures. (A) With the capillary pressure effect; (B) without the capillary pressure effect.

oil and gas production and oil recovery factor after 30 years with and without the capillary pressure effect are 11.2%, 36.3%, and 27.0%, respectively. Comparison of pressure distribution after 30 years of production with and without considering the capillary pressure effect is presented in Fig. 9.23. It can be clearly seen that a larger pressure drop occurs for the scenario with the capillary pressure effect than the scenario without the capillary pressure effect.

REFERENCES

Adamson, A.W., 1990. Physical Chemistry of Surfaces, In: fifth ed. John Wiley & Sons, New York City.

Alharthy, N.S., Nguyen, T.N., Teklu, T.W., Kazemi, H., Graves, R.M., 2013. Multiphase compositional modeling in small-scale pores of unconventional shale reservoirs. Paper SPE 166306, SPE Annual Technical Conference and Exhibition, New Orleans, Louisiana.

Brusilovsky, A.I., 1992. Mathematical simulation of phase behavior of natural multicomponent systems at high pressures with an equation of state. SPE Reserv. Eng. 7 (1), 117–122.

Chu, L., Ye, P., Harmawan, I., Du, L., Shepard, L., 2012. Characterizing and simulating the non-stationariness and non-linearity in unconventional oil reservoirs: Bakken application. Paper SPE 161137, SPE Canadian Unconventional Resources Conference, Calgary, Canada.

CMG-GEM, 2016. GEM User's Guide. Computer Modeling Group Ltd, Calgary.

CMG-IMEX, 2012. GEM User's Guide. Computer Modeling Group Ltd, Calgary.

Devegowda, D., Sapmanee, K., Civan, F., Sigal, R.F., 2012. Phase behavior of gas condensates in shales due to pore proximity effects: implications for transport, reserves and well productivity. Paper SPE 160099, SPE Annual Technical Conference and Exhibition, San Antonio, Texas.

Diaz Campos, M., Akkutlu, I.Y., Sigal, R.F., 2009. A molecular dynamics study on natural gas solubility enhancement in water confined to small pores. Paper SPE 124491, SPE Annual Technical Conference and Exhibition, New Orleans, Louisiana.

Fong, D.K.S., Nghiem, L.X. 1980. A viscosity model for reservoir fluid. Computer Modeling Group Research Report, R7.

Honarpour, M.M., Nagarajan, N.R., Orangi, A., Arasteh, F., Yao, Z., 2012. Characterization of critical fluid PVT, rock, and rock-fluid properties-impact on reservoir performance of liquid rich shales. Paper SPE 158042, SPE Annual Technical Conference and Exhibition, San Antonio, Texas.

Jin, L., Hawthorne, S., Sorensen, J., Pekot, L., Kurz, B., Smith, S., Heebink, L., Herdegen, V., Bosshart, N., Torres, J., Dalkhaa, C., Peterson, K., Gorecki, C., Steadman, E., Harju, J., 2017. Advancing CO_2 enhanced oil recovery and storage in unconventional oil play-experimental studies on Bakken shales. Appl. Energy 208, 171–183.

Jossi, J.A., Stiel, L.I., Thodos, G., 1962. The viscosity of pure substances in the dense gaseous and liquid phases. AICHE J. 8 (1), 59–63.

Ko, L., Loucks, R.G., Ruppel, S.C., Zhang, T., Peng, S., 2017. Origin and characterization of Eagle Ford pore networks in the South Texas Upper Cretaceous Shelf. AAPG Bull. 101 (3), 387–418.

Lohrenz, J., Bray, B.G., Clark, C.R., 1964. Calculating viscosities of reservoir fluids from their compositions. J. Pet. Technol. 16 (10), 1171–1176.

Nojabaei, B., Johns, R.T., Chu, L., 2013. Effect of capillary pressure on phase behavior in tight rocks and shales. SPE Reserv. Eval. Eng. 16 (3), 281–289.

Nojabaei, B., Siripatrachai, N., Johns, R.T., Ertekin, T., 2014. Effect of saturation dependent capillary pressure on production in tight rocks and shales: a compositionally-extended black oil formulation. Paper SPE 171028, SPE Eastern Regional Meeting, Charleston, West Virginia.

Pang, J., Zuo, J.Y., Zhang, D., Du, L., 2012. Impact of porous media on saturation pressures of gas and oil in tight reservoirs. SPE Canadian Unconventional Resources Conference, Calgary, Canada. Paper SPE 161143.

Peng, D.Y., Robinson, D.B., 1976. A new two-constant equation of state. Ind. Eng. Chem. Fundam. 15, 59–64.

Qi, Z., Liang, B., Deng, R., Du, Z., Wang, S., Zhao, W., 2007. Phase behavior study in the deep gas-condensate reservoir with low permeability. Paper SPE 107315, SPE Europec/EAGE Annual Conference and Exhibition, London, United Kingdom.

Rachford, H.H., Rice, J.D., 1952. Procedure for use of electronic digital computers in calculating flash vaporization hydrocarbon equilibrium. J. Pet. Technol. 4 (10), 19–20.

Reamer, H.H., Sage, B.H., 1963. Phase equilibria in hydrocarbon systems. Volumetric and phase behavior of the n-Decane-CO_2 system. J. Chem. Eng. Data 8 (4), 508–513.

Reid, R.C., Prausnitz, J.M., Poling, B.E., 1987. The Properties of Gases and Liquids. McGraw Hill, New York.

Rezaveisi, M., Sepehrnoori, K., Pope, G.A., 2015. Compositional simulation including effect of capillary pressure on phase behavior. Paper SPE 175135, SPE Annual Technical Conference and Exhibition, Houston, Texas.

Shapiro, A.A., Stenby, E.H., 2001. Thermodynamics of the multicomponent vapor-liquid equilibrium under capillary pressure difference. Fluid Phase Equilib. 178 (1), 17–32.

Sigmund, P.M., Dranchuk, P.M., Morrow, N.R., 1973. Retrograde condensation in porous media. SPE J. 13 (2), 93–104.

Stiel, L.I., Thodos, G., 1961. The viscosity of nonpolar gases at normal pressures. AICHE J. 7, 611–615.

Tarek, A., 2007. Equations of State and PVT Analysis. Gulf Publishing Company, Texas.

Wang, L., Parsa, E., Gao, Y., Ok, J.T., Neeves, K., Yin, X., Ozkan, E., 2014. Experimental study and modeling of the effect of nanoconfinement on hydrocarbon phase behavior in unconventional reservoirs. Paper SPE 169581, SPE Western North American and Rocky Mountain Joint Meeting, Denver, Colorado.

Yu, W., Lashgari, H.R., Wu, K., Sepehrnoori, K., 2015. CO_2 injection for enhanced oil recovery in Bakken tight oil reservoirs. Fuel 159, 354–363.

Yu, W., Zhang, Y., Varavei, A., Sepehrnoori, K., Zhang, T., Wu, K., Miao, J., 2018. Compositional simulation of CO_2 huff-n-puff in Eagle Ford tight oil reservoirs with CO_2 molecular diffusion, nanopore confinement and complex natural fractures. Paper SPE 190325, SPE Improved Oil Recovery Conference, Tulsa, Oklahoma.

Zarragoicoechea, G.J., Kuz, V.A., 2004. Critical shift of confined fluid in a nanopore. Fluid Phase Equilib. 220 (1), 7–9.

Zhang, Y., Lashgari, H.R., Di, Y., Sepehrnoori, K., 2016. Capillary pressure effect on hydrocarbon phase behavior in unconventional reservoirs. Paper SPE 180235, SPE Low Perm Symposium, Denver, Colorado.

Zhang, T., Sun, X., Milliken, K., Ruppel, S.C., Enriquez, D., 2017a. Empirical relationship between gas composition and thermal maturity in Eagle Ford shale, South Texas. AAPG Bull. 101 (8), 1277–1307.

Zhang, Y., Yu, W., Sepehrnoori, K., Di, Y., 2017b. A comprehensive numerical model for simulating fluid transport in nanopores. Sci. Rep. 7, 40507.

Zhang, Y., Yu, W., Di, Y., Sepehrnoori, K., 2017c. Investigation of nanopore confinement on fluid flow in tight reservoirs. J. Pet. Sci. Eng. 150, 265–271.

Index

Note: Page numbers followed by *f* indicate figures, and *t* indicate tables.

E

F

G

N

T

U

V

W

Y